Physics of Atomic Nuclei, Vol. 67, No. 8, 2004, pp. 1417–1423. Translated from Yadernaya Fizika, Vol. 67, No. 8, 2004, pp. 1443–1449.

NUCLEI
Experiment

Production of Heavy Nuclei in the Interaction of ^{7}Li Ions with Copper Nuclei at an Energy of 35 MeV per Nucleon

N. A. Demekhina*, G. S. Karapetyan[1)], S. M. Lukyanov[2)], Yu. E. Penionzhkevich[2)], N. K. Skobelev[2)], and A. B. Yakushev[2)]

Yerevan Physics Institute, ul. Brat'ev Alikhanian 2, Yerevan, 375036 Armenia

Received September 1, 2003

Abstract—The absolute values of the cross sections for the production of target fragments in the interaction of copper with ^{7}Li ions at an energy of 35 MeV per nucleon were measured. The measurements were performed by recording the yields of radioactive nuclear residues with the aid of a semiconductor detector from ultrapure germanium. The charge and isobaric distributions in the mass-number range 22–69 amu were used to deduce the mass yield of reaction products and to calculate the total interaction cross section. The results are presented that were derived from a comparison with data obtained for ^{12}C + Cu reactions and with estimates based on theoretical models. © *2004 MAIK "Nauka/Interperiodica"*.

INTRODUCTION

The mechanism of nucleus–nucleus interactions is determined primarily by the energy of projectile ions. At low energies (not higher than 10 MeV per nucleon), the processes of fusion and deep-inelastic scattering are governed by the effect of the mean nuclear field [1, 2]. Nucleon–nucleon collisions, whose role becomes more important with increasing projectile energy, become a dominant mechanism at high energies (not less than 100 MeV per nucleon) [3]. In the region of intermediate energies, various mechanisms of nuclear collisions may be operative, leading to the production of nuclear systems whose nucleonic composition may be quite diverse. The majority of experimental and theoretic investigations have been devoted to the regions of low and high energies. As to the region of intermediate energies, it has received less adequate study.

The statistical model, which has been successfully employed to describe the decay of compound nuclei formed in fusion [4, 5], proves to be insufficiently accurate even at energies in excess of 10 MeV per nucleon. This circumstance motivated the development of additional theoretical concepts concerning both the first stage of the interaction process and the decay of an excited compound nucleus [6–8]. Investigation of distributions of target-fragmentation products is one of the means for exploring the dynamics of nucleus–nucleus collisions. Reactions induced by light nuclei make it possible to analyze a simpler pattern of interactions, where a target nucleus is the only source of heavy products.

The energy dependence of some features of such processes was investigated in reactions induced by ^{12}C ions in Fe, Cu, Nb, Ta, and Au nuclei at projectile-nucleus energies up to 47 MeV per nucleon [4, 9–11]. In the region of lighter projectiles, the results published to date include those that were obtained by measuring various distributions of products originating from alpha-particle interaction with ^{59}Co and ^{nat}Cu targets [12, 13]. However, available experimental information is still insufficient for systematizing data and for determining the effect of the projectile-nucleus energy and type on the reaction mechanism.

In the present article, we report on the measurements of the yields of products originating from reactions proceeding in a ^{nat}Cu target irradiated with ^{7}Li ions of energy 35 MeV per nucleon and present the results of these measurements. Also, we compare these results with data obtained previously in [9] for ^{12}C + Cu reactions and with the results of model calculations.

EXPERIMENTAL METHODS

The irradiation of the target used was performed at the U-400M cyclotron of the Joint Institute for Nuclear Research (Dubna, Russia). The yields of radioactive reaction products were measured by a

[1)]Yerevan State University, ul. A. Manukyana 1, Yerevan, 375049 Armenia.
[2)]Joint Institute for Nuclear Research, Dubna, Moscow oblast, 141980 Russia.
*e-mail: nina@lx2.yerphi.am

spectrometer on the basis of a semiconductor detector manufactured from ultrapure germanium, the resolution of the detector being 0.2% at an energy of about 1.0 MeV. The results of the measurements included the yields of radioactive products that possessed nuclear features such that they could be recorded by the induced-activity method.

The relevant gamma spectra were analyzed on the basis of spectral and nuclear properties of reaction products by using the DEIMOS code [14].

The target was made in the form of self-sustaining copper plates 20 μm thick. It was exposed to a ^{7}Li beam of intensity 30 nA (about 10^{10} nucl./s) for 30 minutes, and the spectra were measured for five months. The yields of products originating from a specific interaction channel—that is, independent cross sections (I)—were calculated by the formula

$$\sigma = \frac{S\lambda}{N_n N_p \kappa\varepsilon\eta(1-\exp(-\lambda t_1))\exp(-\lambda t_2)(1-\exp(-\lambda t_3))}, \quad (1)$$

where S is the area under the photopeak, N_p is the beam intensity (1/s), N_n is the number of target nuclei (1/cm^2), t_1 is the irradiation time, t_2 is the time of storage between the end of the irradiation and the beginning of the measurements, t_3 is the time of the measurements, λ is the decay constant, η is the relative intensity of gamma transitions, κ is the coefficient of photon absorption in the target and detector, and ε is the efficiency of the detection of photons associated with nuclear transitions. In the presence of contributions from neighboring isotopes owing to β^- or β^+ decay, the cross sections were calculated by a complicated formula that involved the probability of the formation and decay of radioactive forerunners of the measured product [15]. In the case where it was impossible to measure the yields of parent isotopes, the cross sections for the production of nuclear fragments were determined as cumulant (C) cross sections.

The results of the measurements in the form of the absolute values of the cross sections for various nuclear residues produced either independently or cumulatively are given in Table 1.

ANALYSIS OF THE RESULTS

In terms of mass features, the reaction products can be partitioned into three groups. These are residual nuclei in the region of masses above 60 amu, nuclei from the mass-number range 34–60 amu, and nuclei from the region of relatively light fragments (not heavier than 34 amu).

Similar investigations of the yields from ^{12}C + Cu reactions in the energy range 20–46 MeV per nucleon revealed [9] that the behavior of the excitation functions depends on the mass region to which reaction products belong: the cross sections for the production of nuclei whose mass numbers are close to the target-nucleus mass decrease with increasing projectile-ion energy; the yields of products belonging to the mass range 34–60 amu and appearing predominantly as evaporation residues depend on energy only slightly; and the probability of the formation of light nuclei (predominantly fragmentation products or binary-fission products) grows with increasing reaction energy.

We compared the yields in partial interaction channels for identical total energies in reactions induced by ^{7}Li and ^{12}C nuclei [9]. For products in the mass range 34–60 amu, the (C + Cu)/(Li + Cu) reaction-cross-section ratio is on average 1.18 ± 0.11 (see Fig. 1). A significant distinction between the values of the respective cross sections was observed for reaction products of mass above 60 amu. In the reactions induced by carbon nuclei, nuclei of mass in this range are produced with a higher probability at the same total reaction energy. It can be assumed that the main contribution to the yields from these reactions comes from interactions in the surface region, which involve nucleons from the overlapping regions of the projectile and target nuclei, rather than from the statistical decay of equilibrium states. Such nonequilibrium processes depend greatly on the number of collisions and the number of nucleons in the projectile nucleus [16].

CHARGE DISTRIBUTIONS

The induced-activity detection method makes it possible to determine the probabilities for the formation of elements whose nuclear features are quantities accessible to measurements. In order to obtain a complete pattern of the yields of residual nuclei, it is necessary to estimate the yields of undetectable products by using the well-known laws of charge and mass distributions. For an approximating expression, we used that which was proposed in [17] and which is given by

$$\sigma(A,Z) = \exp[\alpha_1 + \alpha_2 A + \alpha_3 A^2 + \alpha_4 A^3 \quad (2)$$

Table 1. Cross sections for the formation of products of ^{7}Li + ^{nat}Cu reactions at an energy of 35 MeV per nucleon

Element	Reaction type	σ, mb	Element	Reaction type	σ, mb
^{7}Be	I	5.54 ± 0.55	^{55}Co	C	2.20 ± 0.22
					2.99 ± 0.17*
^{22}Na	C	1.5 ± 0.16	^{56}Mn	C	3.00 ± 0.30
					4.93 ± 0.40*
^{24}Na	C	1.20 ± 0.12	^{56}Co	I	18.50 ± 1.90
		1.13 ± 0.09*			25.70 ± 1.20*
^{28}Mg	C	0.02 ± 0.01	^{56}Ni	I	0.068 ± 0.007
					0.10 ± 0.02*
^{34m}Cl	I	≤ 0.25	^{57}Co	I	51.60 ± 5.20
					89.30 ± 12.00*
^{38}S	I	≤ 0.04	^{57}Ni	I	1.60 ± 0.16
					2.28 ± 0.13*
^{38}Cl	I	≤ 0.10	$^{58(m+g)}$Co	I	77.45 ± 7.80
					116.00 ± 11.00*
^{39}Cl	C	≤ 0.16	^{59}Fe	C	2.11 ± 0.21
					2.23 ± 0.17*
^{41}Ar	C	≤ 0.20	$^{60(m+g)}$Co	I	16.20 ± 1.70
					22.80 ± 1.80*
^{42}K	I	0.70 ± 0.09	^{60}Cu	C	3.60 ± 0.43
		0.69 ± 0.12*			21.00 ± 3.90*
^{43}K	C	0.17 ± 0.02	^{61}Co	C	4.56 ± 0.63
		0.16 ± 0.02*			
^{43}Sc	C	1.20 ± 0.12	^{61}Cu	C	18.20 ± 2.00
					74.60 ± 3.10*
^{44}Ar	I	≤ 0.05	^{62}Zn	C	3.00 ± 0.30
					12.40 ± 0.60*
^{44}K	C	≤ 0.15	^{63}Zn	C	8.00 ± 0.88
					74.30 ± 9.20*
^{44g}Sc	I	0.60 ± 0.06	^{64}Cu	I	32.00 ± 3.52
		0.79 ± 0.10*			
^{44m}Sc	I	1.60 ± 0.17	^{65}Ni	I	≤ 0.03
		1.99 ± 0.14*			
^{45}K	C	0.03 ± 0.003	^{65}Zn	I	21.55 ± 2.20
					97.20 ± 10.00*
$^{46(m+g)}$Sc	I	2.83 ± 0.30	^{65}Ga	C	0.50 ± 0.05
		2.67 ± 0.18*			
^{47}Ca	C	0.03 ± 0.003	^{66}Ni	I	2.00 ± 0.20
^{47}Sc	I	1.15 ± 0.12	^{66}Cu		≤ 1.70
		0.79 ± 0.10*			
^{48}Sc	I	0.26 ± 0.03	^{66}Ga	I	1.47 ± 0.15
		0.17 ± 0.02*			26.20 ± 0.90*
^{48}V	I	6.32 ± 0.70	^{66}Ge	C	≤ 0.40
		6.12 ± 0.35*			
^{48}Cr	I	0.10 ± 0.01	^{67}Cu	C	0.25 ± 0.03
		0.11 ± 0.01*			
^{49}Cr	C	0.60 ± 0.06	^{67}Ga	I	1.91 ± 0.20
		1.83 ± 1.35*			20.00 ± 1.00*
^{51}Cr	C	28.00 ± 2.80	^{67}Ge	C	0.40 ± 0.05
		27.7 ± 2.80*			
^{52g}Mn	C	11.33 ± 1.20	^{68}Ga	I	≤ 0.60
		15.70 ± 0.60*			
^{52m}Mn	I	1.40 ± 0.15	^{68}Ge	C	≤ 1.30
		2.00 ± 0.13*			
^{52}Fe	I	0.08 ± 0.01	^{69m}Zn	I	0.02 ± 0.003
		0.08 ± 0.01*			
^{54}Mn	I	44.20 ± 4.42	^{69}Ge	C	0.13 ± 0.02
		48.20 ± 4.60*			

* Data from [6].

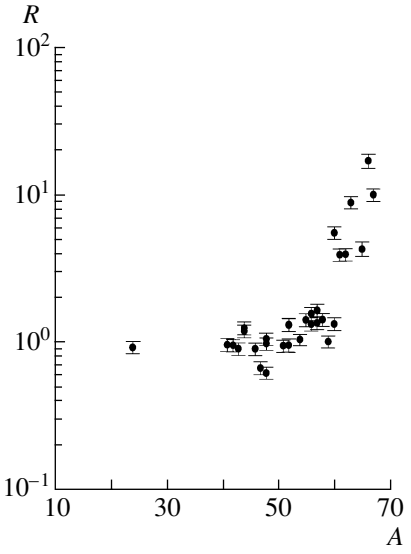

Fig. 1. Ratio (R) of the cross section for the formation of products of $^{12}C + {}^{nat}Cu$ (20.5 MeV per nucleon [9]) and $^{7}Li + {}^{nat}Cu$ (35 MeV per nucleon) reactions.

$$+ (\alpha_5 + \alpha_6 A + \alpha_7 A^2)|Z_p - Z|^{\alpha_8}],$$

where

$$Z_p = \alpha_9 A + a_{10} A^2. \qquad (3)$$

The first four free parameters (α_1–α_4) determine the shape of the mass distribution of reaction yields. The parameters α_5–α_7 are used to calculate the width of the isobaric distribution. The parameter α_8 characterizes the shape of the isobaric distribution at a given mass number, $\alpha_8 = 2$ corresponding to a Gaussian distribution. Formula (3) makes it possible to calculate the most probable charge (Z_p) in the isobaric distribution.

For a first approximation, the reaction yields calculated by formula (1) (independent yields) were used in fitting. After that, cumulative cross sections were corrected with allowance for computed data on the yields of parent isotopes, and the results obtained in this way were employed at the next stage of fitting. The procedure adopted here for calculating the parameters of the approximating function was implemented in a few steps; the resulting parameter values are given in Table 2. For the mass numbers of 48 and 56 amu, the charge distributions of reaction products are given in Fig. 2. The positions of the maxima in these distributions and their FWHM values proved to be close to their counterparts obtained for $^{12}C + Cu$ reactions at the same total energy [9]. Thus, the character of the charge distribution of products originating from the decay of an excited nucleus is obviously controlled by the nuclear properties of residual nuclei and is weakly dependent on the projectile type.

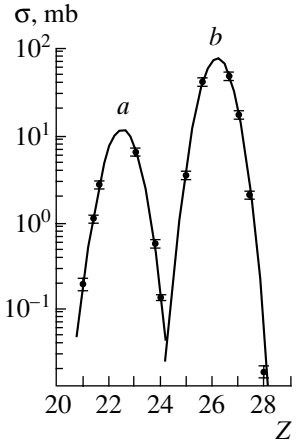

Fig. 2. Charge distributions of reaction products: (*a*) $46 \le A \le 49$, $Z_p = 22.42 \pm 0.05$, and FWHM $= 1.18 \pm 0.12$ and (*b*) $54 \le A \le 57$, $Z_p = 26.15 \pm 0.04$, and FWHM $= 1.12 \pm 0.11$. The points represent our present experimental data, while the curves correspond to the calculations by formula (3).

An analysis of the N/Z distributions of residual nuclei revealed that heavy nuclear residues are produced with a higher probability in the neutron-deficit region adjacent to the nuclear-stability valley.

MASS DISTRIBUTION

For the picture of the mass distribution of residual nuclei to be complete, the experimental data obtained in the present investigation must be supplemented by taking into account a significant contribution of stable isotopes and nuclei that are formed in the reaction being considered, but which cannot be detected by means of the activation method. The probabilities of the formation of such products are usually estimated by employing the well-known Gaussian form to approximate the charge distributions of nuclei. The cross sections for the formation of missing reaction products were determined here with the aid of expressions (2) and (3), which were proposed in [17]. The parameters appearing in these expressions (see Table 2) were determined from a fit to experimental data (on the basis of the χ^2 criterion). From Fig. 2, it can be seen that, for the measured yields of nuclear residues, these calculations lead to quite a reliable picture of the charge distribution ($\chi^2 \sim 0.6$). The mass distribution calculated by formula (2) is displayed in Figs. 3 and 4, the fraction of the measured cross sections for the formation of reaction products in the total isobaric yield being about 60% there.

Figure 3 shows that the proposed form of the approximating function [see Eq. (2)] describes satisfactorily the experimental data in the mass-number range 30–60 amu. The agreement is poorer both for

the yields of products in the immediate vicinity of the target nucleus and for the yields of light nuclei. The point at which the curve representing the mass distribution reaches a maximum corresponds to a mean mass-number value of $\bar{A} = 58.65 \pm 4.1$ amu, the width of the curve being $\Delta A = 5.35 \pm 0.64$ amu. For $^{12}C + Cu$ reactions at the same total energy of ^{12}C ions (20.5 MeV per nucleon), the values presented in [9] for the the analogous parameters of the mass distribution of reaction products are $\bar{A} =$ 59.3 amu and $\Delta A = 4.7 \pm 0.7$ amu.

A descending character of the mass curve in the range 58–38 amu is described by an exponential function. The energy dependence of the slope parameter of the mass curve for reactions initiated in copper by various projectiles was investigated in [18, 19]. The universal curve obtained there was considered as a confirmation of the conjecture that the deexcitation mechanism is determined by the energy transfer, featuring no dependence on the projectile sort. The slope parameter of the mass yield in the present experiment, $(0.31 \pm 0.02)\,A^{-1}$, is consistent with that which was obtained in [9] at the same total energy in $^{12}C + Cu$ reactions, $(0.32 \pm 0.08)\,A^{-1}$. This agreement confirms the assumption that, in determining the mechanism of residual-nucleus formation in the mass range being considered, the total reaction energy plays a dominant role.

The result obtained for the total cross section of ^{7}Li interaction with Cu by integrating the mass distribution (see Fig. 3) is 1.9 ± 0.28 b. The total cross section calculated on the basis of the optical model is 1.8 b. The use of a parametrization that takes into account effects of nucleon–nucleon interaction leads to a value of 2 b [6]. By and large, these estimates agree with our present data within the errors of the measurements.

The ratio of the total cross sections for the interaction of ^{12}C and ^{7}Li nuclei with copper is 1.12 ± 0.17. Since this value is consistent, within the accuracy to which it was determined, with the ratio of the partial cross sections, it can be assumed that the factorization condition in the form $\sigma_i = \sigma_{tot}\Gamma_i$ holds with allowance for the projectile-sort independence of the partial decay-channel width (Γ_i).

DISCUSSION OF THE RESULTS

The model of a compound nucleus formed in the complete-fusion process is usually used to describe the interaction of heavy ions with nuclei at low energies (less than 10 MeV per nucleon). An increase in the probability of incomplete fusion with increasing projectile energy leads to the formation of a set of excited nuclear systems corresponding to the attachment of various products of projectile decay to the target nucleus. In a number of studies, an incomplete fusion was taken into account by presetting initial reaction states, which are intermediate nuclear states characterized by a specific nucleonic composition and a specific value of the excitation energy [17]. In other models, the overlap region of interacting nuclei is introduced and is taken to be dependent on the impact parameter and, accordingly, on the angular-momentum transfer [20, 21]. In order to calculate the production of final reaction products in the evaporation process, use is usually made of the statistical-decay model, which describes the sequential emission of nucleons and light nuclei from excited nuclei [22]. A preequilibrium reaction stage is additionally introduced in some models [1, 8, 17].

Figure 4 shows the results of the calculations performed on the basis of the evaporation model under

Table 2. Fitted values of the parameters in expressions (2) and (3)

Parameter	Value
α_1	19.00 ± 0.19
α_2	-1.90 ± 0.02
α_3	$(5.24 \pm 0.05) \times 10^{-2}$
α_4	$-(4.16 \pm 0.80) \times 10^{-4}$
α_5	$-(4.56 \pm 1.10) \times 10^{-3}$
α_6	$-(8.10 \pm 0.14) \times 10^{-2}$
α_7	$(7.59 \pm 0.23) \times 10^{-4}$
α_8	2.00 ± 0.02
α_9	0.48 ± 0.0
α_{10}	$-(2.15 \pm 0.03) \times 10^{-4}$

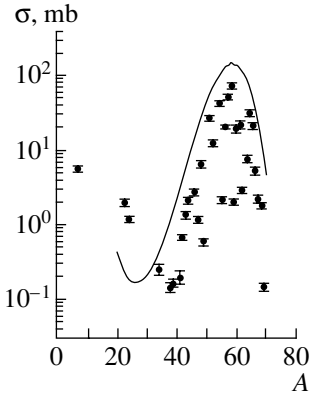

Fig. 3. Mass distribution of products originating from the disintegration of ^{nat}Cu: (points) experimental data obtained in the present study and (curve) mass yield calculated by formula (2).

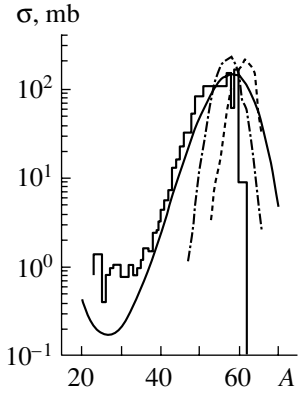

Fig. 4. Results obtained by calculating the mass distributions of products originating from ^{nat}Cu disintegration: (histogram) results of the calculation performed in [9] on the basis of the model proposed in [23]; (dashed curve) approximation of experimental data by formula (2); and (dashed and dash-dotted curves) results of the calculations on the basis of the evaporation model [17] for ^{4}He+^{nat}Cu and ^{6}Li+^{nat}Cu reactions, respectively.

the assumption of complete fusion (Li + Cu) or under the assumption of a transfer of part of the nucleons with an energy of 35 MeV per nucleon (for example, He + Cu) with allowance for a preequilibrium reaction stage [8, 17]. As can be seen from the displayed results of the calculations, the distribution of evaporation products is concentrated in the narrow mass range 45–65 amu and is in poor quantitative agreement with the experimental data.

Thus, the assumption that residual nuclei are produced via the evaporation process does not lead to a satisfactory pattern of the mass distribution.

In analyzing mass distributions of nuclear-reaction products, some authors [9–11] relied on a modified version of the statistical binary model of hot-nucleus decay [23]. Within this model approach, the transfer of a specific number of nucleons from the projectile to the target nucleus is calculated by introducing a set of impact parameters [21] or by invoking the fireball model [24]. The deexcitation of a compound nucleus is considered as a fast statistical-binary-decay process that leads, in the final state, to various configurations of charged fragments and light evaporated particles [23], various decay modes (evaporation, fission, multifragmentation, etc.) being taken into account in the calculations. The ultimate set of interaction products is determined by the sum of distributions associated with each intermediate compound nucleus. In simulating the decay process, Charity *et al.* [25] used the GEMINI Monte Carlo code. The results computed in this way for the mass distributions of products originating from ^{12}C + Cu reactions in the energy range 20–46 MeV per nucleon were presented in [9]. Considering that the features of the charge and mass distributions of residual nuclei produced in reactions initiated in copper by ^{12}C and ^{7}Li ions are similar, we employed the calculated data from [9], which were preliminarily normalized to the total cross section for interaction in Li + Cu reactions (see Fig. 4). The formation of a compound nucleus at the first reaction stage was considered within the fireball model. As can be seen, the region covering disintegration products is described satisfactorily, this being so for the position of the maximum of the mass-distribution curve, its width, and the slope parameter inclusive. Disagreement with computed data for products in the immediate vicinity of the target-nucleus mass may be due to the contribution of nonstatistical processes. The additional investigations in [9, 17] that were performed to explore the features of recoil nuclei having masses close to that of the target nucleus gave sufficient grounds to assume that these products originate from peripheral interactions.

CONCLUSION

The measurements reported in this article have furnished new data on the cross sections for the production of nuclear residues in a ^{nat}Cu target irradiated with ^{7}Li ions of energy 35 MeV per nucleon. On the basis of well-known assumptions on the isobaric and charge distributions of nuclear fragments, we have calculated the mass yields of reaction products and the total interaction cross section. A comparison of these experimental data with theoretical estimates of the total interaction cross section has revealed satisfactory agreement of these results.

The use of a standard code for computing the mass yield on the basis of the evaporation model has failed to provide a satisfactory pattern of the mass distribution. The experimental data in the region of medium-mass and light reaction products are better described within a model that assumes the fireball character of the production of the initial excited nucleus and the statistical mechanism of binary decay in the process of deexcitation. Attempts at describing, within the model concepts considered above, the production of residual nuclei in the immediate vicinity of the target-nucleus mass have proven to be inadequate, which suggests the presence of nonstatistical processes.

REFERENCES

1. Sunita Gupta, B. P. Singh, M. M. Musthafa, *et al.*, Phys. Rev. C **61**, 064613 (2000).
2. A. Navin, A. Chatterjee, S. Kailas, *et al.*, Phys. Rev. C **54**, 767 (1996).
3. T. Lund, D. Molzahn, R. Brandt, *et al.*, Phys. Lett. B **102B**, 239 (1981).

4. P. Vargani, E. Gadioli, E. Vaciago, *et al.*, Phys. Rev. C **48**, 1815 (1993).
5. A. Gavron, Phys. Rev. C **21**, 230 (1980).
6. S. Kox *et al.*, Phys. Rev. C **35**, 1678 (1987).
7. Bernard G. Harvey, Nucl. Phys. A **444**, 498 (1985).
8. M. Blann, Nucl. Phys. A **235**, 211 (1974); **213**, 570 (1973).
9. Li Wenxin, Sun Tongyu, We Dingqing, *et al.*, Radiochim. Acta **72**, 109 (1996).
10. Li Wenxin, Qin Zhi, Zhao Lili, *et al.*, Eur. Phys. J. A **7**, 397 (2000).
11. Li Wenxin, Sun Tongyu, Chin Tahai, *et al.*, Phys. Rev. C **48**, 628 (1993).
12. J. Jastrzebski, P. P. Singh, T. Mróz, *et al.*, Phys. Rev. C **34**, 60 (1986).
13. P. J. Karol, Phys. Rev. C **10**, 150 (1974).
14. J. Frana, Acta Politech. **38**, 127 (1998).
15. I. Adam, V. S. Pronskikh, A. R. Balabekyan, *et al.*, Preprint No. 10-2000-28, OIYaI (Joint Inst. Nucl. Res., Dubna, 2000).
16. C. R. Morton, A. C. Berriman, M. Dasgupta, *et al.*, Phys. Rev. C **60**, 044608 (1999).
17. S. Y. Cho, Y. H. Chung, N. T. Porile, and D. J. Morrissey, Phys. Rev. C **36**, 2349 (1987).
18. S. Y. Cho, N. T. Porile, and D. J. Morrissey, Phys. Rev. C **39**, 227 (1989).
19. J. B. Cumming, P. E. Haustein, T. J. Ruth, *et al.*, Phys. Rev. C **17**, 1632 (1978).
20. K. Siwek-Wilczynska, E. H. du Marchine van Voorthuysen, J. van Popta, *et al.*, Phys. Rev. Lett. **42**, 1599 (1979).
21. J. Wilczynski, K. Siwek-Wilczynska, J. van Driel, *et al.*, Phys. Rev. Lett. **45**, 606 (1980).
22. I. Dostrovsky, Z. Fraenkel, and G. Friedlander, Phys. Rev. C **34**, 2165 (1986).
23. Ben-Hao Sa, Yu-Ming Zhang, and Xioa-Za Zhang, Phys. Rev. C **40**, 2680 (1989).
24. J. Gosset, H. H. Gutbrod, W. G. Poskanzer, *et al.*, Phys. Rev. C **16**, 629 (1977).
25. R. J. Charity, M. A. Mcmahan, G. J. Wozniak, *et al.*, Nucl. Phys. A **483**, 371 (1988).

Translated by A. Isaakyan

Physics of Atomic Nuclei, Vol. 67, No. 8, 2004, pp. 1424–1428. Translated from Yadernaya Fizika, Vol. 67, No. 8, 2004, pp. 1450–1454.

NUCLEI
Experiment

Photofission of Actinide Nuclei in the Nucleon-Resonance Region: First Photonuclear Experiment at the Siberia-2 Storage Ring

A. D. Belyaev[1], N. V. Rudnev[2], V. G. Nedorezov[2], and A. A. Turinge[1]*

Received July 10, 2003; in final form, December 17, 2003

Abstract—Results of an experiment performed to study ^{238}U photofission with the aid of the initial section of the GAMMA channel of the Siberia-2 storage ring at the Kurchatov Institute are presented. These results are predominantly of a methodological value, because a photonuclear experiment was conducted for the first time in this channel. However, the data obtained in this way allowed us to evaluate an upper limit on the probability of the fast fission (fragmentation) of ^{238}U nuclei that was induced by photons of energy up to 2.5 GeV. This is pertinent to the problem of the deviations of the total photoabsorption cross sections for actinide nuclei from a "universal curve." © *2004 MAIK "Nauka/Interperiodica".*

INTRODUCTION

It has been established by now that a "universal behavior" is inherent in the total photoabsorption cross sections for nuclei between lithium and lead in the region of nucleon resonances [1]. This means that the photoabsorption cross section normalized to the number of intranuclear nucleons does not depend on the atomic number of the target nucleus (A). However, the total photoabsorption cross sections for the heaviest actinide nuclei appeared to be 20% above the "universal curve." The first results in this field were obtained for ^{241}Am and ^{243}Am nuclei by using a bremsstrahlung beam in Kharkov [2]; later on, they were corroborated for ^{238}U and ^{237}Np nuclei exposed to a beam of inverse Compton photons in Novosibirsk [3]. Recently, relevant results for ^{232}Th, ^{235}U, ^{238}U, and ^{237}Np were obtained in a beam of tagged bremsstrahlung photons [4, 5]. All of these results are consistent.

Total cross sections were estimated as the ratios of measured photoabsorption cross sections to corresponding fissilities, which were calculated within the cascade–evaporation model [6]. In this case, the total photoabsorption cross sections for all actinide nuclei agree within the experimental uncertainties, which do not exceed 3% in [4, 5] and are about 5% in [3]. Thus, the observed deviation of 20% is far beyond the experimental uncertainties.

Various models have been proposed in order to explain this distinction between the photoabsorption cross sections for actinide and other nuclei. The probability of the inelastic production of e^+e^- pairs on heavy nuclei was estimated in [7] by analogy with the Coulomb dissociation of relativistic ions, in which case the interaction is long-range, so that collective nuclear excitations causing fission arise at low energy and momentum transfers without meson production. According to the theoretical estimates presented in [7], the probability of these photonuclear processes proved to be at least two orders of magnitude less than that which was observed experimentally in [2–5]. Moreover, it should be noted that the pair-production cross section increases monotonically with increasing photon energy, while the excess of the total cross sections in the region of nucleon resonances is about 20% over the entire photon energy range studied in [2–5].

Another explanation of the observed effect can be based on the assumption of fast (prompt) nuclear photofission, in which case the entire energy of the incident photon is transferred to fission fragments (without meson production as well), whereby the total photoabsorption cross section may be enhanced. Such a fast process is usually referred to as fragmentation in order to distinguish it from slow nuclear fission into two fragments. It was shown that, at photon energies below the meson production threshold, the probability of such processes is less than 10^{-5} of the probability of ordinary binary fission [8]. However, there are no such data for photon energies in the region of nucleon resonances. One of the objectives of this study was to fill this gap.

In connection with the problem being discussed, it would also be reasonable to recall that, in contrast

[1]Russian Research Centre Kurchatov Institute, pl. Kurchatova 1, Moscow, 123182 Russia.
[2]Institute for Nuclear Research, Russian Academy of Sciences, pr. Shestidesyatiletiya Oktyabrya 7a, Moscow, 117312 Russia.
*e-mail: andrey@cpc.inr.ac.ru

to what occurs in photon interaction with free nucleons, pion photoproduction is possible on meson-exchange currents [9]. If the probability of such a process is proportional to the number of nucleon pairs in a nucleus—it is equal to $A(A-1)/2$—the effect must be the most pronounced in the heaviest nuclei, about 20% in actinide nuclei; in lighter nuclei, the magnitude of the effect can be commensurate with the experimental uncertainties. If the probability is proportional to A, as follows indirectly from a weak dependence of the nucleon binding energy on the atomic number, the assumption that data on the total photoabsorption cross section suggest the existence of mesons in nuclei becomes less justified. In this connection, we note that no direct indication of the existence of mesons in nuclei has so far been obtained experimentally.

EXPERIMENTAL PROCEDURE

Figure 1 shows the layout of the GAMMA channel, which is under construction in the Siberia-2 electron storage ring at the Russian Research Centre Kurchatov Institute. Our experiment was performed in the initial section of this channel, which permitted extracting a bremsstrahlung beam of endpoint energy 2.5 GeV from the straight section of the storage ring, the beam intensity being 10^5/s (radiation from the residual gas). The exit flange used to let out hard γ radiation was manufactured from stainless steel 1.0 mm thick.

The results of the simulation in [10] show that, if use is made of lasers, two versions of photon-beam formation are in sight, these two differing in the beam-energy range and beam intensity. An argon laser would make it possible to have a beam of energy between 100 and 500 MeV and intensity up to 10^7/s; the energy resolution would be about 10 MeV if a tagging system is used. A limitation on the intensity is due to a decrease in the beam lifetime because of the removal of electrons from the storage-ring orbit by the laser beam. Long-wavelength lasers of CO_2 type could provide a beam of energy between 1 and 20 MeV and intensity up to 10^9/s. There are prospects for obtaining, in the future, a beam of higher intensity (up to 10^{12}/s) in the same energy range with the aid of a free-electron laser.

At the first stage of the experiment, the beam parameters were measured with ^{238}U targets and solid-state tracking fission-fragment detectors, for which we took polycarbonate films of the Macrofol-KG type. These detectors record heavy charged particles having masses above 16 amu and specific ionization energy losses above 4 MeV/(mg cm^2) [11].

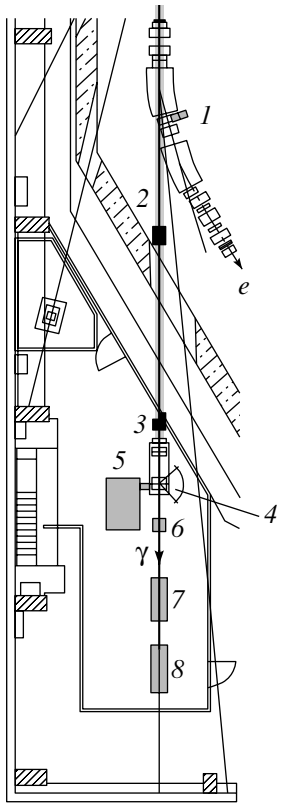

Fig. 1. Layout of the GAMMA photonuclear channel: (*1*) system of photon-energy tagging in energy, (*2*) radiation plug, (*3*) vacuum post, (*4*) mirror used to inject laser radiation into the storage ring, (*5*) laser, (*6*) beam monitor, (*7*) collimator involving a cleaning magnet, and (*8*) photonuclear detector. [At present, the initial section of the channel and some elements (*3*–*8*) have been mounted in the storage-ring hall].

Films of cross-sectional area 100 × 100 mm and thickness 10 μm were assembled into a sandwich together with uranium layers 1 mg/cm^2 thick and 100 mm in diameter and a lead radiator 1 mm thick. The resulting assemblies were placed on the beam axis (its coordinates were determined by means of geodetic measurements) in the storage-ring hall near the radiation-shield wall (Fig. 1). Bremsstrahlung having an endpoint energy of 2.5 GeV and coming from the straight section of the accelerator successively traversed the radiator, the uranium layers, and the films.

Photofission fragments produced within the uranium layers generated tracks in the films; the coordinate distribution of these tracks corresponded to the γ-beam profile. After the exposure, the films were etched for 80 min in a KOH solution at 60°C, which was maintained by a thermostat to a precision of 0.1°C. The tracks were counted and visualized automatically by the electric-spark method described in [12].

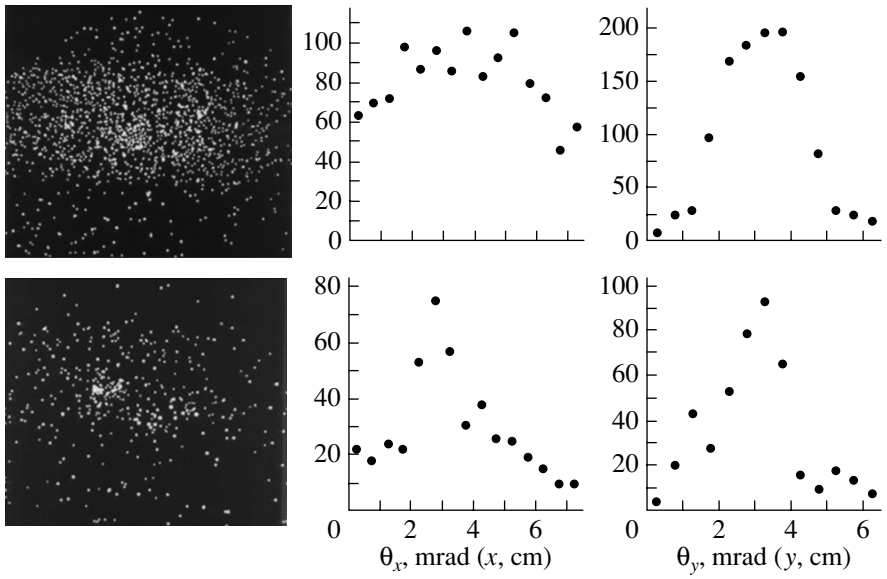

Fig. 2. Photographs of tracking detectors from one of the irradiation runs for exposures characterized by doses of (top left) 135 and (bottom left) 54 mA/h and profiles of the bremsstrahlung-photon beam (on the right) corresponding to the photographs on the left. The profiles were obtained at a distance of 6 m from the straight section of the storage ring (the distance from the straight-section center to the detector was 10 m; therefore, 1 mrad corresponded to 1 cm).

A Dacron film covered with a thin aluminum layer was used as one of the electrodes to obtain an electric-spark breakdown. This made it possible to magnify the image of the tracks and to match thereby the coinciding tracks in the neighboring films in searches for long-range fission fragments. The coinciding tracks were monitored by means of scanner- and computer-aided digital processing of the track images.

RESULTS AND DISCUSSION

By way of example, the photographs of the films located in direct contact with the uranium layers (films no. 1) are shown in Fig. 2. The track-coordinate distributions along the horizontal and vertical axes were calculated on the basis of these data and are also given in Fig. 2. These two films differed in their exposure time (4.5 and 1 h). These displayed distributions illustrate the distinction between a short and a long exposure. The mean current of the storage ring was 30 mA. Figure 2 shows that, in the case of the short exposure, the beam is about 1 cm in height and about 4 cm in diameter, which corresponds to an angular divergence of 1 to 2 mrad. In the case of the long exposure, the beam profile is larger in size, about 3 cm in height and about 12 cm in diameter (FWHM). This means that the position of the beam is not quite stable in the long exposure, and that is why we used 10-cm films. Nevertheless, our result confirms the correctness of channel alignment and permits performing the final stage of beam extraction through the radiation-shield wall. Here, additional precautions are necessary for ensuring the stability of the beam position in the orbit.

Among the advantages of the method used, we can indicate a high photon-beam-energy threshold (the fission threshold is 6 MeV) separating bremsstrahlung from synchrotron radiation, a low level of the background, and a rather high efficiency.

In order to test the assumption that uranium nuclei may undergo photon-induced fast fragmentation in the region of nucleon resonances, measurements of long-range fission fragments were performed with a large number of films (up to 10) in an assembly featuring uranium layers. An increase in the fragment range can be associated with an energy–momentum transfer of up to 2.5 GeV from an incident photon. In this case, the fragment mass can be relatively small if, for example, the possibility of ternary fission is taken into account. It is assumed that, in this case, the energy of an incident photon is transferred almost entirely to a fission fragment without meson production. In the case of ordinary binary fission, the range in Macrofol-KG films is 22 μm [8] at the fragment mean kinetic energy of about 100 MeV. The presumed increase in the fragment energy up to 500 MeV would lead to a longer range of up to 50 μm [13].

Since a bremsstrahlung beam has a continuous spectrum, the probability of the expected effect is averaged over a broad energy range from the fission threshold (about 6 MeV) to 2.5 GeV. The results of a simulation show that, for ^{238}U, the fraction of events

Number of uranium-fission-fragment tracks with coordinates coinciding in different films

Film number	Maximum fragment range, μm	Number of coinciding tracks
2–3	30	5
3–4	40	0
4–5	50	3
5–6	60	3
6–7	70	2
7–8	80	0
8–9	90	0
9–10	100	0
3–4–5	50*	2
3–4–5–6	60*	1

Note: Asterisks label punchthrough tracks coinciding in three or four films; the remaining tracks coincide only in two adjacent films (see main body of the text).

where the energy transfer lies in the region between the pion-production threshold (about 150 MeV) and the endpoint energy of the spectrum is about 60% with respect to the total yield of fission fragments.

The results of our measurements are summarized in the table. Only one event is observed where the tracks coincide in four films from the third film (the films are numbered from the target). The probability of this event is 10^{-4} with respect to the total yield of fission fragments. However, there are 13 events (this corresponds to the probability of their appearance at a level of 10^{-3}) where the tracks coincide in two adjacent films (see table). The observed discontinuity in the fragment range can be associated with an insufficiently high density of ionization energy losses for a high-energy fragment (above 10 MeV per nucleon), with the result that no spark breakdown necessary for track visualization occurs after etching. In any case, the probability of the appearance of long-range fission fragments does not exceed 10^{-3} with respect to the probability of ordinary fission. This means that the fragmentation of actinide nuclei cannot lead to a sizable increase (by 20%) in the total photoabsorption cross section. Thus, the problem of the deviation of the total cross section for photoabsorption on the actinide nuclei from the universal curve remains open.

CONCLUSION

The first photonuclear experiment has been performed at the GAMMA setup, which is under construction at the Kurchatov Center of Synchrotron Radiation. In this experiment, an upper limit on the probability of ^{238}U fragmentation was determined to be 10^{-3} with respect to the probability of ordinary binary fission, this value being averaged over the energy range between the fission threshold and 2.5 GeV. Thus, it has been shown that the observation in [1–5] according to which there is a 20% excess of the total cross section above the universal-curve values in the region of nucleon resonances cannot be explained by the prompt fragmentation of actinide nuclei. In order to study this effect, it is necessary to complete construction of the GAMMA setup.

Our experiment made it possible to obtain data on the angular divergence and stability of the electron beam inside the storage ring. Future measurements along this line would permit obtaining more comprehensive information about the residual-gas pressure in the straight section with allowance for the accumulation of ions in the vicinity of the orbit and would furnish other data that are important for optimizing the storage-ring operation and for increasing the beam lifetime. For this purpose, as well as for studying photonuclear reactions, it is necessary to extract the photon beam from the storage-ring hall and to finish the planned methodological work. It should be recalled that there are similar setups in all of the leading synchrotron-radiation centers worldwide—for example, ESRF (France), Spring-8 (Japan), and NSLS (USA). Construction of the first dedicated source of synchrotron radiation in Russia on the basis of the Siberia-2 electron storage ring offers favorable prospects for carrying out studies along the lines indicated above.

ACKNOWLEDGMENTS

We are grateful to our colleagues from the Russian Research Centre Kurchatov Institute and the Institute for Nuclear Research (Russian Academy of Sciences) for their interest in the problem and for stimulating discussions.

This work was supported by the Russian Foundation for Basic Research (project no. 01-02-17235).

REFERENCES

1. J. Ahrens, Nucl. Phys. A **446**, 229 (1985).
2. Yu. A. Vinogradov, V. I. Kasilov, L. E. Lazareva, *et al.,* Yad. Fiz. **24**, 686 (1976) [Sov. J. Nucl. Phys. **24**, 357 (1976)].
3. A. S. Iljinov, D. I. Ivanov, M. V. Mebel, *et al.*, Nucl. Phys. A **539**, 263 (1992).
4. J. C. Sanabria, B. L. Berman, C. Cetina, *et al.*, Phys. Rev. C **61**, 034604 (2000).
5. C. Cetina, P. Heimberg, B. L. Berman, *et al.*, Phys. Rev. C **65**, 044622 (2002).

6. I. A. Pshenichnov, B. L. Berman, W. J. Briscoe, *et al.*, nucl-th/0303070.
7. D. I. Ivanov, G. Ya. Kezerashvili, A. I. L'vov, *et al.*, Yad. Fiz. **55**, 3 (1992) [Sov. J. Nucl. Phys. **55**, 1 (1992)].
8. D. I. Ivanov, V. G. Nedorezov, and A. S. Sudov, Preprint No. P-0471, IYaI Akad. Nauk SSSR (Inst. Nucl. Res., USSR Acad. Sci., Moscow, 1986).
9. A. I. Lebedev, Vopr. At. Nauki Tekh., Ser. Obshch. Yad. Fiz. **1**, 33 (1978).
10. A. D. Belyaev, V. G. Nedorezov, A. A. Turinge, *et al.,* in *Proceedings of the X Seminar on the Electromagnetic Interactions of Nuclei, Moscow, 2003*, Ed. by G. M. Gurevich (IYaI RAN, Moscow, 2003).
11. R. L. Fleischer *et al.*, Annu. Rev. Nucl. Sci. **15**, 1 (1965).
12. L. Z. Dzhilavyan, V. L. Kuznetsov, N. P. Kucher, *et al.,* Preprint No. P-1021, IYaI AN SSSR (Inst. Nucl. Res., USSR Acad. Sci., Moscow, 1989).
13. V. M. Gorbachev, Yu. S. Zamyatnin, and A. A. Lbov, *Interaction of Radiation with Heavy Nuclei and Nuclear Fission* (Atomizdat, Moscow, 1976), p. 332 [in Russian].

Translated by E. Kozlovsky

Physics of Atomic Nuclei, Vol. 67, No. 8, 2004, pp. 1429–1441. Translated from Yadernaya Fizika, Vol. 67, No. 8, 2004, pp. 1455–1467.

NUCLEI
Theory

Exact Inclusion of the Coulomb Field in the Photobeta Decay of a Nucleus and Problem of Bypassed Elements

I. V. Kopytin, K. N. Karelin*, and A. A. Nekipelov

Voronezh State University, Universitetskaya pl. 1, Voronezh, 394693 Russia

Received July 28, 2003

Abstract—The probability of the endothermic β^- decay of nuclei that is stimulated by an electromagnetic field of Planck frequency spectrum (photobeta decay) is calculated, the effect of the Coulomb field on a relativistic electron and a virtual relativistic positron being exactly taken into account in this calculation. It is shown that the inclusion of Coulomb effects is of paramount importance and that the results of the calculations may differ by an order of magnitude from those that were obtained previously in the plane-wave approximation, depending on the energy range being considered. A model for the synthesis of bypassed elements in the interior of massive stars is proposed on the basis of the mechanism of the photobeta decay of stable elements that originate from s and r processes. © *2004 MAIK "Nauka/Interperiodica".*

1. INTRODUCTION

For the first time, the photobeta decay of a nucleus was theoretically studied in [1]. This is an endothermic process where photon absorption by a beta-stable nucleus stimulates its β^- decay. It was shown in [1] that, among all possible mechanisms of nuclear photobeta decay, that which is realized through the process in which the production of an electron–positron pair by a photon is followed by positron absorption by the nucleus involved and antineutrino emission is characterized by the highest probability. Since the rate of such a process, which involves weak interaction, is rather low for this reason, the authors of [2–5] considered, as its possible realization, the astrophysical application to the problem of the synthesis of bypassed elements in the interior of massive stars (in a number of those studies, direct positron capture was examined as an alternative to photobeta decay).

This is one of the oldest problems in nuclear astrophysics. The term "bypassed nuclides" (which are also known as p-nuclei) is applied to the most proton-rich beta-stable nuclides whose charge numbers lie in the range $34 \le Z \le 80$ (in all, there are 35 of them), their abundances being two to three orders of magnitude less than those of neighboring stable elements formed in neutron-capture processes. The origin of p-nuclei is not explained by the standard theory of nucleosynthesis [6, 7]. According to this theory, medium-mass and heavy nuclei were formed in the interior of massive stars upon slow (s process) or fast (r process) neutron capture followed (or accompanied) by the β^- decay of product elements. The chain of these beta decays usually ends up in the formation of a beta-stable nucleus [we denote it by (A, Z), where A and Z are, respectively, the mass number and the charge number], so that a further transition to a bypassed stable nucleus [we denote it by $(A, Z+2)$] proves to be impossible because of the energy threshold separating the (A, Z) and $(A, Z+1)$ nuclei (see Fig. 1), which has a height of 1 to 3 MeV. This is the reason why $(A, Z+2)$ nuclei are bypassed in neutrino-capture processes.

Owing to the energy of an electromagnetic field in the substance of a star, the physical mechanism of the photobeta decay of an (A, Z) beta-stable nucleus makes it possible to overcome the aforementioned energy barrier and to implement thereby the $(A, Z) \to (A, Z+1)$ beta transition. Since $(A, Z+1)$ nuclei are usually β^--active, their natural beta decay would lead to the formation of $(A, Z+2)$ p-nuclei. Thus, the inclusion of photobeta decay in the chain of natural beta decays at the stage of the synthesis of (A, Z) stable nuclides would permit completing this chain with an $(A, Z+2)$ bypassed nuclide, whereby it would be possible to solve this problem in principle. However, the ultimate yield of p-nuclei would of course be determined by the electromagnetic-radiation density in a medium (that is, by the temperature of stellar substance) and by the duration of that stage of the evolution of a star which makes it possible to reach the required temperatures. The analysis performed in [2–5] revealed that the required temperatures must lie in the range between 2×10^9 and 3×10^9 K and that they can indeed take such values in the zone of the hydrostatic combustion of oxygen in the phase

*e-mail: dayna@mail.ru

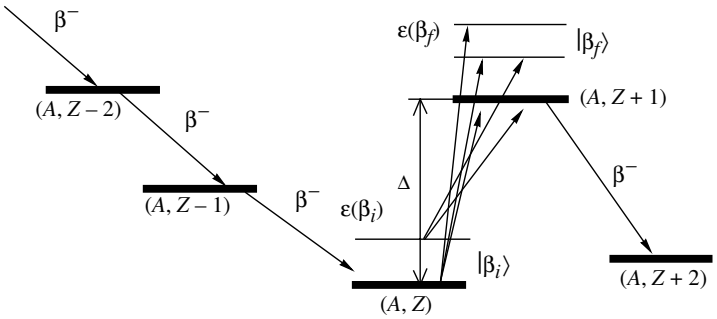

Fig. 1. Chain of beta transformations involving photobeta decay and leading to the formation of an $(A, Z+2)$ p-nucleus.

preceding the explosion of supernovae. Although no detailed calculations of the abundances of p-nuclei on the basis of the photobeta-decay phenomenon were performed in [2–5], the authors of those studies drew the conclusion that, by and large, this model is insufficiently efficient; however, they did not rule out the possibility that synthesis may proceed according to this scheme in some cases. In drawing this conclusion, those authors considered that beta-decay nuclear matrix elements fluctuate widely from one nucleus to another and that the curve of the abundances of p-nuclei is rather smooth.

In considering specific $(A, Z) \to (A, Z+1) \to (A, Z+2)$ triplets with allowance for photobeta decay and natural beta transitions, beta-decay matrix elements would indeed fluctuate widely if, at each stage, it were legitimate to examine beta transitions only between the ground states of the nuclei involved. In this case, one frequently has to deal with beta transitions forbidden to different degrees, with the result that the respective nuclear matrix elements have different orders of magnitude. As was indicated in [5], however, excited states will also be populated in a medium where the temperature is on the same order of magnitude as nuclear temperatures ($T \approx 0.1$–0.5 MeV). Therefore, one can consider, for example, photobeta decay proceeding from excited states of an (A, Z) nucleus rather than from its ground state; it is only necessary in this case to introduce corrections for the population of excited states. As to the final states of a photobeta decay transition, they may be arbitrary if the photon energy is sufficiently high, and it is necessary to perform summation over them in calculating the total transition probability. In a similar way, one can also consider the natural β^- decay of an $(A, Z+1)$ nucleus from excited states, taking into account their population. From an analysis of all beta-decay chains leading to $(A,\ Z+2)$ bypassed nuclei [that is, of $(A, Z) \to (A, Z+1) \to (A, Z+2)$ triplets], it was deduced in [5] that, at all stages of beta decay, allowed beta transitions can be found almost always. This circumstance reduces the structural fluctuations of beta-decay nuclear matrix elements significantly and removes the aforementioned objection that the model including photobeta decay is insufficiently efficient. In addition, we note that, if the effect of the nuclear Coulomb field on the electron from the dilepton pair involved had been taken into account in the formula given in [1] for the total probability of photobeta decay (this was not done), there would have arisen an additional stabilizing factor similar to the so-called integrated Fermi function f_0 (it is well known that the reduced lifetime $f_0 t$ with respect to allowed beta transitions fluctuates only slightly).

The Coulomb field of a nucleus was not taken into account either in [1], where a formula was obtained for the probability of photobeta decay in an electromagnetic field of Planck frequency spectrum, or in [5], where a model of the synthesis of p-nuclei was developed on the basis of the photobeta-decay phenomenon. In [1], the basic expression for the rate of photobeta decay was derived by using the plane-wave approximation both in describing electron and antineutrino states and in constructing the positron Green's function. It seems that the use of this formula in quantitatively calculating the abundances of bypassed nuclei may lead to significant errors.

Since the production of an electron–positron pair with the subsequent positron absorption by the nucleus involved plays a dominant role in the photobeta-decay process, as was shown in [1], it is indeed of paramount importance to take into account the Coulomb field of this nucleus. It is well known that the production of a dilepton pair by a free photon is forbidden by the kinematics of the process. But if, in calculating the basic diagram for the pair-production process, the plane-wave approximation is used at all stages (that is, all of the participant particles are in a free state), the transfer of an "extra" momentum to the nucleus in pair production may only be due to weak interaction, which is also involved in photobeta decay. In an actual situation, however, there exists, a nuclear electromagnetic field, which is much stronger

and which must obviously increase the probability of the production of an electron–positron pair by a photon, on one hand, and affect the process of virtual-positron absorption, on the other hand, to say nothing of its effect on the state of the emitted electron (for example, this effect leads to the emergence of an analog of the beta-decay Fermi function in the final expressions for the probability of the process). In view of the foregoing, the inclusion of the nuclear Coulomb field may substantially change both the probability of the photon-induced beta process (previously, it was calculated in [1] in the plane-wave approximation) and the quantitative results obtained by calculating the abundances of p-nuclei on the basis of models in which the photobeta decay of a stable nucleus is included as the main physical mechanism for overcoming the aforementioned energy threshold.

The objective of the present study is to calculate the probability of the photobeta decay of a stable nucleus within a procedure that would permit exactly taking into account the effect of its Coulomb field on all relativistic charged particles involved in the photobeta-decay process and to formulate a model that would describe the synthesis of bypassed nuclei in the interior of massive stars. It will be based on beta-decay processes stimulated by an electromagnetic field of Planck frequency spectrum in stable elements that originate from s and r processes. We do not expect that this model will prove to be universal or will make it possible to obtain the entire spectrum of the abundances of p-nuclei. Our main task here is to assess the degree to which the exact inclusion of the Coulomb field in calculating the probability of the photobeta-decay process would affect the conclusions drawn previously in [2–5] on the problem of the synthesis of bypassed elements. At the same time, the results obtained previously in [5] give every reason to hope that the proposed model would enable us to determine physical conditions that are necessary for the synthesis of at least some of the bypassed p-nuclei and to relate them to specific stages of the evolution of a massive star.

In accordance with the objective pursued here, we will not give an overview of all of the existing approaches to the problem of the synthesis of bypassed elements, referring the interested reader to the review article of Wallerstein *et al.* [7], which was devoted to advances made in nuclear astrophysics over the past 40 years since the appearance of the preceding survey of this kind [6]. We would only like to note that no comprehensive solution to this problem has been found so far, albeit some steps have been made toward it. In particular, the most spectacular success was achieved by Rayet and his coauthors, who considered the synthesis of p-nuclei in (γ, n) reactions on nuclei from s and r processes in the explosions of type-II supernovae and who reported their results in [8] (references to the preceding studies of those authors can also be found there). For almost 60% of the bypassed elements, the authors of [8] were able to obtain abundances that differ from their observed counterparts only by a factor of 2 to 3, although the choice of some parameters used there in the calculations is questionable. Nonetheless, it was indicated both in [8] and in the review article of Wallerstein *et al.* [7] that models studying the synthesis of only individual elements and trying to specify their position in the spatial and time evolution of a massive star are still of interest in the problem of bypassed nuclei.

2. PHOTOBETA-DECAY RATE

Suppose that the (A, Z) nucleus is β^--stable. This means that the energy threshold $\Delta = (M(A, Z+1) - M(A, Z) + m_e)c^2 > 0$ (see Fig. 1), where $M(A, Z)$ is the mass of the (A, Z) nucleus, m_e is the electron mass, and c is the speed of light, prevents the β^- transition $(A, Z) \xrightarrow{\beta^-} (A, Z+1)$. If an $(A,\ Z)$ nucleus absorbs a photon of energy ϵ_γ sufficient for overcoming the threshold Δ, there can occur photobeta decay—that is, the β^- transition $(A, Z) \xrightarrow{\beta,\gamma} (A, Z+1)$ initiated by photon absorption (it is assumed that relevant quantum selection rules are satisfied). Thus, the photobeta decay of an (A, Z) stable nucleus is the endothermic reaction

$$\gamma + (A, Z) \to (A, Z+1) + e^- + \bar{\nu}_e, \qquad (1)$$

which proceeds under the condition $\epsilon_\gamma > \Delta$. The Feynman diagrams corresponding to this process are displayed in Fig. 2. The diagram in Fig. 2*a* describes the process in which the production of a virtual electron–positron pair in the Coulomb field of the (A, Z) nucleus involved is followed by positron absorption and antineutrino emission, while the diagram in Fig. 2*b* represents a virtual excitation of nuclear states that is followed by their beta decay ("bypass" nuclear transitions). The analysis performed in [1] revealed that, in relation to the process in Fig. 2*a*, a bypass process is suppressed in proportion to $(m_e/m_p)^2$, where m_p is the proton mass. For this reason, we consider here only the diagram in Fig. 2*a*.

We assume that the photon state prior to the reaction and the antineutrino state after the reaction are described by plane waves characterized by momenta $\mathbf{k}$ (for the photon) and $\mathbf{q}$ (for the antineutrino) and by the respective polarization vectors $\mathbf{e}$ and $\boldsymbol{\sigma}_\nu$. After the reaction, the product electron is in a continuum state and has an energy ϵ and a polarization vector $\boldsymbol{\sigma}_e$ in the Coulomb field of an $(A, Z+1)$ nucleus. The transition amplitude corresponding to the diagram in

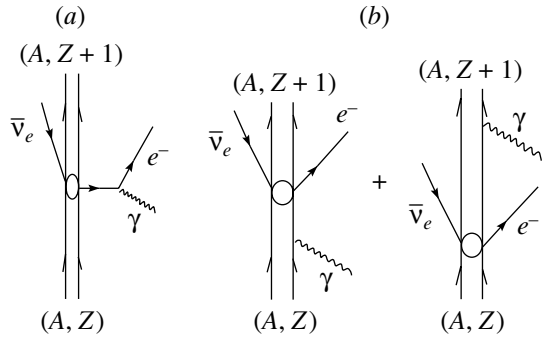

Fig. 2. Diagrams for the endothermic beta-decay process induced by electromagnetic radiation.

Fig. 2*a* can be represented in the form (hereafter, we use the system of units where $\hbar = c = m_e = 1$)

$$A = e\sum_{K\lambda\mu\zeta}(-1)^{K+\mu}\int dr_1 r_1^2\int d\mathbf{r}_2 \qquad (2)$$
$$\times\left\{\int d\Omega'\left[\psi_f^+(\mathbf{r}')T^{\mu}_{K\lambda\zeta}(\mathbf{n}')\right.\right.$$
$$\left.\left.\times(g_V - g_A\gamma_5)\tau_+\psi_i(\mathbf{r}')\right]\right\}\Bigg|_{r'=r_1}$$
$$\times\left\{\int d\Omega''\left[\varphi_e^+(\mathbf{r}_2)(\mathbf{A}(\mathbf{r}_2)\cdot\boldsymbol{\gamma})G_E(\mathbf{r}_2,\mathbf{r}'')\right.\right.$$
$$\left.\left.\times(1+\gamma_5)T^{-\mu}_{K\lambda\zeta}(\mathbf{n}'')\varphi_\nu(\mathbf{r}'')\right]\right\}\Bigg|_{r''=r_1},$$

where the tensor operator $T^{\mu}_{K\lambda\zeta}(\mathbf{n})$ has the form [9]

$$T^{\mu}_{K\lambda\zeta}(\mathbf{n}) = \sum_v i^\lambda C^{K\mu}_{\lambda\mu-v\zeta v}(\sigma_v\gamma_5)^\zeta Y_{\lambda\mu-v}(\mathbf{n}), \quad (3)$$
$$\zeta = 0, 1.$$

In expressions (2) and (3), we have used the following notation: e is the electron charge; ψ and φ are, respectively, the nuclear and lepton wave functions (the subscripts i and f label, respectively, the initial and the final state, while e and ν refer to the electron and the antineutrino); $\boldsymbol{\gamma}$ and γ_5 are the Dirac matrices in the standard representation [10]; σ_v are the cyclic components of the spin Pauli matrices ($v = -1, 0, 1$); $\tau_+ = (\tau_1 + i\tau_2)/2$ and τ_i are the isospin matrices; $C^{jm}_{j_1m_1j_2m_2}$ is a Clebsch–Gordan coefficient; $Y_{\lambda m}(\mathbf{n})$ is a spherical harmonic; $\mathbf{n} \equiv \mathbf{r}/r$; $\mathbf{A}(\mathbf{r}) = \sqrt{2\pi/k}\mathbf{e}e^{i\mathbf{k}\cdot\mathbf{r}}$ is the vector potential of the electromagnetic field; and $G_E(\mathbf{r}_1, \mathbf{r}_2)$ is the relativistic Green's function for the positron of energy $E = k - \epsilon$ in the Coulomb field of the nucleus. In our calculations, we will employ the Green's function in the form obtained in [11]. For an electron moving in the field of a nucleus with a charge Z, it can be represented in the form

$$G_E(\mathbf{r}_1, \mathbf{r}_2) = -\frac{2}{a_0\nu_g} \qquad (4)$$
$$\times\sum_{JLM}\frac{\Gamma(\lambda_g - \eta_g)}{\Gamma(2\lambda_g + 1)}\Psi^{(I)}_{JLM}(\mathbf{r}_1)\overline{\Psi^{(R)}_{JLM}}(\mathbf{r}_2), \quad r_1 > r_2,$$

where $a_0 = \alpha_e^{-1}$ is the Bohr radius; $\alpha_e = e^2$ is the fine-structure constant;

$$\nu_g = \frac{\alpha_e}{(1 - E^2)^{1/2}}, \qquad (5)$$
$$\lambda_g = ((J + 1/2)^2 - (\alpha_e Z)^2)^{1/2}, \quad \eta_g = EZ\nu_g;$$

$\Gamma(z)$ is the complete Euler gamma function;

$$\Psi^{(R)}_{JLM}(\mathbf{r}) = x^{-3/2}\begin{pmatrix} f^{(R)}_+(x)\Omega_{JLM}(\mathbf{n}) \\ if^{(R)}_-(x)\Omega_{JL'M}(\mathbf{n})\end{pmatrix}, \qquad (6)$$

$$\Psi^{(I)}_{JLM}(\mathbf{r}) = x^{-3/2}\begin{pmatrix} f^{(I)}_+(x)\Omega_{JLM}(\mathbf{n}) \\ if^{(I)}_-(x)\Omega_{JL'M}(\mathbf{n})\end{pmatrix} \qquad (7)$$

are solutions to the Dirac equation that are, respectively, regular and irregular at the origin;

$$L' = 2J - L, x = \frac{2r}{a_0\nu_g},$$

$$f^{(R)}_\pm(x) = (1 \pm E)^{1/2} \qquad (8)$$
$$\times\left[(\lambda_g - \eta_g)M_{\eta_g-\frac{1}{2},\lambda_g}(x)\right.$$
$$\left.\pm(Z\nu_g - \kappa_g)M_{\eta_g+\frac{1}{2},\lambda_g}(x)\right],$$

$$f^{(I)}_\pm(x) = (1 \pm E)^{1/2} \qquad (9)$$
$$\times\left[(Z\nu_g + \kappa_g)W_{\eta_g-\frac{1}{2},\lambda_g}(x) \pm W_{\eta_g+\frac{1}{2},\lambda_g}(x)\right];$$

$M_{\kappa,\eta}(x)$ and $W_{\kappa,\eta}(x)$ are Whittaker functions [12]; and

$$\kappa_g = (J + \frac{1}{2})(-1)^{J-1/2}.$$

The spherical spinors appearing in expressions (6) and (7) are defined in a standard way as

$$\Omega_{JLM}(\mathbf{n}) = \sum_m C^{JM}_{LM-m\frac{1}{2}m}Y_{LM-m}(\mathbf{n})\chi_m, \quad (10)$$

where χ_m is a spinor.

The required positron Green's function is obtained from the electron Green's function by making the substitution $Z \to -Z$ in Eqs. (4)–(9).

Only Gamow–Teller beta transitions are of interest for our purposes since they are the most intense. In this case, only the term featuring the coupling constant g_A and the tensor operator T_{101} can be retained in Eq. (2), this corresponding to the Gamow–Teller matrix element $g_A \int \boldsymbol{\sigma}$ in the Cartesian notation (the Fermi nuclear matrix element $g_V \int 1$ does not vanish only if very stringent selection rules hold; for this reason, we will not consider it here). We take the direction of the photon momentum $\mathbf{k}$ for the quantization axis and represent the photon, antineutrino, and electron wave functions in the form of expansions in spherical harmonics [13]. For the vector potential $\mathbf{A}(\mathbf{r})$, we have

$$\mathbf{A}(\mathbf{r}) = \sqrt{\frac{2\pi}{k}}\mathbf{e}e^{i\mathbf{k}\cdot\mathbf{r}} \tag{11}$$
$$= 2\pi s\sqrt{\frac{2}{k}}\sum_{j_\gamma l_\gamma} i^{l_\gamma}\Pi_{l_\gamma}C^{j_\gamma s}_{1sl_\gamma 0}j_{l_\gamma}(kr)\mathbf{Y}_{j_\gamma l_\gamma s}(\mathbf{n}).$$

Here and below, j and l stand for, respectively, the angular and orbital angular momenta of the particles involved; the index γ (in the following, the indices ν and e on the angular momenta as well) refer to the photon (antineutrino and electron, respectively); $\Pi_{l_\gamma} = (2l_\gamma + 1)^{1/2}$,

$$\Pi_{l_1 l_2 \ldots l_n} = \left[\prod_{k=1}^{n}(2l_k+1)\right]^{1/2};$$

s is the photon polarization ($s = \pm 1$); and $j_{l_\gamma}(x)$ is a spherical Bessel function. Vector spherical harmonics are defined in a standard way as

$$\mathbf{Y}_{jlm}(\mathbf{n}) = \sum_\mu C^{jm}_{lm-\mu 1\mu}Y_{lm-\mu}(\mathbf{n})\boldsymbol{\xi}_\mu, \tag{12}$$

where the vectors $\boldsymbol{\xi}_\mu (\mu = 0, \pm 1)$ form a three-dimensional cyclic basis.

For the antineutrino wave function, we have

$$\varphi_\nu(\mathbf{r}) = \sqrt{4\pi}\sum_{j_\nu l_\nu m_\nu}\Pi_{l_\nu}C^{j_\nu\sigma_\nu}_{l_\nu 0\frac{1}{2}\sigma_\nu}D^{j_\nu}_{m_\nu\sigma_\nu}(\mathbf{n}_\nu) \tag{13}$$
$$\times\begin{pmatrix} f_{l_\nu}(qr)\Omega_{j_\nu l_\nu m_\nu} \\ -ig_{l'_\nu}(qr)\Omega_{j_\nu l'_\nu m_\nu}\end{pmatrix},$$

where $\mathbf{n}_\nu$ is a unit vector in the direction of antineutrino emission; $D^j_{m_1 m_2}(\mathbf{n})$ is the rotation matrix; $l'_\nu = 2j_\nu - l_\nu$; and

$$f_{l_\nu}(qr) = \frac{1}{\sqrt{2}}j_{l_\nu}(qr), \quad g_{l'_\nu}(qr) = \frac{1}{\sqrt{2}}j_{l'_\nu}(qr). \tag{14}$$

The expansion of the electron wave function has the form

$$\varphi_e(\mathbf{r}) = \sqrt{4\pi}\sum_{j_e l_e m_e}\Pi_{l_e}C^{j_e\sigma_e}_{l_e 0\frac{1}{2}\sigma_e} \tag{15}$$
$$\times\exp[i\Delta(l_e, j_e)]D^{j_e}_{m_e\sigma_e}(\mathbf{n}_e)$$
$$\times\begin{pmatrix} f_{l_e}(r)\Omega_{j_e l_e m_e} \\ (-1)^{\frac{1+l_e-l'_e}{2}}g_{l_e}(r)\Omega_{j_e l'_e m_e}\end{pmatrix},$$

where $\mathbf{n}_e$ is a unit vector in the direction of electron emission; $\Delta(l_e, j_e)$ is the Coulomb phase,

$$\Delta(l_e, j_e) = \frac{1}{2}\arg\left[\frac{-\kappa_e + i\xi_e/\epsilon}{\gamma_e + i\xi_e}\right] - \arg\Gamma(\xi_e + i\gamma_e)$$
$$-\frac{1}{2}\pi(\gamma_e - |\kappa_e|) - \frac{1}{4}\pi\left(1 + \frac{\kappa_e}{|\kappa_e|}\right),$$
$$\xi_e = \frac{\alpha_e Z}{p}\epsilon, \quad p = (\epsilon^2 - 1)^{1/2}, \quad \kappa_e = \mp(j_e + 1/2)$$
$$\text{for } j_e = l_e \pm 1/2, \quad \gamma_e = (\kappa_e^2 - (\alpha_e Z)^2)^{1/2};$$

$l'_e = 2j_e - l_e$; and $f_{l_e}(r)$ and $g_{l_e}(r)$ are, respectively, the large and the small component of the radial wave function for the electron (the explicit expressions for these components are given, for example, in [10]).

Substituting expressions (4), (13) and (15) into (2) and using the ξ approximation [14], which is known to be valid to a rather high degree of precision in beta decay, we can factorize the amplitude A of the process into the nuclear and the lepton part as

$$A = 3\pi e\sum_{\substack{j_e l_e m_e \\ j_\gamma l_\gamma \mu \\ j_\nu l_\nu m_\nu \\ JLM}} i^{l_\gamma+1}(-1)^{l_\gamma+1+2J+m_e+\mu} \tag{16}$$
$$\times s\sqrt{\frac{2}{k}}\frac{\Pi_{l_\nu j_\nu l_e j_e l_\gamma J}}{\Pi_{J_f}}\exp\left(-i\Delta(l_e, j_e)\right)D^{j_e *}_{m_e\sigma_e}(\mathbf{n}_e)$$
$$\times D^{j_\nu}_{m_\nu\sigma_\nu}(\mathbf{n}_\nu)C^{j_\nu\sigma_\nu}_{l_\nu 0\frac{1}{2}\sigma_\nu}C^{j_e\sigma_e}_{l_e 0\frac{1}{2}\sigma_e}C^{j_\gamma s}_{1sl_\gamma 0}C^{j_\gamma -s}_{j_e -m_e JM}$$
$$\times C^{J_f M_f}_{J_i M_i 1\mu}C^{JM}_{j_\nu m_\nu 1-\mu}N\cdot L_e.$$

Here, J_i (J_f) is the nuclear spin in the initial (final) state; N is the nuclear part of the amplitude,

$$N = \frac{(\nu_g a_0)^2}{R^{3/2}_{\text{nucl}}}\Bigg\{\left[(-1)^{l_\nu}\left(f^{(R)}_+(x_{\text{nucl}})\right)^* f_{l_\nu}(R_{\text{nucl}})\delta_{Ll_\nu}\right. \tag{17}$$
$$\left.+(-1)^{l'_\nu+1/2}\left(f^{(R)}_+(x_{\text{nucl}})\right)^* g_{l'_\nu}(R_{\text{nucl}})\delta_{Ll'_\nu}\right]$$
$$\times W\left(\frac{1}{2}j_\nu\frac{1}{2}J; L1\right)$$
$$+\left[(-1)^{l'_\nu}\left(f^{(R)}_-(x_{\text{nucl}})\right)^* g_{l'_\nu}(R_{\text{nucl}})\delta_{L'l'_\nu}\right.$$

$$-(-1)^{l_\nu+\frac{1}{2}}\left(f_-^{(R)}(x_{\rm nucl})\right)^* f_{l_\nu}(R_{\rm nucl})\delta_{L'l_\nu}\Big]$$
$$\times W\left(\frac{1}{2}j_\nu\frac{1}{2}J;L'1\right)\Bigg\}g_A\int\boldsymbol{\sigma},$$

where $\int\boldsymbol{\sigma}$ is the Gamow–Teller nuclear matrix element for the beta transition $|\beta_i\rangle\to|\beta_f\rangle$ (β_i and β_f are the corresponding sets of quantum numbers for these states), $W(abcd;ef)$ is a Racah coefficient, and $x_{\rm nucl}=2R_{\rm nucl}(\nu_g a_0)^{-1}$ is the value of x at the boundary of the nucleus of radius $R_{\rm nucl}$; and L_e is the lepton part of the amplitude,

$$L_e=\frac{\Gamma(\lambda_g-\eta_g)}{\Gamma(2\lambda_g+1)} \tag{18}$$
$$\times\left((-1)^{l_e+\frac{3}{2}}\Pi_{l_eL'}C^{l_\gamma 0}_{l_e0L'0}\begin{Bmatrix}l_e & j_e & 1/2\\ L' & J & 1/2\\ l_\gamma & j_\gamma & 1\end{Bmatrix}I_1\right.$$
$$\left.+(-1)^{\frac{1+l_e+l'_e}{2}}\Pi_{l'_eL}C^{l_\gamma 0}_{l'_e0L0}\begin{Bmatrix}l'_e & j_e & \frac{1}{2}\\ L & J & \frac{1}{2}\\ l_\gamma & j_\gamma & 1\end{Bmatrix}I_2\right),$$

where

$$I_1\equiv\int_0^\infty dr\sqrt{r}f_{l_e}(r)f_-^{(I)}(x)j_{l_\gamma}(kr), \tag{19}$$
$$I_2\equiv\int_0^\infty dr\sqrt{r}g_{l_e}(r)f_+^{(I)}(x)j_{l_\gamma}(kr).$$

In numerically calculating the radial integrals in (19), it is necessary to consider that, for energies of $E<1$ in the Green's function, they converge fast (this follows from the fact that the asymptotic behavior of the integrand is $\sin(r)/r^{1+\alpha}$, where $\alpha>0$), but that, for $E>1$, these integrals converge rather slowly [the asymptotic behavior of the integrand is $\sin(r)/r$ in this region]. In the latter case, the evaluation of the integrals with the aid of a computer, for example, by the Gauss method leads to such large computational errors that it becomes impossible to determine I_1 and I_2. This problem can be solved by breaking down, for the integral I_1 (and for the integral I_2 as well), the interval of integration into two subintervals separated by an intermediate point r_0 that is rather far off the origin of coordinates:

$$I_1=\int_0^{r_0} dr\sqrt{r}f_{l_e}(r)f_-^{(I)}(x)j_{l_\gamma}(kr) \tag{20}$$
$$+\int_{r_0}^\infty dr\sqrt{r}f_{l_e}(r)f_-^{(I)}(x)j_{l_\gamma}(kr).$$

As a result, the first term can be calculated to the required degree of precision by applying methods of numerical integration (the Gauss method or any other fast method ensuring the accuracy of the calculations), while the second term can be evaluated analytically by using the asymptotic expansions of the integrands (see Appendix).

The differential probability of the transition $(A,Z)\xrightarrow{\beta,\gamma}(A,Z+1)$ can be obtained by averaging the quantity AA^* over the projections of the nuclear spin in the initial state and by performing summation in the resulting expression over the nuclear-spin projections in the final state and over the polarizations of the photon, electron, and antineutrino involved. In order to derive the expression for the total probability of the process, we must also perform integration with respect to the energies of the electron and antineutrino and with respect to their emission angles, taking into account the energy-conservation law, which, in the expression for the differential transition probability, leads to the emergence of the delta function

$$\delta(k-\Delta+1-\epsilon-q).$$

At a fixed energy k of the photon inducing photobeta decay from the state $|\beta_i\rangle$ of an (A,Z) nucleus to the state $|\beta_f\rangle$ of an $(A,Z+1)$ nucleus, the rate of this decay process is

$$P^{(\gamma)}_{\beta,k}(\beta_i\to\beta_f) \tag{21}$$
$$=12\frac{\alpha_e}{\pi^2}\sum_{j_\gamma l_\gamma j_e j_\nu}\Pi^2_{j_e}\Pi^4_{j_\gamma}\left(W(l_\gamma 1 j_e\frac{1}{2};j_\gamma j_\nu)\right)^2$$
$$\times\int_1^{k-\Delta+1}d\epsilon\frac{(k+1-\epsilon-\Delta)^2}{k}(\epsilon^2-1)^{1/2}\epsilon|N|^2|L_e|^2.$$

In an equilibrium medium of temperature T, the energy of a photon that may initiate the photobeta-decay reaction varies between Δ and ∞ with a probability specified by the Planck formula $f(k)=(\exp(k/T)-1)^{-1}$ (the temperature is defined in terms of an energy scale). Upon integration in (21) over the admissible range of energies of photons having the Planck frequency spectrum, there arises the following expression for the total probability of the photobeta-decay transition $(A,Z)\xrightarrow{\beta,\gamma}(A,Z+1)$:

$$P^{(\gamma)}_{\beta}(\beta_i\to\beta_f) \tag{22}$$
$$=\frac{1}{\pi^2}\int_\Delta^\infty\frac{k^2dk}{\exp(k/T)-1}P^{(\gamma)}_{\beta,k}(\beta_i\to\beta_f).$$

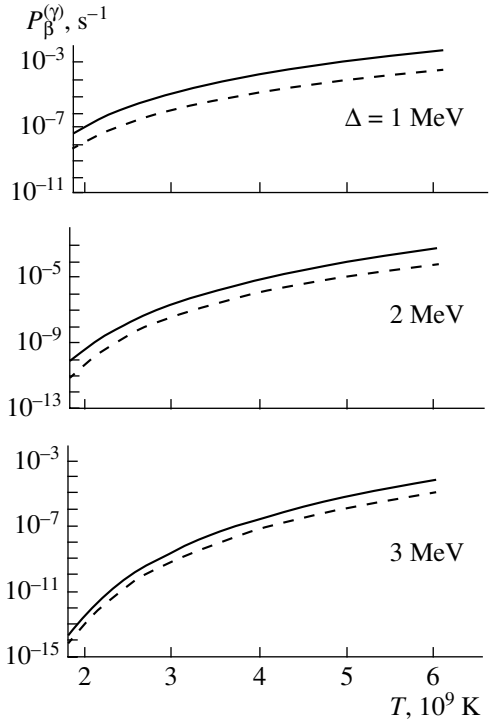

Fig. 3. Photobeta-decay rate as a function of temperature at various values of Δ: (solid curve) results obtained by exactly taking into account the nuclear Coulomb field ($P_\beta^{(\gamma)}$) and (dashed curve) results in the plane-wave approximation ($\widetilde{P}_\beta^{(\gamma)}$).

3. RESULTS OF THE CALCULATION OF THE PHOTOBETA-DECAY RATE

It was mentioned in the Introduction that an analog of expression (22) in the plane-wave approximation was derived in [1] in the form

$$\widetilde{P}_\beta^{(\gamma)}(\beta_i \to \beta_f) \tag{23}$$
$$= \frac{\alpha_e}{2\pi^4}\left|g_A\int \boldsymbol{\sigma}\right|^2 \int\limits_\Delta^\infty \frac{dk}{k\exp(k/T)-1}$$
$$\times \int\limits_1^{k-\Delta+1} d\epsilon(k+1-\epsilon-\Delta)^2\big[2(k-\epsilon)(\epsilon^2-1)^{1/2}$$
$$+ (k^2-2k\epsilon+2\epsilon^2)\ln(\epsilon+(\epsilon^2-1)^{1/2})\big].$$

In order to assess the degree to which it is of importance to take into account the nuclear Coulomb field in the photobeta-decay process, we have calculated the quantities $P_\beta^{(\gamma)}(\beta_i \to \beta_f)$ [formula (22)] and $\widetilde{P}_\beta^{(\gamma)}(\beta_i \to \beta_f)$ [formula (23)] versus the energy threshold Δ, the temperature T of the medium, and the charge number Z and compared the results, which are presented in Figs. 3–5 in units of the nuclear matrix element $g_A\int\boldsymbol{\sigma}$.

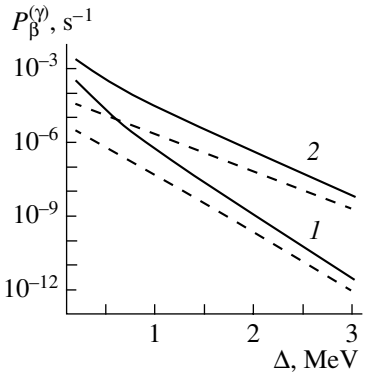

Fig. 4. Photobeta-decay rate as a function of the threshold energy Δ at temperatures of (*1*) $T = 2\times10^9$ K and (*2*) $T = 3\times10^9$ K. The notation for the curves is identical to that in Fig. 3.

For a model nucleus of charge number $Z = 32$, Fig. 3 shows the photobeta-decay rate as a function of temperature T at various values of the threshold energy Δ. It can be seen that, in all cases, the photobeta-decay rate grows with increasing temperature, tending to saturation. This result is quite understandable. The Planck spectrum is known to peak at about $3T$, the threshold energy Δ cutting off the region of energies that does not correspond to the condition $k > \Delta$. Naturally, the higher the temperature T at a given threshold energy, the wider the section of the Planck spectrum that is covered by the integration in formulas (22) and (23). But if the condition $T \gg \Delta$ holds, the result of integration in (22) is virtually independent of Δ, so that there arises saturation.

The dependence of the photobeta-decay rate on the threshold energy Δ at a fixed temperature (see Fig. 4) can be explained in a similar way: the greater the parameter Δ, the narrower the section of the Planck spectrum that contributes to the integrals in (22) and (23). From a comparison of the curves in Figs. 3 and 4, we can also deduce that the nuclear Coulomb field has a pronounced effect on the respective results. Depending on the energy range and on the values of the parameters Δ and T, the photobeta-decay rate calculated on the basis of the procedure that takes exactly into account the nuclear Coulomb field may differ from its counterpart in the plane-wave approximation by more than one order of magnitude, the inclusion of Coulomb effects leading to an increase in the probability of the thermal-radiation-stimulated beta decay of stable nuclei.

The photobeta-decay rate calculated by formula (22) is shown in Fig. 5 as a function of temperature at

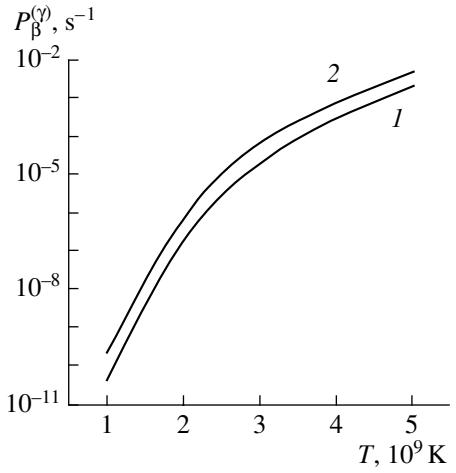

Fig. 5. Photobeta-decay rate as a function of temperature at the charge-number values of $Z = (1)$ 32 and (2) 68 ($\Delta = 1$ MeV).

various values of the charge number Z {in the plane-wave approximation, this rate is independent of Z [see formula (23)]}. It can be seen that, with increasing charge number, the reaction yield grows sizably, the shape of the respective curves being virtually identical.

On the basis of the results presented in Figs. 3–5, we can conclude that the disregard of the nuclear Coulomb field in calculating the diagram that makes a dominant contribution to the probability of photobeta decay leads to significant errors in the result, at least in the temperature region $T \geq 1 \times 10^9$ K.

4. TWO-STEP MODEL OF THE SYNTHESIS OF p-NUCLEI

As was indicated in the Introduction, the photobeta decay of stable nuclei was used in a number of studies as a basis for models aimed at explaining the synthesis of bypassed elements in the interior of massive stars. The beta decay of (A, Z) stable nuclei that is stimulated by thermal radiation from a star makes it possible to overcome the energy threshold separating (A, Z) and $(A, Z+1)$ nuclei and to trigger the chain of beta transitions $(A, Z) \xrightarrow{\beta,\gamma} (A, Z+1) \xrightarrow{\beta} (A, Z+2)$ toward the bypassed element $(A, Z+2)$. The calculation of the photobeta-decay rate in the preceding section revealed that it is not overly small in a medium of temperature in the region $T \geq (2-3) \times 10^9$ K, the corresponding mean energy of thermal photons being $\bar{k} \sim 300-500$ keV. Photons of such energies are present in the matter of hot stars at some stages of their evolution, so that the synthesis of p-nuclei via the photobeta-decay process is possible in principle. Of course, the result of the practical realization of this mechanism depends both on the presence of sufficient numbers of (A, Z) progenitor nuclei in the matter of a star at the above temperatures and on the time duration of the relevant stage of its evolution.

In this section, we will formulate a model in which the photobeta decay of stable nuclei is the main physical mechanism responsible for the synthesis of p-nuclei. On the basis of this model, we will try to estimate the key parameters at which the yield of bypassed elements is close to that which is observed and to find out, in this way, whether the proposed mechanism of the synthesis of bypassed elements is realistic.

The most detailed calculations of the abundances of p-nuclei on the basis of photobeta decay were performed in [5]. However, the calculation of the photobeta-decay rate in [5] relied on the expression obtained in [1] in the plane-wave approximation. As was shown above, this approximation is incorrect, since, for the reaction rate, it leads to a value much less than that which was obtained by exactly taking into account the nuclear Coulomb field. Moreover, only the β^- transitions $|\beta_i\rangle \to |\beta_f\rangle$ between the ground states of the (A, Z) and $(A, Z+1)$ nuclei were considered in [5]. In a number of cases, however, such a beta transition in the pair of (A, Z) and $(A, Z+1)$ nuclei is not allowed by quantum selection rules, while beta transitions from excited states of the (A, Z) nucleus prove to be allowed.

In the present study, we retain the basic features of the model from [5], modifying it with allowance for the aforesaid. In the $(A, Z) \xrightarrow{\beta,\gamma} (A, Z+1) \xrightarrow{\beta} (A, Z+2)$ scheme, the synthesis of p-nuclei, which involves photobeta decay, is considered as a two-step process. At the first step, the aforementioned mechanism of the photobeta decay of an (A, Z) progenitor nucleus is used to overcome the energy threshold Δ. At the second step, the natural β^- transition $(A, Z+1) \xrightarrow{\beta} (A, Z+2)$ is assumed to occur, producing an $(A, Z+2)$ p-nucleus.

Let us examine the first step. We denote by $P_\beta^{(\gamma)}(\beta_i \to \beta_f)$ the rate of photobeta decay from the state $|\beta_i\rangle$ of an (A, Z) nucleus to the state $|\beta_f\rangle$ of an $(A, Z+1)$ nucleus [see Eq. (22)]. In calculating this quantity, we take into account, for photobeta decays, only allowed beta transitions, since they are the most intense. It was indicated above that, for some $(A, Z) \xrightarrow{\beta,\gamma} (A, Z+1)$ photobeta transformations, the transition between the ground states of the nuclei involved is not allowed. However, excited states will also be populated in a medium of temperature about nuclear temperatures ($0.1 \lesssim T \lesssim 0.5$ MeV). In this

case, one can consider photobeta decay from an excited state of an (A, Z) nucleus (rather than from its ground state), arriving at a situation where the beta decay of this nucleus is allowed by quantum selection rules. In accordance with the Boltzmann distribution, the probability of the population of the excited state $|\beta_i\rangle$ of the (A, Z) progenitor nucleus is given by

$$W_{\beta_i} = \frac{2J_i + 1}{P(T)} \exp\left(-\frac{\epsilon(\beta_i)}{T}\right), \qquad (24)$$

where $\epsilon(\beta_i)$ is the energy spacing between the state $|\beta_i\rangle$ of the progenitor nucleus and its ground state (see Fig. 1), J_i is the spin of this state, and the nuclear partition function $P(T)$ is given by

$$P(T) = \sum_{\beta_i} (2J_i + 1) \exp\left(-\frac{\epsilon(\beta_i)}{T}\right). \qquad (25)$$

Since the main contribution to $P(T)$ comes from the ground state, the partition function can be set, in this case, to the statistical weight $P(T) \approx 2J_0 + 1 = 1$ of the ground state of the nucleus [here, it is considered that the spin is $J_0 = 0$ in the ground state of an even–even nucleus—almost all of the (A, Z) nuclei belong to this class].

The state $|\beta_f\rangle$ of the $(A, Z+1)$ parent nucleus can be arbitrary within the limits admitted by the energy conditions. For a specific beta transition $|\beta_i\rangle \to |\beta_f\rangle$, the threshold energy Δ can then be set to $\Delta_{if} = \Delta - \epsilon(\beta_i) + \epsilon(\beta_f)$, where $\epsilon(\beta_f)$ is the energy spacing between the state $|\beta_f\rangle$ of the $(A, Z+1)$ nucleus and its ground state (see Fig. 1). An analysis reveals that, for the (A, Z) and $(A, Z+1)$ nuclei, states between which an allowed beta transition is possible can be found almost always.

As a result, the total photobeta-decay rate that receives contributions from all of the transitions allowed by quantum selection rules can be represented in the form

$$\mathcal{P}_\beta^{(\gamma)} = \sum_{\beta_i \beta_f} W_{\beta_i} P_\beta^{(\gamma)}(\beta_i \to \beta_f), \qquad (26)$$

where $P_\beta^{(\gamma)}(\beta_i \to \beta_f)$ is the photobeta-decay rate associated with the beta transition $|\beta_i\rangle \to |\beta_f\rangle$ and calculated by formula (22).

Let us now consider the second step. It was indicated above that, at this step, there naturally proceeds the β^- decay of an $(A, Z+1)$ parent nucleus according to the scheme $(A, Z+1) \xrightarrow{\beta,\gamma} (A, Z+2)$. We denote by $W_{\beta^-}[(A, Z+1) \to (A, Z+2)]$ the corresponding probability. In estimating it, we consider that the lifetime of $(A, Z+1)$ unstable nuclei is much shorter than the characteristic times of nuclear-synthesis processes. Therefore, we can regard the natural β^- decay of these nuclei, which leads to $(A, Z+2)$ p-nuclei, as an authentic event and take into account only the corresponding branching fraction $K_{\beta^-}[(A, Z+1) \to (A, Z+2)]$. In the total probability of the decay of an $(A, Z+1)$ nucleus, it reflects the fraction of precisely β^- decay rather than that of electron capture or β^+ decay [the last two processes also usually occur, but they lead to the (A, Z) progenitor nucleus]. In the majority of cases, these branching fractions are known from experimental data (however, they were obtained under terrestrial conditions and may change at high temperatures in the matter of massive stars).

As a result, the ultimate expression for the probability of the production of a p-nucleus according to the scheme outlined above has the form

$$P[(A, Z) \to (A, Z+2)] \qquad (27)$$
$$= \mathcal{P}_\beta^{(\gamma)} K_{\beta^-}[(A, Z+1) \to (A, Z+2)].$$

The absolute values of the abundances of p-nuclei [we denote them by $N(A, Z+2)$] formed in accordance with the proposed model can be calculated if the concentration of (A, Z) progenitor nuclei in a star [we denote it by $N(A, Z)$] and the time interval τ within which the process in question is studied are known. Specifically, we have

$$N(A, Z+2) \qquad (28)$$
$$= N(A, Z) \int_0^\tau P[(A, Z) \to (A, Z+2)] T(t) dt,$$

where the time dependence of the probability $P[(A, Z) \to (A, Z+2)]$ (if this dependence is taken into account) is determined by the function $T(t)$ [see expression (22)].

5. CALCULATION OF THE ABUNDANCES OF p-NUCLEI IN THE UNIVERSE

According to present-day data, the evolution of a massive star involves two stages within which the temperature of matter in the star is $(2–3) \times 10^9$ K [15]. These are the stage of a hydrostatic combustion of oxygen (its duration is about six months) and the stage of the explosion of a supernova (the duration of this stage is about one second). In our calculations, we assumed that the photobeta decay of stable nuclei occurs in the interior of massive stars within the quasi-steady-state stage of evolution during the combustion of oxygen.

In calculating the probability of the production of p-nuclei by formula (27), a direct evaluation of the

Basic information about transitions that is used in calculating the abundances of p-nuclei

Progenitor nucleus	Abundance of progenitor nuclei	Parent nucleus	$J_i \to J_f$ transition	$\log f_0 t$	Δ_{if}, MeV	Branching fraction	p-nucleus
1	2	3	4	5	6	7	8
$^{74}_{32}$Ge	42.8	$^{74}_{33}$As	$0^+ \to 1^+$	4.6	1.98	0.32	$^{74}_{34}$Se
			$2^+ \to 1^+$		1.384		
$^{80}_{34}$Se	33.4	$^{80}_{35}$Br	$0^+ \to 1^+$	4.6	1.081	0.917	$^{80}_{36}$Kr
			$2^+ \to 1^+$		0.415		
$^{108}_{46}$Pd	0.347	$^{108}_{47}$Ag	$0^+ \to 1^+$	4.8	1.132	0.977	$^{108}_{48}$Cd
			$2^+ \to 1^+$		0.698		
$^{112}_{48}$Cd	0.373	$^{112}_{49}$In	$0^+ \to 1^+$	4.7	1.789	0.44	$^{112}_{50}$Sn
			$2^+ \to 1^+$		1.171		
$^{114}_{48}$Cd	0.447	$^{114}_{49}$In	$0^+ \to 1^+$	4.8	0.655	0.981	$^{114}_{50}$Sn
			$2^+ \to 1^+$		0.096		
$^{152}_{62}$Sm	0.0641	$^{152}_{63}$Eu	$4^+ \to 4^+$	4.5	0.811	0.27	$^{152}_{64}$Gd
$^{158}_{64}$Gd	0.104	$^{158}_{65}$Tb	$4^+ \to 5^+$	4.5	1.085	0.18	$^{158}_{66}$Dy
$^{164}_{66}$Dy	0.104	$^{164}_{67}$Ho	$0^+ \to 1^+$	4.6	1.029	0.42	$^{164}_{68}$Er
$^{168}_{68}$Er	0.0623	$^{168}_{69}$Tm	$2^+ \to 3^+$	4.5	0.810	0.02	$^{168}_{70}$Yb

Note: Data given in columns 2 and 4–7 were borrowed from [7] and [16], respectively.

nuclear matrix element $\int \boldsymbol{\sigma}$ [see Eq. (17)] presents a nontrivial problem. This evaluation inevitably involves specific model assumptions concerning the structure of nuclear states between which the transition in question proceeds. At the present time, there is no reliable computational scheme or a universal nuclear model that would make it possible to deduce realistic wave functions for nuclear states in cases other than the simplest ones (by no means do the beta transitions under study belong to the class of those simplest cases). For this reason, we did not perform a direct calculation of nuclear matrix elements $\int \boldsymbol{\sigma}$; instead, we extracted their values either from typical values of $\log f_0 t$ for unfavored beta transitions of the allowed type or, when possible, from the experimental values of $\log f_0 t$. Considering that the values of $\log f_0 t$ lie predominantly in the range 4.0–5.0, we took the value of 4.5 in the former case. This minimizes errors that stem from the ignorance of the actual structure of nuclear states. Thus, we did not perform a direct calculation of the matrix element $\int \boldsymbol{\sigma}$ in either case; instead, we used the formula

$$g_A^2 \left| \int \boldsymbol{\sigma} \right|^2 = \frac{2\pi^3 \ln 2}{f_0 t}, \qquad (29)$$

to obtain it from a typical or the experimental value of the reduced lifetime $f_0 t$ with respect to the relevant beta transition of the allowed type.

For the absolute values of the abundances of nine p-nuclei, the results of the calculations on the basis of the proposed model are given in Fig. 6. For the model parameters, we used the following values: the duration of the stage being considered was taken to be $\tau = 1.6 \times 10^7$ s; the concentrations of the progenitor nuclei were set to their abundances in the solar system (these abundances are given in the table, along with other features of relevant beta transitions); and the temperature T was assumed to be independent of time and was taken to be 2.5×10^9 K. In order to assess the applicability of the model to calculating the yields of p-nuclei, we selected $(A, Z) \xrightarrow{\beta,\gamma} (A, Z+1) \xrightarrow{\beta} (A, Z+2)$ triplets such that nuclides entering into them had properties determined to a fairly high precision. From Fig. 6, it can be seen that, in some cases, the agreement with experimental data is rather good, although the general trend is such that the temperature of the medium should be somewhat increased for lighter and somewhat decreased for heavier p-nuclei. Figure 7 gives specific temperature values that the medium should have for the yields of the p-nuclei indicated there to be coincident with their experimental values, the values of all other

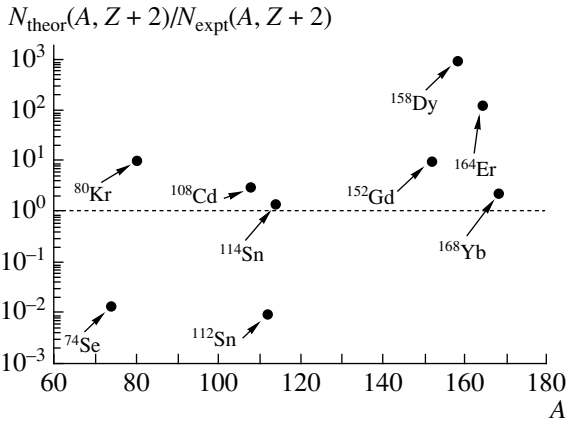

Fig. 6. Ratio of the calculated concentration of p-nuclei, $N_{theor}(A, Z+2)$, to their observed concentration $N_{expt}(A, Z+2)$ at $T = 2.5 \times 10^9$ K ($\tau = 0.5$ yr).

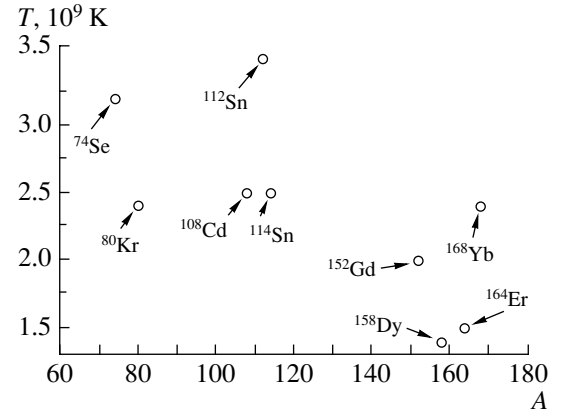

Fig. 7. Temperatures of the medium that make it possible to reproduce experimental data for the quantity $N(A, Z+2)$ ($\tau = 0.5$ yr).

relevant quantities being the same. We note that, for all other stages of the evolution, with the exception of the explosive stage, values close to the observed ones can in principle be obtained for the abundances of some of the p-nuclei by simultaneously varying, within some specific limits, the parameters T, τ, and $N(A, Z)$, as well as the branching fractions K_{β^-}, for which we have taken values determined under terrestrial conditions.

6. CONCLUSIONS

Our present investigation has made it possible to draw the following conclusions:

(i) The role of the nuclear Coulomb field is significant in the photobeta-decay process, which was previously studied in [1] in the plane-wave approximation. Therefore, model simulating the synthesis of p-nuclei on the basis of the formulas derived in [1] may lead to considerable errors in calculations and, accordingly, in conclusions.

(ii) Under rather realistic physical conditions, the proposed model of the synthesis of p-nuclei on the basis of the photobeta decay of stable nuclei originating from s and r processes makes it possible, in principle, to reproduce the observed concentrations for some of the bypassed elements.

(iii) The proposed model does not provide a universal mechanism of the synthesis of bypassed element. In particular, structural uncertainties for some of the beta transitions in $(A, Z) \xrightarrow{\beta,\gamma} (A, Z+1) \xrightarrow{\beta} (A, Z+2)$ triplets presently give no way, even if the parameters T and τ are fixed, to extend the explored range of p-nuclei. There are also uncertainties in associating their production with a specific stage of the evolution of a massive star and, accordingly, in choosing values for the parameters T and τ.

ACKNOWLEDGMENTS

This work was supported by the Ministry of Education of the Russian Federation (grant no. A03-2.9-450).

APPENDIX

Let us consider a method that makes it possible to calculate integrals of the type in (19), which involve quickly oscillating functions in the integrand. In the integral I_1 [formula (20)], the second term at energies in the region $E > 1$ will be calculated by using the asymptotic expansions of the factors in the integrand

$$F(r) \equiv \sqrt{r} f_{l_e}(r) f_-^{(I)}(x) j_{l_\gamma}(kr). \qquad \text{(A.1)}$$

For the large and the small component of the radial electron wave function in the Coulomb field of a nucleus, we have [10]

$$\left.\begin{matrix} f_{l_e}(r) \\ g_{l_e}(r) \end{matrix}\right\} = \sqrt{\frac{2}{\epsilon}} \exp\left(\frac{\pi\xi_e}{2}\right) \qquad \text{(A.2)}$$
$$\times \frac{|\Gamma(\gamma_e + 1 + i\xi_e)|}{\Gamma(2\gamma_e + 1)} \frac{(2pr)^{\gamma_e}}{r}$$
$$\times \left\{\begin{matrix} \sqrt{\epsilon+1} \cdot \mathrm{Im} \\ \sqrt{\epsilon-1} \cdot \mathrm{Re} \end{matrix}\right\} [e^{i(pr+\zeta_e)} {}_1\mathrm{F}_1(\gamma_e$$
$$- i\xi_e, 2\gamma_e + 1, -2ipr)],$$

where ${}_1\mathrm{F}_1(a, c, x)$ is a confluent hypergeometric function and

$$e^{-2i\zeta_e} = (\gamma_e - i\xi_e) / (\kappa_e - i\xi_e/\epsilon)$$

[the rest of the notation is given in the explanations to formula (15)].

The asymptotic expansion of the function ${}_1\mathrm{F}_1(a,c,x)$ has the form [17]

$$
\begin{aligned}
{}_1\mathrm{F}_1(a,c,x) &= \frac{\Gamma(c)}{\Gamma(c-a)}\left(\frac{e^{-i\pi}}{x}\right)^a \qquad \text{(A.3)}\\
&\times \sum_{n=0}^{M}\frac{(a)_n(a-c+1)_n}{n!}(-x)^{-n} + O(|x|^{-a-M-1})\\
&+ \frac{\Gamma(c)}{\Gamma(a)}e^x x^{a-c}\sum_{n=0}^{N}\frac{(c-a)_n(1-a)_n}{n!}x^{-n}\\
&+ O(|e^x x^{a-c-N-1}|),
\end{aligned}
$$

where $(a)_n = a(a+1)(a+2)...(a+n-1)$ is the Pochhammer symbol.

We can determine the asymptotic behavior of the function $f_-^{(I)}(x)$ [and the function $f_+^{(I)}(x)$ as well], knowing the expression for the Whittaker function $W(x)$ at large values of the argument [17],

$$
\begin{aligned}
W_{\kappa,\mu}(x) &= e^{-x/2}x^{\mu+1/2}\sum_{n=0}^{N}(-1)^n \qquad \text{(A.4)}\\
&\times \frac{\left(\frac{1}{2}-\kappa+\mu\right)_n(1/2-\kappa-\mu)_n}{n!}x^{-1/2+\kappa-\mu-n}\\
&+ O(|x|^{-1/2+\kappa-\mu-N-1}).
\end{aligned}
$$

We also employ the well-known asymptotic expression for the spherical Bessel function $j_{l_\gamma}(kr)$ at long distances [18],

$$
j_{l_\gamma}(kr) = \frac{\sin(kr-\pi l_\gamma/2)}{kr}. \qquad \text{(A.5)}
$$

Substituting (A.2)–(A.5) into (A.1) and multiplying those terms of the sums that involve identical powers of the coordinate r, we obtain the asymptotic expansion of the function $F(r)$ in the form

$$
F(r) = \sum_{n=1}^{N} a_n\frac{e^{ib_n r}}{r^{\alpha_n}} + O\left(r^{-\mathrm{Re}(\alpha_n)-1}\right), \qquad \text{(A.6)}
$$

where a_n and α_n are complex-values coefficients and b_n are real-valued coefficients; they are obtained upon the multiplication of those terms in the above sums that involve identical powers of the arguments.

By way of example, we present the expression for the first terms of the sum in (A.6). Retaining only the r^{-1} terms in the series in (A.3) and (A.4), we obtain, for $F(r)$, the sum of four terms for which we have the following:

$n = 1, 2$

$$
\begin{aligned}
a_{1,2} &= (-1)^{n+1}\frac{2^{i(\xi_g+\xi_e)-1}}{k}\\
&\times \left(\frac{(1-E)(1+\epsilon)P}{\epsilon}\right)^{1/2}\\
&\times \exp\left[i\left(\delta_e + (-1)^n\frac{\pi l_\gamma}{2}+\frac{\pi}{4}\right) - \frac{\pi}{2}\xi_g\right]P^{i\xi_g}p^{i\xi_e},\\
b_{1,2} &= -P + p - (-1)^n k,\\
\alpha_{1,2} &= 1 - i(\xi_g+\xi_e);
\end{aligned}
$$

$n = 3, 4$

$$
\begin{aligned}
a_{3,4} &= (-1)^n\frac{2^{i(\xi_g-\xi_e)-1}}{k}\left(\frac{(1-E)(1+\epsilon)P}{\epsilon}\right)^{1/2}\\
&\times \exp\left[i\left(-\delta_e + (-1)^n\frac{\pi l_\gamma}{2}+\frac{\pi}{4}\right)\right.\\
&\left. - \frac{\pi}{2}\xi_g\right]P^{i\xi_g}p^{-i\xi_e},\\
b_{3,4} &= -P - p - (-1)^n k,\\
\alpha_{3,4} &= 1 - i(\xi_g-\xi_e),
\end{aligned}
$$

where $P = (E^2-1)^{1/2}$, $\xi_g = \alpha_e ZE/P$, and $\delta_e = \zeta_e - \arg\Gamma(\gamma_e+1+i\xi_e) - \pi\gamma_e/2$.

Formula (A.6) makes it possible to calculate the second term of the integral I_1 by using the relation [18]

$$
\int_{r_0}^{\infty}\frac{e^{ix}}{x^\alpha}dx = i^{1-\alpha}\Gamma(1-\alpha,-ir_0), \qquad \text{(A.7)}
$$

where $\Gamma(1-\alpha,-ir_0)$ is the incomplete gamma function. Ultimately, we obtain

$$
\int_{r_0}^{\infty}F(r)dr = \sum_n a_n\left(\frac{i}{b_n}\right)^{1-\alpha_n}\Gamma(1-\alpha_n,-ib_n r_0). \qquad \text{(A.8)}
$$

Thus, the integral I_1 assumes the form

$$
\begin{aligned}
I_1 &= \int_0^{r_0} dr\sqrt{r}f_{l_e}(r)f_-^{(I)}(x)j_{l_\gamma}(kr) \qquad \text{(A.9)}\\
&+ \sum_n a_n\left(\frac{i}{b_n}\right)^{1-\alpha_n}\Gamma(1-\alpha_n,-ib_n r_0).
\end{aligned}
$$

In practice, the number of terms in (A.3) and (A.4) [and, accordingly, in (A.9)] could be restricted. Indeed, it was mentioned above that, in numerically calculating the first term of the integral in (A.9), the error of the calculation grew with increasing r_0. Therefore, it was necessary to choose, for r_0, a value at which the error of the calculation was within the preset precision of the calculation. After that, the number of terms retained in the series in (A.3) and (A.4) should have been specified in such a way that

the asymptotic expression for the integrand in (A.1) at the point r_0 was matched with its precise value within the admissible error. The calculations revealed that it was sufficient to retain two terms in each of the sums indicated above.

REFERENCES

1. P. B. Shaw, D. D. Clayton, and F. C. Michel, Phys. Rev. **140**, B1433 (1965).
2. M. Arnould, Nucl. Phys. A **100**, 657 (1967).
3. M. Arnould and C. Brihaye, Astron. Astrophys. **1**, 193 (1969).
4. A. A. Joukoff, Astron. Astrophys. **3**, 186 (1969).
5. I. V. Kopytin and T. A. Krylovetskaya, Izv. Akad. Nauk, Ser. Fiz. **64**, 935 (2000).
6. E. M. Burbidge, G. R. Burbidge, W. A. Fowler, and F. Hoyle, Rev. Mod. Phys. **29**, 547 (1957).
7. G. Wallerstein, I. Iben, P. Parker, *et al.*, Rev. Mod. Phys. **69**, 995 (1997).
8. M. Rayet, M. Arnould, M. Hashimoto, *et al.*, Astron. Astrophys. **298**, 517 (1995).
9. H. A. Wiedenmuller, Rev. Mod. Phys. **33**, 574 (1961).
10. V. B. Berestetskiĭ, E. M. Lifshitz, and L. P. Pitaevskiĭ, *Quantum Electrodynamics* (Nauka, Moscow, 1980; Pergamon, Oxford, 1982).
11. S. A. Zapryagaev, N. L. Manakov, and V. G. Pal'chikov, *Theory of Polyvalent Ions with One or Two Electrons* (Énergoatomizdat, Moscow, 1985), p. 144 [in Russian].
12. E. T. Whittaker and G. N. Watson, *A Course of Modern Analysis*, 4th ed. (Cambridge Univ. Press, Cambridge, 1927; Inostr. Lit., Moscow, 1963), Vol. 2, p. 515.
13. A. Z. Dolginov, in *Gamma Rays* (Akad. Nauk SSSR, Moscow, 1961), p. 720 [in Russian].
14. E. Konopinskiĭ and M. Rouz, in *Alpha, Beta, and Gamma Spectroscopy* (Atomizdat, Moscow, 1969), Vol. 4, p. 272 [in Russian].
15. B. S. Ishkhanov, I. M. Kapitonov, and I. M. Tutyn, *Nucleosynthesis in the Universe* (Mosk. Gos. Univ., Moscow, 1999), p. 128.
16. C. M. Lederer, J. M. Hollander, and J. Perlman, *Table of Isotopes* (Wiley, New York, 1967).
17. H. Bateman and A. Erdelyi, *Higher Transcendental Functions* (McGraw-Hill, New York, 1953; Nauka, Moscow, 1974), Vol. 1.
18. H. Bateman and A. Erdelyi, *Higher Transcendental Functions* (McGraw-Hill, New York, 1953; Nauka, Moscow, 1974), Vol. 2.

Translated by A. Isaakyan

Physics of Atomic Nuclei, Vol. 67, No. 8, 2004, pp. 1442–1447. Translated from Yadernaya Fizika, Vol. 67, No. 8, 2004, pp. 1468–1473.

NUCLEI
Theory

Parity-Nonconservation Effects in the Photodisintegration of Polarized Deuterons

R. V. Korkin

Budker Institute of Nuclear Physics, Siberian Division, Russian Academy of Sciences, pr. Akademika Lavrent'eva 11, Novosibirsk, 630090 Russia
Novosibirsk State University, ul. Pirogova 2, Novosibirsk, 630090 Russia
Received October 15, 2003

Abstract—P-odd correlations in deuteron photodisintegration are considered. It is shown that, in the case of unpolarized deuterons, π-meson exchanges do not contribute to these correlations. For polarized deuterons, the contribution of π-meson exchanges to the P-odd correlation is about 0.3×10^{-8}. The contribution to P-odd effects from weak interactions at short distances substantially exceeds the contribution from π-meson exchanges. © *2004 MAIK "Nauka/Interperiodica"*.

1. INTRODUCTION

In the past few years, parity nonconservation in deuteron photodisintegration has been widely discussed in the literature. An analysis of the problem became particularly interesting in view of advances in experimental techniques, such as the creation of intense beams of polarized photons, neutrons, and electrons. In addition, theoretical investigations of the deuteron are relatively reliable owing to its low binding energy. The problem is especially interesting because the measured anapole moment of ^{133}Cs [1] is in reasonable agreement with the theoretical predictions from [2, 3] if the so-called best values [4] are chosen for the parameters of P-odd forces. It is worth noting that the results of nuclear experiments are indicative of a substantially lower constant for π-meson exchange [5]. We can expect that the deuteron experiments that are being discussed at the present time would resolve the existing discrepancy.

Theoretical investigations of P-odd effects were initiated in [6–10]; *ed* scattering was explored in [10–12]. However, measurement of parity violation in these processes was hindered by a strong background from neutral currents. Numerical estimates for such effects were given in [13–15]. Deuteron disintegration by polarized photons was previously considered in a number of studies (see, for example, [7, 8, 15–20]). Despite a small magnitude of the effect, this process is more interesting since it features no neutral currents.

Experiments aimed at implementing deuteron disintegration by polarized photons with the aim of measuring the weak π-meson constant $\bar{g}$ have been extensively discussed in recent years. As was shown in [21], however, π-meson exchange does not contribute to the asymmetry of the total cross section for unpolarized-deuteron disintegration by polarized photons. In addition, the exchange of vector mesons (contribution of short distances) is significant, having a relative value of about 10^{-7} at the maximum. However, a typical range of ρ- and ω-meson exchange is $r_V \sim 1/m_V \sim 0.25$ fm, which is substantially less than the nucleon size of 0.8 fm. Since the respective theoretical estimates are unreliable, this contribution is not of significant interest. In view of the results obtained in [21], there can arise the question of why the π-meson contribution is canceled in the total photodisintegration cross section. It is necessary to find out whether this contribution vanishes upon integrating the differential cross section with respect to angles or whether there is merely no correction in the differential cross section. If the correction to the differential cross section were nonzero in some angular interval, it would be possible to measure it precisely in this region. In this study, we show that the correction to the differential cross section also vanishes, so that it is impossible to measure the π-meson constant by using polarized photons and unpolarized deuterons. Therefore, we consider parity-violation effects in polarized-deuteron disintegration induced by unpolarized photons. It turns out that, in this case, the weak correction to the differential cross section from π-meson exchange is different from zero. Although it is very difficult to measure this quantity, the problem associated with it is interesting at least theoretically.

We perform all calculations on the basis of the potential model.

We use the deuteron wave function in the zero-

1063-7788/04/6708-1442$26.00

range approximation,

$$\psi_d = \sqrt{\frac{\kappa}{2\pi(1-\kappa r_t)}}\frac{e^{-\kappa r}}{r}\chi^\sigma, \qquad (1)$$

where χ^σ is the spin wave function.

This approximation provides a correct description at distances longer than the effective radius of the triplet state—that is, for $r \gg r_t$. The matrix element for the electric dipole transition does not depend on the form of the wave function at short distances; therefore, the use of the zero-range approximation is quite legitimate here. However, the situation is less favorable in the case of the matrix elements for the magnetic dipole transition and the weak potential, because these quantities are sensitive to the behavior of the wave function at short distances. The zero-range wave function does not satisfy the normalization condition; in order to perform calculations sensitive to short distances, it is therefore necessary to modify the deuteron wave function in such a way as to reduce it to a normalized form. For this, it is sufficient to discard the "correction" factor $\sqrt{1-\kappa r_t}$ [22].

As for final states, we need only s and p waves in the continuous spectrum (see, for example, [11]). We neglect a small admixture of the d wave in the deuteron ground state.

2. CALCULATION OF THE AMPLITUDES OF π-MESON EXCHANGE

We represent the operators of electric and magnetic dipole transitions in the form [22]

$$H_{E1} = -ie\sqrt{2\pi\omega}\mathbf{n}\cdot\mathbf{e}\frac{r}{2}, \qquad (2)$$

$$H_{M1} = -i\frac{e}{2m}\sqrt{2\pi\omega} \times \left(\mu_p\boldsymbol{\sigma}_p + \mu_n\boldsymbol{\sigma}_n + \frac{\mathbf{l}}{2}\right)\cdot\frac{\mathbf{k}\times\mathbf{e}}{k},$$

where $r/2$, $\mathbf{n}$, and $\mathbf{l}/2$ are, respectively, the coordinate, the unit radius vector, and the angular momentum of the proton and $\mathbf{e}$ and $\mathbf{k}$ are the photon polarization vector and momentum, respectively.

Let us calculate the amplitude for a typical electric dipole transition in deuteron photodisintegration. The deuteron wave function ψ_d appears to be the initial state. The final state is obviously a p wave of the continuous spectrum. Further, we can use a plane wave instead of the p wave in the amplitude, because the $E1$-transition operator automatically selects the p-wave state in the plane wave.

The amplitude of the $E1$ transition then takes the form

$$A_{E1} = -2e\sqrt{2\pi\omega}\sqrt{2\pi\kappa}\frac{\mathbf{p}\cdot\mathbf{e}}{\sqrt{1-\kappa r_t}(\kappa^2+p^2)^2}. \qquad (3)$$

Owing to weak P-odd interaction, the deuteron ground state acquires an admixture of the p wave, while, in the p wave of the continuous spectrum in the final state, there arises an admixture of the s wave. Thus, intruder $M1$ transitions become possible.

The P-odd potential of π-meson exchange can be represented in the form [23]

$$V = -i\frac{g\bar{g}}{4\pi m}(\boldsymbol{\sigma}_p + \boldsymbol{\sigma}_n)\cdot\boldsymbol{\nabla}\frac{e^{-m_\pi r}}{r}. \qquad (4)$$

Here, g and $\bar{g}$ are the coupling constants for, respectively, strong and weak P-odd πNN interaction.

The total transition amplitude is then given by

$$A = \langle\mathbf{p},\sigma'|H_{E1}|\psi_d,\sigma\rangle + \sum_n\frac{\langle\mathbf{p},\sigma'|H_{M1}|n\rangle\langle n|V|\psi_d,\sigma\rangle}{E_d-E_n} + \sum_n\frac{\langle\mathbf{p},\sigma'|V|n\rangle\langle n|H_{M1}|\psi_d,\sigma\rangle}{E_p-E_n}, \qquad (5)$$

where the subscript n is used to denote summation over all intermediate states and σ is the deuteron spin. We further consider the second term in (5) and calculate the matrix element of the weak potential for the transition from the deuteron ground state to any intermediate state, for which we can take the plane wave $\psi(p) = e^{i\mathbf{p}\cdot\mathbf{r}}|\chi^\sigma\rangle$.

The matrix element is

$$\langle\mathbf{p},\sigma''|V|\psi_d\rangle = -i\frac{g\bar{g}}{4\pi m}\langle\chi^{\sigma''}|(\boldsymbol{\sigma}_p+\boldsymbol{\sigma}_n)|\chi^\sigma\rangle \times\sqrt{\frac{\kappa}{2\pi}}\int e^{-i\mathbf{k}\cdot\mathbf{r}}\boldsymbol{\nabla}\left(\frac{e^{-m_\pi r}}{r}\right)\frac{e^{-\kappa r}}{r}d\mathbf{r}. \qquad (6)$$

We will postpone the calculation of the spin part for the time being. A simple integration in (6) leads to the following expression for the matrix element of the weak potential:

$$\sqrt{\frac{\kappa}{2\pi}}\frac{g\bar{g}}{km}\langle\chi^{\sigma''}|\mathbf{p}\cdot(\boldsymbol{\sigma}_p-\boldsymbol{\sigma}_n)|\chi^\sigma\rangle f(p). \qquad (7)$$

The function $f(p)$ appearing in (7) is given by

$$f(p) = \frac{1}{2}\left[\frac{m_\pi-\kappa}{p} \times\left(1-\frac{m_\pi+\kappa}{p}\arctan\frac{p}{m_\pi+\kappa}\right) + \arctan\frac{p}{m_\pi+\kappa}\right]. \qquad (8)$$

The matrix element of the $M1$ transition in the second term on the right-hand side of (5) is

$$\langle\mathbf{p},\chi^{\sigma'}|H_{M1}|\mathbf{k},\chi^{\sigma''}\rangle = -i(2\pi)^3\frac{e}{2m}\sqrt{2\pi\omega}[\mathbf{n}_k\times\mathbf{e}] \qquad (9)$$

$$\times \left\langle \sigma' \left| \left(\mu_p \boldsymbol{\sigma}_p + \mu_n \boldsymbol{\sigma}_n - i\frac{\mathbf{p}\times\boldsymbol{\nabla}_p}{2} \right) \right| \sigma'' \right\rangle \delta(\mathbf{k}-\mathbf{p}).$$

After simplification and summation over intermediate states, the second term in (5) then assumes a relatively simple form,

$$i\frac{eg\bar{g}f(p)\sqrt{2\pi\omega}}{2pm(\kappa^2+p^2)}\sqrt{\frac{\kappa}{2\pi}}[\mathbf{n}_k\times\mathbf{e}] \quad (10)$$
$$\times \left\langle \chi^{\sigma'} \left| \left(\mu_p \boldsymbol{\sigma}_p + \mu_n \boldsymbol{\sigma}_n - \frac{i[\mathbf{p}\times\boldsymbol{\nabla}_p]}{2} \right) \right.\right.$$
$$\left.\left. \times\, \mathbf{p}\cdot(\boldsymbol{\sigma}_p+\boldsymbol{\sigma}_n) \right| \chi^{\sigma} \right\rangle.$$

Here, we have used the well-known completeness relation $\sum_\sigma |\chi_\sigma\rangle\langle\chi_\sigma| = 1$ to perform summation over intermediate spin states.

Owing to the orthogonality of the radial parts of the s-wave functions in the last (third) term of (5), the intermediate state n must be the deuteron ground state. Therefore, the operator of the orbital angular momentum of the magnetic dipole transition is not operative here. Upon cumbersome calculations similar to those considered above, we arrive at the following expression for the third term in (5):

$$-i\frac{eg\bar{g}f(p)\sqrt{2\pi\omega}}{2pm(\kappa^2+p^2)}\sqrt{\frac{\kappa}{2\pi}}\,[\mathbf{n}_k\times\mathbf{e}] \quad (11)$$
$$\times\, \langle\chi^{\sigma'}|\mathbf{p}\cdot(\boldsymbol{\sigma}_p+\boldsymbol{\sigma}_n)(\mu_p\boldsymbol{\sigma}_p+\mu_n\boldsymbol{\sigma}_n)|\chi^{\sigma}\rangle.$$

The total amplitude (5) then assumes the form

$$A = -2e\sqrt{2\pi\omega}\sqrt{2\pi\kappa} \quad (12)$$
$$\times \frac{\mathbf{p}\cdot\mathbf{e}}{\sqrt{(1-\kappa r_t)}(\kappa^2+p^2)^2}\delta_{\sigma\sigma'} + i\frac{eg\bar{g}f(p)\sqrt{2\pi\omega}}{2pm(\kappa^2+p^2)}$$
$$\times \sqrt{\frac{\kappa}{2\pi}}\,[\mathbf{n}_k\times\mathbf{e}]\,\langle\chi^{\sigma'}|(\mu_p\boldsymbol{\sigma}_p+\mu_n\boldsymbol{\sigma}_n)\cdot\mathbf{p}$$
$$\times(\boldsymbol{\sigma}_p+\boldsymbol{\sigma}_n) - \mathbf{p}\cdot(\boldsymbol{\sigma}_p+\boldsymbol{\sigma}_n)(\mu_p\boldsymbol{\sigma}_p+\mu_n\boldsymbol{\sigma}_n)|\chi^{\sigma}\rangle$$
$$+ \frac{eg\bar{g}f(p)\sqrt{2\pi\omega}}{2pm(\kappa^2+p^2)}\sqrt{\frac{\kappa}{2\pi}}\,[\mathbf{n}_k\times\mathbf{e}]$$
$$\times \left\langle \chi^{\sigma'} \left| \frac{[\mathbf{p}\times\boldsymbol{\nabla}_p]}{2}\mathbf{p}\cdot(\boldsymbol{\sigma}_p+\boldsymbol{\sigma}_n) \right| \chi^{\sigma} \right\rangle.$$

3. DIFFERENTIAL AND TOTAL CROSS SECTIONS

The differential cross section for the disintegration of unpolarized deuterons has the form

$$\frac{d\sigma}{d\Omega} = \frac{1}{3}\sum_\sigma \frac{2e^2\kappa p(\mathbf{p}\cdot\mathbf{e})^2}{(1-\kappa r_t)(\kappa^2+p^2)^3}$$
$$-\frac{i}{3}\sum_\sigma \frac{eg\bar{g}\kappa f(p)(\mathbf{p}\cdot\mathbf{e}^*)[\mathbf{n}\times\mathbf{e}]}{2\pi\sqrt{1-\kappa r_t}m(\kappa^2+p^2)^2}$$
$$\times\, \langle\chi^{\sigma}|2(\mu_p+\mu_n)(\mathbf{I}(\mathbf{p}\cdot\mathbf{I}) - (\mathbf{p}\cdot\mathbf{I})\mathbf{I}) - i[\mathbf{p}\times\mathbf{I}]|\chi^{\sigma}\rangle,$$

where $\mathbf{I}$ is the deuteron spin. The term responsible for magnetic moments is the commutator of the deuteron spins; that is, it is expressed in terms of the deuteron spin. Thus, the correction to the regular cross section is proportional in the case being considered to the mean spin of the primary (unpolarized) deuteron; that is, it is identically equal to zero [21].

Let us now consider effects associated with polarized deuterons and unpolarized photons. For this, we average the last expression over photon polarizations.

Upon some simple algebra, we reduce the differential cross section to the form

$$\left(\frac{d\sigma}{d\Omega}\right)_{\text{tot}} = \left(\frac{d\sigma}{d\Omega}\right)_{E1} + \Delta\frac{d\sigma}{d\Omega}, \quad (13)$$

where

$$\left(\frac{d\sigma}{d\Omega}\right)_{E1} = e^2\frac{\kappa p(p^2-(\mathbf{p}\cdot\mathbf{n})^2)}{(1-\kappa r_t)(\kappa^2+p^2)^3} \quad (14)$$

is the ordinary expression for the electric dipole disintegration of a deuteron and

$$\Delta\frac{d\sigma}{d\Omega} = -\frac{e^2g\bar{g}\kappa p^2 f(p)}{2\pi m\sqrt{1-\kappa r_t}(\kappa^2+p^2)^2} \quad (15)$$
$$\times \left(\mu_p+\mu_n-\frac{1}{2}\right)\left(\mathbf{n}\cdot\mathbf{I} - \frac{\mathbf{I}\cdot\mathbf{p}\mathbf{n}\cdot\mathbf{p}}{p^2}\right)$$

is the P-odd correction to the differential cross section from π-meson exchange.

Upon integration with respect to angles, we obtain the total cross section

$$\sigma = \frac{8\pi e^2\kappa p^3}{3(1-\kappa r_t)(\kappa^2+p^2)^3} \quad (16)$$
$$-\frac{4e^2g\bar{g}\kappa p^2 f(p)}{3m\sqrt{1-\kappa r_t}(\kappa^2+p^2)^2}\left(\mu_p+\mu_n-\frac{1}{2}\right)\mathbf{n}\cdot\mathbf{I}.$$

4. CONTRIBUTION OF SHORT DISTANCES

Unfortunately, the π-meson contribution to the amplitude is not dominant. There are also two types of contributions from weak interaction at short distances. The first is dominant near the threshold, while the second has a structure similar to that of the π-meson contribution. The contributions from short distances defy all attempts at a reliable calculation, but we will try to estimate it within the potential model. It is important to do this for obtaining deeper insight into the relation between the contributions of π-meson exchange and the contribution of short distances.

In order to obtain weak odd admixtures to the wave functions owing to exchanges of vector mesons, we introduce the Jastrow factor, which takes into account the repulsion of nucleons at short distances [21,

24]. Following [7], we represent the perturbed wave functions in the form

$$\delta\psi_d = -i\lambda_t(\mathbf{\Sigma}\cdot\boldsymbol{\nabla})\sqrt{\frac{\kappa}{2\pi}}\frac{e^{-\kappa r}}{r}. \qquad (17)$$

The admixtures to the s and p waves of the continuous spectrum then assume the form

$$\delta\psi_s = i\frac{\alpha_s}{1+ip\alpha_s}\lambda_s\mathbf{\Sigma}\cdot\boldsymbol{\nabla}\left(\frac{e^{ipr}}{r}\right), \qquad (18)$$

$$\delta\psi_p = -\lambda_s\frac{\alpha_s}{1+ip\alpha_s}\mathbf{\Sigma}\cdot\mathbf{p}\frac{e^{ipr}}{r},$$

where α_s is the triplet scattering length; $\mathbf{\Sigma} = \boldsymbol{\sigma}_p - \boldsymbol{\sigma}_n$ is the spin difference; and λ_t and λ_s are the P-odd constants given by [21]

$$\lambda_t = (0.032h_\rho^0 + 0.001h_\omega^0)\times 10^{-7}m_\pi^{-1}, \qquad (19)$$
$$\lambda_s = (0.028h_\rho^0 - 0.023h_\rho^2 + 0.028h_\omega^0)\times 10^{-7}m_\pi^{-1}.$$

Let us consider the regular $E1$ transition from the deuteron to the continuous spectrum. Owing to parity violation, an $M1$ amplitude appears here. Using (18) and (19) to calculate this amplitude, we arrive at the following expression for the total amplitude:

$$A = -2e\sqrt{2\pi\omega}\sqrt{2\pi\kappa}\frac{\mathbf{p}\cdot\mathbf{e}}{\sqrt{1-\kappa r_t}(\kappa^2+p^2)^2}\delta_{\sigma'\sigma}$$
$$-i\frac{e}{2m}\sqrt{2\pi\omega}\sqrt{2\pi\kappa}(\mu_p-\mu_n)$$
$$\times\left(\frac{\lambda_t}{\kappa^2+p^2}\langle\chi^{\sigma'}|\mathbf{\Sigma}\cdot[\mathbf{n}\times\mathbf{e}]\,\mathbf{\Sigma}\cdot\mathbf{p}|\chi^\sigma\rangle\right.$$
$$\left.-\frac{\alpha_s\lambda_s}{(1-ip\alpha_s)(\kappa+ip)}\langle\chi^{\sigma'}|\mathbf{\Sigma}\cdot\mathbf{p}\mathbf{\Sigma}\cdot[\mathbf{n}\times\mathbf{e}]\,|\chi^\sigma\rangle\right).$$

The short-distance correction to the differential cross section for deuteron disintegration is given by

$$\Delta\frac{d\sigma}{d\Omega} = \frac{\kappa e^2(\mu_p-\mu_n)p^3}{m\sqrt{1-\kappa r_t}(\kappa^2+p^2)^2} \qquad (20)$$
$$\times\left[\left(\lambda_t+\alpha_s\frac{\kappa+p^2\alpha_s}{1+p^2\alpha_s^2}\lambda_s\right)\left(\mathbf{I}\cdot\mathbf{n}-\frac{\mathbf{I}\cdot\mathbf{p}\mathbf{n}\cdot\mathbf{p}}{p^2}\right)\right.$$
$$+\lambda_s\frac{\alpha_s}{p}\frac{1-\kappa\alpha_s}{1+p^2\alpha_s^2}(\mathbf{p}\cdot\mathbf{I}[\mathbf{n}\times\mathbf{p}]\cdot\mathbf{I}$$
$$\left.+\mathbf{I}\cdot[\mathbf{n}\times\mathbf{p}]\mathbf{p}\cdot\mathbf{I})\right].$$

We averaged this correction over photon polarizations. Upon integration with respect to angles, the correction to the total cross section assumes the form

$$\Delta\sigma = \frac{8\pi\kappa e^2(\mu_p-\mu_n)p^3}{3m\sqrt{1-\kappa r_t}(\kappa^2+p^2)^2} \qquad (21)$$
$$\times\left(\lambda_t+\alpha_s\frac{\kappa+p^2\alpha_s}{1+p^2\alpha_s^2}\lambda_s\right)\mathbf{I}\cdot\mathbf{n}.$$

5. CONTRIBUTION OF SHORT DISTANCES NEAR THE THRESHOLD

Let us now consider the deuteron photodisintegration at the threshold. This region is obviously dominated by the magnetic dipole transition from the deuteron to the singlet state ($^3S_1 \to {}^1S_0$). We can see that the operator of this transition violates the conservation of the total spin. However, the total spin is conserved in the $E1$ transition; therefore, weak interaction, which is responsible for the intruder $E1$ transition, must also violate the conservation of the total spin. This property is due to that part of weak interaction which corresponds to the exchange of vector mesons.

All calculation are rather simple and lead to the result

$$A = -i\frac{e}{2m}\sqrt{2\pi\omega}\sqrt{2\pi\kappa}(\mu_p-\mu_n) \qquad (22)$$
$$\times\frac{1-\kappa\alpha_s}{(1-ip\alpha_s)(\kappa^2+p^2)}\mathbf{\Sigma}\cdot[\mathbf{n}\times\mathbf{e}]$$
$$+\frac{e\sqrt{2\pi\omega}\sqrt{2\pi\kappa}}{3}(\lambda_t I_t+\lambda_s I_s)\mathbf{\Sigma}\cdot\mathbf{e},$$

where I_t and I_s are radial integrals,

$$I_t = \frac{3\kappa^2+p^2}{(\kappa^2+p^2)^2} - \frac{\alpha_s(2\kappa+ip)}{(1-ip\alpha_s)(\kappa+ip)^2}, \qquad (23)$$

$$I_s = \frac{\kappa+2ip}{(1-ip\alpha_s)(\kappa+ip)^2}. \qquad (24)$$

Upon some simple algebraic transformations, we obtain the differential cross section in the form

$$\frac{d\sigma}{d\Omega} = \frac{\kappa e^2(\mu_p-\mu_n)^2(1-\kappa\alpha_s)^2p}{4m^2(1+p^2\alpha_s^2)(\kappa^2+p^2)}(\mathbf{I}\cdot\mathbf{n})^2 \qquad (25)$$
$$+\frac{\kappa e^2(\mu_p-\mu_n)(1-\kappa\alpha_s)p}{3m(1+p^2\alpha_s^2)}\frac{3\kappa^2+p^2}{(\kappa^2+p^2)^2}$$
$$\times\left(\lambda_t\left(1-\frac{2\alpha_s\kappa^3}{3\kappa^2+p^2}\right)+\kappa\alpha_s\lambda_s\frac{\kappa^2+3p^2}{3\kappa^2+p^2}\right)\mathbf{n}\cdot\mathbf{I}.$$

Owing to spherical symmetry, the total cross section is obtained by multiplying this expression by 4π. We have

$$\sigma = \frac{\pi\kappa e^2(\mu_p-\mu_n)^2(1-\kappa\alpha_s)^2p}{m^2(1+p^2\alpha_s^2)(\kappa^2+p^2)}(\mathbf{I}\cdot\mathbf{n})^2 \qquad (26)$$
$$+\frac{4\pi\kappa e^2(\mu_p-\mu_n)(1-\kappa\alpha_s)p}{3m(1+p^2\alpha_s^2)}\frac{3\kappa^2+p^2}{(\kappa^2+p^2)^2}$$
$$\times\left(\lambda_t\left(1-\frac{2\alpha_s\kappa^3}{3\kappa^2+p^2}\right)+\kappa\alpha_s\lambda_s\frac{\kappa^2+3p^2}{3\kappa^2+p^2}\right)\mathbf{n}\cdot\mathbf{I}.$$

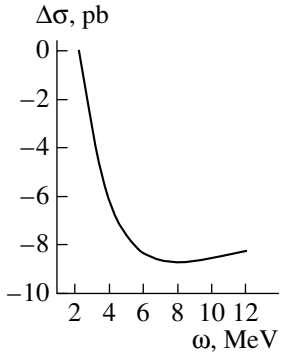

Fig. 1. π-meson contribution to the correlation.

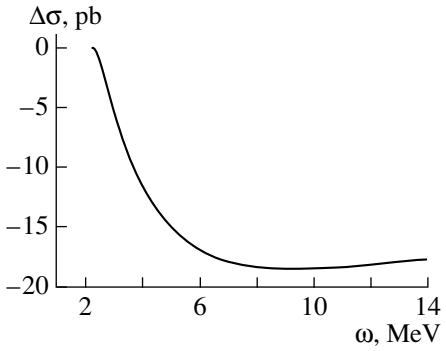

Fig. 2. Contribution from short distances to the correlation: the regular $E1$ transition.

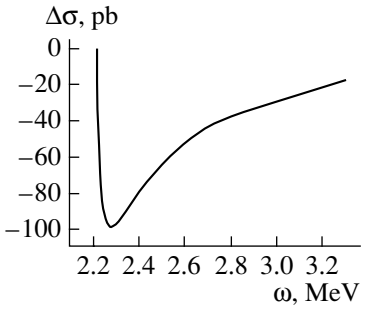

Fig. 3. Contribution from short distances to the correlation: the regular $M1$ transition.

6. CONCLUSION

The resulting total cross section can be represented in the form

$$\sigma = \sigma_{E1} + \sigma_{M1} + \Delta\sigma_\pi + \Delta\sigma_{V1} + \Delta\sigma_{V2},$$

$$\sigma_{E1} = \frac{8\pi e^2 \kappa p^3}{3(1-\kappa r_t)(\kappa^2+p^2)^3},$$

$$\sigma_{M1} = \frac{\pi\kappa e^2(\mu_p-\mu_n)^2(1-\kappa\alpha_s)^2 p}{m^2(1+p^2\alpha_s^2)(\kappa^2+p^2)}(\mathbf{I}\cdot\mathbf{n})^2,$$

$$\Delta\sigma_\pi = -\frac{4e^2 g\bar{g}\kappa p^2 f(p)}{3m\sqrt{1-\kappa r_t}(\kappa^2+p^2)^2} \times \left(\mu_p+\mu_n-\frac{1}{2}\right)\mathbf{I}\cdot\mathbf{n},$$

$$\Delta\sigma_{V1} = \frac{8\pi\kappa e^2(\mu_p-\mu_n)p^3}{3m\sqrt{1-\kappa r_t}(\kappa^2+p^2)^2} \times \left(\lambda_t + \alpha_s\frac{\kappa+p^2\alpha_s}{1+p^2\alpha_s^2}\lambda_s\right)\mathbf{I}\cdot\mathbf{n},$$

$$\Delta\sigma_{V2} = \frac{4\pi\kappa e^2(\mu_p-\mu_n)(1-\kappa\alpha_s)p}{3m(1+p^2\alpha_s^2)}\frac{3\kappa^2+p^2}{(\kappa^2+p^2)^2} \times \left(\lambda_t\left(1-\frac{2\alpha_s\kappa^3}{3\kappa^2+p^2}\right)+\kappa\alpha_s\lambda_s\frac{\kappa^2+3p^2}{3\kappa^2+p^2}\right)\mathbf{I}\cdot\mathbf{n}.$$

As was indicated above, the P-odd corrections to the total and differential cross sections from π-meson exchange vanish in the case of unpolarized deuterons. Therefore, it is impossible to measure the P-odd π-meson constant $\bar{g}$ in processes featuring only polarized photons and unpolarized deuterons. This is the main result of the present study since the numerical estimates given below seem to dash any hope for measuring this constant in processes with polarized deuterons.

Let us now consider the magnitude of P violation in the total cross section and the accuracy of the results. As has already been mentioned, we adopt the so-called best values of the weak constants (these are confirmed by experimental data on the anapole moment of ^{133}Cs [1]). The corresponding constant of π-meson exchange is

$$\bar{g} = 3.3\times10^{-7},$$

while the vector-meson exchange constants are [21]

$$\lambda_s = -0.16\times10^{-7}m_\pi^{-1},$$
$$\lambda_t = -0.37\times10^{-7}m_\pi^{-1}.$$

Figures 1–3 present the corrections to the total cross sections (here, we assume that $\mathbf{n}\cdot\mathbf{I}=1$).

Far from the threshold, there are two types of contributions in the region of a dominant $E1$ transition. We consider the exchanges of π mesons (Fig. 1) and vector mesons (Fig. 2) separately. Unfortunately, a theoretical consideration of weak interactions at short distances is unreliable; therefore, the accuracy in the latter case is low (see above). The main error arises in calculating the constants λ_t and λ_s. We employ the constant values obtained in [21]. The accuracy of the calculations can be estimated on the basis of the difference of the results obtained with and without the Jastrow factor, which takes into account the repulsion of nucleons at short distances. The coefficient characterizing the discrepancy of the two results (it is less than 1.7) measures the accuracy; that is, we can expect an error at a level of 40%, if

the so-called best values were determined precisely. We can also estimate the π-meson contribution by employing a trial function that behaves correctly at the origin [21] and again introducing the Jastrow factor. The distinction between the respective results leads to an error at a level of 20%. The contribution of vector-meson exchange, which is dominant in this region, exceeds the contribution of π-meson exchange approximately by a factor of 2. However, the two contributions are summed; therefore, the result can be considered to be relatively reliable. The most interesting correlation is that which is associated with π-meson exchange, $\Delta\sigma_\pi/\sigma$, its typical value being about 0.3×10^{-8}, which is substantially less than the maximum value of the corresponding contribution from vector mesons.

The maximum correction corresponds to the exchange of vector mesons in the threshold region (Fig. 3); its relative value at the threshold, $\Delta\sigma/\sigma$, is about 4×10^{-8}. The accuracy of this value is again 40%.

ACKNOWLEDGMENTS

I am grateful to I.B. Khriplovich for stimulating discussions and enlightening comments.

This work was supported by the Russian Foundation for Basic Research (project nos. 01-02-16898, 00-15-96811) and the Ministry of Education of the Russian Federation (project no. E00-3.3-148).

REFERENCES

1. C. S. Woods *et al.*, Science **275**, 1759 (1997).
2. V. V. Flambaum and I. B. Khriplovich, Zh. Éksp. Teor. Fiz. **79**, 1656 (1980) [Sov. Phys. JETP **52**, 835 (1980)].
3. V. V. Flambaum, I. B. Khriplovich, and O. P. Sushkov, Phys. Lett. B **146B**, 367 (1984).
4. B. Desplanques, J. F. Donoghue, and B. R. Holstein, Ann. Phys. (N.Y.) **124**, 449 (1980).
5. E. Adelberger and W. Haxton, Annu. Rev. Nucl. Part. Sci. **35**, 501 (1985).
6. F. Partovi, Ann. Phys. (N.Y.) **27**, 114 (1964).
7. G. S. Danilov, Phys. Lett. **18**, 40 (1965).
8. G. S. Danilov, Yad. Fiz. **14**, 788 (1972) [Sov. J. Nucl. Phys. **14**, 443 (1972)].
9. D. Tadić, Phys. Rev. **174**, 1694 (1968).
10. R. J. Blin-Stoyle and F. Feshbach, Nucl. Phys. **27**, 395 (1961).
11. A. I. Mikhaĭlov, A. N. Moskalev, R. M. Ryndin, and G. V. Frolov, Yad. Fiz. **35**, 887 (1982) [Sov. J. Nucl. Phys. **35**, 516 (1982)].
12. M. Porrmann and M. Gari, Phys. Rev. Lett. **38**, 947 (1977).
13. W. Y. P. Hwang and E. M. Henley, Ann. Phys. (N.Y.) **129**, 47 (1980).
14. W. Y. P. Hwang, E. M. Henley, and G. A. Miller, Ann. Phys. (N.Y.) **137**, 378 (1981).
15. H. C. Lee, Phys. Rev. Lett. **41**, 843 (1978).
16. B. Desplanques, Nucl. Phys. A **242**, 423 (1975).
17. K. R. Lassey and B. H. J. McKellar, Phys. Rev. C **11**, 349 (1975).
18. M. Gari and J. Schlitter, Phys. Lett. B **59B**, 118 (1975).
19. J. P. Leroy, J. Micheli, and D. Pignon, Nucl. Phys. A **280**, 377 (1977).
20. T. Oka, Phys. Rev. D **27**, 523 (1983).
21. I. B. Khriplovich and R. V. Korkin, Nucl. Phys. A **690**, 610 (2001).
22. V. B. Berestetskiĭ, E. M. Lifshitz, and L. P. Pitaevskiĭ, *Quantum Electrodynamics* (Nauka, Moscow, 1980; Pergamon, Oxford, 1982).
23. I. B. Khriplovich and R. V. Korkin, Nucl. Phys. A **665**, 365 (2000).
24. V. V. Flambaum, V. B. Telitsin, and O. P. Sushkov, Nucl. Phys. A **444**, 611 (1985).

Translated by M. Kobrinsky

Physics of Atomic Nuclei, Vol. 67, No. 8, 2004, pp. 1448–1453. Translated from Yadernaya Fizika, Vol. 67, No. 8, 2004, pp. 1474–1479.

NUCLEI
Theory

Elastic Scattering of Intermediate-Energy Protons on ^{9}Be Nuclei within the $2\alpha n$ Model

Yu. A. Berezhnoy and V. P. Mikhailyuk[1)]

Kharkov State University, Sumskaya ul. 35, Kharkov, 310022 Ukraine

Received October 13, 2003

Abstract—The α-cluster model involving dispersion is adapted to the case of the ^{9}Be nucleus. Two configurations of the ground state of this nucleus are employed in calculations: (i) a core (^{8}Be nucleus) and a complementary cluster (neutron), which oscillates with the highest probability about the center of mass of the core, and (ii) an isosceles triangle formed by two alpha-particle clusters and a neutron. Polarization observables of elastic proton scattering on ^{9}Be nuclei are calculated on basis of this approach and the theory of multiple diffractive scattering. The results of these calculations are in good agreement with available experimental data. © *2004 MAIK "Nauka/Interperiodica".*

The α-cluster model involving dispersion has been successfully employed to describe the elastic scattering of intermediate-energy electrons and hadrons on ^{12}C, ^{16}O, and ^{20}Ne nuclei (see, for example, [1–4]). It is of interest to examine particle scattering on ^{9}Be nuclei on the basis of this model.

The ^{9}Be nucleus has a large quadrupole moment ($Q = 53$ mb) and a rather small binding energy ($\epsilon = 1.57$ MeV) with respect to disintegration into two α particles and a neutron, this suggesting a high degree of clustering in this nucleus. On the other hand, its spin is 3/2, since it is determined by the total angular momentum of the unpaired neutron in the $1p_{3/2}$ shell. In view of this, four form factors (an electric monopole, an electric quadrupole, a magnetic dipole, and a magnetic octupole one) are required for describing electron scattering on these nuclei. In the case of small-angle scattering ($q \leq 2$ fm^{-1}), however, the main contribution to the electron-scattering cross section comes from the monopole (charge) form factor. If $q \geq 2$ fm^{-1}, the quadrupole form factor fills the minimum of the cross section, this leading to a smooth momentum-transfer dependence of the form factor.

The features of the ^{9}Be nucleus have been considered within various approaches. For example, the processes of elastic and inelastic p^9Be scattering were described on the basis of the optical model, the distorted-wave method, and the coupled-channel method (see [5–8]). The differential cross sections calculated for elastic p^9Be scattering within these approaches agree with available experimental data. On the contrary, polarization (analyzing power) and differential cross sections for inelastic scattering that were calculated within the optical model exhibited not quite adequate behavior and disagreed with available experimental data. The same quantities calculated within the coupled-channel method demonstrated better agreement with experimental data, but the choice of potential in fitting observables was ambiguous—more specifically, the use of some potentials improved agreement between the calculated and measured values of the differential cross sections for elastic scattering, simultaneously spoiling a fit to the measured differential cross sections for inelastic scattering and to the analyzing power for elastic scattering, while the use of other potentials resulted in a poorer fit to the measured differential cross sections for elastic scattering and in better agreement for the differential inelastic-scattering cross sections and for the analyzing powers in elastic scattering.

In [9–11], the observables of elastic proton scattering on ^{9}Be nuclei were considered within the theory of multiple diffractive scattering. The differential cross sections calculated for p^9Be scattering in [9] with allowance for the quadrupole deformation of the nucleus in question agreed well with experimental data. In [10, 11], the differential cross sections and analyzing powers for elastic proton scattering on ^{9}Be were studied within the theory of multiple diffractive scattering by using the wave functions determined on the basis of the $2\alpha n$ model [12], the results being in agreement with corresponding experimental data at 220 and 1000 MeV.

In the present study, the α-cluster model involving dispersion is extended to the case of the ^{9}Be nucleus,

[1)]Institute for Nuclear Research, National Academy of Sciences of Ukraine, pr. Nauki 47, Kiev, 03680 Ukraine.

which is assumed to be formed by two alpha-particle clusters and a neutron. In calculations, we considered two possible configurations of the nucleus: (i) a core (^{8}Be nucleus) and a complementary cluster (neutron), which oscillates with the highest probability about the center of mass of the core, and (ii) two alpha-particle clusters and a neutron, which are located with the highest probability at the vertices of an isosceles triangle, the possibility of a displacement of alpha-particle clusters and of a neutron from their most probable equilibrium positions at the vertices of the triangle being taken into account within this approach.

We will first consider configuration (i). In this case, the multiparticle density of the ^{9}Be nucleus can be represented in the form

$$\rho(\boldsymbol{\xi}, \boldsymbol{\eta}) = \rho_\Delta(\boldsymbol{\xi})\rho_N(\boldsymbol{\eta}), \tag{1}$$

where $\rho_\Delta(\boldsymbol{\xi})$ is the density of the core (^{8}Be nucleus), $\rho_N(\boldsymbol{\eta})$ is the density of the complementary neutron, $\boldsymbol{\xi}$ is the Jacobi coordinate that characterizes the distance between the centers of mass of the alpha-particle clusters belonging to the ^{8}Be nucleus, and $\boldsymbol{\eta}$ is the coordinate of the complementary neutron.

The core density can be written as

$$\rho_\Delta(\boldsymbol{\xi}) = \int d^3\xi' \rho_0(\boldsymbol{\xi}')\Phi_\Delta(\boldsymbol{\xi} - \boldsymbol{\xi}'), \tag{2}$$

$$\rho_0(\boldsymbol{\xi}) = \frac{1}{4\pi d^2}\delta(\xi - d), \tag{3}$$

$$\Phi_\Delta(\xi) = \frac{1}{(2\pi\Delta^2)^{3/2}} \exp\left(-\frac{\xi^2}{2\Delta^2}\right). \tag{4}$$

In (2)–(4), the parameters d and Δ characterize, respectively, the distance between the alpha-particle clusters, which form a rigid dumbbell in this approach, and the probability of their displacement from the dumbbell vertices.

Upon performing integration in (2), we arrive at

$$\rho_\Delta(\boldsymbol{\xi}) = \frac{1}{(2\pi\Delta^2)^{3/2}} \exp\left(-\frac{\xi^2}{2\Delta^2} - \frac{d^2}{2\Delta^2}\right) \frac{\sinh(x)}{x}, \tag{5}$$

where $x = (\xi d)/\Delta^2$.

The complementary-neutron density is taken in the form

$$\rho_N(\boldsymbol{\eta}) = \frac{1}{(\lambda\sqrt{\pi})^3} \exp\left(-\frac{\eta^2}{\lambda^2}\right), \tag{6}$$

where the parameter λ characterizes the most probable distance between the complementary neutron and the center of mass of the core.

The parameters of the density $\rho_\Delta(\boldsymbol{\xi})$ can be determined by fitting the calculated charge form factor for the ^{9}Be nucleus to its experimentally measured counterpart. Considering that, in the region of low momentum transfers, the neutron charge form factor is negligible, we can represent the ^{9}Be charge form factor as

$$F(q) = \exp\left(-\frac{1}{6}q^2\langle r^2\rangle_\alpha - \frac{1}{8}q^2\Delta^2\right) j_0\left(\frac{qd}{2}\right), \tag{7}$$

where $j_0(x) = \sin(x)/x$ is a spherical Bessel function, $\langle r^2\rangle_\alpha^{1/2} = 1.61$ fm is the root-mean-square radius of the alpha particle, and $\mathbf{q}$ is the momentum transfer.

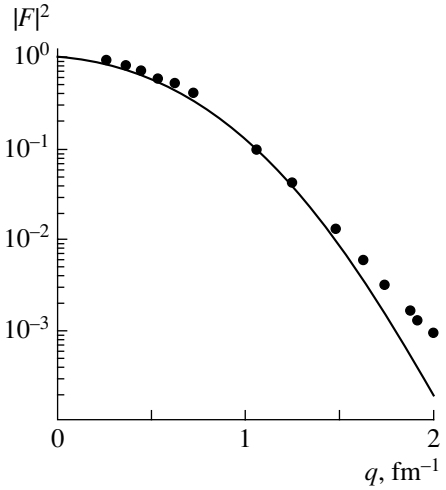

Fig. 1. Charge form factor for the ^{9}Be nucleus as a function of momentum transfer. The displayed experimental data were borrowed from [13, 14].

The ^{9}Be form factor calculated within this approach is presented in Fig. 1, along with experimental data borrowed from [13, 14]. It can be seen that the calculated form factor agrees well with these experimental data in the momentum-transfer region $q \leq 2$ fm^{-1}. The distinction between the calculated and measured form factors at high momentum transfers is likely to be due to the disregard of the quadrupole charge form factor, whose contribution may prove to be significant here.

Comparing the calculated and measured form factors for the ^{9}Be nucleus, we obtained the values of $d = 2.081$ fm and $\Delta = 1.850$ fm for the parameters of the core density $\rho_\Delta(\boldsymbol{\xi})$.

Within this approach, the mean-square radius of the ^{9}Be nucleus has the form

$$\langle r^2\rangle = \langle r^2\rangle_\alpha + \frac{1}{4}d^2 + \frac{3}{4}\Delta^2. \tag{8}$$

Using the values found for the core-density parameters d and Δ, we obtain $\langle r^2\rangle^{1/2} = 2.498$ fm,

which is close to the experimentally measured value of $\langle r^2\rangle^{1/2}_{\rm expt} = 2.519$ fm [15].

It should be noted that the parameter λ, which characterizes the amplitude of neutron oscillations about the center of mass of the core, can be determined from a fit of the calculated charge form factor for the ^{9}Be nucleus to its measured value. A similar model (core plus complementary neutron) was employed in [3, 4, 16] to examine the features of the ^{20}Ne, ^{13}C, and ^{13}N nuclei. In calculating the observables of elastic p^9Be scattering in the present study, we took the value of $\lambda = 1.23$ fm, which is the mean value of the analogous parameter obtained in [3, 4] for the ^{20}Ne nucleus.

A somewhat different configuration (see above) can also be considered in studying the ground-state density of the ^{9}Be nucleus within the α-cluster model involving dispersion. We mean here configuration (ii), where the ^{9}Be nucleus consists of two alpha-particle clusters and a neutron, which are situated with the highest probability at the vertices of an isosceles triangle. This configuration is not typical of the nucleus under consideration, but it is well known to exist, for example, in the molecules of water (H_2O) and ozone (O_3) [17].

In this case, the multiparticle density of the ^{9}Be nucleus can be written as

$$\rho(\boldsymbol{\zeta},\boldsymbol{\chi}) = \int d^3\zeta' d^3\chi' \rho_0(\boldsymbol{\zeta}',\boldsymbol{\chi}')\Phi_\Delta(\boldsymbol{\zeta}-\boldsymbol{\zeta}',\boldsymbol{\chi}-\boldsymbol{\chi}'), \tag{9}$$

where the density $\rho_0(\boldsymbol{\zeta},\boldsymbol{\chi})$ and the smearing function $\Phi_\Delta(\boldsymbol{\zeta},\boldsymbol{\chi})$ are given by

$$\rho_0(\boldsymbol{\zeta},\boldsymbol{\chi}) = \frac{1}{8\pi^2 d_1 d_2}\delta(\zeta-d_1)\delta(\chi-d_2)\delta(\boldsymbol{\zeta}\cdot\boldsymbol{\chi}), \tag{10}$$

$$\Phi_\Delta(\zeta,\chi) = \frac{1}{(2\pi\Delta_1\Delta_2)^3}\exp\left(-\frac{\zeta^2}{2\Delta_1^2}-\frac{\chi^2}{2\Delta_2^2}\right). \tag{11}$$

In these formulas, $\boldsymbol{\zeta}$ and $\boldsymbol{\chi}$ are the Jacobi coordinates of the clusters forming the ^{9}Be nucleus; the parameters d_1 and d_2 characterize, respectively, the distance between the alpha-particle clusters and the distance between the neutron and the center of mass of the alpha-particle clusters; and Δ_1 and Δ_2 specify the probabilities of the displacement of the alpha-particle clusters and the neutron from the most probable positions at the vertices of an isosceles triangle.

As above, we determine d_1, d_2, Δ_1, and Δ_2 from a fit of the calculated form factors for the ^{9}Be nucleus to their measured values. The charge form factor for this nucleus can be written as

$$F(q) = \exp\left(-\frac{1}{6}q^2\langle r^2\rangle_\alpha\right) \times \int \exp\left(i\mathbf{q}\left(-\frac{1}{9}\boldsymbol{\chi}+\frac{1}{2}\boldsymbol{\zeta}\right)\right)\rho(\boldsymbol{\zeta},\boldsymbol{\chi})d^3\zeta d^3\chi. \tag{12}$$

In the momentum-transfer region $q \le 2$ fm^{-1}, the ^{9}Be charge form factor calculated within this approach shows virtually no distinctions from that which is presented in Fig. 1. A fit of the calculated to the measured form factor led to the following values for the parameters of the density in (9): $d_1 = 2.0$ fm, $\Delta_1 = 1.892$ fm, $d_2 = 1.232$ fm, and $\Delta_2 = 0.00012$ fm.

In this case, the mean-square radius of the ^{9}Be nucleus can be represented in the form

$$\langle r^2\rangle = \langle r^2\rangle_\alpha + \frac{1}{4}d_1^2 + \frac{3}{4}\Delta_1^2 + \frac{1}{81}d_2^2 + \frac{1}{27}\Delta_2^2. \tag{13}$$

This yields $\langle r^2\rangle^{1/2} = 2.509$ fm, which is in good agreement with experimental data from [15].

We now consider the elastic scattering of intermediate-energy protons on ^{9}Be nuclei. According to the theory of multiple diffractive scattering, the amplitude $F^{\rm Be}(\mathbf{q})$ of elastic p^9Be scattering can written as

$$F^{\rm Be}(\mathbf{q}) = A + E(\boldsymbol{\sigma}_0\cdot\mathbf{n}) + F(\boldsymbol{\sigma}_1\cdot\mathbf{n}) + B(\boldsymbol{\sigma}_0\cdot\mathbf{n})(\boldsymbol{\sigma}_1\cdot\mathbf{n}) + C(\boldsymbol{\sigma}_0\cdot\mathbf{q})(\boldsymbol{\sigma}_1\cdot\mathbf{q}) + D(\boldsymbol{\sigma}_0\cdot\mathbf{p})(\boldsymbol{\sigma}_1\cdot\mathbf{p}), \tag{14}$$

where the amplitudes A, B, C, D, E, and F are expressed in terms of the elementary amplitudes of nucleon–nucleon and $p\alpha$ scattering and in terms of the model densities given above for the ^{9}Be nucleus.

In the calculations, the central and spin–orbit components of the $p\alpha$-scattering amplitude were chosen as the sum of two Gaussian functions of the momentum transfer [2], while the nucleon–nucleon amplitude $f_{NN}(q)$ was taken in the most general form [18],

$$f_{NN}(\mathbf{q}) = f_1(\mathbf{q}) + qf_2(\mathbf{q})(\boldsymbol{\sigma}_0\cdot\mathbf{n}+\boldsymbol{\sigma}_1\cdot\mathbf{n}) + f_3(\mathbf{q})(\boldsymbol{\sigma}_0\cdot\boldsymbol{\sigma}_1) + f_4(\mathbf{q})(\boldsymbol{\sigma}_0\cdot\mathbf{q})(\boldsymbol{\sigma}_1\cdot\mathbf{q}) + f_5(\mathbf{q})(\boldsymbol{\sigma}_0\cdot\mathbf{p})(\boldsymbol{\sigma}_1\cdot\mathbf{p}). \tag{15}$$

Here, $\boldsymbol{\sigma}_0$ and $\boldsymbol{\sigma}_1$ are the spin operators of, respectively, the projectile proton and the complementary nucleon of the target nucleus; $\mathbf{n} = [\mathbf{k}\times\mathbf{k}']/|[\mathbf{k}\times\mathbf{k}']|$; $\mathbf{q} = \mathbf{k}-\mathbf{k}'$; and $\mathbf{p} = (\mathbf{k}+\mathbf{k}')/(|\mathbf{k}+\mathbf{k}'|)$, $\mathbf{k}$ and $\mathbf{k}'$ being the wave vectors of the projectile and the scattered proton, respectively. The vectors $\mathbf{n}$, $\mathbf{p}$, and $-\mathbf{q}/|\mathbf{q}|$ form a right-hand triplet of orthonormalized vectors. Neglecting the isospin part of nucleon–nucleon interaction, we take the amplitudes $f_i(\mathbf{q})$ in the form of two Gaussian functions whose parameters were

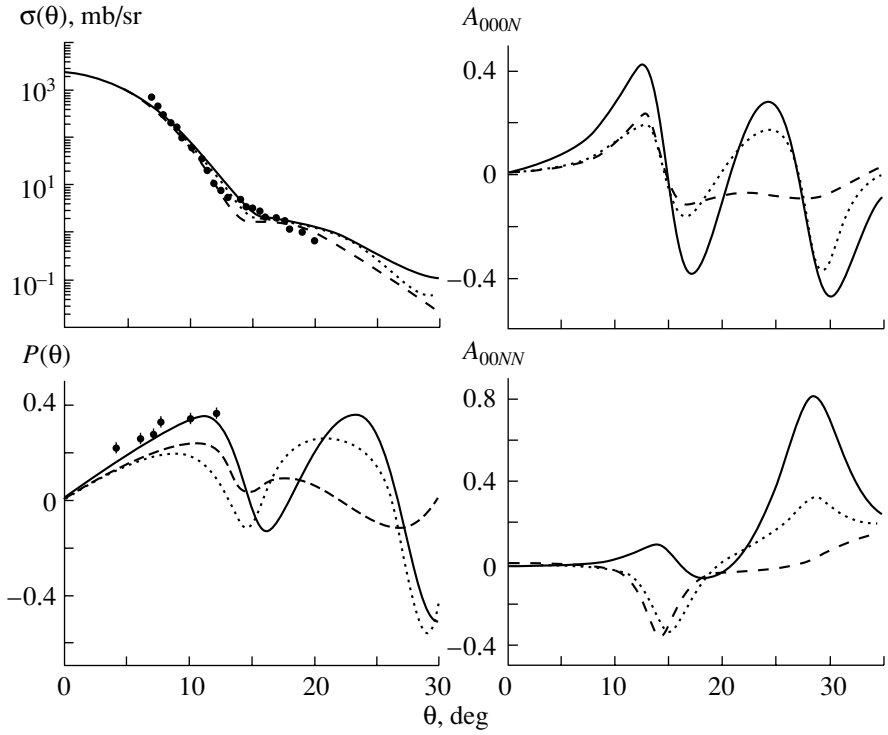

Fig. 2. Differential cross section $\sigma(\theta) \equiv d\sigma/d\Omega$, polarization P($\theta$), and analyzing powers $A_{000N}(\theta)$ and $A_{00NN}(\theta)$ for elastic proton scattering on ^{9}Be nuclei at an energy of 1000 MeV versus the scattering angle θ. The displayed experimental data were borrowed from [13, 23]. The description of the curves is given in the main body of the text.

found in [19] from a partial-wave analysis of nucleon–nucleon scattering.

It is well known that measurement of 11 independent observables is required for describing the elastic scattering of spin-1/2 particles [19]. In the case of the interaction of a spin-1/2 projectile particle (proton) with a spin-3/2 nucleus (^{9}Be), the number of observables necessary for completely describing elastic scattering is still greater.

At the present time, the most comprehensive set of experimental data on the elastic scattering of intermediate-energy protons on odd nuclei is that for p^{13}C scattering at an energy value of 500 MeV [20–22]. The quantities measured for this case as functions on the scattering angle θ include the differential cross section $\sigma(\theta) \equiv d\sigma/d\Omega$ (mb/sr); the polarization (asymmetry) $P(\theta)$; the depolarization parameters $D_{SL}(\theta)$, $D_{SS}(\theta)$, and $D_{NN}(\theta)$; and the analyzing powers $A_{000N}(\theta)$ and $A_{00NN}(\theta)$. The relations between these observables and the amplitudes A, B, C, D, E, and F (14) are given in [16].

Figures 2 and 3 present the calculated polarization observables for elastic p^9Be scattering at an energy value of 1000 MeV. The experimental data displayed in Fig. 2 (points) were borrowed from [13, 23]. The solid curves correspond to configuration (ii) (see above). The dashed curves were calculated under the assumption of configuration (i). From Fig. 2, one can see that the results of the calculations are in good agreement with the experimental data.

The polarization observables of elastic particle scattering on nuclei having a nonzero spin are much more sensitive to the choice of model density for a target nucleus and to the parameters of the elementary amplitude used than the total cross section, the reaction cross section, or the differential cross section. For example, an appropriate choice of parameters for the imaginary part of the spin–orbit nucleon–nucleus interaction is of paramount importance for correctly describing polarization (asymmetry) [24]. In calculating the observables of elastic p^9Be scattering at 1000 MeV, we first use here the parameters of nucleon–nucleon amplitude that were obtained in [19] for 800 MeV (Figs. 2 and 3, dotted curves).

The dotted curves in Figs. 2 and 3 were calculated with these parameter values under the assumption of configuration (ii). It can be seen that this leads only to qualitative agreement between the calculated and measured polarization (asymmetry) and to a somewhat inadequate behavior of the analyzing power $A_{00NN}(\theta)$ (Fig. 2). In order to improve the description of elastic p^9Be scattering, the imaginary part of the spin–orbit nucleon–nucleon

interaction was then somewhat changed to become -4.51 $(\mathrm{GeV}/c)^{-3}$ in [19] and -10.51 $(\mathrm{GeV}/c)^{-3}$ in the present study (solid and dashed curves in Figs. 2 and 3). As to the parameters of the $p\alpha$ amplitude, they were determined from a fit of the calculated features of p^4He scattering to those measured in [25] at 1000 MeV.

Our calculations demonstrate that the proposed approach makes it possible to describe available experimental data on elastic p^9Be scattering at an energy of 1000 MeV. In the region of small scattering angles, the calculated polarization observables proved to be weakly sensitive to the choice of model density for a target nucleus (see Figs. 2 and 3, solid and dashed curves), but they are greatly dependent on the parameters of the imaginary part of the spin–orbit nucleon–nucleon interaction (Figs. 2 and 3, dotted curves). In the region of high momentum transfers ($\theta \geq 15^\circ$), however, the polarization observables calculated under the assumption of configuration (ii) (Figs. 2 and 3, solid curves) are in qualitatively better agreement with the measured features of p^{13}C scattering [20–22] than those calculated under the assumption of configuration (i) (Figs. 2 and 3, dashed curves).

As was mentioned above, elastic p^9Be scattering was studied in [10, 11] within the theory of multiple diffractive scattering by using the wave functions calculated within the $2\alpha n$ model; the differential cross section and the analyzing power for elastic p^9Be scattering were calculated there in the region of moderate momentum transfers ($\theta \sim 15^\circ$). However, the calculations performed in the present study demonstrate that observables calculated with different wave functions (densities) of target nuclei behave differently in the region of high momentum transfers.

In addition, it should be emphasized that, in the region of small scattering angles, the behavior of the analyzing power and especially of the differential cross section for the elastic scattering of intermediate-energy particles on light nuclei is virtually independent of the choice of target-nucleus model (see, for example, [2]). Other polarization observables are more sensitive to the choice of model density for target nuclei and the choice of elementary-amplitude parameters [2, 16]. For example, it was shown in [2] that the agreement between the calculated and the measured observables of elastic p^{16}O scattering is improved (in relation to what we have in the model of independent nucleons) upon taking into account α-cluster-type correlations in ^{16}O nuclei. Also, the spin-rotation functions calculated within the α-cluster model involving dispersion and within the independent-nucleon model were qualitatively different. A similar effect is observed in calculating

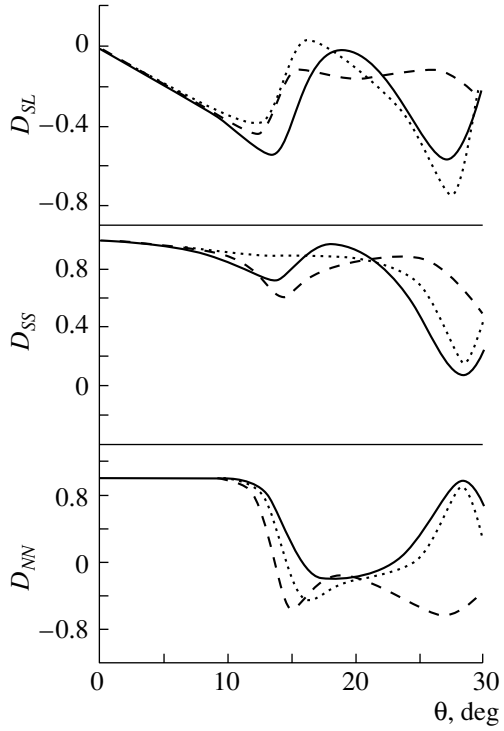

Fig. 3. Depolarization parameters $D_{SL}(\theta)$, $D_{SS}(\theta)$, and $D_{NN}(\theta)$ for elastic proton scattering on ^{9}Be nuclei at 1000 MeV versus the scattering angle θ. The description of the curves is given in the main body of the text.

the polarization observables of elastic p^{13}C and p^{13}N scattering at intermediate energies.

In this connection, it is hardly possible to compare the results of our present calculations with those reported in [10, 11]. There is virtually no doubt that the $2\alpha n$ mode is dominant in the wave function for the ^{9}Be nucleus. Thus, further theoretical and experimental investigations of the interaction between intermediate-energy particles and light nuclei involving one or a few unpaired nucleons would enable us to obtain more detailed information about both the structure of such nuclei and the special features of nucleon–nucleon interaction.

ACKNOWLEDGMENTS

We are grateful to V.V. Pilipenko for stimulating discussions.

REFERENCES

1. Yu. A. Berezhnoy, V. V. Pilipenko, and G. A. Khomenko, J. Phys. G **10**, 63 (1984).
2. Yu. A. Berezhnoy, V. P. Mikhailyuk, and V. V. Pilipenko, J. Phys. G **18**, 85 (1992).
3. Yu. A. Berezhnoy and V. P. Mikhailyuk, Yad. Fiz. **63**, 783 (2000) [Phys. At. Nucl. **63**, 715 (2000)].

4. Yu. A. Berezhnoy and V. P. Mikhailyuk, Izv. Akad. Nauk, Ser. Fiz. **65**, 721 (2001).
5. C. W. Glover *et al.*, Phys. Rev. C **43**, 1664 (1991).
6. G. Roy, Nucl. Phys. A **442**, 686 (1985).
7. D. K. Hassel, Phys. Rev. C **34**, 236 (1986).
8. S. Dixit *et al.*, Phys. Rev. C **43**, 1758 (1991).
9. G. D. Alkhazov, S. L. Belostotskiĭ, A. A. Vorob'ev, *et al.,* Yad. Fiz. **42**, 8 (1985) [Sov. J. Nucl. Phys. **42**, 4 (1985)].
10. M. A. Zhusupov and E. T. Ibraeva, Yad. Fiz. **61**, 51 (1998) [Phys. At. Nucl. **61**, 46 (1998)].
11. M. A. Zhusupov and E. T. Ibraeva, Fiz. Élem. Chastits At. Yadra **31**, 1427 (2000).
12. V. T. Voronchev and V. I. Kukulin, Few-Body Syst. **18**, 191 (1995).
13. G. D. Alkhazov and O. A. Domchenkov, Yad. Fiz. **37**, 84 (1983) [Sov. J. Nucl. Phys. **37**, 46 (1983)].
14. J. P. Glickman *et al.*, Phys. Rev. C **43**, 1740 (1991).
15. H. de Vries, C. W. de Jager, and C. de Vries, At. Data Nucl. Data Tables **36**, 495 (1987).
16. Yu. A. Berezhnoy and V. P. Mikhailyuk, Yad. Fiz. **66**, 702 (2003) [Phys. At. Nucl. **66**, 673 (2003)].
17. W. Greiner, J. Park, and W. Scheid, in *Nuclear Molecules* (World Sci., 1995).
18. J. A. McNeil, L. Ray, and S. J. Wallace, Phys. Rev. C **27**, 2123 (1983).
19. I. N. Kudryavtsev and A. P. Soznik, J. Phys. G **15**, 1377 (1989).
20. G. W. Hoffman, M. L. Barlett, D. Ciskowski, *et al.*, Phys. Rev. C **41**, 1651 (1990).
21. G. W. Hoffman, M. L. Barlett, W. Kielhorn, *et al.*, Phys. Rev. Lett. **65**, 3096 (1990).
22. G. W. Hoffman, L. Ray, D. Read, *et al.*, Phys. Rev. C **53**, 1974 (1996).
23. V. G. Vovchenko *et al.,* Yad. Fiz. **16**, 1145 (1972) [Sov. J. Nucl. Phys. **16**, 628 (1973)].
24. P. Osland and R. G. Glauber, Nucl. Phys. A **326**, 225 (1979).
25. H. Courant *et al.*, Phys. Rev. C **19**, 104 (1979).

Translated by O. Chernavskaya

Physics of Atomic Nuclei, Vol. 67, No. 8, 2004, pp. 1454–1461. Translated from Yadernaya Fizika, Vol. 67, No. 8, 2004, pp. 1480–1487.

NUCLEI
Theory

Interference between Diffractive, Refractive, and Coulomb Effects in the Cross Sections for the Elastic Scattering of Light Nuclei by Nuclei at Intermediate Energies

Yu. A. Berezhnoy and A. S. Molev

Research and Technological Center for Electrophysics, National Academy of Sciences of Ukraine, Kharkov, Ukraine

Received April 16, 2003; in final form, July 16, 2003

Abstract—Patterns typical of Fraunhofer and Fresnel diffractive scattering and of rainbow scattering are considered for elastic nucleus–nucleus scattering in the region of intermediate energies. The interference contributions to the respective differential cross section that are responsible for the formation of these patterns are singled out on the basis of the S-matrix approach. © *2004 MAIK "Nauka/Interperiodica".*

1. INTRODUCTION

In the interaction of intermediate-energy nuclei with nuclei, the presence of strong absorption at moderate orbital angular momenta, of the refraction of scattered waves, and of Coulomb interaction between colliding particles leads to a complicated angular dependence of differential cross sections for scattering. Therefore, investigation of the effect that these factors exert on the pattern of scattering is a problem of importance in scattering theory.

Different combinations of the aforementioned factors may lead to different types of scattering—Fraunhofer or Fresnel diffraction, as well as rainbow scattering or Fraunhofer crossing. These patterns of scattering are usually analyzed in terms of the optical model, which employs a complex-valued interaction potential, including absorptive (imaginary part) and refractive (real part) potentials.

Along with this, there exists an alternative approach to analyzing scattering cross sections, that which employs the scattering matrix. Within this approach, the contributions of absorption and nuclear refraction are determined, respectively, by the modulus of the scattering matrix and by the real part of the phase shift for nuclear scattering. In addition, it is necessary to take into account the Coulomb interaction of colliding particles. Therefore, it is convenient to represent the scattering amplitude as the sum of a few components that are responsible for absorption, refraction, Coulomb interaction, and their interference. Such partitions were constructed in different ways (see, for example, [1–6]) with the aim of studying refractive effects in the differential cross sections for the scattering of light nuclei by nuclei at intermediate energies. In each of the cases being considered, however, an analysis of various special features of the aforementioned patterns requires correctly isolating relevant components in the scattering amplitude. In the present study, we develop precisely such an approach on the basis of the scattering matrix.

2. PARTITION OF THE SCATTERING AMPLITUDE INTO THE DIFFRACTIVE, REFRACTIVE, AND COULOMB COMPONENTS

The amplitude $f(\theta)$ for the elastic scattering of a projectile particle by a nucleus is given by

$$f(\theta) = \frac{i}{2k}\sum_{l=0}^{\infty}(2l+1)(1-S_l)P_l(\cos\theta), \quad (1)$$

where θ is the scattering angle, k is the wave number of the relative motion of colliding particles, S_l is the scattering matrix in the orbital-angular-momentum representation, and $P_l(\cos\theta)$ is a Legendre polynomial.

It is convenient to represent the scattering matrix in the form

$$S_l = \eta_l \exp(2i\delta_l + 2i\sigma_l), \quad (2)$$

where η_l is the modulus of the scattering matrix and δ_l and σ_l are, respectively, the nuclear and the Coulomb phase shift.

Formula (2) demonstrates that the scattering amplitude (1) receives contributions from the components associated with the quantities η_l, δ_l, and σ_l, which characterize absorption, nuclear refraction, and Coulomb interaction, respectively. In order to

1063-7788/04/6708-1454$26.00

determine these components, it is convenient to represent the scattering matrix in the form

$$S_l = 1 - \omega_l^d - \omega_l^r - \omega_l^{\mathrm{C}} - \Delta\omega_l, \tag{3}$$

where

$$\Delta\omega_l = \omega_l^d\omega_l^r\omega_l^{\mathrm{C}} - \omega_l^d\omega_l^r - \omega_l^d\omega_l^{\mathrm{C}} - \omega_l^r\omega_l^{\mathrm{C}}. \tag{4}$$

Here, the diffraction (ω_l^d), refraction (ω_l^r), and Coulomb (ω_l^{C}) profile functions are given by

$$\omega_l^d = 1 - \eta_l, \tag{5}$$

$$\omega_l^r = 1 - \exp(2i\delta_l), \tag{6}$$

$$\omega_l^{\mathrm{C}} = 1 - \exp(2i\sigma_l). \tag{7}$$

Thus, the amplitude in (1) can be represented in the form

$$f(\theta) = f_d(\theta) + f_r(\theta) + f_{\mathrm{C}}(\theta) + \Delta f(\theta), \tag{8}$$

where the diffraction [$f_d(\theta)$], refraction [$f_r(\theta)$], and Coulomb [$f_{\mathrm{C}}(\theta)$] amplitudes are given by

$$f_d(\theta) = \frac{i}{2k}\sum_{l=0}^{\infty}(2l+1)\omega_l^d P_l(\cos\theta), \tag{9}$$

$$f_r(\theta) = \frac{i}{2k}\sum_{l=0}^{\infty}(2l+1)\omega_l^r P_l(\cos\theta), \tag{10}$$

$$f_{\mathrm{C}}(\theta) = \frac{i}{2k}\sum_{l=0}^{\infty}(2l+1)\omega_l^{\mathrm{C}} P_l(\cos\theta), \tag{11}$$

while the interference component of the amplitude, $\Delta f(\theta)$, is written as

$$\Delta f(\theta) = \frac{i}{2k}\sum_{l=0}^{\infty}(2l+1)\Delta\omega_l P_l(\cos\theta). \tag{12}$$

We note that the amplitudes in (9)–(11) are determined by absorption, nuclear refraction, and Coulomb interaction exclusively—that is, they are not distorted by any other factor. Various combinations of the amplitudes in (9)–(11) and of the amplitude components in (12) make it possible to derive components of the elastic-scattering amplitude (1) that are responsible for one combination of nuclear refraction, absorption, and Coulomb interaction of colliding particles or another.

The sum of expressions (9), (10), and (12) is the nuclear amplitude component distorted by Coulomb interaction. In the scattering of intermediate-energy light ions by nuclei, in which case the Coulomb interaction is relatively weak, the effect of their Coulomb fields on the behavior of this amplitude component is insignificant (see, for example, [7, 8]). If the Coulomb interaction of nuclei is strong, which is the case in heavy-ion scattering on medium-mass and heavy nuclei, nuclear and Coulomb interactions strongly interfere.

Along with the differential cross section for elastic scattering,

$$\sigma(\theta) \equiv \frac{d\sigma(\theta)}{d\Omega} = |f(\theta)|^2, \tag{13}$$

we can introduce, in accordance with the partition of the amplitude in (8), its diffraction [$\sigma_d(\theta)$], refraction [$\sigma_r(\theta)$], and Coulomb [$\sigma_{\mathrm{C}}(\theta)$] components; that is,

$$\sigma_d(\theta) \equiv \frac{d\sigma_d(\theta)}{d\Omega} = |f_d(\theta)|^2, \tag{14}$$

$$\sigma_r(\theta) \equiv \frac{d\sigma_r(\theta)}{d\Omega} = |f_r(\theta)|^2,$$

$$\sigma_{\mathrm{C}}(\theta) \equiv \frac{d\sigma_C(\theta)}{d\Omega} = |f_{\mathrm{C}}(\theta)|^2.$$

In order to calculate the differential cross section (13) and its components in (14) numerically, it is necessary to specify the form of the scattering matrix in orbital-angular-momentum space. In specifying the scattering matrix, it is convenient to go over from l to $L = l + 1/2$ and to introduce the notation $\eta(L) = \eta_l$, $\delta(L) = \delta_l$, and $\sigma(L) = \sigma_l$. We parametrize the modulus $\eta(L)$ and the phase shift $\delta(L)$ as

$$\eta(L) = \exp(-2\delta_a(L)), \tag{15}$$

$$2\delta_a(L) = \xi_a[2L\Delta_a G(L, L_a, \Delta_a) + \Delta_a^2 G^2(L, L_a, \Delta_a)]^{1/2} g(L, L_a, \Delta_a), \tag{16}$$

$$2\delta(L) = \xi_r[2L\Delta_r G(L, L_r, \Delta_r) + \Delta_r^2 G^2(L, L_r, \Delta_r)]^{1/2} g^2(L, L_r, \Delta_r), \tag{17}$$

$$G(L, L_j, \Delta_j) = -\frac{\ln[1 - g(L, L_j, \Delta_j)]}{g(L, L_j, \Delta_j)}, \quad j = a, r, \tag{18}$$

$$g(L, L_j, \Delta_j) = \left[1 + \exp\left(\frac{L - L_j}{\Delta_j}\right)\right]^{-1}, \tag{19}$$

where ξ_j is a parameter that characterizes the intensity of absorption ($j = a$) or nuclear refraction ($j = r$), while L_j and Δ_j are parameters that characterize, respectively, the linear dimensions and the smearing of the region of absorption ($j = a$) or nuclear refraction ($j = r$).

For the Coulomb phase shift $\sigma(L)$, we take the semiclassical phase shift for the scattering of a pointlike charge on a uniformly charged sphere of radius R_{C} [9]. This can be done since we consider particle scattering on nuclei at rather high energies.

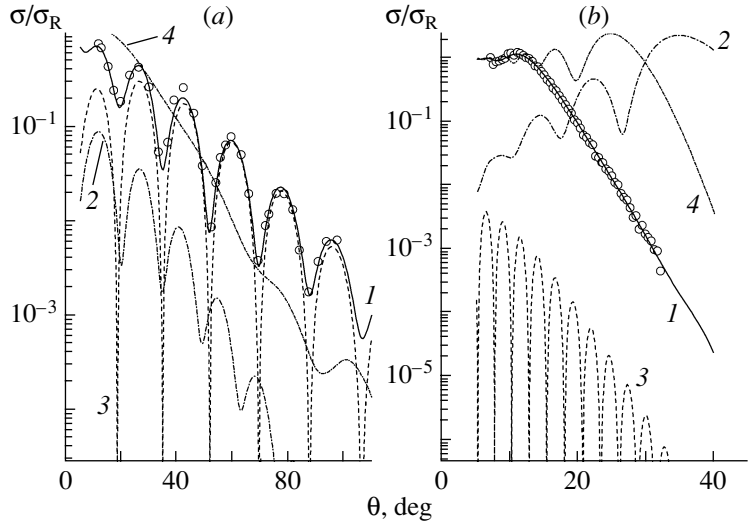

Fig. 1. Ratios of the differential cross sections for elastic (a) ^{3}He–^{26}Mg scattering at $E(^3\mathrm{He}) = 33.67$ MeV and (b) ^{9}Be–^{198}Au scattering at $E(^9\mathrm{Be}) = 158.30$ MeV and of various components of these cross sections to the respective Rutherford cross sections: (curves *1*) results for the total differential cross sections; (curves *2*, *3*, *4*) results for their diffraction, refraction, and Coulomb components, respectively; and (points) experimental data from [10, 11].

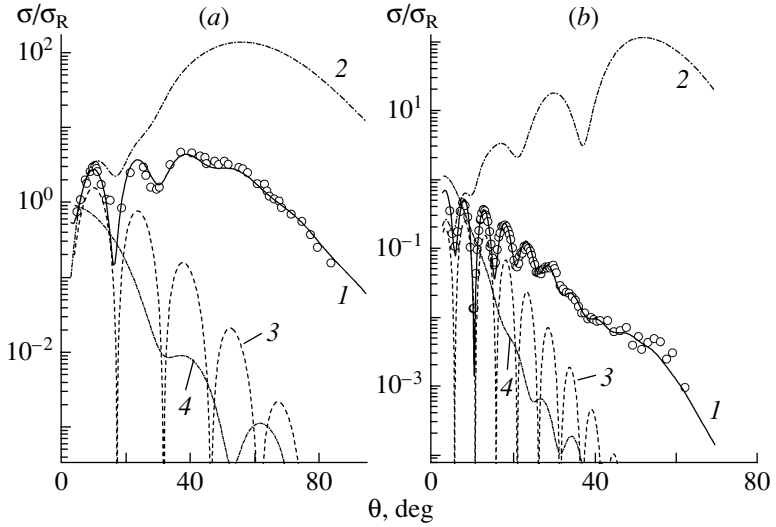

Fig. 2. As in Fig. 1, but for (a) ^{3}He–^{12}C scattering at $E(^3\mathrm{He}) = 82.10$ MeV and (b) ^{13}C–^{12}C scattering at $E(^{13}\mathrm{C}) = 260.00$ MeV. The displayed points represent experimental data from [12, 13].

By using expressions (1), (2), and (13), we have calculated the differential cross sections for the elastic scattering of ^{3}He nuclei by ^{12}C and ^{26}Mg nuclei, of ^{9}Be nuclei by ^{198}Au nuclei, and of ^{13}C nuclei by ^{12}C nuclei at projectile energies lying in the range 11–27 MeV per nucleon. The results of our calculations are displayed in Figs. 1 and 2. The values found for the S-matrix parameters from the best fit of the calculated cross sections to their measured counterparts and used in our calculations are given in the table, along with the resulting values of χ^2. We note that the parameters of the calculations for ^{3}He–^{12}C scattering were borrowed from [14]. In all of the cases considered here, the Coulomb radius R_C was set to the same value as in [15–17]. Along with the differential cross sections, Figs. 1 and 2 also display their diffraction, refraction, and Coulomb components, which were obtained with the aid of expressions (9)–(11) and (14). Figures 1a and 1b show characteristic patterns of Fraunhofer and Fresnel scattering, while Figs. 2a and 2b show characteristic patterns of rainbow scattering. Figures 1 and 2 demonstrate that the interference between the

Parameters used in calculating the differential cross sections for the elastic scattering of ^{3}He, ^{9}Be, and ^{13}C nuclei by, respectively, ^{26}Mg, ^{198}Au, and ^{12}C nuclei

Parameter	Scattering Process			
	^{3}He–^{26}Mg $E = 33.67$ MeV	^{9}Be–^{198}Au $E = 158.00$ MeV	^{3}He–^{12}C $E = 82.10$ MeV	^{13}C–^{12}C $E = 260.00$ MeV
L_a	7.059	59.969	11.003	31.244
L_r	13.304	43.099	8.740	23.600
Δ_a	1.427	6.083	1.941	3.637
Δ_r	1.948	14.972	3.079	7.747
ξ_a	2.6960	0.2558	0.2270	0.1925
ξ_r	0.053	0.731	1.197	1.064
R_C, fm	4.147	7.899	3.205	4.409
χ^2	1.2	0.8	3.3	3.5

different components of the amplitude in (8) plays an important role for the cross section describing elastic nucleus–nucleus scattering, since none of the contributions in (14) is able to reproduce available experimental data completely. By way of example, we indicate that, in the case of ^{3}He–^{26}Mg scattering, the diffraction contribution $\sigma_d(\theta)$ (Fig. 1*a*) for $\theta > 40^\circ$ reproduces, by and large, the shape and the maxima of Fraunhofer oscillations, but it fails to describe the minima of these oscillations. For elastic ^{9}Be–^{198}Au scattering (Fig. 1*b*), the Coulomb contribution $\sigma_C(\theta)$ is responsible for the behavior of the differential cross sections only at small angles ($\theta \leq 12^\circ$).

For the profile functions in (3) and (4), we discuss, in the following, the choice of appropriate combinations that would make it possible to explain the complicated behavior of the differential cross sections for nucleus–nucleus scattering of various types.

3. INTERFERENCE AMPLITUDES FOR DESCRIBING DIFFRACTIVE, REFRACTIVE, AND COULOMB EFFECTS IN THE ELASTIC SCATTERING OF LIGHT NUCLEI

In the present study, we propose determining dominant contributions to the differential cross section for elastic scattering on the basis of which factor—absorption, nuclear refraction, or Coulomb interaction—plays a dominant role in the formation of the cross section in the scattering-angle region being considered, this leading to different patterns of scattering, as was indicated above. In accordance with this, we will single out, in the scattering matrix [see Eqs. (3), (4)], those groups of terms that correspond to strong absorption, strong Coulomb interaction, or strong nuclear refraction. Below, we consider each such case individually.

If the Fraunhofer mode of scattering is realized, in which case there is strong absorption over a rather broad range of orbital angular momenta, it is advisable to single out, in the profile function $\omega(L) = 1 - S(L)$, a group of terms involving $\omega_d(L)$; that is,

$$\Delta\omega_a(L) = \omega_d(L) - \omega_d(L)\omega_r(L) - \omega_d(L)\omega_C(L) + \omega_d(L)\omega_r(L)\omega_C(L). \quad (20)$$

By grouping the remaining terms, which characterize nuclear refraction and Coulomb interaction, we arrive at

$$\Delta\omega_{rC}(L) = \omega_r(L) - \omega_r(L)\omega_C(L) + \omega_C(L). \quad (21)$$

This partition of the profile function (scattering matrix) leads to two interference amplitudes $f^a_{\rm int}(\theta)$ and $f^{rC}_{\rm int}(\theta)$, which are given by

$$f^a_{\rm int}(\theta) = \frac{i}{2k}\sum_{l=0}^{\infty}(2l+1)\Delta\omega_a(L)P_l(\cos\theta), \quad (22)$$

$$\Delta\omega_a(L) = (1-\eta(L))\exp(2i\delta(L) + 2i\sigma(L)); \quad (23)$$

$$f^{rC}_{\rm int}(\theta) = \frac{i}{2k}\sum_{l=0}^{\infty}(2l+1)\Delta\omega_{rC}(L)P_l(\cos\theta), \quad (24)$$

$$\Delta\omega_{rC}(L) = 1 - \exp(2i\delta(L) + 2i\sigma(L)). \quad (25)$$

The amplitude in (22) is determined by strong absorption in the presence of nuclear and Coulomb refraction, while the amplitude in (24) is controlled by nuclear and Coulomb refraction exclusively.

We note that it is advisable to isolate the interference components (22) and (24) in the scattering

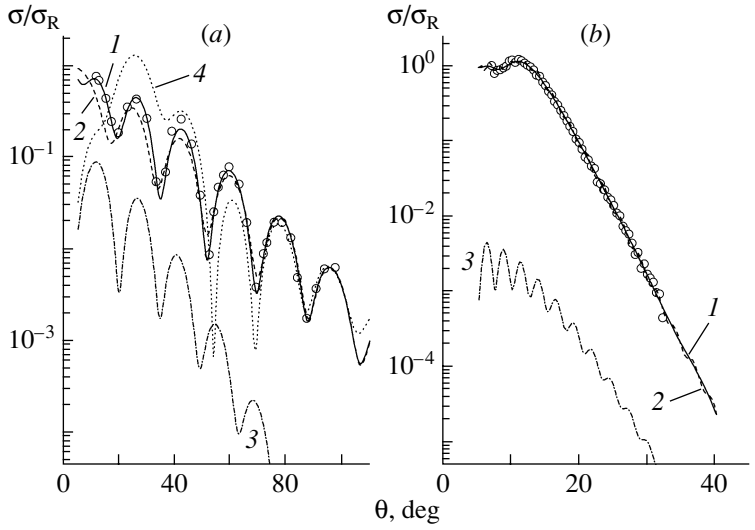

Fig. 3. (*a*) Ratio of the differential cross section for elastic ^{3}He–^{26}Mg scattering at $E(^3\mathrm{He}) = 33.67$ MeV and of the various components of this cross section to the respective Rutherford cross sections: (curve *1*) results for the total differential cross section; (curves *2*, *3*, *4*) results for, respectively, the cross-section components $\sigma_{\mathrm{int}}^{a\mathrm{C}}(\theta)$, $\sigma_r(\theta)$, and $\sigma_{\mathrm{int}}^{a}(\theta)$, which were calculated by formulas (31), (14), and (26); and (points) experimental data from [10]. (*b*) Ratio of the differential cross section for elastic ^{9}Be–^{198}Au scattering at $E(^9\mathrm{Be}) = 158.30$ MeV and of the various components of this cross section to the respective Rutherford cross sections: (curves *1*, *2*, *3*) results for, respectively, the total differential cross sections, the cross-section component (34), and the cross-section component (36) and (points) experimental data from [11]. The parameter values used in calculating the above cross sections are given in the table.

amplitude (1) if the nuclear refraction and Coulomb interaction are weak.

The interference contributions to the differential cross section for scattering that are due to the amplitudes in (22) and (24) are given by

$$\sigma_{\mathrm{int}}^{a}(\theta) = |f_{\mathrm{int}}^{a}(\theta)|^2, \quad \sigma_{\mathrm{int}}^{r\mathrm{C}}(\theta) = \left|f_{\mathrm{int}}^{r\mathrm{C}}(\theta)\right|^2. \quad (26)$$

If the pattern of scattering exhibits features of a diffractive behavior of the Fraunhofer type, its formation being significantly affected by the Coulomb interaction, this pattern will be analyzed here by using the above profile function (20), together with the terms in (21) that involve $\omega_{\mathrm{C}}(L)$,

$$\Delta\omega_{a\mathrm{C}}(L) = \Delta\omega_a(L) + \omega_{\mathrm{C}}(L) - \omega_{\mathrm{C}}(L)\omega_r(L). \quad (27)$$

In this case, the elastic-scattering amplitude can be represented in the form

$$f(\theta) = f_{\mathrm{int}}^{a\mathrm{C}}(\theta) + f_r(\theta), \quad (28)$$

$$f_{\mathrm{int}}^{a\mathrm{C}}(\theta) = \frac{i}{2k}\sum_{l=0}^{\infty}(2l+1)\Delta\omega_{a\mathrm{C}}(L)P_l(\cos\theta), \quad (29)$$

$$\Delta\omega_{a\mathrm{C}}(L) = [1 - \eta(L)\exp(2i\sigma(L))]\exp(2i\delta(L)), \quad (30)$$

where $f_r(\theta)$ is the refraction amplitude (10).

Taking into account relation (28), we introduce the differential cross section

$$\sigma_{\mathrm{int}}^{a\mathrm{C}}(\theta) = \left|f_{\mathrm{int}}^{a\mathrm{C}}(\theta)\right|^2, \quad (31)$$

which is controlled by the interference between the Coulomb and nuclear interactions.

Figure 3*a* displays the results obtained by decomposing the differential cross section for elastic ^{3}He–^{26}Mg scattering at $E(^3\mathrm{He}) = 33.67$ MeV into the components given by (14), (26), and (31). This cross section is typical of diffractive scattering in the case of a weak Coulomb interaction. From Fig. 3*a* and from the table, it can be seen that this example corresponds to the case where the contribution of the form (31) is dominant in the angular region being studied, the interference contribution $\sigma_{\mathrm{int}}^{a}(\theta)$ given by (26) being responsible for the behavior of the cross section only in the range $75^\circ < \theta < 105^\circ$.

In describing the scattering pattern belonging to the Fresnel type and arising in the case of a strong Coulomb interaction of colliding particles, we will use the following procedure to determine that contribution to the differential cross section which is responsible for the features peculiar to this pattern: we break down the profile function $\omega(L)$ into two components in such a way that one component involves all terms containing $\omega_{\mathrm{C}}(L)$, while the other component

involves all of the remaining terms (those that do not enter into the first one):

$$\Delta\omega_{\rm C}(L) = \omega_{\rm C}(L) - \omega_{\rm C}(L)\omega_d(L) - \omega_{\rm C}(L)\omega_r(L) + \omega_{\rm C}(L)\omega_d(L)\omega_r(L), \quad (32)$$

$$\Delta\omega_{rd}(L) = \omega_r(L) - \omega_r(L)\omega_d(L) + \omega_d(L). \quad (33)$$

We note that the profile function $\Delta\omega_{rd}$ is controlled both by a strong absorption and by nuclear refraction, the latter being moderate in the case being considered.

Further, we find the components of the elastic-scattering amplitude that correspond to the partition in (32) and (33) and the respective interference contributions to the differential cross section for the scattering process. We have

$$\sigma^{\rm C}_{\rm int}(\theta) = \left|f^{\rm C}_{\rm int}(\theta)\right|^2, \quad (34)$$

$$f^{\rm C}_{\rm int}(\theta) = \frac{i}{2k}\sum_{l=0}^{\infty}(2l+1)\Delta\omega_{\rm C}(L)P_l(\cos\theta),$$

$$\Delta\omega_{\rm C}(L) = [1 - \exp(2i\sigma(L))]\eta(L)\exp(2i\delta(L)); \quad (35)$$

$$\sigma^{rd}_{\rm int}(\theta) = \left|f^{rd}_{\rm int}(\theta)\right|^2, \quad (36)$$

$$f^{rd}_{\rm int}(\theta) = \frac{i}{2k}\sum_{l=0}^{\infty}(2l+1)\Delta\omega_{rd}(L)P_l(\cos\theta),$$

$$\Delta\omega_{rd}(L) = 1 - \eta(L)\exp(2i\delta(L)). \quad (37)$$

For the example of elastic ^{9}Be–^{198}Au scattering at $E(^9\text{Be}) = 158.30$ MeV, Fig. 3*b* displays the results obtained by analyzing the Fresnel pattern of scattering with the aid of expressions (34)–(37). It can be seen that the interference contribution computed with the aid of expressions (34) is nearly coincident with the differential cross section in the angular region being considered. This contribution is responsible for all special features of the observed pattern of scattering, the contribution given by (36) being small.

Let us now consider the emergence of the interference pattern associated with rainbow scattering or Fraunhofer crossing, in which case there are a strong nuclear refraction and a small transparency with respect to partial waves of low orbital angular momenta. We represent the profile function in the form

$$\omega(L) = \Delta\omega_r(L) + \Delta\omega_{d\rm C}(L), \quad (38)$$

$$\Delta\omega_r(L) = \omega_r(L) - \omega_r(L)\omega_d(L) - \omega_r(L)\omega_{\rm C}(L) + \omega_r(L)\omega_d(L)\omega_{\rm C}(L), \quad (39)$$

$$\Delta\omega_{d\rm C}(L) = \omega_d(L) - \omega_d(L)\omega_{\rm C}(L) + \omega_{\rm C}(L), \quad (40)$$

where the profile function $\Delta\omega_r(L)$ consists of terms involving $\omega_r(L)$, while the function $\Delta\omega_{d\rm C}(L)$ takes into account absorption and the Coulomb interaction of colliding particles.

Using expressions (39) and (40), we now determine the interference amplitudes $f^r_{\rm int}(\theta)$ and $f^{d\rm C}_{\rm int}(\theta)$, which show, in the case being considered, an absorptive behavior and a diffractive behavior, respectively; that is,

$$f^r_{\rm int}(\theta) = \frac{i}{2k}\sum_{l=0}^{\infty}(2l+1)\Delta\omega_r(L)P_l(\cos\theta), \quad (41)$$

$$\Delta\omega_r(L) = [1 - \exp(2i\delta(L))]\eta(L)\exp(2i\sigma(L)); \quad (42)$$

$$f^{d\rm C}_{\rm int}(\theta) = \frac{i}{2k}\sum_{l=0}^{\infty}(2l+1)\Delta\omega_{d\rm C}(L)P_l(\cos\theta), \quad (43)$$

$$\Delta\omega_{d\rm C}(L) = 1 - \eta(L)\exp(2i\sigma(L)). \quad (44)$$

Indeed, the amplitude in (41) is determined by nuclear refraction modified by the absorption and Coulomb interaction, while the amplitude in (43) is controlled exclusively by the absorption of scattered particles, which is distorted by the Coulomb interaction. By evaluating the square of the modulus of the amplitude $f^r_{\rm int}(\theta)$ or $f^{d\rm C}_{\rm int}(\theta)$, we obtain the corresponding interference contribution $\sigma^r_{\rm int}(\theta)$ or $\sigma^{d\rm C}_{\rm int}(\theta)$ to the differential cross section $\sigma(\theta)$. We have

$$\sigma^r_{\rm int}(\theta) = |f^r_{\rm int}(\theta)|^2, \quad (45)$$

$$\sigma^{d\rm C}_{\rm int}(\theta) = \left|f^{d\rm C}_{\rm int}(\theta)\right|^2. \quad (46)$$

Expressions (41)–(46) were used in [3–5] to determine those contributions to the cross sections for the elastic scattering of intermediate-energy stable and radioactive light nuclei on nuclei that are dominant in the diffraction region and in the region where refractive (rainbow) effects manifest themselves.

Figure 4 shows the results obtained by calculating, on the basis of expressions (1), (13), and (41)–(46), the interference contributions to the differential cross sections for elastic ^{3}He–^{12}C and ^{13}C–^{12}C scattering. For the scattering of light ions ^{3}He (see Fig. 4*a*), the interference contribution $\sigma^r_{\rm int}(\theta)$ exhibits a rainbow-type behavior and faithfully reproduces the differential cross section in question within the region where one observes a broad rainbow maximum and an exponential decrease following this maximum. Over the scattering-angle region being considered, the interference contribution $\sigma^{d\rm C}_{\rm int}(\theta)$ displays regular

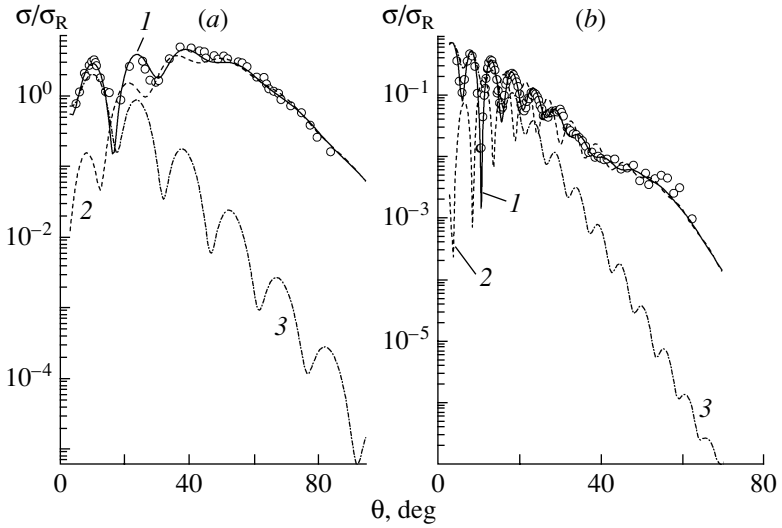

Fig. 4. Ratios of the differential cross sections for elastic (*a*) ^{3}He–^{12}C scattering at $E(^3\mathrm{He}) = 82.10$ MeV and (*b*) ^{13}C–^{12}C scattering at $E(^{13}\mathrm{C}) = 260.00$ MeV and of the various components of these cross sections to the respective Rutherford cross sections: (curves *1*, *2*, *3*) results for, respectively, the total differential cross section, the cross-section component (45), and the cross-section component (46) and (points) experimental data from [12, 13]. The parameter values used in the calculations are given in the table.

diffractive oscillations. This contribution to the differential cross section for elastic ^{3}He–^{12}C scattering proves to be dominant in the region of small angles ($\theta \leq 15^\circ$).

In the scattering of the heavier nuclei ^{13}C, in which case the absorption in the region of moderately low angular momenta is sizably greater than in the scattering of light ions, the contribution $\sigma_{\mathrm{int}}^{dC}(\theta)$, whose behavior is diffractive, is dominant in the scattering-angle region $\theta \leq 20^\circ$ (see Fig. 4*b*). In the region of larger angles, the differential cross section for elastic ^{13}C–^{12}C scattering is determined primarily by the contribution from the interference between the amplitudes in (41) and (43), while, for $\theta \geq 50^\circ$, the cross section in question is faithfully reproduced by the interference contribution $\sigma_{\mathrm{int}}^{r}(\theta)$ alone, which shows a refractive behavior.

4. CONCLUSION

None of those contributions to the differential cross sections for the elastic scattering of intermediate-energy light nuclei by nuclei that are associated with only one factor (absorption, nuclear refraction, or Coulomb absorption) each is able to reproduce the complicated angular dependence of these cross sections over a broad range of scattering angles. In the present study, we have proposed a method for isolating, in the elastic-scattering cross sections, various contributions that are responsible for the formation of special features of these cross sections, this making it possible to find out which specific combination of absorption, nuclear refraction, and Coulomb interaction leads to the observed pattern of scattering. According to this method, the scattering matrix in orbital-angular-momentum space can be represented as the sum of components involving the diffraction, refraction, and Coulomb profile functions and their combinations. The proposed method enables one to pinpoint the profile functions whose interference leads to the different types of behavior of the differential cross section for elastic scattering.

A dominant contribution to the differential cross section for scattering of the Fraunhofer type is determined by all scattering-matrix components involving the diffraction profile function and, in view of the fact that the Coulomb interaction of colliding particles is modest in the case being considered, also by the components involving the Coulomb profile function.

The elastic-scattering differential cross section showing behavior of the Fresnel type is basically reproduced by a contribution that can be found by using the scattering-matrix components involving the Coulomb profile function.

The formation of the differential cross section exhibiting the pattern of rainbow scattering or Fraunhofer crossing can be conveniently represented in terms of two contributions such that one is determined by the diffraction and Coulomb profile functions and their products, while the other is controlled by all scattering-matrix components involving the refraction profile function. The former and the latter are dominant in, respectively, the region of small scattering angles and the region where one observes a

broad rainbow maximum and an exponential decrease that follows this maximum.

Thus, the use of the proposed method, which consists in breaking down the differential cross sections for the elastic scattering of intermediate-energy light nuclei on nuclei into components that have clear physical meaning, makes it possible to deduce important information about observed effects associated with manifestations of strong absorption, nuclear refraction, and the Coulomb interaction of colliding particles.

ACKNOWLEDGMENTS

This work was supported by the State Foundation of Ukraine for Basic Research (project no. 02/07.372).

REFERENCES

1. M. P. Pato and M. S. Hussein, Phys. Lett. B **207**, 121 (1988).
2. M. P. Pato and M. S. Hussein, Phys. Rep. **189**, 127 (1990).
3. A. V. Kuznichenko, A. S. Molev, and G. M. Onishenko, in *Proceedings of the International Meeting on Nuclear Spectroscopy and Nuclear Structure, Alma-Ata, 1992* (Nauka, St. Petersburg, 1992), p. 271.
4. A. S. Molev, Izv. Akad. Nauk, Ser. Fiz. **59**, 96 (1995).
5. R. da Silveira, S. Klarsfeld, A. Bonkour, *et al.*, Phys. Rev. C **48**, 468 (1993).
6. E. Stiliaris, H. G. Bohlen, P. Fröbrich, *et al.*, Phys. Lett. B **223**, 291 (1989).
7. W. E. Frahn, *Diffractive Processes in Nuclear Physics* (Clarendon, Oxford, 1985).
8. A. I. Akhiezer, Yu. A. Berezhnoy, and V. V. Pilipenko, Fiz. Élem. Chastits At. Yadra **31**, 458 (2000).
9. Yu. A. Berezhnoy and V. V. Pilipenko, Mod. Phys. Lett. A **10**, 2305 (1995).
10. T. F. Hill and W. E. Frahn, Ann. Phys. (N.Y.) **124**, 1 (1980).
11. C. B. Fulmer, G. R. Satchler, K. A. Erb, *et al.*, Nucl. Phys. A **427**, 545 (1984).
12. T. Tanabe, K. Koyama, M. Yasue, *et al.*, J. Phys. Soc. Jpn. **41**, 361 (1976).
13. H. G. Bohlen, X. S. Chen, J. G. Cramer, *et al.*, Z. Phys. A **322**, 241 (1985).
14. A. S. Molev, Izv. Akad. Nauk, Ser. Fiz. **64**, 965 (2000).
15. H.-J. Trost, A. Schwarz, U. Feindt, *et al.*, Nucl. Phys. A **337**, 377 (1980).
16. Yu. A. Berezhnoy and V. V. Pilipenko, Heavy Ion Phys. **3**, 249 (1996).
17. M. E. Brandan and G. R. Satchler, Nucl. Phys. A **487**, 477 (1988).

Translated by A. Isaakyan

Physics of Atomic Nuclei, Vol. 67, No. 8, 2004, pp. 1462–1477. Translated from Yadernaya Fizika, Vol. 67, No. 8, 2004, pp. 1488–1502.

NUCLEI
Theory

Near-Barrier Fusion of Heavy Nuclei: Coupling of Channels

V. I. Zagrebaev* **and V. V. Samarin**

Joint Institute for Nuclear Research, Dubna, Moscow oblast, 141980 Russia

Received April 29, 2003; in final form, November 10, 2003

Abstract—The problem of a quantum-mechanical description of a near-barrier fusion of heavy nuclei that occurs under the conditions of a strong coupling of their relative motion to the rotation of deformed nuclei and to a dynamical deformation of their surfaces is studied. A new efficient method is proposed for numerically solving coupled Schrödinger equations with boundary conditions corresponding to a total absorption of the flux that has overcome a multidimensional Coulomb barrier. The new method involves no limitations on the number of channels that are taken into account and makes it possible to calculate cross sections for the fusion of very heavy nuclei that are used in the synthesis of superheavy elements. A global analysis of the relief of the multidimensional potential surface and of the multichannel wave function in the vicinity of the Coulomb barrier provides a clear interpretation of the dynamics of near-barrier nuclear fusion. A comparison with experimental data and with the results produced by the semiempirical model for taking into account the coupling of channels is performed. © *2004 MAIK "Nauka/Interperiodica".*

INTRODUCTION

The near-barrier fusion of nuclei still attracts the attention of theorists and experimentalists. The dynamics of low-energy fusion is governed by quantum tunneling through a Coulomb barrier, this occurring under conditions where relative motion is strongly coupled to internal degrees of freedom—primarily, to vibrations of nuclear surfaces, the rotation of deformed nuclei, and nucleon transfer [1]. We note that this theoretical problem arises in many realms of physics and chemistry. A considerable improvement of experimental techniques that has been achieved over the past few years in this field provides the possibility of performing precision measurements enabling one to study the details of the subbarrier-fusion process and subtle effects accompanying it (see, for example, [2, 3] and the review article of Dasgupta *et al.* [4]). It is hardly possible to solve the respective quantum-mechanical problem (or its semiclassical analog) exactly. As a result, we still do not have an unambiguous interpretation of experimental data in some cases, despite a rather good understanding of the physics of the process in general. The situation is even worse in predicting subbarrier-fusion cross sections for as-yet-unexplored combinations of heavy nuclei, but such predictions are of paramount importance for planning and performing expensive experiments on the synthesis of superheavy elements.

A few algorithms for numerically solving the set of coupled Schrödinger equations that simulates the coupling of channels in the near-barrier fusion of heavy nuclei have been proposed in recent years. These algorithms rely either on employing some approximate method to diagonalize the coupling matrix at the barrier [5] or on directly constructing a numerical solution to the relevant differential equations [6]. As was shown in [7], colliding heavy nuclei develop rather large dynamical deformations upon the inclusion of realistic forces of nucleus–nucleus interactions, and it is necessary to take into account a large number of excited phonons in order to describe these deformations. Following basically the same line of reasoning as in [6], we developed a new algorithm for solving a set of second-order differential equations. This algorithm makes its possible to avoid imposing any limitations on the number of channels that are taken into account. The second distinctive feature of our approach is that we consider boundary conditions on the incident flux more accurately; that is, we ensure a complete absence of waves reflected from the region behind the barrier. In addition to the barrier penetrability, this makes it possible to calculate the multidimensional wave function itself in the near-barrier region. This function can be used to obtain, via a detailed analysis, deeper insight into the dynamics of multidimensional tunneling. In just the same way as in [6], we do not resort to the linear approximation in the coupling interaction, but, in contrast to [6], we use an explicit (quadrature) method for calculating the matrix elements of the interaction, this method ensuring a preset accuracy independent of the number of channels that are taken into account. This approach is used to analyze the fusion of statically deformed and spherically deformed heavy nuclei. We

*e-mail: valeri.zagrebaev@jinr.ru

1063-7788/04/6708-1462$26.00

compare our results with experimental data and with the results obtained on the basis of the semiempirical model developed for taking into account the coupling of channels in fusion processes.

1. INTERACTION OF DEFORMED NUCLEI

The shape of an axisymmetric deformed nucleus can be described by the formula

$$R(\boldsymbol{\beta},\theta)=\tilde{R}\left(1+\sum_{\lambda\geq 2}\beta_\lambda\sqrt{\frac{2\lambda+1}{4\pi}}P_\lambda(\cos\theta)\right), \tag{1}$$

where $\boldsymbol{\beta}\equiv\{\beta_\lambda\}$ are the dimensionless deformation parameters of multipolarity $\lambda=2,3,...$; P_λ are Legendre polynomials;

$$\tilde{R}=R_0\Bigg[1+\frac{3}{4\pi}\sum_\lambda\beta_\lambda^2 + \frac{1}{4\pi}\sum_{\lambda,\lambda',\lambda''}\sqrt{\frac{(2\lambda'+1)(2\lambda''+1)}{4\pi(2\lambda+1)}} \times(\lambda'0\lambda''0|\lambda0)^2\beta_\lambda\beta'_\lambda\beta''_\lambda\Bigg]^{-1/3}; \tag{2}$$

R_0 is the radius of an equivalent sphere that has the same volume as the deformed nucleus being considered; and $(\lambda'0\lambda''0|\lambda0)$ are Clebsch–Gordan coefficients. The potential energy of the interaction of two deformed nuclei can be written as the sum of the Coulomb and nuclear energies and the deformation energy in the harmonic approximation; that is,

$$V_{12}(r;\boldsymbol{\beta}_1,\theta_1,\boldsymbol{\beta}_2,\theta_2)=V_{\rm C}(r;\boldsymbol{\beta}_1,\theta_1,\boldsymbol{\beta}_2,\theta_2) + V_N(r;\boldsymbol{\beta}_1,\theta_1,\boldsymbol{\beta}_2,\theta_2)+\frac{1}{2}\sum_{i=1}^{2}\sum_\lambda C_{i\lambda}(\beta_{i\lambda}-\beta_{i\lambda}^{\rm g.s.})^2. \tag{3}$$

Here and below, the index $i=1,2$ numbers interacting nuclei; $C_{i\lambda}$ are the stiffness parameters of the nuclear surface; $\theta_{1,2}$ specify the orientations of the symmetry axes of deformed nuclei (see Fig. 1); and $\beta_{i\lambda}^{\rm g.s.}$ are the static deformations of the nuclei.

Disregarding multipole–multipole interactions and retaining terms to second order in the deformations inclusive, we can represent the Coulomb interaction of deformed nuclei in the form

$$V_{\rm C}=Z_1Z_2e^2\times\left[F^{(0)}(r)+\sum_{i=1}^{2}\sum_{\lambda\geq 2}F_{i\lambda}^{(1)}(r)\beta_{i\lambda}Y_{\lambda0}(\theta_i)\right] + Z_1Z_2e^2\sum_{i=1}^{2}\sum_{\lambda'}\sum_{\lambda''}\sum_{\lambda=|\lambda'-\lambda''|}^{\lambda'+\lambda''}F_{i\lambda}^{(2)}(r) \tag{4}$$

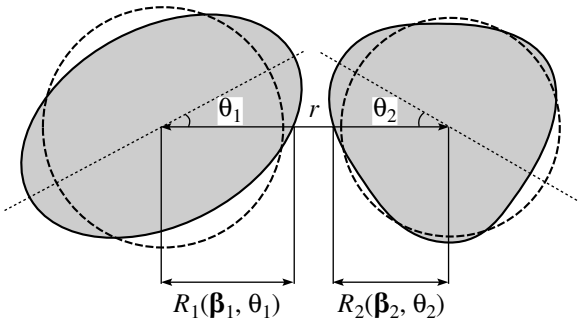

Fig. 1. Relative disposition of two deformed nuclei rotating in the reaction plane ($\boldsymbol{\beta}_i=\{\beta_{i\lambda}\}$).

$$\times\sum_{\mu=-\min\{\lambda',\lambda''\}}^{\min\{\lambda',\lambda''\}}\int Y^*_{\lambda'\mu}Y^*_{\lambda''-\mu}Y_{\lambda0}d\Omega \times\beta_{i\lambda'}\beta_{i\lambda''}Y_{\lambda0}(\theta_i)+\ldots,$$

where $F_\lambda^{(n)}(r)$ are the interaction form factors. For $r>R_1+R_2$, we have

$$F^{(0)}=\frac{1}{r},\quad F_{i\lambda}^{(1)}=\frac{3}{2\lambda+1}\frac{R_i^\lambda}{r^{\lambda+1}},$$
$$F_{i\lambda=2}^{(2)}=\frac{6}{5}\frac{R_i^2}{r^3},\quad F_{i\lambda=4}^{(2)}=\frac{R_i^4}{r^5}.$$

At smaller values of r, in which case the nuclear surfaces are overlap, the form factors $F_\lambda^{(n)}(r)$ are given by more complicated expressions [8], but this is insignificant for fusion processes, because, here, the position of the Coulomb barrier satisfies the condition $R_{\rm C}^B>R_1+R_2$. In describing the rotation of deformed nuclei, one usually takes into account their quadrupole and (or) hexadecapole deformations. Since the strong inequality $\beta_4\ll 1$ holds as a rule, only $\lambda'=\lambda''=2$ terms are retained in the third term, the values of 2 and 4 being taken for λ.

Short-range nuclear interaction depends on the distance between the nuclear surfaces, which is usually set to the distance along the axis connecting the centers of the nuclei involved, $\xi=r-R_1(\boldsymbol{\beta}_1,\theta_1)-R_2(\boldsymbol{\beta}_2,\theta_2)$, or to the minimum distance between their surfaces (see Fig. 1). This interaction is often approximated by the Woods–Saxon potential $V_{\rm WS}(\xi)=V_0[1+\exp(\zeta/a_V)]^{-1}$, where $\zeta=r-R_V-\Delta R_1-\Delta R_2$, $\Delta R_1=R_1(\boldsymbol{\beta}_1,\theta_1)-R_1$, and $\Delta R_2=R_2(\boldsymbol{\beta}_2,\theta_2)-R_2$. It should be recalled that, for the Woods–Saxon potential, the interaction range $R_V=r_0^V(A_1^{1/3}+A_2^{1/3})$ usually does not coincide with the sum of the radii of the nuclei themselves, so that r_0^V is an additional independent parameter. As an alternative possibility, one can describe nuclear

interaction in terms of the "proximity" potential [9]

$$V_{\text{prox}}(\xi) = 4\pi\gamma b P_{\text{sph}}^{-1}\Phi(\xi/b), \quad (5)$$

where $\Phi(\xi/b)$ is a universal dimensionless form factor; b is a parameter that characterizes the surface-layer thickness (about 1 fm); $\gamma = \gamma_0(1 - 1.7826I^2)$, with $\gamma_0 = 0.95$ MeV fm^{-2} being the surface-tension coefficient and I being given by $I = (N - Z)/A$; $\xi = r - R_1(\boldsymbol{\beta}_1, \theta_1) - R_2(\boldsymbol{\beta}_2, \theta_2)$; and $P_{\text{sph}} = 1/\bar{R}_1 + 1/\bar{R}_2$ with $\bar{R}_i = R_i[1 - (b/R_i)^2]$. This interaction is the most sensitive to the choice of matter radii for nuclei. The most realistic results are obtained if use is made of $r_0 \approx 1.16$ fm for the radii of heavy nuclei ($A > 40$) and of $r_0 \approx 1.22$ fm for the radii of $A \sim 16$ nuclei. The most important advantage of the proximity potential is that it is universal in the sense that this potential features no adjustable parameters like V_0, r_0^V, or a_V.

The attraction of two nuclear surfaces also depends on their curvature [9, 10]—that is, on the area of touching surfaces. Usually, this is taken into account by replacing the quantity P_{sph} in (5) by the expression

$$P(\boldsymbol{\beta}_1, \theta_1, \boldsymbol{\beta}_2, \theta_2) = \left[(k_1^{\parallel} + k_2^{\parallel})(k_1^{\perp} + k_2^{\perp})\right]^{1/2}, \quad (6)$$

where $k_i^{\parallel,\perp}$ are the principal parameters of the local curvature of the surfaces of interacting nuclei (see, for example, [11]). For spherical nuclei, $k_i^{\parallel,\perp} = R_i^{-1}$ and $P = P_{\text{sph}}$. In the case of dynamical deformations along the axis connecting the centers of the two nuclei ($\theta_1 = \theta_2 = 0$)—it is realized in slow collisions of dynamically deformable nuclei—the local curvature can be found explicitly (see Appendix 1), which yields

$$P(\boldsymbol{\beta}_1, \theta_1 = 0, \boldsymbol{\beta}_2, \theta_2 = 0) \quad (7)$$
$$= \sum_{i=1,2} \frac{1}{\tilde{R}_i}\left(1 + \sum_{\lambda\geq 2}\sqrt{\frac{2\lambda+1}{4\pi}}\beta_{i\lambda}\right)^{-2}$$
$$\times \left(1 + \sum_{\lambda\geq 2}(1 + \eta(\lambda))\sqrt{\frac{2\lambda+1}{4\pi}}\beta_{i\lambda}\right),$$

where $\eta(\lambda) = 3 \cdot 4 \cdots (\lambda + 1)/(\lambda - 1)!$. For rotating deformed nuclei, it is necessary, in principle, to take into account the difference of the shortest distance ξ_S between the surfaces and the distance ξ calculated along the central line (see Fig. 1). For realistic deformations, however, the resulting effect of taking into account the inequality of ξ_S and ξ in calculating the interaction potentials and fusion cross sections is quite small in relation to the effect of the change in the curvature ($P \neq P_{\text{sph}}$) [12].

Formally, expression (6) can vanish at some negative values of the deformation (the touching of two planar surfaces). This unphysical effect arises because of the disregard of finite dimensions of the areas of touching nuclear surfaces and indicates that it is necessary to go over to a more precise approximation at large negative deformations. The main contribution to the nucleus–nucleus potential comes from the interactions of the most closely spaced nucleons, whose number, albeit depending on the local curvature of the surfaces, is always finite. Thus, we see that, instead of merely substituting the quantity P for P_{sph} in (5), it would be more correct, for the short-range nucleus–nucleus interaction, to employ the expression $V_N = G(\boldsymbol{\beta}_1, \theta_1, \boldsymbol{\beta}_2, \theta_2)V_N^0(r; \boldsymbol{\beta}_1, \theta_1, \boldsymbol{\beta}_2, \theta_2)$, where $V_N^0(r; \boldsymbol{\beta}_1, \boldsymbol{\theta}_1, \boldsymbol{\beta}_2, \theta_2)$ is the interaction that was calculated with allowance for the deformations of the nuclei and their relative orientation but without taking into account the change in the curvature of the surfaces, while $G(\boldsymbol{\beta}_1, \theta_1, \boldsymbol{\beta}_2, \theta_2)$ is a geometric factor that takes into account the change in the number of interacting nucleons that occur in the closely spaced layers of the two nuclei in relation to the case of spherical surfaces. In Appendix 2, we present a derivation of an approximate expression for the geometric factor $G(\boldsymbol{\beta}_1, \theta_1, \boldsymbol{\beta}_2, \theta_2)$, which plays a significant role at not very small deformations.

The nuclear-surface-deformation stiffness C_λ can be found from the experimental value of the probability $B(E\lambda)$ of an electromagnetic transition involving the excitation of one vibrational quantum [13]. Specifically, we have

$$C_\lambda = (2\lambda + 1)\frac{\varepsilon_\lambda}{2\langle\beta_\lambda^0\rangle^2}, \quad (8)$$

where $\varepsilon_\lambda = \hbar\omega_\lambda$ is the energy of a vibrational quantum and

$$\langle\beta_\lambda^0\rangle = \frac{4\pi}{3ZR_0^\lambda}\left[\frac{B(E\lambda)}{e^2}\right]^{1/2}$$

is the root-mean-square value of the total deformation for zero-point vibrations. If there are no relevant experimental data, the parameters of nuclear-surface vibrations can be determined on the basis of the liquid-drop model [13]; that is,

$$C_\lambda^{\text{LD}} = \gamma_0 R_0^2(\lambda - 1)(\lambda + 2) - \frac{3}{2\pi}\frac{Ze^2}{R_0}\frac{(\lambda - 1)}{(2\lambda + 1)}, \quad (9a)$$

$$D_\lambda^{\text{LD}} = \frac{3}{4\pi}\frac{Am_N R_0^2}{\lambda}, \quad \varepsilon_\lambda = \hbar\sqrt{\frac{C_\lambda^{\text{LD}}}{D_\lambda^{\text{LD}}}}, \quad (9b)$$

where D_λ^{LD} is the mass parameter, A is the number of nucleons in the nucleus being considered, and m_N

is the nucleon mass. We note that, in many cases (especially for magic nuclei), the liquid-drop model yields, for the parameters of surface vibrations, values that differ from their experimental counterparts considerably. For the ensuing calculations (we also bear in mind the possibility of parallel calculations employing the equations of classical mechanics), it is convenient to go over to the absolute values of the nuclear deformation, $s_\lambda = \sqrt{(2\lambda+1)/4\pi}R_0\beta_\lambda$. In this case, the potential energy of a specific vibration can be represented in the form $c_\lambda s_\lambda^2/2$, where

$$c_\lambda = C_\lambda \left(\frac{2\lambda+1}{4\pi}R_0^2\right)^{-1} = \frac{\hbar\omega_\lambda}{2\langle s_\lambda^0\rangle^2}$$

and

$$\langle s_\lambda^0\rangle = \frac{R_0}{\sqrt{4\pi}}\langle\beta_\lambda^0\rangle,$$

while the mass parameter is determined from the relation $\omega_\lambda = \sqrt{c_\lambda/d_\lambda}$; within the liquid-drop model, we have

$$d_\lambda^{\mathrm{LD}} = D_\lambda^{\mathrm{LD}}\left(\frac{2\lambda+1}{4\pi}R_0^2\right)^{-1} = \frac{3}{\lambda(2\lambda+1)}Am_N.$$

The two-dimensional interaction potential (3) for the spherical nucleus ^{16}O and the deformed nucleus ^{154}Sm ($\beta_2^{\mathrm{g.s.}} = 0.3$, $\beta_4^{\mathrm{g.s.}} = 0.1$) is displayed in Fig. 2*a* versus the relative orientation of these two nuclei. The potential of interaction of two spherical nuclei ^{40}Ca and ^{90}Zr versus their dynamical quadrupole deformation is shown in Fig. 2*b* according to the calculations with the parameters of the liquid-drop model (for the sake of simplicity, it was assumed here that the deformation energy of the nuclei is proportional to their masses; thus, only one parameter $\beta = \beta_1 + \beta_2$ was used instead of two dynamical-deformation parameters β_1 and β_2). In order to simulate the nuclear part of the interaction, we used the Woods–Saxon potential with parameters $V_0 = -105$ MeV, $r_0^V = 1.12$ fm, and $a_V = 0.75$ fm in the first case and the proximity potential with parameter $r_0^i = 1.16$ for the nuclear radii in the second case. The figures clearly demonstrate the multidimensional character of the potential of the nucleus–nucleus interaction and of the potential barrier itself, which, as is readily seen, cannot be characterized by its height B alone; it would be more correct to consider some continuous distribution $F(B)$ of barriers (see below).

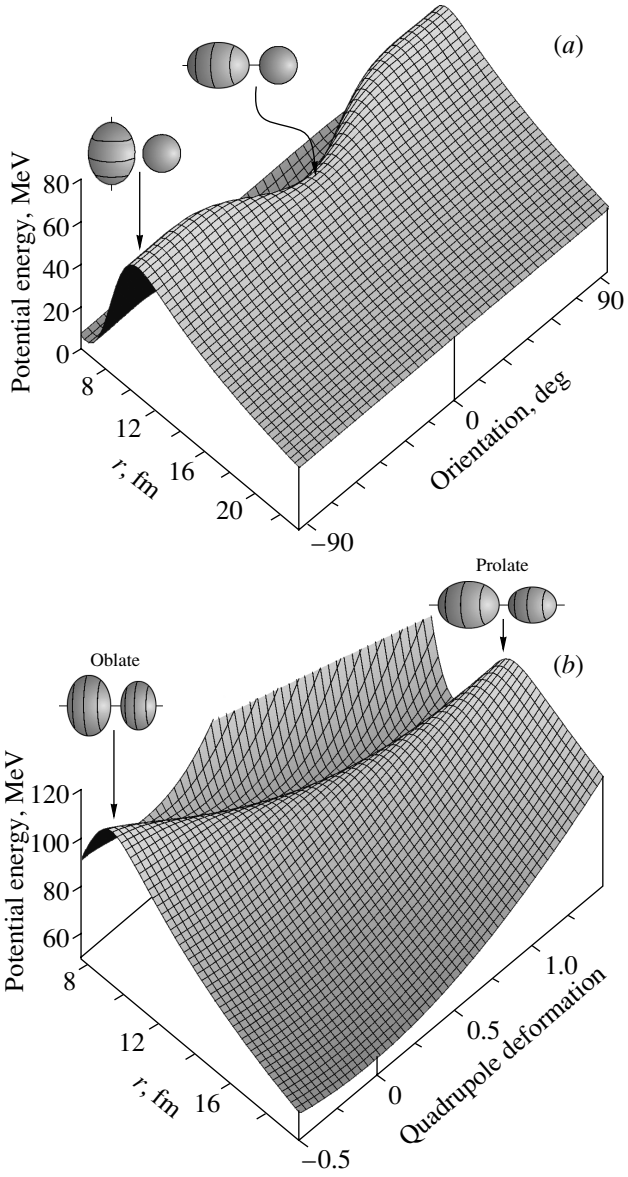

Fig. 2. (*a*) Interaction potential for the ^{16}O and ^{154}Sm ($\beta_2^{\mathrm{g.s.}} = 0.3, \beta_4^{\mathrm{g.s.}} = 0.1$) nuclei versus the distance and relative orientation. (*b*) Potential energy of the interaction of the spherical nuclei ^{40}Ca and ^{90}Zr versus the distance and their dynamical quadrupole deformation.

2. SET OF COUPLED EQUATIONS AND BOUNDARY CONDITIONS

For two deformed nuclei rotating in the reaction plane, the Hamiltonian can be represented in the form

$$H = -\frac{\hbar^2\nabla_r^2}{2\mu} + V_{\mathrm{C}}(r;\boldsymbol{\beta}_1,\theta_1,\boldsymbol{\beta}_2,\theta_2) \qquad (10)$$

$$+ V_N(r;\boldsymbol{\beta}_1,\theta_1,\boldsymbol{\beta}_2,\theta_2) + \sum_{i=1,2}\frac{\hbar^2\hat{I}_i^2}{2\Im_i}$$

$$+ \sum_{i=1,2}\sum_{\lambda\geq 2}\left(-\frac{\hbar^2}{2d_{i\lambda}}\frac{\partial^2}{\partial s_{i\lambda}^2} + \frac{1}{2}c_{i\lambda}s_{i\lambda}^2\right),$$

where μ is the reduced mass of these two nuclei and $\hat{I}_i$ and $\Im_i$ are, respectively, the operator of the angular momentum and the moment of inertia of the ith nucleus. In the algorithm developed for solving the

quantum set of coupled equations, we assumed the independence of vibrations having different multipole orders (not greater than two in each nucleus) and also disregarded the coupling of rotations and vibrations, considering them separately. It turned out that the algorithm used here enabled one to solve, within a reasonable time, a rather large number of coupled equations (about 300 for each partial wave with a computer having 128 Mbytes of random-access memory), this providing the possibility of dispensing, in the following, with approximations where different excitations are considered to be independent. The maximum number of channels whose coupling can be taken into account in the code used is estimated by the formula $N_\nu \sim 500\sqrt{M/N_r}$, where N_r is the number of nodes of the mesh in the radial direction (r) and M is the computer random-access memory in megabytes. In solving the quantum problem in question, we employ the so-called isocentrifugal approximation [14], which consists in disregarding the intrinsic spins of nuclei against the orbital angular momentum of relative motion, this orbital angular momentum being assumed to be identical in all channels (conserved quantum number). This approximation makes it possible to reduce severalfold the dimensionality of the set of differential equations that is to be solved.

Expanding, in terms of partial waves, the total wave function for the system being considered as

$$\Psi_{\mathbf{k}}(r,\vartheta,\boldsymbol{\alpha}) = \frac{1}{kr}\sum_{l=0}^{\infty} i^l e^{i\sigma_l}(2l+1)\chi_l(r,\boldsymbol{\alpha})P_l(\cos\vartheta) \tag{11}$$

and substituting this expansion into the Schrödinger equation, we arrive at the following set of coupled equations:

$$\frac{\partial^2}{\partial r^2}\chi_l(r,\boldsymbol{\alpha}) - \left\{\frac{l(l+1)}{r^2} + \frac{2\mu}{\hbar^2}\right. \tag{12}$$
$$\left.\times\left[E - V(r,\boldsymbol{\alpha}) - \hat{H}_{\rm int}(\boldsymbol{\alpha})\right]\right\}\chi_l(r,\boldsymbol{\alpha}) = 0.$$

Here, α stands for intrinsic variables (deformation parameters or rotation angles), $\hat{H}_{\rm int}(\boldsymbol{\alpha})$ is the Hamiltonian corresponding to these variables, E is the energy of colliding nuclei in the c.m. frame, and $V(r,\boldsymbol{\alpha}) = V_{\rm C}(r,\boldsymbol{\alpha}) + V_N(r,\boldsymbol{\alpha})$. At all values of r, with the exception of those in the region where the nuclei involved are in contact (see below), the function $\chi_l(r,\boldsymbol{\alpha})$ is expanded in the total set of eigenfunctions of the Hamiltonian $\hat{H}_{\rm int}(\boldsymbol{\alpha})$,

$$\chi_l(r,\boldsymbol{\alpha}) = \sum_\nu y_{l,\nu}(r)\varphi_\nu(\boldsymbol{\alpha}), \tag{13}$$

while the radial channel wave functions $y_{l,\nu}(r)$ satisfy a set of second-order ordinary differential equations that, in the following, is solved numerically,

$$y''_{l,\nu} - \left\{\frac{l(l+1)}{r^2} + \frac{2\mu}{\hbar^2}\left[E_\nu - V_{\nu\nu}(r)\right]\right\} y_{l,\nu} \tag{14}$$
$$- \sum_{\mu\neq\nu}\frac{2\mu}{\hbar^2}V_{\nu\mu}(r)y_{l,\mu} = 0.$$

Here, $E_\nu = E - \varepsilon_\nu$, where ε_ν is the excitation of the nuclei in the channel ν, and $V_{\nu\mu}(r) = \langle\varphi_\nu|V(r,\boldsymbol{\alpha})|\varphi_\mu\rangle$ is the channel-coupling matrix.

In a low-energy collision of not very heavy nuclei, nuclei that have overcome the Coulomb barrier undergo fusion (that is, form a compound nucleus) with a probability close to unity as soon as their surfaces come into contact. In this case, the fusion cross section can be measured by examining the total yield of evaporated residues and fragments originating from compound-nucleus fission. In formulating boundary conditions for Eqs. (14), it is therefore usually assumed that the flux in the region behind the Coulomb barrier is fully absorbed; that is, it does not undergo reflection. For this purpose, we require that, for $r < R_{\rm fus}$, the functions $\chi_l(r,\boldsymbol{\alpha})$ have the form of converging waves and not involve components corresponding to waves reflected from the region $0 \le r \le R_{\rm fus}$. For $R_{\rm fus}$, Hagino *et al.* [6] took the point of minimum of the potential

$$V_{\rm eff}(r) = V(r,0) + \frac{\hbar^2}{2\mu}\frac{l(l+1)}{r^2},$$

which, for $r \le R_{\rm fus}$, is replaced by the quantity $V_{\rm eff}(R_{\rm fus})$, the coupling of channels being switched off at the point $r = R_{\rm fus}$. The set of coupled Eqs. (14) then decouples, and we can easily choose their solutions corresponding to converging waves ($\exp(-iqr)$). However, an abrupt charge in the channel-coupling interaction, whose strength reaches maximum values in this region, may in principle lead to an additional unphysical reflection from the sphere $r = R_{\rm fus}$ and, hence, to a significant distortion of the total wave function in the barrier region.

In order to remove this effect, we will first modify the phenomenological potential $V(r,\boldsymbol{\alpha})$ of nucleus–nucleus interaction in the nuclear-surface-overlap region $r \le R_{\rm cont}(\boldsymbol{\alpha}) \le R_1(\boldsymbol{\beta}_1,\theta_1) + R_2(\boldsymbol{\beta}_2,\theta_2)$, rendering it independent of r in this region, $V(r \le R_{\rm cont},\boldsymbol{\alpha}) = V(R_{\rm cont},\boldsymbol{\alpha})$. For $R_{\rm cont}(\boldsymbol{\alpha})$, we will take the minimum of two distances from $r = 0$, that to the point of minimum of the potential $V(r,\boldsymbol{\alpha})$ and that to the point at which the nuclear surfaces touch each other. The boundary-value problem for Eqs. (14) will be considered over the interval $(R_{\rm min}, R_{\rm max})$, where $R_{\rm max} \gg R_1 + R_2$, $R_{\rm min} \le$

$\min\{R_{\rm cont}(\boldsymbol{\alpha})\}$ in the case of rotations, and $R_{\min} \le R_{\rm cont}(-\sqrt{M_1}\langle\boldsymbol{\beta}_1^0\rangle, -\sqrt{M_2}\langle\boldsymbol{\beta}_2^0\rangle)$ in the case of vibrations; here, M_1 and M_2 are the maximum numbers of channels that are taken into account and $\langle\boldsymbol{\beta}_1^0\rangle$ and $\langle\boldsymbol{\beta}_2^0\rangle$ are the vectors of the root-mean-square values of the deformation parameters. The centrifugal potential is also replaced by the constant value

$$U_l = \frac{\hbar^2}{2\mu}\frac{l(l+1)}{R_s^2}$$

for $r < R_s$, where, for $R_s > R_{\min}$, we take the minimum of two distances from $r = 0$, that to the point of minimum of the effective potential for spherical nuclei, $V_{\rm eff}(r)$, and that to the point at which the spherical nuclei touch each other. The choice of $R_{\min}$ is rather arbitrary. It is only of importance that it lie in the region behind the Coulomb barrier: $R_{\min} < R_B(\boldsymbol{\alpha})$. The second item to be mentioned here is that, in formulating boundary conditions at the point $r = R_{\rm fus} = R_s \le R_{\rm cont}$, from which we begin integrating the set of differential Eqs. (14), we will make use of an exact solution to these equations in the region $r \le R_{\rm fus}$. This solution can easily be found if all coefficients in these equations are constant.

For $r \le R_{\rm fus}$, we will further perform the linear transformation

$$y_{l,\nu}(r) = \sum_n Y_{l,n}(r)A_{n,\nu}, \qquad (15)$$

which diagonalizes the matrix $W_{\nu\mu} = V_{\nu\mu}(R_{\rm fus}) + \varepsilon_\nu\delta_{\nu\mu}$, so that $\{A^{-1}WA\}_{nm} = \tilde{W}_{nn}\delta_{nm}$. The new functions $Y_{l,n}(r)$ satisfy the independent equations

$$Y''_{l,n} + K^2_{l,n}Y_{l,n} = 0, \quad K^2_{l,n} = \frac{2\mu}{\hbar^2}[E - \tilde{W}_{nn} - U_l]. \qquad (16)$$

In open channels, the particular solutions $Y_{l,n}(r) = N_{l,n}\exp(-iK_{l,n}r)$ satisfying these equations and the conditions $Y'_{l,n}(r) = -iK_{l,n}Y_{l,n}(r)$ correspond to a flux toward the interior of the nucleus. From the linear transformation (15), we obtain boundary conditions for the sought channel wave functions $y_{l,\nu}(r)$ at $r \le R_{\rm fus}$; that is,

$$y'_{l,\nu}(r) = \sum_n Y'_{l,n}(r)A_{n,\nu} = \sum_\mu C_{\nu\mu}y_{l,\mu}(r), \qquad (17)$$

where

$$C_{\nu\mu} = -i\sum_n A_{n,\nu}K_{l,n}(A^{-1})_{n,\mu}.$$

The values $\tilde{W}_{nn}$ are the eigenvalues of the matrix $W_{\nu\mu}$, while the matrix $A_{n\nu}$ is composed of its normalized eigenvectors. They can be found explicitly by applying the so-called QR method [15].

At large distances, the wave function satisfies standard boundary conditions in the form of an incident and a diverging wave in the elastic channel $\nu = 0$ and in the form of diverging waves in all other channels. For partial wave functions in open channels, this corresponds to the condition

$$y_{l,\nu}(r \to \infty) = \frac{i}{2}\left[h_l^{(-)}(\eta_\nu, k_\nu r)\delta_{\nu 0} - \left(\frac{k_0}{k_\nu}\right)^{1/2} S^l_{\nu 0}h_l^{(+)}(\eta_\nu, k_\nu r)\right], \qquad (18)$$

where $k_\nu^2 = (2\mu/\hbar^2)E_\nu$, $\eta_\nu = k_\nu Z_1 Z_2 e^2/(2E_\nu)$ is the Sommerfeld parameter, $h_l^{(\pm)}(\eta_\nu, k_\nu r)$ are the Coulomb partial wave functions whose asymptotic behavior is $\exp(\pm ix_{l,\nu})$, $x_{l,\nu} = k_\nu r - \eta_\nu \ln 2k_\nu r + \sigma_{l,\nu} - l\pi/2$, $\sigma_{l,\nu} = \arg\Gamma(l+1+i\eta_\nu)$ is the Coulomb phase shift, and $S^l_{\nu 0}$ is the partial-wave scattering matrix. Eliminating the unknown quantities $S^l_{\nu 0}$ in (18), we obtain, at large distances, boundary conditions of the third kind,

$$\left[y_{l,\nu}\frac{dh_l^{(+)}}{dr} - \frac{dy_{l,\nu}}{dr}h_l^{(+)}\right]_{r=R_{\max}} = k_0\delta_{\nu 0}, \qquad (19)$$

which, together with the conditions in (17), are sufficient for numerically solving the set of coupled second-order differential Eqs. (14). For closed channels ($E_\nu < 0$), there arise similar expressions involving Coulomb functions of an imaginary argument.

In specific calculations, the boundary conditions (18) are actually employed at some finite radius, $R_{\max} \sim 30$–40 fm. For very heavy nuclei, which are characterized by large values of Z, the presence of the weakly decreasing ($\sim r^{-3}$) channel-coupling Coulomb interaction (4) results in that, at $r = R_{\max}$, the nuclei involved are already in an excited state, so that it is illegitimate to use the boundary conditions (19) at this point. The physical meaning of more correct boundary conditions is quite obvious. The Coulomb repulsion leads to negative dynamical deformations (oblate nuclei) and to a preferable side-to-side orientation of rotating quadrupolly deformed nuclei. There exist two methods for quantitatively solving this problem. In the region $r \ge R_{\max}$, one can consider a smaller number of coupled channels and solve the problem numerically within the interval $R_{\max} \le r \le R_{\rm MAX}$ by using, for example, the approximation of weak channel coupling. Taking $R_{\rm MAX}$ to be about 300 fm and imposing the "reflection-free" boundary conditions for $r \le R_{\max}$, we can find the values of all channel wave functions at this point and employ thereupon these values instead of the boundary conditions (19) in numerically solving the

full set of Eqs. (14) within the interval $R_{\rm fus} \le r \le R_{\max}$. An alternative method for deriving more correct boundary conditions at the point $r = R_{\max}$ is that of constructing an analytic solution to the problem under study in the adiabatic approximation, which assumes that, with the highest probability, the system in question moves along the bottom of the multidimensional potential surface. In this case, we can find the ground state of the system for the Hamiltonian $H_{\rm int}(\boldsymbol{\alpha}) + V(R_{\max}\boldsymbol{\alpha})$ and expand thereupon this state in the functions $\varphi_\nu(\boldsymbol{\alpha})$. The resulting expansion coefficients will yield the amplitudes of converging waves for $r \le R_{\max}$ in all channels, not only in the $\nu = 0$ channel, as is indicated in relation (18). The results of our analysis of effects of long-range Coulomb excitation in processes of near-barrier nuclear fusion will be reported in a dedicated publication.

The channel-coupling interaction $V(r, \boldsymbol{\alpha})$ can be broken down into the slowly decreasing Coulomb component (4) and the fast decreasing nuclear component; accordingly, the channel-coupling matrix has the form $V_{\nu\mu}(r) = V^{\rm C}_{\nu\mu}(r) + V^N_{\nu\mu}(r)$. The Coulomb component of the channel-coupling matrix is known in an explicit form (see, for example, [6]). In order to take explicitly into account nonlinear effects of nuclear interaction, methods of matrix algebra were applied in [6] in calculating the matrix elements of $V^N_{\nu\mu}(r)$. As a matter of fact, this approach is equivalent to expanding the function $V^N(r, \boldsymbol{\alpha})$ in a series in powers of $\boldsymbol{\alpha}$ to the Mth order inclusive, where M is the maximum number of excited states that are taken into account. In the present study, the quantities $V^N_{\nu\mu}(r)$ at each value of r are calculated explicitly with the aid of the Gauss (for rotations) and Gauss–Hermite (for vibrations) quadrature formulas of order N. If, in the expansion of the function $V^N(r, \boldsymbol{\alpha})$ in powers of $\boldsymbol{\alpha}$, one retains terms to the kth order inclusive, it is sufficient, for obtaining precise values of the matrix elements, to use an order $N \ge M + (k+1)/2$ in each degree of freedom. Our experience has revealed that the choice of $N = M + 10$ for rotations and $N = M + 6$ for vibrations is sufficient for obtaining quite an accurate result if use is made of realistic nucleus–nucleus interactions.

The fusion cross section is determined by the ratio of the absorbed to the incident flux; that is,

$$\sigma_{\rm fus}(E) = \frac{\pi}{k_0^2}\sum_{l=0}^{\infty}(2l+1)T_l(E), \qquad (20)$$

where

$$T_l(E) = \sum_\nu \frac{j_{l,\nu}}{j_0} \qquad (21)$$

are the partial-wave barrier-penetrability coefficients. Here,

$$j_{l,\nu} = -i\frac{\hbar}{2\mu}\left(y_{l,\nu}\frac{dy^*_{l,\nu}}{dr} - y^*_{l,\nu}\frac{dy_{l,\nu}}{dr}\right)\Big|_{r\le R_{\rm fus}}$$

is the partial-wave flux in the channel ν and $j_0 = \hbar k_0/\mu$. In the fusion of heavier nuclei (especially for symmetric combinations), the probability that a compound nucleus is formed after the surfaces of colliding nuclei have come into contact is less than unity because of quasifission processes [16]. It is very difficult to calculate this probability [17], and this presents a problem in itself, which is beyond the scope of the algorithm considered here. For such systems, the cross section calculated by formula (20) will correspond to the so-called capture cross section, which is equal to the sum of the fusion cross section and the quasifission cross section.

3. CONSTRUCTING A NUMERICAL SOLUTION TO OUR SET OF COUPLED EQUATIONS

For a finite number of channel functions, the set of ordinary differential Eqs. (14) supplemented with the boundary conditions (17) and (19) forms a mixed boundary-value problem. In order to solve it numerically, we introduce a mesh and specify mesh functions at its nodes as

$$r_j = r_0 + jh, \quad y^j_{l,\nu} = y_{l,\nu}(r_j), \qquad (22)$$
$$j = 0, 1, \ldots, J, \quad r_0 = R_{\rm fus} - 2h.$$

The boundary conditions involving the first derivative are approximated in terms of a two-point difference scheme. For open channels, the condition in (19) leads to the relation

$$y_{l,\nu}(r_J) = \tau y_{l,\nu}(r_{J-1}) - \zeta, \qquad (23)$$
$$\tau = \frac{2+h\gamma}{2-h\gamma}, \quad \zeta = \frac{2hk_\nu\delta_{\nu 0}}{(2-h\gamma)h^{(+)}_l(\eta_\nu, k_\nu r_{J-1/2})},$$
$$\gamma = \frac{dh^{(+)}_l(\eta_\nu, k_\nu r_{J-1/2})/dr}{h^{(+)}_l(\eta_\nu, k_\nu r_{J-1/2})}.$$

Similar formulas are obtained for closed channels as well. The boundary condition (17) yields the matrix relation

$$y_{l,\nu}(r_0) = \sum_\mu \Theta_{\nu\mu}y_{l,\mu}(r_1), \quad \Theta = D^{-1}F, \qquad (24)$$
$$D_{\nu\mu} = \delta_{\nu\mu} + \frac{h}{2}C_{\nu\mu}, \quad F_{\nu\mu} = \delta_{\nu\mu} - \frac{h}{2}C_{\nu\mu}.$$

In order to approximate differential equations by finite-difference equations, use is usually made of Numerov's method, which has been successfully tested

many times (see, for example, [18]) and which is based on a three-point approximation of the second derivative. As a matter of fact, this method ensures an $O(h^4)$ approximation at one step in solving the Schrödinger equation along the mesh. Numerov's method was used in [6] as well. The finite-difference equations obtained by writing the differential Eqs. (14) at internal nodes of the mesh and taken together with the boundary conditions (23) and (24) for the pair of extreme nodes form a set of linear equations whose matrix is banded. In order to reduce the number of nonzero matrix elements in approximating the second derivative, we employ, instead of Numerov's method, the three-point finite-difference scheme

$$y''(r_j) = h^{-2}(y^{j-1} - 2y^j + y^{j+1}) + O(h^2), \quad (25)$$

the half-width of the resulting matrix appearing to be one-half as great as that in Numerov's method. Although the finite-difference scheme (25) ensures an $O(h^2)$ approximation in solving the Schrödinger equation, this is quite sufficient for deriving a solution to a high precision. It should be noted that the error in numerically solving the boundary-value problem (14) arises and is accumulated not only because of a finite-difference approximation of the derivatives involved but also in solving the set of linear equations. For $h \to 0$, the first component of this error decreases, while the second increases because of an increase in the number of equations and in the number of required computational operations. As a result, the total error first decreases and then begins to increase as the step is reduced. The testing of the two algorithms revealed that the accuracy of Numerov's scheme itself is, as a rule, excessive and that, if use is made of a multisweep algorithm in solving the boundary-value problem, its resulting error may exceed the error of the method based on the scheme in (25).

Since modern computers make it possible to save the matrix in random-access memory entirely, we will use the Gauss reduction method to solve our set of linear equations directly and to determine the values of $y_{l,\nu}(r_j)$ at the nodes of the mesh. The main advantage of the approach based on the Gauss reduction method is its high stability in calculations involving a finite number of digital places. A scheme consisting of one direct and one inverse sweep seems preferable to a scheme involving a few sweeps in one direction that are followed by solving a set of linear equations for determining arbitrary constants. In the latter case, the error can increase because of the loss of the required accuracy of the decreasing solution in the classically inaccessible region, this being especially important in solving problems where there are two turning points. The use of the Gauss reduction method in order to solve the set of linear equations directly enabled us to increase, in relation to the possibility presently realized in the CCFULL code [6], the number of channels that are taken into account almost by an order of magnitude. This is especially important in the case where a few degrees of freedom are excited in both nuclei and for avoiding unphysical nuclear-deexcitation effects associated with stringent constraints on the number of coupled channels that are taken into account. Owing to the storage of all values of $y_{l,\nu}(r_j)$ in computer memory, one can also easily reconstruct the multichannel wave functions (11) and (13) themselves and, hence, obtain deeper and clearer insights into the dynamics of penetration through a multidimensional potential barrier (see below).

4. DISTRIBUTION WITH RESPECT TO BARRIERS AND SEMIEMPIRICAL MODEL OF NUCLEAR FUSION

Precision experiments performed in recent years to measure the energy dependence of the cross section for near-barrier fusion make it possible to estimate quite accurately the second derivative of $E\sigma_{\text{fus}}(E)$ with respect to energy. In the classical limit, this derivative can be identified with the distribution with respect to barriers [19],

$$D(B) = \frac{1}{\pi R_B^2} d^2(E\sigma_{\text{fus}})/dE^2|_{E=B}. \quad (26)$$

The discovery of a rather complicated structure of the function $D(B)$ in the near-barrier region of energies [2–4] (this structure is different for different combinations of nuclei) was the main net result of such measurements. This is indicative of a nontrivial dynamics of passage through the potential barrier under conditions of strong channel coupling.

In the absence of channel coupling (this corresponds to the disregard of all degrees of freedom, with the exception of that which is associated with the relative motion of spherical nuclei), the effective interaction potential

$$V_{\text{eff}}(r) = V(r) + \frac{\hbar^2}{2\mu}\frac{l(l+1)}{r^2}$$

can be approximated near its maximum by an "inverted" parabola,

$$V_{\text{eff}}(r) \approx B(l) + 1/2V''(r)|_{r=R_B}[r - R_B(l)]^2.$$

In this case, the barrier penetrability is determined by the well-known Hill–Wheeler formula [20]

$$T(l,E) = \left[1 + \exp\left(\frac{2\pi}{\hbar\omega_B}[B(l) - E]\right)\right]^{-1}, \quad (27)$$

where $B(l)$ and $R_B(l)$ are the barrier height and position, respectively, and $\omega_B(l) = \sqrt{-V''(R_B)/\mu}$ is the oscillator frequency, which characterizes the barrier

width and which, in general, depends on the energy E. If we now assume that the effective-barrier position $R_B(l)$ changes only slightly in response to a change in l, the barrier height is given by

$$B(l) = B + \frac{\hbar^2}{2\mu R_B^2} l(l+1),$$

where B and R_B are, respectively, the barrier height and position at $l = 0$. In this case, the barrier penetrability $T(l, E)$ does not depend on B and l independently, but it is a function of the combination

$$x = B + \frac{\hbar^2}{2\mu R_B^2} l(l+1) - E;$$

that is, $T(l, E) = f(x)$. By using expression (20) for the fusion cross section, we arrive at

$$\frac{d(E\sigma_{\text{fus}})}{dE} = \frac{\pi\hbar^2}{2\mu} \sum_{l=0}^{\infty} (2l+1) \frac{dT(l,E)}{dE}. \qquad (28)$$

Since

$$\frac{dT}{dE} = -\frac{dT}{dx} = -\frac{dT}{dl}\left(\frac{dx}{dl}\right)^{-1} = -\frac{dT}{dl}\frac{2\mu R_B^2}{\hbar^2}\frac{1}{2l+1},$$

we have

$$\frac{d(E\sigma_{\text{fus}})}{dE} = -\pi R_B^2 \sum_{l=0}^{\infty} \frac{dT(l,E)}{dl}.$$

In a collision of heavy nuclei, in which case the cross section receives large contributions from many partial waves, $T(l, E)$ is a smooth function of l, so that the sum in (28) can be replaced by an integral with respect to l. This integral can be readily evaluated. The result is $d(E\sigma_{\text{fus}})/dE = \pi R_B^2 T(l = 0, E)$ or

$$D(E) = \frac{1}{\pi R_B^2}\frac{d^2(E\sigma_{\text{fus}})}{dE^2} = \frac{dT(l=0,E)}{dE}. \qquad (29)$$

In the classical case, $T(E) = 1$ for $E > B$ and $T(E) = 0$ for $E < B$; that is, $D(E) = \delta(E - B)$. In the quantum case, the penetrability of a one-dimensional barrier has the form (27) and the function $D(E)$ has one maximum at $E = B$, its width being $\Delta_B = \hbar\omega_B \ln(17 + 12\sqrt{2})/2\pi \approx 0.56\hbar\omega_B$ (for a parabolic barrier).

In a realistic case, the potential of nucleus–nucleus interaction is a multidimensional function (see Fig. 2), so that the incident flux overcomes the Coulomb barrier at different points—that is, at different values of B [this corresponds to different values of the dynamical deformation or (and) different orientations of the nuclei]. In order to obtain a simple estimate of the penetrability of such a multidimensional barrier, a semiempirical formula was proposed in [17] on the basis of a parametrized distribution with respect to barriers. Within this approach, the total penetrability is averaged over the barrier height B. Instead of (27), we then have

$$T(l,E) = \int F(B)\left[1 + \exp\left(\frac{2\pi}{\hbar\omega_B}\right.\right. \qquad (30)$$
$$\left.\left. \times \left[B + \frac{\hbar^2}{2\mu R_B^2(l)} l(l+1) - E\right]\right)\right]^{-1} dB,$$

where the function $F(B)$ satisfies the normalization condition $\int F(B)dB = 1$. It can be approximated by a symmetric Gaussian function having the center at $B_0 = (B_1 + B_2)/2$ and the width $\Delta_B = (B_2 - B_1)/2$. For statically deformed nuclei, the quantities B_1 and B_2 are defined as the barriers of the "nose-to-nose" and "side-to-side" configurations (see Fig. 2*a*), which are two limiting configurations. In this case, one can also employ a direct averaging over nuclear orientations, determining the actual barrier $B(\boldsymbol{\beta}_1, \theta_1; \boldsymbol{\beta}_2, \theta_2)$. For nuclei of zero static deformation, B_1 corresponds to the minimum height of the multidimensional barrier with allowance for a dynamical deformation (saddle point in Fig. 2*b*), while B_2 corresponds to the barrier in the case of the interaction of spherical nuclei. Our experience showed that, in order to describe more accurately the cross section for the fusion of heavy nuclei, in which case the difference $(B_2 - B_1)$ is great, it would be better to approximate the function $F(B)$ by a slightly asymmetric Gaussian function having a smaller "intrinsic" half-width (at smaller values of B) [17].

5. FUSION CROSS SECTIONS IN THE PRESENCE OF STRONG CHANNEL COUPLING

In order to compare the results of our calculations for the nuclear-fusion cross sections not only with experimental data but also with the results of the calculations based on the CCFULL code [6], we employ here the Woods–Saxon potential for nucleus–nucleus interaction since the CCFULL code is unable to operate with the proximity potential.

In calculating the cross section for the fusion of a ^{16}O nucleus with a deformed nucleus ^{154}Sm, we set the parameters involved to the following values: $V_0 = -105$ MeV, $r_0^V = 1.12$ fm, $a_V = 0.75$ fm (see Fig. 2*a*), $r_0^1 = 1.2$ fm, and $r_0^2 = 1.06$ fm; also, we took the values of $\beta_2 = 0.3$ and $\beta_4 = 0.1$ for the parameters of, respectively, the static quadrupole and the static hexadecapole deformation of the ^{154}Sm nucleus and the value of $E_{2^+} = 0.084$ MeV for the energy of the first excited rotational level; in addition, we used the values of $R_{\max} = 24$ fm and $h = 0.05$ fm. The fusion cross

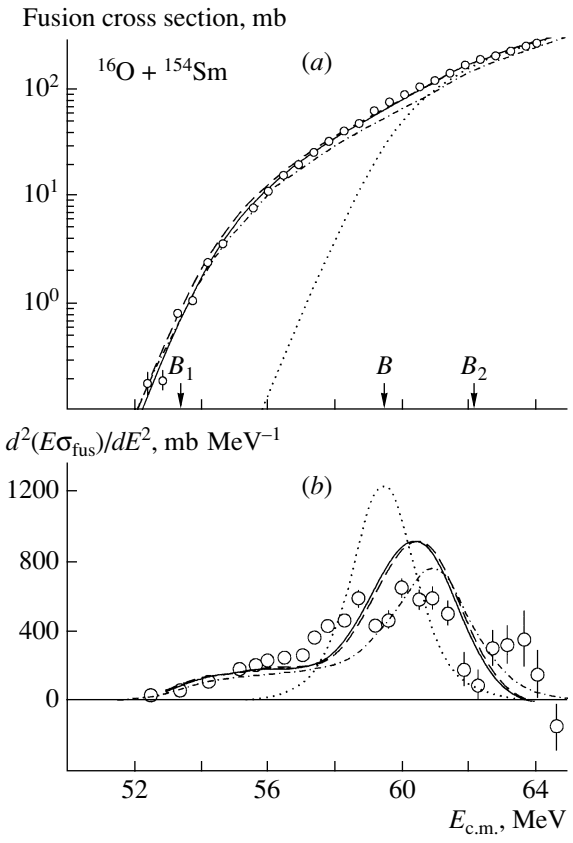

Fig. 3. (*a*) Cross section for the fusion of oxygen nuclei with a deformed nucleus ^{154}Sm and (*b*) distribution with respect to barriers. The dotted curves correspond to the fusion of spherical nuclei. The dashed and solid curves represent the results of the calculations by, respectively, the CCFULL code [6] and our code with allowance for five rotational states of the ^{154}Sm nucleus. The dash-dotted curve for the cross section was obtained by a mere averaging over the orientations of the deformed nucleus. The displayed experimental data were borrowed from [21]. The arrows indicate the positions of the Coulomb barriers for spherical nuclei and for two limiting orientations of the deformed target nucleus.

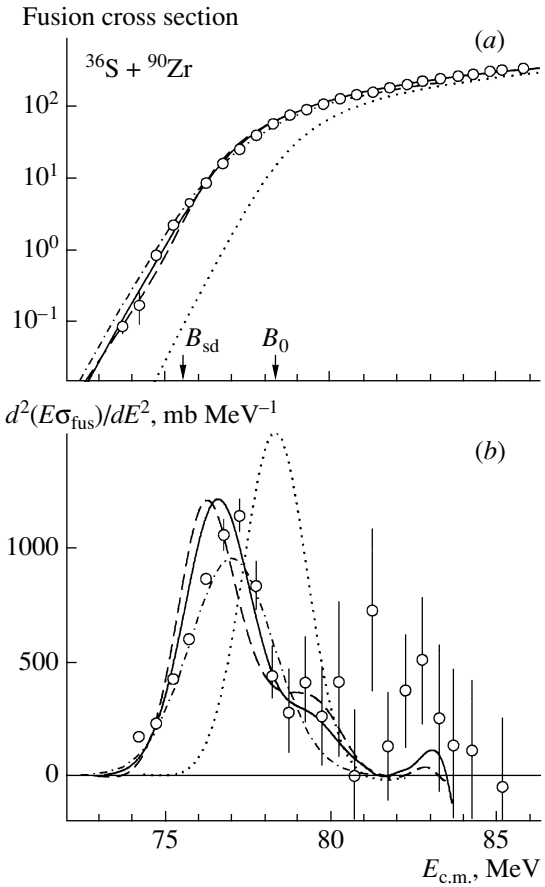

Fig. 4. (*a*) Cross section for the fusion of spherical nuclei ^{36}S and ^{90}Zr and (*b*) distribution with respect to barriers. The dotted curves correspond to the calculation that disregards dynamical deformations. The dashed and solid curves represent the results of the calculations by, respectively, the CCFULL code [6] and our code with allowance for the excitation of four phonons associated with octupole vibrations of the surface of the ^{90}Zr nucleus. The dash-dotted curve for the cross section was calculated on the basis of an empirical model for taking into account dynamical deformations (see main body of the text). The displayed experimental data were borrowed from [22].

sections calculated with allowance for the excitation of five rotational states by using our code and the CCFULL code are displayed in Fig. 3*a* along with experimental data borrowed from [21]. Figure 3*b* shows the distribution with respect to barriers, $d^2(E\sigma_{\text{fus}})/dE^2$, which makes it possible to visualize in greater detail the "fine structure" and the complicated character of barrier penetrability. As can be seen from Fig. 3, the two codes in question lead to nearly identical values for the reaction being considered. It should be noted that, for the fusion of deformed nuclei, a correct choice of internuclear interaction potential in combination with a mere averaging of one-dimensional barrier penetrabilities over the orientations of the nuclei involved (as a matter of fact, over barrier heights—see Fig. 2*a*) leads to quite satisfactory agreement with experimental data both in what is concerned with the magnitude of the fusion cross sections in the subbarrier region and in what is concerned with the shape of the distribution with respect to barriers.

The cross sections for the fusion of spherical nuclei ^{36}S and ^{90}Zr are shown in Fig. 4*a* according to calculations that take into account four phonons associated with octupole vibrations of the surface of the ^{90}Zr nucleus ($\lambda = 3$, $\hbar\omega_\lambda = 2.75$ MeV, $\langle\beta_\lambda^0\rangle = 0.22$). The corresponding distributions with respect to barriers are given in Fig. 4*b*. The displayed experimental data were borrowed from [22]. For this case, the nucleus–nucleus interaction of spherical nuclei was also cho-

sen in the form of the Woods–Saxon potential, its depth, range, and diffuseness parameter being set to $V_0 = -77.5$ MeV, $r_0^V = 1.15$ fm, and $a_V = 0.8$ fm, respectively. This potential leads to the Coulomb barrier height of $B_0 = 78.3$ MeV (right arrow in Fig. 4*a*). Upon taking into account the octupole vibrations of the target nucleus, the fusion cross section becomes much larger in the subbarrier region, the two codes in question (CCFULL [6] and our code) yielding very close results.

An increase in the fusion cross section in the subbarrier region $E < B_0$ can easily be explained with the aid of the data in Fig. 2*b*. For the case of a prolate configuration (positive values of β_λ), a dynamical deformation of the surface leads to the lowering of the Coulomb barrier. As the deformation increases further, the potential energy increases again because of a nonzero stiffness C_λ of the nuclear surface. Thus, we see that, in the total nucleus–nucleus potential, we can single out the saddle point $(r_{\rm sd}, \beta_{\rm sd})$ corresponding to the minimum height $B_{\rm sd}$ of the Coulomb barrier in the (r, β) space (see Fig. 2*b*). Using the experimental value of the energy of the photon associated with octupole vibrations of the ^{90}Zr nucleus ($\hbar\omega_{\lambda=3} = 2.75$ MeV), calculating the stiffness of the corresponding oscillator (see Section 1), and constructing the two-dimensional surface of nucleus–nucleus interaction (similar to that which is shown in Fig. 2*b*), we can easily determine, for this case, the height of the Coulomb barrier at the saddle point, $B_{\rm sd} = 75.6$ MeV (right arrow in Fig. 4*a*). Assuming that the incident flux, moving in the (r, β) space, traverses the two-dimensional barrier at various values of the dynamical deformation in the range $0 \le \beta < \beta_{\rm sd}$, we can approximate the distribution with respect to barriers by a Gaussian function having a center at the point $(B_0 + B_{\rm sd})/2$ and the half-width $(B_0 - B_{\rm sd})/2$ and calculate thereupon the total fusion cross section. The cross section obtained on the basis of this semiempirical approach is in rather satisfactory agreement both with experimental data and with the results of our precise calculations (see dash-dotted curves in Fig. 4), furnishing, at the same time, quite a clear explanation for an increase in the subbarier penetrability and in the width of the distribution with respect to barriers.

The data in Fig. 5, which shows the squared modulus of the two-dimensional wave function describing the relative motion of ^{36}S and ^{90}Zr nuclei in $(r, s_{\lambda=3})$ space, where $s_{\lambda=3} = \sqrt{(2\lambda+1)/4\pi}R_0\beta_{\lambda=3}$ is the absolute value of the octupole deformation of the ^{90}Zr nucleus, provides an additional piece of evidence in support of this qualitative pattern. It can be seen that, at large distances, the multichannel wave function is concentrated in the region of small deformations,

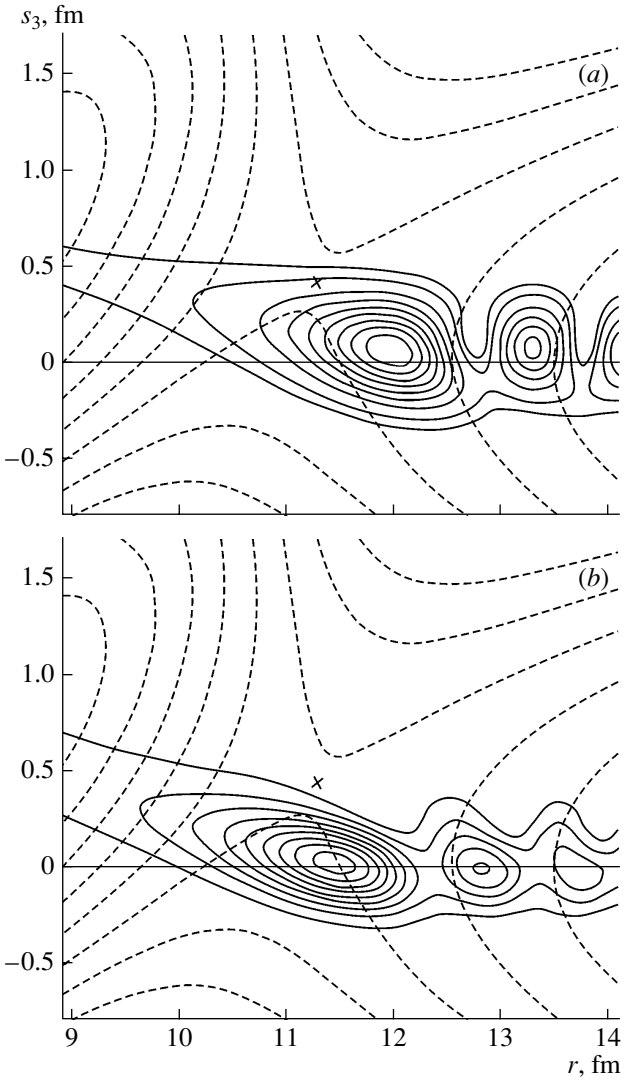

Fig. 5. Topographical landscape of the squared modulus of the two-dimensional wave function (13) (solid curves), which describes the fusion of ^{36}S and ^{90}Zr nuclei at $l = 0$, against the background of the landscape of the potential energy (dashed curves) at energies of $E_{\rm c.m.} = (a)$ 77 and (b) 80 MeV. The cross indicates the position of the saddle point of the Coulomb barrier.

$\beta_3 \approx 0$, this reflecting the dominance of zero-point vibrations of the nuclear ground state $\varphi_{\nu=0}(\beta)$ in the expansion given by (13). At low energies (slow collisions), the nuclei involved undergo considerable deformations at the instant of coming into contact, the Coulomb barrier being overcome predominantly at positive values of the deformation (the stretching of the nuclei toward each other), which lead to the lowering of this barrier (see Fig. 2*a* and the landscape of the potential energy in Fig. 5). That the modulus of the wave function oscillates at large distances is due to the interference between the incident and the reflected wave.

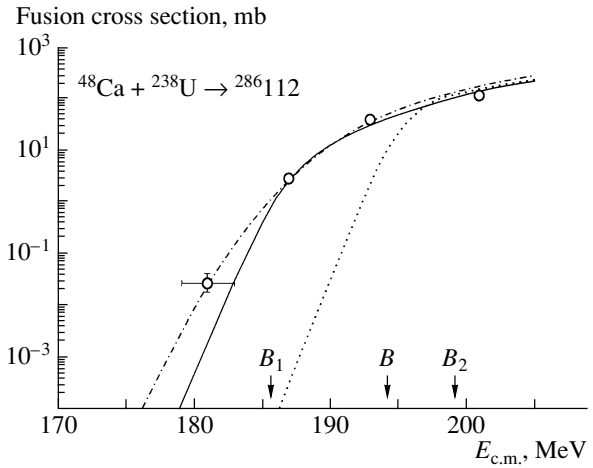

Fig. 6. Cross section for the fusion of a ^{48}Ca nucleus and a deformed ^{238}U nucleus: (dotted curve) fusion of spherical nuclei, (solid curve) results of the calculation by the coupled-channel method with the aid of the algorithm proposed in the present study, (dash-dotted curve) cross section obtained within the semiempirical approach, and (points) experimental data borrowed from [23]. The arrows indicate the positions of the Coulomb barriers for spherical nuclei (Bass barrier) and for two limiting configurations of the deformed target nucleus.

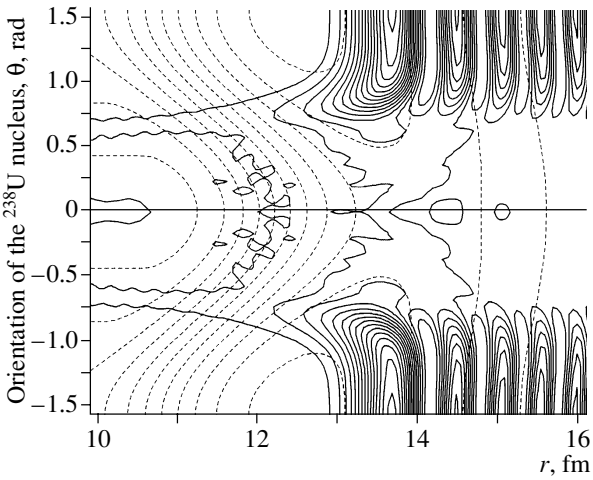

Fig. 7. Topographical landscape of the squared modulus of the two-dimensional wave function (13) at $l = 0$ (solid curves), which describes the fusion of ^{48}Ca and ^{238}U nuclei at an energy of $E_{c.m.} = 194$ MeV, against the background of the landscape of the potential energy (dashed curves).

6. SYNTHESIS OF SUPERHEAVY NUCLEI

In the fusion of very heavy nuclei, which are used, in particular, in the synthesis of superheavy elements, the coupling of channels plays an even more significant role. For this region of nuclei, available experimental data on fusion cross sections are much scarcer; moreover, no experimental data for nuclear combinations close to symmetric ones can be obtained in principle because it is impossible, in this case, to separate products originating from processes of deep-inelastic scattering, on one hand, and from the fission of a compound nucleus, on the other hand. In view of this, theoretical calculations and predictions are of paramount importance in this region of nuclei. The reliability of such predictions is not very high at the present time not only because of problems encountered in taking into account the coupling of several degrees of freedom in the process of near-barrier fusion but also because of inaccuracies in determining the nucleus–nucleus interaction. Until recently, there has been no possibility for performing quantum calculations of the fusion of very heavy nuclei within the coupled-channel method, because the operation of the existing algorithms (including the CCFULL code) is highly unstable in this case. It turned out that our new algorithm for solving a set of a large number of coupled equations makes it possible to perform such calculations.

Figure 6 shows the experimental and theoretical cross sections for the fusion of ^{48}Ca and ^{238}U nuclei. The displayed experimental data, which were taken from [23], correspond to all products of fission (both ordinary fission and prompt fission proceeding without the formation of a compound nucleus); therefore, it is more correct, in this case, to refer to this quantity as the capture cross section (see the comment at the end of Section 2). For the nuclear interaction, we again took the Woods–Saxon potential with parameters $V_0 = -160$ MeV, $r_0^V = 1.14$ fm, and $a_V = 0.65$ fm, which ensure the Coulomb barrier height of $B = 194$ MeV, predicted by the Bass model [24] for these nuclei. The static quadrupole deformation of $\beta_2 = 0.215$ [25], which is realized for the ^{238}U nucleus, leads to the barrier heights of $B_1 = 185.4$ MeV and $B_2 = 199.2$ MeV for two limiting orientations of the nuclei. Employing the semiempirical model of nuclear fusion and approximating the function $F(B)$ in (30) by an asymmetric Gaussian function whose width is $\Delta_B^1 = (B_2 - B_1)/2 \approx 7$ MeV for the right branch (large values of B) and $\Delta_B^2 = 5$ MeV for the left branch (as a matter of fact, this is an adjustable parameter here), we have also obtained quite satisfactory agreement with experimental data (dash-dotted curve in Fig. 6).

The squared modulus of the two-dimensional wave function describing the relative motion of ^{48}Ca and ^{238}U nuclei is shown in Fig. 7 versus the distance r and the angle θ of rotation of the deformed uranium nucleus. For the interaction of these two nuclei, Fig. 7 also displays the potential-energy landscape, which is similar to that in Fig. 2*a*. The value chosen for the collision energy, $E_{c.m.} = 194$ MeV, is above the

Coulomb barrier height at $\theta = 0°$ (about 185 MeV) and below this barrier at $\theta = \pi/2$ (about 200 MeV). As can be seen from the figure, the incident wave therefore overcomes the barrier almost freely only at small θ (in the nose-to-nose configuration), but it is almost completely reflected from the barrier at $\theta \sim \pi/2$. At large distances, this leads to a strong interference between the incident and the reflected wave at $\theta \sim \pi/2$ and to an almost complete absence of interference at small θ.

In conclusion, we note that the algorithms developed by us for calculating the cross sections for the near-barrier fusion of heavy nuclei (coupled-channel method and semiempirical model) and used in the present study can be found, together with the code for computing multidimensional potential surfaces, on the freely accessible Web server quoted in [26].

ACKNOWLEDGMENTS

This work was supported in part by the Russian Foundation for Basic Research (project no. 03-07-90373).

APPENDIX 1

Local Curvature of the Surface of a Deformed Nucleus and Geometric Factor

In terms of polar coordinates, the local curvature of a curve in a plane can be represented as [11, formula (17.1-9)]

$$k = \left[\rho^2 + 2\left(\frac{d\rho}{d\varphi}\right)^2 - \rho\frac{d^2\rho}{d\varphi^2}\right]\left[\rho^2 + \left(\frac{d\rho}{d\varphi}\right)^2\right]^{-3/2}. \quad (A.1)$$

In the case of dynamical deformations along the common symmetry axis of the nuclei (nose-to-nose orientation), any curve lying on the surface of a nucleus in a plane containing the symmetry axis is given by (1); that is, $\rho(\varphi) \equiv R(\theta)$. At small angles ($\theta \ll 1$), we can use an approximate expression for Legendre polynomials,

$$P_\lambda(\cos\theta) \approx 1 - \eta(\lambda)(1 - \cos\theta), \quad \theta \ll 1,$$

where $\eta(\lambda) = 3 \cdot 4 \cdots (\lambda+1)/(\lambda-1)!$, whereupon the equation of the surface takes the form

$$R(\theta) = a + b\cos\theta, \quad (A.2)$$

$$a = \tilde{R}\left[1 + \sum_{\lambda\geq 2}\beta_\lambda\left(1 - \eta(\lambda)\right)\sqrt{\frac{2\lambda+1}{4\pi}}\right],$$

$$b = \tilde{R}\left[1 + \sum_{\lambda\geq 2}\beta_\lambda\eta(\lambda)\sqrt{\frac{2\lambda+1}{4\pi}}\right].$$

At $\theta = 0$, the substitution of (A.2) into (A.1) yields

$$k^\perp = k^{||} = k = \frac{a+2b}{(a+b)^2}, \quad (A.3)$$

$$k = \tilde{R}^{-1}\left(1 + \sum_{\lambda\geq 2}\sqrt{\frac{2\lambda+1}{4\pi}}\beta_\lambda\right)^{-2} \times \left(1 + \sum_{\lambda\geq 2}(1+\eta(\lambda))\sqrt{\frac{2\lambda+1}{4\pi}}\beta_\lambda\right), \quad (A.4)$$

whence we obtain formula (7).

In the case of statically deformed nuclei rotating in the reaction plane, a calculation of a local curvature for an arbitrary orientation of the symmetry axes of the nuclei leads to more cumbersome formulas. A simple expression is obtained for the limiting case of $\theta = \pi/2$ (side-to-side configuration). Since a static quadrupole deformation is the most peculiar to nuclei, we consider here only the case of $\lambda = 2$. Using the expression $(3\cos 2\theta + 1)/4$ for the Legendre polynomial $P_2(\cos\theta)$, we obtain

$$R(\theta) = a' + b'\cos 2\theta, \quad (A.5)$$

where

$$a' = \tilde{R}\left[1 + \frac{1}{4}\beta_2\sqrt{\frac{5}{4\pi}}\right], \quad b' = \frac{3}{4}\tilde{R}\beta_2\sqrt{\frac{5}{4\pi}}.$$

The substitution of (A.5) into (A.1) at $\theta = \pi/2$ yields

$$k^{||} = \frac{a' - 5b'}{(a'-b')^2} = \frac{R_A}{R_B^2}, \quad k^\perp = \frac{1}{R_B} \quad (A.6)$$

where

$$R_A = \tilde{R}\left[1 - \frac{7}{2}\beta_2\sqrt{\frac{5}{4\pi}}\right],$$

$$R_B = R(\theta = \pi/2) = \tilde{R}\left[1 - \frac{1}{2}\beta_2\sqrt{\frac{5}{4\pi}}\right].$$

A further calculation of the local geometric factor $G_{\text{loc}} = P_{\text{sph}}/P$ is performed with the aid of formula (6), which, as was mentioned above, leads to a singularity when two planar surfaces touch each other [$k_1^\perp + k_2^\perp = 0$ or (and) $k_1^{||} + k_2^{||} = 0$].

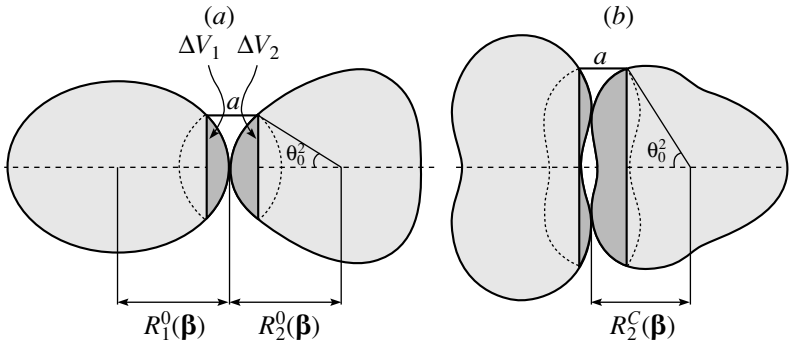

Fig. 8. Schematic representation of two deformed nuclei in the nose-to-nose configuration (the horizontal dashed line is the symmetry axis): (*a*) positive deformations and (*b*) negative deformations. More darkly shaded segments are regions that make a dominant contribution to nucleus–nucleus interaction.

APPENDIX 2

Geometric Factor with Allowance for the Finiteness of the Range of Nuclear Forces and Dimensions of Deformed Nuclei

In principle, a precise value of the geometric factor can be obtained by using the folding procedure for calculating the potential for the nucleus–nucleus interaction. In this case, the finiteness of nuclear sizes and of the range of nucleon–nucleon interaction guarantees the absence of singularities even in the case of zero local curvature at the point where the nuclear surfaces touch each other. In specific applications (especially in dynamical calculations), however, it is more convenient to use, instead of folding potentials, some analytic expression (like the Woods–Saxon potential or the proximity potential) that would represent the nucleus–nucleus interaction and which would take into account the change in the curvature of nuclear surfaces at large deformations. An approximate value of the geometric factor can be obtained with the aid of the expression

$$G = \frac{\Delta V_1(\boldsymbol{\beta}_1, \theta_1; a_1) + \Delta V_2(\boldsymbol{\beta}_2, \theta_2; a_2)}{\Delta V_1^0(a_1) + \Delta V_2^0(a_2)}, \qquad \text{(A.7)}$$

where $\Delta V_i(\boldsymbol{\beta}_i, \theta_i; a_i)$ are the volumes of the most closely spaced small segments of the nuclei being considered (see Fig. 8), $\Delta V_i^0(a_i) = (\pi/3)a_i^2(3R - a_i)$ are the volumes of the segments of the corresponding spherical nuclei, $a_1/a_2 = (R_2 - a/2)/(R_1 - a/2)$, and $a \approx 1$ fm. We will first consider the deformation along the common symmetry axis of the nuclei (Fig. 8*a*). In this case, the volume of the nose segment is given by

$$\Delta V_i = \frac{2\pi}{3}\tilde{R}_i^3 \int\limits_{t_0^i}^{1} \left[1 + \sum_\lambda \beta_{i\lambda}\sqrt{\frac{2\lambda+1}{4\pi}}P_\lambda(t)\right]^3 dt$$
$$- \frac{\pi}{3}(R_i^0 - a_i)^3(1/t_0^{i^2} - 1), \qquad \text{(A.8)}$$

where $R_i^0 = R_i(\boldsymbol{\beta}_i, \theta = 0)$ and t_0^i is found from the equation ($t \equiv \cos\theta$)

$$R(t)t = R_i^0 - a_i. \qquad \text{(A.9)}$$

This equation can be solved explicitly if a parabolic approximation of Legendre polynomials is used in the range $0 < t \leq 1$; that is,

$$P_\lambda(t) \approx -p_\lambda + \alpha_\lambda(t - \tau_\lambda)^2, \qquad \text{(A.10)}$$

where $p_\lambda = \{1/2, \sqrt{1/5}, 3/7\}$, $\tau_\lambda = \{0, \sqrt{1/5}, \sqrt{3/7}\}$, and $\alpha_\lambda = (1 + p_\lambda)/(1 - \tau_\lambda)^2$ at $\lambda = 2$, 3, and 4, respectively. In this case, Eq. (A.9) is a cubic equation, and we must take the positive root of this equation for t_0^i. Integration in (A.8) can also be performed explicitly. For the volume of the nose segment of a deformed nucleus, this yields a rather cumbersome expression, but it is readily calculable. Obviously, the geometric factor (A.7) does not have singularities, remaining finite at any deformations.

At large negative deformations, the nuclear surface at the point $\theta = 0$ first becomes flat and then assumes a concave shape (see Fig. 8*b*). In this case, the "interacting-layer" thickness a must be reckoned not from the point $R_i^0 = R_i(\boldsymbol{\beta}_i, \theta = 0)$, which lies on the symmetry axis, but from the point that lies on the surface and which is the most remote from the center of the nucleus along the axis connecting the centers of the nuclei—that is, from the point $R_i^C \equiv R_i(t_C^i)t_C^i$ in Fig. 8*b*, which is found from the condition $d[R(t)t]/dt|_{t_C} = 0$. In this case, the quantity $t_0^i \equiv \cos\theta_0^i$ is as before determined from Eq. (A.9), where R_i^0 is replaced by R_i^C. In Fig. 9, the geometric factor calculated by formula (A.7) is contrasted against the local approximation $G_{\text{loc}} = P_{\text{sph}}/P$. It can be seen that, in the region of positive and small negative deformations, the approximation of "finite segments" is

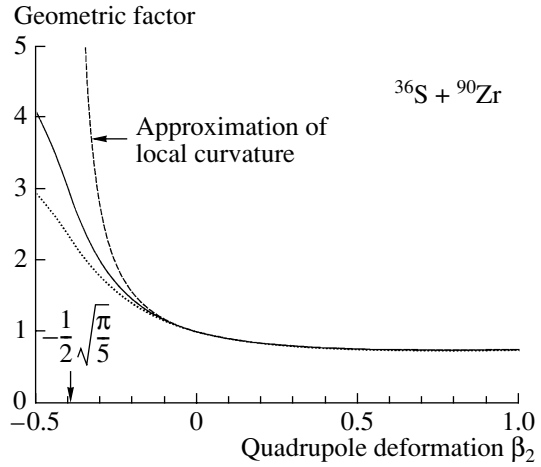

Fig. 9. Geometric factor calculated for the case of identical dynamical quadrupole deformations ($\beta_{1,2} = \beta_{2,2} = \beta_2$) of the interacting nuclei ^{36}S and ^{90}Zr. The dashed curve corresponds to the local approximation $G_{\rm loc} = P_{\rm sph}/P$. The solid and the dotted curve were calculated by formula (A.7) at $a = 1$ and 2 fm, respectively. The arrow indicates the "critical" deformation at which the local curvature of the surface featuring a quadrupole deformation vanishes (contiguity of two flat surfaces).

weakly dependent on a and is virtually coincident with the local approximation.

For rotating deformed nuclei, the volumes of the "interacting segments," $\Delta V_i(\boldsymbol{\beta}_i, \theta_i; a_i)$, depend on the orientation of the symmetry axes of the nuclei. As was indicated above, a static quadrupole deformation is the most peculiar to nuclei—that is, $\beta_{3,4}^{\rm g.s.} \ll \beta_2^{\rm g.s.}$. In addition, we note that, at $a \approx 1$ fm, the deviation of the volumes $\Delta V_i(\boldsymbol{\beta}_i, \theta_i; a_i)$ from the spherical ones is much less for higher multipole orders than for $\lambda = 2$. In calculating the angular dependence of the geometric factor, one can therefore take into account only static quadrupole deformations of interacting nuclei. In order to calculate the volume of the side segment of a nucleus (side-to-side orientation of nuclei—that is, $\theta_i = \pi/2$), we can again use formula (A.9) to find the angle θ_0^i ($t_0^i \equiv \cos\theta_0^i$) of the corresponding cone. In this formula, however, we must replace $R_i^0 = R_i(\boldsymbol{\beta}_i, \theta = 0)$ by $R_i^B = R_i(\boldsymbol{\beta}_i, \theta = \pi/2)$. In this case, the base of the segment is an ellipse whose semiaxes are $A = \sqrt{2R_i^B a_i - a_i^2}$ and $B = (R_i^B - a_i)/\tan\theta_0^i$, its volume being approximately

$$\Delta V_i = \frac{\pi}{2} a_i^2 \sqrt{2R_i^B - a_i}(R_i^B - a_i)/\tan\theta_0^i. \quad \text{(A.11)}$$

Knowing the volumes of the surface segments for the two limiting orientations—ΔV_i^N calculated by formula (A.8) at $\theta_i = 0$ and ΔV_i^S calculated by formula (A.11) at $\theta_i = \pi/2$—one can approximate the volume of the segment of an arbitrarily rotated nucleus by the simple expression $\Delta V_i(\theta_i) = 0.5(\Delta V_i^S + \Delta V_i^N) - 0.5(\Delta V_i^S - \Delta V_i^N)\cos 2\theta_i$ and then use formula (A.7) to calculate the geometric factor in the potential of the interaction of two deformed nuclei arbitrarily rotated in the reaction plane.

REFERENCES

1. M. Beckerman, Rep. Prog. Phys. **51**, 1047 (1988), and references therein.
2. *Heavy Ion Fusion*, Ed. by A. M. Stefanini *et al.* (World Sci., Singapore, 1994).
3. *Papers from Fusion 97*, J. Phys. G **23**, 1157 (1997).
4. M. Dasgupta, D. J. Hinde, N. Rowley, and A. M. Stefanini, Annu. Rev. Nucl. Part. Sci. **48**, 401 (1998).
5. C. H. Dasso and S. Landowne, Comput. Phys. Commun. **46**, 187 (1987); J. Fernandez-Niello, C. H. Dasso, and S. Landowne, Comput. Phys. Commun. **54**, 409 (1989).
6. K. Hagino, N. Rowley, and A. T. Kruppa, Comput. Phys. Commun. **123**, 143 (1999).
7. V. I. Zagrebaev, N. S. Nikolaev, and V. V. Samarin, Izv. Akad. Nauk, Ser. Fiz. **61**, 2157 (1997).
8. N. Takigawa, T. Rumin, and N. Ihara, Phys. Rev. C **61**, 044607 (2000).
9. J. Blocki, J. Randrup, W. J. Swiatecki, and C. F. Tsang, Ann. Phys. (N.Y.) **105**, 427 (1977).
10. R. A. Broglia, C. H. Dasso, and A. Winter, in *Proceedings of the International School of Physics "Enrico Fermi," Course LXXVII, Varenna, 1979*, Ed. by R. A. Broglia, R. A. Ricci, and H. A. Dasso (North-Holland, Amsterdam, 1981), p. 327.
11. G. A. Korn and T. M. Korn, *Mathematical Handbook for Scientists and Engineers* (McGraw-Hill, New York, 1961; Nauka, Moscow, 1971).
12. I. I. Gontchar, M. Dasgupta, D. J. Hinde, *et al.*, Phys. Rev. C **65**, 034610 (2002).
13. A. Bohr and B. R. Mottelson, *Nuclear Structure,* Vol. 2: *Nuclear Deformations* (Benjamin, New York, 1975; Mir, Moscow, 1977), Vol. 2.
14. M. A. Nagarajan, N. Rowley, and R. J. Lindsay, J. Phys. G **12**, 529 (1986).
15. J. H. Wilkinson and C. Reinsch, *Linear Algebra* (Springer-Verlag, Berlin, 1971; Mashinostroenie, Moscow, 1976).
16. J. Tôke, R. Bock, G. X. Dai, *et al.*, Nucl. Phys. A **440**, 327 (1985).
17. V. I. Zagrebaev, Phys. Rev. C **64**, 034606 (2001).
18. *Modern Numerical Methods for Ordinary Differential Equations,* Ed. by G. Hall and J. Watt (Oxford Univ. Press, Oxford, 1976; Mir, Moscow, 1979).
19. N. Rowley, G. R. Satchler, and P. H. Stelson, Phys. Lett. B **254**, 25 (1991).
20. D. L. Hill and J. A. Wheeler, Phys. Rev. **89**, 1102 (1953).
21. J. R. Leigh *et al.*, Phys. Rev. C **52**, 3151 (1995).

22. F. Scarlassara, S. Beghini, G. Montagnoli, *et al.*, in *Proceedings of the International Workshop on Fusion Dynamics at the Extremes, Dubna, 2000*, Ed. by Yu. Ts. Oganessian and V. I. Zagrebaev (World Sci., Singapore, 2001), p. 274.
23. M. G. Itkis *et al.*, in *Proceedings of the International Workshop on Fusion Dynamics at the Extremes*, Dubna, 2000, Ed. by Yu. Ts. Oganessian and V. I. Zagrebaev (World Sci., Singapore, 2001), p. 93.
24. R. Bass, *Nuclear Reactions with Heavy Ions* (Springer-Verlag, Berlin, 1980), p. 326.
25. P. Möller, J. R. Nix, W. D. Myers, and W. J. Swiatecki, At. Data Nucl. Data Tables **59**, 185 (1995).
26. http://nrv.jinr.ru/nrv/.

Translated by A. Isaakyan

Physics of Atomic Nuclei, Vol. 67, No. 8, 2004, pp. 1478–1486. From Yadernaya Fizika, Vol. 67, No. 8, 2004, pp. 1503–1511.

NUCLEI
Theory

Scattering and Pair Production by a Potential Barrier*

A. I. Nikishov**

Lebedev Institute of Physics, Russian Academy of Sciences, Leninskiĭ pr. 53, Moscow, 117924 Russia

Received May 26, 2003; in final form, November 17, 2003

Abstract—Scattering and electron–positron pair production by a one-dimensional electric barrier is considered in the framework of the S-matrix formalism. The solutions of the Dirac equation are classified according to frequency sign. The Bogolyubov transformations relating the in- and out-states are given. We show that the norm of a solution to the wave equation is determined by the largest amplitude of its asymptotic form when $x_3 \to \pm\infty$. For the Sauter-type potential, we give the explicit expressions for the complete in- and out-sets of orthonormalized wave functions. We note that, in principle, virtual vacuum processes in an external field influence the phase of the wave function of the scattered particle.

1. INTRODUCTION

Scattering and pair production by an external field can be treated either by the Feynman propagator method [1, 2] or in the framework of S-matrix formalism [3–5]. In the latter method, the Bogolyubov coefficients, relating the in- and out-states, determine the probabilities of all processes in an external field. So, at first, we have to determine the in- and out-states. Surprisingly enough, there is a controversy on how to choose these states among the stationary solutions of a wave equation with one-dimensional static potential $A_\mu(x_3)$. The choice made in [6] and accepted in [7, 8] disagrees with the one made in [4, 9–11]. For a detailed justification of our choice, see [9–11].

In this paper, we give the in- and out-sets of solutions of the Dirac equation with barrier (electric) potential and the Bogolyubov transformations. We express the normalization of a stationary one-dimensional solution via the largest amplitude of its asymptotic form when $x_3 \to \pm\infty$. For the Sauter-type potential and step potential, we give the explicit solutions to the Dirac equation and also the Bogolyubov coefficients. In contrast to [6, 7], we do not assume that the transverse (to the field) momentum of an electron is zero. The treatment of the spinor case in this paper is similar to that of the scalar case in [9].

2. THE CHOICE OF IN- AND OUT-STATES

We consider the one-dimensional potential $A^0(x_3) = -aF(kx_3)$ and assume that the corresponding electrical field $E_3 = -\partial A^0/\partial x_3 = akF'(kx_3)$ disappears when $x_3 \to \pm\infty$. We use the metric $\eta_{\mu\nu} = \mathrm{diag}(-1, 1, 1, 1)$ and introduce the kinetic energy $\pi^0(x_3)$ and kinetic momentum $\pi_3(x_3)$ of a classical particle defined by the expressions

$$\pi^0(x_3) = p^0 - eA^0(x_3), \tag{1}$$
$$\pi_3(x_3) = \sqrt{\pi_0^2(x_3) - m_\perp^2},$$
$$m_\perp^2 = m^2 + p_1^2 + p_2^2.$$

We also use the notation

$$\pi^0(x_3)\big|_{x_3\to\pm\infty} = \pi^0(\pm), \tag{2}$$
$$\pi_3(x_3)|_{x_3\to\pm\infty} = \pi_3(\pm) = \sqrt{\pi_0^2(\pm) - m_\perp^2},$$
$$\pi^\pm(x_3) = \pi^0(x_3) \pm \pi_3(x_3).$$

The electron charge is denoted as $e = -|e|$. We assume for definiteness that $E_3 > 0$ and consider two regions: electron scattering ($\pi^0(\pm) > m_\perp$) and Klein region

$$\pi^0(-) > m_\perp, \qquad \pi^0(+) < -m_\perp. \tag{3}$$

In the Klein region, the large positive x_3 are accessible only to positrons.

For reasons of brevity, we often write only the wave function factor depending on x_3 (i.e., we drop the factor $\exp\{i[p_1x_1 + p_2x_2 - p^0t]\}$). We denote solutions of the Dirac equation as $f_n(x_3)$, where $n = (p, r)$ and $p = (p^0, p_1, p_2, 0)$ are the eigenvalues of operators $i\partial_0, -i\partial_1, -i\partial_2$; $r = 1, 2$ indicate spin state. f_n can be expressed via solutions $Q_p(x_3, \pm\lambda)$ of the squared Dirac equation

$$[\Pi^2 + m^2 \pm ieE_3(x_3)]Q_p(x_3, \pm\lambda)e^{ipx} = 0. \tag{4}$$

*This article was submitted by the author in English.

**e-mail: nikishov@lpi.ru

Here,

$$\Pi_\mu = -i\partial_\mu - eA_\mu, \quad \mathbf{A} = \mathbf{0}, \quad \lambda = \frac{ea}{k},$$

and ± 1 are the eigenvalues of the Pauli matrix σ_3. It follows from (4) that ($\varphi = kx_3$)

$$\left[\frac{d^2}{d\varphi^2} + \frac{2eap^0}{k^2}F(\varphi) + \lambda^2 F^2(\varphi) + \frac{p_0^2 - m_\perp^2}{k^2} - i\lambda F'(\varphi)\right] Q_p(x_3, \lambda) = 0. \tag{5}$$

We consider solutions with the boundary conditions

$$ {}_\pm Q_p\big|_{x_3\to-\infty} = \exp[\pm i\pi_3(-)x_3], \qquad {}^\pm Q_p\big|_{x_3\to+\infty} = \exp[\pm i\pi_3(+)x_3], \tag{6}$$

independently of the sign in front of λ. The corresponding f_n solutions of the Dirac equation are [12]

$$ {}_\pm f_n = [4|\pi_3(-)\pi^\mp(-)|]^{-1/2} \times [u_r {}_\pm Q_p(x_3, \lambda) + \pi^\mp(-)u'_r {}_\pm Q_p(x_3, -\lambda)], \tag{7}$$

$$ {}^\pm f_n = [4|\pi_3(+)\pi^\mp(+)|]^{-1/2} \times [u_r {}^\pm Q_p(x_3, \lambda) + \pi^\mp(+)u'_r {}^\pm Q_p(x_3, -\lambda)].$$

In the standard representation of γ matrices we have

$$u_1 = \begin{bmatrix} p_1 - ip_2 \\ m \\ p_1 - ip_2 \\ -m \end{bmatrix}, \quad u_2 = \begin{bmatrix} m \\ -p_1 - ip_2 \\ m \\ p_1 + ip_2 \end{bmatrix}, \tag{8}$$

$$u'_1 = \begin{bmatrix} 0 \\ 1 \\ 0 \\ 1 \end{bmatrix}, \quad u'_2 = \begin{bmatrix} 1 \\ 0 \\ -1 \\ 0 \end{bmatrix}.$$

All these spinors are orthogonal:

$$u_1^* u_2 = u_1^* u'_2 = u_1^* u'_1 = \ldots = 0,$$

so that $f^*_{rp} f_{r'p} \propto \delta_{r'r}$. This means that states with $r \neq r'$ are orthogonal. The normalization factors in (7) are chosen in such a way that the current density along the third axis is equal to unity up to a sign. The 4-vector transition current is conserved. For $p^0 = p'^0$, this means that the 3-current is independent of x_3 and can be evaluated using the asymptotic forms of f_n. It is easy to find that (α_3 is the Dirac matrix)

$$j_3(f_{n'}, f_n) = f^*_{n'} \alpha_3 f_n, \tag{9}$$

$$j_3({}^\varepsilon f_{r,p}, {}^{\varepsilon'} f_{r',p}) = \delta_{\varepsilon\varepsilon'}\delta_{rr'} \begin{cases} \varepsilon 1, & \pi^0(+) > m_\perp, \\ -\varepsilon 1, & \pi^0(+) < -m_\perp, \end{cases} \quad \varepsilon, \varepsilon' = \pm;$$

$$j_3({}_\varepsilon f_{r,p}, {}_{\varepsilon'} f_{r',p}) = \delta_{\varepsilon\varepsilon'}\delta_{rr'} \begin{cases} \varepsilon 1, & \pi^0(-) > m_\perp, \\ -\varepsilon 1, & \pi^0(-) < -m_\perp. \end{cases} \tag{10}$$

To obtain the relation between ${}_\pm f_n$ and ${}^\pm f_n$, we first write

$$ {}_+ Q_p(x_3, \lambda) = a(\lambda)^+ Q_p(x_3, \lambda) + b(\lambda)^- Q_p(x_3, \lambda). \tag{11}$$

$a(\lambda)$ and $b(\lambda)$ are defined by this equation. From here, by complex conjugation and substitutions $p \to -p$, $e \to -e$, we get

$$ {}_- Q_p(x_3, \lambda) = a^*(-\lambda)^- Q_p(x_3, \lambda) + b^*(-\lambda)^+ Q_p(x_3, \lambda). \tag{12}$$

Now it can be shown [12] that

$$ {}_+ f_n = c'_{1n} {}^+ f_n + c'_{2n} {}^- f_n, \tag{13}$$

$$ {}_- f_n = \pm c'^*_{2n} {}^+ f_n \pm c'^*_{1n} {}^- f_n, \quad \pm|c'_{1n}|^2 \mp |c'_{2n}|^2 = 1,$$

or equivalently

$$ {}^+ f_n = \pm c'^*_{1n+} f_n - c'_{2n-} f_n, \tag{14}$$

$$ {}^- f_n = \mp c'^*_{2n+} f_n + c'_{1n-} f_n.$$

Here,

$$c'_{1n} = \left(\frac{\pi_3(+)|\pi^-(+)|}{\pi_3(-)|\pi^-(-)|}\right)^{1/2} a(\lambda), \qquad c'_{2n} = \left(\frac{\pi_3(+)|\pi^+(+)|}{\pi_3(-)|\pi^-(-)|}\right)^{1/2} b(\lambda) \tag{15}$$

are independent of spin states $r = 1, 2$. The upper sign in front of c'_{1n}, c'_{2n} (and their complex conjugates) corresponds to the scattering region ($\pi^0(\pm) > m_\perp$ for an electron or $\pi^0(\pm) < -m_\perp$ for a positron), while the lower sign corresponds to the Klein region ($\pi^0(-) > m_\perp, \pi^0(+) < -m_\perp$).

The consistency of Eqs. (13) and (14) can be checked by calculating $j_3({}_+ f_n, {}^+ f_n)$ in two different ways:

$$j_3({}_+ f_n, {}^+ f_n) = \pm c'^*_{1n} j_3({}_+ f_n, {}_+ f_n) = c'^*_{1n} j_3({}^+ f_n, {}^+ f_n). \tag{16}$$

In the first equation here, use has been made of the first equation in (14) and Eq. (10). The last term in

(16) was obtained similarly. The last equality in (16) is consistent (valid) due to (9).

Now we have to classify the solutions as in- and out-states. For the Klein region, we have [4, 9]

$$
\begin{aligned}
{}^{-}\psi_n \equiv {}^{-}\psi_{n\ \mathrm{out}} = \mathcal{N}_{n+} f_n, \qquad (17)\\
{}^{+}\psi_n \equiv {}^{+}\psi_{n\ \mathrm{out}} = \mathcal{N}_n \frac{c'^{\,*}_{2n}}{c'_{2n}} {}^{+}f_n,\\
{}_{-}\psi_n \equiv {}_{-}\psi_{n\ \mathrm{in}} = \mathcal{N}_{n-} f_n,\\
{}_{+}\psi_n \equiv {}_{+}\psi_{n\ \mathrm{in}} = \mathcal{N}_n {}^{-}f_n.
\end{aligned}
$$

Here, the subscripts and superscripts $\pm$ in front of ψ functions indicate the sign of frequencies, i.e., the sign of π^0 of the largest wave. ${}^{-}\psi_n$ is the out-wave because in this state only one current goes out of the barrier (two other currents go to the barrier). Similar arguments hold for other states. The normalization factor $\mathcal{N}_n$ will be determined later [see Eq. (49) and the text below it]. In terms of these ψ functions in (17), relations (13) and (14) take on the form required for application in the S-matrix theory (see [3, 4]),

$$
\begin{aligned}
{}_{+}\psi_n = c_{1n} {}^{+}\psi_n + c_{2n} {}^{-}\psi_n, \qquad (18)\\
{}_{-}\psi_n = -c^*_{2n} {}^{+}\psi_n + c^*_{1n} {}^{-}\psi_n;\\
{}^{+}\psi_n = c^*_{1n+}\psi_n - c_{2n-}\psi_n,\\
{}^{-}\psi_n = c^*_{2n+}\psi_n + c_{1n-}\psi_n;
\end{aligned}
$$

$$
|c_{1n}|^2 + |c_{2n}|^2 = 1, \quad c_{1n} = -\frac{c'_{1n}}{c'^*_{2n}}, \quad c_{2n} = \frac{1}{c'_{2n}}. \qquad (19)
$$

The sign of frequency is not conserved in the Klein region. We note also that the first equation in (19) follows from the last equation in (13) with the lower signs.

The corresponding Bogolyubov transformations for the creation operators $a^\dagger_n$ ($b^\dagger_n$) and destruction operators a_n (b_n) for a particle (antiparticle) are obtainable from the definition of the field operator

$$
\begin{aligned}
\Psi = \sum_n (a_{n\ \mathrm{in}+}\psi_n + b^\dagger_{n\ \mathrm{in}-}\psi_n) \qquad (20)\\
= \sum_n (a_{n\ \mathrm{out}} {}^{+}\psi_n + b^\dagger_{n\ \mathrm{out}} {}^{-}\psi_n).
\end{aligned}
$$

It follows from here and (18), (19) that

$$
\begin{aligned}
a_{n\ \mathrm{out}} = c_{1n} a_{n\ \mathrm{in}} - c^*_{2n} b^\dagger_{n\ \mathrm{in}}, \qquad (21)\\
b^\dagger_{n\ \mathrm{out}} = c_{2n} a_{n\ \mathrm{in}} + c^*_{1n} b^\dagger_{n\ \mathrm{in}}
\end{aligned}
$$

or

$$
\begin{aligned}
a_{n\ \mathrm{in}} = c^*_{1n} a_{n\ \mathrm{out}} + c^*_{2n} b^\dagger_{n\ \mathrm{out}}, \qquad (22)\\
b^\dagger_{n\ \mathrm{in}} = -c_{2n} a_{n\ \mathrm{out}} + c_{1n} b^\dagger_{n\ \mathrm{out}}.
\end{aligned}
$$

In the scattering region $\pi^0(\pm) > m_\perp$, the sign of frequency is conserved, but the sign of kinetic momentum is not. We define

$$
{}^{+}\psi_n(x_3|+) = \frac{c'^*_{1n}}{c'_{1n}} N_{n+} f_n, \quad {}^{+}\psi_n(x_3|-) = N_n {}^{-}f_n, \qquad (23)
$$

$$
{}_{+}\psi_n(x_3|+) = N_n {}^{+}f_n, \quad {}_{+}\psi_n(x_3|-) = N_{n-} f_n.
$$

(The sign in parentheses coincides with the subscript or superscript of the corresponding f function.) ${}^{+}\psi_n(x_3|\pm)$ are functions with two ingoing waves in the past and one outgoing wave in the future. Similarly, ${}_{+}\psi_n(x_3|\pm)$ are functions with one ingoing wave in the past and two outgoing waves in the future. In terms of these ψ functions, relations (13), (14) become

$$
{}_{+}\psi_n(x_3|+) = e_{1n} {}^{+}\psi_n(x_3|+) + e_{2n} {}^{+}\psi_n(x_3|-), \qquad (24)
$$

$$
\begin{aligned}
{}_{+}\psi_n(x_3|-) = -e^*_{2n} {}^{+}\psi_n(x_3|+) + e^*_{1n} {}^{+}\psi_n(x_3|-),\\
{}^{+}\psi_n(x_3|+) = e^*_{1n+}\psi_n(x_3|+) - e_{2n+}\psi_n(x_3|-),\\
{}^{+}\psi_n(x_3|-) = e^*_{2n+}\psi_n(x_3|+) + e_{1n+}\psi_n(x_3|-);
\end{aligned}
$$

$$
e_{1n} = \frac{1}{c'^*_{1n}}, \quad e_{2n} = -\frac{c'_{2n}}{c'_{1n,}}, \quad |e_{1n}|^2 + |e_{2n}|^2 = 1. \qquad (25)
$$

The last equation in (25) is equivalent to the last equation in (13) with upper signs. Proceeding as usual, from these relations and definition (20)

$$
\begin{aligned}
a_{n\,\mathrm{in}}(+)_+\psi_n(x_3|+) + a_{n\,\mathrm{in}}(-)_+\psi_n(x_3|-) \qquad (26)\\
= a_{n\,\mathrm{out}}(+)^+\psi_n(x_3|+) + a_{n\,\mathrm{out}}(-)^+\psi_n(x_3|-),
\end{aligned}
$$

we get

$$
\begin{aligned}
a_{n\ \mathrm{out}}(+) = e_{1n} a_{n\ \mathrm{in}}(+) - e^*_{2n} a_{n\ \mathrm{in}}(-), \qquad (27)\\
a_{n\ \mathrm{out}}(-) = e_{2n} a_{n\ \mathrm{in}}(+) + e^*_{1n} a_{n\ \mathrm{in}}(-).
\end{aligned}
$$

[See also definitions (23), (6), and (7).] Solving (27) for $a_{n\,\mathrm{in}}(\pm)$, we obtain

$$
\begin{aligned}
a_{n\ \mathrm{in}}(+) = e^*_{1n} a_{n\ \mathrm{out}}(+) + e^*_{2n} a_{n\ \mathrm{out}}(-), \qquad (28)\\
a_{n\ \mathrm{in}}(-) = -e_{2n} a_{n\ \mathrm{out}}(+) + e_{1n} a_{n\ \mathrm{out}}(-).
\end{aligned}
$$

3. MATRIX ELEMENTS AND PROBABILITIES

We denote $|0_{n\ \mathrm{in}}\rangle$ the in-vacuum state in the cell with quantum numbers n and similarly for the out-vacuum. To find $\langle 0_{n\ \mathrm{out}}|0_{n\ \mathrm{in}}\rangle$, we rewrite Bogolyubov transformations (21) in the form

$$
a_{n\ \mathrm{out}} = B_n^{-1} a_{n\ \mathrm{in}} B_n, \quad b^\dagger_{n\ \mathrm{out}} = B_n^{-1} b^\dagger_{n\ \mathrm{in}} B_n, \qquad (29)
$$

where [3]

$$B_n = c_{1n}^* + (1 - c_{1n}^*)[a_{n\ \mathrm{in}}^\dagger a_{n\ \mathrm{in}} + b_{n\ \mathrm{in}}^\dagger b_{n\ \mathrm{in}}] \quad (30)$$
$$- c_{2n}^* a_{n\ \mathrm{in}}^\dagger b_{n\ \mathrm{in}}^\dagger - c_{2n} a_{n\ \mathrm{in}} b_{n\ \mathrm{in}}$$
$$+ (c_{1n} + c_{1n}^* - 2) a_{n\ \mathrm{in}}^\dagger a_{n\ \mathrm{in}} b_{n\ \mathrm{in}}^\dagger b_{n\ \mathrm{in}}.$$

Equations (29) imply $\langle 0_{n\ \mathrm{out}}| = \langle 0_{n\ \mathrm{in}}|B_n$ and, hence,

$$\langle 0_{n\ \mathrm{out}}|0_{n\ \mathrm{in}}\rangle = c_{1n}^*. \quad (31)$$

We note now that the unitary operator B is defined by (29) and (21) only up to a phase factor and we set it equal to unity. This is a natural choice. It leads to (31), from which the correct vacuum–vacuum amplitude for a constant electromagnetic field can be obtained [13].

Now we can write the matrix elements. We start with the Klein region. From the second equation in (22), we have

$$b_{n\ \mathrm{in}} = -c_{2n}^* a_{n\ \mathrm{out}}^\dagger + c_{1n}^* b_{n\ \mathrm{out}}. \quad (32)$$

Using this relation, we find

$$b_{n\ \mathrm{out}}|0_{n\ \mathrm{in}}\rangle = c_{2n}^* c_{1n}^{*-1} a_{n\ \mathrm{out}}^\dagger |0_{n\ \mathrm{in}}\rangle. \quad (33)$$

From here, for the pair creation amplitude, we find

$$\langle 0_{n\ \mathrm{out}}|a_{n\ \mathrm{out}} b_{n\ \mathrm{out}}|0_{n\ \mathrm{in}}\rangle \quad (34)$$
$$= c_{2n}^* c_{1n}^{*-1} \langle 0_{n\ \mathrm{out}}|0_{n\ \mathrm{in}}\rangle = c_{2n}^*.$$

The sum of all probabilities in the cell n initially in the vacuum state is

$$|\langle 0_{n\ \mathrm{out}}|0_{n\ \mathrm{in}}\rangle|^2 + |\langle 0_{n\ \mathrm{out}}|a_{n\ \mathrm{out}} b_{n\ \mathrm{out}}|0_{n\ \mathrm{in}}\rangle|^2 = 1 \quad (35)$$

[see (31), (34), and the first equation in (19)]. Similarly, we get the following expression for the scattering amplitude in the Klein region:

$$\langle 0_{n\ \mathrm{out}}|a_{n\ \mathrm{out}} a_{n\ \mathrm{in}}^\dagger|0_{n\ \mathrm{in}}\rangle = c_{1n}^{*-1}\langle 0_{n\ \mathrm{out}}|0_{n\ \mathrm{in}}\rangle = 1. \quad (36)$$

We see that the information on processes in an external field is contained in the solutions of the wave equation, but it has to be decoded. In particular, if the initial state with quantum numbers n is occupied, we know that the electron cannot penetrate deep into the barrier. It is suggested in [14, 15] that the accessible region is defined by the condition $\pi^0(x_3) > 0$.

Now we go to the scattering region, extending its definition to all energies outside the Klein region. In this case, $c_{2n} = 0$ and $c_{1n}c_{1n}^* = 1$ in (18), (19), and (21). Hence,

$${}^+\psi_n = c_{1n}^* {}_+\psi_n, \quad a_{n\ \mathrm{out}} = a_{n\ \mathrm{in}} c_{1n} \quad (37)$$

and similarly for the other quantities. We first consider the scattering region, where the reflection is complete. Then $\pi_3(+)$ is imaginary (namely, $\pi_3(+) = i|\pi_3(+)|$ or $\pi_3(+) = -i|\pi_3(+)|$) and $|c'_{1n}| = |c'_{2n}|$ due to current conservation. The solutions ${}_\pm f_n$ in (13) must be discarded as containing exponentially growing terms when $x_3 \to \infty$ [cf. Eq. (72) below]. Instead of two solutions ${}^\pm f_n$, we are left with only one since there is only one boundary condition when $x_3 \to \infty$ [see the second equation in (6)]: $Q_p|_{x_3 \to +\infty} = \exp[-|\pi_3(+)|x_3]$. The reflection amplitude is

$$\langle 0_{n\mathrm{out}}|a_{n\ \mathrm{out}}(-)a_{n\ \mathrm{in}}^\dagger(+)|0_{n\ \mathrm{in}}\rangle = c_{1n}\langle 0_{n\ \mathrm{out}}|0_{n\ \mathrm{in}}\rangle = 1 \quad (38)$$

[see the second equation in (37), Eq. (31), and the condition $c_{1n}c_{1n}^* = 1$].

The final state ${}^+\psi_n$ in (37) differs from the initial state ${}_+\psi_n$ only by the phase factor given by the (renormalized) value of $\langle 0_{n\ \mathrm{out}}|0_{n\ \mathrm{in}}\rangle$ [see (31)], i.e., by $\langle 0_{n\ \mathrm{out}}|0_{n\ \mathrm{in}}\rangle^{\mathrm{ren}} \equiv e^{i\phi_n}$ [13]. In principle, this factor can be observed in the interference pattern of the incident and reflected waves. Then there will be a way to find ϕ_n experimentally.

We note here that the considered region of complete reflection can be reached from the Klein region by raising the value of p^0. At the top of the Klein region, c_{2n} is very small and the reflected wave resembles the one at the bottom of the complete reflection region; the corresponding c_{1n} just above and below the boundary between two regions must be almost equal.

By raising p^0 still further, we enter into the scattering region where $\pi^0(\pm) > m_\perp$. For the initial state ${}_+\psi_n(x_3|+)$, using (27), we find for the reflection and transmission amplitudes

$$\langle 0_{n\ \mathrm{out}}|a_{n\ \mathrm{out}}(-)a_{n\ \mathrm{in}}^\dagger(+)|0_{n\ \mathrm{in}}\rangle = e_{2n}\langle 0_{n\ \mathrm{out}}|0_{n\ \mathrm{in}}\rangle, \quad (39)$$

$$\langle 0_{n\ \mathrm{out}}|a_{n\ \mathrm{out}}(+)a_{n\ \mathrm{in}}^\dagger(+)|0_{n\ \mathrm{in}}\rangle = e_{1n}\langle 0_{n\ \mathrm{out}}|0_{n\ \mathrm{in}}\rangle. \quad (40)$$

Alternatively, we may say that our solutions ${}^+\psi_n(x_3|\pm)$ are relative ones and the absolute solutions are obtained from them by multiplying by $e^{i\phi_n}$. Then the factor $\langle 0_{n\ \mathrm{out}}|0_{n\ \mathrm{in}}\rangle$ on the right-hand side of (39) and (40) disappears.

The propagator method gives the same results. In the Klein region, we start from ${}_+\psi_n$. The Feynman propagator evolves this state to the relative function $c_{1n}^{*-1}{}^+\psi_n$ [4]. So the absolute final function is ${}^+\psi_n$. In the scattering region, the relative final wave function is the same as the initial one and the absolute final function is $e^{i\phi_n}{}_+\psi_n$. It is a happy occasion when $c_{1n}^{*\mathrm{ren}}$ gives $e^{i\phi_n} \equiv \langle 0_{n\ \mathrm{out}}|0_{n\ \mathrm{in}}\rangle^{\mathrm{ren}}$. In general, $e^{i\phi_n}$ have to be found by other means (see [13]). In quantum mechanics for the state ${}_+\psi_n(x_3|+)$, the amplitudes

of reflection and transmission are obtained directly from the first equation in (24), which says that the reflection (transmission) amplitude is e_{2n} (e_{1n}). In the considered scattering region, $e^{i\phi_n}$ is a phase factor. We see that vacuum virtual processes lead to the appearance of an additional phase shift in the reflected and transmitted waves.

In conclusion of this section, we note that, in the scattering region, instead of (30) and (29), we have (again with natural choice of phase factor)

$$A_n = 1 + (e_{1n} - 1)a^\dagger_{n\ \mathrm{in}}(+)a_{n\ \mathrm{in}}(+) \quad (41)$$
$$+ (e^*_{1n} - 1)a^\dagger_{n\ \mathrm{in}}(-)a_{n\ \mathrm{in}}(-) + e_{2n}a^\dagger_{n\ \mathrm{in}}(-)a_{n\ \mathrm{in}}(+)$$
$$- e^*_{2n}a^\dagger_{n\ \mathrm{in}}(+)a_{n\ \mathrm{in}}(-)$$
$$+ [2 - (e_{1n} + e^*_{1n})]a^\dagger_{n\ \mathrm{in}}(+)a_{n\ \mathrm{in}}(+)a^\dagger_{n\ \mathrm{in}}(-)a_{n\ \mathrm{in}}(-),$$

$$A_n^{-1}a_{n\ \mathrm{in}}(\pm)A_n = a_{n\ \mathrm{out}}(\pm), \quad \langle 0_{n\ \mathrm{in}}| = \langle 0_{n\ \mathrm{in}}|A_n \quad (42)$$

(see Appendix 5 in [16]).

4. NORMALIZATION OF WAVE FUNCTIONS

For our stationary states, the (transition) current conservation gives

$$i(p'^0 - p^0)j^0(f_{n'}, f_n|x_3) = -\frac{\partial}{\partial x_3}j_3(f_{n'}, f_n|x_3). \quad (43)$$

(We recall that, in our metric, $j^3 = j_3$.) Thus,

$$\int_{-L_d}^{L_u} dx_3 j^0(f_{n'}, f_n|x_3) \quad (44)$$
$$= \frac{i}{p'^0 - p^0}[j_3(f_{n'}, f_n|L_u) - j_3(f_{n'}, f_n| - L_d)].$$

First, we consider $f_{n'} = {}_+f_{n'}$, $f_n = {}_+f_n$, where $n' = (p'^0, p_1, p_2, r)$ and $n = (p^0, p_1, p_2, r)$, $r = 1, 2$. For $x_3 \to -\infty$, we can easily calculate $j_3({}_+f_{n'}, {}_+f_n| - L_d)$ because ${}_+f_{n'}$, ${}_+f_n$ are known in this limit [see Eqs. (6) and (7)]. The result is

$$-j_3({}_+f_{n'}, {}_+f_n| - L_d) \quad (45)$$
$$\to -e^{-i[\pi_3(-) - \pi'_3(-)]L_d} = -e^{-iA_d(p^0 - p'^0)},$$
$$A_d = \frac{\pi^0(-) + \pi'^0(-)}{\pi_3(-) + \pi'_3(-)}L_d.$$

Here, $\pi'^0(-)$ and $\pi'_3(-)$ are defined in (1) and (2) with p^0 replaced by p'^0. The arrow means that we set $\pi'_3(-) = \pi_3(-)$, $\pi'^-(-) = \pi^-(-)$ everywhere except in the exponent. This is permissible because, when $L_d \to \infty$, the effectively nonzero result will be achieved only when π' is close to π. In the last equation in (45), we have used the relation

$$\pi_3^2 - \pi'^2_3 = (\pi^0)^2 - (\pi'^0)^2 = (\pi^0 + \pi'^0)(p^0 - p'^0) \quad (46)$$

[see Eqs. (1) and (2)].

The contribution from $j_3({}_+f_{n'}, {}_+f_n|L_u)$ is treated in the same manner. Using the first equation in (13), we have

$$j_3({}_+f_{n'}, {}_+f_n) = c'^*_{1n'}c'_{1n}j_3({}^+f_{n'}, {}^+f_n) \quad (47)$$
$$+ c'^*_{2n'}c'_{2n}j_3({}^-f_{n'}, {}^-f_n) + c'^*_{1n'}c'_{2n}j_3({}^+f_{n'}, {}^-f_n)$$
$$+ c'^*_{2n'}c'_{1n}j_3({}^-f_{n'}, {}^+f_n) \to |c'_{1n}|^2 j_3({}^+f_{n'}, {}^+f_n)$$
$$+ |c'_{2n}|^2 j_3({}^-f_{n'}, {}^-f_n).$$

In the Klein region, this can be written as follows:

$$j_3({}_+f_{n'}, {}_+f_n|L_u) \to -|c'_{1n}|^2 e^{i[\pi_3(+) - \pi'_3(+)]L_u} \quad (48)$$
$$+ |c'_{2n}|^2 e^{-i[\pi_3(+) - \pi'_3(+)]L_u}$$
$$= -|c'_{1n}|^2 e^{-iA_u(p^0 - p'^0)} + |c'_{2n}|^2 e^{iA_u(p^0 - p'^0)},$$
$$A_u = \frac{-\pi^0(+) - \pi'^0(+)}{\pi_3(+) + \pi'_3(+)}L_u.$$

Noting that A_d and A_u are of the same sign, we fix the relation between them: $A_d = A_u$. Using also $|c'_{2n}|^2 = |c'_{1n}|^2 + 1$ [see the last relation (13) with the lower signs], we finally obtain from (44) and (45)

$$\int_{-\infty}^{\infty} dx_3 j^0({}_+f_{n'}, {}_+f_n) = 2\pi|c'_{2n}|^2\delta(p^0 - p'^0) \quad (49)$$

in the Klein region, where the amplitude of the largest wave is c'_{2n}. Thus, choosing $\mathcal{N}_n = |c'_{2n}|^{-1}$, we normalize ψ functions in (17) on $2\pi\delta(p^0 - p'^0)$.

In the scattering region, $|c'_{1n}|^2 = |c'_{2n}|^2 + 1$. So, the amplitude of the largest wave is c'_{1n} and we must substitute $c'_{2n} \to c'_{1n}$ on the right-hand side of (49). This can be seen as follows. Relation (45) remains unchanged. Instead of (48), we have

$$j_3({}_+f_{n'}, {}_+f_n|L_u) \quad (50)$$
$$\to |c'_{1n}|^2 e^{-iA_u(p^0 - p'^0)} - |c'_{2n}|^2 e^{iA_u(p^0 - p'^0)}.$$

In addition, now $A_u = -|A_u|$ and $|c'_{1n}|^2 = |c'_{2n}|^2 + 1$. So, the condition $A_d = |A_u|$ leads to the stated result. In other words, $N_n = |c'_{1n}|^{-1}$ in (23) for normalization on $2\pi\delta(p^0 - p'^0)$. We note here that the condition

$$\frac{\pi^0(-) + \pi'^0(-)}{\pi_3(-) + \pi'_3(-)}L_d = \frac{\pi^0(+) + \pi'^0(+)}{\pi_3(+) + \pi'_3(+)}L_u \quad (51)$$

is a generalization of the usual free field condition $L_d = L_u$ to the scattering region. In the case of a

complete reflection, we have $|c'_{1n}| = |c'_{2n}|$ and (49) remains valid.

Going back to the Klein region, we can show that ${}^{+}\psi_{n'}$ and ${}^{-}\psi_n$ [see (17)] are orthogonal. As ${}^{+}\psi_n \propto {}^{+}f_n$ and ${}^{-}\psi_n \propto {}_{+}f_n$, we write

$$j_3({}^{+}f_{n'}, {}_{+}f_n) = -c'_{1n'} j_3({}_{+}f_{n'}, {}_{+}f_n) - c'^{*}_{2n'} j_3({}_{-}f_{n'}, {}_{+}f_n), \quad (52)$$

where use has been made of the first equation in (14) with lower sign. Arguing as above, we have

$$j_3({}^{+}f_{n'}, {}_{+}f_n|-L_d) \to -c'_{1n} e^{i[\pi_3(-)-\pi'_3(-)](-L_d)} = -c'_{1n} e^{-iA_d(p^0-p'^0)}. \quad (53)$$

Similarly,

$$j_3({}^{+}f_{n'}, {}_{+}f_n|L_u) \to -c'_{1n} e^{-iA_u(p^0-p'^0)}. \quad (54)$$

For $A_d = A_u$, the difference of the last two expressions is zero. So ${}^{+}\psi_{n'}$ and ${}^{-}\psi_n$ are orthogonal. The same is true for ${}_{+}\psi_{n'}$ and ${}_{-}\psi_n$.

In the same manner, it is easy to show that, in the scattering region, ${}^{+}\psi_{n'}(x_3|+)$ and ${}^{+}\psi_n(x_3|-)$ are orthogonal; the same is true for ${}_{+}\psi_{n'}(x_3|+)$ and ${}_{+}\psi_n(x_3|-)$.

Thus, the orthogonal pairs of functions in the Klein region are $({}_{+}f_{n'}, {}^{+}f_n)$ and $({}_{-}f_{n'}, {}^{-}f_n)$ and in the scattering region are $({}_{+}f_{n'}, {}^{-}f_n)$ and $({}_{-}f_{n'}, {}^{+}f_n)$. This assertion must be true for particles of any spin.

For the step potential, considered in Section 6 below, the results of this section were checked by a straightforward calculation of the left-hand side of (44) with $j^0(f_{n'}, f_n) = f^*_{n'} f_n$ and L_d, L_u equal to infinity.

5. SOLVABLE POTENTIAL

For the potential

$$A^0(x_3) = -a\tanh(kx_3), \quad (55)$$

the solution ${}_{+}Q_p(x_3, \lambda)$ of the squared Dirac equation has the form

$${}_{+}Q_p(x_3, \lambda) = (-z)^{i\mu}(1-z)^{i\lambda} F(\alpha, \beta; \gamma; z), \quad (56)$$

where

$$-z = e^{2kx_3}, \quad \lambda = \frac{ea}{k}, \quad (57)$$
$$\pi^0(\pm) = p^0 \pm ea, \quad 2k\nu = \pi_3(+),$$
$$2k\mu = \pi_3(-), \quad \alpha = i\mu + i\nu + i\lambda,$$
$$\beta = i\mu - i\nu + i\lambda, \quad \gamma = 1 + 2i\mu.$$

We assume at first that $\pi_3(\pm)$ are real. The solution ${}_{-}Q_p(x_3, \lambda)$ can be obtained from (56) either by the substitution $\mu \to -\mu$ or by complex conjugation and the substitutions $e \to -e$, $p^0 \to -p^0$.

The solution ${}^{+}Q_p(x_3, \lambda)$ is obtainable from ${}_{+}Q_p(x_3, \lambda)$ by complex conjugation and the substitutions $e \to -e$, $x_3 \to -x_3$ [these operations do not change Eq. (5) with $F(-\varphi) = -F(\varphi)$]:

$${}^{+}Q_p(x_3, \lambda) = (-z^{-1})^{-i\nu}(1-z^{-1})^{i\lambda} \times F(-i\mu - i\nu + i\lambda, i\mu - i\nu + i\lambda; 1 - 2i\nu; z^{-1}). \quad (58)$$

${}^{-}Q_p(x_3, \lambda)$ is obtainable from (58) by the substitution $\nu \to -\nu$. Now, Eq. (11) takes the form

$${}_{+}Q_p(x_3, \lambda) = \frac{\Gamma(1+2i\mu)\Gamma(2i\nu)}{\Gamma(i\mu + i\nu + i\lambda)\Gamma(1 + i\mu + i\nu - i\lambda)} \times {}^{+}Q_p(x_3, \lambda) + \frac{\Gamma(1+2i\mu)\Gamma(-2i\nu)}{\Gamma(i\mu - i\nu + i\lambda)\Gamma(1 + i\mu - i\nu - i\lambda)} {}^{-}Q_p(x_3, \lambda). \quad (59)$$

From here, by complex conjugation and the substitutions $e \to -e$ and $x_3 \to -x_3$, we find

$${}^{+}Q_p(x_3, \lambda) = \frac{\Gamma(-2i\mu)\Gamma(1-2i\nu)}{\Gamma(-i\mu - i\nu + i\lambda)\Gamma(1 - i\mu - i\nu - i\lambda)} \times {}_{+}Q_p(x_3, \lambda) + \frac{\Gamma(1-2i\nu)\Gamma(-2i\mu)}{\Gamma(i\mu - i\nu + i\lambda)\Gamma(1 + i\mu - i\nu - i\lambda)} {}_{-}Q_p(x_3, \lambda). \quad (60)$$

Neglecting $\lambda = ea/(kc\hbar)$ (where we have restored $\hbar$ and c, assumed to be equal to unity throughout the paper), we get the nonrelativistic limit (see Problem 3 in § 25 in [17], where the potential U differs from our eA^0 only by an additive constant).

Now we can rewrite Eq. (15) in the form

$$c'_{1n} = \left(\frac{\pm\pi^-(+)}{\pi^-(-)} \frac{\pi_3(+)}{\pi_3(-)}\right)^{1/2} a(\lambda), \quad (61)$$
$$c'_{2n} = \left(\frac{\pm\pi^+(+)}{\pi^-(-)} \frac{\pi_3(+)}{\pi_3(-)}\right)^{1/2} b(\lambda).$$

The sign + (−) in front of $\pi^-(+)$ and $\pi^+(+)$ refers to the scattering (Klein) region.

We note now that, in the Klein region,

$$\pi^0(-) - \pi^0(+) = -2ea = 2|ea| \quad (62)$$

is the total energy of the e^+e^- pair. Hence, $2|ea| > \pi_3(-) + \pi_3(+)$; i.e., $-\lambda - \mu - \nu > 0$ and all the more so $-\lambda \pm \mu \mp \nu > 0$.

In the scattering region, $\pi^+(+)/\pi^-(-) > 0$, and from here we shall obtain

$$\mu - \nu + \lambda > 0. \quad (63)$$

To this end, we use the relation [4]

$$\frac{\pi^+(+)}{\pi^-(-)} = \frac{\pi^+(-)}{\pi^-(+)} = \frac{\mu-\nu-\lambda}{\mu-\nu+\lambda} = \frac{\pi_3(-)-\pi_3(+)-2ea}{\pi_3(-)-\pi_3(+)+2ea}. \tag{64}$$

In the scattering region, $\pi^0(-) = \pi^0(+) + 2|ea|$ [see (62)]; i.e., $\pi^0(-) > \pi^0(+)$. Hence, $\pi_3(-) > \pi_3(+)$ and all the more so $\pi_3(-) - \pi_3(+) + 2|ea| > 0$. The numerator on the right-hand side of (64) is positive, and so must be the denominator because the left-hand side of the expression is positive.

We note also another useful relation, obtainable from (64) by the substitution $\pi_3(+) \to -\pi_3(+)$,

$$\frac{\pi^-(+)}{\pi^-(-)} = \frac{\pi^+(-)}{\pi^+(+)} = \frac{\mu+\nu-\lambda}{\mu+\nu+\lambda}. \tag{65}$$

With the help of these relations, we find more symmetric expressions for c'_{1n} and c'_{2n}:

$$c'_{1n} = 2\sqrt{\frac{\mu\nu}{\pm(\mu+\nu+\lambda)(\mu+\nu-\lambda)}} \times \frac{\Gamma(2i\mu)\Gamma(2i\nu)}{\Gamma(i\mu+i\nu+i\lambda)\Gamma(i\mu+i\nu-i\lambda)}, \tag{66}$$

$$c'_{2n} = 2\sqrt{\frac{\mu\nu}{\pm(\mu-\nu+\lambda)(\mu-\nu-\lambda)}} \times \frac{\Gamma(2i\mu)\Gamma(-2i\nu)}{\Gamma(i\mu-i\nu+i\lambda)\Gamma(i\mu-i\nu-i\lambda)}.$$

Here and below, the upper sign refers to the scattering region, and the lower one to the Klein region. We see that

$$c'_{1n}(\mu,\nu,\lambda) = c'_{1n}(\nu,\mu,\lambda), \tag{67}$$
$$c'_{2n}(\mu,\nu,\lambda) = c'^*_{2n}(\nu,\mu,\lambda).$$

It is still assumed that μ, ν, and λ are real.

When we approach the complete scattering region from the Klein region, $\pi_3(+) \to 0$, and c'_{1n} and c'_{2n} become unlimited. Then $c_{2n} \to 0$ and c_{1n} becomes a phase factor [see Eq. (19)].

When $k \to 0$, $a \to \infty$, and $ak = E$ in Eq. (55), we get the potential of a constant electric field. This case was studied earlier (see [4, 11, 13]). When $k \to \infty$, we have a step potential. This case is instructive because of its simplicity. In particular, we can verify the orthogonality and normalization in the set of solutions by straightforward calculations.

6. STEP POTENTIAL

From (61), (59), and (57), we find when $k \to \infty$

$$c'_{1n} = \frac{1}{2}\left(\frac{\pm\pi^-(+)}{\pi^-(-)}\frac{\pi_3(+)}{\pi_3(-)}\right)^{1/2} \times \left(1+\frac{\pi_3(-)+2ea}{\pi_3(+)}\right), \tag{68}$$

$$c'_{2n} = \frac{1}{2}\left(\frac{\pm\pi^+(+)}{\pi^-(-)}\frac{\pi_3(+)}{\pi_3(-)}\right)^{1/2} \times \left(1-\frac{\pi_3(-)+2ea}{\pi_3(+)}\right).$$

The notation $\pm$ (or $\mp$) means that the upper sign refers to the scattering region and the lower sign to the Klein region.

Due to relations (64) and (65), there are several other useful forms for c'_{1n} and c'_{2n}. We note these,

$$c'_{1n} = \pm\frac{1}{2}\left(\frac{\pm\{[\pi_3(-)+\pi_3(+)]^2-(2ea)^2\}}{\pi_3(-)\pi_3(+)}\right)^{1/2}, \tag{69}$$

$$c'_{2n} = \mp\frac{1}{2}\left(\frac{\pm\{[\pi_3(-)-\pi_3(+)]^2-(2ea)^2\}}{\pi_3(-)\pi_3(+)}\right)^{1/2},$$

and these,

$$c'_{1n} = \pm\frac{1}{2}\left(\frac{\pi^-(-)}{\pm\pi^-(+)}\frac{\pi_3(-)}{\pi_3(+)}\right)^{1/2} \times \left(1+\frac{\pi_3(+)-2ea}{\pi_3(-)}\right), \tag{70}$$

$$c'_{2n} = -\frac{1}{2}\left(\frac{\pi^+(-)}{\pm\pi^-(+)}\frac{\pi_3(-)}{\pi_3(+)}\right)^{1/2} \times \left(1-\frac{\pi_3(+)-2ea}{\pi_3(-)}\right).$$

From (69) and (19), we find (in both regions)

$$c_{1n} = -\frac{c'_{1n}}{c'^*_{2n}} = \left(\frac{(2ea)^2-[\pi_3(-)+\pi_3(+)]^2}{(2ea)^2-[\pi_3(-)-\pi_3(+)]^2}\right)^{1/2}. \tag{71}$$

We see that $c_{1n} \to 1$ when $\pi_3(+) \to 0$ and probably in this limit $e^{i\phi_n} = 1$.

As mentioned at the end of Section 4, the results of that section were verified using the step potential. Expressions (68) and (70) turn out to be most handy (cf. examples of much less cumbersome calculations for a scalar particle in the first reference in [9]).

The function ${}_+f_{1p}$ in the first equation in (7) takes the form

$$
{}_+f_{1p} = \frac{1}{\sqrt{4\pi_3(-)\pi^-(-)}} \begin{bmatrix} p_1 - ip_2 \\ \pi^-(-) + m \\ p_1 - ip_2 \\ \pi^-(-) - m \end{bmatrix} e^{i\pi_3(-)x_3}\theta(-x_3) \tag{72}
$$

$$
+ \theta(x_3) \left\{ \frac{c'_{1n}}{\sqrt{4\pi_3(+)|\pi^-(+)|}} \begin{bmatrix} p_1 - ip_2 \\ \pi^-(+) + m \\ p_1 - ip_2 \\ \pi^-(+) - m \end{bmatrix} e^{i\pi_3(+)x_3} + \frac{c'_{2n}}{\sqrt{4\pi_3(+)|\pi^+(+)|}} \times \begin{bmatrix} p_1 - ip_2 \\ \pi^+(+) + m \\ p_1 - ip_2 \\ \pi^+(+) - m \end{bmatrix} e^{-i\pi_3(+)x_3} \right\},
$$

$$
\theta(x) = \begin{cases} 1, & x > 0 \\ 0, & x < 0. \end{cases}
$$

Similar expressions can be obtained for other f_n.

In space, where the potential is zero, our spinors $v_r = u_r + p^- u'_r$ [see (8)] are related to the spinors $\tilde{v}_r$ in [6, 7] as follows:

$$
v_1 = b_1\tilde{v}_1 + b_2\tilde{v}_2, \quad v_2 = b_2\tilde{v}_1 - b_1^*\tilde{v}_2,
$$

$$
b_1 = \frac{p_1 - ip_2}{p^0 + m}, \quad b_2 = \frac{p^- + m}{p^0 + m},
$$

$$
\tilde{v}_1 = \begin{bmatrix} p^0 + m \\ 0 \\ p_3 \\ p_1 + ip_2 \end{bmatrix}, \quad \tilde{v}_2 = \begin{bmatrix} 0 \\ p^0 + m \\ p_1 - ip_2 \\ -p_3 \end{bmatrix}. \tag{73}
$$

In our classification, ${}_+f_n$ is a negative-frequency outgoing state [see (17)]. In the classification of [6, 7], it is a positive-frequency ingoing state. In general, both classifications are related by the substitutions

$$
\text{in} \leftrightarrow \text{out}, \quad \text{negative frequency} \leftrightarrow \text{positive frequency}. \tag{74}
$$

The classification of [6, 7] does not satisfy the limit of negligibly small pair creation. On the contrary, our classification holds continuously throughout all regions. On the other hand, the substitutions (74) into (18) do not change the meaning of $|c'_{1n}|^2$, $|c'_{2n}|^2$. Hence, the probabilities of creation of zero or one pair are the same in both classifications [see (31), (34), and (35)]. Yet, roughly speaking, the substitutions (74) change the sign of time. Thus, using the wrong classification will lead to problems with causality, wave packet movement, construction of the propagator via wave functions ψ_n, and so on.

7. CONCLUSION

In general, the S-matrix approach gives the same results as the propagator method. Yet, the former approach gives naturally the expression for $\langle 0_{n\ \text{out}}|0_{n\ \text{in}}\rangle$. Its renormalized value provides the factor distinguishing absolute and relative wave functions. The contribution from (virtual) pair production to any given final wave function must be observable in principle. If the theory is correct, it suggests that particle clock ticking depends upon the field.

ACKNOWLEDGMENTS

I am grateful to V.I. Ritus for encouraging discussions and useful suggestions.

This work was supported in part by the Russian Foundation for Basic Research (project nos. 00-15-96566 and 02-02-16944).

REFERENCES

1. N. B. Narozhny and A. I. Nikishov, Yad. Fiz. **11**, 1072 (1970) [Sov. J. Nucl. Phys. **11**, 596 (1970)].
2. A. I. Nikishov, Nucl. Phys. B **21**, 346 (1970).
3. A. I. Nikishov, Tr. Fiz. Inst. Akad. Nauk SSSR **168**, 157 (1985); in *Issues in Intensive-Field Quantum Electrodynamics*, Ed. by V. L. Ginzburg (Nova Science, Commack, 1987).
4. A. I. Nikishov, Tr. Fiz. Inst. Akad. Nauk SSSR **111**, 152 (1979); J. Sov. Laser Res. **6**, 619 (1985).
5. A. A. Grib, S. G. Mamaev, and V. M. Mostepanenco, *Vacuum Quantum Effects in Strong Fields* (Énergoatomizdat, Moscow, 1988) [in Russian].
6. A. Hansen and F. Ravndal, Phys. Scr. **23**, 1036 (1981).

7. W. Greiner, B. Müller, and J. Rafelski, *Quantum Electrodynamics of Strong Field* (Springer-Verlag, 1985).
8. A. Calogeracos and N. Dombey, Contemp. Phys. **40**, 313 (1999).
9. A. I. Nikishov, hep-th/0111137; *Problems of Atomic Science and Technology, Special Issue Dedicated to the 90th Anniversary of A. I. Akhieser* (Kharkov, Ukraine, 2001), p. 103.
10. A. I. Nikishov, hep-th/0202024; Theor. Math. Phys. **136**, 958 (2003).
11. A. I. Nikishov, hep-th/0211088; *Proceedings of the 3rd International Conference on Physics,* Ed. by A. Semikhatov *et al.* (2003), Vol. 1, p. 787.
12. A. I. Nikishov, Teor. Mat. Fiz. **98**, 60 (1994).
13. A. I. Nikishov, hep-th/0207085; Zh. Éksp. Teor. Fiz. **123**, 211 (2003) [JETP **96**, 180 (2003)].
14. A. I. Nikishov, Zh. Éksp. Teor. Fiz. **91**, 1565 (1986) [Sov. Phys. JETP **64**, 922 (1986)].
15. A. I. Nikishov, Yad. Fiz. **46**, 163 (1987) [Sov. J. Nucl. Phys. **46**, 101 (1987)].
16. F. A. Kaempfer, *Concepts in Quantum Mechanics* (Academic Press, New York, 1965).
17. L. D. Landau and E. M. Lifshits, *Quantum Mechanics: Nonrelativistic Theory* (Nauka, Moscow, 1989, 4th ed.; Pergamon Press, Oxford, 1977, 3rd ed.).

Physics of Atomic Nuclei, Vol. 67, No. 8, 2004, pp. 1487–1494. Translated from Yadernaya Fizika, Vol. 67, No. 8, 2004, pp. 1512–1519.

ELEMENTARY PARTICLES AND FIELDS
Experiment

Searches for Single-Spin Asymmetry in the Inclusive Production of Neutral Pions in the Central Region at a Proton Beam Energy of 70 GeV

A. N. Vasiliev, V. N. Grishin, A. M. Davidenko, A. A. Derevschikov, Yu. A. Matulenko, Yu. M. Melnik, A. P. Meschanin, V. V. Mochalov[*], L. V. Nogach, S. B. Nurushev, A. F. Prudkoglyad, P. A. Semenov, L. F. Soloviev, V. L. Solovianov[†], V. Yu. Khodyrev, K. E. Shestermanov, A. E. Yakutin, N. S. Borisov[1)], V. N. Matafonov[1)], A. B. Neganov[1)], Yu. A. Plis[1)], Yu. A. Usov[1)], A. N. Fedorov[1)], and A. A. Lukhanin[2)]

The PROZA-M Collaboration

Institute for High Energy Physics, Protvino, Moscow oblast, 142284 Russia

Received September 2, 2003

Abstract—Results are presented that were obtained by measuring single-spin asymmetry in the inclusive production of neutral pions in the reaction $p + p \uparrow \to \pi^0 + X$ at $x_{\rm F} \approx 0$. A beam of 70-GeV protons was extracted directly from the vacuum chamber of the accelerator by means of a bent single crystal. For transverse momenta in the range $1.0 < p_T < 3.0$ GeV/c, the single-spin asymmetry independently measured by two detectors is zero within the errors. This result is in agreement with Fermilab data obtained at 200 GeV, but it is at odds with CERN data measured at 24 GeV. © *2004 MAIK "Nauka/Interperiodica".*

INTRODUCTION

Investigation of spin physical observables makes it possible to test theoretical models at a much more profound level than measurement of spin-averaged quantities. Among observables associated with polarizations, transverse single-spin asymmetries in high-energy processes involving nucleons are the most puzzling and interesting. Within perturbative QCD, single-spin effects in inclusive reactions must tend to zero in the limit of high energies and high transverse momenta.

A number of experiments devoted to measuring the asymmetry in inclusive neutral-pion production were performed over a period between the 1970s and the 1990s. A CERN experiment in the central region at a Feynman variable value of $x_{\rm F} \sim 0$ revealed significant effects at an energy of 24 GeV in $p + p_\uparrow \to \pi^0 + X$ reactions [1]. However, statistical uncertainties were large in that experiment, so that the result could only be treated as an indication of a possibly large asymmetry in hard processes. An experiment performed at the Institute for High Energy Physics (IHEP, Protvino, Russia) exhibited a large asymmetry in the inclusive production of neutral pions and eta mesons in the scattering of 40-GeV/c negatively charged pions on a polarized target [2, 3]. According to measurements performed at Fermilab, the asymmetry A_N in the production of neutral pions at a polarized-beam energy of 200 GeV is zero [4].

Taken together, these three results may imply the following: either the asymmetry in the central region decreases with increasing energy, or the effect in question depends on the sort of interacting quarks.

The objective of the PROZA-M experiment was to measure the asymmetry A_N in the inclusive production of neutral pions in the reaction

$$p + p_\uparrow \to \pi^0 + X \qquad (1)$$

at an angle of 90° in the c.m. frame, with the proton-beam energy being 70 GeV, which is an energy value intermediate between the energies of the experiments at CERN and Fermilab.

In this article, we present the results obtained by processing data of an experiment performed at the IHEP accelerator in March 1996.

[†]Deceased.

[1)]Joint Institute for Nuclear Research, Dubna, Moscow oblast, 141980 Russia.

[2)]Kharkov Institute for Physics and Technology, Akademicheskaya ul. 1, Kharkov, 61108 Ukraine.

[*]e-mail: mochalov@mx.ihep.su

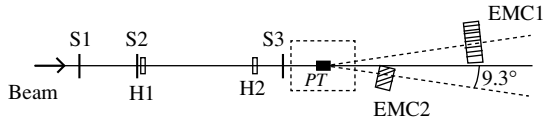

Fig. 1. Layout of the PROZA-M facility: (S1–S3) scintillation counters of the total flux, (H1, H2) hodoscopes, (EMC1, EMC2) electromagnetic calorimeters, and (PT) polarized target.

1. DESCRIPTION OF THE EXPERIMENT

Our investigations were performed with the aid of the PROZA-M facility, which was described in detail elsewhere [5]. The layout of this facility is shown in Fig. 1. Protons of momentum 70 GeV/c were scattered on a polarized frozen-type hydrogen target, where propanediol ($C_3H_8O_2$) was employed as a working substance [6]. The mean polarization of the target and its relaxation time were, respectively, 80% and about 1000 h. The pumping of polarization, together with its reversal, took about four hours. On average, it was performed once every two days.

1.1. Beam Equipment and Generation of a 70-GeV/c Proton Beam

The investigations in question were performed in beamline 14 of the U-70 accelerator complex. For the first time in the world, a bent single crystal was used for a hard-focusing accelerator to extract a 70-GeV proton beam owing to the channeling effect [7]. A crystal deflector in the form of a silicon single crystal bent at angle of 80 mrad was installed within the vacuum chamber of the accelerator.

The number of particles incident on the target was determined by the coincidence of signals from three scintillation counters (S1–S3). Two hodoscopes, H1 (with a step of 5 mm) and H2 (with a step of 2 mm), arranged in front of the polarized target at distances of 8.7 and 3.2 m, respectively, served for determining the coordinates of charged particles incident on the target. The dimensions of the beam were $\sigma_x = 4$ mm in the horizontal direction and $\sigma_y = 3$ mm in the vertical direction. The respective angular divergences of the beam were 2 and 1 mrad. The momentum spread of the beam was $\Delta p/p \sim 10^{-3}$. A description of the procedure for extracting the proton beam to the zone of beamline 14 can be found in [7, 8].

1.2. Electromagnetic Calorimeters

Photons from neutral-pion decays were recorded by two electromagnetic calorimeters (EMC1, EMC2). The mean multiplicity of photons per event was about 2.3. In seeking neutral pions, we selected photons of energy in the range between 1 and 20 GeV.

The calorimeters were arranged at angle of 9.3° with respect to the direction to the target center in the horizontal plane, this corresponding to an angle of 90° in the c.m. frame at a beam momentum of 70 GeV/c. If viewed from the polarized-target center, they covered the same solid angle. The distances to the calorimeters from the target center were 6.9 m for EMC1 and 2.8 m for EMC2. Total-absorption Cherenkov counters manufactured from TF1-00 lead glass were employed for photon detectors [9]. The EMC1 calorimeter consisted of 480 counters grouped into 24 columns containing 20 counters each and forming a rectangular matrix, while the EMC2 calorimeter comprised 144 counters (12 columns of 12 counters). In order to reduce the systematic error in measuring the asymmetry in question, the calorimeters were placed on different sides of the beam axis. An external view of the EMC1 calorimeter and a detailed description of the two calorimeters can be found in [5, 10].

The calibration of the calorimeters was performed by using an electron beam of momentum 26.6 GeV/c. It consisted in determining the coefficients that made it possible to go over from the signal of each counter A_{ij} to the energy E_{ij} [11]. Upon subtracting the beam-momentum spread of 2%, the energy resolution proved to be $\sigma(E)/E \approx 2.5\%$, which is characteristic of lead-glass electromagnetic calorimeters at the energy value being considered.

The energy scale of the calorimeters was additionally matched with the neutral-pion mass. The calibration accuracy reached within five hours of the measurements was 0.1% for EMC1 and 0.15% for EMC2.

1.3. Electronic Equipment and Transverse-Momentum Trigger

The electronic equipment used consisted of modules performed within the SUMMA standard [12]. Beam electronics included hodoscope registers and the rescaling instruments of the monitoring system. A zero-level trigger for an incident particle was formed within a 60-ns gate. A level-1 trigger (formed within a 350-ns gate), which was independent for each detector, ensured a selection of events where the transverse momentum was in excess of 1 GeV/c. A detailed description of the trigger was given in [5, 10]. The electronic equipment for a pulse-height analysis was based on P-267 12-bit analog-to-digital converters [13]. Data were read out by an SM-1420 computer and were logged on magnetic tapes. The electronic equipment used for data readout was described elsewhere [14].

With allowance for the efficiency of data-acquisition-system operation, about 350 events were recorded per accelerator spill, 250 and 100 of these coming from EMC1 and EMC2, respectively. In all, 20 million events were recorded over a 10-day run with a polarized target.

2. DATA ANALYSIS AND RESULTS

Preliminary data were reported in [15]. The resulting asymmetry was close to zero over the entire range considered there. Yet, neutral pions were reconstructed only for the EMC1 calorimeter at transverse momenta above 2.35 GeV/c. In order to reconstruct neutral pions at high energies, we modified the algorithm for reconstructing showers. Our main objective was to improve the separation of overlapping showers in EMC2, where the spacing between photons at transverse momenta in excess of 2 GeV/c became small because of the proximity of EMC2 to the target.

2.1. Reconstruction of Electromagnetic Showers

The algorithm for reconstructing photons is based on isolating an electromagnetic shower by the known shape. First, we found clusters containing at least three cells and satisfying the condition that there is an excess above the threshold of 300 MeV for a counter where the energy deposition is maximal. Upon selecting individual clusters, each of them was treated with the aid of the shower-reconstruction procedure involving the algorithm described in [16]:

(i) A cell where the energy deposition was maximal was found. The primary shower was considered in the region of a 3×3 cell in the vicinity of the maximum.

(ii) It was found out whether a given cluster consists of one or two photons. For this, the MINUIT code [17] was applied to a given shower (in the region of the 3×3 cell) with the aim of constructing, at a fixed energy E_0, a two-parameter fit (in terms of the coordinates X and Y) that minimizes the functional χ^2,

$$\chi^2 = \sum_i (E_i - F_i(X,Y))^2/\sigma_i^2, \qquad (2)$$

where E_i and $F_i(X,Y)$ are, respectively, the measured and the theoretical (from the shape of a shower) value of the energy in each cell and

$$\sigma_i^2 = cE_i(1 - E_i/E_0) + q. \qquad (3)$$

Here, c is a parameter that describes fluctuations of a shower and which is directly related to the resolution of lead-glass calorimeters ($\sqrt{c} \sim \sigma(E)/\sqrt{E}$, $c = 30$ MeV), $q = 1$ MeV^2 takes into account noise in the electronic equipment used, and $E_0 = \sum_i E_i$ is the total measured energy of the shower over the region of the 3×3 cell. The initial values of the parameters were determined as the coordinates of the shower center of gravity. If a value in the region $\chi^2/N < 3$, where N is the number of degrees of freedom, was obtained as the result of fitting, the cluster being considered was treated as a single shower, its energy being corrected for a leakage beyond the region of shower-shape summation in the 3×3 cell.

(iii) Otherwise, we considered the hypothesis that the cluster consists of two overlapping showers and that, in the region of a 5×5 cell around the maximum, there was a counter where the energy deposition was the closest to its maximum value. In seeking two showers, we had to determine six parameters, the energies and the coordinates of each photon. The total energy and the coordinates X_c and Y_c of the cluster center of gravity (in all, three quantities) are fixed. Therefore, the functional χ^2 was minimized with respect to three parameters—the asymmetry $Z_g = |E1 - E2|/(E1 + E2)$ of the energy between two showers, $\Delta X = X_1 - X_2$, and $\Delta Y = Y_1 - Y_2$—in the regions of a 3×3 cell around each maximum. The initial values of ΔX and ΔY were calculated on the basis of the second central moments M_{xx}, M_{yy}, and M_{xy}. The initial value of the asymmetry of the energy between the showers is $Z_g = (E_{\max 1} - E_{\max 2})/(E_{\max 1} + E_{\max 2})$, where $E_{\max 1}$ and $E_{\max 2}$ are the energy values in two counters of the cluster that are characterized by the two largest values of the energy deposition. The condition that $\chi^2_{2\gamma}/N$ is less than unity or is less than $\chi^2_{1\gamma}/N$ by five was used as the criterion for terminating the operation of the algorithm and for concluding that there were two photons in the cluster being considered. If this condition was not satisfied, the cluster was treated as a discrete unit. After that, a single shower was fitted anew, but, this time, over the region of a 5×5 cell.

(iv) After applying the above procedure, signals in the cells that were used for fitting were discarded, and a new shower was sought over the entire area of the calorimeter.

The shower shape, which is necessary for fitting, was obtained experimentally with the aid of a 26.6-GeV electron beam and is described in terms of an analytic function [16].

The algorithm described above made it possible to separate overlapping showers even in the case where the spacing between them did not exceed that which corresponded to one counter. A Monte Carlo simulation was performed to test the algorithm. The efficiency of the algorithm is given in Table 1 for the photon-pair energy of $E_{2\gamma} = 15$ GeV.

In analyzing our experimental data, we used only those showers for which $\chi^2/N < 3$, the asymmetry

Table 1. Efficiency of the algorithm for separating overlapping showers at the photon-pair energy of $E_{2\gamma} = 15$ GeV versus the spacing between photons

Spacing (in the size of a cell)	Efficiency (%)
1.5	91
1.2	88
1.0	71

Z_g of energy was less than 0.8, and the primary photon was at distance not less than half the counter size from the edge of the detector.

Figure 2 shows the mass spectra for the two calorimeters used. Distinct peaks associated with neutral pions can be seen there at all values of the transverse momentum p_T in the region being studied. The mass resolution for the neutral pion is 10 MeV for the far calorimeter EMC1 and 12 to 17 MeV for the near calorimeter EMC2 at different values of the neutral-pion energy.

The algorithm ensured an efficient reconstruction of neutral pions in the EMC2 calorimeter for transverse-momentum values up to $p_T = 3$ GeV/c. The distribution of photon pairs with respect to kinematical variables is displayed in Fig. 3*a* for the neutral-pion-mass region. The distribution is virtually symmetric in x_F, the mean value of x_F being zero.

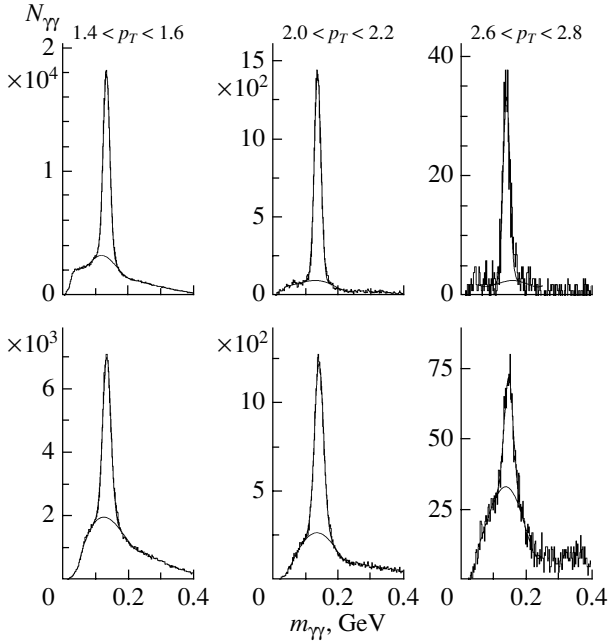

Fig. 2. Mass spectra obtained for proton pairs with (upper plots) EMC1 and (lower plots) EMC2 for various intervals of the transverse momentum p_T (in GeV/c).

In order to test the quality of data, we also determined the transverse-momentum dependence of the number of neutral pions that is normalized to the flux of beam particles that traversed the target (see Fig. 3*b*). The result proved to be in good agreement with data obtained with the aid of the FODS facility (Protvino) on the invariant cross sections for the inclusive production of charged pions for $p_T > 1.8$ GeV/c at 70 GeV [18], where the exponent in these cross sections was -5.68 ± 0.02 $[N/(\mathrm{GeV}/c)]^{-1}$ for positively charged pions and -5.88 ± 0.02 $[N/(\mathrm{GeV}/c)]^{-1}$ for negatively charged pions.

2.2. Calculation of the Single-Spin Asymmetry

For the EMC1 calorimeter, which is positioned to the left of the beam axis, the single-spin asymmetry A_N is defined as

$$A_N(x_\mathrm{F}, p_T) = \frac{1}{P_\mathrm{targ}} \frac{1}{\langle \cos\phi \rangle} \frac{\sigma_\uparrow^\mathrm{H}(x_\mathrm{F}, p_T) - \sigma_\downarrow^\mathrm{H}(x_\mathrm{F}, p_T)}{\sigma_\uparrow^\mathrm{H}(x_\mathrm{F}, p_T) + \sigma_\downarrow^\mathrm{H}(x_\mathrm{F}, p_T)}, \quad (4)$$

where P_targ is the polarization of the target, $\cos\phi$ is the cosine of the azimuthal angle between the target polarization vector and the normal to the plane spanned by the beam axis and the momentum of the outgoing neutral pion, and $\sigma_\uparrow^\mathrm{H}$ and $\sigma_\downarrow^\mathrm{H}$ are the invariant differential cross sections for neutral-pion production on hydrogen for opposite target-polarization directions. In our experiment, the azimuthal angle at which neutral pions were detected was in the range $0^\circ \pm 15^\circ$; therefore, $\cos\phi$ was set to unity over the entire range in question.

For a detector positioned to the left of the beam axis, the raw asymmetry A_N^raw actually measured in the experiment is related to A_N by the equation

$$A_N = \frac{D}{P_\mathrm{targ}} A_N^\mathrm{raw} = \frac{D}{P_\mathrm{targ}} \frac{n_\uparrow - n_\downarrow}{n_\uparrow + n_\downarrow}, \quad (5)$$

where D is the target-dilution factor and $n_\uparrow$ and $n_\downarrow$ are the normalized (to the monitor) numbers of recorded neutral pions for opposite directions of the target polarization vector. For the EMC2 calorimeter, which is arranged to the right of the beam axis, the asymmetry is taken with the opposite sign.

In measurements of the asymmetry, there can arise an additional instrumental asymmetry associated with a trigger-electronics jitter, failures of the monitor counters, or some other reasons. In view of this, the measured asymmetry is the sum of the actual and the instrumental asymmetry. In [10], a method was developed that makes it possible to remove this systematic bias under the assumption that the asymmetry of the background (that is, of photons off the neutral-pion-mass peak) is zero.

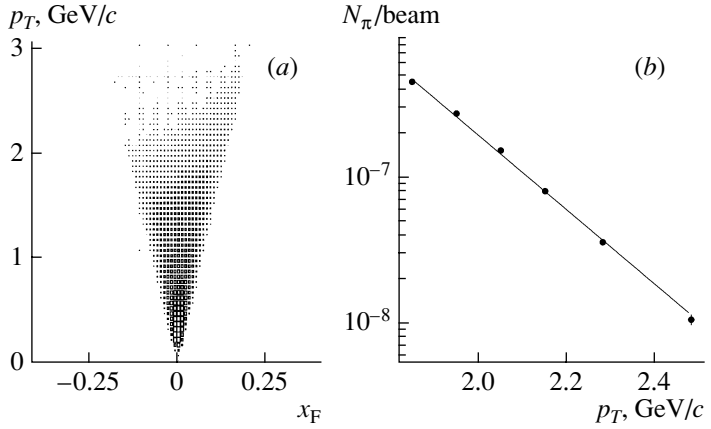

Fig. 3. (*a*) Two-dimensional distribution of neutral pions with respect to p_T and x_F and (*b*) p_T dependence of the relative cross section for $p_T > 1.8$ GeV/c (the word *beam* in the denominator on the ordinate stands for the number of beam particles that traversed the target), the respective exponent being $-5.89 \pm 0.08\,[N_\pi/(\,GeV/c)]^{-1}$. The resolution in p_T is 0.08 GeV/c.

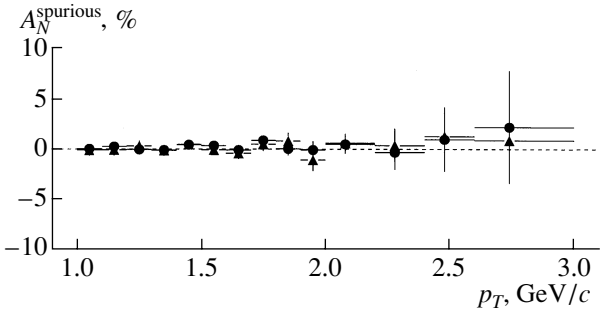

Fig. 4. Raw spurious asymmetry as a function of p_T for (●) EMC1 and (▲) EMC2.

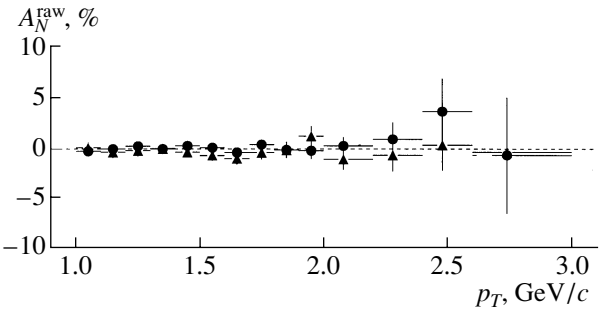

Fig. 5. Asymmetry A_N^{raw} for the two detectors: (●) data for EMC1 and (▲) data for EMC2.

2.3. Analysis of a Spurious Asymmetry

A spurious asymmetry is determined predominantly by the drift of the calorimeter energy scale, this leading to an inaccurate reconstruction of the kinematical parameters of the photon pair. The instability of the calorimeter energy scale was less than 0.1% for the EMC1 calorimeter and less than 0.15% for the EMC2 calorimeter. Accordingly, the contribution to the spurious asymmetry from the instability of the energy scale was less than 0.2 and 0.3% for, respectively, the former and the latter calorimeter (with allowance for the dilution factor and the target polarization, $D/P_{\text{targ}} \sim 10$, this yields values below 2 and 3% for the spurious contribution to the sought quantity).

In order to estimate the spurious asymmetry, we broke down the total data sample for the same direction of the target polarization vector into two equal subsamples of events and determined the asymmetry for these two subsamples.

The result obtained by calculating the spurious asymmetry for the two calorimeters is presented in Fig. 4. The spurious asymmetry proved to be zero within the errors.

In order to verify the consistency of data on the asymmetry A_N^{raw}, we compared the results of the measurements for the two detectors (see Fig. 5). For the two calorimeters, the asymmetry takes values that are compatible with each other within the errors over the entire transverse-momentum range, this being also indicative of a small spurious asymmetry.

2.4. Determination of the Dilution Factor

In order to obtain the ultimate value of the asymmetry according to Eq. (5), it is necessary to determine the target-dilution factor. The procedure for calculating the target-dilution factor D was described in detail elsewhere [10]. In order to test the respective calculations, we used the experimental results for the dilution factor from [2]. A compendium of the data on the dilution factor is given in Table 2.

In the range $1.2 < p_T < 2.0$ GeV/c, the dilution factor is 8.1 ± 0.5, its value increasing to 10.1 ± 2.5

Table 2. Target-dilution factor versus the transverse momentum

p_T, GeV/c	D from [2]	D for the calculation
1.2–1.4	8.0 ± 1.0	8.1
1.4–1.6	8.1 ± 1.2	8.1
1.6–1.8	8.1 ± 0.7	8.1
1.8–2.0	8.2 ± 0.9	8.3
2.0–2.2	8.8 ± 1.3	8.7
2.2–2.4	9.2 ± 1.6	9.1
2.4–2.6	9.5 ± 2.0	9.5
2.6–3.2	10.1 ± 2.5	10.2

for $p_T > 2.6$ GeV/c. In the run of 1996, we tested the dilution factor on the basis of scarcer statistics. It complies well with the results of previous dedicated measurements and with calculated values. By way of example, we indicate that the dilution factor is $D = 8.4 \pm 1.2$ at $p_T \sim 1.8$ GeV/c and $D = 9.2 \pm 1.5$ at $p_T \sim 2.1$ GeV/c.

In assessing the asymmetry, we used the calculated values of the dilution factor from Table 2 without allowance for errors.

2.5. Results

The asymmetry summed over the two calorimeters is given in Fig. 6*a* and in Table 3. Over the entire range of the measurements, the resulting asymmetry is compatible with zero.

3. DISCUSSION OF THE RESULTS

3.1. Comparison with Other Results

The asymmetry A_N in the inclusive production of neutral pions in the central region of *pp* interaction was previously measured in two experiments (at 24 GeV in [1] and at 200 GeV in [4]), the results of those experiments being displayed in Fig. 6*b*. The asymmetry A_N that we measured in the reaction $p + p_\uparrow \to \pi^0 + X$ is zero within the errors over the entire range under study. Comparing our results at 70 GeV with the data for the same reaction at 24 GeV, we therefore arrive at the conclusion that it is advisable to perform measurements aimed at searches for the asymmetry at beam energies between 24 and 70 GeV.

At the same time, the measurements in the PROZA-M experiment (Protvino) for the reaction $\pi^- + p_\uparrow \to \pi^0 + X$ at 40 GeV yielded, for the asymmetry of neutral-pion production, a value of -30% for $p_T > 2.5$ GeV/c [3], this being indicative of the dependence of the asymmetry on the type of interacting particles.

Table 3. Asymmetry versus the transverse momentum

$\langle p_T \rangle$, GeV/c	A_N^{sum}, %	$\langle p_T \rangle$, GeV/c	A_N^{sum}, %
1.05	-1.0 ± 3.2	1.75	1.7 ± 4.1
1.15	-0.8 ± 3.2	1.85	-0.8 ± 5.0
1.25	1.5 ± 3.1	1.95	4.7 ± 6.6
1.35	0.2 ± 3.0	2.08	-3.1 ± 7.4
1.45	1.3 ± 3.0	2.28	1.7 ± 13.4
1.55	-1.1 ± 3.0	2.48	19.5 ± 23.6
1.65	-5.4 ± 3.5	2.74	-4.7 ± 35.4

3.2. Predictions of Theoretical Models

Owing primarily to the results obtained in the PROZA-M and E-704 experiments (see [2, 3] and [4], respectively), models have been developed over the past decade that explain large single-spin asymmetries in terms of various mechanisms.

These are

(i) the mechanism assuming the presence of an additional quark transverse momentum $\mathbf{k}_T$ in a polarized nucleon—the asymmetry of the quark-density distribution for opposite proton-polarization directions in the initial state (Sivers mechanism) [19–21] or the asymmetry of the fragmentation functions for opposite quark-polarization directions in the final state (Collins mechanism) [22];

(ii) the contribution of higher twists [23–28];

(iii) the effect of the orbital angular momentum of valence quarks (Berlin model) [29, 30] or current quarks within a constituent quark (U-matrix quark model) [31];

(iv) the interaction of the quark magnetic moment with a chromomagnetic field [32, 33];

(v) the formation of resonances or of excited states [34].

An overview of these models is given [30, 35, 36].

For the central region of the reaction $p_\uparrow + p \to \pi^0 + X$, almost all of these models predict an asymmetry of small magnitude. By way of example, Fig. 6*b* shows the results of Anselmino's calculations for the E704 experiment in the central region [37]. The behavior of the asymmetry within the Collins and Sivers models at an energy of 70 GeV is expected to differ only slightly in what is concerned with predictions for the E704 experiment [38].

The fact that, in the central region of the reaction being considered, a neutral pion is produced predominantly from gluons is thought to be the main reason for a small asymmetry in this reaction: since the contribution of the gluon component to the transverse

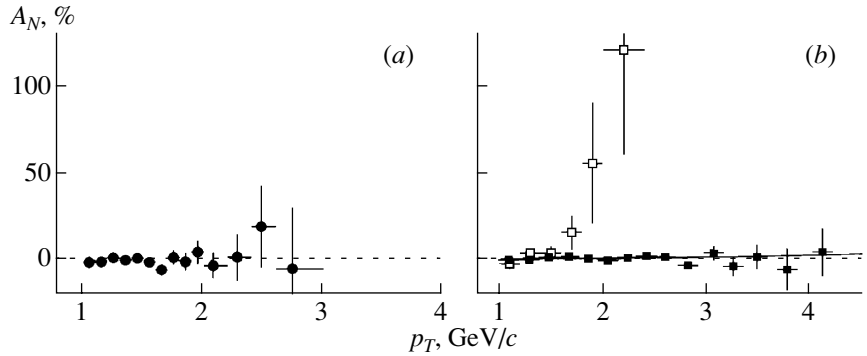

Fig. 6. (*a*) Total (for the two calorimeters) asymmetry A_N as a function of transverse momentum (the results of the present experiment are given here). (*b*) Asymmetry at (□) 24 GeV [1] and (■) 200 GeV [4] in the central region; the curve represents the results of Anselmino's calculations for 200 GeV and $x_F = 0$ [37].

proton spin is small in these models, the asymmetry is not expected to exceed a few percent. In this case, there must not be any difference between $pp_\uparrow$ and $\pi^- p_\uparrow$ interactions; yet, a significant asymmetry (up to -30%) was discovered in the latter case at 40 GeV [3].

Therefore, we have to assume either that a considerable contribution to neutral-pion production at an angle of 90° in the c.m. frame comes from quarks or that interaction dynamics changes strongly in response to the increase in energy from 40 to 70 GeV. In the case of the contribution to the asymmetry from quark interactions, the asymmetry is canceled in $pp_\uparrow$ interaction because of opposite-sign polarizations of u and d quarks in the proton and because of the mixing of channels from a polarized and an unpolarized proton. But in $\pi^- p_\uparrow$ interaction, a large asymmetry may arise in neutral-pion production from a valence $\overline{u}$ antiquark of the incident negatively charged pion and a valence u quark of a polarized proton, the contribution of the valence d quark of the proton being substantially suppressed in this case.

CONCLUSIONS

The basic results of the present study are the following:

(i) The asymmetry in the reaction $p + p_\uparrow \to \pi^0 + X$ at 70 GeV in the region $1 < p_T < 3$ GeV/c is zero within the errors. This result is in good agreement with the E704 data at 200 GeV, but it is at odds with the results obtained for 24 GeV at CERN, where a significant asymmetry was discovered. Thus, the asymmetry in the energy range between 70 and 200 GeV is indeed small and is independent of energy. If the asymmetry depends on energy, this takes place as the beam energy changes from 24 to 70 GeV.

(ii) Comparing the results presented here with those that were obtained by measuring the asymmetry over the same kinematical region at 40 GeV, but in a beam of negatively charged pions, we can conclude that the asymmetry depends on the sort of interacting particles; otherwise, we have to assume that the dynamics of interaction undergoes considerable changes as the beam energy grows from 40 to 70 GeV.

(iii) The predictions of the theoretical models considered above are compatible with the data reported here.

ACKNOWLEDGMENTS

We are indebted to the Directorate of the Institute for High Energy Physics for support of the present investigation and to the U-70 Accelerator Department and the Beam Division for ensuring a stable operation of the U-70 accelerator and beamline 14. Special thanks are due to M. Anselmino, J. Collins, M. Ryskin, and S. Troshin for stimulating discussions and to N.I. Belikov, Yu.M. Goncharenko, V.A. Kormilitsyn, N.E. Mikhalin, and A.I. Myskin for technical support during this run of our experiments.

This work was supported in part by the Russian Foundation for Basic Research (project no. 03-02-16919).

REFERENCES

1. J. Antille *et al.*, Phys. Lett. **94**, 523 (1980).
2. N. S. Amaglobeli, V. D. Apokin, Yu. I. Arestov, *et al.,* Yad. Fiz. **50**, 695 (1989) [Sov. J. Nucl. Phys. **50**, 432 (1989)].
3. V. D. Apokin *et al.*, Phys. Lett. **243**, 461 (1990).
4. D. L. Adams *et al.*, Preprint No. 94-88, IHEP (Inst. High Energy Phys., Protvino, 1994); Phys. Rev. D **53**, 4747 (1996).

5. V. D. Apokin *et al.,* Preprint No. 97-38, IFVÉ (Inst. High Energy Phys., Protvino, 1997); V. D. Apokin *et al.*, Instrum. Exp. Tech. **41**, 464 (1998).
6. N. S. Borisov *et al.,* Preprint No. 1-80-98, OIYaI (Joint Inst. Nucl. Res., Dubna, 1980).
7. A. A. Aseev *et al.,* Preprint No. 91-46, IFVÉ (Inst. High Energy Phys., Protvino, 1991); A. A. Aseev *et al.*, Nucl. Instrum. Methods Phys. Res. A **330**, 39 (1993).
8. A. P. Bugorskiĭ *et al.,* Preprint No. 00-11, IFVÉ (Inst. High Energy Phys., Protvino, 2000); Prib. Tekh. Éksp., No. 1, 14 (2001).
9. G. A. Akopdjanov *et al.*, Nucl. Instrum. Methods **140**, 441 (1977); F. Binon *et al.*, Nucl. Instrum. Methods **188**, 507 (1981).
10. A. N. Vasil'ev *et al.,* Preprint No. 2003-21, IFVÉ (Inst. High Energy Phys., Protvino, 2003).
11. D. L. Adams *et al.,* Preprint No. 91-99, IFVÉ (Inst. High Energy Phys., Protvino, 1991).
12. Yu. V. Bushnin *et al.,* Preprint No. 72-49, IFVÉ (Inst. High Energy Phys., Protvino, 1972); O. I. Alferova *et al.,* Prib. Tekh. Éksp., No. 4, 56 (1975).
13. S. A. Zimin *et al.,* Preprint No. 93-50, IFVÉ (Inst. High Energy Phys., Protvino, 1993).
14. N. I. Belikov *et al.,* Preprint No. 87-58, IFVÉ (Inst. High Energy Phys., Protvino, 1987).
15. N. I. Belikov *et al.,* Preprint No. 97-51, IFVÉ (Inst. High Energy Phys., Protvino, 1997).
16. A. A. Lednev, Preprint No. 93-153, IFVÉ (Inst. High Energy Phys., Protvino, 1993).
17. F. James and M. Roos, Comput. Phys. Commun. **10**, 343 (1975); CERN-DD-75-20.
18. V. V. Abramov *et al.,* Preprint No. 84-88, IFVÉ (Inst. High Energy Phys., Protvino, 1984).
19. D. Sivers, Phys. Rev. D **41**, 83 (1990).
20. D. Sivers, Phys. Rev. D **43**, 261 (1991).
21. T. T. Chou and C. N. Yang, Nucl. Phys. B **107**, 1 (1976).
22. J. C. Collins, Nucl. Phys. B **396**, 161 (1993).
23. A. A. Efremov and O. V. Teryaev, Yad. Fiz. **36**, 242 (1982) [Sov. J. Nucl. Phys. **36**, 140 (1982)]; **36**, 950 (1982) [**36**, 557 (1982)]; **39**, 1517 (1984) [**39**, 962 (1984)]; A. V. Efremov and O. V. Teryaev, Phys. Lett. B **150B**, 383 (1985).
24. A. V. Efremov, V. M. Korotkiyan, and O. V. Teryaev, Phys. Lett. B **348**, 577 (1995).
25. J. Qiu and G. Sterman, Phys. Rev. Lett. **67**, 2264 (1991); Nucl. Phys. B **378**, 52 (1992).
26. A. Schäfer, L. Mankiewicz, P. Gornicki, and S. Güllenstern, Phys. Rev. D **47**, R1 (1993); B. Ehrnsperger, A. Schäfer, W. Greiner, and L. Mankiewicz, Phys. Lett. B **321**, 121 (1994).
27. J. Qiu and G. Sterman, ITP-SB-98-28, BNL-HET-98-17; Phys. Rev. D **59**, 014004 (1999); hep-ph/9806356.
28. Y. Kanazawa and Y. Koike, Phys. Lett. B **490**, 99 (2000); hep-ph/0007272.
29. Meng Ta-Chung, in *Proceedings of the 4th Workshop on High-Energy Spin Physics, Protvino, Russia, 1991*.
30. Zuo-tang Liang and C. Boros, Int. J. Mod. Phys. A **15**, 927 (2000); hep-ph/0001330.
31. S. M. Troshin and N. E. Tyurin, Phys. Rev. D **52**, 3862 (1995); **54**, 838 (1996).
32. M. G. Ryskin, Yad. Fiz. **48**, 1114 (1988) [Sov. J. Nucl. Phys. **48**, 708 (1988)]; D. I. D'yakonov and V. Yu. Petrov, Zh. Éksp. Teor. Fiz. **89**, 361 (1985) [Sov. Phys. JETP **62**, 204 (1985)].
33. V. V. Abramov, Preprint No. 98-84, IFVÉ (Inst. High Energy Phys., Protvino, 1998); Eur. Phys. J. C **14**, 427 (2000); hep-ph/0110152.
34. G. Musulmanbekov and M. Tokarev, in *Proceedings of the VI Workshop on High-Energy Spin Physics, Protvino, Russia, 1995*, p. 132.
35. M. Anselmino *et al.*, *Talk at 3rd Circum-Pan-Pacific Symposium on High-Energy Spin Physics (SPIN 2001), Beijing, China, 2001*; hep-ph/0201076.
36. M. Anselmino, *Lectures at Advanced Study Institute on Symmetries and Spin (PRAHA SPIN 2001), Prague, Czech Republic, 2001*; hep-ph/0201150.
37. M. Anselmino and F. Murgia, Phys. Lett. B **442**, 470 (1998); hep-ph/9808426.
38. M. Anselmino, S. Troshin, and J. Collins, private communication.

Translated by A. Isaakyan

Physics of Atomic Nuclei, Vol. 67, No. 8, 2004, pp. 1495–1504. Translated from Yadernaya Fizika, Vol. 67, No. 8, 2004, pp. 1520–1528.

ELEMENTARY PARTICLES AND FIELDS
Experiment

Single-Spin Asymmetry of Inclusive π^0-Meson Production in 40-GeV Pion Interactions with a Polarized Target in the Target-Fragmentation Region

A. N. Vasiliev, V. N. Grishin, A. A. Derevschikov, V. I. Kravtsov, Yu. A. Matulenko, V. A. Medvedev, Yu. M. Melnik, A. P. Meschanin, D. A. Morozov, V. V. Mochalov*, A. I. Mysnik, L. V. Nogach, S. B. Nurushev, A. F. Prudkoglyad, P. A. Semenov, L. F. Soloviev, V. L. Solovianov†, M. N. Ukhanov, Yu. V. Kharlov, V. Yu. Khodyrev, B. V. Chujko, K. E. Shestermanov, A. E. Yakutin, N. S. Borisov[1)], V. N. Matafonov[1)], A. B. Neganov[1)], Yu. A. Plis[1)], Yu. A. Usov[1)], A. N. Fedorov[1)], and A. A. Lukhanin[2)]

PROZA-2 Collaboration

Institute for High Energy Physics, Protvino, Moscow oblast, 142284 Russia

Received September 2, 2003

Abstract—Data on the single-spin asymmetry (A_N) of inclusive π^0 production in 40-GeV pion interactions with a polarized target, $\pi^- + p_\uparrow \to \pi^0 + X$, are presented for the target-fragmentation region. The result is $A_N = (-13.8 \pm 3.8)\%$ for $-0.8 < x_\mathrm{F} < -0.4$ and $1 < p_T < 2$ GeV/c and is compatible with zero for $-0.4 < x_\mathrm{F} < -0.1$ and $0.5 < p_T < 1.5$ GeV/c. At a π^0 momentum of about 1.7 GeV/c in the c.m. frame, the asymmetry becomes nonzero both in the central and in the target-fragmentation region. The behavior of the asymmetry is similar to that observed in the beam-fragmentation region of the E-704 (FNAL, 200 GeV) and STAR (BNL, 20 TeV) experiments, which employed a polarized proton beam.

INTRODUCTION

The spin is one of the fundamental properties of elementary particles. Since the advent of polarized targets and polarized beams, investigation into spin effects has become one of the most important fields in high-energy physics.

Within perturbative QCD (pQCD), transverse single-spin effects tend to zero in the limit of high energies and high momentum transfers. However, even the first experiments with polarized targets yielded results contradicting these expectations. A significant asymmetry was revealed in elastic and charge-exchange reactions. Experiments in the region of polarized-beam fragmentation at the Argonne National Laboratory (ANL) disclosed considerable effects in $p_\uparrow + p \to \pi^\pm + X$ reactions at beam energies of 6 and about 12 GeV [1, 2]. In 1990, a detailed study of the asymmetry was performed by the E-704 experiment in a 200-GeV beam at the Fermi National Accelerator Laboratory (FNAL). The E-704 Collaboration reported a substantial value of the π-meson asymmetry in the beam-fragmentation region [3]. The absolute value of the asymmetry of inclusive charged-pion production was 40% in the E-925 experiment performed in a 22-GeV polarized-proton beam at the Brookhaven National Laboratory (BNL) in the late 1990s [4].

The main purpose of the PROZA-2 experiment [5] was to measure the asymmetry in question in the region of polarized-target fragmentation. No experiments were performed in this kinematical region previously. A feature peculiar to the PROZA-2 experiment is that, in contrast to all previous experiments, which sought the asymmetry of inclusive π^0-meson production either in the fragmentation region at high longitudinal momenta ($x_\mathrm{F} \gg x_T$, where $x_\mathrm{F} \approx 2p_L/\sqrt{s}$ is the Feynman variable and $x_T = 2p_T/\sqrt{s}$, p_L and p_T being, respectively, the longitudinal and the transverse secondary-particle momentum) or in the central region ($x_\mathrm{F} \approx 0$), the contributions of both the

†Deceased.
1)Joint Institute for Nuclear Research, Dubna, Moscow oblast, 141980 Russia.
2)Kharkov Institute for Physics and Technology, ul. Akademicheskaya 1, Kharkov, 61108 Ukraine.
*e-mail: mochalov@mx.ihep.su

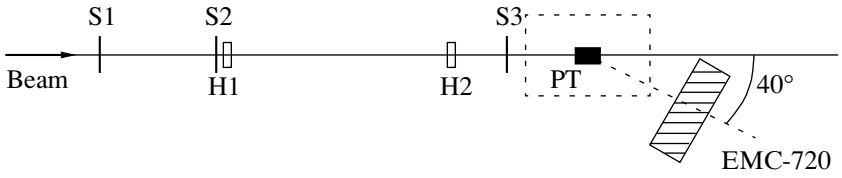

Fig. 1. Layout of the PROZA-2 experimental setup: (S1–S3) scintillation counters of the total flux, (H1, H2) hodoscopes, (PT) polarized target, and (EMC-720) electromagnetic calorimeter placed at an angle of 40° or 30° with respect to the beam axis.

longitudinal and the transverse momentum components are significant here.

1. EXPERIMENTAL SETUP

Our experiment was conducted with the aid of the PROZA-2 setup installed in the beamline 14 of the U-70 accelerator complex. In a 40-GeV beam, we measured the asymmetry of inclusive π^0-meson production in the reaction

$$\pi^- + p_\uparrow \to \pi^0 + X. \qquad (1)$$

The setup consisted of beam detectors, a polarized target, and an electromagnetic calorimeter. Figure 1 shows the layout of the experimental setup, which was described in detail elsewhere [6].

1.1. Beam Formation and Beam Detectors

The beam of negatively charged particles produced in the internal target was deflected into beamline 14 by the magnetic field of the accelerator. The system of three magnets and eight lenses permitted us to select particles of specific energy and to focus the resulting beam onto the polarized target of the setup. The beam formed in this way contained π^- mesons, K^- mesons, and antiprotons (about 98, 1.8, and 0.3%, respectively), the beam intensity being 10^6 particles per spill. The spread in particle momenta was about 2% and was determined by the acceptance of a pulsed collimator.

The beam foci in the horizontal and vertical planes were close to the target center. The beam dimensions at the target were $\sigma_x \simeq \sigma_y \simeq 3.5$ mm. More than 97% of beam particles hit the target, which was 18 mm in diameter.

The number of particles incident on the target was determined by three scintillation counters, S1–S3; the first two of them were 10 cm in diameter, while the last one, located near the target, was 1.8 cm in diameter.

The coordinates of beam particles incident on the target were determined by two hodoscopes, H1 and H2, placed at distances of, respectively, 8.7 and 3.2 m from the target center. The hodoscope H1 comprised two planes, each containing 16 counters of size $5 \times 5 \times 85$ mm; the hodoscope H2 had two planes with 12 counters per plane, each of them being of size $2 \times 5 \times 40$ mm (the 2-mm side was oriented along the direction transverse to the beam).

1.1.1. Polarized target

A frozen polarized-proton target based on propanediol ($C_3H_8O_2$) was used in the experiment [7]. The mean polarization of hydrogen nuclei there was 80% during the accumulation of data. The pumping of the polarization, with its simultaneous reverse, took about four hours. On average, it was performed once every 48 hours. A special compact magnet ensuring a field of high uniformity (up to 10^{-4}) was designed for the polarized target at the Institute for High Energy Physics (IHEP, Protvino) [8].

A thin-walled horizontal cryostat was used in the target. Low-energy secondary particles could be recorded owing to thin side walls of the cryostat. This property was of special importance for measurements of the asymmetry in the target-fragmentation region.

We note that the mass of hydrogen nuclei was about 1/10 of the entire target material. In calculating the asymmetry, it is therefore necessary to take into account the target-dilution factor D, which is defined as the ratio of the total number of beam interactions with the target to the number of interactions with hydrogen nuclei.

1.1.2. Electromagnetic calorimeter

Photons from π^0-meson decay were recorded by a total-absorption electromagnetic calorimeter. The calorimeter comprised 720 counters (EMC-720) from TF1-00 lead glass [9]. It was shaped as a rectangular matrix containing 30 column of 24 counters. The calorimeter was placed at a distance of about 2.3 m from the target. The counters were of size $38 \times 38 \times 450$ mm (18 radiation-length units); they were wrapped with an aluminized Mylar film 20 μm thick. Cherenkov light produced by electromagnetic showers in the glass was recorded by a 12-dynode

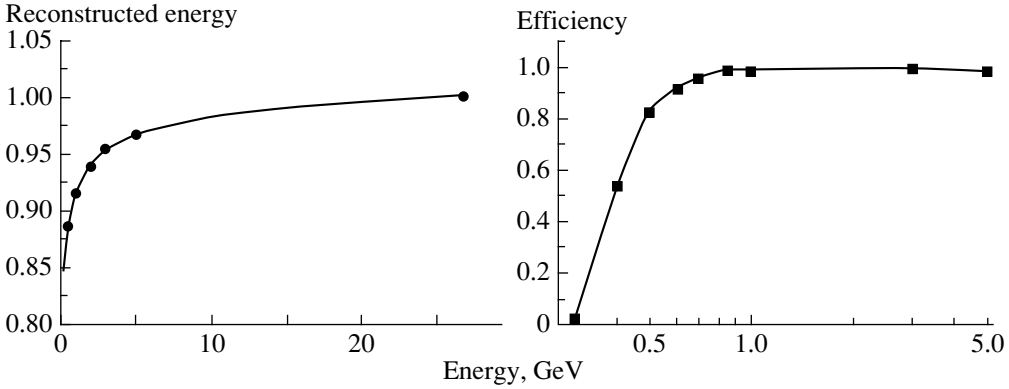

Fig. 2. Energy fraction recorded by the calorimeter (left panel) and efficiency of electromagnetic-shower reconstruction in the detector (right panel) versus the true photon energy in a simulation.

photomultiplier tube (PMT-84/3), the photocathode being 34 mm in diameter.

The coefficients used to convert the pulse from each detector cell to the energy deposited inside this cell were determined by means of a detector calibration with a 26.6-GeV electron beam [10]. The calorimeter design permitted moving the detector in the horizontal and vertical directions orthogonal to the beam in such a way that the electron beam could irradiate all of the calorimeter cells. The calorimeter resolution was $\sigma(E)/E = 2.5\%$ at the energy value used (the beam-momentum spread of 2% was subtracted).

A monitoring system based on photodiodes [11] was used to test the calorimeter stability with time. The energy scale was monitored by means of an additional calibration against the π^0-meson mass to a precision of 0.1% in the course of five-hour measurements.

The EMC-720 central counters were arranged in the horizontal plane at a viewing angle of 30° with respect to the target center in the run of 1999 for measurements in the range $-0.4 < x_{\mathrm{F}} < -0.1$ and at an angle of 40° in two runs of 2000 for measurements in the range $-0.8 < x_{\mathrm{F}} < -0.3$.

1.2. Electronic System and Transverse-Energy Trigger

The electronic system consisted of unified nanosecond-electronics modules, circuits of pulse-height converters, rescaling circuits, registers, and other additional systems manufactured in the SUMMA standard [12].

The coincidence of signals from three scintillation counters S1–S3 was a zero-level trigger for an incident particle. In addition, a response from each plane of the hodoscopes was required. The trigger was formed within a 60-ns gate if another particle did not pass within this time gate.

A level-1 trigger within a 350-ns gate was developed on the basis of an analysis of the total transverse energy deposition in the calorimeter. A fraction of the pulse from each counter (about 5%) was fed into an analogous adder, the angle at which this counter was viewed from the target being taken into account. To introduce angular corrections, use was made of shunting resistors whose resistances were proportional to $\sin\theta$, where θ was the mean angle corresponding to a given column. Thus, the total signal was proportional to the transverse energy $E_T = E\sin\theta$ recorded by the detector. The detector trigger was adjusted at a level of 1.1 GeV in the run of 1999 and at a level of 1.4 GeV in the runs of 2000.

For electronics of the pulse-height analysis, we used 12-bit analog-to-digital converters (P-267) [13]. The data were read out by a computer based on the MC68030 processor and controlled by the OS-9 real-time operating system and were then transferred by a local network to an individual computer in order to perform on-line processing and to log them on a magnetic tape. With allowance for the efficiency of the data-acquisition system, about 300 events were recorded per accelerator cycle. In all, about 100 million events were obtained over 30 days of data accumulation.

2. DATA ANALYSIS AND RESULTS

Analyzing our experimental data, we selected, among all of the recorded photons, those whose energy ranged between 0.5 and 3.5 GeV. The mean multiplicity of recorded photons was about 1.3.

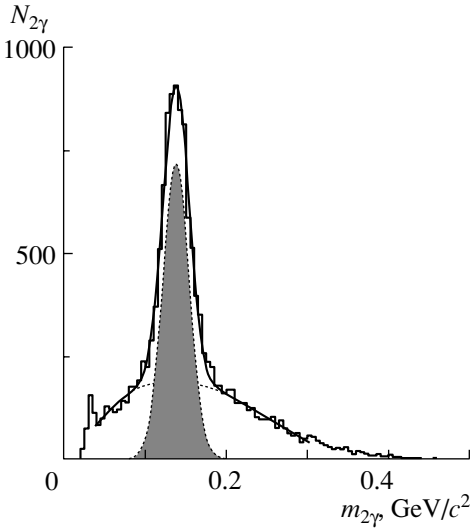

Fig. 3. Mass distribution of photon pairs recorded in the EMC-720 electromagnetic calorimeter. The distribution is approximated by a Gaussian and a polynomial of third degree (solid curve). The dotted curve represents the background in the region of the π^0-meson mass peak, while the shaded area corresponds to the Gaussian function describing the π^0 mass distribution.

2.1. Simulation of an Electromagnetic Shower in the Calorimeter

To test the algorithm for reconstructing photons and π^0 mesons, the development of electromagnetic showers in lead glass was simulated on the basis of the GEANT 3.21 code [14]. In the simulation of Cherenkov light, we took into account the effects caused by its propagation through matter and its reflection from the surface of the crystal wrapped with a Mylar film, as well as the quantum properties of PMT-84/3 photomultiplier tubes. The number of photoelectrons was about 1000 GeV^{-1}, which corresponds to experimental data obtained for this type of glass [15].

The simulation revealed that a substantial fraction of energy (up to 20%) was lost in recording low-energy photons mainly because of the detection threshold of the electronics. Figure 2 shows the ratio of the recorded energy to the true energy. It can also be seen from this figure that the efficiency of electromagnetic-shower reconstruction in the calorimeter without the background is close to 100% for energies above 0.8 GeV and exceeds 80% at an energy of 0.5 GeV.

2.2. Properties of Reconstructed Neutral Pions

Corrections to the shower energy that were obtained in the simulation permitted us to take into account the energy losses and to reconstruct the energy and the mass of π^0 mesons correctly. Figure 3 shows the mass distribution of a photon pair, its width σ_m being about 15 MeV/c^2.

The chosen geometry and trigger made it possible to record π^0 mesons in the target-fragmentation region for transverse momenta in excess of 0.5 GeV/c. Figure 4 shows the distribution of photon pairs in the region of the π^0-meson mass versus some kinematical variables. The correlation between p_T and x_F is clearly seen in this figure.

2.3. Algorithm for Calculating Single-Spin Asymmetry

The single-spin asymmetry A_N observed physically is defined as

$$A_N(x_\mathrm{F}, p_T) = \frac{1}{P_\mathrm{targ}} \frac{1}{\langle \cos\phi \rangle} \frac{\sigma_\uparrow^\mathrm{H}(x_\mathrm{F}, p_T) - \sigma_\downarrow^\mathrm{H}(x_\mathrm{F}, p_T)}{\sigma_\uparrow^\mathrm{H}(x_\mathrm{F}, p_T) + \sigma_\downarrow^\mathrm{H}(x_\mathrm{F}, p_T)}, \quad (2)$$

where P_targ is the target polarization, $\cos\phi$ is the cosine of the azimuthal angle between the target-polarization vector and the normal to the plane spanned by the beam axis and the momentum of the outgoing π^0 meson, and $\sigma_\uparrow^\mathrm{H}$ and $\sigma_\downarrow^\mathrm{H}$ are the cross sections for π^0-meson production on hydrogen for opposite directions of the target polarization. In our case, π^0 mesons were recorded at an azimuthal angle in the range $180^\circ \pm 15^\circ$; therefore, $\cos\phi$ was set to -1.

The raw asymmetry A_N^raw actually measured in our experiment for the detector placed to the right of the beam axis is related to A_N by the equation

$$A_N = \frac{D}{P_\mathrm{targ}} A_N^\mathrm{raw} = \frac{D}{P_\mathrm{targ}} \frac{n_\downarrow - n_\uparrow}{n_\downarrow + n_\uparrow}, \quad (3)$$

where D is the target-dilution factor and $n_\downarrow$ and $n_\uparrow$ are the normalized (to the monitor) numbers of π^0 mesons produced on the propanediol target for opposite directions of the polarization vector.

The number of particles that traversed the setup target was used as a monitor with allowance for the efficiency of the hodoscopes—that is, with allowance for the number of triggers T_0 formed upon a simultaneous actuation of the telescope consisting of three scintillation counters and each plane of the hodoscopes.

In measuring the asymmetry, there can arise an additional instrumental asymmetry caused by trigger-electronics jitter, failures of the monitor counters, and other reasons. As a consequence, the

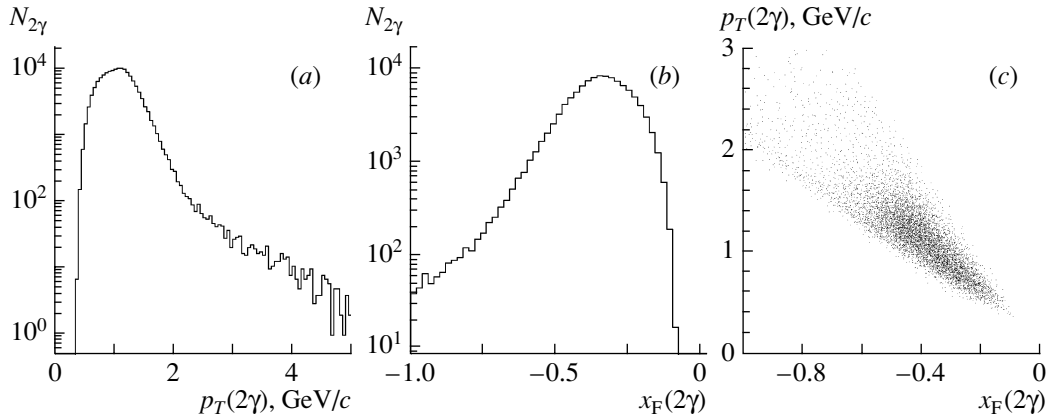

Fig. 4. (*a*) Transverse-momentum (p_T) and (*b*) x_F distributions of photon pairs and (*c*) p_T as a function of x_F in the region of the π^0 meson mass according to measurements with EMC-720 during the run in the fall of 2000. The efficiency of π^0-meson reconstruction is not taken into account in the displayed distributions.

measured asymmetry is a sum of the real and the instrumental asymmetry (A_{backgr}); that is,

$$A_{2\gamma}^{\text{meas}} = kA_{\pi^0}^{\text{real}} + A_{\text{backgr}}, \qquad (4)$$

where k is the relative number of π^0 mesons, which depends on the photon-pair mass. In order to remove this systematic bias of the asymmetry, we developed a method based on the assumption that the background asymmetry is zero. By the background asymmetry A_{backgr}, we mean the asymmetry of photon pairs off the region of the π^0-meson mass peak. This assumption is based on the results of the PROZA-M and E-704 experiments performed previously. The asymmetry A_N for photon pairs off the π^0-meson mass region was $A_N = (-1.0 \pm 0.8)\%$ in the E704 experiment [16] and $(0.04 \pm 0.4)\%$ in the raw data of the PROZA-M experiment, where it was averaged over the range $1.8 < p_T < 3.2$ GeV/c. In our calculation, we set the background asymmetry to zero, disregarding the uncertainty in the measurements.

In order to suppress systematic uncertainties associated with the instability of electronics operation, the data from counters that were actuated much more often, on average, than neighboring ones at least in one of the event sets (hot counters) were excluded from the analysis of the whole statistics. Hot counters were tested over three-hour intervals. In all, two groups of 16 counters, each corresponding to two analog-to-digital converters and nine separate counters were discarded. It should also be noted that we selected only clusters described by an electromagnetic shower of shape known from the experimental data.

Figure 5 shows an example illustrating the calculation of the asymmetry $A_{\pi^0}^{\text{raw}}$. The asymmetry is derived as the ratio of the difference of the normalized numbers of photon pairs as a function of their mass for two opposite directions of the target polarization vector to the sum of these numbers, $\dfrac{n_\downarrow - n_\uparrow}{n_\downarrow + n_\uparrow}$. The background asymmetry A_{backgr} is fitted off the region of the mass peak. The resulting value is subtracted, at each point, from the measured asymmetry $A_{2\gamma}^{\text{meas}}$. In this way, we obtained the raw asymmetry $A_N^{\text{raw}}(2\gamma)$ as a function of mass. The resulting distribution was fitted with allowance for the weight factor k for π^0 mesons at each point of the mass spectrum.

The systematic error of this method is determined primarily by the statistics of photon pairs off the region of the π^0-meson mass and, for different intervals of x_F, is 50 to 100% of the statistical uncertainty in assessing the number of π^0 mesons. In the results presented in this article, we took into account both the statistical and the systematic uncertainty.

2.4. Analysis of the Spurious Asymmetry

The spurious asymmetry is caused by a drift of the calorimeter-energy scale and by the respective inaccuracy in reconstructing the kinematical parameters of the photon pair. The cross section for the inclusive production of π^0 mesons depends greatly on p_T. Therefore, a 1% difference in the energy scale of the detector between the data for positive and negative target polarizations leads to a spurious raw asymmetry on the order of 2%—that is, to a spurious asymmetry of 20% upon taking into account the dilution factor. In our case, the instability of the calorimeter energy scale was below 0.1%. Thus, the spurious asymmetry caused by the instability of the energy scale was below 0.2% for the raw asymmetry and

Table 1. Dilution factor versus the transverse momentum

p_T [GeV/c]	1.3	1.5	1.7	1.9	2.1	2.3	2.5	2.8
D from [17]	8.0 ± 1.0	8.1 ± 1.2	8.1 ± 0.7	8.2 ± 0.9	8.8 ± 1.3	9.2 ± 1.6	9.5 ± 2.0	10.1 ± 2.5

2% for the quantity under study (the dilution factor and target polarization $D/P_{\text{targ}} \sim 10$ were taken into account).

In order to estimate the spurious asymmetry, the total data set obtained for the same direction of the target polarization vector was broken down into two equal subsets, and the asymmetry for these subsets was determined (opposite signs of target polarization were arbitrarily assigned to these subsets). Figure 6 shows the result calculated for the spurious asymmetry in one of the three experimental runs. The spurious asymmetry is zero within the errors. The same result was obtained for the other experimental runs as well; however, the uncertainties are rather large. In order to be sure that the data obtained in the different measurements are consistent, we compared the results on the asymmetry from the three experimental runs performed in different periods. The results are in agreement within the errors.

2.5. Determination of the Dilution Factor

In order to calculate the physically observed asymmetry A_N on the basis of Eq. (3), it is necessary to determine the target-dilution factor. For this, we must know the composition of the target material (in percent). Interactions can also occur on the target iron walls 0.3 mm thick. The cross section for the production of charged π mesons is proportional to A^α, with α lying in the range between 0.85 and 1.2 for $p_T > 1$ GeV/c [18]. According to our calculations, the dilution-factor value must range between about 8 and about 10.5 if the transverse momentum p_T varies between 1 and 3 GeV/c. To test the calculations, we used the results of dedicated measurements from previous runs [17] with an empty target and with a carbon equivalent of our target. The effect for an unpolarized propanediol target was determined as the mean effect for two orientations of the target polarization vector. Table 1 summarizes the data from these measurements. It should be noted that our study is performed with the same polarized target from the same material. In 1996, we also measured the dilution factor, but on the basis of scarcer statistics. The results were $D = 8.4 \pm 1.2$ and $D = 9.2 \pm 1.5$ at $p_T \sim 1.8$ GeV/c and $p_T \sim 2.1$ GeV/c, respectively, these values being in agreement with previous results. We adopted the value of $D = 8.1$ for our calculations.

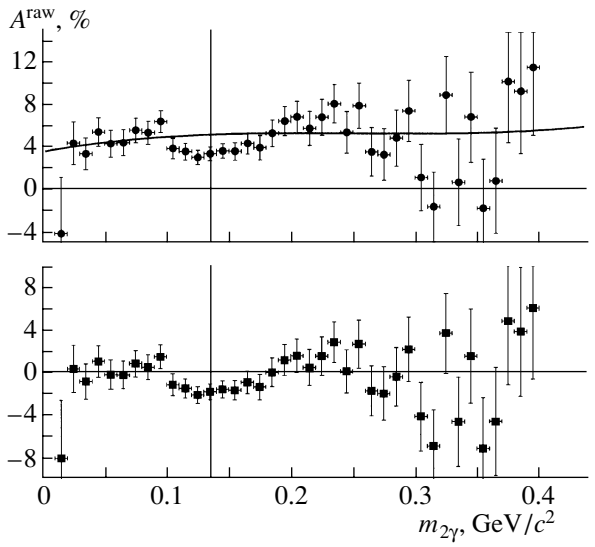

Fig. 5. Raw asymmetry A^{raw} as a function of the photon-pair mass (upper panel) and result obtained upon subtracting the background asymmetry (lower panel). The curve represents a fit to the background asymmetry—that is, for photon pairs off the π^0-meson mass peak.

2.6. Measurements of the Asymmetry

Figure 7 and Table 2 display the ultimate results with allowance for the dilution factor and the target polarization. In the calculation of the physically observed asymmetry A_N, the uncertainties in the dilution factor D and in the target polarization (about 10%) were disregarded.

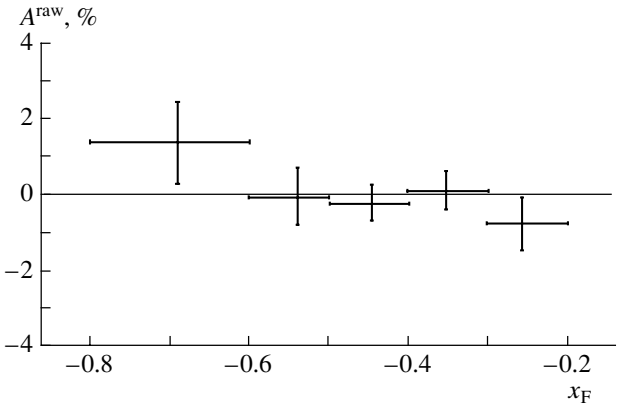

Fig. 6. Spurious asymmetry as a function of x_{F} in the spring run of 2000.

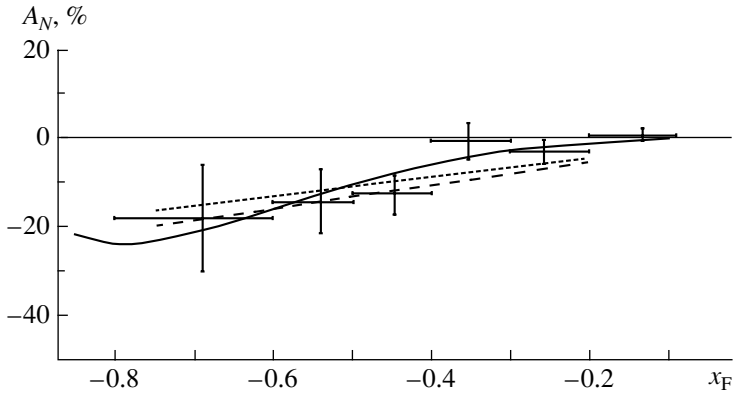

Fig. 7. Asymmetry A_N of π^0-meson production in the target-fragmentation region as a function of x_F. The resolution in x_F varies from 0.03 for $-0.3 < x_F < -0.1$ to 0.07 for $-0.8 < x_F < -0.6$. The solid curve represents the prediction obtained in [23] on the basis of the Collins model; the dotted and dashed curves are the predictions of the U-matrix quark model at various values of $\langle L_{\{\bar{q}q\}}\rangle$ ($\langle L_{\{\bar{q}q\}}\rangle$ is the mean angular momentum of current quarks inside the constituent quark) [30].

The asymmetry proves to be $A_N = (-13.8 \pm 3.8)\%$ in the range $-0.8 < x_F < -0.4$ and is close to zero in the range $-0.4 < x_F < -0.1$.

3. DISCUSSION

3.1. Comparison with Other Experimental Data

The asymmetry of inclusive π^0 production in the polarized-particle-fragmentation region was also measured in experiments at FNAL (E-704) and BNL [19] at, respectively, 200 GeV and 20 TeV in the target rest frame (the latter energy value was rescaled from the c.m. energy of two 100-GeV beams of the RHIC collider to the beam energy in the laboratory frame). Table 3 summarizes the results of the three experiments in the polarized-particle-fragmentation region.

In all of the experiments, the absolute value of the asymmetry grows with increasing $|x_F|$, reaching a value of 10 to 15% at high values of $|x_F|$. Therefore, we can conclude that the asymmetry of inclusive π^0-meson production in the polarized-proton-fragmentation region is virtually independent of energy in the range 40–20 000 GeV in the laboratory frame. The measured analyzing power is rather high in the reaction being studied (10–15%), and the cross section for π^0 production is quite large. Thus, this reaction can be used to measure the polarization of proton beams.

The asymmetry A_N in the central π^0-production region of the reaction $\pi^- + p_\uparrow \to \pi^0 + X$ was previously measured with the PROZA-M setup at 40 GeV/c [17]. In that case, the asymmetry grew in magnitude with increasing p_T, reaching a value of −30%. If the asymmetry was approximated by a linear function, it intersected the abscissa at $p_T^0 = 1.67 \pm 0.09$ GeV/c. In order to compare our new data with the results from [17], we plotted the asymmetry versus the π^0-meson energy in the c.m. frame, E. The asymmetry begins to grow in magnitude at $p_0 = 1.75 \pm 0.2$ GeV/c (Fig. 8). The measurements in [17] were carried out at an angle of 90° in the c.m. frame; therefore, the transverse momentum p_T there was

Table 2. Asymmetry in the reaction $\pi^- + p_\uparrow \to \pi^0 + X$ at a beam momentum of 40 GeV/c versus x_F

$\langle x_F\rangle$	$\langle p_T\rangle$, GeV/c	A_N, %
−0.133	0.8	0.4 ± 1.4
−0.258	1.1	-3.3 ± 2.4
−0.353	1.3	-1.0 ± 3.9
−0.446	1.5	-12.7 ± 4.8
−0.54	1.65	-14.4 ± 7.2
−0.69	1.8	-18.3 ± 11.9

Table 3. Data from different experiments on the asymmetry A_N measured in the polarized-proton-fragmentation region for $1 < p_T < 2$ GeV/c

Experiment	$\lvert A_N\rvert$, %
E-704, FNAL [3]	12.4 ± 1.4
STAR, BNL [19]	14 ± 4
Present experiment	13.8 ± 3.8

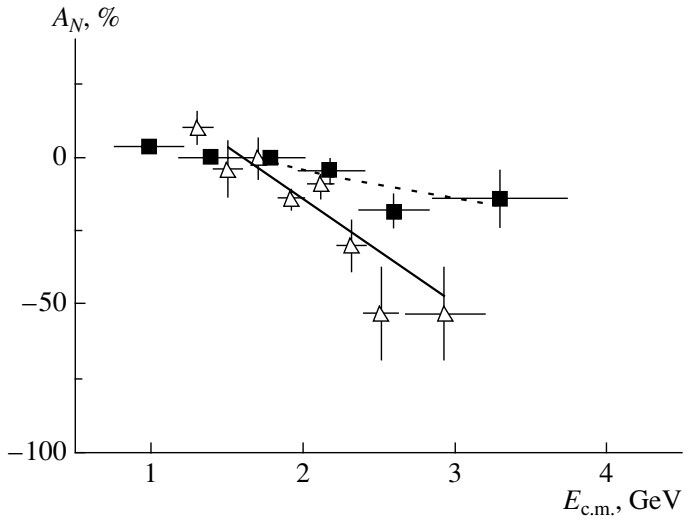

Fig. 8. Asymmetry A_N of π^0-meson production in the reaction $\pi^- + p_\uparrow \to \pi^0 + X$ as a function of the π^0-meson energy in the c.m. frame (E) for the target-fragmentation region (■, our experiment) and for the central region (△, data from [17].

virtually coincident with the π^0-meson momentum in the c.m. frame. Thus, we can see that, in the two kinematical regions, the asymmetry begins growing in magnitude at the same π^0-meson energy in the c.m. frame.

3.2. Mechanism of Asymmetry Generation within Various Theoretical Models

The pQCD model predicts zero asymmetry. In order to explain the observed high single-spin asymmetry, Sivers [20, 21] introduced an additional internal transverse momentum $\mathbf{k}_T$ of quarks in the parton distributions within polarized nucleons. Collins [22] assumed that an additional transverse momentum appears in the fragmentation functions $D_{\pi/c}$. Thus, the single-spin asymmetry appears because of the spin dependence of initial-state interaction in the Sivers model and because of the spin dependence of final-state interaction in the Collins model. Figure 7 shows Anselmino's predictions for the single-spin asymmetry A_N in the reaction $\pi^- + p_\uparrow \to \pi^0 + X$ within the Collins model [23] (solid curve). His predictions within the Sivers model deviate only slightly from this curve.

Efremov and Teryaev [24, 25] proposed taking into account the contribution of higher twists or the quark–gluon correlation, which reflects quark interaction with a hadron color field [26, 27]. The predictions of Qiu and Sterman [28] within this model also adequately describe the experimental data in the polarized-particle-fragmentation region.

A high-asymmetry generation can also be associated with the orbital angular momentum of quarks. Troshin and Tyurin [29] formulated a quark model within the U-matrix approach where the main contribution to the asymmetry comes from the orbital angular momentum of current quarks inside a constituent quark. For the reaction being studied, Fig. 7 shows the asymmetry values predicted within the U-matrix quark model [30] (dotted and dashed curves).

Ryskin [31] proposed a model where the asymmetry arises owing to the interaction of the quark chromomagnetic moment with a chromomagnetic field. Using Ryskin's basic idea, Abramov [32] put forward his own model, which also describes the data in question quite well.

The basic models are reviewed in [33–35].

The results on the asymmetry in inclusive π-meson production that were obtained in the PROZA (IHEP) [17] and E-704 (FNAL) [3] experiments gave impetus to the development of these models. The parameters of the models were chosen in such a way as to describe well the results of the E-704 experiment. Since the data presented in this article are similar to those obtained in the E-704 experiment, they are in good agreement with the predictions of the theoretical models.

We also note that the gluon component makes a large contribution to the cross section in the region of small $|x_{\text{F}}|$; therefore, the asymmetry must be small in the region $|x_{\text{F}}| < 0.4$ because the transverse gluon functions depend only slightly on the proton polarization.

4. CONCLUSIONS

The basic results of our study are the following.

(i) The asymmetry in inclusive π^0 production has been measured for the first time in the polarized-target-fragmentation region. The asymmetry measured in the reaction $\pi^- + p_\uparrow \to \pi^0 + X$ is $A_N = (-13.8 \pm 3.8)\%$ in the range $-0.8 < x_\mathrm{F} < -0.4$ for p_T values ranging between 1 and 2 GeV/c.

(ii) The asymmetry is close to zero in the range $-0.4 < x_\mathrm{F} < -0.1$ for p_T values between 0.5 and 1.5 GeV/c.

(iii) Within the uncertainties, the asymmetry measured in our experiment for $|x_\mathrm{F}| > 0.4$ is consistent with the results of the measurements performed at FNAL (E-704, 200 GeV) and BNL (20 TeV in the rest-target frame) in the polarized-proton-beam fragmentation region at the same values of $|x_\mathrm{F}|$. Therefore, it has been established in a fixed-target experiment that the asymmetry arises in the polarized-proton-fragmentation region and is independent of whether this proton is a beam or a target particle.

(iv) Inclusive π^0-meson production in the polarized-proton-fragmentation region is a new reaction for polarimetry, the experimentally established analyzing power being about 10 to 15%.

(v) From a comparison with the asymmetry measured at an angle of 90° in the c.m. frame, it follows that the absolute value of the asymmetry in the reaction $\pi^- + p_\uparrow \to \pi^0 + X$ at 40 GeV begins growing at the same value of the π^0-meson momentum in the c.m. frame for two different kinematical regions, this value being $p_0 \approx 1.7$ GeV/c.

(vi) The existing theoretical models describe well the experimental data in question.

ACKNOWLEDGMENTS

We are grateful to the leadership of the Institute for High Energy Physics for their support of our studies and to the staff of the U-70 Accelerator Department and the Beam Division, who ensured a high-quality operation of the accelerator complex and the beamline 14. We are also indebted to V.V. Abramov, M. Anselmino, A.M. Zaitsev, J.C. Collins, M.G. Ryskin, and S.M. Troshin for stimulating discussion and to Yu.M. Goncharenko, V.A. Kormilitsin, and N.E. Mikhalin for their technical assistance during the runs.

This work was supported in part by the Russian Foundation for Basic Research (project no. 03-02-16919).

REFERENCES

1. R. D. Klem *et al.*, Phys. Rev. Lett. **36**, 929 (1976).
2. W. H. Dragoset *et al.*, Phys. Rev. D **18**, 3939 (1978).
3. D. L. Adams *et al.*, Z. Phys. C **56**, 181 (1992).
4. C. E. Allgower *et al.*, Phys. Rev. D **65**, 092008 (2002).
5. N. I. Belikov *et al.*, Preprint No. 97-17, IHEP (Protvino, 1997).
6. V. D. Apokin *et al.*, Instrum. Exp. Tech. **41**, 464 (1998).
7. N. S. Borisov *et al.*, Preprint No. 1-80-98, JINR (Dubna, 1980).
8. M. M. Bukharin *et al.*, Prib. Tekh. Éksp., No. 1, 30 (1981); O. A. Grachev *et al.*, Prib. Tekh. Éksp., No. 3, 189 (1993).
9. G. A. Akopdjanov *et al.*, Nucl. Instrum. Methods **140**, 441 (1977).
10. D. L. Adams *et al.*, Preprint No. 91-99, IHEP (Protvino, 1991).
11. A. N. Vasiliev *et al.*, Preprint No. 97-60, IHEP (Protvino, 1997).
12. Yu. V. Bushnin *et al.*, Preprint No. 72-49, IHEP (Serpukhov, 1972); O. I. Alferova *et al.*, Prib. Tekh. Éksp., No. 4, 56 (1975).
13. S. A. Zimin *et al.*, Preprint No. 93-50, IHEP (Protvino, 1993).
14. *GEANT—Detector Description and Simulation Tool* (CERN, 1994).
15. F. Binon *et al.*, Nucl. Instrum. Methods **188**, 507 (1981).
16. E704 Collab., private communication.
17. N. S. Amaglobeli, V. D. Apokin, Yu. N. Arestov, *et al.*, Yad. Fiz. **50**, 695 (1989) [Sov. J. Nucl. Phys. **50**, 432 (1989)]; V. D. Apokin *et al.*, Phys. Lett. B **243**, 461 (1990).
18. R. M. Sulyaev, Preprint No. 88-100, IHEP (Protvino, 1988); R. M. Sulyaev, in *Relativistic Nuclear Physics and Quantum Chromodynamics, Dubna, 1988*, Vol. 1, p. 237.
19. L. C. Bland, in *Proceedings of the 15th International Spin Physics Symposium (SPIN 2002), Long Island, New York, 2002*; hep-ex/0212013.
20. D. Sivers, Phys. Rev. D **41**, 83 (1990).
21. D. Sivers, Phys. Rev. D **43**, 261 (1991).
22. J. C. Collins, Nucl. Phys. B **396**, 161 (1993).
23. M. Anselmino, private communication; M. Anselmino, M. Boglione, and F. Murgia, Phys. Rev. D **60**, 054027 (1999); Phys. Lett. B **362**, 164 (1995); M. Anselmino and F. Murgia, Phys. Lett. B **442**, 470 (1998); hep-ph/9808426.
24. A. V. Efremov and O. V. Teryaev, Yad. Fiz. **36**, 242 (1982) [Sov. J. Nucl. Phys. **36**, 140 (1982)]; **36**, 950 (1982) [**36**, 557 (1982)]; **39**, 1517 (1984) [**39**, 962 (1984)]; Phys. Lett. B **150B**, 383 (1985).
25. A. V. Efremov, V. M. Korotkiyan, and O. V. Teryaev, Phys. Lett. B **348**, 577 (1995).
26. J. Qiu and G. Sterman, Phys. Rev. Lett. **67**, 2264 (1991); Nucl. Phys. B **378**, 52 (1992).

27. A. Schäfer, L. Mankiewicz, P. Gornicki, and S. Güllenstern, Phys. Rev. D **47**, R1 (1993); B. Ehrnsperger, A. Schäfer, W. Greiner, and L. Mankiewicz, Phys. Lett. B **321**, 121 (1994).
28. J. Qiu and G. Sterman, Phys. Rev. D **59**, 014004 (1999).
29. S. M. Troshin and N. E. Tyurin, Phys. Rev. D **52**, 3862 (1995); **54**, 838 (1996).
30. S. M. Troshin, private communication.
31. M. G. Ryskin, Yad. Fiz. **48**, 1114 (1988) [Sov. J. Nucl. Phys. **48**, 708 (1988)].
32. V. V. Abamov, Preprint No. 98-84, IHEP (Protvino, 1998); V. V. Abramov, Eur. Phys. J. C **14**, 427 (2000); hep-ph/0110152; Preprint No. 2001-13, IHEP (Protvino, 2001); hep-ph/0111128.
33. Zuo-tang Liang and C. Boros, Int. J. Mod. Phys. A **15**, 927 (2000); hep-ph/0001330.
34. M. Anselmino, *Lectures at Advanced Study Institute on Symmetries and Spin (PRAHA SPIN 2001), Prague, 2001*; hep-ph/0201150.
35. M. Anselmino *et al.*, *Talk at 3rd Circum-Pan-Pacific Symposium on High-Energy Spin Physics (SPIN 2001), Beijing, China, 2001*; hep-ph/0201076.

Translated by E. Kozlovsky

Physics of Atomic Nuclei, Vol. 67, No. 8, 2004, pp. 1505–1512. Translated from Yadernaya Fizika, Vol. 67, No. 8, 2004, pp. 1529–1536.

ELEMENTARY PARTICLES AND FIELDS
Experiment

Measurement of Cross Sections for Gamma Transitions Induced in Excited Nuclei by the Interaction of 1.1-GeV Protons with Silicon Nuclei

A. A. Vasenko, N. D. Galanina, K. E. Gusev, V. S. Demidov, E. V. Demidova, I. V. Kirpichnikov, V. A. Kuznetsov, B. N. Pavlov, A. Yu. Sokolov, A. S. Starostin, and N. A. Khaldeeva

Institute of Theoretical and Experimental Physics, Bol'shaya Cheremushkinskaya ul. 25, Moscow, 117259 Russia

Received June 21, 2003

Abstract—The cross sections for the production of excited nuclei were measured in the reaction $^{28}\mathrm{Si}(p, xpyn)A^*$ followed by a gamma transition to a state of lower excitation energy or to the ground state. The experiment was performed in an extracted proton beam from the accelerator of the Institute of Theoretical and Experimental Physics (ITEP, Moscow). The reaction in question was identified by a Ge(Li)–NaI(Tl) anticoincidence spectrometer that recorded prompt gamma radiation emitted by the excited final nucleus. The sensitivity of the experiment was 1.5 mb. The cross-section values were obtained for 24 gamma transitions in 17 nuclear products. The cross sections for spallation reactions were estimated. A comparison was performed with known experimental data and with the results of calculations by a semiempirical formula, as well as with the results obtained by simulating hadron interactions on the basis of the GEANT and INUCL codes. © *2004 MAIK "Nauka/Interperiodica".*

1. INTRODUCTION

Measurement of cross sections for the yield of nuclear products originating from the spallation of nuclei that is induced by protons of energy about a few GeV is necessary both for testing various theoretical models of nuclear reactions and for solving applied problems associated with the conversion of nuclear wastes.

Such measurements have been performed in various laboratories worldwide, and their results are included both in monographs, such as that which is cited in [1], and in modern databases (see, for example, [2]). In what is concerned with theoretical models that describe the spallation of nuclei, we would like to mention the semiempirical dependences presented in [3–5], cascade–evaporation models and their realization in the form of Monte Carlo codes for computers (see, for example, [6–8]), and models developed at the present time on the basis of quantum molecular dynamics [9–11].

In the overwhelming majority of the experiments performed in this energy region, use is made of the method where the products of nuclear spallation are accumulated during the irradiation of targets with proton beams. The amount of radioactive isotopes accumulated in this way is determined by the intensity of so-called delayed emission that is radiated in the process of radioactive decay. Mass spectrometers are used to separate some stable isotopes of inert gases—for example, helium and neon. One of the recent articles devoted to this subject presents results obtained by applying this method to measuring cross sections for the yield of nuclear products originating from the interaction of 0.8- to 2.6-GeV protons with various nuclei ($7 < Z < 30$) [12]. The yields of radioactive nuclides were measured in [13–15] for a wider range of elements ($6 < Z < 92$).

With the aid of the accumulation method, it is impossible to measure the yields of stable nuclei not belonging to the class of inert gases and the yields of radioactive nuclei having a short half-life, these cases constituting a considerable fraction of spallation reactions. The problem of measuring cross sections for reactions involving the production of such nuclei can be solved by recording prompt gamma radiation that is emitted in transitions of excited nuclei to states of lower excitation energy or to the ground state. A feature peculiar to this method is that one measures partial cross sections for transitions primarily from the first excited state to the ground-state level rather than the total yields of nuclei (it is virtually impossible to record all gamma transitions). It is well known [16, 17], however, that, in the case of even–even nuclei, more than 90% of cascade transitions proceed through the first excited state at the last

1063-7788/04/6708-1505$26.00

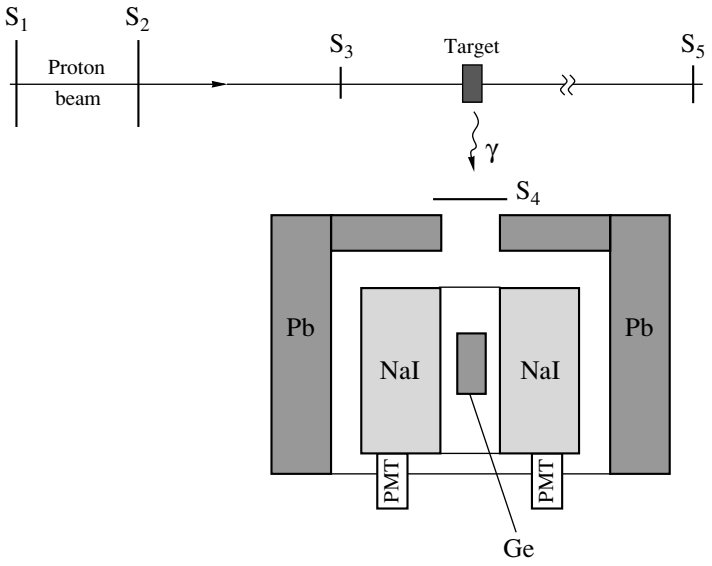

Fig. 1. Layout of the Ge(Li)–NaI(Tl) gamma spectrometer used.

stage. In this case, the gamma-transition cross section can therefore be considered to be close to the cross section for the yield of the respective nucleus; for nuclei belonging to a different type, it is only possible to estimate the yields. Semiconductor (germanium or silicon) spectrometers are used to measure the energy of prompt gamma radiation. However, their application in accelerator experiments at proton energies in excess of 500 MeV, in which case background conditions deteriorate, requires taking additional measures for separating a useful signal.

The method of gamma spectroscopy in a beam was applied in [17]. This made it possible to measure the cross sections for the yields of stable nuclei and radioactive nuclei of short half-life. These data were obtained there for Al and Fe targets at a proton energy of 0.8 GeV.

In the present experiments, we measured cross sections for gamma transitions in excited nuclei originating from the interaction of 1.1-GeV protons with ^{28}Si nuclei.

In order to identify the reaction being considered, prompt gamma radiation emitted by an excited final nucleus was recorded by a Ge(Li)–NaI(Tl) anticoincidence spectrometer. In [18], we reported our preliminary results on the cross sections for the formation of nuclear products in the spallation of Mg, Al, and Si nuclei that was induced by 1.1- to 2.5-GeV protons.

2. DESCRIPTION OF THE EXPERIMENT

Our experiment was performed in a proton beam extracted from the U-10 accelerator of the Institute of Theoretical and Experimental Physics (ITEP, Moscow). A Ge(Li)–NaI(Tl) gamma spectrometer was used to record photons and measure their energy, this spectrometer being part of the MAG facility [19, 20]. The layout of our experiment is displayed in Fig. 1. A beam of protons with a momentum of 1.81 ± 0.02 GeV/c was focused onto the target used by means of a system of magnets and lenses. Coincidences of the $S_1 \times S_2 \times S_3$ counters served as a beam monitor, their dimensions being 4×4 cm^2 for S_3 and 10×10 cm^2 for S_1 and S_2. The beam intensity was maintained at a level of 5×10^5 protons per accelerator spill, the spill duration being approximately 0.5 s. For a target, we used crystalline silicon of natural isotopic composition (92.2% ^{28}Si, 4.7% ^{29}Si, and 3.1% ^{30}Si) in the form of a cylinder 8 cm in diameter and 2.7 cm in height. The beam was directed to the center of the cylinder along its generatrix, so that the amount of substance that the beam traversed was 6.0 g/cm^2. We performed three runs of measurements in the beam. A detailed description of experimental conditions in the runs can be found in [21]. The number of protons that hit the target over the time of the measurements was $N_0 = 5.6 \times 10^{10}$, while the number of "triggers" transferred to a computer was $N_T = 1.18 \times 10^6$.

2.1. Gamma Spectrometer

The Ge(Li)–NaI(Tl) spectrometer was arranged in the direction orthogonal to the beam axis below the target (Fig. 1). The detecting part of the spectrometer was a Ge(Li) crystal of volume 100 cm^3 placed in a cryostat of special configuration. The distance from the center of the crystal to the target was 35.7 cm.

In order to reduce the gamma-ray and neutron background associated with the operation of the accelerator, the gamma detector was protected by a passive shield from lead and was placed within a six-section NaI(Tl) assembly in the form of a well having a height of 30 cm and an external diameter of 45 cm, the diameter of the inner hole being 10 cm. A signal from six NaI crystals was required to be in anticoincidence with a signal from a germanium detector, whereby the continuous background component was suppressed by a factor of 20 to 30 [19].

The scintillation counter S_4 used in the anticoincidence mode prevented the actuation of the spectrometer from charged particles finding their way to the detector. The trigger for the readout of information by a computer was formed by an $S_1S_2S_3\overline{S_4S_5}Ge\overline{NaI}$ signal. The S_5 counter, placed in the beam at a distance greater than 5 m from the target, was used in the anticoincidence mode in order suppress signals from particles that traversed the target without undergoing interaction. The S_5 counter recorded beam protons with an efficiency of 80%. An analogous signal from the germanium detector was recast into digital information $A_{g.d}$ by an analog-to-digital converter with a step of 0.9 keV. The energy interval of recorded photons was 150–3400 keV. The on-line monitoring of spectrometer operation was accomplished with the aid of a 4096-channel analyzer of the NOKIA type.

2.2. Efficiency of the Gamma Spectrometer

The gamma-spectrometer efficiency $\Omega_{\text{eff}}(E_\gamma)$ is determined as the product of two factors, $\Omega_{\text{eff}}(E_\gamma) = \Omega_g(E_\gamma)\eta(E_\gamma)$, where Ω_g describes the geometric component of the efficiency [that is, this factor takes into account the probability that a photon finds its way to the detector and the probability of its loss via the escape of part of the respective electromagnetic shower from the Ge(Li) crystal], while $\eta(E_\gamma)$ characterizes the efficiency of triggering-signal formation.

The dependence $\Omega_g(E_\gamma)$ was determined experimentally in detecting, with the spectrometer, gamma radiation from four reference spectrometric gamma-radiation sources (^{60}Co, ^{88}Y, ^{137}Cs, and ^{228}Th) having well-known intensities. The gamma lines of these sources covered the energy range under study. For the conditions of photon detection to be as close as possible to the conditions of the measurements, the sources were placed at the position of the target being investigated.

The factor $\eta(E_\gamma)$ reflects the decrease in the efficiency because of restricting the time gate δt within which the arrival of a signal from the Ge(Li) detector to the coincidence circuit involving beam counters was allowed. In our measurements, this time gate was $\delta t = 50$ ns. Because of a large scatter of the duration of the leading edge of pulses from the Ge(Li) detector, the gating at a level of $\delta t = 50$ ns restricted the efficiency of the spectrometer. The function $\eta(E_\gamma)$ was determined experimentally by comparing the spectra of gamma radiation from the target that were collected for $\delta t = 50$ ns and $\delta t = 250$ ns.

The photon-detection efficiency decreases with increasing photon energy. It is 2.3×10^{-4} at an energy of 200 keV, falling to 0.77×10^{-4} at 1000 keV and to 0.51×10^{-4} at 1800 keV.

It should be emphasized that the inaccuracy in the efficiency is one of the main sources of errors in measuring cross sections and that, while the geometric efficiency Ω_g can be determined to within a few percent, $\eta(E_\gamma)$ is known to a lower degree of precision, this leading to systematic errors that may be as great as $\pm 10\%$.

The gate δt for the time of delay of a recorded pulse from the Ge(Li) detector sets an upper limit on the half-lives $T_{1/2}$ of levels that can be observed in our experiment. In all probability, the intensities of levels characterized by $T_{1/2} \leq 10$–20 ns can be measured without distortions; however, corrections for the fraction of undetected decays must be introduced for more long-lived states. A lower bound on the recorded lifetimes is determined by the distortion of the gamma-line shape owing to the Doppler effect [22]. Our calculations performed by the Monte Carlo method revealed that distortions can be considered to be insignificant for times longer than 100 fs.

2.3. Energy Calibration

The energy scale of the germanium detector was calibrated on the basis of 14 known gamma lines of a ^{226}Ra source in the range between 180 and 3100 keV. Up to an energy of 1200 GeV, the shape of the recorded gamma line—the spectrometer resolution is affected by this shape—is well described by the Gaussian distribution

$$f(x) = \frac{a}{s}\exp\left[-\left(\frac{x-\mu}{s}\right)^2 \Big/ 2\right], \qquad (1)$$

where a is a normalization factor, μ is the position of the line, and s is the root-mean-square deviation. At high energies, the gamma-line shape becomes asymmetric, more extended toward smaller values of the argument. Up to an energy of 3100 keV, it is approximated by the empirical distribution

$$f(x) = \frac{a}{s}\exp\left[\frac{x-\mu}{s}\right] - \exp\left[\frac{x-\mu}{s}\right], \qquad (2)$$

which is similar to the distribution of extreme values in [23]. In this expression, s is the shape parameter,

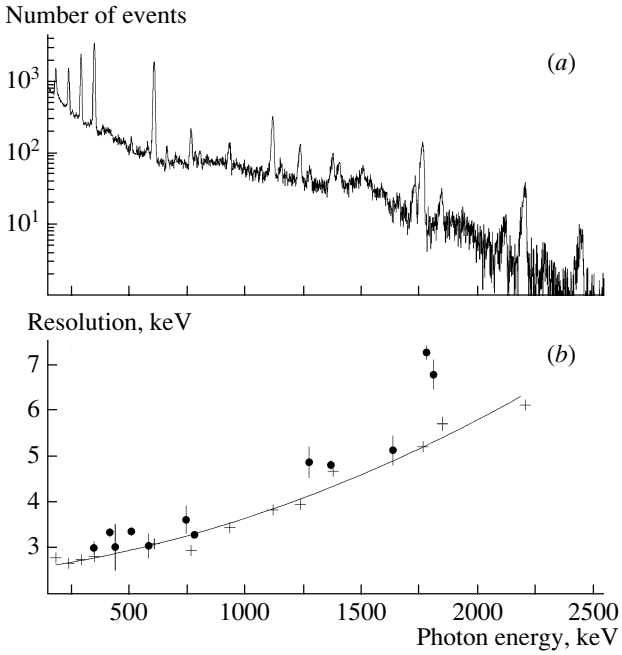

Fig. 2. (*a*) Spectrum recorded by the gamma spectrometer in the irradiation with a ^{226}Ra source. (*b*) Gamma-spectrometer resolution as a function of the photon energy for gamma lines of a ^{226}Ra source (crosses) (the curve represents an approximation by a polynomial of second degree) and for gamma lines excited in the interaction of protons with a silicon target (closed circles).

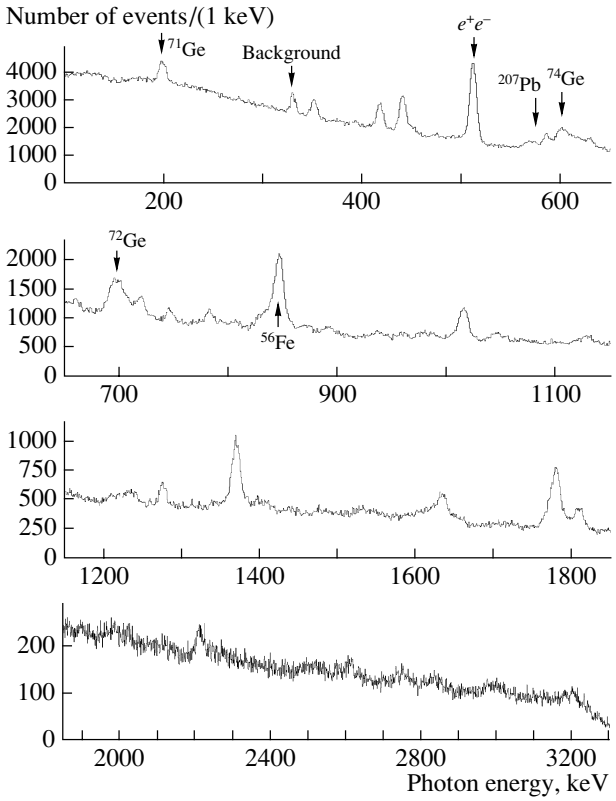

Fig. 3. Spectrum of photons originating from the interaction of 1.1-GeV protons with silicon nuclei. The background peaks are indicated.

which is related to the variance of the distribution by the equation $D = 1.645\ s^2$, while $\mu = \langle x \rangle - 0.58$, where $\langle x \rangle$ is the mean value.

In the vicinity of each of the 14 lines, the distributions of experimental events over channel number of the analog-to-digital converter in the calibration run were described by the sum of a linear background and the resolution function $f(x)$. The relationship between the photon energy (tabulated values) and the number of that channel of the analog-to-digital converter which corresponds to the parameter μ of the function f was approximated by the power-law function E_g [keV] $= b(A_{\mathrm{g.d}} - c)^d$, where the coefficients b, c, and d were determined by the method of least squares.

The calibration dependence approximated well the relationship between the photon energy and the amplitude—the maximum difference between the tabulated values of the energies of photons from the ^{226}Ra source and their counterparts calculated by the respective formula did not exceed ± 1.0 keV. A slight drift of the calibration dependence was observed in the case of a long-term operation of the spectrometer. In order to ensure the required accuracy, measurements with the ^{226}Ra source were performed every day. Figure 2*a* displays an example of the spectrum obtained in the calibration run. Figure 2*b* shows the spectrometer resolution (root-mean-square deviation) as a function of the photon energy: crosses represent the FWHM values for ^{226}Ra gamma lines (these data were approximated by a polynomial of second degree). It should be noted that the resolution of the detector in accelerator experiments is somewhat lower than its standard resolution. This is because the adaptation of the detector to conditions of a heavy background from accidental photons and neutrons requires applying special electronic circuits for pulse formation [20], which shorten the analogous pulse in time and distort its shape. In Fig. 2*b*, the circles represent the widths of the distributions for lines that are observed in the measurements with the ^{28}Si target in the beam. Because of line broadening caused by the Doppler effect and because of the admixture of other gamma transitions, experimental points lie, as a rule, above the calibration dependence.

2.4. Calculation of Cross Sections

The gamma spectrum obtained in a proton beam with a silicon target is given in Fig. 3. The continuous component of the spectrum (continuum) is formed predominantly by photons whose energy was not

completely recorded (because of the escape of shower particles from the detector), by Compton scattering, and by gamma radiation of a background origin. The maxima in the spectrum are due to gamma transitions in nuclei formed in proton-induced reactions from excited states to the ground state or to a state of lower excitation energy.

In the vicinity of each maximum, the spectra were approximated by the function f, which specifies the line shape, and a linear function extrapolating the continuum. In order to describe spectral regions containing a few gamma lines, several functions f were included in the approximating function. The position μ of the maximum, the shape parameter s, and the parameter a related to the amplitude of a function f were found for each of them as the result of fitting. The values found for μ served for identifying gamma transitions on the basis of tables known from [2, 16].

The identification of transitions is complicated by the fact that, among the recorded maxima, there are those that are caused by the interaction of the accelerator neutron background with nuclei of structural material occurring near the detector—in particular, aluminum, iron, and lead nuclei. There can proceed both (n,γ) reactions and (n,n') reactions accompanied by the excitation of the nucleus involved. There is also background gamma radiation caused by neutron absorption within the detector itself. The energies of background gamma lines are known, and their presence was taken into account in processing the measured spectra. The background maxima are indicated in Fig. 3. The parameters s and a were used to calculate the area of the spectrum under the curve representing the function f, and the cross section for the corresponding gamma transition was determined on the basis of this area. That some regions of the spectrum contained several gamma transitions in different excited nuclei of close energies presented a serious difficulty. The error in measuring transition probabilities in such regions increased considerably.

In order to rescale the number N of events recorded in the photon spectrum at an energy E_γ into the cross section, we employed the formula

$$\sigma[\mathrm{cm}^2] = \frac{4\pi AN}{N_{\mathrm{Av}} x \Omega_{\mathrm{eff}}(E_\gamma) k(E_\gamma) m \xi N_{\mathrm{o}}}, \qquad (3)$$

where N is the area under the peak in terms of the number of events, A = 28 is the atomic number of the target nucleus, N_{Av} is Avogadro's number, $x = 6.0$ g/cm^2 is the target thickness, $\Omega_{\mathrm{eff}}(E_\gamma)$ is the germanium-detector efficiency in steradians, $k(E_\gamma)$ is a coefficient that takes into account photon absorption in the target and in the S_4 counter, the coefficient $m = 0.95$ takes into account the correction for the detector dead time, ξ introduces a correction for the angular distribution of photons in nuclear transitions ($\xi = 1.05$ for $2^+_{(1)} \to 0^+_{(\mathrm{g.s.})}$ transitions [24], and $\xi = 1.0$ for all other transitions), and $N_0 = 5.6 \times 10^{10}$ is the number of beam particles that hit the target over the time of the measurements.

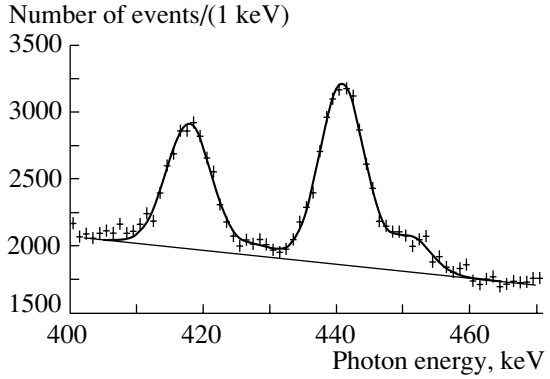

Fig. 4. Photon spectrum in the energy range 400–470 keV. The curve describes the spectrum in terms of a linear background and four Gaussian distributions. The thin straight line represents a linear background.

The coefficient of photon absorption in matter as a function of the photon energy, $k(E_\gamma)$, was calculated by the Monte Carlo method. Its value changes from 0.35 at an energy of 200 keV to 0.7 at an energy of 2500 keV.

An example of a fit to the spectrum in the energy range 400–470 keV is given in Fig. 4. We can see two distinct peaks, which are identified as the 416.8-keV transition from the second level of the ^{26}Al nucleus to its ground-state level and the 440.7-keV transition from the first level of the ^{23}Na nucleus to its ground-state level. Between these two large peaks, there is a modest maximum, which is introduced to improve the approximation and which is probably a manifestation of the 429.1-keV transition from the first level of the ^{7}Be nucleus to its ground-state level. In addition, a peak at 451 keV, which can be identified in terms of the transition from the first level of the $^{23}_{12}$Mg or the $^{25}_{13}$Al nucleus to the respective ground-state level, is taken into account in this fit.

Table 1 presents the results obtained by measuring the cross sections for gamma transitions occurring upon the interaction of 1.1-GeV protons with silicon nuclei. Data are arranged in order of decreasing atomic number of nuclear products formed in the respective reaction. Presented in this table are the value obtained in our experiment for the transition energy, its tabular value (taken from the NNDC database [2]), a product nucleus and emitted particles, the quantum numbers of a transition, and the cross section in millibarns. The quoted errors in the cross sections are purely statistical and are determined by the errors

Table 1. Gamma transitions in nuclei upon the spallation of ^{28}Si nuclei bombarded with 1.1-GeV protons and respective cross sections

E(expt.), keV	E(NNDC), keV	Product nucleus	Emitted particles	Transition	Cross section, mb
1780.3 ± 0.2	1779.0	^{28}Si		$2^+_{(1)} \to 0^+_{(g.s.)}$	35.9 ± 1.8
782.7 ± 0.3	780.8	^{27}Si	n	$1/2^+_{(1)} \to 5/2^+_{(g.s.)}$	5.0 ± 0.9
960.3 ± 0.7	957.3			$3/2^+_{(2)} \to 5/2^+_{(g.s.)}$	2.5 ± 0.8
1796.0 ± 0.9	1795.8	^{26}Si	$2n$	$2^+_{(1)} \to 0^+_{(g.s.)}$	1.4 ± 0.9
841.5 ± 0.1	843.7	^{27}Al	p	$1/2^+_{(1)} \to 5/2^+_{(g.s.)}$	11.3 ± 1.5
1015.0 ± 0.4	1014.4			$3/2^+_{(2)} \to 5/2^+_{(g.s.)}$	11.0 ± 8.0
2214.1 ± 2.0	2211.0			$7/3^+_{(2)} \to 5/2^+_{(g.s.)}$	6.7 ± 1.4
418.2 ± 0.1	416.8	^{26}Al	pn	$3^+_{(2)} \to 5^+_{(g.s.)}$	19.7 ± 0.9
831.4 ± 0.8	829.4			$1^+_{(3)} \to 5^+_{(1)}$	4.6 ± 1.5
451.5 ± 0.4	451.5	^{25}Al	$p2n$	$1/2^+_{(1)} \to 5/2^+_{(g.s.)}$	3.9 ± 1.1
1810.3 ± 0.4	1808.7	^{26}Mg	$2p$	$2^+_{(1)} \to 0^+_{(g.s.)}$	10.9 ± 1.1
1129.8 ± 0.6	1129.7			$2^+_{(2)} \to 2^+_{(1)}$	5.4 ± 0.8
585.8 ± 0.2	585.0	^{25}Mg	$2pn$	$1/2^+_{(1)} \to 5/2^+_{(g.s.)}$	8.2 ± 1.2
978.1 ± 0.6	974.7			$3/2^+_{(2)} \to 5/2^+_{(g.s.)}$	2.2 ± 1.0
1369.8 ± 0.3	1368.6	^{24}Mg	$2p2n$	$2^+_{(1)} \to 0^+_{(g.s.)}$	29.0 ± 1.6
441.2 ± 0.1	440.0	^{23}Na	$3p2n$	$5/2^+_{(1)} \to 3/2^+_{(g.s.)}$	27.5 ± 1.5
892.1 ± 0.7	890.9	^{22}Na	$3p3n$	$4^+_{(3)} \to 3^+_{(g.s.)}$	4.0 ± 1.5
1530.8 ± 1.4	1528.0			$5^+_{(4)} \to 3^+_{(g.s.)}$	2.7 ± 1.0
1276.0 ± 0.3	1274.5	^{22}Ne	$4p2n$	$2^+_{(1)} \to 0^+_{(g.s.)}$	6.9 ± 1.3
351.7 ± 0.2	350.7	^{21}Ne	$4p3n$	$5/2^+_{(1)} \to 3/2^+_{(g.s.)}$	10.6 ± 1.1
1634.9 ± 0.4	1633.7	^{20}Ne	$4p4n$	$2^+_{(1)} \to 0^+_{(g.s.)}$	14.4 ± 1.9
659.2 ± 0.6	656.0	^{20}F	$5p3n$	$3^+_{(1)} \to 2^+_{(g.s.)}$	4.1 ± 0.9
936.7 ± 1.2	937.2	^{18}F	$5p5n$	$3^+_{(1)} \to 1^+_{(g.s.)}$	3.5 ± 1.0
719.2 ± 0.4	718.3	^{10}B	$9p9n$	$1^+_{(1)} \to 3^+_{(g.s.)}$	10.1 ± 1.0

with which the parameters were determined from a fit to the peaks. In addition, there are errors associated with choosing the boundaries of fitting and intervals of the background, with misidentifying peaks, and with including nearby peaks in the fitting procedure. The inaccuracy stemming from these errors can be estimated at 2% for intense peaks (for example, those at 1780, 418, 1369, 441, and 1276 keV) and at 5% for the remaining peaks. A systematic error in determining the efficiency of the spectrometer and in beam monitoring is also possible—it is approximately 10%.

In calculating the transition cross section, we introduced a correction of $1/0.9223 = 1.084$ for the isotopic composition of ^{28}Si. Also, we estimated the correction for the content of the ^{29}Si and ^{30}Si isotopes—it proved to be less than 1 mb. Presented immediately below are some comments to Table 1:

(i) We have estimated the correction for the contribution of closely lying transitions from different reactions. A sizable contribution (3.1 ± 0.6 mb) comes only from the 1780.0-keV transition occurring from the third level of the ^{26}Mg nucleus to its first level. In deriving this estimate, we used our experimental data on the cross sections for the transition from the first level of the ^{26}Mg nucleus to its ground-state level and the transition from its second to its first level.

(ii) For the ^{27}Al nucleus, the energy of the transition from the first to the ground-state level (843.7 keV) is very close to the energy of the background peak from the $(n, n\gamma)$ reaction on a ^{56}Fe

Table 2. Our data along with data from other experiments and results of theoretical calculations (cross-section values are given in millibarns)

Nucleus	Experiment			Calculation			
	Our study	Michel *et al.* [12]	Webber *et al.* [25]	ST	UNUCL	GHEISHA	FLUKA
^{27}Si	7.5 ± 0.9		31.2 ± 0.5	7.8	25.0	38.3	0.4
^{26}Si	1.4 ± 0.9		1.4 ± 0.1	1.4			
^{27}Al	29.0 ± 8.3		51.8 ± 0.8	21.5	22.9	24.6	0.3
^{26}Al	24.3 ± 1.7	20.3 ± 1.7(c)	30.3 ± 0.5	18.5	36.5	84.4	1.0
^{26}Mg	10.9 ± 1.1		15.9 ± 0.3	9.1	6.8	21.8	0.4
^{25}Mg	10.4 ± 1.5		27.2 ± 0.4	17.8			
^{24}Mg	29.0 ± 1.6		33.0 ± 0.4	16.4			
^{23}Na	27.5 ± 1.5		18.9 ± 0.3	14.7	13.3	34.9	3.2
^{22}Na	6.7 ± 1.8	19.3 ± 1.4(c)	11.4 ± 0.3	17.4			
^{22}Ne	6.9 ± 1.3	9.2 ± 1.2	7.8 ± 0.2	5.4	1.7	3.3	2.7
^{21}Ne	10.6 ± 1.1	24.2 ± 1.0(c)	12.3 ± 0.2	9.7	10.3	16.1	4.7
^{20}Ne	14.4 ± 1.9	26.5 ± 1.6(c)	13.3 ± 0.2	12.7	11.7	17.5	6.1
^{20}F	4.1 ± 0.9			4.1			

nucleus (846.8 keV). The presence of the respective peak in exposures where carbon was used for a target proves that the peak in question receives a contribution from the above background reaction. An $(n, n'\gamma)$ reaction can also proceed on aluminum. In order to test the effect of the neutron background, we implemented exposures where the detector was covered with an additional shield from neutrons. In that case, the 843.7- and 1014.4-keV peaks became less intense, at least by 30%. A large error in determining the cross section for the peak at 1014.4 keV stems from the fact that, in constructing a fit, we took into account the 1017.0-keV transition from the first level of the ^{23}Ne nucleus to its ground-state level.

(iii) The first excited state of the ^{26}Al nucleus decays, emitting a positron, the respective half-life being 6.3 s. The transition from the second level of this nucleus to its ground-state level is clearly seen. The peak corresponding to the (830.9 ± 1.2)-keV transition from the third to the first level lies at the edge of a large background peak, so that its cross section is determined with large errors.

(iv) The peak at 451.2 ± 0.2 keV can be identified in two ways, as a transition from the first to the ground-state level either for the ^{25}Al or for the ^{23}Mg nucleus.

(v) The peak associated with the transition from the first level of the ^{25}Mg nucleus to its ground-state level lies at the edge of a large background peak.

(vi) For the ^{22}Na nucleus, the 583.0-keV transition from the first to the ground-state level is characterized by the half-life value of 244 ns and cannot be recorded by our spectrometer. The transition from the second to the first level cannot be recorded either because of a low transition energy. Only the transitions from the third and the fourth level to the ground-state level are recorded.

(vii) The main contribution to the peak at 1634.9 keV comes from the transition proceeding in the ^{20}Ne nucleus from the first excited to the ground-state level. However, the 1636.0-keV transition from the second to the first level of the ^{23}Na nucleus can be superimposed on it. The spectra were processed with allowance for two closely lying transitions, the 1611.7-keV transition in the ^{25}Mg nucleus from the third to the ground-state level and the 1651.9-keV transition in the ^{26}Al nucleus from the sixth to the second level. This can lead to an additional error in the respective cross section.

(viii) The peak at 719.4 keV lies at the edge of a large background peak. The contribution from the background $(n, n'\gamma)$ reaction on a ^{10}B nucleus is possible here.

In Table 2, our data are contrasted against data from other experiments and the results of theoretical calculations. Only the most reliably determined cross sections are quoted there. The second column gives lower limits on the cross sections for the production

of a given nucleus, while the third column displays the results of Michel *et al.* [12]. The procedure applied by those authors to determine cross sections does not rule out, in the cases labeled with the symbol (c), the contribution from radioactive forerunners and yields, as a rule, an upper limit on reaction cross sections.

Presented in the next column of the table are data obtained by Webber *et al.* [25] in an experiment where ^{28}Si nuclei accelerated to an energy of 600 MeV per nucleon interacted with a proton at rest. The product nuclei were separated there by the mass-spectrometry method. The results of that experiment are close to our results for ^{26}Si, ^{24}Mg, ^{22}Ne, ^{21}Ne, and ^{20}Ne nuclei.

In the columns that follow, one can find the result of our calculations based on the semiempirical formula of Silberberg and Tsao (ST) [26, 4] and the result of Monte Carlo simulations performed with the aid of the GEANT 3.21 (FLUKA, GHEISHA) and INUCL codes (see [6] and [7], respectively).

The results of the calculation by the Silberberg–Tsao formula proved to be the closest to the experimental data for neon isotopes, but they show significant deviations for ^{25}Mg, ^{24}Mg, and ^{23}Na nuclei.

The INUCL code employs the cascade–evaporation model. From Table 2, one can see that the INUCL code does not always provide a satisfactory description of spallation cross section, but, for some nuclei (for example, ^{27}Al, ^{21}Ne, and ^{20}Ne), the results of the INUCL calculations are close to the experimental values. As to the calculations based on the GEANT package, they lead to cross-section values deviating dramatically from the experimental data.

3. CONCLUSIONS

(i) By recording gamma radiation emitted upon the interaction of 1-GeV protons with ^{28}Si nuclei, we have measured cross sections for 24 gamma transitions in 17 excited nuclei.

(ii) The results are compared with experimental data available from other studies and with the results of theoretical calculations.

REFERENCES

1. V. S. Barashenkov and V. D. Toneev, *Interaction of High-Energy Particles and Nuclei with Nuclei* (Atomizdat, Moscow, 1972) [in Russian].
2. Brookhaven National Laboratory, Nuclear Data Center (Online Computer Data Service), http://www.nndc.bnl.gov/nndc/nndcnsdd.html.
3. G. Rudstam, Naturforsch A **21**, 1027 (1966).
4. R. Silberberg, C. H. Tsao, and J. R. Letaw, Astrophys. J., Suppl. Ser. **58**, 873 (1985).
5. T. A. Gabriel and J. S. G. Mashnik, Preprint No. +4-96-43, JINR (Dubna, 1996).
6. CERN Program Library Long Writeup W5013, GEANT Detector Description and Simulation Tool, CERN Geneva, Switzerland.
7. G. A. Lobov *et al.,* Preprint No. 83-91, ITEP (Moscow, 1983).
8. J. P. Bondorf, A. S. Botvina, A. S. Iljinov, *et al.*, Phys. Rep. **257**, 134 (1995).
9. S. Chiba *et al.*, Phys. Rev. C **54**, 285 (1996).
10. J. Aichelin, Phys. Rep. **202**, 234 (1991).
11. K. Niita *et al.*, Phys. Rev. C **52**, 2620 (1995).
12. R. Michel *et al.*, Nucl. Instrum. Methods Phys. Res. B **103**, 183 (1995).
13. Yu. E. Titarenko *et al.*, LANL Report LA-UR-00-3599 (Los Alamos, 2000).
14. Yu. E. Titarenko, O. V. Shvedov, M. M. Igumnov, *et al.*, Nucl. Instrum. Methods Phys. Res. A **414**, 739 (1998).
15. O. V. Shvedov *et al.,* Preprint No. 81-93, ITEP (Moscow, 1993).
16. R. M. Endt, Nucl. Phys. A **521**, 1 (1990).
17. H. Vonach *et al.*, Phys. Rev. C **55**, 2458 (1997).
18. A. A. Vasenko *et al.*, *Proceedings of the 11 International Seminar on Precise Measurements in Nuclear Spectroscopy, Sarov, 1996* (1997), Vopr. At. Nauki Tekh., Ser.: Fiz. Yad. Reaktorov, p. 115.
19. M. P. Bezuglov, E. T. Bogdanov, E. V. Bystritskaya, *et al.*, Prib. Tekh. Éksp., No. 1, 13 (2002).
20. M. P. Bezuglov *et al.*, Preprint No. 7-01, ITEP (Moscow, 2001).
21. M. P. Bezuglov *et al.*, Preprint No. 30-99, ITEP (Moscow, 1999).
22. I. Kh. Lemberg and A. A. Pasternak, *Contemporary Methods of Nuclear Spectroscopy* (Nauka, Leningrad, 1985), p. 39.
23. W. T. Eadie *et al. Statistical Methods and Experimental Physics* (North-Holland, Amsterdam, 1971; Atomizdat, Moscow, 1976).
24. I. V. Kirpichnikov, V. A. Kuznetsov, I. I. Levintov, and A. S. Starostin, Yad. Fiz. **41**, 21 (1985) [Sov. J. Nucl. Phys. **41**, 13 (1985)].
25. W. R. Webber, J. C. Kich, and D. A. Schrier, Phys. Rev. C **41**, 547 (1990).
26. R. Silberberg and C. H. Tsao, Astrophys. J., Suppl. Ser. **25**, 315 (1973).

Translated by A. Isaakyan

Physics of Atomic Nuclei, Vol. 67, No. 8, 2004, pp. 1513–1522. Translated from Yadernaya Fizika, Vol. 67, No. 8, 2004, pp. 1537–1545.

ELEMENTARY PARTICLES AND FIELDS
Experiment

Associated $\phi\Lambda^0$ Production in the EXCHARM Experiment

A. N. Aleev, N. S. Amaglobeli[†1)], V. P. Balandin, O. V. Bulekov[2)], I. M. Geshkov[3)], T. S. Grigalashvili[4)], E. A. Goudzovski, D. K. Guriev, D. D. Emelianov, S. V. Eremin[2)], A. I. Zinchenko, Z. M. Ivanchenko, I. M. Ivanchenko, M. N. Kapishin, A. A. Loktionov[5)], V. D. Kekelidze, Z. I. Kozhenkova, V. V. Korenkov, I. G. Kosarev, N. A. Kuzmin, A. L. Ljubimov, D. T. Madigozhin, V. G. Maznyj, A. S. Mestvirishvili, N. A. Molokanova[*], A. N. Morozov, R. E. Pismenyj, V. D. Poze, I. A. Polenkevich, A. K. Ponosov[2)], T. Ponta[6)], Yu. K. Potrebenikov, F. M. Sergeev[2)], L. A. Slepets, and V. N. Spaskov

The EXCHARM Collaboration

Joint Institute for Nuclear Research, Dubna, Moscow oblast, 141980 Russia

Received October 3, 2003; in final form, February 6, 2004

Abstract—The features of the associated production of ϕ mesons with Λ^0 hyperons in neutron–carbon interactions were investigated. The experiment was performed with the aid of the EXCHARM spectrometer at the Serpukhov accelerator in a neutron beam of energy in the interval 20–70 GeV. The differential cross section for inclusive associated $\phi\Lambda^0$ production was measured. © *2004 MAIK "Nauka/Interperiodica".*

1. INTRODUCTION

Within the quark model of broken $SU(3)$ symmetry, the ϕ meson can be represented as a particle entering into the vector-meson nonet, consisting of $s\bar{s}$ valence quarks, and involving a small admixture of $q\bar{q}$ nonstrange quark pairs; it is the first member of the family of vector mesons featuring hidden flavors (ϕ, J/ψ, Υ).

The dynamics of the interaction of systems composed of quarks manifests itself in the Okubo–Zweig–Iizuka rule [1]. According to this rule, disconnected quark diagrams are forbidden in strong interactions; as a consequence, the production and annihilation of quark–antiquark pairs fully belonging to the same hadron are also forbidden. This means, among other things, that, if the ϕ meson were a pure $s\bar{s}$ state, it could not be produced in the interactions of hadrons not containing strange quarks in the initial state or without the emergence of additional strange particles in the final state.

Investigation of the features of ϕ production can be of use for obtaining deeper insight into the mechanisms of the production of heavier vector mesons featuring hidden flavors (J/ψ and Υ) and for determining those regularities in hadron processes that are associated with the flavors of the quarks entering into the hadron involved.

In this article, we present the results obtained by studying the associated production of ϕ mesons with Λ^0 hyperons in neutron–carbon interactions detected at neutron energies in the range 20–70 GeV by the EXCHARM spectrometer. Events of the associated production ϕ mesons with Λ^0 hyperons were selected among about 172×10^6 original neutron–carbon interactions recorded by the spectrometer in one of the exposures of the EXCHARM facility.

2. EXCHARM EXPERIMENT

The EXCHARM spectrometer is situated in the 5N neutron channel of the U-70 Serpukhov accelerator. A beam of neutrons is produced upon the interaction of 70-GeV protons circulating in the accelerator ring with the internal beryllium target and is formed by a system of collimators arranged along the axis

[†]Deceased.
[1)]High Energy Physics Institute, Universitetskaya ul. 9, Tbilisi State University, GE-380086 Tbilisi, Republic of Georgia.
[2)]Moscow State Engineering Physics Institute (Technical University), Kashirskoe sh. 31, Moscow, 115409 Russia.
[3)]Institute for Nuclear Research and Nuclear Energy, Blvd. Tsarigradsko chausse 72, BG-1784 Sofia, Bulgaria.
[4)]Institute of Physics, Georgian Academy of Sciences, ul. Tamarashvili 6, GE-380077 Tbilisi, Republic of Georgia.
[5)]Institute for Physics and Technology, Kazakh Academy of Sciences, Almaty, Republic of Kazakhstan.
[6)]Institute of Atomic Physics, R-76900 Bucharest-Magurele, Romania.
[*]e-mail: natalia.molokanova@jinr.ru

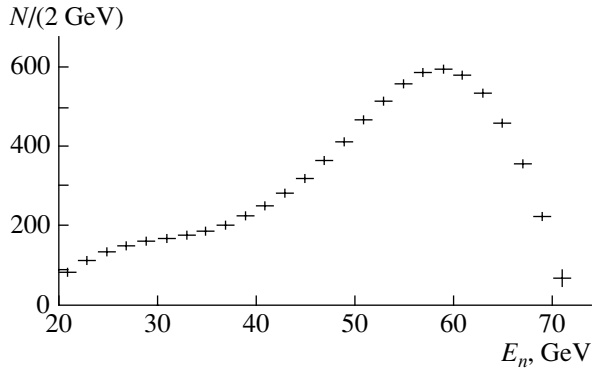

Fig. 1. Energy spectrum of beam neutrons. Here and in the figures that follow, N is the number of combinations.

that is nearly parallel to the momentum of incident protons. Figure 1 shows the energy spectrum of beam neutrons that was obtained in [2] by measuring neutron energies with the aid of the hadronic calorimeter entering into the composition of the spectrometer. The energy spectrum of the beam has a maximum in the vicinity of 58 GeV and a width of about 12 GeV.

In order to reduce the admixture of photons, a lead filter of variable thickness (from 0 to 20 cm, depending on the position along the beam) was installed in a beam. The admixture of charged particles was removed by the deflecting magnets of the accelerator and the SP-129 magnet, which was arranged in the nose part of the experimental zone.

The intensity of the beam during an accelerator spill was about 6×10^6 neutrons per 5×10^{11} protons dumped onto the internal target.

The arrangement of basic units of the operating EXCHARM spectrometer is displayed in Fig. 2. The spectrometer includes the following elements:

(i) a carbon target T of thickness 1.3 g/cm^2 along the beam,

(ii) an analyzing magnet SP-40A having an aperture of 274×49 cm^2 and generating a magnetic field of maximum strength 0.79 T (the system of the magnet power supply provides the possibility of a fast reversal of its polarity);

(iii) a system of 11 multiwire proportional chambers PC [3, 4] (25 signal planes) positioned upstream (PC 1–8) and downstream (PC A–C) of the magnet (the maximum dimensions of the chambers were 100×60 cm^2 upstream and 200×100 cm^2 downstream of the magnet);

(iv) hodoscopes H1 and H2 of scintillation counters (these hodoscopes are used to develop a signal triggering the facility);

(v) neutron-beam monitor Mn;

(vi) a hadronic calorimeter HC, which is used to measure the energy spectrum of beam neutrons;

(vii) a 14-channel (MTGCC-14) and a 32-channel (MTGCC-32) threshold gas Cherenkov counter [5, 6], which are used to identify charged particles.

The MTGCC-14 and MTGCC-32 counters are filled with, respectively, Freon-12 and air at atmospheric pressure. The calculated thresholds for charged-particle detection are given in Table 1.

Table 1. Thresholds for charged-particle detection

Counter	Gas	Detection thresholds, GeV/c			
		μ	π	K	p
MTGCC-14	Freon-12	2.3	3.1	10.8	20.5
MTGCC-32	Air	4.5	6.0	21.2	40.3

The spectrometer is described in terms of a right-hand coordinate frame specified in such a way that its z and y axes are directed, respectively, along the neutron-beam axis and upward along the main component of the magnetic field, the origin of coordinates being coincident with the center of the SP-40A magnet.

The facility is triggered by pulses formed by a majority scheme of coincidence from two hodoscopic planes of proportional chambers upstream of the magnet, one such plane downstream of the magnet, and two hodoscopes of scintillation counters. The system of triggering the spectrometer requires that not less than four charged particles traverse the main units of the facility.

The EXCHARM spectrometer is described in greater detail elsewhere [7].

Associated $\phi\Lambda^0$ production was investigated by two independent methods. In calculating the cross section for associated $\phi\Lambda^0$ production, different models of the production of this pair of particles were used within these two methods.

3. EVENT SELECTION

Events involving the associated production of ϕ mesons and Λ^0 hyperons were selected in the reaction

$$n + N \longrightarrow \phi + \Lambda^0 + X. \qquad (1)$$

We identified Λ^0 hyperons by their decays to a proton and a pion:

$$\Lambda^0 \longrightarrow p\pi^-. \qquad (2)$$

Neutral-vee (V^0) topology corresponds to the decay process in (2). For V^0, we took a pair of unlikely charged particles whose trajectories were spaced by a distance not less than 0.5 cm, this corresponding to

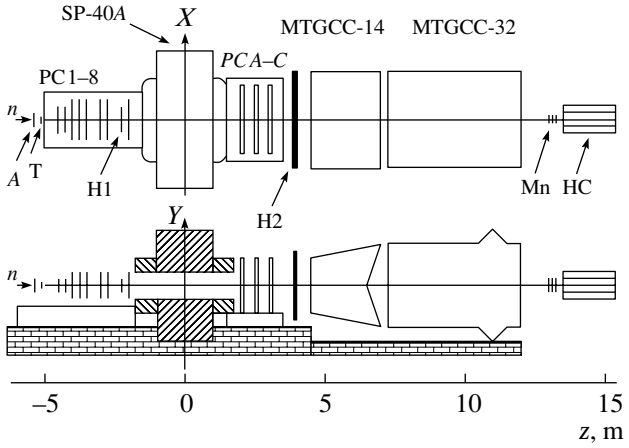

Fig. 2. Layout of the EXCHARM spectrometer.

the tripled experimental resolution in this parameter. In addition, it was required that the decay vertex occur within the decay volume beginning at a distance of 10 cm from the target edge along the z axis. This made it possible to suppress a major part of the background from interactions within the target. As a result, we selected V^0 vees that were identified with K^0, Λ^0, and $\bar{\Lambda}^0$ strange particles. For a V^0 vee corresponding to Λ^0, the effective mass of the $p\pi^-$ system was required to be within $\pm$ 4.5 MeV/c^2 around the tabular value of the Λ^0 mass, this approximately corresponding to the tripled value of the experimental resolution in this quantity (about 1.5 MeV/c^2).

In order to separate ϕ mesons, we considered their decay to two charged kaons:

$$\phi \longrightarrow K^+K^-. \tag{3}$$

In order to reduce the background from misidentified kaons in the final state being investigated, we employed information from MTGCC-14 and MTGCC-32. For each charged particle, we calculated the relative probabilities of its identification as a specific hadron (so-called weight), $W(i)$, where $i = \pi^\pm$, $K^\pm$, or $p/\bar{p}$. For this, the recorded pulses from both Cherenkov counters were compared with their computed counterparts that were obtained under the assumption that the charged particles in question correspond to the above presumed types. The values found for $W(i)$ are normalized in such a way that, for each charged particle, we have

$$W(\pi^\pm) + W(K^\pm) + W(p/\bar{p}) = 3.$$

The value of $W(i) = 3$ then implies a 100% identification of a particle with the type i, while the value of $W(i) = 1$ corresponds to a complete indeterminacy in the type of particle. The cuts on the Cherenkov weights $W(K^\pm)$ in the selection procedure were specified on the basis of the following requirements: on one hand, it was necessary to achieve a maximum suppression of the background from misidentified particles; on the other hand, it was desirable to minimize losses of combinations involving K^+K^-.

As a criterion for identifying $K^\pm$ in the final states of ϕ-meson decay, we choose the condition

$$W(K^\pm) \geq 1.3, \tag{4}$$

in which case the number of background combinations decreases by about 90%, while the losses of the signal do not exceed 10%.

In order to select events of the reaction in (1), we have also imposed the following constraints:

(i) The minimum distance between the reconstructed trajectories of ϕ and Λ^0 particles must not exceed 0.5 cm.

(ii) In the event being considered, the vertex composed of the reconstructed ϕ and Λ^0 particles must be within $\pm$5 cm from the target surface along the beam axis (the spectrometer resolution in the coordinate z is about 1 cm).

Figures 3*a* and 3*b* show, respectively, the $M(K^+K^-)$ and the $M(p\pi^-)$ distribution for events selected with allowance for the cuts listed above. The presence of a clear-cut structure in each of the distributions makes it possible to study their features.

4. BASIC FEATURES OF THE SIGNALS BEING STUDIED

The parameters of the structure in the $M(K^+K^-)$ spectrum were determined by means of approximating this spectrum by a superposition of the convolution of a Breit–Wigner (BW) function with a Gaussian (G) resolution function and a function that

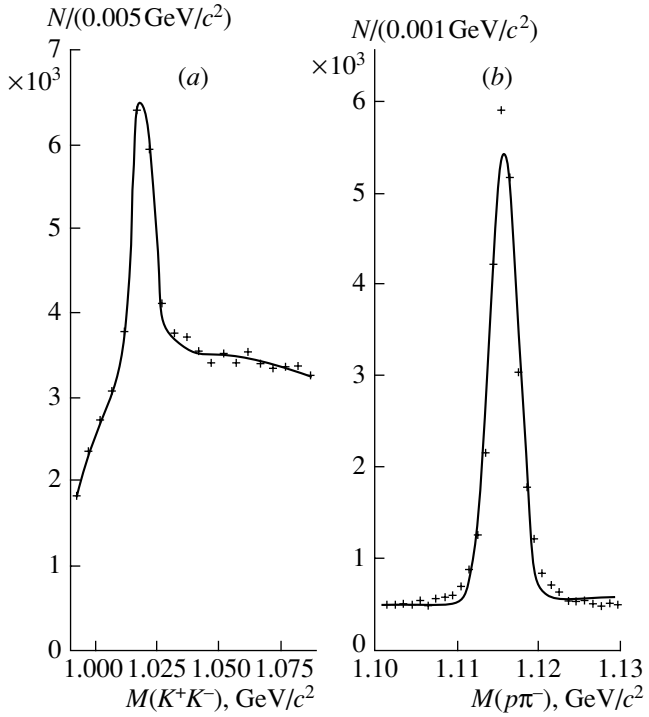

Fig. 3. Effective-mass spectra of the (*a*) K^+K^- and (*b*) $p\pi^-$ systems. The curves represent fits to these spectra.

describes the background (BG). This superposition can be taken in the form

$$F(M) = \widetilde{BW}(M) + BG(M), \qquad (5)$$

where

$$\widetilde{BW}(M) = \int BW(m)G(m-M)dm. \qquad (6)$$

The Breit–Wigner and Gaussian functions were parametrized as

$$BW(m) = \frac{1}{\pi}\frac{mM_0\Gamma}{(m^2-M_0^2)^2+M_0^2\Gamma^2}, \qquad (7)$$

$$G(m) = \frac{1}{\sqrt{2\pi\delta^2}}\exp\left(-\frac{m^2}{2\delta^2}\right), \qquad (8)$$

where Γ is the width of a structure, M_0 is the mean value of the effective mass $M(K^+K^-)$ for this structure, and δ is the mass resolution of the spectrometer in the ϕ-meson region (its value obtained by the Monte Carlo method is 1.7 ± 0.3 MeV/c^2).

The background was approximated by the function

$$BG(m) = A + B\sqrt{(m^2-M_{\text{th}}^2)} + Cm, \qquad (9)$$
$$m > M_{\text{th}},$$

where $M_{\text{th}} = M(K^+) + M(K^-)$ and A, B, and C are free parameters.

The solid curve in Fig. 3*a* represents the result obtained by approximating the spectrum of the effective masses $M(K^+K^-)$ by the function in (5). The background function describes well the $M(K^+K^-)$ spectra off the region of the structure.

This approximation made it possible to determine the features of the structure. The measured values of the ϕ-meson mass and width are given in Table 2.

The effective-mass spectrum of the $p\pi^-$ system is displayed in Fig. 3*b*. In the region around the tabular value of the Λ^0-hyperon mass, there is a structure, which was approximated by a Gaussian function, the background being approximated by a linear function. As a result, we determined the Λ^0 mass (Table 2).

Within the errors, the resulting features of ϕ and Λ^0 agree well with their counterparts in the Particle Data Group tables [8].

5. ESTIMATING THE NUMBER OF EVENTS OF THE ASSOCIATED PRODUCTION OF ϕ AND Λ^0 PARTICLES

We have considered the two-dimensional effective-mass distribution of K^+K^- and $p\pi^-$ combinations (Fig. 4).

The number of events involving the associated production of ϕ and Λ^0 particles was estimated by two methods:

Table 2. Features of the ϕ meson and Λ hyperon (in MeV/c^2)

	$M(\phi)$	$\Gamma(\phi)$	$M(\Lambda^0)$
Our study	1019.6 ± 0.9	4.4 ± 0.3	1115.8 ± 0.2
Particle Data Group [8]	1019.456 ± 0.020	4.26 ± 0.05	1115.683 ± 0.006

(i) The number of combinations in the structure generated by a ϕ meson (N_ϕ) was calculated in successive intervals of the effective mass $M(p\pi^-)$ with a step of 2 MeV/c^2, and the one-dimensional distribution of the $M(p\pi^-)$ dependence of N_ϕ was constructed on this basis. The latter made it possible to estimate the number of ϕ and Λ^0 particles emerging from their associated production.

(ii) The number of combinations in the structure associated with a Λ^0 hyperon (N_Λ) was calculated for successive intervals of the effective mass $M(K^+K^-)$ with a step of 4 MeV/c^2, and the total number of events featuring ϕ and Λ^0 was determined thereupon.

Figure 5*a* displays the number N_ϕ of combinations as a function of the effective mass $M(p\pi^-)$. The approximation of this dependence by a superposition of a Gaussian function and a linear function (solid curve in the figure) made it possible to calculate the structure associated with $\phi\Lambda^0$ (dashed curve); it involved 2885 ± 208 $\phi\Lambda^0$ events.

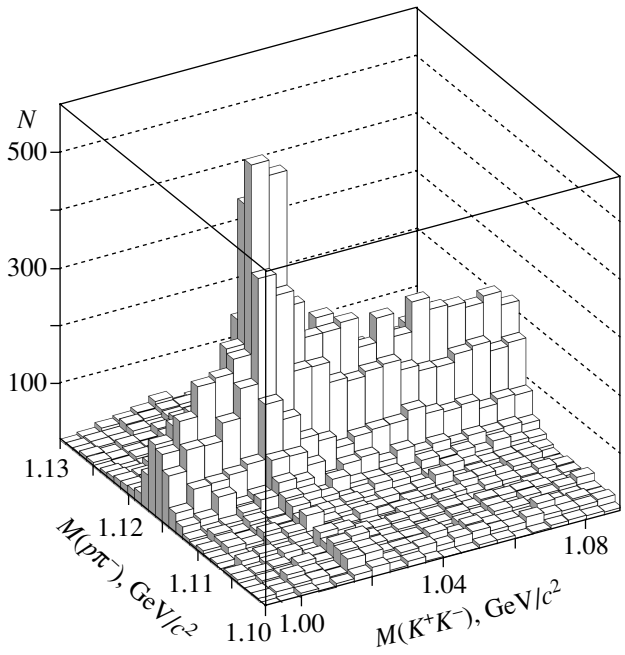

Fig. 4. Distribution of the effective mass $M(K^+K^-)$ versus the effective mass $M(p\pi^-)$.

Figure 5*b* shows the number N_Λ of combinations as a function of the effective mass $M(K^+K^-)$. The approximation of this dependence by the function in (5) (solid curve) made it possible to evaluate the structure associated with $\phi\Lambda^0$ (dashed curve), and it proved to involve 2818 ± 160 $\phi\Lambda^0$ events.

The results obtained by calculating the numbers of combinations by the above two methods agree within the errors.

The $M(p\pi^-)$ distributions have a symmetric shape and involve a smooth modest background, while the M (K^+K^-) distributions look like a complicated superposition of functions describing a structure against a heavy background [a superposition of the form in (5)]. Therefore, it is preferable to begin determining the parameters of the structure due to associated production by deriving the number of combinations in the structure generated by Λ^0 (N_Λ) in

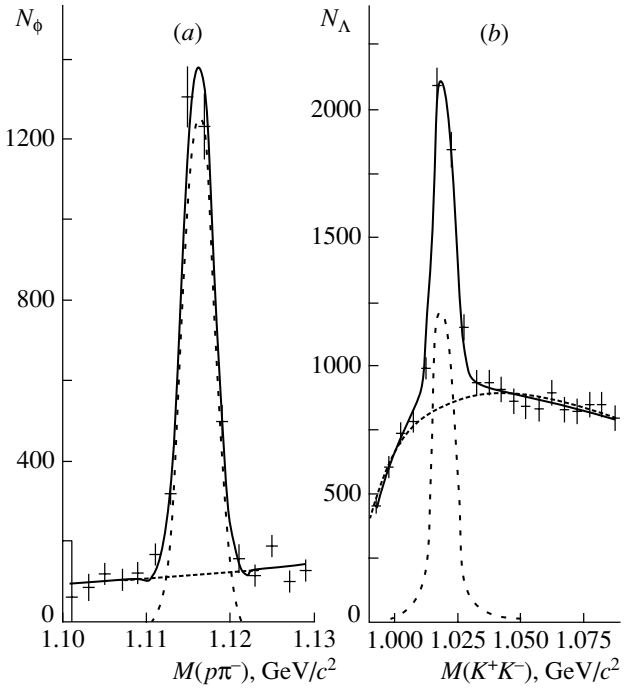

Fig. 5. (*a*) Number of ϕ mesons in various intervals of the effective mass M $(p\pi^-)$ and (*b*) number of Λ^0 hyperons in various intervals of the effective mass $M(K^+K^-)$: (solid curves) results of fitting, (dashed curves) structures, and (dotted curves) background.

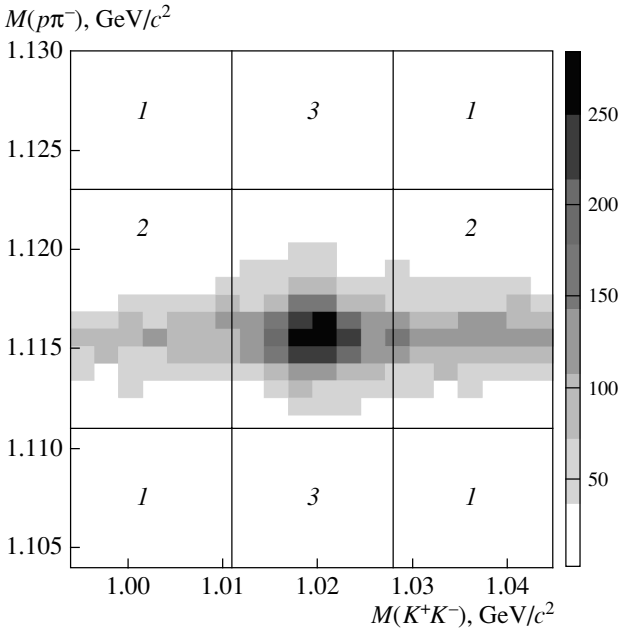

Fig. 6. Distribution of the effective mass $M(p\pi^-)$ versus the effective mass $M(K^+K^-)$. The notation for the regions is explained in the main body of the text.

various intervals of the effective mass $M(K^+K^-)$—that is, to employ the second method for determining the number of combinations, since, even in the case of scarce statistics in these intervals, the spectra in question can be correctly approximated by a superposition of a Gaussian function and a linear function.

Thus, the number of events in which $\phi\Lambda^0$ pairs originate from associated production is 2818 ± 160. In the region of the structure, the combinatorial background is small.

6. ANALYSIS OF MOMENTUM SPECTRA AND OF DISTRIBUTIONS WITH RESPECT TO THE MULTIPLICITY OF TRACKS IN EVENTS

In order to subtract the background in the spectra corresponding to associated $\phi\Lambda^0$ production, we analyzed respective combinations in eight two-dimensional mass regions situated around the structure and displayed in Fig. 6. We considered three sources of the background:

(*1*) noncorrelated background (F_0) from events where K^+K^- and $p\pi^-$ pairs do not originate from, respectively, ϕ-meson and Λ^0-hyperon decay (it is determined by averaging the numbers of combinations in four intervals off the region of the ϕ-meson and Λ^0-hyperon masses);

(*2*) correlated background (F_1) from events of Λ^0-hyperon production accompanied by random K^+K^- pairs [it is determined as the averaged number of combinations in two regions around the Λ^0 mass and off the region of the ϕ mass (the number of combinations in these mass intervals corresponds to $F_0 + F_1$)];

(*3*) correlated background (F_2) from events of ϕ-meson production accompanied by random $p\pi^-$ pairs that are not products of Λ^0 decay [it is determined as the result of averaging the number of combinations in two intervals off the region of the Λ^0-hyperon mass and in the region of the ϕ-meson mass (the number of combinations in these mass intervals corresponds to $F_0 + F_2$)].

Each two-dimensional mass region around the structure in the distribution of the effective mass $M(p\pi^-)$ versus the effective mass $M(K^+K^-)$ is labeled in Fig. 6 with a figure corresponding to the aforementioned sources of the background.

Upon subtracting the background ($F_0 + F_1 + F_2$), we obtained the longitudinal-momentum (P_l) and transverse-momentum (P_t^2) spectra of ϕ and Λ^0 particles from associated production (histograms in Fig. 7) and the distribution of events with respect to the multiplicity of charged particles (histogram in Fig. 8).

7. DETERMINING THE EFFICIENCY OF THE DETECTION OF ASSOCIATED $\phi\Lambda^0$ PRODUCTION

In order to calculate the efficiency of the detection of $\phi\Lambda^0$ production, we performed a simulation by two methods, on the basis of a corrected FRITIOF generator and on the basis of the so-called compound-particle model, which considers a two-body decay of a variable-particle mass and employs a parametrization of the differential cross section for its production with respect to the Feynman variable x_F and the square of the transverse momentum, (P_t^2).

7.1. Corrected FRITIOF Model

In simulating the reaction

$$n + N \longrightarrow \phi + \Lambda^0 + X,$$

we first employed the FRITIOF generator [9], whereupon, in accordance with experimental distributions, we corrected the momentum spectra of ϕ and Λ^0 particles from the associated-production process by assigning, to the events being studied, a weight function depending on the momenta of the particles in question. Specifically, the weight function (WF) was taken in the form

$$WF = (1 - |x_\mathrm{F}|)^k \exp(-bP_t^2)Pn, \qquad (10)$$

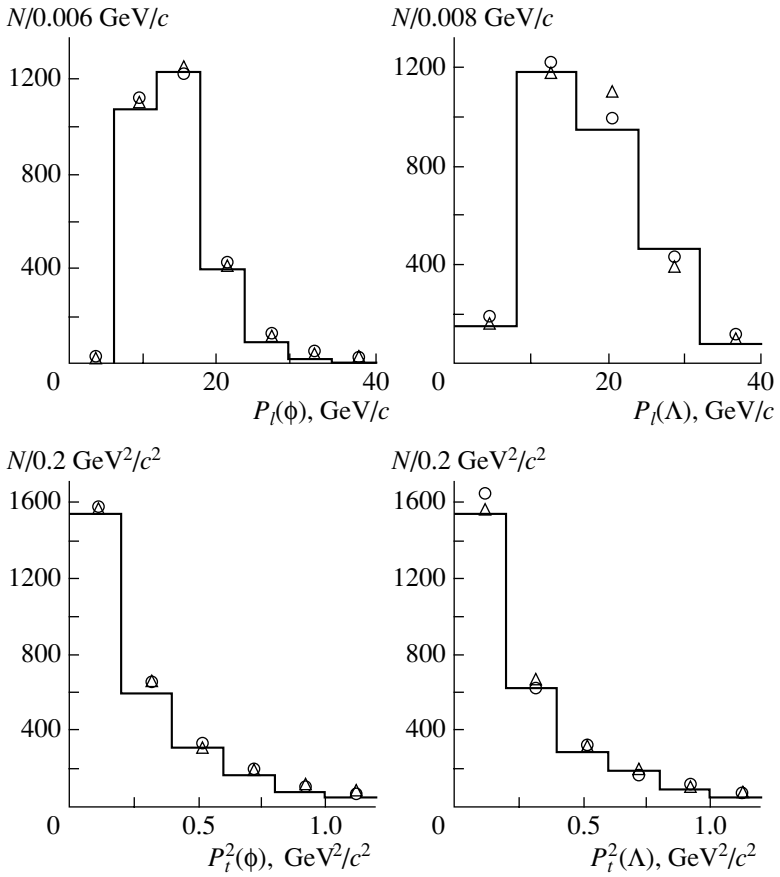

Fig. 7. Momentum spectra of ϕ and Λ^0 from associated production. Here and in the figures that follow, histograms represent experimental data, while open circles and open triangles correspond to the FRITIOF and compound-particle models, respectively.

where k and b are free parameters and Pn is a function that depends on the beam-neutron momentum $P_l(n)$ and on the momentum P_l of the corresponding particle.

We used the values of $k = 3.25$, $b = -0.41$, and $Pn = 1$ for the ϕ meson and the values of $k = 1.00$, $b = -1.08$, and $Pn = 3.35 - 17.64p + 41.59p^2 - 33.28p^3$ with $p = P_l(\Lambda^0)/P_l(n)$ for the Λ^0 hyperon.

As a result, we attained (see Figs. 7, 8) good agreement between the experimental and simulated results for the longitudinal- and transverse-momentum (P_l and P_t^2, respectively) spectra of $\phi\Lambda^0$ pairs from the associated-production process and for the spectra of charged-particle multiplicity (N_{trk}). The simulated spectra were normalized to the number of experimental events.

7.2. Compound-Particle Model

Within this model, it was assumed that ϕ and Λ^0 particles are generated via the process in which the production of a compound particle B of variable invariant mass,

$$n + N \longrightarrow B + K^0 + N + X, \qquad (11)$$

is followed by its decay

$$B \longrightarrow \phi + \Lambda^0. \qquad (12)$$

In (11), X stands for additional particles whose production was simulated within the JETSET model [10].

At the first step, the momentum of the B particle was generated in the reference frame comoving with the center of mass of the incident neutron and a target nucleon (a proton or a neutron with an identical probability), the constraints imposed by conservation laws being taken into account. The differential cross section for B production was parametrized in the form

$$\frac{d^2\sigma}{dx_{\text{F}}dP_t^2} \propto (1 - |x_{\text{F}}|)^k \exp(-bP_t^2), \qquad (13)$$

where k and b are free parameters of the model (see [11]) that characterize the production of the corresponding particle. For the reaction in (11), we

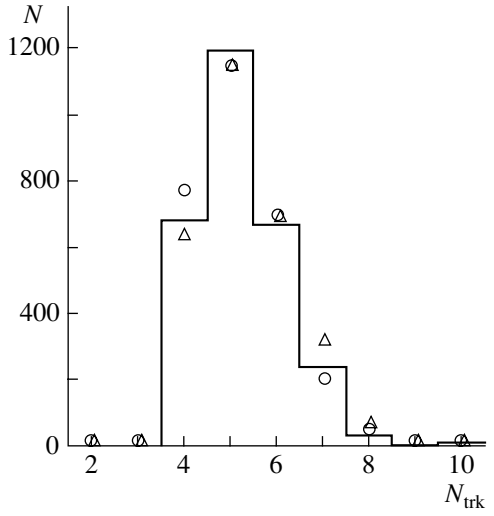

Fig. 8. Distribution with respect to the multiplicity N_{trk} of charged particles. In our experiment, the mean value $\langle N_{trk}\rangle$ was 5.211 (the root-mean-square deviation was RMS = 0.969); the respective results of the simulations were $\langle N_{trk}\rangle = 5.154$ (RMS = 0.949) within the corrected FRITIOF model and $\langle N_{trk}\rangle = 5.296$ (RMS = 0.998) within the compound-particle model.

selected the following values for the parameters of compound-particle production: $k = 2.3$ and $b = 2.0$.

Further, we corrected the momentum spectra of B, ϕ, and Λ^0 particles and the spectrum of the effective masses $M(B)$ in accordance with the experimental distributions by selecting probabilities for the rejection of simulated events. In doing this, we minimized the χ^2 functional by fitting each simulated distribution to its experimental counterpart.

In Fig. 7, the simulated spectra of longitudinal momenta (P_l) and the squares of transverse momenta (P_t^2) of ϕ and Λ^0 particles from the associated-production process are contrasted against their experimental counterparts. The spectra of the longitudinal and transverse momenta of a compound particle are displayed in Fig. 9, along with the spectrum of the effective masses $M(K^+K^-p\pi^-)$. The simulated spectra were normalized to the number of experimental events. Good agreement between the experimental and simulated spectra was attained. In order to improve the agreement for the distribution of events with respect to the multiplicity of charged particles, we fitted the probabilities for the rejection of simulated events, and this made it possible to match the mean values of the experimental and simulated multiplicities of charged particles (Fig. 8).

Table 3. Detection efficiencies

	ϵ, %
Corrected FRITIOF Model	0.097 ± 0.002(stat.) ± 0.010(syst.)
Compound-particle model	0.100 ± 0.004(stat.) ± 0.020(syst.)

7.3. Calculation of the Efficiency of the Detection of $\phi\Lambda^0$

In order to determine the cross section for the inclusive production of particle pairs under study, we have calculated the efficiency of their detection, ϵ.

In employing the corrected FRITIOF model, the systematic error in the detection efficiency was determined by varying the probabilities for the rejection of simulated events. They were varied in such a way that, in comparing the experimental and simulated distributions, χ^2 changed by not more than the value of 1.07, which was determined by a 70% confidence level [12]. This led to variations of 10% in the detection efficiency.

In employing the compound-particle model, the main contribution to the systematic error came from the sensitivity of the result to the multiplicity of charged particles in events. From an additional analysis that made it possible to attain good agreement between the experimental and simulated multiplicities of charged particles (see Subsection 7.2), we found a change of 19% in the detection efficiency.

For both models, the values obtained for the efficiency of the detection of $\phi\Lambda^0$ pairs with allowance for the aforesaid are given in Table 3.

The good agreement of independent results emphasizes their stability to the criteria used in the analysis. For the ultimate value of the cross section for inclusive $\phi\Lambda^0$ production, we took the result obtained by using the corrected FRITIOF model, since, in this model, better agreement between the experimental and simulated results was attained for the momentum spectra and for the multiplicity distribution of charged particles. The distinction between the detection-efficiency values obtained within the different models was taken into account in the systematic error in the final result. Ultimately, the efficiency of the detection of $\phi\Lambda^0$ pairs was

$$\epsilon = (0.097 \pm 0.002(\text{stat.}) \pm 0.010(\text{syst.}))\%.$$

8. DETERMINATION OF THE DIFFERENTIAL CROSS SECTION FOR INCLUSIVE ASSOCIATED $\phi\Lambda^0$ PRODUCTION

The differential cross section for inclusive associated $\phi\Lambda^0$ production was calculated by the formula

$$\sigma = \frac{NA}{MnTN_A\epsilon \mathrm{Br}_1\mathrm{Br}_2}, \qquad (14)$$

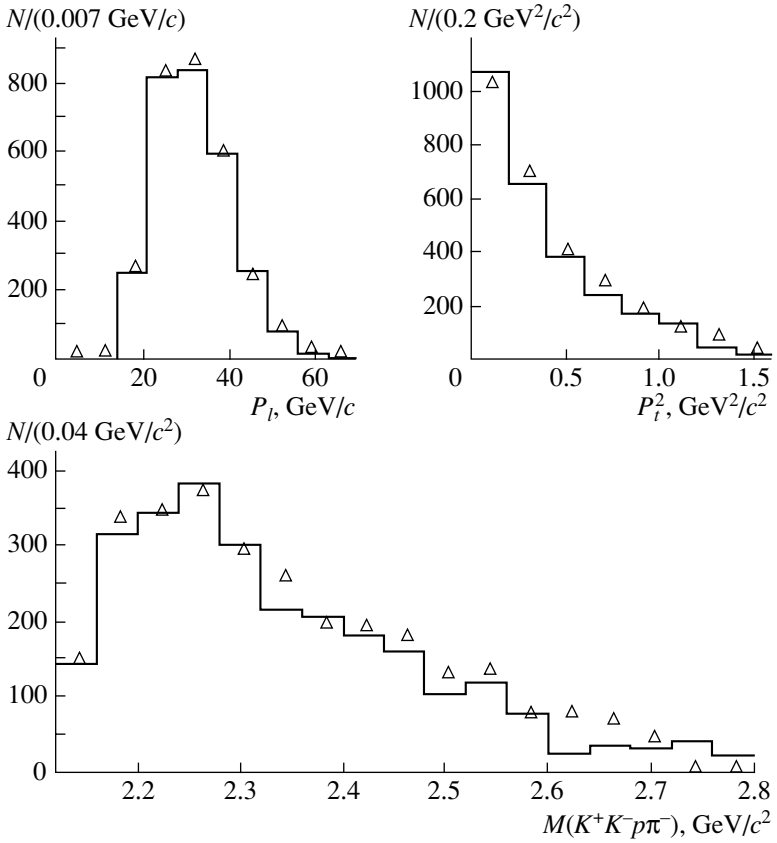

Fig. 9. Results obtained within the compound-particle model. Presented in the figure are the spectra of longitudinal and transverse momenta of a compound particle, as well as the spectrum of the effective masses $M(K^+K^-p\pi^-)$.

where $N = 2818 \pm 160$ is the number of events of associated $\phi\Lambda^0$ production, $A = 12.011$ is the atomic weight of the target nucleus, $Mn = (2.311 \pm 0.084) \times 10^{11}$ is the number of neutrons that traversed the target over the exposure time, $T = 1.3$ g/cm^2 is the target thickness, N_A is Avogadro's number, ϵ is the detection efficiency, $\mathrm{Br}_1 = (49.1 \pm 0.8)\%$ is the branching fraction of the decay $\phi \longrightarrow K^+K^-$, and $\mathrm{Br}_2 = (63.9 \pm 0.5)\%$ is the branching fraction of the decay $\Lambda^0 \longrightarrow p\pi^-$.

The statistical error in the cross section was determined from the error in the result calculated in Section 5 for the number of events of associated $\phi\Lambda^0$ production.

The systematic error in determining the cross section receives contributions from the error in the efficiency of the detection of ϕ and Λ^0 particles emerging from the associated-production process, the error in determining the number of neutrons that traversed the whole facility over the exposure time, and the uncertainty in the measured branching fractions of the decays $\phi \to K^+K^-$ and $\Lambda^0 \to p\pi^-$.

Upon substituting all relevant quantities into (14) and taking into account the aforementioned uncertainties, we eventually obtained

$$\sigma(\phi\Lambda^0 X) = 614 \pm 35(\mathrm{stat.}) \pm 67(\mathrm{syst.})\ \mu\mathrm{b/nucleus}. \quad (15)$$

9. CONCLUSION

By studying in detail associated $\phi\Lambda^0$ production in neutron–carbon interactions with the aid of the EXCHARM facility at the Serpukhov accelerator, we have determined the cross section for inclusive associated $\phi\Lambda^0$ production to the highest precision at present:

$$\sigma(\phi\Lambda^0 X) = 614 \pm 35(\mathrm{stat.}) \pm 67(\mathrm{syst.})\ \mu\mathrm{b/nucleus}.$$

The only estimate of the inclusive cross section for associated $\phi\Lambda^0$ production in hadron interactions was obtained in the BIS-2 experiment [13], which was performed at the Serpukhov accelerator. The contribution of associated $\phi\Lambda^0$ production in neutron–proton interactions at neutron-beam energies in the range 30–70 GeV to the inclusive cross section for ϕ-meson production was $(20 \pm 4)\%$. By using the value presented in [13] for the cross section characterizing

inclusive ϕ production and assuming its linear dependence on the atomic number of the target, we can estimate the cross section for associated $\phi\Lambda^0$ production at 528 ± 216 μb/nucleus. Within the errors, the result of our present study agrees with the value extracted from the BIS-2 data reported in [13], but the former has a much higher accuracy.

ACKNOWLEDGMENTS

This work was performed at the Laboratory of Particle Physics at the Joint Institute for Nuclear Research (Dubna) and was supported by the Russian Foundation for Basic Research (project no. 03-07-90385).

REFERENCES

1. S. Okubo, Phys. Lett. **5**, 165 (1963); G. Zweig, CERN TH-412 (1964); J. Iizuka, Prog. Theor. Phys. Suppl. **37–38**, 21 (1996).
2. A. N. Aleev *et al.,* Preprint No. R13-94-312, OIYaI (Joint Inst. Nucl. Res., Dubna, 1994).
3. A. N. Aleev *et al.,* Prib. Tekh. Éksp., No. 4, 8 (1995).
4. G. Aĭkhner *et al.,* Preprint No. 1-80-644, OIYaI (Joint Inst. Nucl. Res., Dubna, 1980); G. Aĭkhner *et al.,* Prib. Tekh. Éksp., No. 3, 40 (1982); A. N. Aleev *et al.,* Prib. Tekh. Éksp., No. 1, 50, (1991).
5. M. N. Voĭchishin *et al.,* Prib. Tekh. Éksp., No. 3, 71 (1985).
6. A. N. Aleev *et al.,* Preprint No. R13-94-520, OIYaI (Joint Inst. Nucl. Res., Dubna, 1994).
7. A. N. Aleev *et al.*, Instrum. Exp. Tech. **42**, 481 (1999).
8. K. Hagiwara *et al.* (PDG), Phys. Rev. D **66**, 010001 (2002); http://pdg.lbl.gov.
9. Hong Pi, Comput. Phys. Commun. **71**, 173 (1992).
10. T. Sjostrand, Comput. Phys. Commun. **82**, 74 (1994).
11. A. B. Kaidalov and O. I. Piskunova, Z. Phys. C **30**, 145 (1986).
12. *MINUIT, Reference Manual,* Version 94.1, CERN Preprint (1994).
13. A. N. Aleev *et al.*, Preprint No. E1-90-316, JINR (Joint Inst. Nucl. Res., Dubna, 1990).

Translated by A. Isaakyan

Physics of Atomic Nuclei, Vol. 67, No. 8, 2004, pp. 1523–1528. Translated from Yadernaya Fizika, Vol. 67, No. 8, 2004, pp. 1546–1551.

ELEMENTARY PARTICLES AND FIELDS
Experiment

Two-Proton Correlations in ^{4}Hep Interactions at a Primary Momentum of 5 GeV/c

A. V. Blinov*, V. F. Turov, and M. V. Chadeyeva*****

Institute of Theoretical and Experimental Physics, Bol'shaya Cheremushkinskaya ul., Moscow, 117259 Russia

Received June 18, 2003; in final form, September 8, 2003

Abstract—Correlations of secondary protons in ^{4}Hep interactions are investigated in an exclusive experiment with the aid of a 2-m liquid-hydrogen bubble chamber exposed to an alpha-particle beam of momentum 5 GeV/c (the kinetic energy of primary protons in the rest frame of the nucleus is T_p = 620 MeV). By using data obtained in 4π geometry for six basic channels of ^{4}Hep interaction that lead to the production of two protons, the total correlation function for the pp system is determined, along with two-proton correlation functions for individual channels. Experimental results are compared with the predictions of the modified Lednicky–Lyuboshitz model. The value of $R = 1.6 \pm 0.3$ fm is obtained for the root-mean-square spacetime radius of pp emission in ^{4}Hep interactions. The dependence of the correlation function on the total momentum of two emitted protons and on the momentum-transfer direction is investigated.

1. INTRODUCTION

In contemporary nuclear physics, two-particle interferometry based on an analysis of the correlation function for two emitted identical particles of momenta $\mathbf{p}_1$ and $\mathbf{p}_2$,

$$C(\mathbf{p}_1, \mathbf{p}_2) = \frac{d^2N/d\mathbf{p}_1 d\mathbf{p}_2}{(dN/d\mathbf{p}_1)(dN/d\mathbf{p}_2)}, \qquad (1)$$

where $dN/d\mathbf{p}_{1(2)}$ and $d^2N/d\mathbf{p}_1 d\mathbf{p}_2$ are, respectively, the inclusive single- and the two-particle distribution of emitted particles, is an efficient tool for determining the spacetime size of the particle-emission region in nuclear reactions [1–9]. Data on nuclear reactions involving ^{4}He, which is the most compact nucleus, are of particular interest from the point of view of studying the above correlations. However, there are virtually no such data in the literature. We are aware only of the study reported in [4], where, on the basis of experimental data obtained by exposing, to an alpha-particle beam of momentum taking values of 8.6 and 13.6 GeV/c, a 1-m liquid-hydrogen bubble chamber installed at the Joint Institute for Nuclear Research (JINR, Dubna), the authors determined the correlation functions for two protons and the spacetime dimensions of the region of their emission in ^{4}Hep interactions,

$$^4\mathrm{He}p \to (pp)X, \qquad (2)$$

where X is the system comprising secondary particles and nuclear fragments.

In the present study, a similar experimental scheme (where a liquid-hydrogen bubble chamber is exposed to ^{4}He nuclei) is employed to examine two-proton correlations in reaction (2) at a momentum of 5 GeV/c (the kinetic energy of primary protons in the rest frame of the nucleus is T_p = 620 MeV). It should be noted that, at this primary momentum, secondary protons and pions can be identified almost over the entire phase space.

In correlation experiments, the quantity C in the form (1) usually cannot be studied as a function of all six variables $(\mathbf{p}_1, \mathbf{p}_2)$ because of insufficient statistics. In the present experiment, the two-proton correlation function C_{pp} is determined in a standard way as a function of the modulus of half the difference of the proton momenta in the rest frame of the pair, $q_{\mathrm{inv}} \equiv k^* = \frac{1}{2}|\mathbf{p}_1^* - \mathbf{p}_2^*|$; that is,

$$C_{pp} = K\frac{N_{\mathrm{c}}}{N_{\mathrm{nc}}}, \qquad (3)$$

where N_{c} and N_{nc} are the numbers of events of reaction (2) that feature a given value of q_{inv} and which correspond to, respectively, the experimentally observed (correlated) and the background (uncorrelated) distribution, the latter being generated by

*e-mail: blinov@itep.ru
**e-mail: turov@itep.ru
***e-mail: marina.chadeyeva@itep.ru

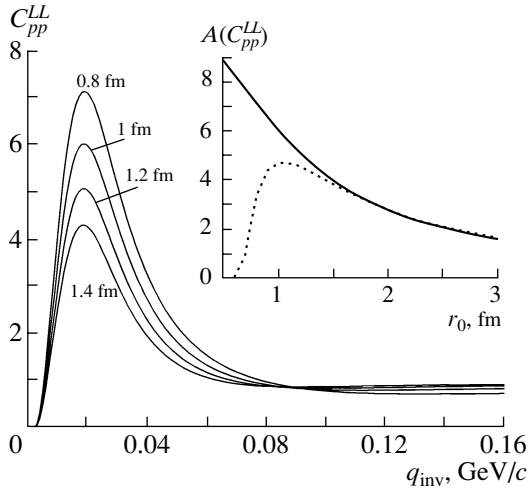

Fig. 1. Two-proton correlation function $C_{pp}^{LL}(q_{\text{inv}})$ calculated within the theoretical model used here (see main body of the text) for the values of r_0 that are indicated in the figure. The inset shows the correlation-function amplitude $A(C_{pp}^{LL})$ versus r_0 for (solid curve) the model used here and (dotted curve) the "traditional" Lednicki–Lyuboshitz model.

mixing the momenta of protons from different events, and K is a normalization constant defined in such a way that $C_{pp} \to 1$ in the limit of large q_{inv}, for which there are no correlations.

We note that the determination of C_{pp} in the form (3) by the so-called mixing method, which is used in the majority of experimental studies devoted to the subject [4–9], and the determination in the form (1) by the method of inclusive single-particle distributions are equivalent (see, for example, [7]).

It is of great interest to study the correlation function in question versus the momenta of secondary protons. It is well known (see, for example, [6, 8]) that, even for collisions of heavy nuclei, the dependence of the two-proton correlation function on the modulus of the total momentum of the pair in the rest frame of the nucleus, $P_{\text{tot}} = |\mathbf{p}_1 + \mathbf{p}_2|$, is significant. In the case of ^{4}Hep interaction, it is natural to expect the enhancement of this dependence.

It is also of interest to study the behavior of the correlation function versus the direction of the relative momentum $\mathbf{q} = \mathbf{p}_1 - \mathbf{p}_2$ in the pair of emitted protons with respect to the primary-proton momentum $\mathbf{p}_{\text{in}}$ in the rest frame of the nucleus—such data make it possible to obtain information about the shape of the emission region [3].

In correlation experiments employing electronics, where a beam is directed to a target nucleus, there is usually a natural limitation on the magnitude of the momenta of secondaries in the rest frame of the nucleus; that is,

$$p_{\text{lab}} > p_{\text{min}}, \tag{4}$$

where $p_{\text{min}} \sim 0.3$ GeV/c [5]. In the present experiment, where a beam of nuclei bombards a target proton and where the efficiency of the detection of nuclear-fragmentation products (which are slow in the rest frame of the nucleus) is maximal, the P_{tot} dependence of the correlation function can be studied in detail over a broad range of momenta and directions of $\mathbf{q}$. Moreover, there appears a unique possibility for determining the correlation function for so-called evaporated protons, which are characterized by relatively low values of P_{tot}.

2. THEORETICAL MODEL

A theoretical calculation of correlations of two nonrelativistic protons having low relative momenta that takes into account final-state interaction was performed for the first time by Koonin [1], who relied on numerically solving the Schrödinger equation with the Reid nucleon–nucleon potential and the Coulomb potential. In a later study [2], Lednicky and Luboshitz proposed a model that took into account both the Coulomb interaction and an S-wave short-range nuclear interaction and which made it possible to obtain an analytic expression for the two-proton correlation function depending on the spacetime parameters r_0 and τ_0 of the particle-emission region (those authors assumed that nucleon-generation points are independent and that their distribution is of a Gaussian character), the root-mean-square radius of the generation region being $R = \sqrt{3}r_0$. The expressions obtained in [2] enable one, at $r_0 \geq 1.5$ fm, to reproduce the two-proton correlation function adequately without knowing an explicit solution ψ to the Schrödinger equation [$\psi = \exp(-i\mathbf{k}^* \cdot \mathbf{r}) + \phi_{\mathbf{k}^*}(\mathbf{r})$] within the region where nuclear forces are operative. In the region $r_0 \leq 1$ fm (which can play a significant role in the emission of protons in ^{4}Hep interactions), however, some formulas from [2] [in particular, expression (21) there] become inapplicable. In this case, the result is entirely determined by the behavior of the function ϕ in the region of action of the short-range potential and is sensitive to the form of the potential (see [2]). In the present study, we analyze our data on the basis of the simplest modification of the Lednicky–Lyuboshitz model, taking, for ψ, an exact solution to the Schrödinger equation with a potential of the square-well form (the explicit expression for the function ϕ can be found in the Appendix to [2]). We also relied on the usual assumption of equal emission times in the c.m. frame of particles ($\tau_0 = 0$).

Figure 1 displays the two-proton correlation function $C_{pp}^{LL}(q_{\text{inv}})$ calculated on the basis of our theoretical model for various values of r_0. The inset shows the r_0 dependence of the correlation-function amplitude (that is, the maximum value of the correlation function) $A(C_{pp}^{LL})$ for (solid curve) the theoretical model proposed here and (dotted curve) the traditional Lednicky–Lyuboshitz model [2]. It can be seen that, for $r_0 \geq 1.5$ fm, the two curves are nearly coincident, but that, for $r_0 \leq 1$ fm, the results are sizably different. We note that a detailed theoretical analysis of the behavior of the correlation function at small r_0 on the basis of calculations employing realistic nucleon–nucleon potentials would be of great interest, but such an analysis is beyond the scope of our experimental study.

3. DESCRIPTION OF THE EXPERIMENT

The 2-m liquid-hydrogen bubble chamber installed at the Institute of Theoretical and Experimental Physics (ITEP, Moscow) was exposed to a separated beam of ^{4}He nuclei accelerated to a momentum of 5 GeV/c. The chamber was placed in a magnetic field of strength 0.92 T. Background particles in the primary beam (predominantly deuterons) were reliably separated by track ionization. We obtained about 120 000 photographs at a mean load of about five to eight particles per chamber development. In all, we measured 18 736 interactions. The total cross section for ^{4}Hep interaction was determined in a standard way [10] by counting the number of interactions over the chosen volume of the chamber and proved to be 121.5 ± 2.9 mb (the quoted error is purely statistical). The systematic error in the absolute normalization of the cross sections was about 3%. In order to identify particles in αp interactions, we used the standard (for bubble-chamber experiments) procedure of selecting mass hypotheses with allowance for data on the visible ionization of secondary-particle tracks. The procedure adopted in the present experiment and procedure for data processing are described in greater detail elsewhere [10, 11]. We would like to emphasize that our experimental procedure makes it possible to analyze data under conditions of 4π geometry.

At the energy being considered, there are six basic channels of reaction (2), which are listed in the table, along with statistics accumulated for each of them in the present experiment. In the case of the channel $^4\text{He}p \to pppnn(\pi^0)$, which involves the production of three protons, two spectator protons, which are the slowest in the rest frame of the nucleus, were selected for our analysis. For the subsequent correlation analysis, we select events of reaction (2) that satisfy the condition

$$q_{\text{inv}} < q_{\text{max}}, \tag{5}$$

Basic reaction channels involving the production of two protons in ^{4}Hep interaction at a momentum of 5 GeV/c ($T_p = 620$ MeV)

Reaction channel	Number of events	Number of events satisfying the selection $q_{\text{inv}} < 0.4$ GeV/c
$^4\text{He}p \to dppn$	2567	1084
$^4\text{He}p \to pppnn(\pi^0)$	1394	1331
$^4\text{He}p \to tpp$	1952	59
$^4\text{He}p \to ppnnn\pi^+$	79	75
$^4\text{He}p \to dppn\pi^0$	93	87
$^4\text{He}p \to tpp\pi^0$	117	106
$^4\text{He}p \to (pp)X$	6202	2742

where q_{max} is determined by the primary momentum. At the primary momenta used in this study, we set $q_{\text{max}} = 0.4$ GeV/c (the number of events in each channel for this selection is given in the table). These restrictions have no effect on the distribution of N_{c} [see expression (3)] at rather low values of q_{inv}, but they are of importance for correctly taking into account the background of N_{nc} in this kinematical region. In all probability, the significant discrepancies between the theoretical and experimental results at $q_{\text{inv}} = 0$ in [4] are due to incorrectly taking into account the background in this region—more specifically, to including, in the analysis, all possible combinations without selections and cuts.

4. RESULTS AND CONCLUSIONS

4.1. Two-Proton Correlation Functions

Figure 2 shows the two-proton correlation function C_{pp} in ^{4}Hep interactions versus q_{inv}. The closed circles represent the results of an imaginable "electronic" experiment where data for all six basic channels leading to the production of two protons are analyzed, while the open and closed triangles correspond to the results for, respectively, the reaction $^4\text{He}p \to pppnn(\pi^0)$ and the reaction $^4\text{He}p \to dppn$ [the correlation functions were determined by formula (3)].

In determining the spacetime size of the proton-emission region, the data were approximated by a theoretical curve obtained within the modified Lednicky–Lyuboshitz model (see Section 2). In fitting the data, the resolution of the facility used was taken into account with the aid of the expression

$$\tilde{C}_{pp}^{LL}(q_{\text{inv}}) = \frac{1}{(2\pi)^{1/2}} \int \frac{C_{pp}^{LL}(q'_{\text{inv}})}{\sigma(q'_{\text{inv}})} \tag{6}$$

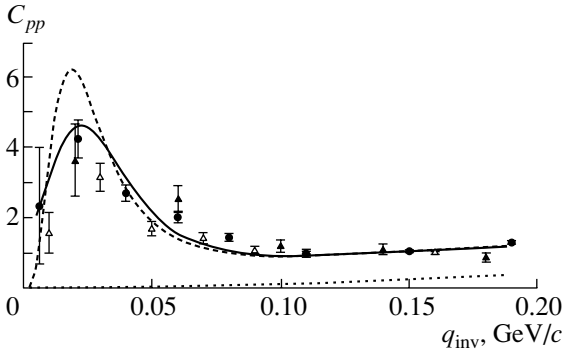

Fig. 2. Two-proton correlation function C_{pp} for ^{4}Hep interaction versus q_{inv}: (closed circles) data on six basic channels leading to the production of two protons; (open triangles) results for the reaction $^4\text{He}p \to pppnn(\pi^0)$; (closed triangles) results for the reaction $^4\text{He}p \to dppn$; (solid and dashed curves) predictions of the modified Lednicky–Lyuboshitz model, respectively, with and without allowance for the errors of the measurements; and (dotted curve) conjectured contribution of the kinematical background.

$$\times \exp\left(-\frac{(q_{\text{inv}} - q'_{\text{inv}})^2}{2\sigma^2(q'_{\text{inv}})}\right) dq'_{\text{inv}},$$

where $\tilde{C}_{pp}^{LL}$ and C_{pp}^{LL} are the model predictions, respectively, with and without allowance for the errors of the measurements, while $\sigma(q_{\text{inv}})$ is the experimental error in determining q_{inv}. In the calculations, we used a linear parametrization of $\sigma(q_{\text{inv}})$ in the form

$$\sigma(q_{\text{inv}}) = 0.01 + 0.032 q_{\text{inv}}\ [\text{GeV}/c]. \qquad (7)$$

For the root-mean-square spacetime radius of pp emission, the best fit of a theoretical curve to the data on all channels for $q_{\text{inv}} < 0.1$ GeV/c yields $R = 1.6 \pm 0.3$ fm. The curves in Fig. 2 represent the predictions of the modified Lednicky–Lyuboshitz model with allowance for the presumed kinematical-background contribution (dotted curve) and correspond to the calculation that either takes into account the errors of the measurements in the form (6) (solid curve) or disregards these errors (dashed curve). The curves in this figure were plotted for the case where the parameter corresponding to the root-mean-square spacetime radius of pp emission is $R = 1.6$ fm. We note that the approximation of the experimental data within the model without taking into account the errors yields a close result, $R = 1.65 \pm 0.4$ fm. For the kinematical-background contribution, we employed the simplest parametrization in the form

$$KB = a q_{\text{inv}}^2, \qquad (8)$$

where the coefficient equal to $a = 10.0 \pm 1.2\,(\text{GeV}/c^2)$ was determined by fitting the quantity $C_{pp} - 1$ (for all channels) in the region $q_{\text{inv}} > 0.1$ GeV/c.

From the analysis of the distributions displayed in Fig. 2, we can draw the following conclusions.

(i) Within the errors of the measurements, the two-proton correlation functions for all six channels and for the reactions $^4\text{He}p \to pppnn(\pi^0)$ and $^4\text{He}p \to dppn$ are consistent. We note that, in the present experiment, the accuracy in measuring the proton momenta proved to be sufficient for experimentally observing the characteristic decrease in the correlation function for $q_{\text{inv}} \to 0$ because of the interference between the Coulomb and the nuclear component of C_{pp}.

(ii) The agreement between the theoretical and experimental results is improved by taking into account the errors of the measurements (especially in the region of the interference maximum), but this does not have a significant effect on the result that the best fit to the experimental data yields for the spacetime radius of pp emission. This justifies the use of the model without allowance for the errors in deriving rough estimates of this parameter in the analysis of the dependence of C_{pp} on various kinematical parameters (in particular, on the modulus of the sum of the proton momenta, P_{tot}).

(iii) The root-mean-square spacetime radius of pp emission in $^4\text{He}p$ interactions proves to be close to the root-mean-square charge radius of the ^{4}He nucleus, $R_{^4\text{He}}^{\text{ch}} = 1.67$ fm [12], and to the root-mean-square radius of the density distribution in this nucleus, $R_{^4\text{He}} = 1.53$–1.66 fm. The latter was used in [10, 13] to analyze data on proton scattering by ^{4}He nuclei at intermediate energies. We note that $R_{^4\text{He}} = \sqrt{3/2}a_0$ for the parametrization of the ground-state nuclear density in the Gaussian form $\rho(r) \sim \exp(-r^2/a_0^2)$. Thus, our results confirm the main conclusion of Gałazka-Friedman *et al.* [4] that the spacetime radius of pp emission is close to the radius of the nucleus involved. Moreover, a comparison of C_{pp} at primary projectile momenta of 5 GeV/c (our data) and at 8.6 and 13.6 GeV/c (data from [4]) suggests that there is a trend toward an increase in the size of the proton-emission region with increasing primary momentum (the value of $R = 1.7 \pm 0.3$ fm was obtained in [4]).

4.2. Dependence of the Correlation Function on P_{tot}

For events of the six basic channels leading to the production of two protons, the inset in Fig. 3 shows the distribution with respect to the modulus of the sum of the momenta of two protons, P_{tot}, the constraint in (5) being imposed. It is obvious that, at a primary momentum of 5 GeV/c, there is a considerable fraction ($\sim$40%) of events featuring relatively low momenta of $P_{\text{tot}} < 0.6$ GeV/c (unshaded part

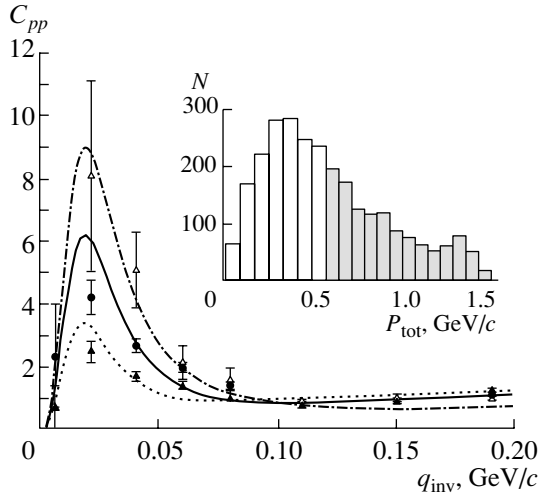

Fig. 3. Two-proton correlation function C_{pp} in ^{4}Hep interactions for events of six basic channels versus the momentum transfer q_{inv} (closed triangles) for the kinematical cut $P_{\text{tot}} < 0.6$ GeV/c, (open triangles) for the kinematical cut $P_{\text{tot}} > 0.6$ GeV/c, and (closed curcles) without any cuts on P_{tot}. The inset shows the distribution with respect to P_{tot}. The curves represent the predictions of the modified Lednicky–Lyuboshitz model for the r_0 values corresponding to the R values of (dotted curve) 2.55, (solid curve) 1.65, and (dash-dotted curve) 0.8 fm.

of the histogram in the inset in Fig. 3). The two-proton correlation function in ^{4}Hep interactions for the six basic channels is displayed in Fig. 3 versus the momentum transfer q_{inv} for the kinematical cut $P_{\text{tot}} < 0.6$ GeV/c (closed triangles), for the kinematical cut $P_{\text{tot}} > 0.6$ GeV/c (open triangles), and without any cuts on P_{tot} (closed circles). The curves in Fig. 3 represent the predictions of the modified Lednicky–Lyuboshitz model without allowance for the errors of the measurements at the values of the parameter r_0 that correspond to the values of $R = 2.55$ ($\sim 1.5R_{^4\text{He}}$), 1.65 ($\sim R_{^4\text{He}}$), and 0.8 fm ($\sim R_p$, where $R_p = 0.8$ fm is the root-mean-square radius of the proton) for the root-mean-square spacetime radius of pp emission, this corresponding to the best fit to the data for $q_{\text{inv}} < 0.1$ GeV/c. The added kinematical background is taken here in the form (8). A very strong dependence of C_{pp} on the cut on P_{tot} is observed. Moreover, it follows from a formal comparison of our theoretical and experimental results that emitted proton pairs characterized by relatively high momenta P_{tot} originate from a region of size about the proton radius and that the pairs of evaporated protons, for which P_{tot} is relatively low, seem as if they come from a region off the nucleus or from a region inside the nucleus but within different time intervals, this being equivalent from the point of view of the spacetime particle-emission pattern discussed here.

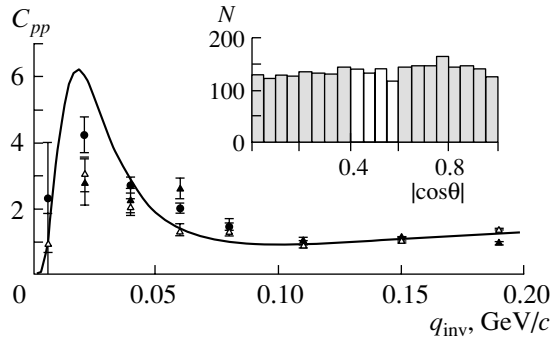

Fig. 4. Two-proton correlation function C_{pp} in ^{4}Hep interactions for events of the six basic channels versus the momentum transfer q_{inv} (open trianges) for the kinematical cut $|\cos\theta| < 0.4$, (closed triangles) for the kinematical cut $|\cos\theta| > 0.6$, and (closed circles) without any cuts on $|\cos\theta|$. The inset shows the distribution with respect to $|\cos\theta|$. The curve represents the predictions of the modified Lednicky–Lyuboshitz model.

4.3. Dependence of the Correlation Function on the Direction of $\boldsymbol{q}$

For events of the six basic channels leading to the production of two protons, the inset in Fig. 4 shows the distribution with respect $|\cos\theta|$, where θ is the angle between the vectors $\mathbf{q}$ and $\mathbf{p}_{\text{in}}$ (the latter is the primary-proton momentum in the rest frame of the nucleus), the constraint in (5) being imposed. The distribution proves to be nearly isotropic. For events of the same six channels, Fig. 4 displays the two-proton correlation function in ^{4}Hep interactions versus the momentum transfer q_{inv} for the kinematical cut $|\cos\theta| < 0.4$ (open triangles), for the kinematical cut $|\cos\theta| > 0.6$ (closed triangles), and without any cuts on $|\cos\theta|$ (closed circles). The curve represents the predictions of the modified Lednicky–Lyuboshitz model without allowance for the errors of the measurements, the parameter r_0 corresponding here to $R = 1.65$ fm. Within the errors of the measurements, all distributions in Fig. 4 are consistent. This suggests that the region of proton-pair emission in ^{4}Hep interactions has a spherically symmetric shape.

5. CONCLUSION

With the aid of a 2-m liquid-hydrogen bubble chamber exposed to a beam of alpha particles accelerated to a momentum of 5 GeV/c, we have studied the correlations of secondary protons in ^{4}Hep interactions—specifically, we have determined the total correlation function for the pp system and the two-proton correlation functions for individual channels. For the root-mean-square spacetime radius of pp emission in ^{4}Hep interactions, we have obtained the value of $R = 1.6 \pm 0.3$ fm. We have examined the

dependence of the correlation function in question on the modulus of the total momentum of an emitted proton pair and on the direction of the momentum transfer. We have determined the correlation function for pairs of evaporated protons, which have relatively low momenta in the rest frame of the nucleus. An analysis of the dependence of the correlation function on the direction of the momentum transfer gives every reason to assume that the region of proton-pair emission in ^{4}Hep interactions is spherically symmetric. A trend toward an increase in the size of the proton-emission region with increasing primary projectile momentum—this is revealed in comparing the results of the present study with the results reported in [4]—can be attributed to the growth of multiplicity (see the discussion of this issue in the review article of Boal *et al.* [3]).

We note that the experimental procedure used in the present study also makes it possible to obtain correlation functions for pairs of various secondary particles and nuclear fragments in ^{4}Hep interaction that have isospin values of $T_z = \pm 1$ (^{3}Hep, ^{3}Hn) and $T_z = 0$ (^{3}Hen, ^{3}Hp, dd). We are planning to do this in a dedicated investigation.

ACKNOWLEDGMENTS

We are grateful to V.V. Kulikov, G.A. Leksin, K.R. Mikhailov, and especially A.V. Stavinsky for interest in this study and numerous stimulating discussions. We are also indebted to V.V. Glagolev for kindly placing an electronic copy of his article at our disposal.

This work was supported in part by the Russian Foundation for Basic Research (project no. 04-02-16500).

REFERENCES

1. S. E. Koonin, Phys. Lett. B **70B**, 43 (1977).
2. R. Lednicky and V. A. Lyuboshits, Yad. Fiz. **35**, 1316 (1982) [Sov. J. Nucl. Phys. **35**, 770 (1982)].
3. D. H. Boal, C.-K. Gelbke, and B. K. Jennings, Rev. Mod. Phys. **62**, 553 (1990).
4. J. Gałazka-Friedman *et al.*, Z. Phys. A **345**, 125 (1993).
5. Yu. D. Bayukov *et al.,* Yad. Fiz. **34**, 95 (1981) [Sov. J. Nucl. Phys. **34**, 54 (1981)]; A. V. Vlasov *et al.,* Yad. Fiz. **36**, 915 (1982) [Sov. J. Nucl. Phys. **36**, 536 (1982)]; Yu. D. Bayukov *et al.,* Yad. Fiz. **50**, 719 (1989) [Sov. J. Nucl. Phys. **50**, 447 (1989)]; **52**, 480 (1990) [**52**, 305 (1990)].
6. R. Ghetti *et al.*, Nucl. Phys. A **674**, 277 (2000).
7. M. A. Lisa *et al.*, Phys. Rev. C **44**, 2865 (1991).
8. W. G. Gong *et al.*, Phys. Rev. Lett. **65**, 2114 (1990); Phys. Rev. C **43**, 1804 (1991).
9. J. Barrette *et al.*, Phys. Rev. C **60**, 054905 (1999); S. Y. Panitkin *et al.* (E895 Collab.), nucl-ex/9905008; S. Y. Panitkin and D. A. Brown, Phys. Rev. C **61**, 021901 (2000).
10. A. V. Blinov *et al.*, Yad. Fiz. **64**, 975 (2001) [Phys. At. Nucl. **64**, 907 (2001)].
11. A. V. Blinov, V. F. Turov, and M. V. Chadeyeva, Yad. Fiz. **65**, 1340 (2002) [Phys. At. Nucl. **65**, 1307 (2002)].
12. R. F. Frosh *et al.*, Phys. Rev. **160**, 874 (1967); J. S. McCarthy *et al.*, Phys. Rev. C **15**, 1396 (1977); C. R. Ottermann *et al.*, Nucl. Phys. A **436**, 688 (1985).
13. E. T. Boschitz *et al.*, Phys. Rev. Lett. **20**, 1116 (1968); W. Czyz and L. Lesniak, Phys. Lett. B **24B**, 227 (1967); Phys. Lett. B **25B**, 319 (1967); R. H. Bassel and C. Wilkin, Phys. Rev. **174**, 1179 (1968).

Translated by A. Isaakyan

Physics of Atomic Nuclei, Vol. 67, No. 8, 2004, pp. 1529–1535. From Yadernaya Fizika, Vol. 67, No. 8, 2004, pp. 1552–1557.

ELEMENTARY PARTICLES AND FIELDS
Theory

Radiative Decays of ϕ Meson and Nature of Light Scalar Resonances*

N. N. Achasov**

Sobolev Institute for Mathematics, Siberian Division, Russian Academy of Sciences, Novosibirsk, 630090 Russia

Received May 20, 2003; in final form, November 20, 2003

Abstract—We show on gauge invariance grounds that a new threshold phenomenon has been discovered in the radiative decays $\phi \to \gamma a_0 \to \gamma\pi^0\eta$ and $\phi \to \gamma f_0 \to \gamma\pi^0\pi^0$. This enables us to conclude that production of the light scalar mesons $a_0(980)$ and $f_0(980)$ in these decays is caused by the four-quark transitions, resulting in strong restrictions on the large-N_c expansions of the decay amplitudes. The analysis shows that these constraints give new evidence in favor of the four-quark nature of $a_0(980)$ and $f_0(980)$ mesons.

1. INTRODUCTION

The light scalar mesons $a_0(980)$ and $f_0(980)$, discovered more than thirty years ago, became a hard problem for the naive quark–antiquark ($q\bar{q}$) model from the outset. Really, on the one hand, the almost exact degeneration of the masses of the isovector $a_0(980)$ and isoscalar $f_0(980)$ states seemingly revealed a structure similar to the structure of the vector ρ and ω mesons, and, on the other hand, the strong coupling of $f_0(980)$ with the $K\bar{K}$ channel pointed unambiguously to a considerable part of the strange-quark pair $s\bar{s}$ in the wave function of $f_0(980)$.

In 1977, Jaffe [1] noted that, in the MIT-bag model, which incorporates confinement phenomenologically, there are light four-quark scalar states. He suggested also that $a_0(980)$ and $f_0(980)$ might be these states with symbolic structures $a_0^0(980) = (us\bar{u}\bar{s} - ds\bar{d}\bar{s})/\sqrt{2}$ and $f_0(980) = (us\bar{u}\bar{s} + ds\bar{d}\bar{s})/\sqrt{2}$. From that time, the $a_0(980)$ and $f_0(980)$ resonances became beloved children of light-quark spectroscopy (see, for example, [2–4]).

Ten years later, we showed [5] that the study of the radiative decays $\phi \to \gamma a_0 \to \gamma\pi\eta$ and $\phi \to \gamma f_0 \to \gamma\pi\pi$ can shed light on the problem of $a_0(980)$ and $f_0(980)$ mesons. Over the next ten years before experiments (1998), the question was considered from different points of view [6–10].

Now these decays have been studied not only theoretically but also experimentally.

The first measurements have been reported by the SND [11, 12] and CMD-2 [13] collaborations, which obtained the following branching ratios:

$$\mathrm{BR}(\phi \to \gamma\pi^0\eta) = (0.88 \pm 0.14 \pm 0.09) \times 10^{-4}\,[11],$$

$$\mathrm{BR}(\phi \to \gamma\pi^0\pi^0) = (1.221 \pm 0.098 \pm 0.061) \times 10^{-4}\,[12],$$

$$\mathrm{BR}(\phi \to \gamma\pi^0\eta) = (0.9 \pm 0.24 \pm 0.1) \times 10^{-4}\,[13],$$

$$\mathrm{BR}(\phi \to \gamma\pi^0\pi^0) = (0.92 \pm 0.08 \pm 0.06) \times 10^{-4}\,[13].$$

More recently, the KLOE Collaboration has measured [14, 15]

$$\mathrm{BR}(\phi \to \gamma\pi^0\eta) = (0.851 \pm 0.051 \pm 0.057) \times 10^{-4} \text{ in } \eta \to \gamma\gamma\,[14],$$

$$\mathrm{BR}(\phi \to \gamma\pi^0\eta) = (0.796 \pm 0.060 \pm 0.040) \times 10^{-4} \text{ in } \eta \to \pi^+\pi^-\pi^0\,[14],$$

$$\mathrm{BR}(\phi \to \gamma\pi^0\pi^0) = (1.09 \pm 0.03 \pm 0.05) \times 10^{-4}\,[15],$$

in agreement with the Novosibirsk data [11–13], but with a considerably smaller error.

Note that the isovector $a_0(980)$ meson is produced in radiative ϕ-meson decay as intensively as the well-studied $\eta'(958)$ meson, which contains $\approx 66\%$ $s\bar{s}$, responsible for the decay ($\phi \approx s\bar{s} \to \gamma s\bar{s} \to \gamma\eta'(958)$). It is a clear qualitative argument for the presence of the $s\bar{s}$ pair in the isovector $a_0(980)$ state, i.e., for its four-quark nature.

Since the one-loop model $\phi \to K^+K^- \to \gamma a_0$ and $\phi \to K^+K^- \to \gamma f_0$ (see Fig. 1), suggested on the basis of the experimental investigations [5], is used in the data treatment [11–15], the question on the mechanism of the scalar-meson production in ϕ radiative decays is put into the shade.

We show in Section 2 that the present data give conclusive arguments in favor of the K^+K^--loop transition as the principal mechanism of $a_0(980)$- and $f_0(980)$-meson production in ϕ radiative decays. In Section 3, we show that knowledge of this mechanism allows us to conclude that the production of

*This article was submitted by the author in English.

**e-mail: achasov@math.nsc.ru

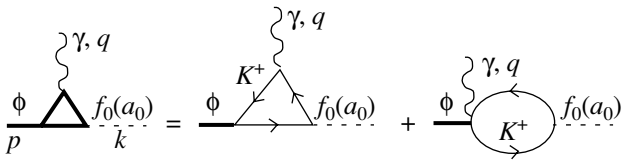

Fig. 1. Diagrams of the K^+K^- loop model.

$a_0(980)$ and $f_0(980)$ in ϕ radiative decays is caused by the four-quark transitions. This constrains the large-N_c expansions of the decay amplitudes and gives new impressive evidence in favor of the four-quark nature of $a_0(980)$ and $f_0(980)$ [1, 3–5, 7, 16–18]. Section 4 contains concluding remarks.

2. THE MECHANISM OF $a_0(980)$ AND $f_0(980)$ PRODUCTION IN ϕ RADIATIVE DECAYS

In Figs. 2 and 3 are shown the KLOE data on $\phi \to \gamma\pi^0\eta$ [14] and the SND data on $\phi \to \gamma\pi^0\pi^0$ [12] (2000), respectively. The excitations of the $a_0(980)$ resonance, similar to the one in Fig. 2, are also observed by the SND [11] and CMD-2 [13] collaborations. The excitations of the $f_0(980)$ resonance, similar to the one in Fig. 3, are also observed by the CMD-2 [13] and KLOE [15] collaborations. The data are described in the model $\phi \to (\gamma a_0 + \pi^0\rho) \to \gamma\pi^0\eta$ and $\phi \to (\gamma f_0 + \pi^0\rho) \to \gamma\pi^0\pi^0$ (see details in [18]).

As Figs. 2 [19] and 3 suggest, the $\phi \to \gamma a_0 \to \gamma\pi^0\eta$ process dominates everywhere over the region of the $\pi^0\eta$ invariant mass $m_{\pi^0\eta} = m$, and the $\phi \to \gamma f_0 \to \gamma\pi^0\pi^0$ process dominates in the resonance region of the $\pi^0\pi^0$ system, the $\pi^0\pi^0$ invariant mass $m_{\pi^0\pi^0} = m > 780$ MeV.[1)]

The resonance mass spectrum is of the form[2)]

$$S_R(m) = d\Gamma(\phi \to \gamma R \to \gamma ab, m)/dm \qquad (1)$$
$$= \frac{2}{\pi}\frac{m^2\Gamma(\phi \to \gamma R, m)\Gamma(R \to ab, m)}{|D_R(m)|^2}$$
$$= \frac{4|g_R(m)|^2\omega(m)p_{ab}(m)}{3(4\pi)^3 m_\phi^2}\left|\frac{g_{Rab}}{D_R(m)}\right|^2,$$

where $R = a_0$ or f_0 and $ab = \pi^0\eta$ or $\pi^0\pi^0$, respectively; $\omega(m) = (m_\phi^2 - m^2)/2m_\phi$ is the photon energy in the ϕ-meson rest frame; $p_{ab}(m)$ is the modulus of the a- or b-particle momentum in the a and b mass-center frame; g_{Rab} is the coupling constant; $g_{f_0\pi^0\pi^0} = g_{f_0\pi^+\pi^-}/\sqrt{2}$; $D_R(m)$ is the R-resonance propagator, the form of which everywhere over the m region can be found in [5, 20, 21]; and $g_R(m)$ is the invariant amplitude that describes the vertex of the $\phi(p) \to \gamma(k)R(q)$ transition with $q^2 = m^2$. This is precisely the function which is the subject of our investigation.

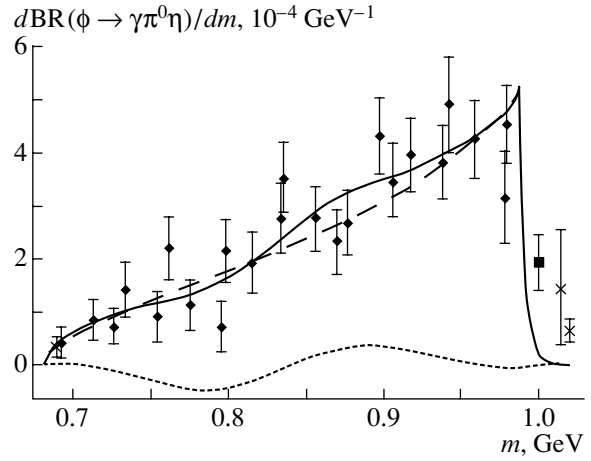

Fig. 2. Fitting of $d\mathrm{BR}(\phi \to \gamma\pi^0\eta)/dm$ with the background (solid curve). The signal contribution and interference contributions are shown by the dashed and dotted curves, respectively. The data are from the KLOE detector.

By gauge invariance, the transition amplitude is proportional to the electromagnetic-field strength tensor $F_{\mu\nu}$ (in our case to the electric field in the ϕ-meson rest frame):

$$A\left[\phi(p) \to \gamma(k)R(q)\right] \qquad (2)$$
$$= G_R(m)\left[p_\mu e_\nu(\phi) - p_\nu e_\mu(\phi)\right]\left[k_\mu e_\nu(\gamma) - k_\nu e_\mu(\gamma)\right],$$

where $e(\phi)$ and $e(\gamma)$ are the ϕ-meson and γ-quantum polarization four-vectors, and $G_R(m)$ is the invariant amplitude, free from kinematical singularities. Since there are no charged particles or particles with magnetic moments in the process, there is no pole in $G_R(m)$. Consequently, the function

$$g_R(m) = -2(pk)G_R(m) = -2\omega(m)m_\phi G_R(m) \quad (3)$$

is proportional to $\omega(m)$ (at least!) in the soft-photon region.

To describe the experimental spectra similar to the ones in Figs. 2 and 3,[3)] the function $|g_R(m)|^2$ should be smooth (almost constant) in the range $m \le 0.99$ GeV [see Eq. (1)]. Stopping the function $(\omega(m))^2$ at $\omega(990\,\mathrm{MeV}) = 29$ MeV with the help of the form factor $1/\left[1 + (R\omega(m))^2\right]$ requires $R \approx$

[1)] A.V. Kiselev noted kindly that in [18] the solid curve at $m <$ 780 MeV is drawn incorrectly. He also kindly prepared the correct figure.

[2)] Notice that in [18] we took into account the mixing of the $f_0(980)$ meson with another scalar–isoscalar resonance (see also [7]), but such a complication is not essential for the present investigation.

[3)] Note that $S_R(m) = \Gamma_\phi d\mathrm{BR}(\phi \to \gamma R \to \gamma ab, m)/dm$.

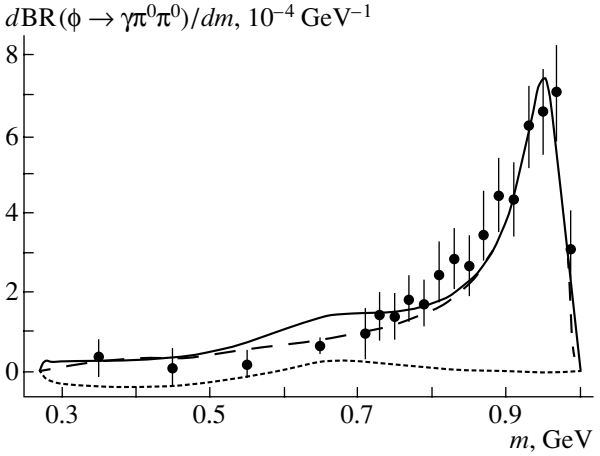

Fig. 3. Fitting of $d\mathrm{BR}(\phi \to \gamma\pi^0\pi^0)/dm$ with the background (solid curve). The signal contribution is shown by the dashed curve. The dotted curve is the interference term. The data are from the SND detector.

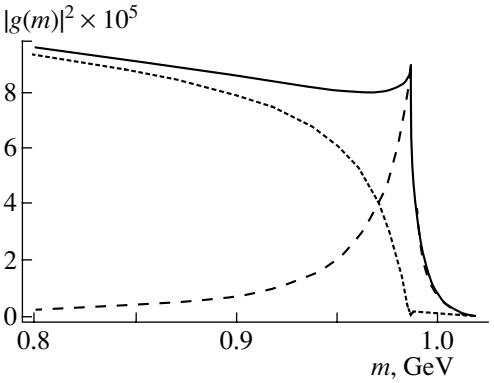

Fig. 4. The function $|g(m)|^2$ (solid curve). The contributions of the imaginary part and the real part are shown by dashed and dotted curves, respectively.

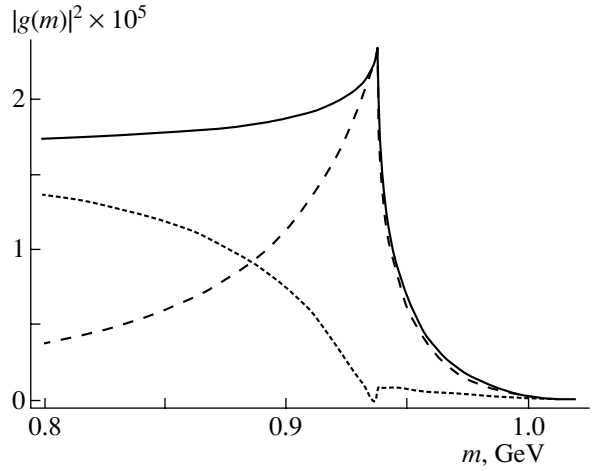

Fig. 5. The function $|g(m)|^2$ for $m_{K^+} = 469$ MeV (solid curve). The contributions of the imaginary part and the real part are shown by the dashed and dotted curves, respectively.

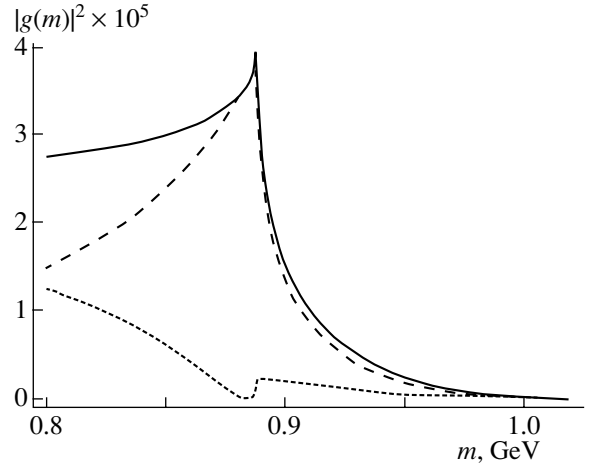

Fig. 6. The function $|g(m)|^2$ for $m_{K^+} = 444$ MeV is shown by the solid curve. The contributions of the imaginary part and the real part are shown by the dashed and dotted curves, respectively.

100 GeV^{-1}. It seems to be incredible to explain the formation of such a huge radius in hadron physics. Based on the large, by hadron physics' standards, $R \approx 10$ GeV^{-1}, one can obtain an effective maximum of the mass spectrum under discussion only near 900 MeV. To exemplify this trouble, let us consider the contribution of the isolated R resonance: $g_R(m) = -2\omega(m)m_\phi G_R(m_R)$. Let also the mass and the width of the R resonance equal 980 and 60 MeV, then $S_R(920\ \mathrm{MeV}) : S_R(950\ \mathrm{MeV}) : S_R(970\ \mathrm{MeV}) : S_R(980\ \mathrm{MeV}) = 3 : 2.7 : 1.8 : 1$.

So stopping the $g_R(m)$ function is the crucial point in understanding the mechanism of the production of $a_0(980)$ and $f_0(980)$ resonances in ϕ radiative decays.

The K^+K^- loop model $\phi \to K^+K^- \to \gamma R$ [5] solves this problem in an elegant way: the fine threshold phenomenon is discovered (see Fig. 4), where the universal K^+K^--loop-model function $|g(m)|^2 = |g_R(m)/g_{RK^+K^-}|^2$ is shown.[4)]

To demonstrate the threshold character of this effect, we present Figs. 5 and 6, in which the function $|g(m)|^2$ is shown in the case where the K^+-meson mass is 25 and 50 MeV less than that in reality.

One can see from Figs. 5 and 6 that the function $|g(m)|^2$ is suppressed by the $(\omega(m))^2$ law in the region 950–1020 and 900–1020 MeV, respectively.

In the mass spectrum, this suppression is increased by one more power of $\omega(m)$ [see Eq. (1)],

[4)]The forms of $g_R(m)$ and $g(m) = g_R(m)/g_{RK^+K^-}$ everywhere over the m region are in [5] and [19, 21], respectively.

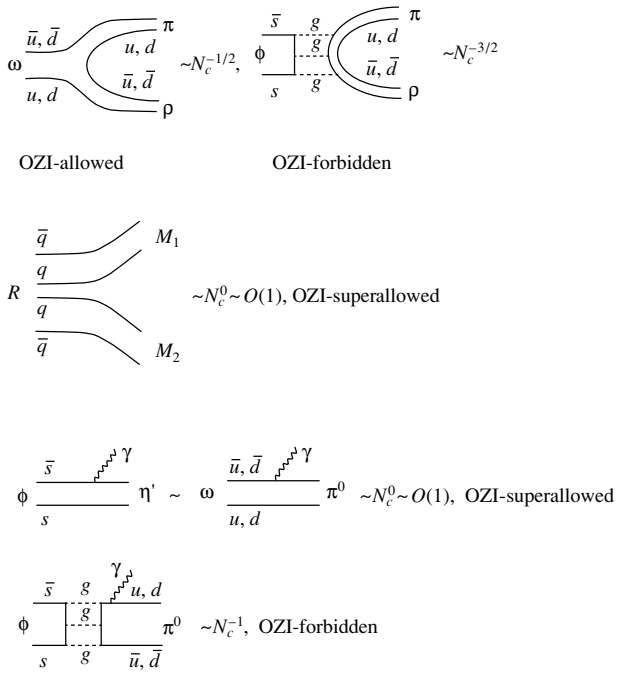

Fig. 7. The large-N_c expansion of some well-known decay amplitudes.

so that we cannot see the resonance in the region 980–995 MeV.[5)] The maximum in the spectrum is effectively shifted to the region 935–950 MeV and 880–900 MeV, respectively.

In truth, this means that the $a_0(980)$ and $f_0(980)$ resonances are seen in the radiative decays of the ϕ meson owing to the K^+K^- intermediate state, otherwise the maxima in the spectra would be shifted to 900 MeV.

Thus, the mechanism of production of $a_0(980)$ and $f_0(980)$ mesons in ϕ radiative decays is established.

3. THE LARGE-N_c EXPANSION OF THE $\phi \to \gamma a_0$ AND $\phi \to \gamma f_0$ AMPLITUDES

Both real and imaginary parts of the $\phi \to \gamma R$ amplitude are caused by the K^+K^- intermediate state. The imaginary part is caused by the real K^+K^- intermediate state, while the real part is caused by the virtual compact K^+K^- intermediate state; i.e., we are dealing here with the four-quark transition.[6)] Needless to say, radiative four-quark transitions can occur between two $q\bar{q}$ states as well as between $q\bar{q}$ and $q^2\bar{q}^2$ states, but their intensities depend strongly on the

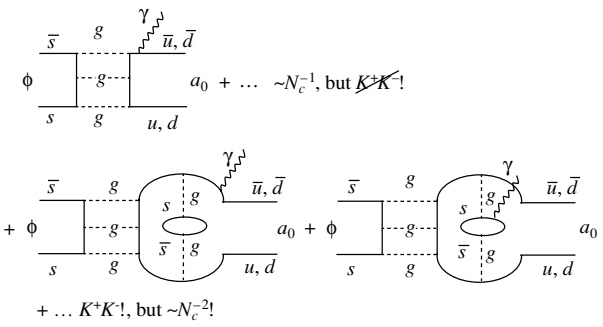

Fig. 8. The large-N_c expansion of the $\phi \to \gamma a_0(980)$ amplitude in the two-quark model $a_0^0(980) = (u\bar{u} - d\bar{d})/\sqrt{2}$.

type of transitions. A radiative four-quark transition between two $q\bar{q}$ states requires creation and annihilation of an additional $q\bar{q}$ pair [i.e., such a transition is forbidden according to the Okubo–Zweig–Iizuka (OZI) rule], while a radiative four-quark transition between $q\bar{q}$ and $q^2\bar{q}^2$ states requires only creation of an additional $q\bar{q}$ pair (i.e., such a transition is allowed according to the OZI rule).

Let us consider this problem from the large-N_c expansion standpoint, using the G. 't Hooft rules [22]: $g_s^2 N_c \to$ const at $N_c \to \infty$ and a gluon is equivalent to a quark–antiquark pair ($A^i_j \sim q^i \bar{q}_j$).

Figure 7 reminds us of the large-N_c expansion of some well-known decay amplitudes.[7)]

Let us begin our consideration with the $q\bar{q}$ model.

In the two-quark model $a_0^0(980) = (u\bar{u} - d\bar{d})/\sqrt{2}$, the large-$N_c$ expansion of the $\phi \approx s\bar{s} \to \gamma a_0(980)$ amplitude starts with the OZI-forbidden transition of the $1/N_c$ order: $s\bar{s}$ annihilation and $u\bar{u}, d\bar{d}$ creation (see Fig. 8). But its weight is bound to be small, because this term does not contain the K^+K^- intermediate state, which emerges only in the next-to-leading term of the $(1/N_c)^2$ (!) order for creation and annihilation of additional $q\bar{q}$ pairs (see Fig. 8). Note that the $\phi \approx s\bar{s} \to \gamma s\bar{s} \to \gamma\eta'(958)$ transition (as intensive experimentally as $\phi \to \gamma a_0(980)$) does not require creation of an additional $q\bar{q}$ pair at all (the OZI-superallowed transition) and has the $(N_c)^0$ order (see Fig. 7).

In the two-quark model $f_0(980) = (u\bar{u} + d\bar{d})/\sqrt{2}$, which involves a_0–f_0 mass degeneration, the large-N_c expansion of the $\phi \approx s\bar{s} \to \gamma f_0(980)$ amplitude also starts with the OZI-forbidden transition of

[5)] The actual absence of a background at a soft photon energy region $\omega(m) < 112$ MeV ($m > 900$ MeV) is due to gauge invariance also.

[6)] It will be recalled that the imaginary part of every hadronic amplitude describes a multiquark transition.

[7)] In Figs. 7–11, the graphs are understood with the obvious permutations of the gamma quantum. In addition, not shown in Figs. 7–11 are exchanges by planar gluons which do not change the large-N_c behavior.

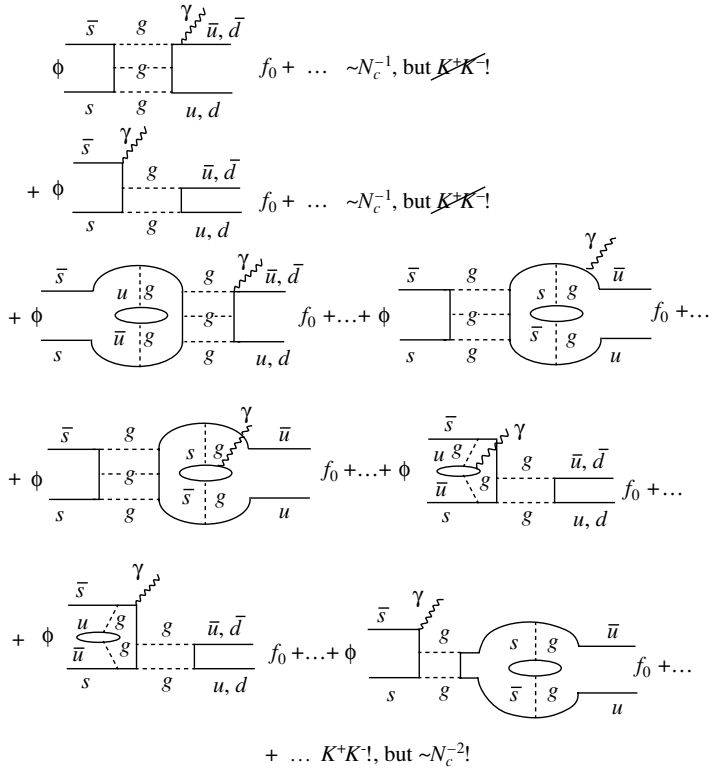

Fig. 9. The large-N_c expansion of the $\phi \to \gamma f_0(980)$ amplitude in the two-quark model $f_0(980) = (u\bar{u} + d\bar{d})/\sqrt{2}$.

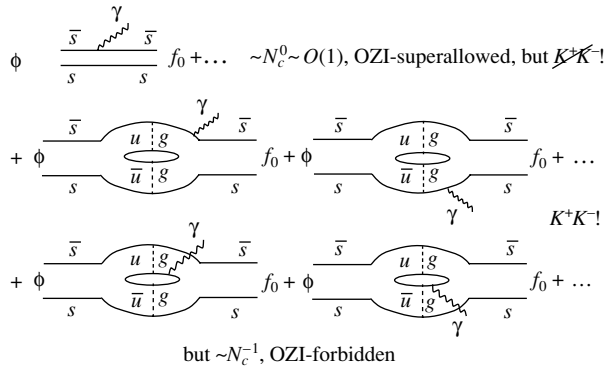

Fig. 10. The large-N_c expansion of the $\phi \to \gamma f_0(980)$ amplitude in the two-quark model $f_0(980) = s\bar{s}$.

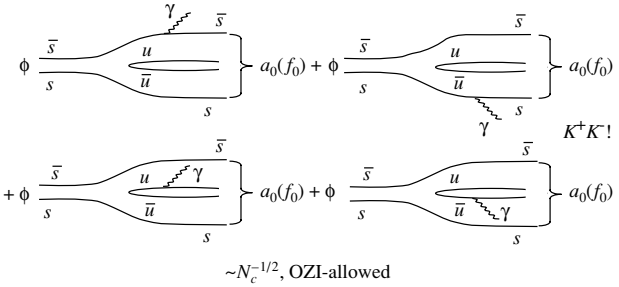

Fig. 11. The large-N_c expansion of the $\phi \to \gamma a_0(980)$ and $\phi \to \gamma f_0(980)$ amplitudes in the four-quark model $a_0^0(980) = (u\bar{s}s\bar{u} - d\bar{s}sd\bar{)}/\sqrt{2}$ and $f_0(980) = (u\bar{s}s\bar{u} + d\bar{s}sd\bar{)}/\sqrt{2}$.

the $1/N_c$ order: $s\bar{s}$ annihilation and $u\bar{u}, d\bar{d}$ creation (see Fig. 9), whose weight also is bound to be small, because this term does not contain the K^+K^- intermediate state, which emerges only in the next-to-leading term of the $(1/N_c)^2$ order (see Fig. 9).

In the two-quark model $f_0(980) \approx s\bar{s}$, which has serious trouble with the $a_0 - f_0$ mass degeneration, the $(N_c)^0$-order transition without creation of an additional $q\bar{q}$ pair $\phi \approx s\bar{s} \to \gamma s\bar{s} \to \gamma f_0(980)$[8] (see Fig. 10) is bound to have a small weight in the large-N_c expansion of the $\phi \approx s\bar{s} \to \gamma f_0(980)$ amplitude, because this term does not contain the K^+K^- intermediate state, which emerges only in the next-to-leading term of the $1/N_c$ order, i.e., in the OZI-forbidden transition (see Fig. 10). We emphasize that

[8] In this regard, the $(N_c)^0$-order mechanism is similar to the principal mechanism of the $\phi \approx s\bar{s} \to \gamma s\bar{s} \to \gamma\eta'(958)$ decay (see Fig. 7).

the mechanism without creation and annihilation of the additional $u\bar{u}$ pair cannot explain the $S_{f_0}(m)$ spectrum because such a mechanism does not include the K^+K^- intermediate state!

But if $a_0^0(980)$ and $f_0(980)$ mesons are compact $K\bar{K}$ states $a_0^0(980) = (u\bar{s}s\bar{u} - d\bar{s}s\bar{d})/\sqrt{2}$ and $f_0(980) = (u\bar{s}s\bar{u} + d\bar{s}s\bar{d})/\sqrt{2}$, respectively, i.e., four-quark states similar to states of the MIT-bag model,[9] the large-N_c expansions of the $\phi \approx s\bar{s} \to \gamma a_0(980)$ and $\phi \approx s\bar{s} \to \gamma f_0(980)$ amplitudes start with the OZI-allowed transitions of the $(1/N_c)^{1/2}$ order, which require only creation of an additional $u\bar{u}$ pair for the K^+K^- intermediate state (see Fig. 11). It will be recalled that an OZI-allowed hadronic decay amplitude, for example, the $\rho \to \pi\pi$ amplitude, has the $(1/N_c)^{1/2}$ order, as well as the $\omega \to \pi\rho$ one (see Fig. 7).

4. CONCLUSIONS

In summary, the fine threshold phenomenon has been discovered, which is to say that the K^+K^--loop mechanism of the $a_0(980)$- and $f_0(980)$-scalar-meson production in ϕ radiative decays has been established at a physical level of proof. The case is the rarest in hadron physics. This production mechanism is the four-quark transition that constrains the large-N_c expansion of the $\phi \to \gamma a_0(980)$ and $\phi \to \gamma f_0(980)$ amplitudes and gives new strong (if not crucial) evidence in favor of the four-quark nature of $a_0(980)$ and $f_0(980)$ mesons.

ACKNOWLEDGMENTS

I thank A.V. Kiselev very much for his help.

This work was supported in part by the Russian Foundation for Basic Research (project no. 02-02-16061) and by a Presidential grant (no. 2339.2003.2) for support of Leading Scientific Schools.

[9] In the case of the $K\bar{K}$ bound states with the binding energy close to 20 MeV, i.e., in the extended molecule case, the contribution of the virtual intermediate K^+K^- states in the K^+K^- loop is suppressed by the momentum distribution in the molecule, and the real part of the loop amplitude is negligible [8]. It leads to branching ratios [8] much less than the experimental ones. In addition, the $S_R(m)$ spectra in the $K\bar{K}$ molecule case are much narrower than the experimental ones (see the behavior of the imaginary part contribution in Fig. 4).

REFERENCES

1. R. L. Jaffe, Phys. Rev. D **15**, 267, 281 (1977).
2. L. Montanet, Rep. Prog. Phys. **46**, 337 (1983); L. G. Landsberg, Usp. Fiz. Nauk **160** (3), 1 (1990) [Sov. Phys. Usp. **33**, 169 (1990)]; M. R. Pennington, in *HADRON'95, Proceedings of the 6th International Conference on Hadron Spectroscopy, Manchester, UK, 1995*, Ed. by M. C. Birse, G. D. Lafferty, and J. A. McGovern (World Sci., Singapore, 1996), p. 3; T. Barnes, AIP Conf. Proc. **432**, 3 (1998); C. Amsler, Rev. Mod. Phys. **70**, 1293 (1998); Muneyuki Ishida, Shin Ishida, and Taku Ishida, Prog. Theor. Phys. **99**, 1031 (1998); R. Delbourgo and M. D. Scadron, Int. J. Mod. Phys. A **13**, 657 (1998); S. Godfrey and J. Napolitano, Rev. Mod. Phys. **71**, 1411 (1999); P. Minkowski and W. Ochs, Eur. Phys. J. C **9**, 283 (1999); E. van Beveren, hep-ph/0201006; F. E. Close and N. A. Törnqvist, J. Phys. G **28**, R249 (2002); hep-ph/0204205; H. Y. Cheng, Phys. Rev. D **67**, 034024 (2003); hep-ph/0212117.
3. N. N. Achasov, S. A. Devyanin, and G. N. Shestakov, Phys. Lett. B **96B**, 168 (1980); Usp. Fiz. Nauk **142**, 361 (1984) [Sov. Phys. Usp. **27**, 161 (1984)]; N. N. Achasov and G. N. Shestakov, Usp. Fiz. Nauk **161** (6), 53 (1991) [Sov. Phys. Usp. **34**, 471 (1991)]; N. N. Achasov, Nucl. Phys. B (Proc. Suppl.) **21**, 189 (1991).
4. N. N. Achasov, Usp. Fiz. Nauk **168**, 1257 (1998); Nucl. Phys. A **675**, 279 (2000); Yad. Fiz. **65**, 573 (2002) [Phys. At. Nucl. **65**, 546 (2002)].
5. N. N. Achasov and V. N. Ivanchenko, Nucl. Phys. B **315**, 465 (1989); Preprint No. 87-129, INP (Novosibirsk, 1987).
6. A. Bramon, A. Grau, and G. Pancheri, Phys. Lett. B **289**, 97 (1992); F. E. Close, N. Isgur, and S. Kumano, Nucl. Phys. B **389**, 513 (1993); J. L. Lucio and M. Napsuciale, Phys. Lett. B **331**, 418 (1994).
7. N. N. Achasov and V. V. Gubin, Phys. Rev. D **56**, 4084 (1997); Yad. Fiz. **61**, 274 (1998) [Phys. At. Nucl. **61**, 224 (1998)].
8. N. N. Achasov, V. V. Gubin, and V. I. Shevchenko, Phys. Rev. D **56**, 203 (1997); Int. J. Mod. Phys. A **12**, 5019 (1997); Yad. Fiz. **60**, 89 (1997) [Phys. At. Nucl. **60**, 81 (1997)].
9. N. N. Achasov, V. V. Gubin, and E. P. Solodov, Phys. Rev. D **55**, 2672 (1997); Yad. Fiz. **60**, 1279 (1997) [Phys. At. Nucl. **60**, 1152 (1997)].
10. N. N. Achasov and V. V. Gubin, Phys. Rev. D **57**, 1987 (1998); Yad. Fiz. **61**, 1473 (1998) [Phys. At. Nucl. **61**, 1367 (1998)].
11. M. N. Achasov *et al.*, Phys. Lett. B **438**, 441 (1998); **479**, 53 (2000).
12. M. N. Achasov *et al.*, Phys. Lett. B **440**, 442 (1998); **485**, 349 (2000).
13. R. R. Akhmetshin *et al.*, Phys. Lett. B **462**, 380 (1999).
14. A. Aloisio *et al.*, Phys. Lett. B **536**, 209 (2002).
15. A. Aloisio *et al.*, Phys. Lett. B **537**, 21 (2002).
16. O. Black, A. Fariborz, F. Sannino, and J. Schechter, Phys. Rev. D **59**, 074026 (1999).

17. N. N. Achasov, AIP Conf. Proc. **619**, 112 (2002); hep-ph/0110059; J. Schechter, AIP Conf. Proc. **619**, 178 (2002); hep-ph/0110356; S. F. Tuan, AIP Conf. Proc. **619**, 495 (2002); hep-ph/0109191; T. Teshima, AIP Conf. Proc. **619**, 487 (2002); hep-ph/0105107.
18. N. N. Achasov and V. V. Gubin, Phys. Rev. D **63**, 094007 (2001); Yad. Fiz. **65**, 1566 (2002) [Phys. At. Nucl. **65**, 1528 (2002)].
19. N. N. Achasov and A. V. Kiselev, Phys. Rev. D **68**, 014006 (2003); Yad. Fiz. **67**, 653 (2004) [Phys. At. Nucl. **67**, 633 (2004)].
20. N. N. Achasov, S. A. Devyanin, and G. N. Shestakov, Yad. Fiz. **32**, 1098 (1980) [Sov. J. Nucl. Phys. **32**, 566 (1980)].
21. N. N. Achasov and V. V. Gubin, Phys. Rev. D **64**, 094016 (2001); Yad. Fiz. **65**, 1939 (2002) [Phys. At. Nucl. **65**, 1887 (2002)].
22. G. 't Hooft, Nucl. Phys. B **72**, 461 (1974).

Physics of Atomic Nuclei, Vol. 67, No. 8, 2004, pp. 1536–1558. Translated from Yadernaya Fizika, Vol. 67, No. 8, 2004, pp. 1558–1580.

ELEMENTARY PARTICLES AND FIELDS
Theory

Field-Theory Approach to the Dibaryon Model of Nuclear Forces

V. I. Kukulin* and M. A. Shikhalev[1)]

Institute of Nuclear Physics, Moscow State University, Vorob'evy gory, Moscow, 119899 Russia

Received July 14, 2003; in final form, February 17, 2004

Abstract—A covariant field-theory formulation of the recently developed dibaryon model of nuclear forces is given. The model involves an intermediate dibaryon dressed with π, σ, ρ, and other fields; the corresponding mesons can be in various orbitally excited states with respect to a six-quark bag; and scalar, pseudoscalar, vector, and axial-vector fields are taken into account for the dressed dibaryon. Particular attention is given to nucleon–nucleon interaction in even partial waves. A relativistically covariant nucleon–nucleon potential is derived. It is shown that a simple generalization of the single-channel model makes it possible to take into account coupling to other baryon channels of the $N\Delta$, $\Delta\Delta$, $NN^*(1535)$, etc., types, this in turn leading to a description of the production of various mesons within this approach. The model also enables one to describe, in a natural way, 2π production in nucleon–nucleon collisions in the isoscalar and in the isovector channel and provides a new formulation of the theory of meson-exchange currents in the physics of electromagnetic interactions. The possible applications of the developed approach in the physics of hadron interactions and in nuclear physics on the whole are discussed.

1. INTRODUCTION: QUALITATIVE CONSIDERATION OF THE DIBARYON MODEL OF NUCLEAR FORCES

On the basis of the traditional one-boson-exchange (OBE) model of nuclear forces, considerable advances have recently been made in explaining the properties of few-nucleon and light nuclei. Despite this, the model has run into rather serious and hardly removable difficulties both at the fundamental level and in various applications [1–4]. The main difficulty arises here in describing any processes (of strong, weak, and electromagnetic interactions) accompanied by a high momentum (and energy) transfer, in which case one has to specify form factors for the coupling of meson and nucleon degrees of freedom—such as $F_{\pi NN}$ and $F_{\pi N\Delta}$. Data from numerous experiments with extremely light and light nuclei show that the probability of finding, in nuclei, high-momentum components of wave functions is quite significant (in terms of an alternative description, the probability that a high projectile momentum is distributed among the remaining intranuclear nucleons is sizable); at the same time, rather "soft" meson–nucleon form factors required both by experiments and by all fundamental theories (featuring cutoff-parameter values in the ranges $\Lambda \sim 0.5$–0.7 GeV/c) [1, 2, 5] give no way to distribute, with the required probability, a high projectile momentum among the other intranuclear nucleons [6, 7]. For the same reason, a significant deficit of high-momentum components is observed in nuclei [2-4, 6–8].[2)] This fundamental flaw in one-boson-exchange theories becomes noticeable even at $A = 2$—that is, from the deuteron [4, 6, 10]. The discovery and subsequent detailed investigation of cumulative processes [11–14], which are kinematically forbidden on a single nucleon, was one of the most spectacular manifestations of such a deficit. As a result, it became clear that, in nuclei, there are rather tight two- and three-nucleon correlations, which are completely disregarded in the one-boson-exchange scheme. In order to adapt the meson-exchange model, in one way or another, to describing a large number of such experiments (to begin from elastic nucleon–nucleon scattering at energies in the region $E > 200$ MeV), the cutoff parameters Λ in all meson–nucleon form factors are increased by hand by a factor of 2 to 3 (that is, $\Lambda_{\pi NN} \sim 1.5$–$1.7$ GeV/c is usually taken instead of $\Lambda_{\pi NN} \sim 0.6$ GeV/c), this making it possible to increase the hardness of nuclear wave functions. A similar ad hoc increase in the cutoff parameters Λ by a factor of 2 to 3 is introduced for the operators of all meson-exchange currents (MEC), whereby one is able to distribute a high projectile

[1)]Joint Institute for Nuclear Research, Dubna, Moscow oblast, 141980 Russia;
e-mail: shehalev@phys.vsu.ru
*e-mail: kukulin@nucl-th.sinp.msu.ru

[2)]It is interesting to note that the first indications of such a deficit of high-momentum components in nuclear wave functions were obtained as far back as the early 1960s in studying the emission of fast nucleons from nuclei [9].

momentum (of a virtual photon, for example) among the other intranuclear nucleons. In addition to the aforementioned inconsistencies with all fundamental theories of meson–nucleon interaction, the following clearly demonstrates that the above ad hoc enhancement of the meson–nucleon form factors is unnatural:

(i) The description of $\pi^{\pm}$-meson production in inelastic proton–proton collisions and the description of elastic nucleon–nucleon scattering require radically different values of the cutoff parameters Λ ($\Lambda_{\pi NN} \approx \Lambda_{\rho NN} \sim 0.6$–$0.7$ GeV/c versus $\Lambda_{\pi NN} \sim 1.5$ GeV/c), and the threshold production of neutral pions can hardly be described within a consistent one-boson-exchange model.

(ii) As to the currently adopted models of three-particle forces (all of them are based on the two-boson-exchange mechanism), they require intermediate values of the cutoff parameters ($\Lambda_{\pi NN} \sim 0.8$ GeV/c).

Thus, we can state that, in order to describe processes of four independent types (that is, elastic nucleon–nucleon scattering, the production of $\pi^{\pm}$ and π^0 mesons, and the contribution of three-nucleon forces to the properties of the ^{3}H and ^{3,4}He nuclei), one needs three drastically different values of the same quantity $\Lambda_{\pi NN}$ (this also concerns other cutoff parameters, such as $\Lambda_{\pi N\Delta}$ and $\Lambda_{\rho NN}$).

This obviously indicates that the force model in question is not adequate. In order to improve the situation in one way or another, especially the description of processes involving a high momentum transfer, quark models on the basis of quark bags of various types (MIT [15], QCB [16], and others) have been widely used since the mid-1970s. A feature common to these hybrid models was that quark bags ($6q$, $9q$, or $12q$) did not include meson degrees of freedom explicitly, and this gave no way to develop a smooth interpolation between the low-momentum-transfer region (dominated by nucleon currents) and the high-momentum-transfer region (dominated by quark currents). At the same time, it is well known that, even in deuteron photodisintegration, which is the simplest electromagnetic nuclear process, meson currents make a dominant contribution from an energy of $E_\gamma > 100$ MeV [17]. Moreover, it is generally recognized that the meson cloud of a nucleon (that is, of a $3q$ cluster) plays an important role in a great number of strong-, weak-, and electromagnetic-interaction processes, including those that are responsible for the origin of the nucleon spin [18]. But it would then be necessary to recognize that the meson cloud of a six-quark cluster (the integrated coupling of this cloud to the six-quark core must be stronger than that for nucleons) must play a role that is at least as significant as that in the nucleon (if fact, the role of the meson cloud in the six-quark system is much more pronounced than in the nucleon because of the emergence of a strong scalar sigma field).

Such a model of a dressed six-quark bag was proposed by our group in the late 1990s [19]; it was based on previous studies devoted to constructing the Moscow nucleon–nucleon potential [20–22]. The model relied on the following three ideas:

(i) A clustered nucleon–nucleon channel must be dominated by the mixed spatial symmetry of the six-quark wave function $|s^4p^2[42]; L = 0, 2, ST\rangle$; at the same time, the second allowed symmetry $|s^6[6]; L = 0, ST\rangle$ is associated with the six-quark-bag component and is naturally orthogonal to the nucleon–nucleon channel.

(ii) In the space of quark channels, the components having the mixed symmetry $|s^4p^2[42]; LST\rangle$ and corresponding to the nucleon–nucleon channel involve two excitation quanta; therefore, the transition becomes possible that proceeds to a nonexcited state of symmetry $|s^6\rangle$ and which involves the emission of two s-wave pions,

$$|s^4p^2[42]\rangle \longrightarrow |s^6[6] + (\pi\pi)_{l=0}\rangle,$$

which can form a scalar sigma meson in the field of the six-quark core.

(iii) Owing to the scalar character of the sigma-meson cloud formed in this way and owing to the purely s-wave structure of the six-quark core, this cloud will "contract" quarks to a bag of smaller radius, whereby there will arise a large gain in energy (see, for example, a similar pattern for a "small" chiral bag in [23]). Because of the high density of quarks, the sigma-meson mass, as well as the sigma-meson width, must decrease sizably in such a bag, this corresponding to a partial restoration of chiral symmetry in the six-quark bag. This partial restoration of chiral symmetry in dense nuclear matter due to the reduction of the sigma-meson mass (and of the constituent-quark mass as well) was investigated in detail and was well confirmed in a number of recent studies (see [24–26]). The total effect of such a phase transition will manifest itself as a strong attraction of nucleons in the nucleon channel.

In traditional one-boson-exchange models, this attraction (which is dominant at intermediate distances) is described by t-channel sigma-meson exchange [27]. In recent years, however, it was shown that the t-channel exchange of a correlated 2π pair (in the $L_{\pi\pi} = 0$, $T = 0$ channel) is unable to yield an attraction of the required strength in the nucleon–nucleon channel, leading either to a nucleon–nucleon

repulsion or to a weak attraction.[3)] Thus, the introduction of an s-channel dressed dibaryon in the nucleon–nucleon interaction makes it possible to fill this obvious gap in the one-boson-exchange pattern of nuclear interaction.

In recent studies of our group, the model of a dressed six-quark bag [referred to as the dressed-bag intermediate state (DBS) or the dressed-bag model (DBM)] was improved to such an extent as to provide a realistic nucleon–nucleon potential that made it possible to describe quite accurately nucleon–nucleon phase shifts (in the lowest partial waves) from 0 to 1000 MeV [28–30]. Moreover, the constructed nucleon–nucleon potential was tested in a three-body problem, and it was found in [31] that the respective description of the main static properties of the ^{3}H and ^{3}He nuclei, including the ^{3}He Coulomb energy, which could not have been explained before within traditional one-boson-exchange models, is excellent.

Yet, the DBS model constructed in previous studies of our group to describe nucleon–nucleon forces had some significant drawbacks. First, the entire pattern was by and large nonrelativistic, but our main interest lies in the energy region $E_N > 500$ MeV, where relativistic effects are expected to be quite significant. Second, the whole model heavily relied on the microscopic content of the quark shell model (see, for example, [29]), and this complicated its generalization to high partial waves and high energies. Difficulties associated with the inclusion of odd nucleon–nucleon partial waves are an indirect corollary of this.

But the most important point here is the following. In the region of low energies ($E_N < 200$ MeV), the development at present is predominantly proceeding along the lines of chiral perturbation theory (ChPT) [32–35] and the formulation of nucleon–nucleon interaction in terms of effective field theory [36], this providing a universal approach to various processes in the realms of hadron physics. However, chiral perturbation theory is inapplicable in the region $E_N > 200$–300 MeV, since the expansion parameter $p/\Lambda_{\rm QCD}$ is on the order of unity in this region, and there are presently no workable approaches of this type that would make it possible to advance toward the energy region $E \sim 1$–3 GeV. In the present study, we therefore made an attempt to give a consistent covariant field-theory description of the dibaryon model of nuclear forces, which permits reaching the intermediate-energy region (1–3 GeV), which is inaccessible to chiral perturbation theory. This, more advanced, approach immediately led to an important modification of this model: there arises a consistent scheme for dressing a six-quark bag in terms of an effective field theory (see below). In this case, an additional inclusion of π- or ρ-meson degrees of freedom or both of them simultaneously within the DBS model merely amounts to supplementing the total dibaryon polarization operator $\Pi(P^2)$ with the corresponding loops; previously, it was necessary for this to change completely the vertex functions in the transition $NN \to D + m$ (where $m = \sigma, \pi, \rho, \ldots$).

Such a field-theory pattern naturally admits the matching of the low- and the high-energy region, since each of these is already described in similar field-theory terms. It should be recalled that, within chiral perturbation theory at low energies, the short-range nucleon–nucleon interaction, in which we are interested, is assumed to be pointlike and is parametrized in terms of a constant [which is fitted (rather than calculated) to experimental data in the spirit of the interaction constants in Landau–Migdal theory], while the peripheral part of the nucleon–nucleon interaction is treated on the basis of a convergent perturbation theory in the multiplicity of the πN interaction. But in our approach, the external part of the interaction is described in terms of t-channel π and 2π exchanges, while the main, internal, part of the nucleon–nucleon interaction is represented as an expansion in the number of quanta of the excitation of a color string that simulates a dressed dibaryon. Therefore, it is quite clear that, taking a superposition of two field Lagrangians for the external and the internal component of the interaction, we arrive, in a natural way, at a unified field-theory model of nuclear forces (although the problem of explicitly unifying the two patterns in question can be quite nontrivial).

2. DESCRIPTION OF NUCLEON–NUCLEON INTERACTION AT INTERMEDIATE AND SHORT DISTANCES

We begin by specifying what we mean here by a CC state. Any nonconfined state—a nucleon–nucleon or a delta–delta state—can be represented as a combination of two three-quark clusters, the quarks in each of these clusters being connected by a color string (Fig. 1a). Further, we consider the interaction of two quarks belonging to different quark clusters and exchanging color; this can lead to the formation of either a nonconfined six-quark state (Fig. 1b) (in which case such an interaction is in principle analogous in action to meson exchange) or a confined six-quark state (Fig. 1c), which has zero projection onto any nonconfined state. This closed CC configuration can be illustratively represented in the form of three diquarks connected by a double string.

[3)] This contradiction is yet another problem of importance in one-boson-exchange models of nuclear forces.

Here, we will briefly touch upon the distinctions between the dressed-dibaryon pattern, which was considered in previous studies of our group [28–30], and the new pattern proposed in the present study. Here, two nucleons form, at the first stage, a rather extended color string (of length about 1 fm) with $3q(C)$ clusters at its ends [or two strings with diquarks at its ends (see Fig. 1*c*)] rather than a spherically symmetric (or weakly deformed) six-quark bag, as in the preceding version. In the present case, the nonexcited states of this color string (in terms of the six-quark shell model—here, it is not quite accurate—these are $|s^6; L=0\rangle$ or $|s^5p; L=1\rangle$ configurations) lie rather high on the energy scale and make but a small contribution to the nucleon–nucleon attraction induced by the string interaction. Recent microscopic calculations within the six-quark resonating-group method [37, 38] revealed that, if one takes into account the one-gluon-exchange or the one-pion-exchange interaction between quarks (plus the confining interaction), the resulting nucleon–nucleon interaction leads to a strong repulsion in the states of $|s^6[6]\rangle$ or $|s^5p[51]\rangle$ six-quark symmetry. This nonlocal short-range repulsion is not directly related to the dibarion pattern discussed in the present study and is simulated in the approach used here by a nonlocal (separable) repulsive potential $\lambda|\phi\rangle\langle\phi|$.

Excited states of the string can (because of coupling to meson degrees of freedom) emit mesons—in particular, a scalar sigma meson—this strongly shifting highly excited states downward along the energy scale. Concurrently, there arises a nonexcited dressed spherically symmetric bag of structure $|s^6+\sigma\rangle$ or weakly deformed dressed bag of structure $|s^5p+\sigma\rangle$ in, respectively, even or odd partial waves.

Thus, we can see that, to a good approximation, the whole process of nucleon–nucleon interaction can be broken down into three stages corresponding to long, intermediate, and short nucleon–nucleon distances:

(i) the region of classical one- and two-pion exchanges, $r_{NN} > 1$ fm;

(ii) the intermediate region of an excited color string, $0.5 \le r_{NN} \le 1$ fm;

(iii) the region of a spherical or weakly deformed six-quark bag dressed with meson fields (mainly π, σ, ρ, and ω fields), $r_{NN} < 0.5$ fm.

In the first region, the interaction is described by traditional meson-exchange models and is not considered here (see, for example, the review article of Machleidt [27]). We focus here on the dynamics of nucleon–nucleon interaction in the second and the third region.

In order to derive the amplitude corresponding to the process $NN \to D(CC) \to NN$, we use

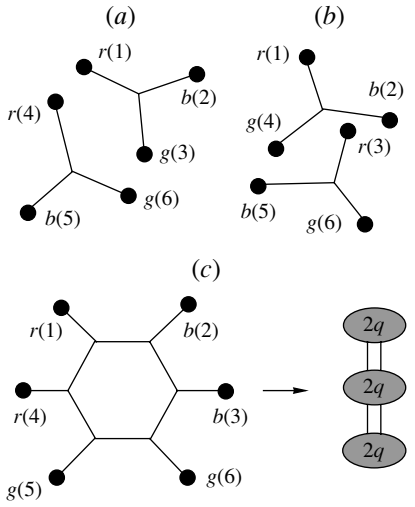

Fig. 1. Graphs illustrating various states of the $6q$ system: (a, b) nucleon–nucleon and delta–delta states, respectively, and (c) confined CC state. The symbols r (red), b (blue), and g (green) stand for the color of a quark.

the Stückelberg–Feynman pattern, which interprets an antiparticle as a particle having a negative energy and moving in the opposite direction in spacetime. First, we consider the structure of the vertices for the $NN \to D$ transition. In the case of pointlike (structureless) nucleons and a pointlike (structureless) dibaryon, we can compose five local nucleon currents $J_N(x)$ associated with the corresponding dibaryon fields: scalar $\tilde{N}N$, pseudoscalar $\tilde{N}\gamma_5 N$, vector $\tilde{N}\gamma_\mu N$, axially vector $\tilde{N}\gamma_5\gamma_\mu N$, and tensor $\tilde{N}\sigma_{\mu\nu}N$ currents. Here, $\tilde{N} \equiv N^T C^{-1}\gamma_5 i\tau_2$ has the same transformation properties as the Dirac-conjugate nucleon-field operator $\bar{N} = N^\dagger\gamma_0$ in the Lorentz and isospin groups, $C = i\gamma_2\gamma_0$ is the charge-conjugation operator, τ_2 is a Pauli matrix, and N^T stands for a transposed matrix. These currents can easily be derived from conventional chiral Lagrangians describing a contact nucleon–nucleon interaction of the $(\bar{N}N)^2$ type if they are reduced to the form $(\bar{N}N)(N^T C^{-1} C\bar{N}^T)$ and if the Fierz transformation is performed. For the Lagrangian describing the $NN \to D$ transition, we then have (for example, in the state of isospin $I=0$)[4)]

$$\mathcal{L}_{NND} = \tilde{N}(x)\{\alpha_S^0 S(x) + \alpha_P^0\gamma_5 P(x) + \alpha_V^0\gamma^\mu V_\mu(x) + \alpha_A^0\gamma_5\gamma^\mu A_\mu(x) + \alpha_T^0\sigma^{\mu\nu}V_{\mu\nu}(x)\}N(x), \quad (1)$$

where α_i^I (I labels an isospin state) are coupling constants; S, P, V_μ, and A_μ stand for, respectively, scalar,

[4)] As usual, we mean that the summation is performed over the dummy Greek indices.

pseudoscalar, vector, and axially vector dibaryon fields; $\sigma_{\mu\nu} = i[\gamma_\mu, \gamma_\nu]/2$; and $V_{\mu\nu} = \partial_\mu V_\nu - \partial_\nu V_\mu$.

In our model, a dibaryon is produced upon color exchange between two quarks belonging to different nucleons. Since this interaction can occur not only in the interior of nucleons but also at their periphery, the dimensions of the product dibaryon appear to be commensurate with the dimensions of the NN-interaction range of interest (that is, ≤ 1.0 fm); therefore, the dibaryon is not a pointlike particle. It follows that the nucleon current J_N and, hence, the interaction Lagrangian $\mathcal{L}_{NND}$ become nonlocal functions of coordinates. As a result, the required amplitude for the $NN \to D(CC) \to NN$ transition can be represented as the amplitude describing the scattering of a nucleon on an antinucleon moving in the opposite direction in Minkowski space; that is,

$$M_{fi} = \frac{i}{2!} \times \sum_{S,I,P} \int d^4x_1 d^4x_2 d^4x_3 d^4x_4 \langle 4,3|\mathrm{T}[J_N^{(SI)^P\dagger}(x_3,x_4)\Psi_{\mathrm{DB}}^{(SI)^P}(x_3,x_4)\Psi_{\mathrm{DB}}^{(SI)^P}(x_1,x_2)J_N^{(SI)^P}(x_1,x_2)]|2,1\rangle, \quad (2)$$

where T is the symbol of chronological ordering in the respective product; the operator

$$J_N^{(SI)^P}(x_1,x_2) = \tilde{N}(x_1)\Gamma^{(S,T)^P}N(x_2)$$

corresponds to a nonlocal nucleon current; $\Gamma^{(S,I)^P}$ is the vertex operator transforming a nonconfined nucleon–nucleon state into a confined dibaryon state D; $\Psi_{\mathrm{DB}}^{(SI)^P}(x_1,x_2)$ is the operator of the field that corresponds to the deformed six-quark bag (excited string) in the state specified by the spin S, the isospin I, and the parity P; and summation is performed over all possible values of S, I, and P.

The only result of an individual chronological ordering with respect to the coordinates x_3, x_4 and x_1, x_2 is that, in integration, the time components of the relative coordinates $x = x_1 - x_2$ and $x' = x_3 - x_4$ can take both positive and negative values. A mixed chronological ordering—for example, with respect to the coordinates x_1, x_3 and x_2, x_4—leads to the appearance of two types of exchange interaction that are shown in Fig. 2. The first type of interaction (first diagram in Fig. 2)—this is s-channel dibaryon exchange—is resonant, and the terms proportional to $\theta(x_1^0 - x_3^0)\theta(x_2^0 - x_4^0)$ and $\theta(x_3^0 - x_1^0)\theta(x_4^0 - x_2^0)$ [where $\theta(x)$ is a theta function] correspond to it in the matrix element (2). The second type of interaction is nonresonant, and t- and u-channel dibaryon exchanges generate it. In the following, we will disregard this interaction.[5)]

As a result, the matrix element assumes the form

$$M_{fi} = \frac{1}{2!} \times \sum_{S,I,P} \int d^4x_1 d^4x_2 d^4x_3 d^4x_4 \langle 4,3|\bar{N}(x_4)(\Gamma^{(SI)^P})^\dagger \bar{\tilde{N}}(x_3)\mathcal{G}^{(SI)^P}(x_3,x_4;x_1,x_2)\tilde{N}(x_1)\Gamma^{(SI)^P}N(x_2)|2,1\rangle, \quad (3)$$

where

$$\mathcal{G}^{(SI)^P}(x_3,x_4;x_1,x_2) = i\langle 0|\mathrm{T}_{X,X'}[\Psi_{\mathrm{DB}}^{(SI)^P}(x_3,x_4)\Psi_{\mathrm{DB}}^{(SI)^P}(x_1,x_2)]|0\rangle$$

is an exact dibaryon Green's function that takes into account the dressing of a dibaryon with meson fields and where the chronological ordering is performed with respect to the coordinates X and X' of the dibaryon center of mass. The dressed-dibaryon Green's function is found by solving the Dyson equation

$$\mathcal{G}^{(SI)^P}(x_3,x_4;x_1,x_2) = G^{(SI)^P}(x_3,x_4;x_1,x_2) + \int d^4x_1' d_4x_2' d^4x_3' d^4x_4' G^{(SI)^P}(x_3,x_4;x_3',x_4') \times \Pi^{(SI)^P}(x_3',x_4';x_1',x_2')\mathcal{G}^{(SI)^P}(x_1',x_2';x_1,x_2), \quad (4)$$

where Π stands for a polarization operator.

Since we neglect here color tensor interaction between quarks, which, as is well known, is rather weak, the total spin of the system is conserved in the $NN \to D$ transition. Therefore, $(0,1)^+$ or $(1,0)^+$ and $(0,0)^-$

[5)] This six-quark state corresponds to a heavy exotic $\bar{N}N$ meson rather than to a dibaryon, since it is produced in the s channel of the cross-symmetric reaction of nucleon–antinucleon scattering.

or $(1,1)^-$ states are the possible $(S,I)^P$ states of a dibaryon in, respectively, even and odd partial waves. In this case, summation in the matrix element (3) will be performed over precisely these allowed states.

The zeroth-order Green's function $G^{(SI)^P}$ is defined as the vacuum expectation value over the bare dibaryon state. Since a dibaryon is a free particle, its Green's function depends only on the difference of the coordinates of its center of mass rather than on these coordinates individually (the same is valid for the polarization operator $\Pi^{(SI)^P}$). In the $(S,I)^P = (0,1)^+$ channel, we have[6)]

$$G^{(0,1)^+}(x,x',X-X') = i\sum_{N_e=\text{even}} f_{N_e}(x;P) \quad (5)$$
$$\times \langle 0|\mathrm{T}_{\mathrm{X,X'}}[S_{N_e}(X)S^\dagger_{N_e}(X')]|0\rangle f_{N_e}(x';P)$$
$$= \sum_{N_e=\text{even}} f_{N_e}(x;P)f_{N_e}(x';P)G_{N_e}(X-X'),$$

where $f_{N_e}(x;P)$ is the wave function describing the relative motion of two $3q(C)$ clusters and N_e is the number of string-excitation quanta. For the $(S,I)^P = (1,0)^+$ state, we similarly have

$$G^{(1,0)^+}_{\mu\nu}(x,x',X-X') = i\sum_{N_e=\text{even}} f_{N_e}(x;P) \quad (6)$$
$$\times \langle 0|\mathrm{T}_{\mathrm{X,X'}}[A_{N_e,\mu}(X)A^\dagger_{N_e,\nu}(X')]|0\rangle f_{N_e}(x';P)$$
$$= \sum_{N_e=\text{even}} f_{N_e}(x;P)f_{N_e}(x';P)G_{N_e,\mu\nu}(X-X').$$

The Green's functions G_{N_e} and $G_{N_e,\mu\nu}$ are ordinary propagators for scalar and vector particles; that is,

$$\frac{1}{P^2-M^2_{N_e}+i0} = \int e^{iP\xi}G_{N_e}(\xi)d^4\xi,$$
$$\frac{-g_{\mu\nu}+P_\mu P_\nu/M^2_{N_e}}{P^2-M^2_{N_e}+i0} = \int e^{iP\xi}G_{N_e,\mu\nu}(\xi)d^4\xi,$$

where $g_{\mu\nu}$ is the metric tensor and M_{N_e} is the mass of a bare dibaryon in a state where the number of string-excitation quanta is N_e. Similar considerations hold for the Green's functions in odd partial waves. Accordingly, we have

$$G^{(0,0)^-}(x,x',X-X') = i\sum_{N_e=\text{odd}} f_{N_e}(x;P) \quad (7)$$
$$\times \langle 0|\mathrm{T}_{\mathrm{X,X'}}[S_{N_e}(X)S^\dagger_{N_e}(X')]|0\rangle f_{N_e}(x';P)$$
$$= \sum_{N_e=\text{odd}} f_{N_e}(x;P)f_{N_e}(x';P)G_{N_e}(X-X'),$$

$$G^{(1,1)^-}_{\mu\nu}(x,x',X-X') = i\sum_{N_e=\text{odd}} f_{N_e}(x;P) \quad (8)$$
$$\times \langle 0|\mathrm{T}_{\mathrm{X,X'}}[A_{N_e,\mu}(X)A^\dagger_{N_e,\nu}(X')]|0\rangle f_{N_e}(x';P)$$
$$= \sum_{N_e=\text{odd}} f_{N_e}(x;P)f_{N_e}(x';P)G_{N_e,\mu\nu}(X-X').$$

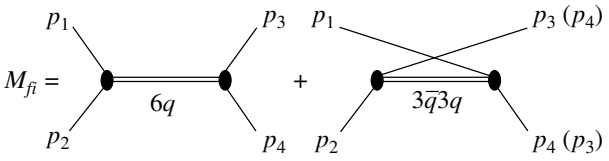

Fig. 2. Diagrams representing the amplitude in (2). The first diagram corresponds to s-channel dibaryon exchange, while the second diagram describes the u- or the t-channel exchange of a heavy $\bar{N}N$ meson having an exotic $3\bar{q}3q$ structure.

In Eqs. (5)–(8), summation is performed over all eigenstates of the string. The spin wave functions S and A_μ corresponding to scalar and pseudovector fields, respectively, are rank-2 tensors in spinor space and are constructed from combinations of two spinor functions for a positive definite value of energy. Here, we have disregarded the possible states of the pseudoscalar and vector types, since they have a relativistic nature caused by the mixing of positive- and negative-energy spinors and correspond to the t- or u-channel (rather than the s-channel) dibaryon-exchange mechanism (see Fig. 2, the second diagram).

Upon the substitution of expression (5) into Eq. (4), the exact Green's function in the $(S,I)^P = (0,1)^+$ channel can be represented in the form

$$\mathcal{G}^{(0,1)^+}(x,x',X-X') \quad (9)$$
$$= \sum_{N_e,N'_e=\text{even}} f_{N_e}(x;P)\mathcal{G}^{(0,1)^+}_{N_eN'_e}(X-X')f_{N'_e}(x';P),$$

where $\mathcal{G}^{(0,1)^+}_{N_eN'_e}$ satisfies the modified Dyson equation

$$\mathcal{G}^{(0,1)^+}_{N_eN'_e}(X-X') = G_{N_e}(X-X')\delta_{N_eN'_e} \quad (10)$$
$$+\sum_{N''_e}\int d^4x''d^4x'''d^4X''d^4X'''G_{N_e}(X-X'')$$
$$\times f_{N_e}(x'';P)\Pi^{(0,1)^+}(x'',x''',X''-X''')$$
$$\times f_{N''_e}(x''';P)\mathcal{G}^{(0,1)^+}_{N''_eN'_e}(X'''-X').$$

[6)]For the sake of simplicity, we will henceforth consider dibaryon states of total angular momentum $J=0,1$ and orbital angular momentum $L=0,1$. The spin wave-function components corresponding to higher values of J are rank-J tensors in Lorentz indices and are contracted with the corresponding components of the orbital parts of the wave functions.

Further, we determine the polarization operator projected onto the space of functions $f_{N_e}(x;P)$,

$$\tilde{\Pi}^{(SI)^P}_{N_eN'_e}(X''-X''') = \int d^4x''d^4x''' f_{N_e}(x'';P) \quad (11)$$
$$\times\, \Pi^{(SI)^P}(x'',x''',X''-X''')f_{N'_e}(x''';P),$$

and go over to the momentum representation. As a result, we obtain, for the matrix operator $\mathcal{G}^{(0,1)^+}_{N_eN'_e}$, the set of coupled algebraic equations

$$\mathcal{G}^{(0,1)^+}_{N_eN'_e}(P^2) = \frac{\delta_{N_eN'_e}}{P^2-M^2_{N_e}+i0} \quad (12)$$
$$+\sum_{N''_e}\frac{\tilde{\Pi}^{(0,1)^+}_{N_eN''_e}(P^2)}{P^2-M^2_{N_e}+i0}\mathcal{G}^{(0,1)^+}_{N''_eN'_e}(P^2).$$

A similar argument is applicable to the exact propagator in the $(1,0)^+$ state. This yields

$$\mathcal{G}^{(1,0)^+}_{\mu\nu}(x,x',X-X') \quad (13)$$
$$=\sum_{N_e,N'_e=\text{even}} f_{N_e}(x;P)\mathcal{G}^{(1,0)^+}_{N_eN'_e,\mu\nu}(X-X')f_{N'_e}(x';P),$$

where the function $\mathcal{G}^{(1,0)^+}_{N_eN'_e,\mu\nu}$ in the momentum representation satisfies the set of equations[7)]

$$\mathcal{G}^{(1,0)^+,\mu\nu}_{N_eN'_e}(P) = G^{\mu\nu}_{N_e}(P)\delta_{N_eN'_e} \quad (14)$$
$$+\sum_{N''_e}G^{\mu\alpha}_{N_e}(P)\tilde{\Pi}^{(1,0)^+}_{N_eN''_e,\alpha\beta}(P)\mathcal{G}^{(1,0)^+,\beta\nu}_{N''_eN'_e}(P).$$

The projected operator $\tilde{\Pi}^{(1,0)^+}_{N_eN''_e,\alpha\beta}(P)$ is defined in the same way as that in (11), but, now, the polarization operator $\Pi^{(SI)^P}$ is a rank-2 tensor in 4-vector indices. The functions $G^{\mu\nu}_{N_e}(P)$, $\tilde{\Pi}^{(S,I)^P}_{N_eN'_e,\mu\nu}(P)$, and $\mathcal{G}^{(SI)^P,\mu\nu}_{N_eN'_e}(P)$ depend only on the 4-vector P, which is the dibaryon 4-momentum. In terms of this 4-vector, one can construct two independent rank-2 tensors $\mathcal{P}^0_{\mu\nu}=P_\mu P_\nu/P^2$ and $\mathcal{P}^1_{\mu\nu}=g_{\mu\nu}-P_\mu P_\nu/P^2$, which have the meaning of the operators of projection onto spin-0 and spin-1 states, respectively. With allowance for this, the tensor structure of the above functions can be represented in the form

$$G^{\mu\nu}_{N_e}(P) = -\frac{\mathcal{P}^{1,\mu\nu}}{P^2-M^2_{N_e}+i0}+\frac{\mathcal{P}^{0,\mu\nu}}{M^2_{N_e}}, \quad (15)$$

$$\tilde{\Pi}_{\mu\nu}(P) = -\tilde{\Pi}_{(1)}(P^2)\mathcal{P}^1_{\mu\nu}+\tilde{\Pi}_{(0)}(P^2)\mathcal{P}^0_{\mu\nu}, \quad (16)$$

$$\mathcal{G}^{\mu\nu}(P) = -\mathcal{G}_{(1)}(P^2)\mathcal{P}^{1,\mu\nu}+\mathcal{G}_{(0)}(P^2)\mathcal{P}^{0,\mu\nu} \quad (17)$$

(for the sake of simplicity, we have suppressed the remaining indices on $\tilde{\Pi}$ and $\mathcal{G}$). Instead of the set of Eqs. (14), we then have the following decoupled set of equations for the individual components $\mathcal{G}_{(1)}$ and $\mathcal{G}_{(0)}$ of the resolvent matrix; that is,

$$\mathcal{G}^{(1,0)^+}_{(1),N_eN'_e}(P^2) = \frac{\delta_{N_eN'_e}}{P^2-M^2_{N_e}+i0} \quad (18)$$
$$+\sum_{N''_e}\frac{\tilde{\Pi}^{(1,0)^+}_{(1),N_eN''_e}(P^2)}{P^2-M^2_{N_e}+i0}\mathcal{G}^{(1,0)^+}_{(1),N''_eN'_e}(P^2),$$

$$\mathcal{G}^{(1,0)^+}_{(0),N_eN'_e}(P^2) = \frac{\delta_{N_eN'_e}}{M^2_{N_e}} \quad (19)$$
$$+\sum_{N''_e}\frac{\tilde{\Pi}^{(1,0)^+}_{(0),N_eN''_e}(P^2)}{M^2_{N_e}}\mathcal{G}^{(1,0)^+}_{(0),N''_eN'_e}(P^2).$$

Since the functions $\tilde{\Pi}^{(SI)^P}_{(i),N_eN''_e}(P^2)$ are analytic, the pole singularity can appear only in that part of the dibaryon propagator which corresponds to spin-1 states [that is, $\mathcal{G}^{(1,0)^+}_{(1),N_eN'_e}(P^2)$]. This also applies to the propagator in the $(0,1)^+$ channel [it is determined by the set of Eqs. (12)]. Because of the dressing of the dibaryon with a meson cloud, the pole position appears to be shifted from the real axis to the plane of complex values of P^2 and corresponds to a resonance state of the dressed six-quark bag. As for the contribution to the nucleon–nucleon potential from unphysical states of spin zero, which are developed for an off-shell vector particle and which are inherent in a field-theory description of particles having higher spins, it is of order $1/M^2_{N_e}$ and is therefore disregarded in the following.

The dibaryon Green's functions in the $(S,I)^P=(0,0)^-$ and $(1,1)^-$ odd channels, $\mathcal{G}^{(0,0)^-}_{N_eN_{e'}}$ and $\mathcal{G}^{(1,1)^-}_{(1),N_eN'_e}$, are also determined by relations that are similar to (12) and (18), but which involve an odd number N_e of string-excitation quanta.

In order to determine the wave functions $f_{N_e}(x;P)$, we will use the covariant-harmonic-oscillator formalism [39, 40]. Although there is presently no direct connection between this formalism and QCD, its application appeared to be quite successful in describing the baryon spectra and the systematics of $\bar{q}q$ meson states; in addition, it leads to hadron form factors whose behavior agrees well with experimental data. For its microscopic basis, one can employ the formalism of a Dirac harmonic oscillator [41, 42], where the Dirac equation with

[7)] For the sake of convenience, we will henceforth use subscripts or superscripts on 4-vectors and 4-tensors without implying multiplication by the metric tensor.

a linear vector potential corresponding to a string-type interaction reduces to an equation of the Klein–Gordon type with a conventional quadratic oscillator potential (see also [43]).

In the covariant-harmonic-oscillator formalism, spin wave functions satisfy the standard Klein–Gordon equation

$$\left(\partial^2/\partial X_\mu^2 - M_{N_e}^2\right) S_{N_e}(X;P) = 0, \qquad (20)$$

and the identical equation holds for A_μ, the relation $P^\mu A_\mu = 0$ being valid.

The relative-motion wave function $f_{N_e}(x;P)$ is a rank-N_e tensor in the $O(3,1)_{\text{Lorentz}}$ space and satisfies the equation [44]

$$\mathcal{M}^2(x_\mu, \partial/\partial x_\mu) f_{N_e}(x;P) = M_{N_e}^2 f_{N_e}(x;P). \quad (21)$$

The square of the mass operator is given by

$$\mathcal{M}^2 \equiv d\left(-\frac{1}{2\mu}\frac{\partial^2}{\partial x_\mu^2} + U(x)\right), \qquad (22)$$

$$d = 2(m_1+m_2), \quad \mu = m_1 m_2/(m_1+m_2),$$

where m_i are the kinematical masses of the $3q(C)$ clusters forming the dibaryon D. The potential $U(x)$ can be represented as the sum

$$U = U_{\text{conf}} + U_{\text{pert.QCD}}, \qquad (23)$$

where the first term corresponds to confinement, while the second term takes into account various perturbative effects—in particular, one-gluon exchange. In the present study, the potential U_{conf} is determined by the potential energy of the string and a nonperturbative interaction of the instanton type; that is,

$$U(x) = (1/2)Kx_\mu^2 + C. \qquad (24)$$

As to the perturbative term $U_{\text{pert.QCD}}$, whose effect reduces to deviating the Regge trajectory from a linear dependence and to somewhat modifying the oscillator wave function at small x, it is disregarded here. With allowance for (21), (22), and (24), we then have

$$f_0(x;P) \equiv \langle x|G(P)\rangle \qquad (25)$$

$$= \frac{\beta}{\pi}\exp\left[\frac{\beta}{2}\left(x^2 - 2\frac{(Px)^2}{P^2}\right)\right],$$

$$f_{N_e}(x;P) = \langle x|a^\dagger_{\nu_{N_e}}\ldots a^\dagger_{\nu_1}|G(P)\rangle, \qquad (26)$$

$$M_{N_e}^2 = dC + (N_e+1)\Omega = M_0^2 + N_e\Omega, \qquad (27)$$

where $a_\nu^\dagger = (\beta x_\nu + \partial/\partial x_\nu)/(2\beta)^{1/2}$ is the operator of oscillator-quantum creation, $\beta^{-1} = (\mu K)^{-1/2}$ is the square of the oscillator radius, and $\Omega = d(K/\mu)^{1/2}$ is the oscillator frequency. For the mass spectrum, we thus obtain a linear Regge trajectory. The operators $a_\nu^\dagger$ are defined in such a way that a physical state satisfies the condition,

$$P^\nu a_\nu^\dagger|\text{phys}\rangle = 0,$$

which rules out the appearance of an unphysical spectrum with respect to the time coordinate.

For example, the function corresponding to a single-quantum excitation of the oscillator can be represented in the form

$$f_\mu(x;P) = \sqrt{2\beta}\left(x_\mu - \frac{(Px)P_\mu}{P^2}\right) f_0(x;P).$$

This function is normalized by the condition

$$N_{\mu\nu} \equiv \int f_\mu(x;P) f_\nu(x;P) d^4x = -g_{\mu\nu} + \frac{P_\mu P_\nu}{P^2}.$$

In the case of a two-quantum excitation, two oscillator states are possible,

$$f_{\mu\nu}(x;P) = \left[g_{\mu\nu} - \frac{P_\mu P_\nu}{P^2}\right.$$

$$\left. + 2\beta\left(x_\mu - \frac{(Px)P_\mu}{P^2}\right)\left(x_\nu - \frac{(Px)P_\nu}{P^2}\right)\right] f_0(x),$$

$$f_{\mu\mu}(x;P) = \left(3 + 2\beta x^2 - 2\beta\frac{(Px)^2}{P^2}\right) f_0(x;P),$$

which are normalized as follows:

$$N_{\mu\nu,\alpha\beta} \equiv \int f_{\mu\nu}(x) f_{\alpha\beta}(x) d^4x$$

$$= \left(g_{\mu\alpha} - \frac{P_\mu P_\alpha}{P^2}\right)\left(g_{\nu\beta} - \frac{P_\nu P_\beta}{P^2}\right)$$

$$+ \left(g_{\mu\beta} - \frac{P_\mu P_\beta}{P^2}\right)\left(g_{\nu\alpha} - \frac{P_\nu P_\alpha}{P^2}\right).$$

We now return to expression (3) for the reaction amplitude. The vertex operators $\Gamma^{(SI)^P}$ are determined by the Lorentz-invariant structure of the Lagrangian $\mathcal{L}_{NND}$ and, in various $(S,I)^P$ channels, have the form

$$\Gamma_\mu^{(1,0)^+} = \alpha_A^0 \gamma_5\gamma_\mu, \quad \Gamma_a^{(0,1)^+} = \alpha_S^1\tau_a,$$

$$\Gamma^{(0,0)^-} = \alpha_S^0, \quad \Gamma_{\mu,a}^{(1,1)^-} = \alpha_A^1\gamma_5\gamma_\mu\tau_a,$$

where a is the isospin index and the constants α correspond to the $NN \to D$ Lagrangian (1). Further, we use the relationship between the bispinors corresponding to positive- and negative-energy states (the notation here was borrowed from [45]),

$$v(\mathbf{p},s) = C\bar{u}^T(\mathbf{p},s), \qquad (28)$$

$$\bar{v}(\mathbf{p},s) = -u^T(\mathbf{p},s)C^{-1},$$

and go over to the relative coordinates and the coordinates of the nucleon center of mass. For the matrix

elements in the $(S,I)^P = (0,1)^+$, $(1,0)^+$, $(0,0)^-$, and $(1,1)^-$ channels, we then obtain the expressions

$$M_{fi}^{(0,1)^+} = -2(\alpha_S^1)^2[\bar{u}(\mathbf{p}_4,s_4)\gamma_5 v(\mathbf{p}_3,s_3)] \times [\bar{v}(\mathbf{p}_1,s_1)\gamma_5 u(\mathbf{p}_2,s_2)] I_1 F^{(0,1)^+} \times \delta^4(p_1+p_2-p_3-p_4), \quad (29)$$

$$M_{fi}^{(1,0)^+} = -2(\alpha_A^0)^2[\bar{u}(\mathbf{p}_4,s_4)\gamma^\mu v(\mathbf{p}_3,s_3)] \times [\bar{v}(\mathbf{p}_1,s_1)\gamma^\nu u(\mathbf{p}_2,s_2)]\mathcal{P}^1_{\mu\nu} I_0 F^{(1,0)^+} \times \delta^4(p_1+p_2-p_3-p_4), \quad (30)$$

$$M_{fi}^{(0,0)^-} = -2(\alpha_S^0)^2[\bar{u}(\mathbf{p}_4,s_4)\gamma_5 v(\mathbf{p}_3,s_3)] \times [\bar{v}(\mathbf{p}_1,s_1)\gamma_5 u(\mathbf{p}_2,s_2)] I_0 F^{(0,0)^-} \times \delta^4(p_1+p_2-p_3-p_4), \quad (31)$$

$$M_{fi}^{(1,1)^-} = -2(\alpha_A^1)^2[\bar{u}(\mathbf{p}_4,s_4)\gamma^\mu v(\mathbf{p}_3,s_3)] \times [\bar{v}(\mathbf{p}_1,s_1)\gamma^\nu u(\mathbf{p}_2,s_2)]\mathcal{P}^1_{\mu\nu} I_1 F^{(1,1)^-} \times \delta^4(p_1+p_2-p_3-p_4), \quad (32)$$

where the factor of 2 arises in the amplitude because of antisymmetrization with respect to the nucleon variables. In contrast to the t-channel interaction mechanism, where antisymmetrization occurs at the level of Feynman diagrams, it is achieved here even at the level of vertices, with the result that the amplitude M_{fi} appears to be automatically antisymmetrized.

In the $I=1$ channels, the isospin factor is given by

$$I_1 = (\chi_4^\dagger \boldsymbol{\tau}\tau_2\chi_3)(\chi_1^\dagger\tau_2\boldsymbol{\tau}\chi_2) = \begin{cases} 1 \text{ for } pn \text{ scattering} \\ 2 \text{ for } pp \text{ scattering}, \end{cases} \quad (33)$$

while, in the $I=0$ channels, it is

$$I_0 = (\chi_4^\dagger\tau_2\chi_3)(\chi_1^\dagger\tau_2\chi_2) = 1, \quad (34)$$

where χ_i is the isospin part of the ith-nucleon wave function. It should be mentioned here that, owing to the isospin factor, the proton–proton potential is two times greater than the proton–neutron potential. However, it should be borne in mind that the resulting proton–proton potential appears to be antisymmetrized. In calculating the proton–proton phase shifts, it must therefore be divided by a factor of 2 (whereupon we obtain isotopic invariance). But in subsequently calculating the cross sections or other features, we must again multiply by a factor of 2 the final amplitude derived with this potential.

The form factors F in expressions (29)–(32) play the role of invariant amplitudes (that is, the amplitude obtained upon the separation of the spin and isospin variables) and ensure the necessary splitting of the nucleon–nucleon potential in the orbital angular momentum.

Let us demonstrate how there occurs the reduction of the transition matrix elements $M_{fi}^{(SI)^P}$. Taking into account the results for the dibaryon Green's functions (9) and (13), we can represent the form factors $F^{(SI)^P}$ as

$$F^{(0,1)^+} = \sum_{N_e,N_e'=\text{even}} f_{N_e}(q',P)\mathcal{G}^{(0,1)^+}_{N_eN_e'}(P^2) f_{N_e'}(q,P), \quad (35)$$

$$F^{(1,0)^+} = \sum_{N_e,N_e'=\text{even}} f_{N_e}(q',P)\mathcal{G}^{(1,0)^+}_{(1),N_eN_e'}(P^2) f_{N_e'}(q,P), \quad (36)$$

$$F^{(0,0)^-} = \sum_{N_e,N_e'=\text{odd}} f_{N_e}(q',P)\mathcal{G}^{(0,0)^-}_{N_eN_e'}(P^2) f_{N_e'}(q,P), \quad (37)$$

$$F^{(1,1)^-} = \sum_{N_e,N_e'=\text{odd}} f_{N_e}(q',P)\mathcal{G}^{(1,1)^-}_{(1),N_eN_e'}(P^2) f_{N_e'}(q,P), \quad (38)$$

where $q' = (p_3-p_4)/2$ and $q=(p_1-p_2)/2$ are, respectively, the final and the initial relative 4-momentum of nucleons and

$$f_{N_e}(q,P) = \int d^4x e^{iqx} f_{N_e}(x;P) \quad (39)$$

is the Fourier component of the dibaryon wave function for a state where the number of excitation quanta is N_e. The propagators for the spin-0 and spin-1 dibaryons of positive parity are determined by Eqs. (12) and (18).

In principle, summation in (35)–(38) is performed over all possible values of N_e. However, the $N_e=0$ and $N_e=1$ terms, which correspond to the coupling of the nucleon–nucleon channel to the closed dibaryon state $D(CC)$ occurring in the maximally symmetric six-quark configurations $|s^6\rangle$ or $|s^5p\rangle$, yield, at low energies ($E<1$ GeV), only a weak attraction in the nucleon–nucleon system against the background of a strong nucleon–nucleon repulsion in these six-quark configurations that is induced by the one-gluon-exchange and one-pion-exchange mechanisms that describe the interaction between quarks and which take into account the effects of antisymmetrization with respect to the quark variables [37, 38]. On the other hand, the effects of antisymmetrization in deformed six-quark configurations play an insignificant role, the effective masses of these

states being strongly shifted toward the low-energy region because of the strong coupling of the excited string to meson fields. As a result, the coupling to low-lying excited dibaryon states featuring $N_e = 2$ and $N_e = 3$ string-excitation quanta (these values of N_e corresponds to the six-quark configurations $|s^4p^2[42]\rangle$ and $|s^3p^3[33]\rangle$, respectively[8]) leads to a strong attraction in the nucleon–nucleon system even at rather low interaction energies. In this model, the attraction in question plays the same role as the t-channel exchange of a sigma meson and also as coupling to the $N\Delta$ and $\Delta\Delta$ channels in the standard one-boson-exchange model.[9]

From expressions (29)–(32), it can be seen that the potentials in the $(S,I)^P = (0,1)^+$ and $(0,0)^-$ states have identical spinor components, and so do the potentials in the $(1,0)^+$ and $(1,1)^-$ states. In the above form, their structure is more appropriate for describing the cross-symmetry reaction of nucleon–antinucleon scattering. In order to accomplish a transition to the nucleon–nucleon channel, it is necessary to use the Fierz transformation

$$[\bar\psi\Gamma_i\phi][\bar\phi\Gamma_j\psi] = \frac{1}{16}\sum_{k,l=1}^{16}\mathrm{Tr}(\Gamma_i\Gamma_k\Gamma_j\Gamma_l)[\bar\psi\Gamma^k\psi][\bar\phi\Gamma^l\phi], \tag{40}$$

where Γ_i corresponds to one of the 16 Dirac matrices $\{\mathbf{1}, \gamma_5, \gamma_\mu, \gamma_5\gamma_\mu, \sigma_{\mu\nu}\}$ forming a basis in the space of 4×4 matrices and ψ and ϕ stand for spinor functions. By using relation (28) and the fact that the Dirac matrices satisfy the relations $\gamma_\mu^T = -C^{-1}\gamma_\mu C$ and $[C,\gamma_5] = 0$, we then obtain in the c.m. frame ($p_1 = q$, $p_2 = -q$, $p_3 = q'$, and $p_4 = -q'$)

$$\begin{aligned}
&[\bar u(-\mathbf{q}')\gamma_5 v(\mathbf{q}')][\bar v(\mathbf{q})\gamma_5 u(-\mathbf{q})] \qquad (41)\\
&= -\frac{1}{4}[\bar u(\mathbf{q}')u(\mathbf{q})][\bar u(-\mathbf{q}')u(-\mathbf{q})]\\
&-\frac{1}{4}[\bar u(\mathbf{q}')\gamma_\mu u(\mathbf{q})][\bar u(-\mathbf{q}')\gamma^\mu u(-\mathbf{q})]\\
&+\frac{1}{8}[\bar u(\mathbf{q}')\sigma_{\mu\nu} u(\mathbf{q})][\bar u(-\mathbf{q}')\sigma^{\mu\nu} u(-\mathbf{q})]\\
&-\frac{1}{4}[\bar u(\mathbf{q}')\gamma_5\gamma_\mu u(\mathbf{q})][\bar u(-\mathbf{q}')\gamma_5\gamma^\mu u(-\mathbf{q})]\\
&-\frac{1}{4}[\bar u(\mathbf{q}')\gamma_5 u(\mathbf{q})][\bar u(-\mathbf{q}')\gamma_5 u(-\mathbf{q})],
\end{aligned}$$

$$\begin{aligned}
&[\bar u(-\mathbf{q}')\gamma^\mu v(\mathbf{q}')][\bar v(\mathbf{q})\gamma^\nu u(-\mathbf{q})]\mathcal{P}^1_{\mu\nu} \qquad (42)\\
&= -[\bar u(-\mathbf{q}')\boldsymbol{\gamma} v(\mathbf{q}')][\bar v(\mathbf{q})\boldsymbol{\gamma} u(-\mathbf{q})]\\
&= -\frac{3}{4}[\bar u(\mathbf{q}')u(\mathbf{q})][\bar u(-\mathbf{q}')u(-\mathbf{q})]\\
&-\frac{1}{2}[\bar u(\mathbf{q}')\gamma_0 u(\mathbf{q})][\bar u(-\mathbf{q}')\gamma_0 u(-\mathbf{q})]\\
&-\frac{1}{4}[\bar u(\mathbf{q}')\gamma_\mu u(\mathbf{q})][\bar u(-\mathbf{q}')\gamma^\mu u(-\mathbf{q})]\\
&-\frac{1}{8}[\bar u(\mathbf{q}')\sigma_{\mu\nu} u(\mathbf{q})][\bar u(-\mathbf{q}')\sigma^{\mu\nu} u(-\mathbf{q})]\\
&+\frac{1}{2}[\bar u(\mathbf{q}')\sigma_{0\mu} u(\mathbf{q})][\bar u(-\mathbf{q}')\sigma^{0\mu} u(-\mathbf{q})]\\
&+\frac{1}{4}[\bar u(\mathbf{q}')\gamma_5\gamma_\mu u(\mathbf{q})][\bar u(-\mathbf{q}')\gamma_5\gamma^\mu u(-\mathbf{q})]\\
&+\frac{1}{2}[\bar u(\mathbf{q}')\gamma_5\gamma_0 u(\mathbf{q})][\bar u(-\mathbf{q}')\gamma_5\gamma_0 u(-\mathbf{q})]\\
&+\frac{3}{4}[\bar u(\mathbf{q}')\gamma_5 u(\mathbf{q})][\bar u(-\mathbf{q}')\gamma_5 u(-\mathbf{q})].
\end{aligned}$$

By using the expressions presented in the Appendix for the matrix elements of bispinors, we finally arrive at

$$\begin{aligned}
&[\bar u(-\mathbf{q}')\gamma_5 v(\mathbf{q}')][\bar v(\mathbf{q})\gamma_5 u(-\mathbf{q})] \qquad (43)\\
&= -\frac{(1-\boldsymbol{\sigma}_1\cdot\boldsymbol{\sigma}_2)}{2}W\left(1+\frac{\mathbf{q}'^2}{(E_{q'}+m_N)^2}\right)\\
&\times\left(1+\frac{\mathbf{q}^2}{(E_q+m_N)^2}\right),
\end{aligned}$$

$$\begin{aligned}
&[\bar u(-\mathbf{q}')\gamma^\mu v(\mathbf{q}')][\bar v(\mathbf{q})\gamma^\nu u(-\mathbf{q})]\mathcal{P}^1_{\mu\nu} \qquad (44)\\
&= -\frac{(3+\boldsymbol{\sigma}_1\cdot\boldsymbol{\sigma}_2)}{2}W\left(1+\frac{\mathbf{q}'^2+S_{12}(\mathbf{q}')}{3(E_{q'}+m_N)^2}\right)\\
&\times\left(1+\frac{\mathbf{q}^2+S_{12}(\mathbf{q})}{3(E_q+m_N)^2}\right).
\end{aligned}$$

Here, the factor W is given by the expression $W = (E_{q'}+m_N)(E_q+m_N)/(4m_N^2)$, where $E_q = (\mathbf{q}^2 + m_N^2)^{1/2}$ and m_N is the nucleon mass; the Pauli matrices $\boldsymbol{\sigma}_1$ and $\boldsymbol{\sigma}_2$ are defined in such a way that the operator $\boldsymbol{S} = (\boldsymbol{\sigma}_1+\boldsymbol{\sigma}_2)/2$ corresponds to the total spin of the nucleon–nucleon system; and $S_{12}(q) = 3(\boldsymbol{\sigma}_1\cdot\mathbf{q})(\boldsymbol{\sigma}_2\cdot\mathbf{q}) - \mathbf{q}^2(\boldsymbol{\sigma}_1\cdot\boldsymbol{\sigma}_2)$ stands for the tensor-interaction operator. For the expectation values in the spin-0 and spin-1 states, we have

$$\begin{aligned}
&\langle S=0|(1-\boldsymbol{\sigma}_1\cdot\boldsymbol{\sigma}_2)/2|S=0\rangle = 2,\\
&\langle S=1|(1-\boldsymbol{\sigma}_1\cdot\boldsymbol{\sigma}_2)/2|S=1\rangle = 0,\\
&\langle S=0|(3+\boldsymbol{\sigma}_1\cdot\boldsymbol{\sigma}_2)/2|S=0\rangle = 0,\\
&\langle S=1|(3+\boldsymbol{\sigma}_1\cdot\boldsymbol{\sigma}_2)/2|S=1\rangle = 2.
\end{aligned}$$

[8] These six-quark configurations appear to be basic ones if the motion of the collective center of mass is taken into account within the microscopic model.

[9] It should be noted, however, that, in order to achieve the required strength of the attractive force, the cutoff parameters $\Lambda_{\sigma NN}$ and $\Lambda_{\pi N\Delta}$ in one-boson-exchange models are increased by hand in relation to the values obtained from meson–nucleon dynamics and from numerous theoretical calculations.

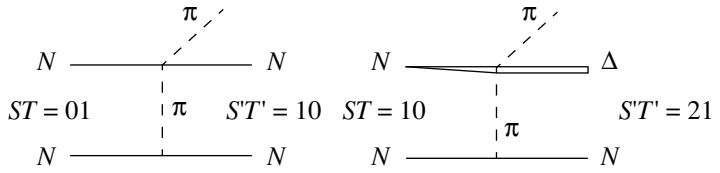

Fig. 3. Example of diagrams for $(S,T) \to (S',T')$ transitions within traditional one-boson-exchange models of the nucleon–nucleon interaction.

3. DERIVATION OF THE COVARIANT NUCLEON–NUCLEON POTENTIAL IN EVEN PARTIAL WAVES

In order that the complicated NN-interaction operator obtained within the formalism developed in the preceding section could be used in specific calculations, it is necessary to specify expressions for the form factors $F^{(SI)^P}$ explicitly. For this, we must determine the particular structure of the polarization operators $\Pi(x,x',X-X')$. We investigate this issue by considering the example of even partial waves.

In principle, the dibaryon polarization operator is predominantly determined by the $D\sigma$ and $D\pi$ loops, while its imaginary part is determined by the NN loop and is responsible for dibaryon decay to two real nucleons, which is followed by their fusion back into a dibaryon. In this case, however, we must exclude coupling to an intermediate nucleon–nucleon state, since, in the equation for nucleon–nucleon scattering, this channel is automatically taken into account by virtue of the requirement that the scattering amplitude satisfy two-particle unitarity. Therefore, the main contribution to the polarization operator comes from the dressing of the dibaryon D with meson clouds—namely, from pion- or sigma-meson-cloud-formation-induced transition of this dibaryon (featuring $N_e \geq 2$ string-excitation quanta) to the ground state $|s^6\rangle$ at low energies. At the same time, the interaction with rho and omega mesons makes a much smaller contribution both because of their rather large mass and because of the fact that these mesons can exist only in odd partial waves with respect to the dibaryon $|s^6\rangle$ or in even partial waves with respect to the excited configuration $|s^5p\rangle$, which has one excitation quantum Ω with respect to the excited configuration $|s^6\rangle$.

In view of parity and total-isospin conservation, transitions between the following $(S,I)^P$ states are possible:

$$(0,1)^+ \longrightarrow (0,1)^+|s^6\rangle + \sigma(L=\text{even}),$$
$$(0,1)^+ \longrightarrow (1,0)^+|s^6\rangle + \pi(L=\text{odd}),$$
$$(1,0)^+ \longrightarrow (1,0)^+|s^6\rangle + \sigma(L=\text{even}),$$
$$(1,0)^+ \longrightarrow (0,1)^+|s^6\rangle + \pi(L=\text{odd}),$$
$$(1,0)^+ \longrightarrow (2,1)^+|s^6\rangle + \pi(L=\text{odd}).$$

Here, we emphasize an important fact that directly follows from the above quantum numbers for the allowed transitions $NN \longrightarrow 6q+m$, where $m=\sigma$ or π. The s-channel transitions forming the intermediate states of the dressed dibaryon are fully in accord with ordinary t-channel transitions (see, for example, Fig. 3). It is precisely for this reason that the s-channel mechanisms considered here make those contributions to various high-momentum-transfer processes that were missing in the traditional one-boson-exchange approach. Within the present model, this important conclusion becomes clear even without specific calculations.

We would also like to indicate that a $(2,1)^+$ dibaryon state may be formed owing to the dressing of the dibaryon with a pion cloud. It was mentioned above that, since the instanton-induced interaction of the tensor type between quarks is rather weak, this state does not decay directly through the nucleon–nucleon channel, but it has a strong coupling to the $N\Delta$ channel. It is well known that the behavior of the $^1D_2$ phase shift for nucleon–nucleon scattering is indicative of the presence of a strong $N\Delta$ correlation, which is sizable even at energies of about 400 MeV in the laboratory frame. In contrast to one-boson-exchange models, however, where the formation of this state is due to t-channel pion exchange and requires the use of hard pion form factors,[10] our model proposes a totally new mechanism that is responsible for the formation of a $N\Delta$ state at short and intermediate distances and which is caused by the dressing of the dibaryon with the pion field; that is,

$$(0,1)^+ \longrightarrow (1,0)^+|s^6\rangle + \pi(L=\text{odd})$$
$$\longrightarrow (2,1)^+ \longrightarrow N\Delta(L_{N\Delta}=0, S=2, I=1).$$

[10] In particular, there are quite reliable indications in the literature that the cutoff parameter $\Lambda_{\pi N\Delta}$ must be at least 100 MeV less than $\Lambda_{\pi NN}$—that is, the $\pi N\Delta$ transition form factor must be rather soft ($\Lambda_{\pi N\Delta} \sim 400$–$500$ MeV/c)—this being in sharp contrast with the values of $\Lambda_{\pi N\Delta}$ that appear in the traditional one-boson-exchange model of the nucleon–nucleon interaction.

The elementary Lagrangians that correspond to the above transitions and which are responsible for dressing a bare intermediate dibaryon have the form

$$\mathcal{L}_{(0,1)^+(0,1)^+\sigma} = h^{(0)}_{D\sigma}\sigma(\mathbf{S}\cdot\mathbf{S}), \tag{45}$$

$$\mathcal{L}_{(1,0)^+(1,0)^+\sigma} = h^{(1)}_{D\sigma}\sigma(A_\mu A^\mu),$$

$$\mathcal{L}_{(0,1)^+(1,0)^+\pi} = \frac{h_{D\pi}}{m_\pi}(\mathbf{S}\cdot\partial_\mu\boldsymbol{\pi})A^\mu,$$

$$\mathcal{L}_{(1,0)^+(2,1)^+\pi} = \frac{h^{(1)}_{D\pi}}{m_\pi}(\mathbf{T}_{\mu\nu}\cdot\partial_\mu\boldsymbol{\pi})A_\nu,$$

where $\mathbf{S}$, A_μ, and $\mathbf{T}_{\mu\nu}$ are the operators of, respectively, the scalar, the axial-vector, and the tensor dibaryon fields; $\boldsymbol{\pi}$ and σ are the operators of, respectively, the isovector pion field and the isoscalar sigma-meson field; and m_π is the pion mass. The parameters $h_{D\pi}$ and $h_{D\sigma}$ correspond to the couplings of the respective mesons to the dibaryon. However, this structure of the Lagrangians implies the locality (pointlike character) of the interaction and, strictly speaking, is valid only for structureless particles. The inclusion of the internal structure—that is, the presence of the radial component of the wave function $f_{N_e}(x;P)$—results in that the Lagrangians become nonlocal functions of the particle coordinates. Hence, additional factors, which are form factors in the interaction vertices, can arise.

We begin by considering the polarization operator in the $(0,1)^+$ state and restrict ourselves to the one-channel approximation for the time being; that is,

$$\Pi^{(0,1)^+} = \Pi^{(0,1)^+}_\sigma + \Pi^{(0,1)^+}_\pi,$$

where the first and the second term correspond to, respectively, the interaction with the sigma-meson field and the interaction with the pion field. Taking into account (45), we then find, for example, for $\Pi^{(0,1)^+}_\sigma$ that

$$\Pi^{(0,1)^+}_\sigma(x,x',X-X') \tag{46}$$
$$= i\sum_{\substack{i,j=1\\ i\neq j}}^{2}\Gamma^\dagger_i f_0(x)\mathcal{G}^{(0,1)^+}_{00}(X-X')$$
$$\times G_\sigma(x_i-x'_j)f_0(x')\Gamma_j.$$

Here, $f_0(x)$ is the oscillator wave function (25), $\mathcal{G}^{(0,1)^+}_{00}$ is the exact propagator for the $|s^6;L=0\rangle$ dibaryon with $N_e=0$, and $G_\sigma(x)$ is the propagator for the sigma meson in the six-quark bag. Introducing the sigma-meson Green's function in the momentum representation, $G_\sigma(k^2)$, through the relation

$$G_\sigma(x_i-x'_j) = \int\frac{d^4k}{(2\pi)^4}e^{-ik(x_i-x'_j)}G_\sigma(k^2)$$

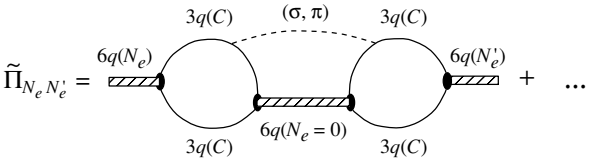

Fig. 4. Example of the diagrams determining the projected polarization operator. The sum also includes three analogous diagrams differing only in the permutation of the $3q(C)$ clusters.

and going over from the coordinates x_i and x'_j of the $3q(C)$ clusters to the relative coordinates x and x' and to the center-of-mass coordinates X and X', we can write the polarization operator in the form

$$\Pi^{(0,1)^+}_\sigma(x,x',X-X') \tag{47}$$
$$= i\frac{h^{(0)2}_{D\sigma}}{4}\int\frac{d^4k}{(2\pi)^4}(e^{ikx/2}+e^{-ikx/2})$$
$$\times f_0(x)G_\sigma(k^2)\mathcal{G}^{(0,1)^+}_{00}(X-X')e^{-ik(X-X')}$$
$$\times(e^{ikx'/2}+e^{-ikx'/2})f_0(x').$$

For the polarization operator describing the pion cloud in odd waves, we similarly have

$$\Pi^{(0,1)^+}_{\pi(\mathrm{odd})}(x,x',X-X') \tag{48}$$
$$= i\frac{h^2_{D\pi}}{4m^2_\pi}\int\frac{d^4k}{(2\pi)^4}(e^{ikx/2}+e^{-ikx/2})$$
$$\times f_0(x)G_\pi(k^2)k^\mu k^\nu\mathcal{G}^{(1,0)^+}_{00,\mu\nu}(X-X')e^{-ik(X-X')}$$
$$\times(e^{ikx'/2}+e^{-ikx'/2})f_0(x').$$

For the polarization operator $\tilde{\Pi}^{(0,1)^+}_{N_eN'_e}$ defined in (11) and projected onto the space of solutions obtained within the covariant-harmonic-oscillator formalism, we find in the momentum representation that (the Feynman diagrams corresponding to the polarization operator in question are shown in Fig. 4)

$$\tilde{\Pi}^{(0,1)^+}_{N_eN'_e}(P^2) = i\int\frac{d^4k}{(2\pi)^4}\Phi^{(\mathrm{even})}_{0N_e}(k,P) \tag{49}$$
$$\times\left(\frac{h^{(0)2}_{D\sigma}}{4}G_\sigma(k^2)\mathcal{G}^{(0,1)^+}_{00}(P-k)\right.$$
$$\left.+\frac{h^2_{D\pi}}{4m^2_\pi}G_\pi(k^2)k^\mu k^\nu\mathcal{G}^{(1,0)^+}_{00,\mu\nu}(P-k)\right)\Phi^{(\mathrm{even})}_{0N'_e}(k,P),$$

where

$$\Phi^{(\mathrm{even})}_{0N_e}(k,P) = \int d^4x(e^{ikx/2}+e^{-ikx/2})$$
$$\times f_0(x;P-k)f_{N_e}(x;P)$$

corresponds to the form factor in the vertices for the transitions $D \longrightarrow |s^6 + \sigma(L = \text{even})\rangle$ and $D \longrightarrow |s^6 + \pi(L = \text{odd})\rangle$, which do not change the intrinsic parity of the dibaryon.

We now proceed to consider the polarization operator in the $(1,0)^+$ state; that is, $\Pi^{(1,0)^+}_{\mu\nu}$. It can also be represented as the sum of two terms.[11] Using the Lagrangians in (45) for this state and following the same line of reasoning as above in deriving (47) and (48), we obtain

$$\Pi^{(1,0)^+}_{\sigma,\mu\nu}(x,x',X-X') \tag{50}$$
$$= i\frac{h^{(1)2}_{D\sigma}}{4}\int \frac{d^4k}{(2\pi)^4}(e^{ikx/2}+e^{-ikx/2})$$
$$\times f_0(x)G_\sigma(k^2)\mathcal{G}^{(1,0)^+}_{00,\mu\nu}(X-X')e^{-ik(X-X')}$$
$$\times (e^{ikx'/2}+e^{-ikx'/2})f_0(x'),$$

$$\Pi^{(1,0)^+}_{\pi(\text{odd}),\mu\nu}(x,x',X-X') \tag{51}$$
$$= i\frac{3h^2_{D\pi}}{4m^2_\pi}\int \frac{d^4k}{(2\pi)^4}(e^{ikx/2}+e^{-ikx/2})$$
$$\times f_0(x)G_\pi(k^2)k_\mu k_\nu\mathcal{G}^{(0,1)^+}_{00}(X-X')e^{-ik(X-X')}$$
$$\times (e^{ikx'/2}+e^{-ikx'/2})f_0(x'),$$

where the coefficient 3 appears because of the isospin factor.

As a result, we find for the polarization operator $\tilde{\Pi}^{(1,0)^+}_{N_eN'_e}$ that

$$\tilde{\Pi}^{(1,0)^+}_{N_eN'_e,\mu\nu}(P) = i\int\frac{d^4k}{(2\pi)^4}\Phi^{(\text{even})}_{0N_e}(k,P) \tag{52}$$
$$\times\left(\frac{h^{(1)2}_{D\sigma}}{4}G_\sigma(k^2)\mathcal{G}^{(1,0)^+}_{00,\mu\nu}(P-k)\right.$$
$$\left.+\frac{3h^2_{D\pi}}{4m^2_\pi}G_\pi(k^2)k_\mu k_\nu\mathcal{G}^{(0,1)^+}_{00}(P-k)\right)\Phi^{(\text{even})}_{0N'_e}(k,P).$$

According to expression (16), that part of this operator which corresponds to the spin-1 dibaryon state is given by

$$\tilde{\Pi}^{(1,0)^+}_{(1)} = -\mathcal{P}^{1,\mu\nu}\tilde{\Pi}^{(1,0)^+}_{\mu\nu}/3.$$

Before we go over to a practical calculation of the resulting integrals and finally obtain a closed expression for the covariant nucleon–nucleon potential, we note that any rank-N_e tensor can be represented as a set of irreducible tensors of rank N_e, N_e-2, N_e-4, etc. For example, any tensor of rank $N_e = 4$ can be represented as the sum of three tensors of the same rank such that the first is an irreducible rank-4 tensor, the second is the tensor product of an irreducible rank-2 tensor and the metric tensor $g_{\mu\nu}$, and the third is a symmetric combination of the metric tensors. By way of example, we indicate that, in the dibaryon c.m. frame, the wave function $f_{N_e}(x;P)$ is a rank-N_e tensor in conventional $O(3)$ space and can be expanded in spherical harmonics Y_{lm}, where l takes a finite number of values: $l = 0, 2, \ldots, N_e$ in the case of even partial waves and $l = 1, 3, \ldots, N_e$ in the case of odd partial waves.

In going over to the lm representation, we must therefore make the substitution $f_{N_e}(x;P) \to f_{N_elm}(x;P)$, where N_e now stands for the number of string-excitation quanta rather than being the rank of a tensor. As a result, the expressions for the polarization operators change as

$$\tilde{\Pi}^{(0,1)^+}_{N_eN'_e} \longrightarrow \tilde{\Pi}^{(0,1)^+}_{N_elm,N'_el'm'},$$
$$\tilde{\Pi}^{(1,0)^+}_{(1),N_eN'_e} \longrightarrow \tilde{\Pi}^{(1,0)^+}_{(1);N_elm,N'_el'm'},$$

and the expressions for the dibaryon Green's functions change analogously.

From the structure of the integrals in (49) and (52), it can easily be seen that integration with respect to the momentum k does not change the values of the orbital angular momentum l and of its projection m. Moreover, the polarization operators appear to be independent of m. It follows that, if we retain only the two lowest states with $N_e = 0$, 2 in the sums in (35) and (36) and set $q_0 = q'_0 = 0$ in the functions $f_{N_elm}(q,P)$ (this is always so for real nucleons in their c.m. frame), the form factors F in the $(1,0)^+$ and $(0,1)^+$ states can be represented as

$$F^{(i)} = \sum_{N_e,N'_e}\sum_{l=0}^{\min(N_e,N'_e)}\sum_{m=-l}^{l} f_{N'_elm}(\mathbf{q}') \tag{53}$$
$$\times\,\mathcal{G}^{(i)}_{N'_el,N_el}(P^2)f_{N_elm}(\mathbf{q}),$$

where the superscript is $(i) = (0,1)^+$ or $(1,0)^+$ and $f(\mathbf{q})$ stands for a conventional eigenfunction of a three-dimensional harmonic oscillator.

In order to calculate the Green's functions $\mathcal{G}^{(i)}_{N'_el,N_el}(P^2)$, we must consider that the dibaryon in the $l = 0$ state can involve $N_e = 0$, 2 excitation quanta. This means that, upon dressing, the s-wave dibaryon can go over from the configuration $|s^4p^2\rangle$ to the configuration $|s^6\rangle$ and also from the latter to the former configuration, so that, in calculating the Green's functions in question, it is necessary to take into account the possible mixing of these configurations. From expression (12) or (18) for the

[11] For the sake of simplicity and clarity, we disregard here the coupling to the $(2,1)^+$ state.

Green's functions, we obtain a set of four equations for the elements of the matrix $\mathcal{G}^{(i)}_{N'_e0,N_e0} \equiv \mathcal{G}^{(i)}_{N'_e,N_e}$. In particular, we find for the elements $\mathcal{G}^{(i)}_{2,2}$ and $\mathcal{G}^{(i)}_{0,2}$ that

$$\mathcal{G}^{(i)}_{2,2} = \frac{1+\tilde{\Pi}^{(i)}_{2,0}\mathcal{G}^{(i)}_{0,2}+\tilde{\Pi}^{(i)}_{2,2}\mathcal{G}^{(i)}_{2,2}}{P^2-M_2^2+i0},$$

$$\mathcal{G}^{(i)}_{0,2} = \frac{\tilde{\Pi}^{(i)}_{0,0}\mathcal{G}^{(i)}_{0,2}+\tilde{\Pi}^{(i)}_{0,2}\mathcal{G}^{(i)}_{2,2}}{P^2-M_0^2+i0}.$$

Solving this set of equations (and the analogous set of equations for $\mathcal{G}^{(i)}_{0,0}$ and $\mathcal{G}^{(i)}_{2,0}$), we represent the diagonal elements of the dibaryon propagators in the form

$$\mathcal{G}^{(i)}_{0,0}(P^2) = \frac{P^2-M_2^2-\tilde{\Pi}^{(i)}_{2,2}}{(P^2-M_2^2-\tilde{\Pi}^{(i)}_{2,2})(P^2-M_0^2-\tilde{\Pi}^{(i)}_{0,0})-(\tilde{\Pi}^{(i)}_{2,0})^2},$$

$$\mathcal{G}^{(i)}_{2,2}(P^2) = \frac{P^2-M_0^2-\tilde{\Pi}^{(i)}_{0,0}}{(P^2-M_2^2-\tilde{\Pi}^{(i)}_{2,2})(P^2-M_0^2-\tilde{\Pi}^{(i)}_{0,0})-(\tilde{\Pi}^{(i)}_{2,0})^2}.$$

Here, we have considered that $\tilde{\Pi}^{(i)}_{2,0} = \tilde{\Pi}^{(i)}_{0,2}$. If the operator $\tilde{\Pi}^{(i)}_{2,0}$, which mixes the configurations featuring $N_e = 2$ and $N_e = 0$ excitation quanta, is rather small (which, in all probability, is so, since the transition from the six-quark configuration $|s^6\rangle$ to the configuration $|s^4p^2\rangle$ must be accompanied by an additional energy transfer 2Ω), we obtain the ordinary one-channel expressions for the Green's functions; that is,

$$\mathcal{G}^{(i)}_{0,0}(P^2) = \frac{1}{P^2-M_0^2-\tilde{\Pi}^{(i)}_{0,0}(P^2)}, \quad (54)$$

$$\mathcal{G}^{(i)}_{2,2}(P^2) = \frac{1}{P^2-M_2^2-\tilde{\Pi}^{(i)}_{2,2}(P^2)}. \quad (55)$$

The propagators for the d-wave dibaryons ($l = 2$) have the ordinary one-channel form[12)]

$$\mathcal{G}^{(i)}_{22,22}(P^2) = \frac{1}{P^2-M_2^2-\tilde{\Pi}^{(i)}_{22,22}(P^2)}. \quad (56)$$

Disregarding the small contribution of the off-diagonal propagator elements, we can represent the form factors $F^{(i)}$ as

$$F^{(i)} = f_0(\mathbf{q}')\mathcal{G}^{(i)}_{0,0}(P^2)f_0(\mathbf{q}) + \sum_{l=0,2}\sum_{m=-l}^{l} f_{2lm}(\mathbf{q}')\mathcal{G}^{(i)}_{2l,2l}(P^2)f_{2lm}(\mathbf{q}). \quad (57)$$

[12)]If one disregards coupling to the $N\Delta$ channel.

If we also take into account states involving $N_e = 4$ excitation quanta, there arises the possibility of describing G-wave scattering. However, it is necessary to consider here that, at low energies, the behavior of the phase shifts in higher partial waves ($l > 3$) is determined primarily by the interaction at long distances ($r > 1$ fm) and is governed by one- and two-pion exchanges. But at higher energies, in which case the mechanisms of short-range interaction come into play, the interactions with vector (rho- and omega-meson) fields and also the possible transitions both to the $|s^6\rangle$ and to the $|s^5p\rangle$ state must be taken into account in the polarization operators.

In various $(S,I)^P$ channels, the nucleon–nucleon potential is determined by expressions (29)–(32) for the matrix elements if we eliminate the delta function from them. Bringing together the results for the spinor components (43) and (44) and for the form factors (57), we obtain the following expression for that component of the nucleon–nucleon potential which describes the interaction at short and intermediate distances in even partial waves:

$$V^{(i)}_{NN} = \lambda^{(i)}\phi^{(i)}_0(\mathbf{q}')\phi^{(i)}_0(\mathbf{q}) + V^{(i)}_D(\mathbf{q}',\mathbf{q}), \quad \lambda^{(i)} > 0.$$

Here, the first term simulates the repulsive interaction arising in the $|s^6\rangle$ configuration owing to one-gluon and one-pion exchanges between quarks, antisymmetrization being taken into account, and $V^{(i)}_D(\mathbf{q}',\mathbf{q})$ is the potential allowing for the coupling of the nucleon–nucleon state to the dibaryon; in the singlet S and D waves, this potential has the separable form

$$V^{(i)}_D(\mathbf{q}',\mathbf{q}) = 4(\alpha^{(i)})^2\left(\phi^{(i)}_0(\mathbf{q}')\mathcal{G}^{(i)}_{0,0}(P^2)\phi^{(i)}_0(\mathbf{q}) + \sum_{l=0,2}\sum_{m=-l}^{l}\phi^{(i)}_{2lm}(\mathbf{q}')\mathcal{G}^{(i)}_{2l,2l}(P^2)\phi^{(i)}_{2lm}(\mathbf{q})\right), \quad (58)$$

where

$$\alpha^{(0,1)^+} = \alpha^{(1)}_S, \quad \alpha^{(1,0)^+} = \alpha^{(0)}_A.$$

The functions $\phi^{(i)}(\mathbf{q})$ are related to the oscillator wave function $f(\mathbf{q})$ by kinematical factors; that is,

$$\phi^{(0,1)^+}(\mathbf{q}) = \frac{E_q+m_N}{2m_N}\left(1+\frac{\mathbf{q}^2}{(E_q+m_N)^2}\right)f(\mathbf{q}), \quad (59)$$

$$\phi^{(1,0)^+}(\mathbf{q}) = \frac{E_q + m_N}{2m_N}\left(1 + \frac{\mathbf{q}^2 + S_{12}(\mathbf{q})}{3(E_q + m_N)^2}\right) f(\mathbf{q}). \quad (60)$$

In analyzing the resulting expression for the nucleon–nucleon potential, we notice first of all that its structure—at least in the singlet waves (the problem of describing tensor interactions within the present formalism will be discussed below)—is virtually coincident with the structure of the semiphenomenological potential that was obtained in [29] and which made it possible to describe well both the phase shifts up to an energy of $E = 1$ GeV in the laboratory frame and the main properties of the deuteron. Indeed, we have $\phi^{(i)}(\mathbf{q}) = f(\mathbf{q})$ in the nonrelativistic limit. Disregarding, in the potential $V_D^{(i)}(\mathbf{q}', \mathbf{q})$, the term responsible for a rather weak attraction in the $|s^6\rangle$ configuration, we then arrive at a nucleon–nucleon potential of the form

$$V_{NN}^{(i)} = \lambda^{(i)} f_0(\mathbf{q}') f_0(\mathbf{q}) + \sum_{l=0,2}\sum_{m=-l}^{l} f_{2lm}(\mathbf{q}')\lambda_l^{(i)}(E) f_{2lm}(\mathbf{q}), \quad (61)$$

which is identical to that of the potential in [29]. Here, $\lambda_l^{(i)}(E) = 4(\alpha^{(i)})^2 \mathcal{G}_{2l,2l}(P^2)$ and the invariant quantity P^2 is related to the kinetic energy in the laboratory frame by the equation $P^2 = 4m_N^2 + 2m_N E$.

We also note that, in the present model, the polarization operators (49) and (52) and, hence, the form factors $F^{(i)}$ (57) (and the entire nucleon–nucleon potential as well) are complex-valued functions. Their imaginary parts are related to open inelastic channels and are determined by the discontinuities of these quantities at the unitary cut in the complex plane of energy. In the example considered here, we have two inelastic channels corresponding to real intermediate states, $NN\pi$ and $NN\pi\pi$. Indeed, three propagators G_π, G_σ, and $\mathcal{G}_{0,0}^{(i)}$ appear in expressions (49) and (52). The imaginary part of the propagator G_π is responsible for the production of a real pion. In order to obtain a real s-wave $\pi\pi$ state, one must take into account the strong coupling of the sigma meson to this state. In this case, the sigma-meson propagator takes the form

$$G_\sigma(k^2) = \frac{1}{k^2 - m_\sigma^2 - \Pi_\sigma(k^2)},$$

where the imaginary part of the operator $\Pi_\sigma(k^2)$ is associated with the mechanisms of sigma-meson decay to two real pions that is followed by their fusion into a sigma meson and can be found from the condition requiring the unitarity of the S matrix for this process. As for the coupling to the real nucleon–nucleon state, it is determined by the imaginary parts of the polarization operators $\tilde{\Pi}_{0,0}^{(i)}$ appearing in the dibaryon propagators $\mathcal{G}_{0,0}^{(i)}(P^2)$, which in turn appear in the integrals in (49) and (52).

Finally, we will briefly dwell upon an important aspect concerning the description of a tensor interaction in the scheme developed here. We recall that, at the present time, the problem of tensor nucleon–nucleon interaction is quite nontrivial. This especially concerns the description of tensor nucleon–nucleon forces at short distances. For example, it follows from the calculations performed within the resonating-group method that conventional meson-exchange interactions and one-gluon-exchange quark–quark interaction cannot make a significant contribution to tensor nucleon–nucleon forces [38]. At the same time, experimental phase shifts favor unambiguously a considerable strength of such forces at short and intermediate distances. In ordinary one-boson-exchange models, pions and rho mesons are the main sources of tensor forces. However, the required strength of this interaction is achieved via the use of large values for the cutoff parameters $\Lambda_{\pi NN}$ and $\Lambda_{\rho NN}$. Moreover, almost all of the meson-exchange nucleon–nucleon models use a value of $\kappa_\rho \approx 6$–7 for the tensor coupling of the rho meson to the nucleon. At the same time, an analysis of data on pion–nucleon scattering yields a much more modest value of $\kappa_\rho \approx 1$–3 for this parameter (see, for example, [46]). Thus, the tensor nucleon–nucleon force in one-boson-exchange models is enhanced by hand to reproduce the experimental phase shifts.

Within our approach, the short-range tensor nucleon–nucleon interaction arises owing to the following three sources:

(i) In the dressed $NN \to D$ vertex, there is a combination of a relatively short-range tensor one-pion-exchange interaction and a relatively long-range potential form factor $\phi_{2lm}^{(i)}(\mathbf{q})$ appearing in (58). As a result, the contribution of the tensor one-pion-exchange potential is effectively enhanced.

(ii) For the same reason, the mechanism of Goldstone boson exchange can make a significant contribution to the structure of the wave function $\Psi_{\mathrm{DB}}(x_1, x_2)$ for the dressed dibaryon. As a consequence, the exact propagators for dibaryons featuring $N_e \geq 2$ string-excitation quanta will develop nonvanishing elements that are off-diagonal in the orbital angular momentum l and which are determined by polarization operators belonging to the same type as those presented in Figs. 4 and 5. As a result, the nucleon–nucleon potential will in turn develop elements that are off-diagonal in l and which will lead

to a new type of tensor interaction at intermediate and short distances.

(iii) Additional terms that are completely due to relativistic effects also have tensor components proportional to $(\mathbf{q}^2 + S_{12}(\mathbf{q}))/[3(E_q + m_N)^2]$ [see (60)]. Owing to internal nodes of the scattering wave functions [21, 22], the total kinetic energy in the nucleon–nucleon channel increases strongly in relation to what we have in traditional approaches of the one-boson-exchange type, with the result that the contribution from relativistic effects will be sizably greater in our case.

4. ILLUSTRATIVE MODEL OF THE NUCLEON–NUCLEON POTENTIAL

Expression (61), derived in the preceding section for the effective nucleon–nucleon potential in the nonrelativistic limit, can be tested in an actual situation—for instance, in describing nucleon–nucleon phase shifts over a rather broad energy interval. First of all, we address the question of which energy interval can be described if we take into account zero- and two-quantum excitations of our color string for even S and D partial waves (or one- and three-quantum excitations for P and F partial waves). Simple dimensional estimates show that the energy corresponding to a single quantum of string excitation is $\Omega \sim 300$–350 MeV. On the laboratory scale, the excitation energy 2Ω corresponds to an energy of about 1.2 to 1.4 GeV in the nucleon–nucleon system. It follows that, taking into account only the zero- and two-quantum string excitations, we can hope to describe, on the basis of the potential in the form (61), the nucleon–nucleon amplitudes (both elastic and inelastic ones) up to an energy of about 1.2 GeV in the laboratory frame. In the present study, we consider only the amplitudes for elastic nucleon–nucleon scattering, postponing the description of inelastic processes until the next publication.

For the purpose of illustration, we consider here the $^1S_0$ and $^3S_1$–$^3D_1$ nucleon–nucleon channels. In deriving the polarization operators $\tilde{\Pi}^{(i)}_{0,0}(P^2)$, we restrict ourselves, in either case, to the leading loop graphs featuring a sigma meson and retain one-pion exchange in the external potential not related to the formation of an excited string. For the sake of simplicity, we also neglect the coupling of an intermediate sigma meson to the 2π channel, which is of importance only for describing inelastic processes that involve the production of two-pion pairs in nucleon–nucleon collisions. According to (61), the sought potential in the $^1S_0$ partial wave will then have the form

$$V_{NN}(^1S_0) = V_{\rm OPE} + V_{\rm TPE} + V_{NqN}, \qquad (62)$$

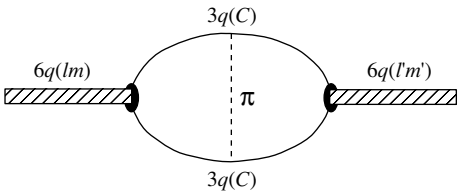

Fig. 5. Diagram corresponding to the dibaryon polarization operator leading to the mixing of six-quark states characterized by different values of the orbital angular momentum l.

where $V_{\rm OPE}$ is the potential that corresponds to t-channel one-pion exchange and which is softly cut off at short distances, with the cutoff parameter being $\Lambda_{\pi NN} \sim 700$ MeV, and $V_{\rm TPE} = V^0_{\rm TPE}(\alpha r^2)^2 \times \exp(-\alpha r^2)$ is a local potential that represents the external component ($r > 1$ fm) of two-pion exchange (TPE) and which is also suppressed at short distances r. The potential component

$$V_{NqN} = \lambda^{(0)} f_0(\mathbf{q}') f_0(\mathbf{q}) + \lambda^{(2)}_{00}(E) f_2(\mathbf{q}') f_2(\mathbf{q})$$

is responsible for dibaryon formation. Here, $\lambda^{(0)}$ is a large positive constant, while the energy-dependent strength constant $\lambda^{(2)}_{00}(E)$ is calculated directly from the sigma-meson-loop diagram shown in Fig. 4. The potential form factors $f_0(\mathbf{q})$ and $f_2(\mathbf{q})$ are merely the nonrelativistic harmonic-oscillator wave functions for the states featuring, respectively, zero and two excitation quanta. Thus, we have four adjustable parameters in the $^1S_0$ channel: two in the expression for $V_{\rm TPE}$ ($V^0_{\rm TPE}$ and α) and two in the expression for V_{NqN} (the oscillator radius $r_0 = \beta^{-1/2}$ associated with the functions f_0 and f_2 and the general normalization constant $\lambda^{(2)}_{00}(0)$ of the polarization operator). The energy dependence of $\lambda^{(2)}_{00}(E)$ is determined here by the bare dibaryon mass M_0 (we chose the value of $M_0 = 2.25$ GeV) and by the effective sigma-meson mass m_σ (we set it to $m_\sigma = 400$ MeV).

The numerical calculation of the loop integral leads to the conclusion that, to a good accuracy, it can be represented (over the broad energy interval from zero to 1 GeV) as the Padè approximant

$$\lambda^{(2)}_{00}(E) = \lambda^{(2)}_{00}(0)\frac{E_0 + aE}{E_0 - E},$$

the values of the parameters a and E_0 being given in Table 1. In the potential V_{NqN}, there remain only two adjustable parameters, $\lambda^{(2)}_{00}(0)$ and r_0, to be varied in describing the empirical $^1S_0$ phase shift, but the value of r_0 must be close to the conventional quark radius of the nucleon, $r_0^{(N)} \sim 0.4$–0.5 fm. To our great surprise, it turned out that a variation of only one pa-

Table 1. Parameters of the potential model that were determined on the basis of calculating the polarization operator and on the basis of the fitting procedure

Channel	r_0, fm	r_2, fm	$\lambda_{00}^{(2)}(0)$, MeV	$\lambda_{22}^{(2)}(0)$, MeV	$\lambda_{02}^{(2)}(0)$, MeV	E_0, MeV	a	$V_{\rm TPE}^0$, MeV	α^{-2}, fm^{-2}
$^3S_1-^3D_1$	0.38113	0.59423	−385.089	−18.1305	−416 384	855.29	−0.25	−4.62843	0.53936
$^1S_0$	0.39797	–	−379.961	–	–	855.29	−0.25	−11.6287	0.717044

rameter $\lambda_{00}^{(2)}(0)$, together with quite a modest tuning of r_0 values from a rather narrow admissible interval, makes it possible to attain an excellent description of the $^1S_0$ phase shift over the entire range from zero energy to 1 GeV (see Fig. 6). We believe that this astoundingly simple and accurate description of the nucleon–nucleon phase shifts is not accidental, but that it is due to the adequacy of the interaction pattern developed here.[13)]

The description of the $^3S_1-^3D_1$ triplet coupled channels proved to be equally simple. Here, the potential has the same form as in (62), with the only difference that now $V_{\rm OPE}$ and V_{NqN} include a tensor interaction. In particular, $V_{\rm OPE}$ involves a peripheral tensor nucleon–nucleon interaction (with the cutoff parameter of $\Lambda = 0.7$ GeV). As to V_{NqN}, it admits the matrix representation [49]

$$V_{NqN} = \begin{pmatrix} \lambda_{00}^{(2)}(E)|2s\rangle\langle 2s| & \lambda_{02}^{(2)}(E)|2s\rangle\langle 2d| \\ \lambda_{20}^{(2)}(E)|2d\rangle\langle 2s| & \lambda_{22}^{(2)}(E)|2d\rangle\langle 2d| \end{pmatrix}, \tag{63}$$

where $|2s\rangle$ and $|2d\rangle$ are the harmonic-oscillator wave functions featuring the parameters r_0 (for the S wave) and r_2 (for the D wave). In principle, quite a satisfactory description of the $^3S_1-^3D_1$ phase shifts can be achieved even at a unified value of the oscillator radius for the s- and d-wave form factors. However, the quality of a fit with different values of r_0 appears to be somewhat better.

We found that the values of the basic parameters $\lambda_{00}^{(2)}(0)$, a, and E_0 in (63) for the $^3S_1$ triplet channel are virtually identical to those for the $^1S_0$ singlet channel (see Table 1), this providing an additional piece of evidence in support of the model constructed here. The quality of the description of nucleon–nucleon phase shifts over the broad energy interval 0–1000 MeV is illustrated in Fig. 6. Table 2 gives the effective-range values corresponding to our model. Again, perfect agreement between the theoretical and experimental values of the effective-range parameters serves as a good additional argument in favor of the force model under consideration. Indeed, a fit of two empirical parameters of the low-energy amplitude—that is, the scattering length and the effective range—in the $^1S_0$ channel, for example, fixes, as a matter of fact, two parameters of the present force model, leaving two variable parameters (of four input ones) for a fit to the $^1S_0$ phase shift in the range from 15 to 1000 MeV (under the assumption that effective-range theory reproduces phase shifts from zero to 15 MeV). Thus, there arises the impression that the model in question faithfully reproduces the energy dependence of the nucleon–nucleon phase shifts over a broad energy range. It should be emphasized once again that the energy dependence of the effective coupling constants $\lambda^{(2)}(E)$ was taken directly from the calculations of the loop diagram featuring a sigma meson (see Fig. 4).

5. IMPLICATIONS OF THE DEVELOPED FORCE MODEL FOR NUCLEAR PHYSICS

The force model developed in the preceding section has many implications for the physics of hadron processes, and we discuss some of them below.

5.1. Meson Production in Proton–Proton and Other Collisions

It is well known that traditional one-boson-exchange models are often unable to describe the cross sections for meson production in nucleon–nucleon collisions—for example, the cross sections for the threshold production of neutral pions [50–52]. There exist serious problems in describing the exclusive cross sections for double pion production in the $I = J = 0$ channel [53]

$$p + p \to p + p + \pi^+ + \pi^-,$$
$$p + p \to p + p + 2\pi^0.$$

Moreover, the so-called ABC puzzle [54–56] consisting in the enhancement of the cross section for the production of a $\pi^+\pi^-$ pair in the scalar–isoscalar channel of reactions like

$$p + n \to d + \pi^+ + \pi^-, \tag{64}$$

[13)] We note for the sake of comparison that a conventional phenomenological nucleon–nucleon potential that is represented in a separable form includes many separable terms and very many adjustable parameters [48] for describing nucleon–nucleon phase shifts in the energy range 0–500 MeV.

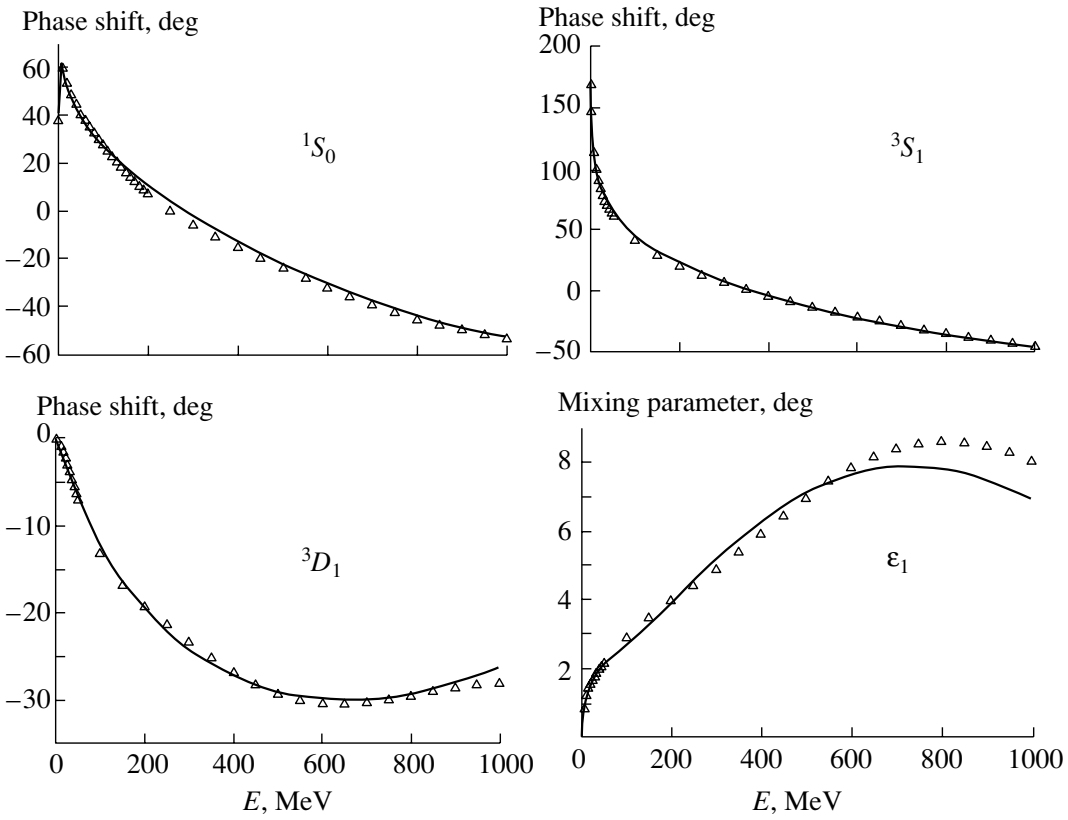

Fig. 6. Phase shifts and tensor-mixing parameter ε_1 for nucleon–nucleon scattering: (solid curves) results of the calculation within the present model and (points) data of the SP99 (SAID) partial-wave analysis [47].

$$p + d \to {}^3\mathrm{He} + \pi^+ + \pi^-$$

has been discussed in the literature over more than the past 40 years. Quite a similar enhancement was recently discovered in the photoproduction of pion pairs on a deuteron [57],

$$d + \gamma \to n + p + 2\pi^0.$$

For some of these puzzles, recent ad hoc explanations made it possible to describe the corresponding experimental data by introducing some free parameters. Unfortunately, there is absolutely no relationship between these explanations and the generally accepted basic mechanisms of elastic nucleon–nucleon scattering; therefore, these explanations cannot be considered as some kind of reliable theoretical guidelines for describing hadron dynamics. Moreover, models presented in the literature for describing similar processes obviously contradict one another. For example, the 2π enhancement and numerous $\pi\pi$, pp, and πp correlations found recently by Patzold *et al.* [58] in proton–proton collisions, $pp \to pp\pi^+\pi^-$, are interpreted at present in terms of the production of the Roper resonance $N(1440)$ and its subsequent 2π and π decays [59], while the analogous 2π enhancement in the reaction $pn \to d\pi^+\pi^-$ (ABC puzzle) is explained by the production and subsequent decay of two delta isobars, etc. It is clear that this situation is far from satisfactory, and a unified approach to describing the aforementioned numerous similar processes would be highly desirable. Such an approach may involve free parameters, but it must be matched in one way or another with the basic mechanism adopted for elastic nucleon–nucleon scattering.

We would like to indicate here that our mechanism of nucleon–nucleon interaction makes it possible, in principle, to create a unified basis for describing meson production in nucleon–nucleon, proton–deuteron, and other collisions. By way of example, we indicate that, in our approach, the enhancement of

Table 2. Scattering lengths and effective ranges in the triplet and singlet nucleon–nucleon channels for the present model along with experimental data

Channel	a, fm		r_0, fm	
	Theory	Experiment	Theory	Experiment
$^3S_1$	5.419	5.419(7)	1.753	1.753(8)
$^1S_0$	−23.741	−23.740(20)	2.77	2.77(5)

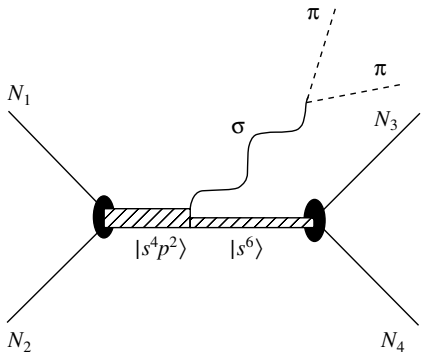

Fig. 7. Example of diagrams describing a new possible mechanism of double pion production in the scalar–isoscalar channel.

double pion production in the scalar–isoscalar channel is a direct consequence of a dominant role of the sigma-meson cloud of the dressed intermediate dibaryon [29, 30] (see Fig. 7). Nearly the same mechanism can be responsible for the enhancement of the yield of a $2\pi^0$ pair in photoproduction on a deuteron and (with the substitution of an off-shell rho meson for a sigma meson) for the enhanced yield of dilepton pairs in proton–proton collisions at proton energies of $E_{\text{c.m.}} \geq 2$ GeV [60]—that is, for the so-called DLS puzzle.

5.2. Production of Nucleon Isobars in Nucleon–Nucleon Collisions

Yet another large range of problems where the existing theory runs into serious difficulties concerns the prediction of cross sections (as well as of the vector and tensor analyzing powers) for nucleon-isobar production in nucleon–nucleon collisions, especially at high momentum transfers. This is also associated with the above difficulties in treating the nucleon–nucleon interaction on the basis of the traditional one-boson-exchange approach at high momentum transfers. Here, the description of short-range $N\Delta$ interaction is one of the most important problems in practice. It is obvious from physical considerations that, since the production of real isobars is accompanied by high momentum (and energy) transfers, the traditional one-meson mechanism is hardly applicable here—especially if soft form factors are used in meson–nucleon vertices. Therefore, the dibaryon mechanism, which makes it possible to transfer, in a collision, a high momentum and a high energy without particular problems, must be especially useful. Simultaneously, the production of mesons arising in the decay of isobars must be enhanced—for example, in the threshold production of omega mesons [61] (see Fig. 8).

All of the aforesaid gives every reason to assume that the dibaryon mechanism of particle production must play a basic role in nucleus–nucleus collisions at energies of $E/A \geq 1$ GeV. The available methods for the diagnostics of quark–gluon plasma—for example, through the measurement of the yield of high-energy e^+e^- pairs—unambiguously indicate that, at energies in the range $E_{2e} \sim 200$–400 MeV, the yield of these pairs is enhanced in relation to the predictions of the existing theories of lepton-pair production through the decays of rho, phi, and other mesons in bare nucleon–nucleon collisions.

5.3. New Meson-Exchange Currents

The use of the present formalism in the Lagrangian formulation also allows one to take readily into account the contribution to various photo- and electronuclear processes from new meson-exchange currents appearing in our model. The need for such short-range electromagnetic currents is clearly seen against the background of the obvious inability of standard one-boson-exchange models (even if they take into account the contribution from delta isobars and other resonances) to describe quantitatively (and sometimes even qualitatively) various experimental data. Even in such elementary photonuclear reactions as bremsstrahlung from nucleon–nucleon scattering [62] and deuteron photodisintegration [63–65], traditional one-boson-exchange models lead to results that are in a strong contradiction with experimental data. Such a situation is observed even in the photon-energy range $E_\gamma \sim 100$–400 MeV, where standard meson dynamics was expected to work well. By way of example, we indicate that, in the reaction $pp \to pp\gamma$ proceeding at a collision energy of about 400 MeV in the laboratory frame [62], the standard one-boson-exchange models of the nucleon–nucleon interaction that also involve delta-isobar excitation and $\rho \to \pi\gamma$ meson-exchange currents lead, at some specific angles of photon emission, to differential-cross-section values that are one-half as large as their experimental counterparts. This comes as no surprise if one considers that, at this energy, the delta isobar (its contribution to the cross section is approximately 50%) is still far off the mass shell, in which case the mean radius of the $N\Delta$ system must be rather small ($r_{N\Delta} \leq 1$ fm), so that conventional meson-exchange mechanisms are inadequate here.

New meson-exchange electromagnetic currents arising in the present model in a natural way (see, for example, Fig. 9) at distances that are critical for various experimentally observable features inspire hopes for improving agreement between theoretical and experimental results.

5.4. Multiparticle Forces in Nuclei

In this subsection, we briefly discuss the implications of the dibaryon model of nuclear forces for the basic theory of the nucleus. First of all, we note that, from the present model {see Eq. (61), as well as formulas (80) and (81) from [29]}, it follows that the pair nucleon–nucleon interaction explicitly depends on energy. It was rigorously shown by Merkuriev *et al.* [66] that, in a three-nucleon system, this dependence inevitably entails the substitution $\mathcal{E}_2 \to E_3 - 3q^2/(4m_N)$, where $\mathcal{E}_2$ and E_3 are, respectively, the pair and the three-particle energy and q is the momentum of the third particle in the c.m. frame of the system. Thus, we can see that, in the three-nucleon system, the coupling constant $\lambda_l^{(i)}(\mathcal{E}_2)$ in (61) transforms into the quantity $\lambda_l^{(i)}(E_3 - 3q^2/(4m_N))$, which depends on the third-particle momentum—that is, the purely pair interaction (apart from one- and two-pion-exchange terms) disappears in our approach, transforming into a three-particle (or multiparticle) interaction. It is interesting to note, however, that, as the mean kinetic energy of particles grows, the effective coupling constant $\lambda_l^{(i)}$ decreases, this corresponding to the appearance of an additional density-dependent repulsive force.[14] Further, we emphasize that, as had been indicated in the first study of this series [19] and as was then confirmed by the quantitative theory developed in [31], the introduction of dibaryon degrees of freedom inevitably leads to the appearance of three- and four-particle forces that are of a scalar character and which are induced by sigma-meson exchange between the dibaryon and neighboring nucleons. These forces prove to be so strong that they (together with the aforementioned fact of the emergence of effective density-dependent repulsive multiparticle forces) change drastically the force balance in nuclei. It was shown in [31] that, in the three-nucleon system, the scalar three-particle forces caused by the interaction of the sigma-meson cloud of the dibaryon with the third nucleon saturate at least half the entire binding energy of this system. We note that this conclusion is strictly quantitative rather than qualitative since the model made it possible to describe quantitatively—and to a high precision—the three-nucleon binding energies in the ^{3}H and ^{3}He nuclei and the main static features of these nuclei [31].

In this connection, it is very interesting to note that a wide variety of data indicate that a strong scalar sigma-meson field must be present in nuclei.

[14] It is reasonable to recall here that, in phenomenological nuclear models (of the Skyrme type), it is the inclusion of three-particle density-dependent repulsive forces that leads to accurate results.

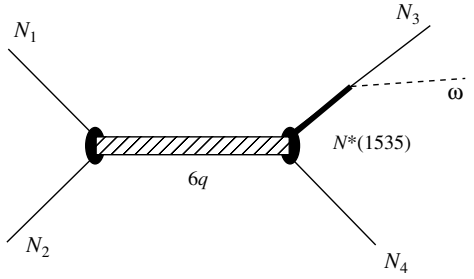

Fig. 8. Diagram describing the enhancement of the probability for the formation of nucleon excited states and, in particular, of the mechanism of omega-meson emission in a nucleon–nucleon collision.

For example, the well-known Walecka field-theory model [67] for nuclei and nuclear matter includes the sigma-meson field as one of the main ingredients. Moreover, the Walecka model was recently generalized in [68, 69] in order to describe the spectra of excited states in heavy nuclei—primarily giant resonances. It was found there that, in order to describe monopole vibrations—that is, in order to reproduce the nuclear compressibility faithfully—it is necessary to enhance additionally the scalar sigma-meson field in the Walecka model (by introducing terms proportional to σ^3 and σ^4 in the Lagrangian). This can serve as a good (albeit indirect) piece of evidence in support of the model of strong scalar three- and four-nucleon forces that directly follows from the dibaryon concept.

Thus, we see that, upon the inclusion of such scalar multiparticle forces, basic nuclear dynamics must change drastically in relation to what we have in theories based on pair forces of the one-boson-exchange type.

6. CONCLUSIONS

It is appropriate here to formulate briefly the main results of the present study.

In previous studies of our group (see [2, 19, 28, 29]), the model of a dressed six-quark bag was proposed for describing the nucleon–nucleon interaction at intermediate and short distances. Here, it has been significantly improved and refined by introducing a color-confined intermediate state whose structure includes, in all probability, three diquarks connected by color strings. In the lowest partial waves, this configuration is of a star type with a central connection of three strings at the center of mass; as the angular momentum in the nucleon–nucleon system grows, the star configuration goes over to a linear string configuration whose rotation approximately corresponds to a linear Regge trajectory. In the present model, it is a rotating double string that mediates interaction in higher partial waves at energies $E_{NN} \sim 1$ GeV

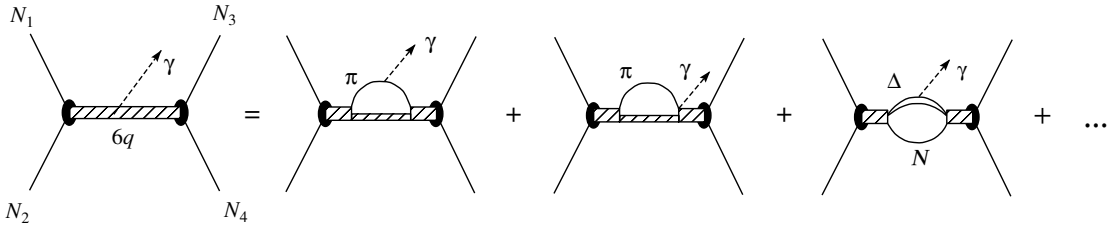

Fig. 9. Examples of diagrams involving new meson-exchange electromagnetic currents that arise in the present model.

and above.[15)] It should be emphasized that, according to the microscopic content of the six-quark model, the clustered nucleon–nucleon component goes over primarily to excited-string states (in the lowest partial waves) that are deexcited through a virtual (or real) emission of 2π pairs in the isoscalar and isovector channels and of (although to a lesser degree) single pions, this corresponding to the dressing of the intermediate dibaryon with meson fields.

The physical picture described above has been recast in the present study into the form of a covariant field-theory model involving effective scalar, pseudoscalar, vector, and axial-vector dibaryon fields, their excitations being described in terms of the corresponding relativistic oscillator. There then arises a conventional (in field theory) model of the dressing of bare particles with meson fields via summation of meson loops in the s channel. This model makes it possible to include, in quite a natural way, coupling to other baryon channels of the $N\Delta$, $\Delta\Delta$, $NN^*(1535)$, etc., types. Because of closely lying poles of the amplitude, the channel coupling will be enhanced near the corresponding thresholds for isobar production. This model allows one to include, along with channel coupling, the production of various mesons via a subsequent decay of excited isobars. In an equally natural way, this model permits including, in the description, real 2π-pair production in the isoscalar and isovector channels and dilepton emission (e^+e^-) in proton–proton and nucleus–nucleus collisions.

It is of paramount importance that all of these particle-production processes can in principle be described within a unified relativistic model involving also the description of elastic nucleon–nucleon scattering, this distinguishing sharply our approach from other currently available approaches. Future investigations will reveal the degree to which these optimistic expectations will come true.

[15)]It should be noted that, at these energies, higher nucleon–nucleon phase shifts for $L \geq 4$ are large, and no one-boson-exchange model can reproduce such values of higher phase shifts.

ACKNOWLEDGMENTS

We are grateful to many colleagues for stimulating discussions and critical comments, especially to V.N. Pomerantsev, P. Grabmayr, H. Clement, A. Faessler, M. Krivoruchenko, and M. Kaskulov (Tubingen University).

This work was supported in part by the Russian Foundation for Basic Research (project nos. 02-02-16612 and 04-02-04001) and by the Deutsche Forschungsgemeinschaft (grant no. Fa-67/20-1).

APPENDIX

For the matrix elements of bispinors, we present here expressions that are necessary for determining the spinor components of the nucleon–nucleon potential by formulas (41) and (42). Using the definition of a bispinor for a positive definite energy,

$$u(\mathbf{q}) = \sqrt{\frac{E_q + m_N}{2m_N}} \begin{pmatrix} 1 \\ \dfrac{(\boldsymbol{\sigma}\cdot\mathbf{q})}{E_q + m_N} \end{pmatrix},$$

and the definition of the Dirac matrices in the standard representation, we obtain

$$[\bar{u}(\mathbf{q}')u(\mathbf{q})][\bar{u}(-\mathbf{q}')u(-\mathbf{q})]$$
$$= W\left(1 - \frac{(\boldsymbol{\sigma}_1\cdot\mathbf{q}')(\boldsymbol{\sigma}_1\cdot\mathbf{q})}{(E_{q'} + m_N)(E_q + m_N)}\right)$$
$$\times\left(1 - \frac{(\boldsymbol{\sigma}_2\cdot\mathbf{q}')(\boldsymbol{\sigma}_2\cdot\mathbf{q})}{(E_{q'} + m_N)(E_q + m_N)}\right),$$

$$[\bar{u}(\mathbf{q}')\gamma_0 u(\mathbf{q})][\bar{u}(-\mathbf{q}')\gamma_0 u(-\mathbf{q})]$$
$$= W\left(1 + \frac{(\boldsymbol{\sigma}_1\cdot\mathbf{q}')(\boldsymbol{\sigma}_1\cdot\mathbf{q})}{(E_{q'} + m_N)(E_q + m_N)}\right)$$
$$\times\left(1 + \frac{(\boldsymbol{\sigma}_2\cdot\mathbf{q}')(\boldsymbol{\sigma}_2\cdot\mathbf{q})}{(E_{q'} + m_N)(E_q + m_N)}\right),$$

$$[\bar{u}(\mathbf{q}')\gamma_\mu u(\mathbf{q})][\bar{u}(-\mathbf{q}')\gamma^\mu u(-\mathbf{q})]$$
$$= [\bar{u}(\mathbf{q}')\gamma_0 u(\mathbf{q})][\bar{u}(-\mathbf{q}')\gamma_0 u(-\mathbf{q})]$$
$$+ W\left(\frac{\boldsymbol{\sigma}_1(\boldsymbol{\sigma}_1\cdot\mathbf{q})}{E_q + m_N} + \frac{(\boldsymbol{\sigma}_1\cdot\mathbf{q}')\boldsymbol{\sigma}_1}{E_{q'} + m_N}\right)$$

$$\times\left(\frac{\boldsymbol{\sigma}_2(\boldsymbol{\sigma}_2\cdot\mathbf{q})}{E_q+m_N}+\frac{(\boldsymbol{\sigma}_2\cdot\mathbf{q}')\boldsymbol{\sigma}_2}{E_{q'}+m_N}\right),$$

$$[\bar{u}(\mathbf{q}')\sigma_{0\mu}u(\mathbf{q})][\bar{u}(-\mathbf{q}')\sigma^{0\mu}u(-\mathbf{q})]$$
$$=-W\left(\frac{\boldsymbol{\sigma}_1(\boldsymbol{\sigma}_1\cdot\mathbf{q})}{E_q+m_N}-\frac{(\boldsymbol{\sigma}_1\cdot\mathbf{q}')\boldsymbol{\sigma}_1}{E_{q'}+m_N}\right)$$
$$\times\left(\frac{\boldsymbol{\sigma}_2(\boldsymbol{\sigma}_2\cdot\mathbf{q})}{E_q+m_N}-\frac{(\boldsymbol{\sigma}_2\cdot\mathbf{q}')\boldsymbol{\sigma}_2}{E_{q'}+m_N}\right),$$

$$[\bar{u}(\mathbf{q}')\sigma_{\mu\nu}u(\mathbf{q})][\bar{u}(-\mathbf{q}')\sigma^{\mu\nu}u(-\mathbf{q})]$$
$$=2[\bar{u}(\mathbf{q}')\sigma_{0\mu}u(\mathbf{q})][\bar{u}(-\mathbf{q}')\sigma^{0\mu}u(-\mathbf{q})]$$
$$+2W\left(\boldsymbol{\sigma}_1-\frac{(\boldsymbol{\sigma}_1\cdot\mathbf{q}')\boldsymbol{\sigma}_1(\boldsymbol{\sigma}_1\cdot\mathbf{q})}{(E_{q'}+m_N)(E_q+m_N)}\right)$$
$$\times\left(\boldsymbol{\sigma}_2-\frac{(\boldsymbol{\sigma}_2\cdot\mathbf{q}')\boldsymbol{\sigma}_2(\boldsymbol{\sigma}_2\cdot\mathbf{q})}{(E_{q'}+m_N)(E_q+m_N)}\right),$$

$$[\bar{u}(\mathbf{q}')\gamma_0\gamma_5u(\mathbf{q})][\bar{u}(-\mathbf{q}')\gamma_0\gamma_5u(-\mathbf{q})]$$
$$=-W\left(\frac{\boldsymbol{\sigma}_1\cdot\mathbf{q}}{E_q+m_N}+\frac{\boldsymbol{\sigma}_1\cdot\mathbf{q}'}{E_{q'}+m_N}\right)$$
$$\times\left(\frac{\boldsymbol{\sigma}_2\cdot\mathbf{q}}{E_q+m_N}+\frac{\boldsymbol{\sigma}_2\cdot\mathbf{q}'}{E_{q'}+m_N}\right),$$

$$[\bar{u}(\mathbf{q}')\gamma_\mu\gamma_5u(\mathbf{q})][\bar{u}(-\mathbf{q}')\gamma^\mu\gamma_5u(-\mathbf{q})]$$
$$=[\bar{u}(\mathbf{q}')\gamma_0\gamma_5u(\mathbf{q})][\bar{u}(-\mathbf{q}')\gamma_0\gamma_5u(-\mathbf{q})]$$
$$-W\left(\boldsymbol{\sigma}_1+\frac{(\boldsymbol{\sigma}_1\cdot\mathbf{q}')\boldsymbol{\sigma}_1(\boldsymbol{\sigma}_1\cdot\mathbf{q})}{(E_{q'}+m_N)(E_q+m_N)}\right)$$
$$\times\left(\boldsymbol{\sigma}_2+\frac{(\boldsymbol{\sigma}_2\cdot\mathbf{q}')\boldsymbol{\sigma}_2(\boldsymbol{\sigma}_2\cdot\mathbf{q})}{(E_{q'}+m_N)(E_q+m_N)}\right),$$

$$[\bar{u}(\mathbf{q}')\gamma_5u(\mathbf{q})][\bar{u}(-\mathbf{q}')\gamma_5u(-\mathbf{q})]$$
$$=-W\left(\frac{\boldsymbol{\sigma}_1\cdot\mathbf{q}}{E_q+m_N}-\frac{\boldsymbol{\sigma}_1\cdot\mathbf{q}'}{E_{q'}+m_N}\right)$$
$$\times\left(\frac{\boldsymbol{\sigma}_2\cdot\mathbf{q}}{E_q+m_N}-\frac{\boldsymbol{\sigma}_2\cdot\mathbf{q}'}{E_{q'}+m_N}\right).$$

REFERENCES

1. D. Plaemper, J. Flender, and M. F. Gari, Phys. Rev. C **49**, 2370 (1994).
2. V. I. Kukulin, I. T. Obukhovsky, V. N. Pomerantsev, and A. Faessler, Yad. Fiz. **64**, 1748 (2001) [Phys. At. Nucl. **64**, 1667 (2001)].
3. D. L. Groep *et al.*, Phys. Rev. C **63**, 014005 (2001); R. Gilman and F. Gross, J. Phys. G **28**, R37 (2002).
4. E. Tomasi-Gustafsson, I. M. Sitnik, C. F. Perdrisat, and M. P. Rekalo, Nucl. Instrum. Methods Phys. Res. A **402**, 361 (1998).
5. H. Kamada *et al.*, Phys. Rev. C **55**, 2563 (1997).
6. K. I. Blomqvist *et al.*, Phys. Lett. B **424**, 33 (1998).
7. Bin Zhang, W. Bertozzi, and Sh. Gilad, *Talk at the 5th Workshop on Electromagnetically Induced Two-Hadron Emission, Lund, 2001*.
8. J. Golak *et al.*, Few-Body Syst. Suppl. **14**, 355 (2003); in *Proceedings of the XVIII European Conference on Few-Body Problems in Physics, Bled, Slovenia, 2002*.
9. *Proceedings of the Manchester International Conference on Nuclear Physics, 1962*.
10. L. A. Sliv, M. N. Strikman, and L. L. Frankfurt, Usp. Fiz. Nauk **145**, 553 (1985).
11. Yu. D. Bayukov *et al.,* Yad. Fiz. **34**, 95 (1981) [Sov. J. Nucl. Phys. **34**, 54 (1981)].
12. Yu. D. Bayukov *et al.,* Yad. Fiz. **34**, 785 (1981) [Sov. J. Nucl. Phys. **34**, 437 (1981)].
13. A. V. Vlasov *et al.,* Yad. Fiz. **36**, 915 (1982) [Sov. J. Nucl. Phys. **36**, 536 (1982)].
14. V. G. Ableev *et al.*, in *Proceedings of the High-Energy Spin Physics, Bonn, Germany, 1990*, Vol. 1, p. 546.
15. A. Chodos, R. L. Jaffe, K. Johnson, *et al.*, Phys. Rev. D **9**, 3471 (1974); A. Chodos *et al.*, Phys. Rev. D **10**, 2599 (1974).
16. Yu. A. Simonov, Yad. Fiz. **36**, 722 (1982) [Sov. J. Nucl. Phys. **36**, 422 (1982)]; **38**, 1542 (1983); Yu. S. Kalashnikova *et al.*, Phys. Lett. B **155B**, 217 (1985); B. L. G. Bakker and I. M. Narodetskii, Adv. Nucl. Phys. **21**, 1 (1994).
17. A. I. Akhiezer, A. G. Sitenko, and V. K. Tartakovskiĭ, *Nuclear Electrodynamics* (Naukova Dumka, Kiev, 1993) [in Russian].
18. B.-Q. Ma, I. Schmidt, and J.-J. Jong, Eur. Phys. J. A **12**, 353 (2001).
19. V. I. Kukulin, *Proceedings of the XXXIII St. Petersburg Institute for Nuclear Physics Winter School on Nuclear Physics, St. Petersburg, 1999*, p. 207.
20. V. I. Kukulin, V. M. Krasnopolsky, V. N. Pomerantsev, and P. B. Sazonov, Phys. Lett. B **135B**, 20 (1984); **165**, 7 (1985); V. I. Kukulin, V. M. Krasnopolsky, and V. N. Pomerantsev, *Proceedings of the 3rd Leningrad Institute for Nuclear Physics Symposium on Nucleon–Nucleon and Hadron–Nucleus Interactions at Intermediate Energies, Leningrad, 1986*, p. 103.
21. V. I. Kukulin, V. N. Pomerantsev, and A. Faessler, Phys. Rev. C **59**, 3021 (1999).
22. V. I. Kukulin and V. N. Pomerantsev, Nucl. Phys. A **631**, 456 (1998); Prog. Theor. Phys. **88**, 159 (1992).
23. G. E. Brown and M. Rho, Comments Nucl. Part. Phys. **18**, 1 (1988); S. W. Hong and B. K. Jennings, nucl-th/0010067.
24. T. Hatsuda and T. Kunihiro, Phys. Rep. **247**, 221 (1994).
25. T. Hatsuda, T. Kunihiro, and H. Shimizu, Phys. Rev. Lett. **82**, 2840 (1999); H. Saganuma and T. Tatsumi, in *Proceedings of the International Symposium on High-Energy Nuclear Collisions and Quark–Qluon Plasma, Kyoto, Japan, 1990* (World Sci., Singapore, 1991).
26. P. Rehrberg, L. Bot, and J. Aichelin, Nucl. Phys. A **653**, 415 (1999).

27. R. Machleidt, Adv. Nucl. Phys. **19**, 189 (1989).
28. V. I. Kukulin, I. T. Obukhovsky, V. N. Pomerantsev, and A. Faessler, J. Phys. G **27**, 1851 (2001).
29. V. I. Kukulin, I. T. Obukhovsky, V. N. Pomerantsev, and A. Faessler, Int. J. Mod. Phys. E **11**, 1 (2002).
30. V. I. Kukulin, Few-Body Systems Suppl. **14**, 71 (2003); in *Proceedings of the XVIII European Conference on Few-Body Problems in Physics, Bled, Slovenia*, 2002.
31. V. I. Kukulin, V. N. Pomerantsev, M. M. Kaskulov, and A. Faessler, J. Phys. G **30**, 287 (2004); V. I. Kukulin, V. N. Pomerantsev, and A. Faessler, J. Phys. G **30**, 303 (2004).
32. S. Weinberg, Phys. Lett. B **251**, 288 (1990); Nucl. Phys. B **363**, 3 (1991).
33. D. B. Kaplan, nucl-th/9506035; Nucl. Phys. B **494**, 471 (1997).
34. D. B. Kaplan, M. J. Savage, and M. B. Wise, Nucl. Phys. B **478**, 629 (1996); Phys. Lett. B **424**, 390 (1998).
35. E. Epelbaum, W. Gloeckle, and U.-G. Meissner, Nucl. Phys. A **637**, 107 (1998).
36. W. Haxton and C. L. Song, Phys. Rev. Lett. **84**, 5484 (2000).
37. D. Bartz and Fl. Stancu, Phys. Rev. C **63**, 034001 (2001).
38. D. R. Entem, F. Fernández, and A. Valcarce, Phys. Rev. C **62**, 034002 (2000).
39. R. P. Feynman, K. Kislinger, and F. Ravndal, Phys. Rev. D **3**, 2706 (1971); Y. S. Kim and M. E. Noz, Phys. Rev. D **8**, 3521 (1973).
40. S. Ishida, M. Ishida, and T. Maeda, Prog. Theor. Phys. **104**, 785 (2000).
41. M. Moshinsky and A. Szczepaniak, J. Phys. A **22**, L817 (1989).
42. A. Szczepaniak and A. G. Williams, Phys. Rev. D **47**, 1175 (1993).
43. V. I. Kukulin, G. Loyola, and M. Moshinsky, Phys. Lett. A **158**, 19 (1991).
44. S. Ishida, M. Ishida, and M. Oda, Prog. Theor. Phys. **93**, 939 (1995).
45. J. D. Björken and S. D. Drell, *Relativistic Quantum Fields* (McGraw-Hill, New York, 1965).
46. A. D. Lahiff and I. R. Afnan, Phys. Rev. C **60**, 024608 (1999).
47. R. A. Arndt, Chang Heon Oh, I. I. Strakovsky, and R. L. Workman, Phys. Rev. C **56**, 3005 (1997).
48. L. Mathelitsch, W. Plessas, and M. Schweiger, Phys. Rev. C **26**, 65 (1982).
49. V. I. Kukulin, M. A. Shikhalev, and A. Faessler, Phys. Rev. D (in press).
50. H. M. Machner and J. Haidenbauer, J. Phys. G **25**, R231 (1999).
51. S. Abdel Samad *et al.*, nucl-ex/0212024.
52. E. Gedalin, A. Moalem, and L. Razdolskaya, Phys. Rev. C **60**, 31 (1999).
53. J. Johanson *et al.*, Nucl. Phys. A **712**, 75 (2002); J. Patzold *et al.*, PiN Newslett. **16**, 370 (2002).
54. J. Banaigs *et al.*, Nucl. Phys. B **67**, 1 (1973).
55. J. C. Anjos, D. Levy, and A. Santoro, Nucl. Phys. B **67**, 37 (1973).
56. F. Plouin *et al.*, Nucl. Phys. A **302**, 413 (1978).
57. V. Kleber *et al.*, Eur. J. Phys. A **9**, 1 (2000).
58. J. Patzold *et al.*, Phys. Rev. C **67**, 052202 (2003).
59. E. Hernandez and E. Oset, Phys. Rev. C **60**, 025204 (1999).
60. A. Faessler, C. Fuchs, M. I. Krivoruchenko, and B. V. Martemyanov, J. Phys. G **29**, 603 (2003).
61. C. Fuchs, M. I. Krivoruchenko, H. L. Yadav, *et al.*, Phys. Rev. C **67**, 025202 (2003).
62. K. Yasuda *et al.*, Phys. Rev. Lett. **82**, 4775 (1999).
63. G. Blanpied *et al.*, Phys. Rev. C **61**, 024604 (2000).
64. C. Bochna *et al.*, Phys. Rev. Lett. **81**, 4576 (1998).
65. K. Wijesooriya *et al.*, Phys. Rev. Lett. **86**, 2975 (2001).
66. S. P. Merkuriev, A. K. Motovilov, and S. D. Yakovlev, Teor. Mat. Fiz. **94**, 435 (1993); Yu. A. Kuperin *et al.*, in *Properties of Few-Body and Quark–Hadronic Systems* (Vilnus, 1986), p. 28.
67. B. D. Serot and J. D. Walecka, Adv. Nucl. Phys. **16**, 1 (1986); Int. J. Mod. Phys. E **6**, 515 (1997).
68. Z. Y. Ma, H. Toki, B. Chen, and N. Van Giai, Prog. Theor. Phys. **98**, 917 (1998); Z. Y. Ma *et al.*, Nucl. Phys. A **686**, 173 (2001); **703**, 222 (2002).
69. P. Ring *et al.*, Nucl. Phys. A **694**, 249 (2001).

Translated by A. Isaakyan

Physics of Atomic Nuclei, Vol. 67, No. 8, 2004, pp. 1559–1570. From Yadernaya Fizika, Vol. 67, No. 8, 2004, pp. 1581–1592.

ELEMENTARY PARTICLES AND FIELDS
Theory

Prospects for the B_c Studies at LHCb*

I. P. Gouz, V. V. Kiselev[1)], A. K. Likhoded, V. I. Romanovsky, and O. P. Yushchenko

Institute for High Energy Physics, Protvino, Moscow oblast, 142281 Russia

Received April 10, 2003; in final form, November 4, 2003

Abstract—Motivations and perspectives for the studies of the mesons of the (bc) family at LHCb are discussed. The description of production and decays at LHC energies is given in detail. The event yields, detection efficiencies, and background conditions for several B_c decay modes at LHCb are estimated.

1. INTRODUCTION

The B_c meson is the ground state of the $(\bar{b}c)$ system, which in many respects is an intermediate between charmonium and bottonium systems. However, because the B_c mesons carry flavor, they provide a window for studying the heavy-quark dynamics that is very different from that provided by $c\bar{c}$ and $b\bar{b}$ quarkonia.

The first observation of approximately 20 B_c events in the $B_c \to J/\psi l\nu$ decay mode by the CDF Collaboration [1] demonstrates the possibility of experimental study of the B_c meson.

The $(\bar{b}c)$ states have a rich spectroscopy of the orbital and angular-momentum excitations. Below the threshold of decay into a BD pair, one can expect 16 extremely narrow states which decay via a cascade into the ground pseudoscalar state with mass of about 6.3 GeV by radiating photons and pion pairs. The annihilation decays can occur due to weak interactions only and, hence, are suppressed for excited levels.

The production mechanism for the $(\bar{b}c)$ system differs in an essential way from that for the $(\bar{b}b)$ system, because two heavy quark–antiquark pairs must be created in a collision. While the $\bar{b}b$ pair can be created in the parton processes $q\bar{q}, gg \to b\bar{b}$ at the order of α_s^2, the lowest order mechanism for creating the $(\bar{b}c)$ system is at least of α_s^4: $q\bar{q}, gg \to (\bar{b}c)b\bar{c}$, and the gluon–gluon contribution dominates at Tevatron and LHC energies. At LHC with a luminosity of about $\mathcal{L} = 10^{34}\ \mathrm{cm}^{-2}\mathrm{s}^{-1}$, one could expect around 5×10^{10} B_c events per year. At Tevatron energy, the expected yield should be at least one order of magnitude smaller.

The weak decays of B_c mesons are attractive due to the presence of both channels: (i) the b-quark decay with the c quark as a spectator, and (ii) the c-constituent decay with b as a spectator. In addition, the weak annihilation contribution to decay channels is quite visible (around 10%).

The dominant contribution to the B_c lifetime ($\tau_{B_c} \sim 0.5$ ps) comes from the c-quark decays (∼70%), while the b-quark decays and weak annihilation add about 20 and 10%, respectively.

An accurate measurement of the B_c lifetime can provide us with information on both the masses of charm and beauty quarks and the normalization point of the nonleptonic weak Lagrangian in B_c decays.

The experimental study of semileptonic decays and the extraction of the decay form factors can test the spin symmetry derived in the NRQCD and HQET approaches. The measurement of the branching fractions for semileptonic and hadronic modes can provide information about the parameters of the weak Lagrangian and hadronic matrix elements determined by the nonperturbative effects due to quark confinement.

In this paper we, first, summarize our theoretical prediction for the mass spectrum of the B_c-meson family calculated in the framework of potential models (PMs) and describe the radiative transitions between the levels in Section 2. Next, in Section 3, we discuss the estimate of B_c lifetime evaluated in different approaches: the operator product expansion in the inverse heavy-quark mass, the PMs, and QCD sum rules (SRs). Section 4 is devoted to estimates of semileptonic and leptonic branching ratios, basically in the framework of QCD SRs, whose predictions are consistent with those of PMs. The nonleptonic modes are considered in Section 5. The role of Pauli interference and some other effects are stressed. We give a table for a rather long list of the B_c branching

*This article was submitted by the authors in English.

[1)]Institute for High Energy Physics, Protvino, Moscow oblast, 142281 Russia; MIFT, Dolgoprudny, Russia; e-mail: kiselev@th1.ihep.su

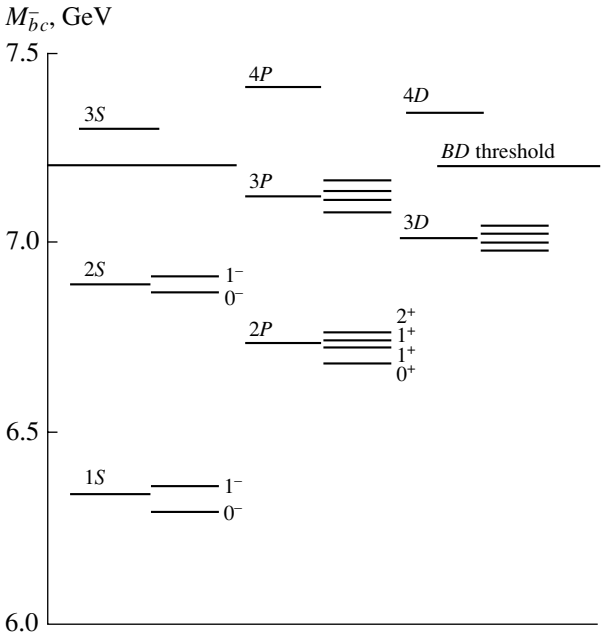

Fig. 1. The mass spectrum of $(\bar{b}c)$ with account of the spin-dependent splittings.

ratios. Section 6 is devoted to the estimates of B_c production at high energies. A competition between two contributions, fragmentation and recombination, at various values of transverse momentum is described. A picture of distributions for the conditions of the LHCb facility at the LHC collider is presented. The basic features of B_c physics at LHCb are summarized in the Conclusions.

2. THE MASS SPECTRUM OF THE B_c FAMILY

The most accurate estimates of $(\bar{b}c)$ masses [2, 3] can be obtained in the framework of nonrelativistic PMs based on the NRQCD expansion over both $1/m_Q$ and $v_{\rm rel} \to 0$ [4].

The uncertainty of evaluation is about 30 MeV. The reason is the following. The PMs [5] were justified for the well-measured masses of charmonium and bottomonium. So, the potentials with different global behavior, i.e., with different $r \to \infty$ and $r \to 0$ asymptotics, have the same form in the range of mean distances between the quarks in heavy quarkonia at $0.2 < r < 1$ fm [6]. The observed regularity in the distances between the excitation levels are approximately flavor independent. The latter is exact for the logarithmic potential (the Feynman–Gell-Mann theorem), where the average kinetic energy of quarks T is a constant value independent of the excitation numbers (the virial theorem) [7]. A slow dependence of the level distances on the reduced mass $m_{\rm red}$ can be taken into account by the use of the Martin potential (power law: $V(r) = A(r/r_0)^a + C$, $a \ll 1$) [8], wherein the predictions are in agreement with the QCD-motivated Buchmüller–Tye (BT) potential with account of the two-loop evolution of the coupling constant at short distances [9].

Thus, one gets the picture of $(\bar{b}c)$ levels (see Fig. 1 and Table 1), which is very close to the texture of charmonium and bottomonium. The difference is the jj binding instead of the LS one.

The spin-dependent perturbation of the potential includes the contribution of the effective one-gluon exchange (the vector part) as well as the scalar confining term [10]:

$$V_{\rm SD}(\mathbf{r}) = \left(\frac{\mathbf{L}\cdot\mathbf{S}_c}{2m_c^2} + \frac{\mathbf{L}\cdot\mathbf{S}_b}{2m_b^2}\right) \times \left(-\frac{dV(r)}{rdr} + \frac{8}{3}\alpha_s\frac{1}{r^3}\right) + \frac{4}{3}\alpha_s\frac{1}{m_c m_b}\frac{\mathbf{L}\cdot\mathbf{S}}{r^3} + \frac{4}{3}\alpha_s\frac{2}{3m_c m_b}\mathbf{S}_c\cdot\mathbf{S}_b\cdot 4\pi\delta(\mathbf{r}) + \frac{4}{3}\alpha_s\frac{1}{m_c m_b}(3(\mathbf{S}_c\cdot\mathbf{n})(\mathbf{S}_b\cdot\mathbf{n}) - \mathbf{S}_c\cdot\mathbf{S}_b)\frac{1}{r^3}, \quad \mathbf{n} = \frac{\mathbf{r}}{r}. \tag{1}$$

The model-dependent value of effective α_s [3] can be extracted from the data on the splitting in the charmonium,

$$M(J/\psi) - M(\eta_c) = \alpha_s\frac{8}{9m_c^2}|R(0)|^2 \approx 117\ \text{MeV}.$$

We take into account the renormalization-group dependence of α_s at the one-loop accuracy by means of introduction of the quarkonium scale [2]

$$\mu^2 = \langle\mathbf{p}^2\rangle = 2\langle T\rangle m_{\rm red}.$$

The estimated difference between the masses of the basic pseudoscalar state and its vector excitation [2] is equal to

$$M(B_c^{*+}) - M(B_c^+) = 65 \pm 15\ \text{MeV}.$$

The mass of the ground state [2] equals

$$M(B_c^+) = 6.25 \pm 0.03\ \text{GeV}, \tag{2}$$

which is in agreement with the CDF measurements $M(B_c) = 6.4 \pm 0.19$ GeV [1].

2.1. Radiative Transitions

The bright feature of the $(\bar{b}c)$ family is that there are no annihilation decay modes due to the strong interaction. Thus, the excitations, in a cascade way, decay into the ground state with the emission of photons and pion–pion pairs.

Table 1. The mass spectrum of $(\bar{b}c)$ with account of the spin-dependent splittings

State	Martin [8]	BT [9]	State	Martin [8]	BT [9]
1^1S_0	6.253	6.264	3^1P_0	7.088	7.108
1^1S_1	6.317	6.337	$3P1^+$	7.113	7.135
2^1S_0	6.867	6.856	$3P1'^+$	7.124	7.142
2^1S_1	6.902	6.899	3^3P_2	7.134	7.153
2^1P_0	6.683	6.700	$3D2^-$	7.001	7.009
$2P1^+$	6.717	6.730	3^5D_3	7.007	7.005
$2P1'^+$	6.729	6.736	3^3D_1	7.008	7.012
2^3P_2	6.743	6.747	$3D2'^-$	7.016	7.012

The formulas for the $E1$ transitions are slightly modified:

$$\Gamma(\bar{n}P_J \to n^1S_1 + \gamma) \tag{3}$$
$$= \frac{4}{9}\alpha_{\rm em}Q_{\rm eff}^2\omega^3 I^2(\bar{n}P; nS)w_J(\bar{n}P),$$
$$\Gamma(\bar{n}P_J \to n^1S_0 + \gamma)$$
$$= \frac{4}{9}\alpha_{\rm em}Q_{\rm eff}^2\omega^3 I^2(\bar{n}P; nS)(1 - w_J(\bar{n}P)),$$
$$\Gamma(n^1S_1 \to \bar{n}P_J + \gamma)$$
$$= \frac{4}{27}\alpha_{\rm em}Q_{\rm eff}^2\omega^3 I^2(nS; \bar{n}P)(2J+1)w_J(\bar{n}P),$$
$$\Gamma(n^1S_0 \to \bar{n}P_J + \gamma)$$
$$= \frac{4}{9}\alpha_{\rm em}Q_{\rm eff}^2\omega^3 I^2(nS; \bar{n}P)(2J+1)(1 - w_J(\bar{n}P)),$$
$$\Gamma(\bar{n}P_J \to nD_{J'} + \gamma)$$
$$= \frac{4}{27}\alpha_{\rm em}Q_{\rm eff}^2\omega^3 I^2(nD; \bar{n}P)(2J'+1)w_J(\bar{n}P))$$
$$\times w_{J'}(nD)S_{JJ'},$$
$$\Gamma(nD_J \to \bar{n}P_{J'} + \gamma)$$
$$= \frac{4}{27}\alpha_{\rm em}Q_{\rm eff}^2\omega^3 I^2(nD; \bar{n}P)(2J'+1)w_{J'}(\bar{n}P))$$
$$\times w_J(nD)S_{J'J},$$

where ω is the photon energy and $\alpha_{\rm em}$ is the electromagnetic fine structure constant. In Eq. (3), one uses

$$Q_{\rm eff} = \frac{m_cQ_{\bar{b}} - m_bQ_c}{m_c + m_b}, \tag{4}$$

where $Q_{c,b}$ are the electric charges of the quarks. For the B_c meson with the parameters from the Martin potential, one gets $Q_{\rm eff} = 0.41$. $w_J(nL)$ is the probability that the spin $S = 1$ in the nL state. $S_{JJ'}$ are the statistical factors. The $I(\bar{n}L; nL')$ value is expressed through the radial wave functions,

$$I(\bar{n}L; nL') = \left|\int R_{\bar{n}L}(r)R_{nL'}(r)r^3dr\right|. \tag{5}$$

Table 2. The total widths of $(\bar{b}c)$ states with the Martin potential

State	$\Gamma_{\rm tot}$, keV	Dominant decay mode	BR, %
1^1S_1	0.06	$1^1S_0 + \gamma$	100
2^1S_0	67.8	$1^1S_0 + \pi\pi$	74
2^1S_1	86.3	$1^1S_1 + \pi\pi$	58
2^1P_0	65.3	$1^1S_1 + \gamma$	100
$2P1^+$	89.4	$1^1S_1 + \gamma$	87
$2P1'^+$	139.2	$1^1S_0 + \gamma$	94
2^3P_2	102.9	$1^1S_1 + \gamma$	100
3^1P_0	44.8	$2^1S_1 + \gamma$	57
$3P1^+$	65.3	$2^1S_1 + \gamma$	49
$3P1'^+$	92.8	$2^1S_0 + \gamma$	63
3^3P_2	71.6	$2^1S_1 + \gamma$	69
$3D2^-$	95.0	$2P1^+ + \gamma$	47
3^5D_3	107.9	$2^3P_2 + \gamma$	71
3^3D_1	155.4	$2^1P_0 + \gamma$	51
$3D2'^-$	122.0	$2P1'^+ + \gamma$	38

For the dipole magnetic $M1$ transitions, one has

$$\Gamma(\bar{n}^1S_i \to n^1S_f + \gamma) = \frac{16}{3}\mu_{\rm eff}^2\omega^3(2f+1)A_{if}^2, \tag{6}$$

where

$$A_{if} = \int R_{\bar{n}S}(r)R_{nS}(r)j_0(\omega r/2)r^2dr$$

and

$$\mu_{\rm eff} = \frac{1}{2}\frac{\sqrt{\alpha_{\rm em}}}{2m_cm_b}(Q_cm_b - Q_{\bar{b}}m_c). \tag{7}$$

Note that, in contrast to the ψ and Υ particles, the total width of the B_c^* meson is equal to the width of its radiative decay into the $B_c(0^-)$ state.

Thus, below the threshold of decay into the BD pair, the theory predicts the existence of 16 narrow $(\bar{b}c)$ states (see Table 1), which do not annihilate due to the strong interactions, but they have cascade radiative transitions into the ground long-lived pseudoscalar state, the B_c^+ meson.

Table 3. The branching ratios of the B_c decay modes calculated in the framework of the inclusive OPE approach by summing up the exclusive modes in the potential model [12, 13] and according to the semi-inclusive estimates in the sum rules of QCD and NRQCD [14, 15]

B_c decay mode	OPE, %	PM, %	SR, %
$\bar{b} \to \bar{c}l^+\nu_l$	3.9 ± 1.0	3.7 ± 0.9	2.9 ± 0.3
$\bar{b} \to \bar{c}u\bar{d}$	16.2 ± 4.1	16.7 ± 4.2	13.1 ± 1.3
$\sum \bar{b} \to \bar{c}$	25.0 ± 6.2	25.0 ± 6.2	19.6 ± 1.9
$c \to sl^+\nu_l$	8.5 ± 2.1	10.1 ± 2.5	9.0 ± 0.9
$c \to su\bar{d}$	47.3 ± 11.8	45.4 ± 11.4	54.0 ± 5.4
$\sum c \to s$	64.3 ± 16.1	65.6 ± 16.4	72.0 ± 7.2
$B_c^+ \to \tau^+\nu_\tau$	2.9 ± 0.7	2.0 ± 0.5	1.8 ± 0.2
$B_c^+ \to c\bar{s}$	7.2 ± 1.8	7.2 ± 1.8	6.6 ± 0.7

3. B_c LIFETIME AND INCLUSIVE DECAY RATES

The B_c-meson decay processes can be subdivided into three classes: (1) the $\bar{b}$-quark decay with the spectator c quark; (2) the c-quark decay with the spectator $\bar{b}$ quark; and (3) the annihilation channel $B_c^+ \to l^+\nu_l(c\bar{s}, u\bar{s})$, where $l = e, \mu, \tau$.

In $\bar{b} \to \bar{c}c\bar{s}$ decays, one also separates the Pauli interference with the c quark from the initial state. In accordance with the given classification, the total width is the sum over the partial widths

$$\Gamma(B_c \to X) = \Gamma(b \to X) + \Gamma(c \to X) + \Gamma(\text{ann.}) + \Gamma(\text{PI}).$$

For the annihilation channel, the Γ(ann.) width can be reliably estimated in the framework of an inclusive approach where one takes the sum of the leptonic and quark decay modes with account of the hard gluon corrections to the effective four-quark interaction of weak currents. These corrections result in the factor $a_1 = 1.22 \pm 0.04$. The width is expressed through the leptonic constant $f_{B_c} \approx 400$ MeV. This estimate of the quark contribution does not depend on a hadronization model, since a large energy release of the order of the meson mass takes place. From the following expression, one can see that the contribution by light leptons and quarks can be neglected:

$$\Gamma(\text{ann.}) = \sum_{i=\tau,c} \frac{G_F^2}{8\pi} |V_{bc}|^2 f_{B_c}^2 M m_i^2 (1 - m_i^2/m_{B_c}^2)^2 C_i,$$

where $C_\tau = 1$ for the $\tau^+\nu_\tau$ channel and $C_c = 3|V_{cs}|^2 a_1^2$ for the $c\bar{s}$ channel.

As for the nonannihilation decays, in the approach of the operator product expansion (OPE) for the quark currents of weak decays [11], one takes into account the α_s corrections to the free-quark decays and uses the quark–hadron duality for the final states. Then one considers the matrix element for the transition operator over the bound meson state. The latter allows one also to take into account the effects caused by the motion and virtuality of a decaying quark inside the meson because of the interaction with the spectator. In this way, the $\bar{b} \to \bar{c}c\bar{s}$ decay mode turns out to be suppressed almost completely due to the Pauli interference with the charm quark from the initial state. In addition, the c-quark decays with the spectator $\bar{b}$ quark are significantly suppressed in comparison with the free-quark decays because of a large bound energy in the initial state.

In the framework of an exclusive approach, it is necessary to sum up widths of different decay modes calculated in the PMs. While considering the semileptonic decays due to the $\bar{b} \to \bar{c}l^+\nu_l$ and $c \to sl^+\nu_l$ transitions, one finds that the hadronic final states are practically saturated by the lightest bound $1S$ state in the $(\bar{c}c)$ system, i.e., by the η_c and J/ψ particles, and the $1S$ states in the $(\bar{b}s)$ system, i.e., B_s and B_s^*, which can only enter the accessible energetic gap.

Further, the $\bar{b} \to \bar{c}u\bar{d}$ channel, for example, can be calculated through the given decay width of $\bar{b} \to \bar{c}l^+\nu_l$ with account of the color factor and hard gluon corrections to the four-quark interaction. It can be also obtained as a sum over the widths of decays with the $(u\bar{d})$-system bound states.

The results of calculation for the total B_c width in the inclusive OPE and exclusive PM approaches give values consistent with each other (see Table 3), if one takes into account the most significant uncertainty related to the choice of quark masses (especially for the charm quark), so that finally we have

$$\tau[B_c^+]_{\text{OPE, PM}} = 0.55 \pm 0.15 \text{ ps}, \qquad (8)$$

which agrees with the measured value of B_c lifetime.

The OPE estimates of inclusive decay rates agree with recent semi-inclusive calculations in the SRs of QCD and NRQCD [14, 15], where one assumed the saturation of hadronic final states by the ground levels in the $(c\bar{c})$ and $(\bar{b}s)$ systems as well as the factorization allowing one to relate the semileptonic and hadronic decay modes. The Coulomb-like corrections in the heavy-quarkonium states play an essential role in the B_c decays and allow one to remove the disagreement between the estimates in SRs and OPE. In contrast to OPE, where the basic uncertainty is given by the variation of heavy-quark masses, these parameters are fixed by the two-point SRs for bottomonia and charmonia, so that the accuracy of SR calculations for the total width of B_c is determined

by the choice of scale μ for the hadronic weak Lagrangian in decays of charmed quarks. We show this dependence in Fig. 2, where $m_c/2 < \mu < m_c$ and the dark shaded region corresponds to the scales preferred by data on the charmed-meson lifetimes.

Assuming the preferable choice of scale in the $c \to s$ decays of B_c to be equal to $\mu^2_{B_c} \approx (0.85\ \text{GeV})^2$, setting $a_1(\mu_{B_c}) = 1.20$, and neglecting the contributions caused by nonzero a_2 in charmed-quark decays [15], in the framework of semi-inclusive SR calculations, we predict

$$\tau[B_c]_{\text{SR}} = 0.48 \pm 0.05\ \text{ps}, \qquad (9)$$

which agrees with the direct summation of exclusive channels calculated in the next sections. In Fig. 2, we show the exclusive estimate of lifetime too.

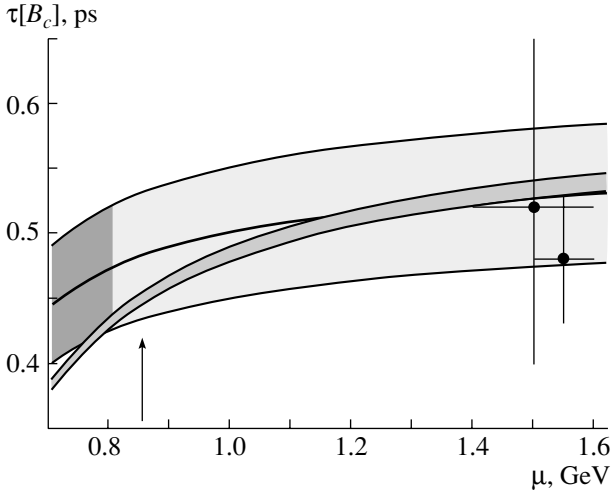

Fig. 2. The B_c lifetime calculated in QCD sum rules vs. the scale of hadronic weak Lagrangian in the decays of charmed quarks. The wide shaded region shows the uncertainty of semi-inclusive estimates, the dark shaded region is the preferable choice as given by the lifetimes of charmed mesons. The dots represent the values in the OPE approach taken from [11]. The narrow shaded region represents the result obtained by summing up the exclusive channels with the variation of hadronic scale in the decays of beauty antiquarks in the range of $1 < \mu_b < 5$ GeV. The arrow points to the preferable prescription of $\mu = 0.85$ GeV as discussed in [15].

4. SEMILEPTONIC AND LEPTONIC MODES

4.1. Semileptonic Decays

The semileptonic decay rates are underestimated in the QCD SR approach of [16], because large Coulomb-like corrections were not taken into account. The recent analysis of SRs in [14, 15, 17] decreased the uncertainty, so that the estimates agree with the calculations in the PMs.

The absolute values of semileptonic widths are presented in Table 4 in comparison with the estimates obtained in PMs.

In practice, the most constructive information is given by the J/ψ mode, since this charmonium is clearly detected in experiments due to the pure leptonic decays [1]. In addition to the investigation of various form factors and their dependence on the transfer squared, we would like to stress that the measurement of decay to the excited state of charmonium, i.e., ψ', could answer the question on the reliability of QCD predictions for the decays to the excited states. We see that, at the moment, the finite-energy SRs predict the width of $B_c^+ \to \psi' l^+ \nu$ decays in reasonable agreement with the PMs.

4.2. Leptonic Decays

The dominant leptonic decay of B_c is given by the $\tau\nu_\tau$ mode (see Table 3). However, it has a low experimental efficiency of detection because of hadronic background in the τ decays or a missing energy. Recently, in [24], the enhancement of muon and electron channels in the radiative modes was studied. The additional photon allows one to remove the helicity suppression for the leptonic decay of a pseudoscalar particle, which leads, say, to the double increase of the muonic mode.

5. NONLEPTONIC MODES

In comparison with the inclusive nonleptonic widths, which can be estimated in the framework of quark–hadron duality (see Table 3), the calculations of exclusive modes usually involve the approximation of factorization [25], which, as expected, can be quite accurate for the B_c, since the quark–gluon sea is suppressed in the heavy quarkonium. Thus, the important parameters are the factors a_1 and a_2 in the nonleptonic weak Lagrangian, which depend on the normalization point suitable for the B_c decays.

The QCD SR estimates for the nonleptonic decays of charmed quarks in B_c give agreement of results with the values predicted by the PMs which is rather good for the direct transitions with no permutation of color lines, i.e., the class-I processes with the factor of a_1 in the nonleptonic amplitude determined by the effective Lagrangian. In contrast, the SR predictions are significantly enhanced in comparison with the values calculated in the PMs for the transitions with color permutation, i.e., for the class-II processes with the factor of a_2.

Further, for the transitions wherein the Pauli interference is significantly involved, the class-III processes, we find that the absolute values of different terms given by the squares of a_1 and a_2 calculated in the SRs are in agreement with the estimates of

Table 4. Exclusive widths (in 10^{-15} GeV) of semileptonic B_c^+ decays

Mode	[18]	[19]	[20]	[21]	[22]	[23]
$B_c^+ \to \eta_c e^+ \nu$	11	11.1	14.2	14	10.4	8.6
$B_c^+ \to \eta_c \tau^+ \nu$	3.3			3.8		2.9
$B_c^+ \to \eta_c' e^+ \nu$	0.60		0.73		0.74	
$B_c^+ \to \eta_c' \tau^+ \nu$	0.050					
$B_c^+ \to J/\psi e^+ \nu$	28	30.2	34.4	33	16.5	18
$B_c^+ \to J/\psi \tau^+ \nu$	7.0			8.4		5.0
$B_c^+ \to \psi' e^+ \nu$	1.94		1.45		3.1	
$B_c^+ \to \psi' \tau^+ \nu$	0.17					
$B_c^+ \to D^0 e^+ \nu$	0.059	0.049	0.094	0.26	0.026	
$B_c^+ \to D^0 \tau^+ \nu$	0.032			0.14		
$B_c^+ \to D^{*0} e^+ \nu$	0.27	0.192	0.269	0.49	0.053	
$B_c^+ \to D^{*0} \tau^+ \nu$	0.12			0.27		
$B_c^+ \to B_s^0 e^+ \nu$	59	14.3	26.6	29	13.8	15
$B_c^+ \to B_s^{*0} e^+ \nu$	65	50.4	44.0	37	16.9	34
$B_c^+ \to B^0 e^+ \nu$	4.9	1.14	2.30	2.1		
$B_c^+ \to B^{*0} e^+ \nu$	8.5	3.53	3.32	2.3		

PMs. However, we stress that we have found that, due to the Pauli interference determining the negative sign of two amplitudes with a_1 and a_2, the overall sign in some modes should be different from those obtained in the PM. Taking into account the negative value of a_2 with respect to a_1, we see that half of the decays should be enhanced in comparison with the case of Pauli interference switched off, while the other half is suppressed. The characteristic values of effects caused by the Pauli interference are presented in Table 5, where we put the widths in the form

$$\Gamma = \Gamma_0 + \Delta\Gamma, \qquad \Gamma_0 = x_1 a_1^2 + x_2 a_2^2,$$
$$\Delta\Gamma = z a_1 a_2.$$

Then, we conclude that the Pauli interference can be straightforwardly tested in the listed decays, wherein its significance reaches about 50%.

At large recoils as in $B_c^+ \to J/\psi\pi^+(\rho^+)$, the spectator picture of transition can be broken by the hard gluon exchanges [26]. The spin effects in such decays were studied in [27]. However, we emphasize that the significant rates of B_c decays to the P- and D-wave charmonium states point out that the corrections in the second order of the heavy-quark velocity in the heavy quarkonia under study could be quite substantial and suppress the corresponding decay rates, since the relative momentum of heavy quarks inside the quarkonium, if different from zero, should enhance the virtuality of gluon exchange, which suppresses the decay amplitudes.

The widths of nonleptonic c-quark decays in the framework of the SR are greater than those of PM. In this respect, we check that our calculations are consistent with the inclusive ones. So, we sum up the calculated exclusive widths and estimate the total width of the B_c meson as shown in Fig. 2, which points to good agreement of our calculations with those of OPE and semi-inclusive estimates.

Another interesting point is the possibility of extracting the factorization parameters a_1 and a_2 in the c-quark decays by measuring the branching ratios

$$\frac{\Gamma[B_c^+ \to B^+ \bar{K}^0]}{\Gamma[B_c^+ \to B^0 K^+]} = \frac{\Gamma[B_c^+ \to B^+ \bar{K}^{*0}]}{\Gamma[B_c^+ \to B^0 K^{*+}]} \qquad (10)$$
$$= \frac{\Gamma[B_c^+ \to B^{*+} \bar{K}^0]}{\Gamma[B_c^+ \to B^{*0} K^+]} = \frac{\Gamma[B_c^+ \to B^{*+} \bar{K}^{*0}]}{\Gamma[B_c^+ \to B^{*0} K^{*+}]}$$
$$= \left|\frac{V_{cs}}{V_{cd}^2}\right|^2 \left(\frac{a_2}{a_1}\right)^2.$$

This procedure can give the test for the factorization approach itself.

The suppressed decays caused by the flavor-changing neutral currents were studied in [28].

The CP violation in B_c decays can be investigated in the same manner as is done in charged B decays. The expected CP asymmetry of $\mathcal{A}(B_c^{\pm} \to J/\psi D^{\pm})$ is about 4×10^{-3} when the corresponding branching ratio is suppressed as 10^{-4} [29]. The reference-triangle ideology can be applied for the model-independent extraction of CKM-matrix angle γ. However, the corresponding branchings are suppressed, e.g., $\mathrm{BR}(B_c^+ \to D_s^+ D^0) \sim 10^{-5}$. Thus, the direct study of CP violation in B_c decays is difficult in practice because of the low relative yield of B_c with respect to ordinary B mesons: $\sigma(B_c)/\sigma(B) \sim 10^{-3}$.

Another possibility is the lepton tagging of B_s in $B_c^{\pm} \to B_s^{(*)} l^{\pm} \nu$ decays for the study of mixing and CP violation in the B_s sector [30].

We present here the current status of B_c-meson decays. We have found that the various approaches, OPE, PMs, and QCD SRs, result in close estimates, while the SRs as explored for the various heavy-quark systems lead to a smaller uncertainty due to quite accurate knowledge of the heavy-quark masses. So, summarizing, we expect that the dominant contribution to the B_c lifetime is given by the charmed-quark decays ($\sim$70%), while the b-quark decays and the weak annihilation add about 20 and 10%, respectively. The Coulomb-like α_s/v corrections play an essential role in the determination of exclusive form factors in the QCD SRs. The form factors obey the relations dictated by the spin symmetry of NRQCD and HQET with quite good accuracy expected.

The predictions of QCD SRs for the exclusive decays of B_c are summarized in Table 6 at fixed values of factors $a_{1,2}$ and lifetime. In addition to the decay channels with the heavy charmonium J/ψ well detectable through its leptonic mode, one could expect significant information on the dynamics of B_c decays from the channels with single heavy meson, if the experimental efficiency allows one to extract a signal from the cascade decays. An interesting opportunity is presented by the relations for the ratios in (10), which can shed light on characteristics of the nonleptonic decays in an explicit form.

We have found that the $\bar{b}$ decay to the doubly charmed states gives

$$\mathrm{BR}[B_c^+ \to \bar{c}cc\bar{s}] \approx 3.26\%,$$

so that, in the absolute value of width, it can be compared with the estimate of spectator decay [11],

$$\Gamma[B_c^+ \to \bar{c}cc\bar{s}]\big|_{\mathrm{sr}} \approx 48 \times 10^{-15}\ \mathrm{GeV},$$

$$\Gamma[B_c^+ \to \bar{c}cc\bar{s}]\big|_{\mathrm{spect}} \approx 90 \times 10^{-15}\ \mathrm{GeV},$$

and we find the suppression factor of about 1/2. This result is in agreement with the estimate in OPE [11], where a strong dependence of the negative term caused by the Pauli interference on the normalization scale of the nonleptonic weak Lagrangian was emphasized, so that, at large scales, one gets approximately the same suppression factor of 1/2 too.

Table 5. The effect of Pauli interference in the exclusive nonleptonic decay widths of the B_c meson with the c quark as the spectator at $a_1 = 1.18$, $a_2 = -0.22$

Mode	$\Delta\Gamma/\Gamma_0$, %
$B_c^+ \to \eta_c D_s^+$	59
$B_c^+ \to \eta_c D_s^{*+}$	−41
$B_c^+ \to J/\psi D_s^+$	−55
$B_c^+ \to J/\psi D_s^{*+}$	53
$B_c^+ \to \eta_c D^+$	43
$B_c^+ \to \eta_c D^{*+}$	−47
$B_c^+ \to J/\psi D^+$	−46
$B_c^+ \to J/\psi D^{*+}$	48

At the moment, we certainly state that an accurate direct measurement of B_c lifetime can provide us with information on both the masses of charmed and beauty quarks and the normalization point of the nonleptonic weak Lagrangian in B_c decays (the a_1 and a_2 factors). The experimental study of semileptonic decays and the extraction of ratios for the form factors can test the spin symmetry derived in the NRQCD and HQET approaches and decrease the theoretical uncertainties in the corresponding theoretical evaluation of quark parameters, as well as the hadronic matrix elements, determined by the nonperturbative effects caused by the quark confinement. The measurement of branching fractions for the semileptonic and nonleptonic modes and their ratios can give information on the values of factorization parameters, which depend again on the normalization of the nonleptonic weak Lagrangian. The charmed quark counting in B_c decays is related to the overall contribution of b-quark decays, as well as to the suppression of the $\bar{b} \to c\bar{c}\bar{s}$ transition because of the destructive Pauli interference, whose value depends on the nonperturbative parameters (roughly estimated, the leptonic constant) and nonleptonic weak Lagrangian.

Thus, progress in measuring the B_c lifetime and decays could altogether improve the theoretical understanding of what really happens in heavy-quark decays.

We point also to papers wherein some aspects of B_c decays and spectroscopy were studied: nonleptonic decays in [31], polarization effects in the radiative leptonic decays [32], relativistic effects [33],

Table 6. Branching ratios [18] of exclusive B_c^+ decays at the fixed choice of factors: $a_1^c = 1.20$ and $a_2^c = -0.317$ in the nonleptonic decays of c quark, and $a_1^b = 1.14$ and $a_2^b = -0.20$ in the nonleptonic decays of $\bar{b}$ quark (the lifetime of B_c is appropriately normalized by $\tau[B_c] \approx 0.45$ ps)

Mode	BR, %	Mode	BR, %	Mode	BR, %
$B_c^+ \to \eta_c e^+ \nu$	0.75	$B_c^+ \to J/\psi K^+$	0.011	$B_c^+ \to B_s^0 K^+$	1.06
$B_c^+ \to \eta_c \tau^+ \nu$	0.23	$B_c \to J/\psi K^{*+}$	0.022	$B_c^+ \to B_s^{*0} K^+$	0.37
$B_c^+ \to \eta_c' e^+ \nu$	0.041	$B_c^+ \to D^+ \bar{D}^0$	0.0053	$B_c^+ \to B_s^0 K^{*+}$	–
$B_c^+ \to \eta_c' \tau^+ \nu$	0.0034	$B_c^+ \to D^+ \bar{D}^{*0}$	0.0075	$B_c^+ \to B_s^{*0} K^{*+}$	–
$B_c^+ \to J/\psi e^+ \nu$	1.9	$B_c^+ \to D^{*+} \bar{D}^0$	0.0049	$B_c^+ \to B^0 \pi^+$	1.06
$B_c^+ \to J/\psi \tau^+ \nu$	0.48	$B_c^+ \to D^{*+} \bar{D}^{*0}$	0.033	$B_c^+ \to B^0 \rho^+$	0.96
$B_c^+ \to \psi' e^+ \nu$	0.132	$B_c^+ \to D_s^+ \bar{D}^0$	0.00048	$B_c^+ \to B^{*0} \pi^+$	0.95
$B_c^+ \to \psi' \tau^+ \nu$	0.011	$B_c^+ \to D_s^+ \bar{D}^{*0}$	0.00071	$B_c^+ \to B^{*0} \rho^+$	2.57
$B_c^+ \to D^0 e^+ \nu$	0.004	$B_c^+ \to D_s^{*+} \bar{D}^0$	0.00045	$B_c^+ \to B^0 K^+$	0.07
$B_c^+ \to D^0 \tau^+ \nu$	0.002	$B_c^+ \to D_s^{*+} \bar{D}^{*0}$	0.0026	$B_c^+ \to B^0 K^{*+}$	0.015
$B_c^+ \to D^{*0} e^+ \nu$	0.018	$B_c^+ \to \eta_c D_s^+$	0.86	$B_c^+ \to B^{*0} K^+$	0.055
$B_c^+ \to D^{*0} \tau^+ \nu$	0.008	$B_c^+ \to \eta_c D_s^{*+}$	0.26	$B_c^+ \to B^{*0} K^{*+}$	0.058
$B_c^+ \to B_s^0 e^+ \nu$	4.03	$B_c^+ \to J/\psi D_s^+$	0.17	$B_c^+ \to B^+ \bar{K}^0$	1.98
$B_c^+ \to B_s^{*0} e^+ \nu$	5.06	$B_c^+ \to J/\psi D_s^{*+}$	1.97	$B_c^+ \to B^+ \bar{K}^{*0}$	0.43
$B_c^+ \to B^0 e^+ \nu$	0.34	$B_c^+ \to \eta_c D^+$	0.032	$B_c^+ \to B^{*+} \bar{K}^0$	1.60
$B_c^+ \to B^{*0} e^+ \nu$	0.58	$B_c^+ \to \eta_c D^{*+}$	0.010	$B_c^+ \to B^{*+} \bar{K}^{*0}$	1.67
$B_c^+ \to \eta_c \pi^+$	0.20	$B_c^+ \to J/\psi D^+$	0.009	$B_c^+ \to B^+ \pi^0$	0.037
$B_c^+ \to \eta_c \rho^+$	0.42	$B_c^+ \to J/\psi D^{*+}$	0.074	$B_c^+ \to B^+ \rho^0$	0.034
$B_c^+ \to J/\psi \pi^+$	0.13	$B_c^+ \to B_s^0 \pi^+$	16.4	$B_c^+ \to B^{*+} \pi^0$	0.033
$B_c^+ \to J/\psi \rho^+$	0.40	$B_c^+ \to B_s^0 \rho^+$	7.2	$B_c^+ \to B^{*+} \rho^0$	0.09
$B_c^+ \to \eta_c K^+$	0.013	$B_c^+ \to B_s^{*0} \pi^+$	6.5	$B_c^+ \to \tau^+ \nu_\tau$	1.6
$B_c^+ \to \eta_c K^{*+}$	0.020	$B_c^+ \to B_s^{*0} \rho^+$	20.2	$B_c^+ \to c\bar{s}$	4.9

spectroscopy in the systematic approach of potential nonrelativistic QCD in [34], nonperturbative effects in semileptonic decays [35], exclusive and inclusive decays of B_c states into a lepton pair and hadrons [36], rare decays in [37], and spectroscopy and radiative decays in [38].

6. B_c PRODUCTION

The $(\bar{b}c)$ system is a heavy quarkonium; i.e., it contains two heavy quarks. This determines the general features for the B_c-meson production in various interactions:

(i) Perturbative calculations for the hard associative production of two heavy pairs of $\bar{c}c$ and $\bar{b}b$.

(ii) A soft nonperturbative binding of nonrelativistic quarks in the color-singlet state can be described in the framework of PMs.

The two above conditions result in the suppression of the B_c yield of the order of 10^{-3} with respect to beauty hadrons.

As was mentioned above, the consideration of mechanisms for the hadronic production of different spin B_c states is based on the factorization of hard parton production of heavy quarks $(\bar{b}b\bar{c}c)$ and soft coupling of the $(\bar{b}c)$ bound state [39]. In the first stage of description, the hard subprocess can be reliably calculated in the framework of QCD perturbation theory, while in the second stage the quark binding in the heavy quarkonium can be described in the nonrelativistic PM assigned to the $(\bar{b}c)$-pair rest system. The latter means that one performs the integration of the final quark state over the quarkonium wave function in momentum space. Since the relative quark velocity inside the meson is close to zero, the

perturbative matrix element can be expanded in series over the relative quark momentum, which is low in comparison with the quark masses determining the scale of virtualities and energies in the matrix element. In the leading approximation, one considers only the first nonzero term of such an expansion, so that, for the S-wave states, the matrix element of the parton subprocess for the B_c production is expressed through the perturbative matrix element for the production of four heavy quarks ($gg \to \bar{b}b\bar{c}c$) with the corresponding projection to the vector or pseudoscalar spin state of the ($\bar{b}c$) system, which is the color singlet, and through the factor of the radial wave function at the origin, $R_{nS}(0)$, for the given quarkonium. The perturbative matrix element is calculated for the ($\bar{b}c$) state, where the quarks move with the same velocity; i.e., one neglects the relative motion of $\bar{b}$ and c.

For the P-wave states, the PM gives the factor in the form of the first derivative of the radial wave function at the origin, $R'_{nL}(0)$. In the perturbative part, one has to calculate the first derivative of the matrix element over the relative quark momentum at the point where the velocities of quarks entering the quarkonium are equal to each other.

Thus, in addition to the heavy-quark masses, the values of $R_{nS}(0)$, $R'_{nL}(0)$, and α_s are the parameters of calculation for the partonic production of B_c mesons. In calculations, we use the wave function parameters equal to the values calculated in [2] and $R'_{2P}(0) = 0.50$ GeV$^{3/2}$. The value of $R(0)$ can be related with the leptonic constant, $\tilde{f}$, so that we have

$$\tilde{f}_{1S} = 0.47 \text{ GeV}, \qquad \tilde{f}_{2S} = 0.32 \text{ GeV},$$

$$\tilde{f}_n = \sqrt{\frac{3}{\pi M_n}} R_{nS}(0).$$

In the approximation of the weak quark binding inside the meson, one has $M_{B_c} = m_b + m_c$, so that the performable phase space in calculations is close to the physical one at the choices of $m_b = 4.8$ GeV, $m_c = 1.5$ GeV for the $1S$ state; $m_b = 5.1$ GeV, $m_c = 1.8$ GeV for the $2S$ state; and $m_b = 5.0$ GeV, $m_c = 1.7$ GeV for the $2P$ state.

At large transverse momenta of the B_c meson, $p_T \gg M_{B_c}$, the production mechanism enters the regime of $\bar{b}$-quark fragmentation (see Fig. 3), so that the scale determining the QCD coupling constant in hard $\bar{b}b$ production is given by $\mu^2_{\bar{b}b} \sim M^2_{B_c} + p^2_T$, and in the hard fragmentation production of the additional pair of heavy quarks $\bar{c}c$, we get $\mu_{\bar{c}c} \sim m_c$. This scale choice is caused by the high-order corrections of perturbation theory to the hard gluon propagators, where the summing of logarithms over the virtualities leads to the indicated μ values. Therefore, the normalization

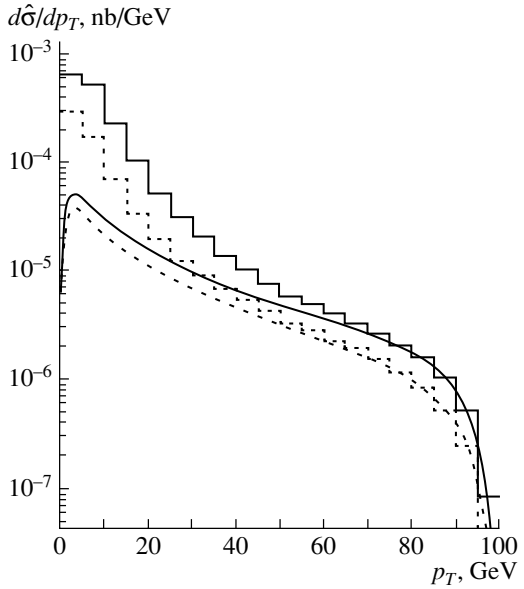

Fig. 3. The differential cross section for the $B_c^{(*)}$-meson production in gluon–gluon collisions as calculated in the perturbative QCD over the complete set of diagrams in the $O(\alpha_s^4)$ order at 200 GeV. The dashed and solid histograms present the pseudoscalar and vector states, respectively, in comparison with the corresponding results of the fragmentation model shown by the smooth curves.

of the matrix element is determined by the value of $\alpha_s(\mu_{\bar{b}b})\alpha_s(\mu_{\bar{c}c}) \approx 0.18 \cdot 0.28$. In calculations, we use the single combined value of $\alpha_s = 0.22$.

The parton subprocess of gluon–gluon fusion $gg \to B_c^+ + b + \bar{c}$ dominates in the hadron–hadron production of B_c mesons. In the leading approximation of QCD perturbation theory, it requires the calculation of 36 diagrams in the fourth order over the α_s coupling constant.

By the general theorem on factorization, it is clear that, at high transverse momenta, the fragmentation of the heavier quark $Q \to (Q\bar{q}) + q$ must dominate. It is described by the factorized formula

$$\frac{d\sigma}{dp_T} = \int \left.\frac{d\hat{\sigma}(\mu; gg \to Q\bar{Q})}{dk_T}\right|_{k_T = p_T/x} \times D^{Q\to(Q\bar{q})}(x;\mu)\frac{dx}{x}, \tag{11}$$

where μ is the factorization scale, $d\hat{\sigma}/dk_T$ is the cross section for the gluon–gluon production of quarks $Q + \bar{Q}$, and D is the fragmentation function.

The calculation for the complete set of diagrams of the $O(\alpha_s^4)$ contribution [39] allows one to determine a value of the transverse momentum $p_T^{\min}$, which is the low boundary of the region, where the subprocess of gluon–gluon B_c-meson production enters the regime of factorization for the hard production of a $b\bar{b}$ pair

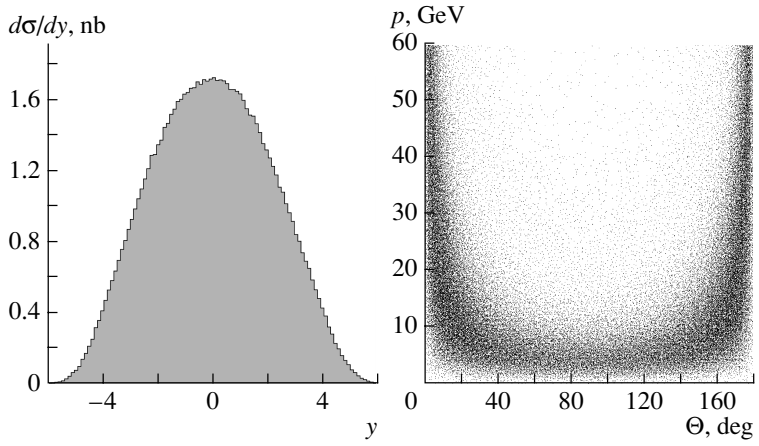

Fig. 4. $d\sigma/dy$ (left) and B_c momentum vs. angle (right) for the $B_c^+(1S_0)$ at LHC energy.

and the subsequent fragmentation of a $\bar{b}$ quark into the bound $(\bar{b}c)$ state, as follows from the theorem on the factorization of the hard processes in perturbative QCD.

The $p_T^{\min}$ value turns out to be much greater than the M_{B_c} mass, so that the dominant contribution to the total cross section of gluon–gluon B_c production is given by the diagrams of nonfragmentational type, i.e., by the recombination of heavy quarks. Furthermore, the convolution of the parton cross section with the gluon distributions inside the initial hadrons leads to the suppression of contributions at large transverse momenta, as well as the subprocesses with large energy in the system of parton mass center, so that the main contribution to the total cross section of hadronic B_c production is given by the region of energies less than or comparable to the B_c-meson mass, where the fragmentation model cannot be applied by its construction. Therefore, one must perform the calculations taking into account all contributions in the given order under consideration in the region near the threshold.

The large numeric value of $p_T^{\min}$ means that the majority of events of the hadronic $B_c^{(*)}$ production certainly do not allow a description in the framework of the fragmentation model. This conclusion looks more evident if one considers the B_c-meson spectrum over the energy.

The basic part of events for the gluon–gluon production of B_c is accumulated in the region of low z close to 0, where the recombination dominates. One can draw a conclusion on the essential destructive interference in the region of z close to 1 and $p_T < p_T^{\min}$ for the pseudoscalar state.

We have considered in detail the contributions of each diagram in the region of $z \to 1$. In the covariant Feynman gauge, the diagrams of the gluon–gluon production of $Q + \bar{Q}$ with the subsequent $Q \to (Q\bar{q})$ fragmentation dominate, as well as the diagrams when the $q\bar{q}$ pair is produced in the region of the initial gluon splitting. However, the contribution of the latter diagrams leads to a destructive interference with the fragmentation amplitude, and this results in the "reduction" of the production cross section in the region of z close to 1. In the axial gauge with the vector $n^\mu = p_{\bar{Q}}^\mu$, this effect of the interference manifests itself still brighter, since the diagrams like the splitting of gluons dominate by several orders of magnitude over the fragmentation, but the destructive interference results in the cancellation of such extremely large contributions. This interference is caused by the non-Abelian nature of QCD, i.e., by the presence of the gluon self-action vertices.

The use of the CTEQ5L parametrization for the structure functions of a nucleon [40] leads to the total hadronic cross sections for the B_c mesons of about 0.8 μb, receiving contributions from the following:

$1S_0$	$1S_1$	$2S_0$	$2S_1$
0.19 μb	0.47 μb	0.05 μb	0.11 μb.

After summing over the different spin states, the total cross sections for the production of P-wave levels is equal to 7% of the S-state cross section.

At LHC with the luminosity $\mathcal{L} = 10^{34}$ cm^{-2}s^{-1} and $\sqrt{s} = 14$ TeV, one could expect $4.5 \times 10^{10} B_c^+$ events/yr.

Nevertheless, the P-wave states could be of particular interest due to their radiative decays with relatively energetic photons (around 500 MeV in the B_c rest frame). For P-wave states, the leading color-singlet matrix element and the leading color-octet matrix elements are both suppressed by a factor of v^2 (relative velocity of the charmed quark) relative to the

color-singlet matrix element for the S wave, which can enhance the P-wave contribution.

In Fig. 4, the $d\sigma/dy$ distribution is presented. The y distribution shows a maximum in the central region; however, considering the experimental observability of the B_c states, one should care about the momentum of the meson to ensure a reasonable γ factor for B_c and visible separation of the B_c decay vertex from the primary one.

The right part of the same figure shows the dependence of the B_c momentum on the angle. One can see that the central region is dominated by low-momentum mesons, which makes the observation of these states in the central region quite a difficult task. On the other hand, the forward–backward (LHCb acceptance) regions are dominated by very energetic mesons.

In the region of the LHCb acceptance ($\Theta < 17^\circ$), the expected number of events with the nominal luminosity of 2×10^{32} cm^{-2} s^{-1} is about 10^9 per year. Taking the value of ~ 0.1 as an approximation for the reconstruction efficiency of the decay $B_c \to J/\psi\pi \to \mu\mu\pi$, for example, one gets a total number of 2×10^4 reconstructed events per year.

The topology of the events with B_c-meson production is somewhat specific due to extreme kinematics which, particularly, is responsible for the enhancement of the forward–backward regions. The main feature of the topology of these events consists in the strong correlation in the direction of B_c and associated D- and b-meson momenta. One should expect an associated production of all three heavy mesons in the same hemisphere and, moreover, in a sufficiently narrow cone.

7. CONCLUSIONS

The family of $(\bar{b}c)$ mesons contains 16 narrow states. The S-wave ones will be produced in pp collisions at LHC energies with relatively large cross sections, ~ 0.1 μb. The total cross section of the B_c production, taking into account the cascade decays of the narrow excited states, can be as high as ~ 1 μb. This value is more than an order of magnitude larger than that at Tevatron energy.

With the total luminosity of about $\mathcal{L} = 10^{34}$ cm^{-2}s^{-1}, one could expect the total amount of B_c mesons produced to be of the order of $N_{B_c} \sim 5 \times 10^{10}$ per year.

The forward–backward regions of the B_c-meson production are more favorable in view of experimental observation due to the strong Lorentz boost of the initial parton system. One can expect $\sim 10^9$ B_c events per year inside LHCb acceptance. This amount is quite sufficient to study the spectroscopy and various decay modes, as well as the lifetime of the ground state.

The inclusive decay mode $B_c \to J/\psi X$ has a branching of about 17%, in comparison with $\sim$1% in $B_{d,s}$-meson decays. These channels produce very well visible signatures, and one could expect $\sim (2\text{–}4) \times 10^4$ events in the decay mode $B_c \to J/\psi\pi \to \mu\mu\pi$ and $\sim 8 \times 10^4$ events in the $B_c \to J/\psi\mu\nu \to \mu\mu\mu\nu$ mode. The Cabbibo-suppressed mode $B_c \to J/\psi K \to \mu\mu K$ can be observed at the level of $\sim 10^3$ events.

The most probable b-spectator decay modes are saturated by the two-body decays $B_c \to B_s^{(*)}\pi^\pm$ and $B_c \to B_s^{(*)}\rho^\pm$, which makes these channels quite interesting for the study of the c-quark decays in the B_c meson. The estimated yield of the reconstructed events could be $\sim 10^3$ events per year in the $B_c \to B_s\pi^\pm$ mode. Approximately the same number of events can be observed in other modes with B_s in the final state, although with worse background conditions.

Rare decay modes, e.g., $B_c \to D^\pm D^0$, could be interesting in view of CP-violation studies; however, the preliminary estimates of the detection efficiencies and branchings involved are not too optimistic and additional studies of the reconstruction and selection procedures are required.

ACKNOWLEDGMENTS

We are very grateful for the contribution of A. Berezhnoy to this work. We also would like to thank the LHCb Collaboration for its warm hospitality and the IHEP group (Protvino) in LHCb for providing support for this work.

This work is partially supported by the Russian Foundation for Basic Research, project nos. 01-02-99315 and 01-02-16585, and by grants of the RF President for Young Doctors of Science no. MD-297.2003.02 and for Scientific Schools no. NSc-1303.2003.2.

REFERENCES

1. F. Abe *et al.* (CDF Collab.), Phys. Rev. Lett. **81**, 2432 (1998); Phys. Rev. D **58**, 112004 (1998).
2. S. S. Gershtein *et al.*, Phys. Rev. D **51**, 3613 (1995).
3. E. Eichten and C. Quigg, Phys. Rev. D **49**, 5845 (1994).
4. G. T. Bodwin, E. Braaten, and G. P. Lepage, Phys. Rev. D **51**, 1125 (1995); T. Mannel and G. A. Schuller, Z. Phys. C **67**, 159 (1995).
5. C. Quigg and J. L. Rosner, Phys. Rep. **56**, 167 (1979).
6. E. Eichten, Preprint FERMILAB-Conf-85/29-T (1985).

7. C. Quigg and J. L. Rosner, Phys. Lett. B **71B**, 153 (1977).
8. A. Martin, Phys. Lett. B **93B**, 338 (1980).
9. W. Buchmüller and S.-H. H. Tye, Phys. Rev. D **24**, 132 (1981).
10. E. Eichten and F. Feinberg, Phys. Rev. Lett. **43**, 1205 (1979); Phys. Rev. D **23**, 2724 (1981); D. Gromes, Z. Phys. C **26**, 401 (1984).
11. I. Bigi, Phys. Lett. B **371**, 105 (1996); M. Beneke and G. Buchalla, Phys. Rev. D **53**, 4991 (1996); A. I. Onishchenko, hep-ph/9912424; Ch.-H. Chang, Sh.-L. Chen, T.-F. Feng, and X.-Q. Li, Commun. Theor. Phys. **35**, 51 (2001); Phys. Rev. D **64**, 014003 (2001).
12. V. V. Kiselev, Mod. Phys. Lett. A **10**, 1049 (1995); Int. J. Mod. Phys. A **9**, 4987 (1994).
13. V. V. Kiselev, A. K. Likhoded, and A. V. Tkabladze, Yad. Fiz. **56**, 128 (1993) [Phys. At. Nucl. **56**, 643 (1993)].
14. V. V. Kiselev, A. K. Likhoded, and A. I. Onishchenko, Nucl. Phys. B **569**, 473 (2000).
15. V. V. Kiselev, A. K. Likhoded, and A. E. Kovalsky, Nucl. Phys. B **585**, 353 (2000); hep-ph/0006104 (2000); hep-ph/0006104.
16. P. Colangelo, G. Nardulli, and N. Paver, Z. Phys. C **57**, 43 (1993); E. Bagan *et al.*, Z. Phys. C **64**, 57 (1994).
17. V. V. Kiselev and A. V. Tkabladze, Phys. Rev. D **48**, 5208 (1993).
18. V. V. Kiselev, hep-ph/0211021.
19. A. Abd El-Hady, J. H. Munoz, and J. P. Vary, Phys. Rev. D **62**, 014019 (2000).
20. C. H. Chang and Y. Q. Chen, Phys. Rev. D **49**, 3399 (1994).
21. M. A. Ivanov, J. G. Korner, and P. Santorelli, Phys. Rev. D **63**, 074010 (2001).
22. D. Scora and N. Isgur, Phys. Rev. D **52**, 2783 (1995).
23. A. Yu. Anisimov, I. M. Narodetskii, C. Semay, and B. Silvestre-Brac, Phys. Lett. B **452**, 129 (1999); A. Yu. Anisimov, P. Yu. Kulikov, I. M. Narodetsky, and K. A. Ter-Martirosian, Yad. Fiz. **62**, 1868 (1999) [Phys. At. Nucl. **62**, 1739 (1999)].
24. G. Chiladze, A. F. Falk, and A. A. Petrov, Phys. Rev. D **60**, 034011 (1999); hep-ph/9811405; C. H. Chang, J. P. Cheng, and C. D. Lu, Phys. Lett. B **425**, 166 (1998); hep-ph/9712325; T. M. Aliev and M. Savci, Phys. Lett. B **434**, 358 (1998); hep-ph/9804407; J. Phys. G **24**, 2223 (1998); hep-ph/9805239; P. Colangelo and F. De Fazio, Mod. Phys. Lett. A **14**, 2303 (1999); hep-ph/9904363.
25. M. Dugan and B. Grinstein, Phys. Lett. B **255**, 583 (1991); M. A. Shifman, Nucl. Phys. B **388**, 346 (1992); B. Blok and M. Shifman, Nucl. Phys. B **389**, 534 (1993).
26. S. S. Gershtein *et al.*, hep-ph/9803433; V. V. Kiselev, Phys. Lett. B **372**, 326 (1996); hep-ph/9605451.
27. O. N. Pakhomova and V. A. Saleev, Yad. Fiz. **63**, 2091 (2000) [Phys. At. Nucl. **63**, 1999 (2000)]; hep-ph/9911313; V. A. Saleev, Yad. Fiz. **64**, 2113 (2001) [Phys. At. Nucl. **64**, 2027 (2001)]; hep-ph/0007352; V. V. Kiselev, O. N. Pakhomova, and V. A. Saleev, J. Phys. G **28**, 595 (2002); hep-ph/0110180; G. Lopez Castro, H. B. Mayorga, and J. H. Munoz, J. Phys. G **28**, 2241 (2002); hep-ph/0205273.
28. D.-s. Du, X.-l. Li, and Y.-d. Yang, Phys. Lett. B **380**, 193 (1996); hep-ph/9603291; S. Fajfer, S. Prelovsek, and P. Singer, Phys. Rev. D **59**, 114003 (1999); **64**, 099903(E) (2001); hep-ph/9901252; T. M. Aliev and M. Savci, Phys. Lett. B **480**, 97 (2000); hep-ph/9908203.
29. M. Masetti, Phys. Lett. B **286**, 160 (1992); Y. S. Dai and D. S. Du, Eur. Phys. J. C **9**, 557 (1999); hep-ph/9809386; J. F. Liu and K. T. Chao, Phys. Rev. D **56**, 4133 (1997).
30. C. Quigg, in *Proceedings of the Workshop on B Physics at Hadron Accelerators, Snowmass, Colorado, 1993*, Ed. by P. McBride and C. S. Mishra (Fermilab, Batavia, 1994).
31. R. C. Verma and A. Sharma, Phys. Rev. D **65**, 114007 (2002).
32. C. H. Chang, A. K. Giri, R. Mohanta, and G. L. Wang, J. Phys. G **28**, 1403 (2002); hep-ph/0204279.
33. M. A. Nobes and R. M. Woloshyn, J. Phys. G **26**, 1079 (2000); hep-ph/0005056.
34. N. Brambilla and A. Vairo, Phys. Rev. D **62**, 094019 (2000); hep-ph/0002075.
35. T. Mannel and S. Wolf, Phys. Rev. D **65**, 074012 (2002); hep-ph/0109250.
36. J. P. Ma and J. S. Xu, Eur. Phys. J. C **24**, 261 (2002); X. G. Wu, C. H. Chang, Y. Q. Chen, and Z. Y. Fang, hep-ph/0209125; C. H. Chang, hep-ph/0205112.
37. A. Faessler, T. Gutsche, M. A. Ivanov, *et al.*, hep-ph/0205287; C. Q. Geng, C. W. Hwang, and C. C. Liu, Phys. Rev. D **65**, 094037 (2002); hep-ph/0110376.
38. D. Ebert, R. N. Faustov, and V. O. Galkin, hep-ph/0210381.
39. A. V. Berezhnoy, A. K. Likhoded, and M. V. Shevlyagin, Yad. Fiz. **58**, 730 (1995) [Phys. At. Nucl. **58**, 672 (1995)]; A. V. Berezhnoy, A. K. Likhoded, and O. P. Yuschenko, Yad. Fiz. **59**, 742 (1996) [Phys. At. Nucl. **59**, 709 (1996)]; C.-H. Chang *et al.*, Phys. Lett. B **364**, 78 (1995); K. Kolodziej, A. Leike, and R. Rückl, Phys. Lett. B **355**, 337 (1995); A. V. Berezhnoy, V. V. Kiselev, and A. K. Likhoded, Z. Phys. A **356**, 79 (1996).
40. H. L. Lai *et al.* (CTEQ Collab.), hep-ph/9606399.

Physics of Atomic Nuclei, Vol. 67, No. 8, 2004, pp. 1571–1579. From Yadernaya Fizika, Vol. 67, No. 8, 2004, pp. 1593–1601.

ELEMENTARY PARTICLES AND FIELDS
Theory

$D_s^+ \to \pi^+\pi^+\pi^-$ Decay: The $1^3P_0 s\bar{s}$ Component in Scalar–Isoscalar Mesons*

V. V. Anisovich, L. G. Dakhno, and V. A. Nikonov

Received May 5, 2003; in final form, December 2, 2003

Abstract—We calculate the processes $D_s^+ \to \pi^+ s\bar{s}$ and $D_s^+ \to \pi^+ resonance$, respectively, in the spectator and W-annihilation mechanisms. The data on the reaction $D_s^+ \to \pi^+\rho^0$, which is due to the W-annihilation mechanism only, point to a negligibly small contribution of the W annihilation to the production of scalar–isoscalar resonances $D_s^+ \to \pi^+ f_0$. As to spectator mechanism, we evaluate the $1^3P_0 s\bar{s}$ component in the resonances $f_0(980)$, $f_0(1300)$, and $f_0(1500)$ and broad state $f_0(1200–1600)$ on the basis of data on the decay ratios $(D_s^+ \to \pi^+ f_0)/(D_s^+ \to \pi^+\phi)$. The data point to a large $s\bar{s}$ component in the $f_0(980)$: $40 \lesssim s\bar{s} \lesssim 70\%$. Nearly 30% of the $1^3P_0 s\bar{s}$ component flows to the mass region 1300–1500 MeV, being shared by $f_0(1300)$, $f_0(1500)$, and broad state $f_0(1200–1600)$: the interference of these states results in a peak near 1400 MeV with the width around 200 MeV. Our calculations show that the yield of the radial-excitation state $2^3P_0 s\bar{s}$ is relatively suppressed, $\Gamma(D_s^+ \to \pi^+(2^3P_0 s\bar{s}))/\Gamma(D_s^+ \to \pi^+(1^3P_0 s\bar{s})) \lesssim 0.05$.

1. INTRODUCTION

The meson yields in the decay $D_s^+ \to \pi^+\pi^+\pi^-$ [1] immediately evoked great interest and now they are actively discussed (see [2–5] and references therein). The point is that, in this decay, the production of strange quarkonium is dominant, $D_s^+ \to \pi^+ s\bar{s}$, with a subsequent transition $s\bar{s} \to f_J \to \pi^+\pi^-$. Therefore, the reaction $D_s^+ \to \pi^+\pi^+\pi^-$ may serve as a tool for the estimation of $s\bar{s}$ components in the f_J mesons. This possibility is particularly important in context of the determination of quark content of the f_0 mesons, since the classification of $q\bar{q}$ scalar–isoscalar states is a key problem in the search for exotics.

In D_s^+ decay, the production of f_0 mesons proceeds mainly via the spectator mechanism (Fig. 1*a*): this very mechanism implements the transition $s\bar{s} \to f_0$. In addition, the spectator mechanism provides a strong production of the $\phi(1020)$ meson. To evaluate the $s\bar{s}$ components in f_0 mesons, we use the process $D_s^+ \to \pi^+\phi(1020)$ as a standard: we consider the ratio $(D_s^+ \to \pi^+ f_0)/(D_s^+ \to \pi^+\phi(1020))$, where the uncertainty related to the coupling $c \to \pi^+ s$ is absent.

Calculation of the transition of Fig. 1*a* is performed in the spectral integration technique; this technique was developed in the study of deuteron form factors [6] and deuteron photodisintegration [7]; it was used in the analysis of radiative decays of light mesons [8, 9] and weak decays of D and B mesons [10]. The cuttings of the triangle diagram related to the double spectral integrals are shown in Fig. 1*b*.

In addition, the $\pi^+ f_0$ production can originate from the W-annihilation process of Figs. 1*c* and 1*d*. It is a relatively weak transition; nevertheless, we take it into account, and the reaction $D_s^+ \to \pi^+\rho^0$ serves as a scale to determine the W-annihilation coupling $c\bar{s} \to u\bar{d}$. Let us emphasize that the processes shown in Fig. 1 are of the leading order in terms of the $1/N_c$ expansion rule [11].

In Section 2, we present the data set used for the analysis and write the amplitudes for the spectator and W-annihilation processes. The results of calculations are presented and discussed in Section 3. In this section, we demonstrate that (i) the W annihilation contributes weakly to the f_J-meson production, and (ii) the 1^3P_0 state dominates the transition $s\bar{s} \to f_0$, while the production of the $2^3P_0 s\bar{s}$ component is relatively suppressed, so the transition $D_s^+ \to \pi^+ s\bar{s} \to \pi^+ f_0$ is in fact a measure for the $1^3P_0 s\bar{s}$ component in scalar–isoscalar mesons.

In the Conclusions, we sum up what the data on the decay $D_s^+ \to \pi^+\pi^+\pi^-$ tell us, in particular, with respect to the identification of the lightest scalar $q\bar{q}$ nonet.

2. DATA SET AND THE AMPLITUDES FOR THE SPECTATOR AND W-ANNIHILATION MECHANISMS

In this section, we present the data used in the analysis and write formulas for the spectator and W-annihilation mechanisms (Fig. 1*a* and Figs. 1*c*, 1*d*, respectively).

*This article was submitted by the authors in English.

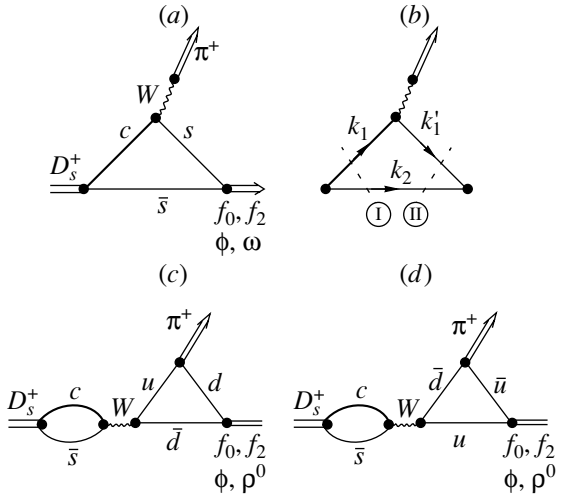

Fig. 1. Diagrams determining the decay $D_s^+ \to \pi^+\pi^+\pi^-$. ($a$) Diagram for the spectator mechanism; (b) energy-off-shell triangle diagram for the integrand of the double spectral representation; (c, d) diagrams for the W-annihilation mechanism $D_s^+ \to u\bar{d}$ with subsequent production of $u\bar{u}$ and $d\bar{d}$ pairs.

2.1. The Data Set

In the recently measured spectra from the reaction $D_s^+ \to \pi^+\pi^+\pi^-$ [1], the relative weight of channels $\pi^+ f_0(980)$ and $\pi^+\rho^0(770)$ is evaluated,

$$\begin{aligned} \mathrm{BR}\left(\pi^+ f_0(980)\right) &= (57 \pm 9)\%, \\ \mathrm{BR}\left(\pi^+\rho^0(770)\right) &= (6 \pm 6)\%, \end{aligned} \tag{1}$$

and the ratio of yields,

$$\begin{aligned} \Gamma(D_s^+ \to \pi^+\pi^+\pi^-)/\Gamma(D_s^+ \to \pi^+\phi(1020)) \\ = 0.245 \pm 0.028^{+0.019}_{-0.012}, \end{aligned} \tag{2}$$

is measured. These values are the basis to determine relative weight of the $s\bar{s}$ component in the $f_0(980)$.

Moreover, in [1], a bump in the wave ($IJ^{PC} = 00^{++}$) is seen at 1434 ± 18 MeV with the width 173 ± 32 MeV; this should be a contribution from the nearby resonances $f_0(1300)$ and $f_0(1500)$ and the broad state $f_0(1200{-}1600)$. The relative weight of this bump is equal to

$$\begin{aligned} \mathrm{BR}\left(\pi^+(f_0(1300) + f_0(1500)\right. \\ \left. + f_0(1200{-}1600))\right) = (26 \pm 11)\%. \end{aligned} \tag{3}$$

This magnitude allows us to determine the total weight of the $1^3P_0 s\bar{s}$ component in the states $f_0(1300)$, $f_0(1500)$, and $f_0(1200{-}1600)$.

Now the data of the FOCUS Collaboration [12] on the decay $D_s^+ \to \pi^+ f_0(980)$ are available. These data are compatible with those of [1], so we do not use them in our estimates, and we base our work on the ratios $\pi^+ f_0/\pi^+\phi$ measured in [1].

In addition, the production of $f_2(1270)$ is seen in [1]: $\mathrm{BR}\,(\pi^+ f_2(1270)) = (20 \pm 4)\%$. This makes it necessary to include tensor mesons in the calculation machinery.

2.2. Decay Amplitudes and Partial Widths

The spin structure of the amplitude depends on the type of meson produced—it is different for scalar (f_0), vector (ϕ, ω, ρ), or tensor (f_2) mesons. Let us denote the momenta of the produced scalar (S), vector (V), and tensor (T) mesons by p_M, where $M = S, V, T$; the D_s^+-meson momentum is referred to as p.

The production amplitude is written as

$$A(D_s^+ \to \pi^+ M) = \widehat{O}_M(p, p_M) A_M(q^2), \tag{4}$$

where the spin operators $\widehat{O}_M(p, p_M)$ for scalar, vector, and tensor mesons read as follows:

$$\begin{aligned} \widehat{O}_S(p, p_S) = 1, \quad \widehat{O}_V(p, p_V) = p_{V\perp\mu}, \\ \widehat{O}_T(p, p_T) = \frac{p_{T\perp\mu} p_{T\perp\nu}}{p_{T\perp}^2} - \frac{1}{3} g_{\mu\nu}^{\perp}. \end{aligned} \tag{5}$$

The momenta $p_{V\perp}$ and $p_{T\perp}$ are orthogonal to the D_s^+-meson momentum p:

$$\begin{aligned} p_{V\perp\mu} = g_{\mu\mu'}^{\perp} p_{V\mu'}, \quad p_{T\perp\mu} = g_{\mu\mu'}^{\perp} p_{T\mu'}, \\ g_{\mu\mu'}^{\perp} = g_{\mu\mu'} - \frac{p_\mu p_{\mu'}}{p^2}. \end{aligned} \tag{6}$$

In the spectral integration technique, the invariant production amplitude $A_M(q^2)$ is calculated as a function of $q^2 = (p - p_M)^2 = m_\pi^2$.

In terms of the spin-dependent operators $\widehat{O}_M(p, p_M)$, the partial width for the transition $D_s^+ \to \pi^+ M$ reads

$$\begin{aligned} m_{D_s}\Gamma(D_s^+ \to \pi^+ M) = \left|A_M(q^2 = m_\pi^2)\right|^2 \\ \times \left(\widehat{O}_M(p, p_M)\right)^2 \frac{\sqrt{-p_{M\perp}^2}}{8\pi m_{D_s}}, \end{aligned} \tag{7}$$

where

$$\begin{aligned} \left(\widehat{O}_S(p, p_S)\right)^2 = 1, \quad \left(\widehat{O}_V(p, p_V)\right)^2 = -p_{V\perp}^2, \\ \left(\widehat{O}_T(p, p_T)\right) = \frac{2}{3}. \end{aligned} \tag{8}$$

In (7), the value $\sqrt{-p_{M\perp}^2}$ is equal to the center-of-mass relative momentum of mesons in the final state; it is determined by the magnitudes of the meson masses as follows:

$$\sqrt{-p_{M\perp}^2} = \sqrt{[m_{D_s}^2 - (m_M + m_\pi)^2][m_{D_s}^2 - (m_M - m_\pi)^2]}/(2m_{D_s}).$$

2.3. Amplitudes for the Spectator and W-Annihilation Processes in the Light-Cone Variables

In the leading order of the $1/N_c$ expansion, there exist two types of processes which govern the decays $D_s^+ \to \pi^+ f_0, \pi^+ f_2, \pi^+\phi/\omega, \pi^+\rho^0$. They are shown in Figs. 1*a*, 1*c*, and 1*d*. We refer to the process of Fig. 1*a* as a spectator one, while that shown in Figs. 1*c* and 1*d* is called the W-annihilation process. The transition $s\bar{s} \to meson$ is a characteristic feature of the spectator mechanism; it contributes to the production of isoscalar mesons, $D_s^+ \to \pi^+ f_0$, $\pi^+ f_2$, $\pi^+\phi$, $\pi^+\omega$, whereas ρ^0 cannot be produced within the spectator mechanism. The W annihilation contributes to the production of mesons with both $I = 1$ and $I = 0$, $D_s^+ \to \pi^+ f_0$, $\pi^+ f_2$, $\pi^+\phi$, $\pi^+\omega$ and $D_s^+ \to \pi^+\rho^0$. Therefore, the latter reaction, $D_s^+ \to \pi^+\rho^0$, allows us to evaluate the relative weight of the effective coupling constant for W annihilation, thus making it possible to estimate the W-annihilation contribution to the channels of interest: $D_s^+ \to \pi^+ f_0$, $\pi^+ f_2$, $\pi^+\phi$. This estimate tells us that the W annihilation is relatively weak, which agrees with conventional evaluations (see, for example, [10]).

The amplitudes for the spectator production of mesons (Fig. 1*a*) and for W annihilation (Figs. 1*c*, 1*d*) can be calculated in terms of the double spectral integral representation developed for the quark three-point diagrams in [8, 10]. The calculation scheme for the diagram of Fig. 1*a* in the spectral integration technique is as follows. We consider the relevant energy-off-shell diagram shown in Fig. 1*b* for which the momentum of the $c\bar{s}$ system, $P = k_1 + k_2$, obeys the requirement $P^2 \equiv s > (m_c + m_s)^2$, while the $s\bar{s}$ system, with the momentum $P' = k_1' + k_2$, satisfies the constraint $P'^2 \equiv s' > 4m_s^2$; here, $m_{s,c}$ are the masses of the constituent s, c quarks, which are taken to be $m_s = 500$ MeV and $m_c = 1500$ MeV. The next step consists in the calculation of the double discontinuity of the triangle diagram (cuttings I and II in Fig. 1*b*) which corresponds to real processes, and the double discontinuity is the integrand of the double dispersion representation.

The double dispersion integrals may be rewritten in terms of the light-cone variables by introducing the light-cone wave functions for the D_s^+ meson and produced mesons f_0, f_2, ϕ, ω, ρ^0: the calculations performed here are done by using these variables.

Our calculations have been carried out in the limit of negligibly small pion mass, $m_\pi \to 0$, which is a reasonable approach, because in the ratio $D_s^+ \to \pi^+ f_J/D_s^+ \to \pi^+\phi$ the uncertainties related to this limit are mainly canceled.

2.3.1. Spectator-production form factor. The form factor for the spectator process given by the triangle diagram of Fig. 1*a* reads

$$F_M^{(\mathrm{sp})}(q^2) = \frac{G_{\mathrm{sp}}}{16\pi^3}\int_0^1 \frac{dx}{x(1-x)^2} \times \int d^2k_\perp \psi_{D_s}(s)\psi_M(s')S_{D_s\to\pi M}(s,s',q^2). \quad (9)$$

Here, G_{sp} is the vertex for the decay transition $c \to \pi^+ s$; the light-cone variables x and $\mathbf{k}_\perp$ refer to the momenta of quarks in the intermediate states. The energies squared for initial and final quark states ($c\bar{s}$ and $s\bar{s}$) are written in terms of the light-cone variables as follows:

$$s = \frac{m_c^2 + k_\perp^2}{1-x} + \frac{m_s^2 + k_\perp^2}{x}, \quad (10)$$
$$s' = \frac{m_s^2 + (\mathbf{k}_\perp + x\mathbf{q}_\perp)^2}{x(1-x)}.$$

The limit of the negligibly small pion mass corresponds to $\mathbf{q}_\perp \to 0$; in (9), this limit is attained within numerical calculation of $F_M^{(\mathrm{sp})}(q^2)$ at small negative q^2.

In the spectral integration technique, wave functions of the initial and final states are determined as ratios of vertices to the dispersion-relation denominators, $\psi_{D_s}(s) = G_{D_s}(s)/(s - m_{D_s}^2)$ and $\psi_M(s') = G_M(s')/(s' - m_M^2)$ (see [8, 10] for details).

In our calculations, the D_s^+-meson wave functions and $s\bar{s}$ component in the meson M are parametrized as follows:

$$\psi_{D_s}(s) = C_{D_s}\exp(-b_{D_s}s), \quad (11)$$
$$\psi_M(s') = C_M\exp(-b_M s'),$$

where C_{D_s} and C_M are the normalization constants for the wave functions, and b_{D_s} and b_M characterize the mean radii squared of the $c\bar{s}$ and $s\bar{s}$ systems, $R_{D_s}^2$ and R_M^2. In approximation (11), the mean radii squared are the only parameters for the description of quark wave functions. Based on the results of the analysis of the radiative decays [9], we set R_M^2 for $f_0(980)$, $\phi(1020)$, and $f_2(1270)$ to be of the order of the pion radius squared, $R_M^2 \sim R_\pi^2 = 10$ GeV^{-2},

which corresponds to the following wave function parameters for $s\bar{s}$ components (in GeV units; recall that 1 fm$^2 \simeq 25$ GeV^{-2}):

$$b_{f_0(980)} = 1.25, \quad b_{\phi(1020)} = 2.50, \qquad (12)$$
$$b_{f_2(1270)} = 1.25, \quad C_{f_0(980)} = 98.92,$$
$$C_{\phi(1020)} = 374.76, \quad C_{f_2(1270)} = 68.85.$$

Recall that, in [9], the mean radius squared was defined through the Q^2 dependence of the meson form factor at small momentum transfers, $F_M(Q^2) \simeq 1 - Q^2R_M^2/6$, and the normalization factor C_M is given by $F_M(0) = 1$, which actually represents the convolution $\psi_M \otimes \psi_M = 1$.

For the D_s^+ meson, the charge radius squared $R_{D_s}^2$ is of the order of 3.5–5.5 GeV^{-2} [10], which corresponds to

$$b_{D_s} \simeq 0.70\text{–}1.50 \text{ GeV}^{-2}, \qquad (13)$$
$$C_{D_s} \simeq 157.6\text{–}7205.4 \text{ GeV}^{-2}.$$

One should keep in mind that the D_s^+-meson charge radius squared is determined by two form factors, $F_c(Q^2)$ and $F_{\bar{s}}(Q^2)$, when the photon interacts with c and $\bar{s}$ quarks: $2F_c(Q^2)/3 + F_{\bar{s}}(Q^2)/3 \simeq 1 - R_{D_s}^2Q^2/6$.

The factor $S_{D_s\to\pi M}(s,s',q^2)$ is defined by the spin structure of the quark loop in the diagram of Fig. 1*b*. The corresponding trace of the three-point quark loop is equal to

$$\widehat{S}_M \qquad (14)$$
$$= -\mathrm{Tr}[\widehat{Q}_M(-\hat{k}_2 + m_s)i\gamma_5(\hat{k}_1 + m_c)i\gamma_5(\hat{k}_1' + m_s)],$$

where $i\gamma_5$ stands for the D_s^+ meson and pion vertices, and $\widehat{Q}_M$ is the spin operator for the transition ($s\bar{s} \to M$), which is defined for scalar, vector, and tensor mesons as follows:

$$\widehat{Q}_S = 1, \qquad (15)$$
$$\widehat{Q}_V = \gamma'_{\perp\mu},$$
$$\frac{1}{2}\widehat{Q}_T = k'_\mu\gamma'_{\perp\nu} + k'_\nu\gamma'_{\perp\mu} - \frac{2}{3}\hat{k}'g'^{\perp}_{\mu\nu}.$$

Here, $k' = (k_1' - k_2)/2$ and $\gamma'_{\perp\mu} = g'^{\perp}_{\mu\nu}\gamma_{\perp\nu}$, where $g'^{\perp}_{\mu\nu} = g_{\mu\nu} - P'_\mu P'_\nu/P'^2$. The operator $\widehat{Q}_T$ stands for the production of f_2 mesons belonging to the basic $1^3P_2q\bar{q}$ multiplet.

With these definitions, the factor $S_{D_s\to\pi M}(s,s',q^2)$ can be calculated through normalized convolution of the quark-loop operator (14) with the spin operator of the amplitude given by (5) but determined in the space of internal momenta, by substituting $p \to P$ and $p_M \to P'$, namely,

$$S_{D_s\to\pi M}(s,s',q^2) = \frac{\left(\widehat{S}_M \cdot \widehat{O}_M(P,P')\right)}{\left(\widehat{O}_M(P,P')\right)^2}. \qquad (16)$$

Let us emphasize once again that we calculate the integrand of the spectral integral for the energy-off-shell process of Fig. 1*b*. Because of that, the invariant spin-dependent structure $S_{D_s\to\pi M}(s,s',q^2)$ should be calculated through (16) with the energy-off-shell operators $\widehat{O}_M(P,P')$ and mass-on-shell constituents. The spin factors determined by (16) read

$$S_{D_s\to\pi f_0}(s,s',q^2) = 2(sm_s - 2m_c^2m_s \qquad (17)$$
$$- m_cs' + 4m_cm_s^2 + q^2m_s - 2m_s^3),$$
$$S_{D_s\to\pi\phi/\omega}(s,s',q^2) = \frac{-8s'}{\lambda}(sm_c^2 - sm_cm_s - sq^2$$
$$- m_c^4 + 2m_c^3m_s - m_c^2s' + m_c^2q^2 + m_cs'm_s$$
$$- m_cq^2m_s - 2m_cm_s^3 + m_s^4),$$
$$S_{D_s\to\pi f_2}(s,s',q^2) = \frac{8s'}{\lambda}(sm_c^2 - sm_cm_s - sq^2$$
$$- m_c^4 + 2m_c^3m_s - m_c^2s' + m_c^2q^2 + m_cs'm_s$$
$$- m_cq^2m_s - 2m_cm_s^3 + m_s^4)(s - 2m_c^2 - s'$$
$$+ q^2 + 2m_s^2),$$

where $\lambda = (s'-s)^2 - 2q^2(s'+s) + q^4$. In the performed calculations, we have used the moment-expansion technique; for the details, see the review paper [13] and references therein.

2.3.2. *W*-annihilation form factor. The right-hand side of the three-point block of Figs. 1*c* and 1*d*, which describes the transitions of the $u\bar{d}$ system into mesons π^+M, can also be calculated with formulas similar to (9). One has

$$F_M^{(W)}(q^2) = \frac{1}{16\pi^3}\int_0^1 \frac{dx}{x(1-x)^2} \qquad (18)$$
$$\times \int d^2k_\perp \frac{G_W}{s - m_{D_s}^2 - i0}\psi_M(s')$$
$$\times S_{D_s(u\bar{d})\to\pi M}(s,s',q^2).$$

For the transition $D_s^+ \to u\bar{d}$, we use the dispersion relation description, and vertex G_W is treated as an energy-independent factor.

The spin factor $S_{D_s(u\bar{d})\to\pi M}(s,s',q^2)$ is determined by the triangle graph of Figs. 1*c* and 1*d*, with light quarks in the intermediate state. Therefore,

$$\widehat{S}_M^{(W)} \qquad (19)$$

$$= -\mathrm{tr}\left[\widehat{Q}_M(-\hat{k}_2 + m)i\gamma_5(\hat{k}_1 + m)i\gamma_5(\hat{k}_1' + m)\right],$$

where $m = 350$ MeV and $\widehat{Q}_M$ is given by (15). Furthermore, the spin factors $S_{D_s(u\bar{d})\to\pi M}(s, s', q^2)$ are calculated with the use of (16). For scalar, vector, and tensor mesons, respectively, they are equal to

$$S_{D_s(u\bar{d})\to\pi f_0}(s, s', q^2) = 2m(s - s' + q^2), \quad (20)$$

$$S_{D_s(u\bar{d})\to\pi\phi/\omega}(s, s', q^2) = \frac{8ss'q^2}{\lambda},$$

$$S_{D_s(u\bar{d})\to\pi f_2}(s, s', q^2) = -\frac{8ss'q^2}{\lambda}(s - s' + q^2).$$

The transition amplitude defined by Eq. (18) is complex-valued.

3. CALCULATIONS AND RESULTS

Here, we write the amplitudes used for the calculation of the decay processes—the corresponding results are presented below.

3.1. Amplitudes for Decay Channels $\pi^+ f_0(980)$, $\pi^+\phi(1020)$, $\pi^+ f_2(1270)$, $\pi^+\rho^0$

Taking into account two decay processes, spectator and W annihilation, we write the transition amplitude as follows:

$$A(D_s^+ \to \pi^+ M) = \xi_M^{(\mathrm{sp})} F_M^{(\mathrm{sp})}(0) + \xi_M^{(W)} F_M^{(W)}(0), \quad (21)$$

where the factors $\xi^{(\mathrm{sp})}$ and $\xi^{(W)}$ are determined by the flavor content of isoscalar mesons. In terms of the quarkonium states $s\bar{s}$ and $n\bar{n} = (u\bar{u} + d\bar{d})/\sqrt{2}$, we define flavor wave functions of isoscalar mesons as

$$\phi(1020): \quad n\bar{n}\sin\varphi_V + s\bar{s}\cos\varphi_V, \quad (22)$$

$$f_0(980): \quad n\bar{n}\cos\varphi[f_0(980)] + s\bar{s}\sin\varphi[f_0(980)],$$

$$f_2(1270): \quad n\bar{n}\cos\varphi_T + s\bar{s}\sin\varphi_T,$$

which serves for the determination of coefficients in (21):

$$D_s^+ \to \pi^+\phi(1020): \quad \xi_\phi^{(\mathrm{sp})} = \cos\varphi_V, \quad (23)$$

$$\xi_\phi^{(W)} = \sqrt{2}\sin\varphi_V;$$

$$D_s^+ \to \pi^+ f_0(980): \quad \xi_{f_0(980)}^{(\mathrm{sp})} = \sin\varphi[f_0(980)],$$

$$\xi_{f_0(980)}^{(W)} = \sqrt{2}\cos\varphi[f_0(980)];$$

$$D_s^+ \to \pi^+ f_2(1270): \quad \xi_{f_2(1270)}^{(\mathrm{sp})} = \sin\varphi_T,$$

$$\xi_{f_2(1270)}^{(W)} = \sqrt{2}\cos\varphi_T.$$

For $\phi(1020)$, which is dominantly the $s\bar{s}$ state, we fix the mixing angle in the interval $|\varphi_V| \le 4^\circ$.

The production of $\pi^+\rho^0$ is due to the direct mechanism only:

$$D_s^+ \to \pi^+\rho^0: \quad \xi_\rho^{(\mathrm{sp})} = 0, \quad \xi_\rho^{(W)} = \sqrt{2}. \quad (24)$$

3.2. Evaluation of the Ratio G_W/G_{sp}

To evaluate the ratio G_W/G_{sp}, we use the reaction $D_s^+ \to \pi^+\rho^0$, with the experimental constraint $\Gamma(\pi^+\rho^0)/\Gamma(\pi^+\phi) \le 0.032$. By using the maximal value of $\Gamma(\pi^+\rho^0)/\Gamma(\pi^+\phi) = 0.032$, we get the following ratios $F_M^{(W)}(0)/F_M^{(\mathrm{sp})}(0)$ for scalar, vector, and tensor mesons at $R_{D_s}^2 = 4.5\ \mathrm{GeV}^{-2}$:

$$\frac{\sqrt{2}F_S^{(W)}(0)}{F_S^{(\mathrm{sp})}(0)} = (0.28 + 0.75i)\times 10^{-3}, \quad (25)$$

$$\frac{\sqrt{2}F_V^{(W)}(0)}{F_V^{(\mathrm{sp})}(0)} = (0.5 + 15.1i)\times 10^{-2},$$

$$\frac{\sqrt{2}F_T^{(W)}(0)}{F_T^{(\mathrm{sp})}(0)} = (0.26 + 1.35i)\times 10^{-3}.$$

This evaluation tells us that the W-annihilation contribution is comparatively small, and one may neglect it when the reactions $D_s^+ \to \pi^+ f_0$ and $D_s^+ \to \pi^+ f_2$ are studied.

3.3. Evaluation of Relative Weights of the $1^3P_0 s\bar{s}$ and $2^3P_0 s\bar{s}$ States for the Decay $D_s^+ \to \pi^+ f_0$

In the region 1000–1500 MeV, one can expect the existence of scalar–isoscalar states which belong to the basic and first radial-excitation $q\bar{q}$ nonets, 1^3P_0 and 2^3P_0. Here, we estimate relative weights of the states $1^3P_0 s\bar{s}$ and $2^3P_0 s\bar{s}$ in the transitions $D_s^+ \to \pi^+ s\bar{s} \to \pi^+ f_0$.

The form factor for the production of a radial-excitation (re) state is given by (9), with a choice of the wave function as follows:

$$\psi_{M(\mathrm{re})}(s) = C_{\mathrm{re}}(d_{\mathrm{re}}s - 1)\exp(-b_{\mathrm{re}}s). \quad (26)$$

Two parameters in (26) can be determined by the normalization and orthogonality conditions, $\psi_{M(\mathrm{re})} \otimes \psi_{M(\mathrm{re})} = 1$ and $\psi_{M(\mathrm{re})} \otimes \psi_{M(\mathrm{basic})} = 0$, while the third one can be related to the mean radius squared, R_{re}^2. In our estimates, we keep R_{re}^2 of the order of the pion radius squared or larger, $1 \le R_{\mathrm{re}}^2/R_\pi^2 \le 1.5$. To be precise, we present as an example the wave function parameters (in GeV units) for the $2^3P_0 s\bar{s}$ state with $R_{\mathrm{re}}^2 = 11.3\ \mathrm{GeV}^{-2}$:

$$b_{\mathrm{re}} = 1.75, \quad C_{\mathrm{re}} = 938.5, \quad d_{\mathrm{re}} = 0.60. \quad (27)$$

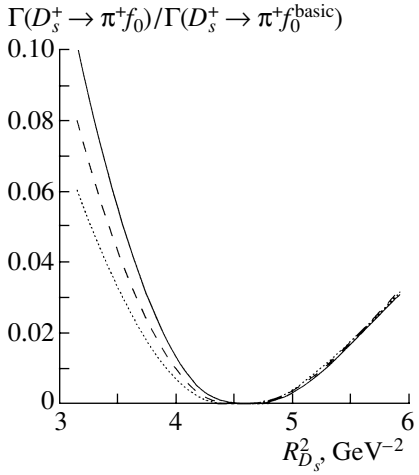

Fig. 2. The ratio $\Gamma\left(D_s^+ \to \pi^+ f_0\right)/\Gamma\left(D_s^+ \to \pi^+ f_0^{\rm basic}\right)$ as a function of radius squared of the D_s^+ meson [see Eq. (13)]. Calculations have been carried out at fixed $R^2[f_0^{\rm basic}] = 10$ GeV^{-2} for several values of $R^2(f_0)$: 10 GeV^{-2} (solid curve), 13 GeV^{-2} (dashed curve), and 16 GeV^{-2} (dotted curve).

In Fig. 2, we show the ratios

$$\frac{\Gamma\left(D_s^+ \to \pi^+(2^3P_0 s\bar{s})\right)}{\Gamma\left(D_s^+ \to \pi^+(1^3P_0 s\bar{s})\right)}$$

for different values of radius squared of the $(2^3P_0 s\bar{s})$ component, $R^2(f_0)$, in the interval $3.5 \lesssim R^2_{D_s} \lesssim 5.5$ GeV^{-2}.

From the point of view of the calculation technique, a suppression of the production of the $2^3P_0 s\bar{s}$ state in the process of Fig. 1*a* is due to the existence of a zero in the wave function ψ_M [see (26)]. As a result, the convolution of wave functions $\psi_{D_s} \otimes \psi_M$ turned out to be considerably less than the convolution $\psi_{D_s} \otimes \psi_M$.

Thus, the production of the radial-excitation state $D_s^+ \to \pi^+(2^3P_0 s\bar{s})$ is relatively suppressed, by a factor of the order of 1/30. This means that, by measuring f_0 resonances, one actually measures the yield of the $1^3P_0 s\bar{s}$ state.

3.4. The Decay $D_s^+ \to \pi^+ f_0(980)$

The channel $D_s^+ \to \pi^+ f_0(980)$ dominates the decay $D_s^+ \to \pi^+\pi^+\pi^-$; it comprises $(57 \pm 9)\%$. Taking into account the branching ratio $\mathrm{BR}(f_0(980) \to \pi^+\pi^-) \simeq 53\%$ [14] and the ratio of yields (2), we have

$$\frac{\Gamma\left(D_s^+ \to \pi^+ f_0(980)\right)}{\Gamma\left(D_s^+ \to \pi^+\phi(1020)\right)} = 0.275(1 \pm 0.25). \quad (28)$$

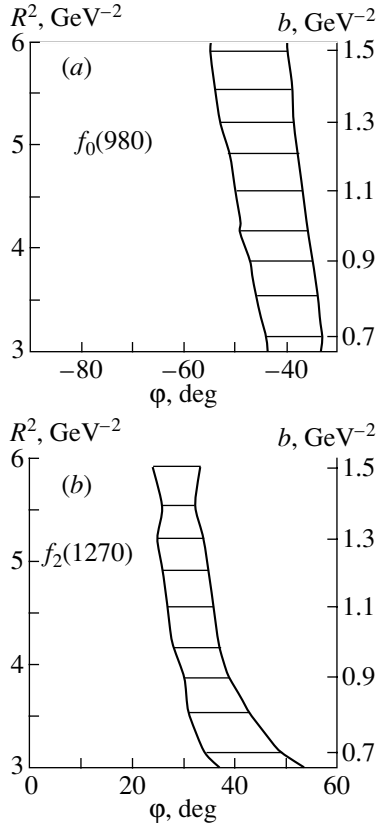

Fig. 3. Allowed areas $(R^2_{D_s}, \varphi_M)$ for flavor wave functions (22) provided by experimental constraints (28) and (30). The right-hand ordinate axis stands for the b_{D_s} values.

Calculations performed with formulas (9), (18), and (21) allow one to satisfy this ratio with

$$35^\circ \le |\varphi| \le 55^\circ, \quad (29)$$

keeping the charge radius of the D_s^+ meson in the interval $3.5 \le R^2_{D_s} \le 5.5$ GeV^{-2} [10] (see Fig. 3*a*).

The data on radiative decays $f_0(980) \to \gamma\gamma$ and $\phi(1020) \to \gamma f_0(980)$ tell us that the mixing angle φ can be either $\varphi = -48^\circ \pm 6^\circ$ or $\varphi = 83^\circ \pm 4^\circ$ [9]. The constraint (29) shows that the D_s^+-meson decay prefers the solution with negative mixing angle, thus supporting the $f_0(980)$ to be a dominantly flavor-octet state. The analysis of hadronic spectra in terms of the K-matrix approach [14, 15] also points to the flavor-octet origin of the $f_0(980)$.

3.5. The Decay $D_s^+ \to \pi^+ f_2(1270)$

Taking into account $\mathrm{BR}[f_2(1270) \to \pi^+\pi^-] \simeq 57\%$, one has

$$\frac{\pi^+ f_2(1270)}{\pi^+\phi(1020)} = 0.09(1 \pm 0.2). \quad (30)$$

The values of φ_T, which satisfy the ratio (30), are shown in Fig. 3*b*. With $R^2_{D_s} \simeq 3.5{-}5.5\ \mathrm{GeV}^{-2}$, we have $|\varphi_T| \simeq 20^\circ{-}40^\circ$, which does not contradict the data on either hadronic decays or the radiative decay $f_2(1270) \to \gamma\gamma$, which give $\varphi_T \simeq 0^\circ{-}20^\circ$. Therefore, the production of $f_2(1270)$ in $D_s^+ \to \pi^+\pi^+\pi^-$ agrees reasonably with the weight of the $s\bar{s}$ component measured in other reactions.

3.6. Bump near 1430 *MeV: The Decays* $D_s^+ \to \pi^+ (f_0(1300) + f_0(1500) + f_0(1200{-}1600))$

In the region 1300–1500 MeV, two comparatively narrow resonances $f_0(1300)$ and $f_0(1500)$ and the broad state $f_0(1200{-}1600)$ are located (for more detail, see [14, 16] and references therein). These resonances are the mixtures of quarkonium states from the multiplets 1^3P_0 and 2^3P_0 and scalar gluonium gg:

$$1^3P_0 s\bar{s}, \quad 1^3P_0 n\bar{n}, \quad 2^3P_0 s\bar{s}, \quad 2^3P_0 n\bar{n}, \quad gg. \tag{31}$$

We denote the probabilities for the f_0 resonance to have $1^3P_0 s\bar{s}$ and $2^3P_0 s\bar{s}$ components as $\sin^2\varphi[f_0]$ and $\sin^2\varphi_{\mathrm{re}}[f_0]$, respectively. Then the amplitude for the production of the S-wave $\pi^+\pi^-$ state due to decays of $f_0(1300)$, $f_0(1500)$, and $f_0(1200{-}1600)$ reads

$$A\left(D_s^+ \to \pi^+(\pi^+\pi^-[\sim 1430\ \mathrm{MeV}])_S\right) \tag{32}$$
$$= \sum_n \frac{m_n\sqrt{\Gamma(D_s^+ \to \pi^+ f_0(n))}\sqrt{\Gamma_n(f_0 \to \pi^+\pi^-)}}{m_n^2 - s - i m_n\Gamma_n}.$$

Here, we are summing over the resonances $n = f_0(1300), f_0(1500), f_0(1200{-}1600)$, with the following parameters [14, 16] (in GeV units):

$$\begin{aligned} f_0(1300):&\quad m = 1.300, \quad \Gamma/2 = 0.12; \\ f_0(1500):&\quad m = 1.500, \quad \Gamma/2 = 0.06; \\ f_0(1200{-}1600):&\quad m = 1.420, \quad \Gamma/2 = 0.508. \end{aligned} \tag{33}$$

$\Gamma\left(D_s^+ \to \pi^+ f_0(n)\right)$ is determined by Eqs. (9) and (21).

The peak which is seen in the $\pi^+\pi^-$ S wave near 1430 MeV is determined by both $s\bar{s}$ components in $f_0(1300)$ and $f_0(1500)$ and relative phases of the amplitudes of $f_0(1300)$ and $f_0(1500)$ which govern the interference with the background given by $f_0(1200{-}1400)$. According to the analysis of hadronic decays [14, 16], the mixing angles of these states are in the intervals

$$\begin{aligned} -25^\circ \lesssim \varphi[f_0(1300)] \lesssim 15^\circ, \\ -3^\circ \lesssim \varphi[f_0(1500)] \lesssim 18^\circ, \\ 28^\circ \lesssim \varphi[f_0(1200{-}1600)] \lesssim 38^\circ. \end{aligned} \tag{34}$$

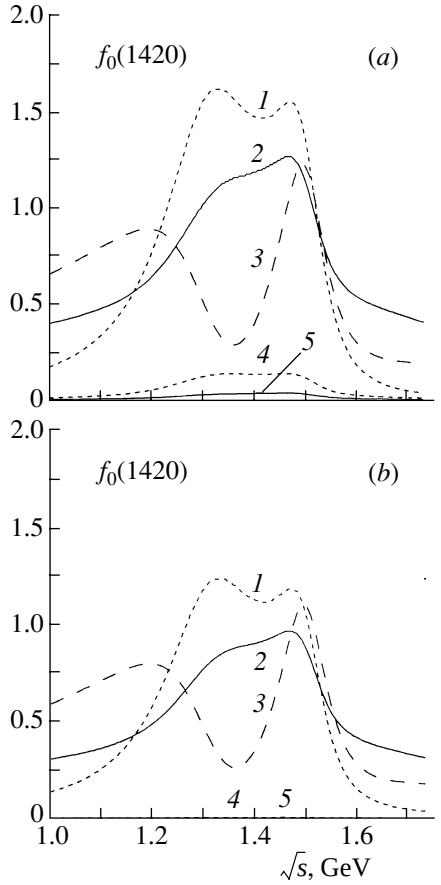

Fig. 4. The $\pi^+\pi^-$ mass spectrum (in arb. units) in the vicinity of 1420 MeV. Calculated curves correspond to the production of $f_0(1300) + f_0(1500)$ and the broad state $f_0(1200{-}1600)$, with (*a*) $R^2_{D_s} = 4.15\ \mathrm{GeV}^{-2}$ and (*b*) $R^2_{D_s} = 5.90\ \mathrm{GeV}^{-2}$. Parameters used in calculations are given in (35) and (36).

Different variants of the calculation of the $\pi^+\pi^-$ spectra near 1400 MeV are shown in Fig. 4 for the values of mixing angles in the intervals (34). The following parameters were used in the calculation of the transitions $D_s^+ \to \pi^+ 1^3P_0 s\bar{s} \to \pi^+(\pi^+\pi^-)_S$ (curves *1*–*3*, Fig. 4):

$$\begin{aligned} (1)&\quad \varphi[f_0(1300)] = -7^\circ, \quad \varphi[f_0(1500)] = 7^\circ, \\ &\qquad \varphi[f_0(1200{-}1600)] = 37^\circ; \\ (2)&\quad \varphi[f_0(1300)] = -25^\circ, \quad \varphi[f_0(1500)] = 17^\circ, \\ &\qquad \varphi[f_0(1200{-}1600)] = 37^\circ; \\ (3)&\quad \varphi[f_0(1300)] = 15^\circ, \quad \varphi[f_0(1500)] = 17^\circ, \\ &\qquad \varphi[f_0(1200{-}1600)] = 37^\circ. \end{aligned} \tag{35}$$

The variants (*1*) and (*2*) in Fig. 4*a* reproduce well the bump observed in the $D_s^+ \to \pi^+\pi^+\pi^-$ decay: the relative weight of the bump for variants (*1*) and (*2*) is of the order of $\sim (15{-}20)\%$, which agrees with the measured weight of the peak [1]. The variant (*3*)

demonstrates that, with the same signs of mixing angles for $f_0(1300)$ and $f_0(1500)$, the calculated curve gives a dip, not bump, near 1400 MeV.

In Fig. 4, one can also see the results of the calculation performed for the radial-excitation state $2^3P_0 s\bar{s}$ (curves *4*, *5*). For transitions $D_s^+ \to \pi^+ 2^3P_0 s\bar{s} \to \pi^+(\pi^+\pi^-)_S$, the following angles are used:

$$(4)\quad \varphi_{\rm re}[f_0(1300)] = -7^\circ, \quad \varphi_{\rm re}[f_0(1500)] = 7^\circ, \quad \varphi_{\rm re}[f_0(1200{-}1600)] = 37^\circ, \tag{36}$$

$$(5)\quad \varphi_{\rm re}[f_0(1300)] = -25^\circ, \quad \varphi_{\rm re}[f_0(1500)] = 17^\circ, \quad \varphi_{\rm re}[f_0(1200{-}1600)] = 37^\circ.$$

These curves illustrate well the suppression rate of the production of the $2^3P_0 s\bar{s}$ in the decay $D_s^+ \to \pi^+\pi^+\pi^-$.

4. CONCLUSIONS

The performed calculations allow one to trace out the destiny of the $s\bar{s}$ component in the dominating process $D_s^+ \to \pi^+ + s\bar{s} \to \pi^+ + f_0$ of Fig. 1*a*. We show that this transition is realized mainly due to the $1^3P_0 s\bar{s}$ state, while the production of the radial-excitation state, $2^3P_0 s\bar{s}$, is suppressed by a factor of 1/20 or more. Therefore, the reaction $D_s^+ \to \pi^+ + f_0$ is a measure of the $1^3P_0 s\bar{s}$ component in the f_0 mesons.

The data of [1] tell us that $1^3P_0 s\bar{s}$ is dispersed as follows: about two-thirds of this state is held by the $f_0(980)$ and the last one-third is shared between the states with masses in the region 1300–1500 MeV, which are $f_0(1300)$, $f_0(1500)$, and broad state $f_0(1200{-}1600)$. This result is quite recognizable as concerns the percentage of the f_0 states produced in the decay $D_s^+ \to \pi^+\pi^+\pi^-$: $\mathrm{BR}\,(\pi^+ f_0(980)) = (57 \pm 9)\%$ and $\mathrm{BR}(\pi^+ f_0(\text{bump at } 1430\ \text{MeV})) = (26 \pm 11)\%$. The performed calculations demonstrate that nothing prevents this straightforward interpretation. In other words,

(i) the spectator mechanism $D_s^+ \to \pi^+ + s\bar{s} \to \pi^+ + f_0$ dominates;

(ii) the production of the 2^3P_0 states is suppressed;

(iii) the interference of the states $f_0(1300)$, $f_0(1500)$, and $f_0(1200{-}1600)$ may organize a bump with the mass ~ 1400 MeV and width ~ 200 MeV.

The decay $D_s^+ \to \pi^+\pi^+\pi^-$ was discussed in [2–5] from the point of view of the determination of the quark structure of produced resonances—let us emphasize common and different points in the obtained results.

In [5], the hypothesis of the four-quark structure of $f_0(980)$ is advocated: to explain a large yield of $f_0(980)$ within the four-quark model, one needs to assume that the decay $D_s^+ \to \pi^+\pi^+\pi^-$ goes with a strong violation of the $1/N_c$ expansion rules. Recall that, in terms of the $1/N_c$ expansion, the processes shown in Figs. 1*a*, 1*c*, and 1*d* dominate; it is not clear why these rules, though they work well in other decay processes, are violated in $D_s^+ \to \pi^+\pi^+\pi^-$. From the point of view of [5], the yield of the $s\bar{s}$ state is seen only at larger masses, such as the 1400-MeV bump or higher.

In [2–4], the spectator mechanism shown in Fig. 1*a* is adopted, and the authors conclude that the $s\bar{s}$ component dominates the resonance $f_0(980)$. Here, our conclusions are similar but only on a qualitative level: our calculations indicate the existence of a considerable $n\bar{n}$ component in $f_0(980)$, about 30–40%, while according to [2–4] it is negligibly small. Correspondingly, their interpretation of the bump around 1430 MeV differs from ours. Our calculations show that the production of the $2^3P_0 s\bar{s}$ component is suppressed, so the bump at 1430 is a manifestation of the $1^3P_0 s\bar{s}$ component in this mass region, while, as was stated in [3, 4], the component $2^3P_0 s\bar{s}$ is responsible for this bump.

Let us emphasize again that, according to our calculations, relative suppression of the production of $2^3P_0 s\bar{s}$ component is due to the use of realistic wave functions of radial-excitation states [see (26)]: the existence of a zero in the wave function resulted in a suppression of the convolution $\psi_{D_s} \otimes \psi_{2^3P_0 s\bar{s}}$.

The data [1] cannot provide us with more scrupulous information about the weight of the $1^3P_0 s\bar{s}$ component in the resonances $f_0(1300)$, $f_0(1500)$, and $f_0(1750)$ and broad state $f_0(1400{-}1600)$. To get such information, one needs to carry out a combined analysis of the decay $D_s^+ \to \pi^+\pi^+\pi^-$ and hadron reactions with the production of the investigated resonances. The present investigation of the reaction $D_s^+ \to \pi^+\pi^+\pi^-$ is quite in line with the K-matrix analysis of hadronic reactions [14–16] that tells us that, in the scalar–isoscalar sector, the lowest $1^3P_0 q\bar{q}$ state is the flavor octet, while the flavor singlet is a heavier one.

ACKNOWLEDGMENTS

We thank A.V. Anisovich and A.V. Sarantsev for useful discussions.

This work was supported by the Russian Foundation for Basic Research, project no. 04-02-17091.

REFERENCES

1. E. M. Aitala *et al.* (E791 Collab.), Phys. Rev. Lett. **86**, 765 (2001).
2. A. Deandrea, R. Gatto, G. Nardulli, *et al.*, Phys. Lett. B **502**, 79 (2001).
3. F. Kleefeld, E. van Beveren, G. Rupp, and M. D. Scadron, Phys. Rev. D **66**, 034007 (2002).
4. P. Minkowski and W. Ochs, hep-ph/0209223.
5. H. Y. Cheng, hep-ph/0212117.
6. V. V. Anisovich, M. N. Kobrinsky, D. I. Melikhov, and A. V. Sarantsev, Nucl. Phys. A **544**, 747 (1992).
7. A. V. Anisovich and V. A. Sadovnikova, Yad. Fiz. **55**, 2657 (1992) [Sov. J. Nucl. Phys. **55**, 1483 (1992)]; Eur. Phys. J. A **2**, 199 (1998).
8. V. V. Anisovich, D. I. Melikhov, and V. A. Nikonov, Phys. Rev. D **52**, 5295 (1995); **55**, 2918 (1997).
9. A. V. Anisovich, V. V. Anisovich, and V. A. Nikonov, Eur. Phys. J. A **12**, 103 (2001); A. V. Anisovich, V. V. Anisovich, V. N. Markov, and V. A. Nikonov, Yad. Fiz. **65**, 523 (2002) [Phys. At. Nucl. **65**, 497 (2002)]; A. V. Anisovich, V. V. Anisovich, M. A. Matveev, and V. A. Nikonov, Yad. Fiz. **66**, 946 (2003) [Phys. At. Nucl. **66**, 914 (2003)].
10. D. I. Melikhov, Phys. Rev. D **56**, 7089 (1997); D. I. Melikhov and B. Stech, Phys. Rev. D **62**, 014006 (2000).
11. G. 't Hooft, Nucl. Phys. B **72**, 461 (1974).
12. J. M. Link *et al.* (FOCUS Collab.), Phys. Lett. B **541**, 227 (2002).
13. A. V. Anisovich, V. V. Anisovich, V. N. Markov, *et al.*, J. Phys. G **28**, 15 (2002).
14. V. V. Anisovich and A. V. Sarantsev, Eur. Phys. J. A **16**, 229 (2003); V. V. Anisovich, V. A. Nikonov, and A. V. Sarantsev, Yad. Fiz. **65**, 1583 (2002) [Phys. At. Nucl. **65**, 1545 (2002)].
15. V. V. Anisovich and A. V. Sarantsev, Phys. Lett. B **382**, 429 (1996); V. V. Anisovich, Yu. D. Prokoshkin, and A. V. Sarantsev, Phys. Lett. B **389**, 388 (1996).
16. V. V. Anisovich, Usp. Fiz. Nauk (in press); hep-ph/0208123.

Physics of Atomic Nuclei, Vol. 67, No. 8, 2004, pp. 1580–1595. Translated from Yadernaya Fizika, Vol. 67, No. 8, 2004, pp. 1602–1617.

ELEMENTARY PARTICLES AND FIELDS
Theory

Transparency of Nuclei and Mean Free Path of Protons and Pions in Nuclear Matter at Intermediate Energies

I. V. Glavanakov*

Institute of Nuclear Physics, Tomsk Polytechnic University, Tomsk, 634004 Russia

Received April 2, 2003; in final form, September 29, 2003

Abstract—In the second resonance region of photon energies, the differential yields of neutral and charged pions are measured in the $(\gamma, \pi p)$ reactions on Li, C, and Al nuclei versus the proton energy and the azimuthal angle of pion emission. These experimental data are analyzed on the basis of a model that takes into account both single and double quasifree pion photoproduction. This results in deriving the mean free paths of protons and neutral and charged pions and in estimating the transparency of the participant nuclei.

1. INTRODUCTION

In interpreting many nuclear reactions, it is necessary to know various properties of nuclei, such as nuclear transparency with respect to the propagation of nucleons, pions, and other fast particles in a nucleus and the mean free paths of these particles in nuclear matter. In recent years, much attention has been given to these properties of nuclei. This increased interest was generated by two factors. First, Brodsky in [1] and Mueller in [2] predicted a color-transparency phenomenon consisting in that, at high squares of the 4-momentum transfer (Q^2), nuclear transparency may increase substantially owing to the formation a small color-singlet object whose interaction with surrounding intranuclear nucleons occurs with a lower probability. In order to observe this phenomenon experimentally, it is necessary to know, to a high degree of precision, ordinary nuclear transparency at moderate values of Q^2.

The second factor motivating keen interest in the problem of nuclear transparency and of the mean free path of particles is associated with the investigation of ion–ion collisions, which is being intensively conducted at present. Information about the mean free path of nucleons is necessary in this case for estimating the number of nucleon–nucleon collisions. Pions produced in ion–ion collisions are used, in these investigations, as a sensitive probe carrying information about reaction dynamics. For the interpretation of relevant data to be correct, it is therefore necessary to know the pion mean free path, which controls the change in the flux of pions because of their absorption in nuclear matter [3, 4].

As usual, nuclear transparency is defined as the ratio of the measured cross section for a given reaction to the cross section calculated theoretically without allowance for final-state interaction [5]. The transparency defined in this way is an integrated quantity and is, as a rule, a quantity averaged over some part of the reaction phase space; therefore, information obtained from it for final-state interaction often cannot be used in analyzing a different reaction. Data from measurements of mean free paths of particles in a nucleus have a higher degree of universality. Results obtained by estimating the mean free path of a particle on the basis of data on one reaction can be employed in microscopically calculating cross sections for different reactions involving this particle.

In experimentally determining the mean free paths of particles in a nucleus, the results of such an analysis are less model-dependent if they are based on data from measurements of the reaction yield as a function of the atomic number of the target nucleus. It is of importance here to specify the reaction mechanism unambiguously. At intermediate energies, it is difficult to meet the last requirement in experiments where only one particle is recorded. In estimating, for example, the mean free path of a neutral pion in nuclei on the basis of data on quasifree pion photoproduction, an uncontrollable contribution from the elastic channel, featuring a quadratic dependence of the cross section on the mass number of the target nucleus, can distort the results of the analysis significantly. In this respect, experiments that ensure the identification of the quasifree reaction mechanism via the detection of two particles—a scattered or a newly produced one and a recoil nucleon—are the most promising.

Measurement of the cross section for a nuclear reaction as a function of the atomic number of the target

* e-mail: glavanak@npi.tpu.ru

nucleus (A) is an extensively used method for studying final-state interaction. The problems encountered in applying this method to the case of quasifree pion photoproduction in $(\gamma, \pi p)$ reactions are generated by the presence of two strongly interacting particles, and these problems have so far prevented a full-scale implementation of the method in such cases. In the present study, the mean free paths of a proton and a neutral and a charged pion are estimated for the first time on the basis of the A dependence of the yield of pion–proton pairs. The experimental data obtained here are analyzed within a model that takes into account single and double quasifree pion photoproduction.

The ensuing exposition is organized as follows. A brief description of the experimental procedure used is given in Section 2. The theoretical model employed to explain the results of the measurements is presented in Section 3. Section 4 contains the description of the algorithm underlying the code for extracting, from experimental data, information about the mean free path of particles. The resulting estimates of the mean free paths and of the nuclear transparency are discussed in Sections 5 and 6.

2. EXPERIMENTAL PROCEDURE

The experiment was performed in a bremsstrahlung-photon beam from the Tomsk synchrotron. The photon beam was produced as the result of the braking of electrons accelerated to an energy of 900 MeV against the accelerator internal tantalum target of thickness 0.07 radiation-length units. Plates from lithium, carbon, and aluminum of natural isotopic composition were used for nuclear targets, their thicknesses being 6.95×10^{22}, 4.27×10^{22}, and 1.27×10^{22} nucl./cm^2, respectively. The experimental facility involved three detection channels: a proton channel and channels for detecting a neutral and a charged pion. The last two were arranged on the same axis. A scintillation time-of-flight spectrometer was employed for the proton channel. Neutral pions were recorded by one decay photon with the aid of a total-absorption Cherenkov gamma spectrometer, while charged pions were detected by two scintillation counters. For a detailed description of the experimental facility and the procedure used in the measurements, the interested reader is referred to [6].

The charge state of a charged pion was not identified in the experiment. As follows from theoretical estimates, however, about 80% of the yield of charged pions from the relevant $(\gamma, \pi p)$ reactions in the kinematical region being studied was due to negatively charged pions. In the following, quantities associated with neutral and charged pions will therefore be labeled with the indices "0" and "−," respectively.

In the experiment reported here, which studied photon interactions with C, Li, and Al nuclei, the differential yields of neutral and charged pions accompanied by emitted protons were measured versus the proton energy T_p and the azimuthal angle ϕ_π of pion emission.

The energies of the protons recorded in the experiment lay in the range 140–280 MeV. The polar angles of proton and pion emission were 41° and 61°, respectively. The azimuthal angle of proton emission was constant and equal to π, while that for pions was varied with a step of 10° over the range 0°–50°. At an azimuthal angle of $\phi_\pi = 0°$, the primary-photon momentum $\mathbf{p}_\gamma$, the recorded-pion momentum $\mathbf{p}_\pi$, and the proton momentum $\mathbf{p}_p$ lie in the same plane.

The yield $d^3Y/dE_p d\Omega_p d\Omega_\pi$ measured in the experiment is related to the differential cross section $d^3\sigma/dE_p d\Omega_p d\Omega_\pi$ for the relevant $(\gamma, \pi p)$ reaction by the equation

$$\frac{d^3Y}{dE_p d\Omega_p d\Omega_\pi} = \int\limits^{E_{\max}} dE_\gamma f(E_\gamma) \frac{d^3\sigma(E_\gamma)}{dE_p d\Omega_p d\Omega_\pi},$$

where E_γ and E_p are, respectively, the photon energy and the total proton energy; $E_{\max}$ is the endpoint energy of the bremsstrahlung spectrum; and $f(E_\gamma)$ is the bremsstrahlung spectrum, which is normalized by the condition

$$\int\limits_0^{E_{\max}} f(E_\gamma) E_\gamma \, dE_\gamma = E_{\max}.$$

The measured differential yields for the photoproduction of pion–proton pairs on Li and Al nuclei are given in Tables 1–4. The respective data obtained for C nuclei were reported in [6].

3. MODEL OF THE PHOTOPRODUCTION OF PION–PROTON PAIRS

In the second resonance region of photon energy, the production of pion–proton pairs on nuclei proceeds predominantly through the following channels involving proton emission: two single-pion-photoproduction reactions,

$$A(\gamma, \pi^0 p)B, \quad A(\gamma, \pi^- p)C, \tag{1}$$

and three double-pion-photoproduction reactions,

$$A(\gamma, \pi^-\pi^+ p)B, \quad A(\gamma, \pi^-\pi^0 p)C, \quad A(\gamma, \pi^0\pi^0 p)B. \tag{2}$$

The experimental data are analyzed here on the basis of the model developed for describing the production of pion–proton pairs on nuclei with allowance

Table 1. Differential yield $d^3Y_{\pi^0}/dE_p d\Omega_p d\Omega_\pi$ for neutral-pion photoproduction in the reaction $^7\mathrm{Li}(\gamma, \pi p)$ versus the proton kinetic energy T_p and the azimuthal angle ϕ_π of pion emission [in 10^{-32} cm^2/(MeV sr^2) units]

T_p,MeV	ϕ_π, deg					
	0	10	20	30	40	50
150	24.5 ± 2.7	18.5 ± 2.7	12.3 ± 2.0	9.5 ± 2.2	4.0 ± 1.2	3.0 ± 1.0
170	21.8 ± 2.7	14.2 ± 2.4	7.9 ± 1.6	5.2 ± 1.6	5.0 ± 1.4	1.0 ± 1.0
190	18.2 ± 2.5	11.6 ± 2.1	7.0 ± 1.5	3.2 ± 1.3	1.5 ± 0.8	2.6 ± 1.0
210	15.2 ± 2.1	13.3 ± 2.4	5.1 ± 1.3	2.8 ± 1.2	2.1 ± 0.9	1.4 ± 1.0
230	11.6 ± 1.8	7.7 ± 2.0	4.6 ± 1.2	5.0 ± 1.6	2.2 ± 0.9	0.3 ± 1.0
250	7.6 ± 2.1	8.4 ± 2.0	5.4 ± 1.3	1.3 ± 0.8	2.8 ± 1.0	1.0 ± 1.0
270	7.8 ± 2.2	5.8 ± 2.0	2.6 ± 0.9	1.8 ± 1.0	1.7 ± 0.8	0.6 ± 1.2

Table 2. Differential yield $d^3Y_{\pi^-}/dE_p d\Omega_p d\Omega_\pi$ for charged-pion photoproduction in the reaction $^7\mathrm{Li}(\gamma, \pi p)$ versus the proton kinetic energy T_p and the azimuthal angle ϕ_π of pion emission [in 10^{-32} cm^2/(MeV sr^2) units]

T_p, MeV	ϕ_π, deg					
	0	10	20	30	40	50
150	37.9 ± 5.0	25.4 ± 4.1	24.2 ± 2.7	11.6 ± 2.4	7.1 ± 1.7	6.4 ± 1.4
170	38.4 ± 4.5	30.5 ± 3.6	22.1 ± 2.6	11.8 ± 2.4	7.1 ± 1.7	4.3 ± 1.2
190	35.7 ± 3.2	30.0 ± 3.3	11.7 ± 2.6	7.5 ± 1.9	4.4 ± 1.7	5.0 ± 1.2
210	32.2 ± 3.0	22.4 ± 2.9	11.0 ± 1.8	6.6 ± 1.8	6.8 ± 1.6	1.9 ± 1.0
230	27.3 ± 3.3	17.5 ± 2.6	7.5 ± 1.5	5.4 ± 1.6	3.0 ± 1.5	2.1 ± 1.0
250	20.0 ± 2.3	14.7 ± 2.6	7.4 ± 1.5	2.2 ± 1.5	3.1 ± 1.5	2.2 ± 1.0
270	12.6 ± 1.9	7.9 ± 2.3	4.9 ± 1.2	3.7 ± 1.5	3.7 ± 1.5	1.9 ± 0.8

for the results obtained in [6–8]. As its basic ingredients, this model includes the impulse approximation, the shell model of the nucleus, and the optical model of final-state interaction.

A fairly large value for the lower boundary of the energy range over which protons are detected experimentally and the chosen disposition of the proton and pion channels of the facility with respect to the photon beam ensured fulfillment of the condition under which quasifree pion photoproduction was the main mechanism of the production of pion–proton pairs in the kinematical region being studied. In the factorization approximation, the squared modulus of the amplitude for quasifree pion photoproduction, $|M|^2$, can be represented as

$$|M|^2 = |M_0|^2 \frac{N_l}{2l+1} \sum_{m_l} |G_{l,m_l}|^2, \qquad (3)$$

where M_0 is the amplitude of single (M_s) or double (M_d) pion production on a free nucleon; N_l is the number of nucleons (protons or neutrons) in the lth shell of the nucleus; l and m_l are, respectively, the orbital angular momentum of a nucleon bound in the nucleus and its projection; and

$$G_{l,m_l} = \int \Psi_\pi^*(\mathbf{r}) \Psi_p^*(\mathbf{r}) \times \exp(i\mathbf{p}_\gamma \cdot \mathbf{r}) Y_l^{m_l}(\mathbf{r}/r) \Phi_l(r) d\mathbf{r}.$$

Here, $Y_l^{m_l}$ is a spherical harmonic; Φ_l is the orbital wave function for a nucleon bound in the nucleus; and

Table 3. Differential yield $d^3Y_{\pi^0}/dE_p d\Omega_p d\Omega_\pi$ for neutral-pion photoproduction in the reaction $^{27}\mathrm{Al}(\gamma, \pi p)$ versus the proton kinetic energy T_p and the azimuthal angle ϕ_π of pion emission [in 10^{-32} cm^2/(MeV sr^2) units]

T_p, MeV	ϕ_π, deg					
	0	10	20	30	40	50
150	29.3 ± 5.4	39.3 ± 8.4	26.7 ± 5.2	19.5 ± 5.8	21.8 ± 5.8	13.2 ± 4.6
170	32.7 ± 5.6	26.1 ± 5.9	23.6 ± 4.9	13.4 ± 3.9	17.6 ± 5.2	10.3 ± 4.0
190	21.2 ± 4.8	18.3 ± 5.4	22.1 ± 4.7	11.2 ± 4.1	7.9 ± 3.5	6.2 ± 3.1
210	27.0 ± 5.1	13.9 ± 4.7	14.8 ± 3.9	11.0 ± 4.0	3.2 ± 2.2	2.3 ± 3.0
230	16.5 ± 4.2	19.3 ± 5.5	5.2 ± 2.3	5.5 ± 3.0	4.6 ± 2.7	8.5 ± 3.6
250	16.3 ± 4.1	13.1 ± 4.5	6.6 ± 2.6	2.7 ± 2.0	1.8 ± 1.7	3.6 ± 2.4
270	9.7 ± 3.4	8.4 ± 3.0	9.6 ± 3.5	3.3 ± 3.0	6.4 ± 3.1	3.8 ± 3.5

Table 4. Differential yield $d^3Y_{\pi^-}/dE_p d\Omega_p d\Omega_\pi$ for charged-pion photoproduction in the reaction $^{27}\mathrm{Al}(\gamma, \pi p)$ versus the proton kinetic energy T_p and the azimuthal angle ϕ_π of pion emission [in 10^{-32} cm^2/(MeV sr^2) units]

T_p, MeV	ϕ_π, deg					
	0	10	20	30	40	50
150	50.2 ± 6.8	54.6 ± 10.0	43.9 ± 6.7	35.0 ± 9.2	14.9 ± 5.2	9.1 ± 4.3
170	57.1 ± 7.8	32.4 ± 6.8	44.7 ± 6.7	19.3 ± 5.8	11.2 ± 4.7	12.9 ± 4.8
190	41.3 ± 6.4	31.5 ± 7.1	32.8 ± 5.7	4.7 ± 5.0	7.9 ± 4.1	14.9 ± 5.5
210	28.2 ± 5.4	24.1 ± 6.3	29.0 ± 5.4	12.8 ± 4.5	8.9 ± 4.2	8.1 ± 3.0
230	24.6 ± 5.7	17.7 ± 6.0	12.8 ± 4.5	9.7 ± 3.9	5.0 ± 3.3	2.2 ± 3.0
250	15.6 ± 4.1	10.5 ± 5.3	10.4 ± 4.5	10.6 ± 4.0	6.3 ± 3.4	6.1 ± 3.3
270	9.3 ± 3.3	15.7 ± 4.8	3.5 ± 5.0	6.2 ± 3.0	6.9 ± 3.3	1.9 ± 2.1

Ψ_p and Ψ_π are the wave functions for, respectively, the proton and one or two pions formed in reactions (1) or (2).

In order to describe bound states of nucleons in a nucleus and the radial distribution of the nuclear optical potential, we used the oscillator model of the nucleus and determined the parameters of this model on the basis of data on the charge radii $\langle r^2_{\mathrm{ch}}\rangle^{1/2}$ of nuclei [9, 10]:

$$\begin{array}{lccccccc} \text{Nuclei:} & ^7\mathrm{Li} & ^{12}\mathrm{C} & ^{27}\mathrm{Al} & ^{40}\mathrm{Ca} & ^{58}\mathrm{Ni} & ^{181}\mathrm{Ta} & ^{207}\mathrm{Pb}, \\ \langle r^2_{\mathrm{ch}}\rangle^{1/2}, \text{fm}: & 2.41 & 2.45 & 3.05 & 3.48 & 3.76 & 5.5 & 5.51. \end{array} \quad (4)$$

The oscillator parameters of neutrons bound in a nucleus were taken to be identical to the corresponding proton parameters.

The squared modulus of the amplitude for single pion production on nucleons, $|M_s|^2$ [see expression (3)], is related to the differential reaction cross section $d\sigma/d\Omega^*$ in the c.m. frame by the equation

$$\overline{|M_s|^2} = (2\pi)^2 j \frac{m_{\pi p}}{E_p E_\pi p^*_\pi} \frac{d\sigma}{d\Omega^*},$$

where j is the particle flux, p^*_π is the pion momentum in the c.m. frame, and $m_{\pi p}$ is the invariant mass of the πp system. Taking this into account, we will calculate the squared matrix element in question by using the experimental cross sections reported in [11].

There are presently no exclusive experimental cross sections for double pion photoproduction on nucleons in the kinematical region of our prime interest. In order to calculate $|M_d|^2$, we will therefore make use of the isobar phase-space model [8], which

resorts to data on total cross sections and which takes into account the dominant mechanism of the reaction leading to the production of an intermediate $\Delta(1232)$ isobar:

$$\begin{array}{c}\gamma + p \to \Delta + \pi_1 \\ \qquad \hookrightarrow \pi_2 + p.\end{array} \tag{5}$$

In this model, the squared modulus of the amplitude for the reaction in (2), $|M_d|^2$, is expressed in terms of the total reaction cross section $\sigma_{\rm tot}$ as

$$\overline{|M_d|^2} = \frac{(2\pi)^5}{8E_pE_{\pi_1}E_{\pi_2}}\,\frac{\sigma_{\rm tot}}{S_\Delta}\,\frac{B_\Delta(m_{\pi_2 p})}{2m_{\pi_2 p}},$$

where $m_{\pi_2 p}$ is the invariant mass of the $\pi_2 p$ system; $B_\Delta(m)$ is a Breit–Wigner function that describes the distribution of $\Delta(1232)$ isobars with respect to the mass m,

$$B_\Delta(m) = \frac{1}{\pi}\frac{\Gamma_\Delta/2}{(m_\Delta - m)^2 + \Gamma_\Delta^2/4};$$

and

$$S_\Delta = \frac{2\pi^2}{m_0}\int\limits_{m_\pi + m_N}^{m_0 - m_\pi} p^*_{\pi_1} p^{**}_{\pi_2}\frac{B_\Delta(m)}{2m}dm$$

is the convolution of the phase space of final-state particles from the reaction in (5) with the mass distribution of the delta isobar being considered. In the last expression, m_Δ and Γ_Δ are, respectively, the mass and width of the $\Delta(1232)$ isobar; m_0 is the invariant mass of the γN system; and $p^*_{\pi_1}$ and $p^{**}_{\pi_2}$ are the momenta of, respectively, the first pion in the γN c.m. frame and the second pion in the $\pi_2 p$ c.m. frame.

Within the optical model, the multiparticle problem of the interaction of the product pion and of the recoil proton with nucleons of the residual nucleus reduces to the problem of particle interaction with a complex-valued optical potential $V = U + iW$, whose real part U and whose imaginary part W describe, respectively, particle scattering and absorption.

In performing a global analysis of data obtained for some nuclei, it is convenient to represent the optical potential as [12]

$$V(E, r) = V_0(E)\frac{\rho(r)}{\rho_0}, \tag{6}$$

where $\rho(r)$ is the normalized (to unity) radial distribution of the optical-potential density and $\rho_0 = 3/(4\pi R^3)$ is the analogously normalized distribution of the density of a uniformly charged sphere whose radius is

$$R = r_0 A^{1/3}. \tag{7}$$

This representation of the potential makes it possible to take into account the deviation of the densities of individual nuclei from some mean density ρ_0, whereby one can reduce the number of adjustable parameters in the model.

For the radial parameter r_0 in Eq. (7), we take the value

$$r_0 = 1.12 \text{ fm}, \tag{8}$$

which corresponds to the nucleon density of 0.17 nucleon/fm^3 at the center of heavy nuclei [13]. In this case, $V_0 = U_0 + iW_0$ in expression (6) has the meaning of the depth of the optical potential for normal nuclear matter.

For the function $\rho(r)$, which describes in (6) the radial distribution of the pion–nucleus potential, we will take, according to the Frank–Gammel–Watson model [12], the nuclear density. The distribution of the density of the proton–nucleus potential will be described in a similar way. It should be noted that spin–orbit interaction is disregarded for this choice of proton potential. As was shown in [14], however, the effect of proton spin–orbit interaction with the residual nucleus has a negligible effect on the cross section for quasifree pion photoproduction.

In the eikonal approximation, the wave function Ψ for a particle having a momentum $\mathbf{p}$ and propagating in the optical potential $V(E, \mathbf{r})$ acquires the phase $\phi(\mathbf{r})$,

$$\Psi(\mathbf{r}) = \exp(i(\mathbf{p}\cdot\mathbf{r} + \phi(\mathbf{r}))), \tag{9}$$

$$\phi(\mathbf{r}) = -\frac{1}{v}\int\limits_0^\infty V(E, \mathbf{r} + s\mathbf{p}/p)ds,$$

where v is the group velocity of the wave packet representing the propagation of a particle in a nucleus.

The particle energy "within a nucleus," E', and its vacuum component E are related by the equation

$$E' = E - V(E', \mathbf{r}).$$

For the imaginary part of the phase $\phi(\mathbf{r})$ in (9)—it controls the change in the particle flux due to final-state interaction—we will use the representation

$$\mathrm{Im}\phi(\mathbf{r}) = \int\limits_0^\infty \frac{ds}{2\lambda(\mathbf{r} + s\mathbf{p}/p)},$$

where $\lambda(\mathbf{r})$ is the local mean free path of a particle in a nucleus,

$$\frac{1}{\lambda(\mathbf{r})} = \frac{1}{\lambda_0}\frac{v_0}{v}\frac{\rho(r)}{\rho_0}, \tag{10}$$

$\lambda_0 = -v_0/(2W_0)$ and v_0 being, respectively, the mean free path and the group velocity of the wave packet in nuclear matter.

On the basis of the model outlined above, we have calculated the A dependence of the differential yield of pion–proton pairs for protons of kinetic energy 210 MeV at three values of the azimuthal angle of pion emission. The results are given in Fig. 1. Segments of a solid straight line connect points representing yields that were calculated with allowance for final-state interaction in the distorted-wave impulse approximation (DWIA). In the calculation, we employed the pion–nucleus and proton–nucleus optical potentials that, in [6], made it possible to reproduce the energy dependence of the yield of pion–proton pairs from reactions on carbon at small azimuthal angles of pion emission. As can be seen, the yield of pion–proton pairs that was calculated within the DWIA faithfully reproduces the data given in Fig. 1. At large azimuthal angles of pion emission, the model used underestimates the reaction yield somewhat. It is worth noting that the evolution of the A dependence of the yield in response to the change in the azimuthal angle of pion emission is reproduced satisfactorily. A somewhat paradoxical decrease in the reaction yield at $\phi_\pi = 0°$ upon going over from lithium to carbon is explained by two factors caused by the same reason—the distinction between the densities of these nuclei. Because of the higher density of the carbon nucleus, the momentum spectrum of nucleons bound in this nucleus is significantly broader; therefore, the probability of the production of a pion–proton pair in coplanar geometry is lower. The final-state interaction acts here in the same direction.

The points in Fig. 1 that are connected by segments of a dashed straight line represent the yield of pion–proton pairs that was computed in the plane-wave impulse approximation (PWIA) and which was normalized in such a way that, for lithium nuclei, it coincides with the results obtained within the DWIA. By comparing the reaction yields obtained within the DWIA and PWIA, one can assess, within the model used, the sensitivity of experimental data to effects of final-state interaction. It can be seen that the displayed data show approximately identical sensitivity to manifestations of this element of the reaction model. For nuclei in the Li–Al range, the relative decrease in the yield of pion–proton pairs owing to proton and pion interactions with the residual nucleus is about a factor of 2, the coefficient of suppression of the absolute yield in the reactions being studied being about a factor of 4 for aluminum nuclei.

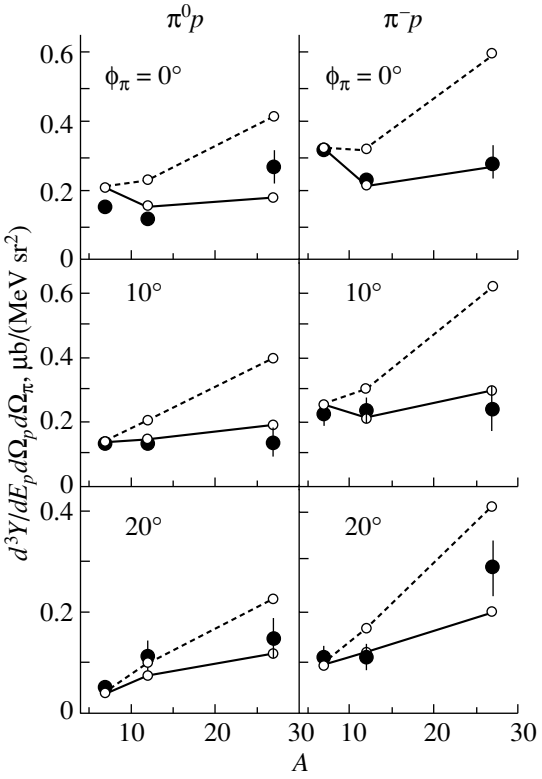

Fig. 1. Differential yields in the photoproduction of $\pi^0 p$ and $\pi^- p$ pairs versus the mass number A of the target nucleus at a proton kinetic energy of 210 MeV for three values of the azimuthal angle ϕ_π of pion emission: (closed circles) data of the present experiment, (solid lines) DWIA results, and (dashed lines) PWIA results for the normalization explained in the main body of the text.

4. ALGORITHM FOR CALCULATING MEAN FREE PATHS

Our experimental data are cross sections integrated with respect to the pion energy. The sensitivity of the experimental data to the dependence of the mean free path of pions on their energy is not as obvious as in the case of protons. In view of this, we will give a brief substantiation of the method used. According to theoretical calculations, the yield of pion–proton pairs at a fixed proton energy receives contributions from two pion groups having partly overlapping spectra and originating from single-pion-production and double-pion-production reactions. The method is based on the fact that the spectra of pions produced via a quasifree reaction mechanism are dome-shaped, peaking at an energy corresponding to the minimum momentum of the residual nucleus.

In Fig. 2, the calculated spectra for single and double pion photoproduction are shown at three experimental points chosen at random. An increase in the azimuthal angle of the detected pion leads to a growth of the mean momentum of the residual nucleus and to a change in the pion energy at the maximum of the spectrum. In view of this, the data in question prove to be sensitive to the energy dependence of the effects caused by proton and pion interaction with the residual nucleus.

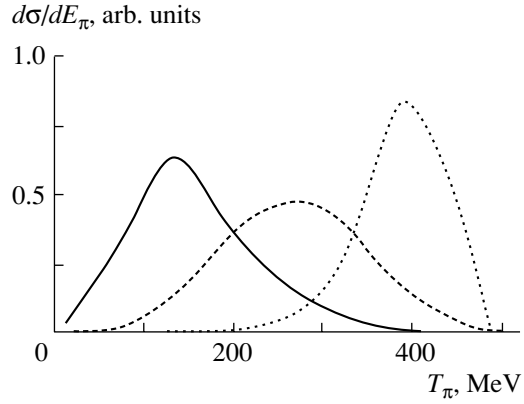

Fig. 2. Spectra of single and double pion photoproduction on carbon nuclei at various values of the proton energy and the azimuthal angle of pion emission: (solid curve) 150 MeV and 0°, reaction (2); (dashed curve) 170 MeV and 30°, reaction (1); and (dotted curve) 270 MeV and 10°, reaction (1).

We will now assess the amount of available experimental information and the number of parameters that we must determine by comparing experimental data with the calculated reaction yields. The yields of $\pi^0 p$ and $\pi^- p$ pairs were measured for three nuclei (Li, C, and Al) at seven points uniformly distributed, with a step of 20 MeV, over the proton-kinetic-energy range $T_p = 150-270$ MeV at six values of the azimuthal angle of pion emission in the interval $0°-50°$ that were spaced by 10°—in all, 252 values of the experimental yields are available. The proton mean free path λ_p was estimated at seven values of the proton energy. The energy dependences of the neutral- and the charged-pion mean free paths (λ_0 and λ_-, respectively) were represented in the form of fourth-degree polynomials; that is,

$$\lambda_{0(-)} = \sum_{j=0}^{4} \Lambda_j^{0(-)} T_\pi^j, \qquad (11)$$

where T_π is the pion kinetic energy. Therefore, 17 parameters characterizing the proton, neutral-pion, and charged-pion mean free paths must be determined from a fit of the calculated reaction yields to experimental data.

In constructing an algorithm for solving this problem, it was of paramount importance that its solution be obtained on the basis of a relative variation in the reaction yields in going over from one target nucleus to another. In this case, many problems associated with the need for absolute experimental values become simpler or even nonexistent, and the results of the respective analysis appear to be less sensitive to possible imperfections of some ingredients of the theoretical model used. This leads to the emergence of additional 84 adjustable parameters ξ.

The algorithm of our fitting procedure is based on the use of the Bayes formula for an a posteriori probability [15]. This formula makes it possible to obtain, on the basis of data on the statistical features of the experimentally measured quantity $Y \equiv d^3Y_{\pi^0(\pi^-)}/dE_p d\Omega_p d\Omega_\pi$, an expression for the probability density $p(\Lambda|Y)$ characterizing the parameter $\Lambda \equiv (\lambda_p, \Lambda^0, \Lambda^-, \xi)$ to be estimated; that is,

$$p(\Lambda|Y) = \frac{p(Y|\Lambda)p(\Lambda)}{\int p(Y|\Lambda)p(\Lambda)d\Lambda}, \qquad (12)$$

where $p(Y|\Lambda)$ is the conditional probability of the distribution of the reaction yield Y at a specific value of Λ and $p(\Lambda)$ is the a priori probability of the distribution of Λ.

The expansion coefficients Λ^0 and Λ^- in (11), as well as the quantities λ_p, are not statistical variables; nonetheless, we will treat them in (12) as statistical variables, this reflecting incompleteness of our knowledge of them.

In order to construct a distribution $p(Y|\Lambda)$ that would specify a relationship between the experimentally measured quantities Y and the parameters Λ of the theoretical model used to describe pion production in reactions (1) and (2), we invoked a model that relies on the "clearest" statistical relation

$$\delta_{mn} = Y_{mn} - \xi_m Y_{mn}^{\text{theor}}(\Lambda), \qquad (13)$$

where m is a generic index corresponding to specific values of the proton energy T_p and of the azimuthal angle ϕ_π of a pion and to its specific charge state $(0/-)$; n is an index that represents the mass number A of the target nucleus; and Y^{theor} is the theoretical reaction yield calculated in the corresponding kinematical region by using specific values of the proton mean free path λ_p and of the expansion coefficients Λ^0 and Λ^- in (11).

By introducing in (13) the adjustable parameter ξ_m, which does not depend on the mass number A of the nucleus, we moderate the effect of the model on the resulting estimates of the sought parameters and render the situation closer to an ideal case. One can then solve the problem, disregarding the dynamics of pion production and treating nuclei as sources that produce pion–proton pairs, which differ in size, and which are distributed in proportion to density.

The majority of the values of the experimental yield Y were estimated on the basis of data samples whose volume exceeds a few tens of events. It is therefore reasonable to assume that the random variables δ_{mn} have a normal distribution whose variance is equal to the square of the root-mean-square error σ in the yield Y.

Since the random variables δ_{mn} are statistically independent, the multidimensional yield-density distribution $p(Y|\Lambda)$ that includes the entire body of experimental data can be represented, with allowance for Eq. (13), in the form of the product

$$p(Y|\Lambda) = \prod_{mn} p(\delta_{mn}|\Lambda).$$

We assume that the mean free path of a particle is a positive definite function and restrict ourselves, for the sake of simplicity, to seeking solutions in the region where the mean free path does not exceed 10 fm; that is,

$$p(\Lambda) = 1, \qquad \lambda \in \Delta\lambda;$$
$$p(\Lambda) = 0, \qquad \lambda \notin \Delta\lambda,$$

where $\lambda \equiv (\lambda_p, \lambda_0, \lambda_-)$ and $\Delta\lambda$ is the range 0–10 fm.

As a result, we obtain

$$p(\Lambda|Y) \tag{14}$$
$$= C\exp\left(-\sum_{mn}(Y_{mn} - \xi_m Y^{\rm th}_{mn}(\Lambda))^2/(2\sigma^2_{mn})\right), \quad \lambda \in \Delta\lambda;$$
$$p(\Lambda|Y) = 0, \qquad \lambda \notin \Delta\lambda,$$

where C is a normalization factor.

The a posteriori distribution of the mean free path for particles of energy T, $p(\lambda(T)|Y)$, is related to the distribution in (14) by the equation

$$p(\lambda(T)|Y) = \int p(\Lambda|Y)\delta(\lambda(T) - \lambda)d\Lambda. \tag{15}$$

According to [15], the moments of the a posteriori distribution in (15) that have the form

$$\hat{\lambda} = \int p(\lambda|Y)\lambda d\lambda. \tag{16}$$

$$\sigma^2_{\hat{\lambda}} = \int p(\lambda|Y)(\lambda - \hat{\lambda})^2 d\lambda \tag{17}$$

provide optimum estimates that minimize the mean-square loss function $\overline{(\lambda - \hat{\lambda}/w)^2}$.

The basic problem that must have been solved in numerically calculating the multidimensional integrals presented above consisted in determining that region $\Delta\Lambda$ of the parameters Λ where the distribution $p(\Lambda|Y)$ was quite large. Prior to calculating the integrals in (16) and (17), it was therefore necessary to determine, through a fit, those values Λ_m of the parameters Λ that minimize the functional

$$\chi^2 = \sum_{mn}\frac{(Y_{mn} - \xi_m Y^{\rm th}_{mn}(\Lambda_m))^2}{\sigma^2_{mn}}. \tag{18}$$

The fitting procedure was implemented in the following order. First, we determined the parameters ξ. In doing this, we took, for the input values λ_p and $\Lambda^{0(-)}$, those that were obtained on the basis of the proton and pion nuclear optical potentials that were used in [16] to reproduce the yield of pion–proton pairs in the relevant reaction on a ^{12}C nucleus at moderate values of the azimuthal angle of pion emission. Further, the functional χ^2 was minimized by simultaneously varying the parameters ξ and λ_p at the input values $\Lambda^{0(-)}$. Preliminarily, the theoretical yield $Y^{\rm theor}$ of pion–proton pairs from reactions (1) and (2) was tabulated in the range 0–10 fm as a function of the pion and proton mean free paths. In the process of fitting, the quantity $Y^{\rm theor}$ was determined by means of interpolation. The ultimate value of Λ_m was determined by globally fitting all of the parameters ξ, λ_p, Λ^0, and Λ^-. The error σ in expressions (14) and (18) was estimated as the root-mean-square value of the statistical error quoted in Tables 1–4 and a 10% systematic error of the measurements, the latter stemming from the errors in measuring the total energy of the photon beam and the thicknesses of the targets, the uncertainty in the energy calibration of the proton time-of-flight spectrometer, and the inaccuracies in calculating the bremsstrahlung spectrum and the detection efficiency for individual channels of the experimental facility. The resulting value of χ^2 per degree of freedom proved to be 1.03, which indicates that the combination of the dynamical and statistical models of the processes being considered is able to reproduce the experimental data in question adequately.

Integration in (15) was performed over the range $\Delta\Lambda$ of the parameters Λ_m. The value of $\Delta\Lambda$ was chosen in such a way that $\overline{p(\Lambda|Y)} \leq 10^{-4}p(\Lambda_m|Y)$.

In order to get an idea of the shape of the distribution density $p(\lambda(T)|Y)$, the results obtained by calculating the distribution in (15) by using the sections of the function $p(\Lambda|Y)$ at parameter values that are not involved in the determination of $\lambda(T)$ and which are equal to Λ_m are displayed in Fig. 3. Integration in (15) over the full volume $\Delta\Lambda$ does not lead to a significant change in $\hat{\lambda}$, somewhat increasing $\sigma_{\hat{\lambda}}$.

The results of the calculations for the proton, neutral-pion, and charged-pion mean free paths in nuclear matter are given in Section 5 below.

5. MEAN FREE PATH OF PARTICLES IN NUCLEAR MATTER

In Fig. 4, the results of the present study (closed circles) are displayed along with three sets of empirical values of the proton mean free path, which

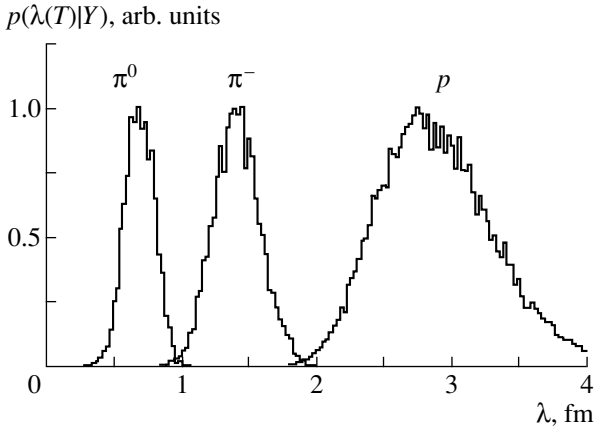

Fig. 3. A posteriori distributions of the mean free paths of a 170-MeV proton, a 150-MeV neutral pion, and a 100-MeV charged pion according to the calculation performed on the basis of (15) by using the sections of the function $p(\Lambda|Y)$ at the parameter values that are not involved in the determination of $\lambda(T)$ and which are equal to Λ_m.

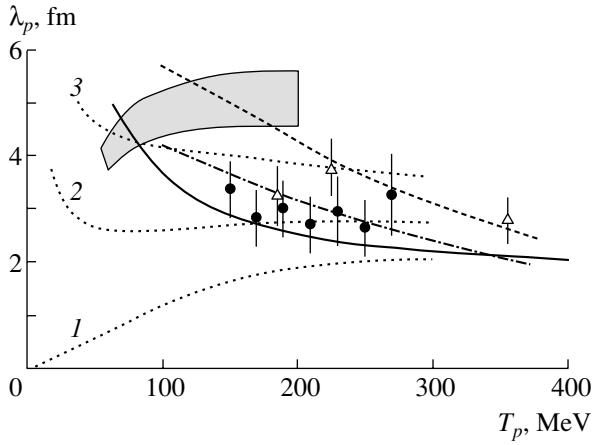

Fig. 4. Proton mean free path in nuclear matter as a function of energy: empirical data from (closed circles) the present study, (triangles) [17], (shaded region) [18], and (solid curve) [19] along with the results of theoretical calculations (dashed, dash-dotted, and dotted curves). The dashed and the dash-dotted curve represent, respectively, the results of a self-consistent relativistic calculation with the Bonn potential [20] and the results of the calculation based on the Walecka model [21]; the dotted curves correspond to three successive approximations from [22] (see main body of the text).

were obtained on the basis of the experimental cross sections for elastic proton scattering on nuclei. Three experimental values represented by triangles are part of the results obtained in [17] (an article reporting on one of the early studies on the subject), where the proton mean free path was estimated for proton energies in the range 220–570 MeV. In [18], the cross sections for elastic proton scattering on ^{40}Ca, ^{90}Zr, and ^{208}Pb nuclei were measured for proton energies of 80 to 180 MeV. Those data were used to determine, through a fit, the parameters of a ten-parameter optical potential, which, in turn, was then applied in calculating the reaction cross section and the mean free path. The shaded region in Fig. 4 covers the calculated values of the proton mean free path in the ^{208}Pb nucleus [18]. A global proton–nucleus optical potential was obtained in [19] by using Dirac's phenomenology. This potential is valid over the energy range 20–1040 MeV and is based on data obtained for elastic proton scattering on ^{12}C, ^{16}O, ^{40}Ca, ^{90}Zr, and ^{208}Pb nuclei. In Fig. 4, the solid curve represents the results obtained in [19] by calculating the energy dependence of the local proton mean free path $\lambda_p(r)$ in the central region ($r = 0$) of the ^{208}Pb nucleus. It can be seen that the results of the present study are compatible with the data from [17, 19], but that they are well below the data from [18].

To illustrate the effect of the main factors determining the energy dependence of the proton mean free path λ_p, the results obtained in [22], where this quantity was calculated in symmetric nuclear matter by using three successive approximations, are shown by the dotted curves in Fig. 4. Curve *1* was computed within the simplest model; that is, the mean free path was defined there as

$$\lambda = \frac{1}{\rho_N \bar{\sigma}_t}, \qquad (19)$$

where ρ_N is the nucleon density and $\bar{\sigma}_t$ is the isotopically averaged total cross section for proton–nucleon scattering in a vacuum. The effect of the Pauli exclusion principle, which reduces the set of possible nucleon states in a nucleus after scattering in relation to what we have in a vacuum, was taken into account in calculating the mean free path represented by curve *2*. In addition, a nonlocality of the optical potential—it leads to a decrease in the nucleon mass and, hence, to an increase in λ_p [23, 24]—was taken into account in computing curve *3*. It can be seen that the effect of the last two factors, which determine almost completely the mean free path at modest photon energies, is less significant in the region where the present measurements were performed. The overestimation of λ_p in this calculation may be partly due to a slight isotopic asymmetry in the nuclei used, this reducing the proton mean free path [25].

In addition, Fig. 4 shows the results of a self-consistent relativistic calculation based on the Bonn potential [20] (dashed curve) and the results of the calculation within the Walecka model [21] (dash-dotted curve). The experimental data obtained in the present study are in better agreement with the latter model, but, as was shown in [20], this model underestimates λ_p at higher proton energies.

We now proceed to consider the pion mean free path in nuclear matter. In Fig. 5, the measured energy dependence of λ_π is represented by open and closed circles for, respectively, neutral and charged pions. Along with the data obtained in the present study, Fig. 5 shows (open boxes) the first empirical data on neutral pions, these also coming from an experiment at the Tomsk synchrotron [26]. In that experiment, the pion mean free path was estimated on the basis of the measured yield of 60-, 85-, 130-, and 195-MeV pions from the interaction of photons with C, Al, Cu, Ag, and Pb nuclei. The measurements were performed in the kinematical region of quasifree pion photoproduction. The estimate of the mean free path in [26] was derived for nuclear matter of density corresponding to the radial-parameter value of $r_0 = 1.3$ fm [29]. In order to perform a comparison with data for normal nuclear matter [see (8)], the results in Fig. 5 from [26] were corrected on the basis of the model used here. The theoretical estimates of the mean free path from [26] were subjected to the same procedure.

The shaded region in Fig. 5 covers the estimated values of the neutral-pion absorption length λ_{abs}, which were derived in [27] from the cross section for the production of π^0 mesons in collisions of ^{36}Ar nuclei with ^{197}Au nuclei at an energy of 95 MeV per projectile nucleon. The estimates of λ_{abs} were obtained in [27] by comparing the experimental cross section for neutral-pion production with its theoretical counterpart calculated within Boltzmann–Uehling–Uhlenbeck transport theory [30].

The dash-dotted curve in Fig. 5 represents the energy dependence of λ_π according to the results obtained in [26] on the basis of the Frank–Gammel–Watson model [12], while the solid curve shows the analogous dependence from [28] for the ^{207}Pb nucleus, the latter stemming from the calculation based on the Klein–Gordon equations with a pion–nucleus optical potential [31].

Qualitatively, the results of the present study are compatible with those presented in [27]. The experiment reported in [27] was inclusive. Inclusive cross sections are sensitive primarily to pion absorption (annihilation). The experiment described in this article is semiexclusive—fast secondaries were recorded here in narrow solid angles. The data of the present experiment are sensitive both to pion absorption and to inelastic rescattering. Since λ_{abs}^{-1} is only a fraction of λ_π^{-1}, then λ_{abs} must exceed λ_π. However, the degree to which the absorption length λ_{abs} measured in [27] exceeds the neutral-pion mean free path λ_π determined here is much greater than the theoretical estimate of the difference of these two quantities at modest pion energies [32]. In this classification, the experiment reported in [26] occupies an intermediate position. It would therefore be natural to expect intermediate results in that case. As can be seen from Fig. 5, however, the results of the present experiment and those from [26] (upon rescaling to normal nuclear matter) are in astonishingly good agreement.

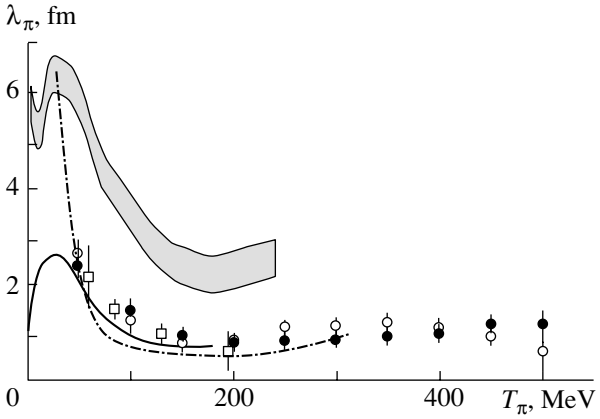

Fig. 5. Pion mean free path in nuclear matter as a function of energy. The displayed empirical data are given according to (open and closed circles) the present study for, respectively, neutral and charged pions; (open boxes) [26] for π^0; and (shaded region) [27] for the π^0 absorption length. The results of the theoretical calculations were borrowed from (solid curve) [28] and (dash-dotted curve) [26].

6. NUCLEAR TRANSPARENCY

The transparency T of a nucleus to particles produced in its interior upon the interaction between this nucleus and a projectile particle to which the nucleus is quite transparent can be represented in the form

$$T = \int d\mathbf{r}\rho(\mathbf{r}) \exp\left(-2\mathrm{Im}\phi(\mathbf{r})\right). \qquad (20)$$

The calculated nuclear transparency of Li, C, and Al to protons is shown in Fig. 6 as a function of energy. These transparencies were calculated by using the definition of the local mean free path according to (10) and the estimates of the proton mean free path in nuclear matter from Section 5.

Along with the data of the present study, Fig. 6 displays the empirical estimates of the nuclear transparency that were obtained on the basis of the results of three experiments performed at the MIT-Bates linear electron accelerator (USA) [33, 38], the Tomsk synchrotron [34, 39], and the 500-MeV Bonn synchrotron [40].

The quasifree electron scattering in the $(e, e'p)$ and (e, e') reactions on C, Al, Ni, and Ta nuclei was studied in [33]. The transparency of the nuclei was determined as a normalization factor that makes it

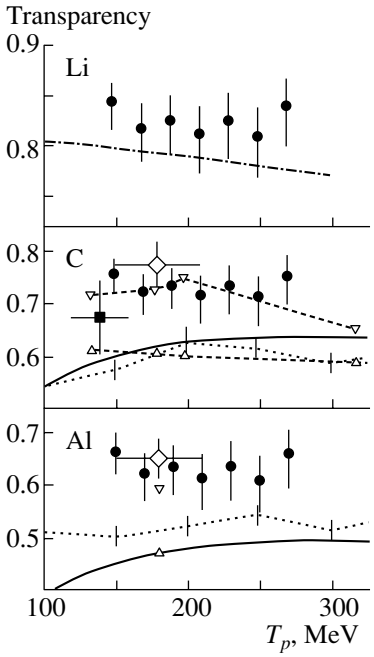

Fig. 6. Transparency of the Li, C, and Al nuclei to protons versus energy. The displayed empirical data are given according to (closed circles) the present study, (diamonds) [33] for $(e, e'p)$ and (e, e') reactions, and (closed boxes) [34] for the $(\gamma, \pi^- p)$ and (γ, π^-) reactions. The theoretical results shown here were obtained (closed circles) within the optical model [35]; (dotted curves) within the microscopic cascade model [36]; (right and inverted open triangles) for $(e, e'p)$ reactions in, respectively, the DWA with the optical potential from [19] and the EEI model [37]; and (dash-dotted curve) for the transparency of the Li nucleus according to a calculation with the optical potential that was used to obtain the input values of λ and the DWIA reaction yields presented in Fig. 1.

possible to fit the results of the PWIA calculations for the ratio of the cross sections $d^2\sigma/d\Omega_e d\Omega_p$ and $d\sigma/d\Omega_e$ for the respective $(e, e'p)$ and (e, e') reactions to the experimental value of this ratio. The resulting estimates of the nuclear transparency for protons of energy 180 ± 30 MeV are represented by diamonds in Fig. 6.

In [34], information about proton interaction with the residual nucleus was deduced from a global analysis of the exclusive cross sections for quasifree pion photoproduction in the reaction $^{12}\mathrm{C}(\gamma, \pi^- p)^{11}\mathrm{C}$ that were measured in the experiment reported in [39] and the inclusive cross sections for the reaction $^{12}\mathrm{C}(\gamma, \pi^-)$ [40]. The effect of proton interaction with a $^{11}\mathrm{C}$ nucleus was determined in terms of the ratio of the sum of the exclusive cross section $d^3\sigma/dE_\pi d\Omega_\pi d\Omega_p$ for the $(p_{3/2})^{-1}$ and $(s_{1/2})^{-1}$ states of the $^{11}\mathrm{C}$ nucleus to the analogous cross section obtained in the quasifree approximation on the basis of data on the inclusive cross section $d^2\sigma/dE_\pi d\Omega_\pi$ for the reaction $^{12}\mathrm{C}(\gamma, \pi^-)$. An estimate of the nuclear transparency to protons of energy 140 ± 20 MeV (closed box in Fig. 6) was obtained in the region of moderate momenta of the residual nucleus, where the effect of the real part of the proton–nucleus optical potential on the sum of the cross sections for s- and p-wave hole states of the residual nucleus is minimal.

As can be seen, the results presented in [34, 38] are consistent with the data of this study. A somewhat smaller value of the transparency estimated on the basis of data on the respective $(\gamma, \pi^- p)$ and (γ, π^-) reactions may possibly be due to a greater contribution to the cross section for the inclusive (γ, π^-) reaction from highly excited states of residual nuclei formed in pion photoproduction on nuclei. This conjecture is suggested by the results obtained in [39, 41] by measuring the excitation spectra of residual nuclei in the reactions $^{12}\mathrm{C}(\gamma, \pi^- p)^{11}\mathrm{C}$ and $^{12}\mathrm{C}(\gamma, \pi^+ n)^{11}\mathrm{B}$.

The empirical estimates given in Fig. 6 for the nuclear transparency to protons are compared with the results of theoretical calculations based on various models. The solid curves represent the results obtained in one of the first studies on the subject [35], where a systematic analysis of the nuclear transparency to particles produced in photon–nucleus interaction was performed within the optical model. There, the nucleus was considered as a uniformly filled sphere of radius given by (7), where the radial parameter r_0 depended on the mass number A. The particle mean free path λ was taken in a form that was similar to (19) and which expressed it in terms of the nucleon density ρ_N and the mean value of the total cross section for particle interaction with intranuclear nucleons, $\bar{\sigma}_t$. The separate points connected by segments of a dotted line show the energy dependence of the nuclear transparency calculated in [36] on the basis of the cascade model by the Monte Carlo model. There, the model of a degenerate Fermi gas was used for the nucleus. The interaction of a particle with a nucleus was considered as a succession of two-particle collisions. Only elastic scattering was taken into account in proton–nucleon collisions. The effect of the Pauli exclusion principle was incorporated in the calculation. Two sets of computed data shown by right and inverted triangles in Fig. 6 correspond to the results obtained in [37], where the transparency of nuclei to protons produced in quasifree electron scattering on nuclei in $(e, e'p)$ reactions was studied in the distorted-wave approximation (DWA). In calculating the transparency represented by the right triangles in Fig. 6, use was made in [37] of the aforementioned global Dirac proton–nucleus optical potential [19] of the EDAD1 version, this potential being based on data obtained for elastic proton–nucleus scattering.

The results of the calculation that are shown by inverted triangles in Fig. 6 were obtained for the empirical effective interaction (EEI) of the model based on the Brueckner–Hartree–Fock approximation for the density-dependent interaction of nucleons in nuclear matter. The EEI parametrization was constructed through a fit to data both on elastic proton–nucleus scattering and on processes accompanied by inelastic nuclear transitions. In contrast to the former, the latter are sensitive to the behavior of the wave function in the interior of the nucleus.

As can be seen from Fig. 6, the transparency of nuclei to protons that was calculated within all model approaches, with the exception of the EEI approach, is insufficiently high for explaining the available experimental data. Within microscopic models, it is of importance to take into account the Pauli exclusion principle, the effective nucleon mass in nuclear matter, and nucleon–nucleon correlations in nuclei [22]. Some of these factors, which increase the transparency of nuclei, were disregarded in [35, 36]. The best description of the energy dependence of the nuclear transparency was attained on the basis of the EEI model, whose parameters were determined from a fit to experimental data, including those on inelastic-scattering processes [37].

The transparency of Li, C, and Al nuclei to neutral and charged pions that was determined as a function of energy according to (20) by using the empirical data of the present study on the pion mean free path in nuclear matter is shown in Fig. 7 by open and closed circles, respectively. The data represented by open boxes are the results obtained in [42], where the semiinclusive cross section for the reaction $^{12}\mathrm{C}(\gamma,\pi^-)$ was measured under kinematical conditions close to those in the present study ($\theta_\pi = 44.2^\circ$ in the laboratory frame). The transparency was estimated there as the ratio of the experimentally measured differential cross section and the theoretical cross section calculated in the plane-wave impulse approximation. In Fig. 7, the notation for the theoretical estimates of the nuclear transparency of C and Al from [35, 36] is identical to that in Fig. 6. In [35], the pion mean free path was determined in terms of the total cross sections for pion–nucleon interaction, while, in [36], the pion–nucleus interaction included elastic-scattering processes, scattering processes involving pion charge exchange, and pion absorption by nucleon pairs.

As can be seen, the empirical transparencies of the carbon nucleus to charged pions in the present study comply well with those obtained in [42]. The theoretical transparency reproduces satisfactorily the empirical data at low pion energies, but it exceeds them systematically at high pion energies. In relation to the theoretical estimates, the energy dependence of the empirical transparency is smoother.

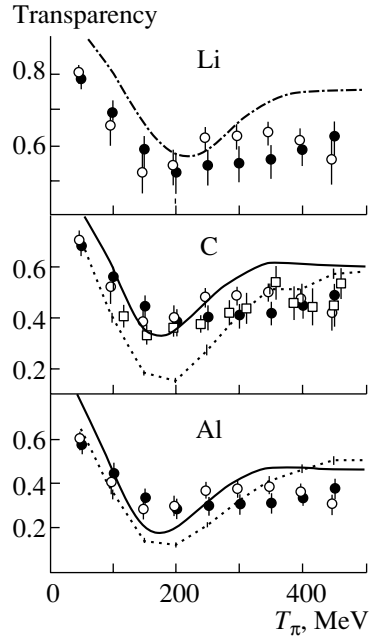

Fig. 7. Transparency of the Li, C, and Al nuclei to neutral and charged pions versus energy. The displayed empirical data are given according to (open and closed circles) the present study for, respectively, neutral and charged pions and (open boxes) [42] for (γ,π^-) reactions. The notation for the curves is identical to that in Fig. 6.

The mean free path averaged over the nuclear volume, $\bar{\lambda}$, is a quantity of use for deriving a simplified estimate of the final-state-interaction effect.

The concept of a mean free path as a global characteristic of the nucleus is straightforwardly introduced within the optical model for nuclei whose matter density is distributed uniformly [23]:

$$\lambda = -\frac{v}{2W}.$$

In defining the particle mean free path in actual nuclei, there arise difficulties generated by the presence of a diffuse external boundary. One method for taking into account the nonuniformity of the nuclear-density distribution—it was employed in [43]—consists in introducing, by analogy with (10), a local mean free path $\lambda(\mathbf{r})$ that is related to the local quantity $W(\mathbf{r})$ and in defining the global quantity $\bar{\lambda}$ as the average of $\lambda(\mathbf{r})$ over the nuclear volume. Within this approach, there arise problems associated with the behavior of $\lambda(\mathbf{r})$ near the nuclear surface.

The quantity λ is not additive, but the potential possesses the property of additivity; therefore, we define $\bar{\lambda}$ in terms of the average of the quantity inverse to $\lambda(\mathbf{r})$; that is,

$$\frac{1}{\bar{\lambda}} = \overline{\left(\frac{1}{\lambda(\mathbf{r})}\right)}.$$

In this case, $\bar{\lambda}$ is expressed in terms of the mean depth of the imaginary part of the optical potential.

Using expression (10) for $\lambda(\mathbf{r})$, we obtain the following relation for the averaged mean free path of a particle in nuclei:

$$\frac{1}{\bar{\lambda}} \simeq \frac{1}{\lambda_0}\frac{v_0}{\bar{v}}\frac{\rho_{\text{opt}}}{\rho_0}. \qquad (21)$$

Here, $\rho_{\text{opt}} = 3/(4\pi R_{\text{opt}}^3)$, where $R_{\text{opt}} = \sqrt{5(\langle r_{\text{ch}}^2\rangle + R_s^2)/3}$ is the equivalent radius of a sphere where the optical-potential density is uniform and which corresponds to the root-mean-square charge radius of the nucleus, $\langle r_{\text{ch}}^2\rangle^{1/2}$, and $R_s = 1.4$ fm is the range of nucleon–nucleon and pion–nucleon interactions.

In this approach to defining $\bar{\lambda}$, the individual properties of a nucleus affect the mean free path through the mean optical-potential density ρ_{opt} and the mean group velocity of a particle, $\bar{v}$, this velocity being dependent on the depth of the real part of the optical potential.

At sufficiently high energies of a particle, the real part of the optical potential has but a slight effect on its velocity. Therefore, we can disregard the velocity ratio $v/v_0 \approx 1$ in (10) and, accordingly, in (21).

Employing $\bar{\lambda}$, we can determine the nuclear transparency to a high precision under the assumption that $\rho(\mathbf{r})$ is constant in (20) and (10). In this case, expression (20) for the transparency T assumes the form

$$T = \frac{3}{x^3}\left(\frac{x^2}{2} - 1 + (1+x)\exp(-x)\right), \qquad (22)$$

where $x = 2R_{\text{opt}}/\bar{\lambda}$.

The A dependence of the nuclear transparency according to the calculations performed on the basis of (22) by using values estimated with the aid of the experimental results quoted in Section 5 for the proton mean free path in nuclear matter is given in Fig. 8*a* along with data from [33], these values of $\bar{\lambda}$ being the following:

Nucleus:	^{7}Li	^{12}C	^{27}Al	^{40}Ca	^{58}Ni	^{181}Ta	^{207}Pb,
$\bar{\lambda}$ [fm]:	14.6 ± 1.3	8.5 ± 0.8	6.4 ± 0.6	6.0 ± 0.6	5.1 ± 0.5	4.6 ± 0.5	4.0 ± 0.4.

The data of the present study, as well as those from [33], were averaged over the proton-energy range 180 ± 30 MeV. In estimating $\bar{\lambda}$, use was made of the values given in (4) for the root-mean-square charge radii of the nuclei being considered.

Figure 8*a* also displays the data obtained in [37] (inverted open triangles) within the EEI model and the results of the calculation performed in [22] (crosses) in the Glauber approximation with allowance for nucleon–nucleon correlations in a nucleus, the effective nucleon mass, and the Pauli exclusion principle. As can be seen, the empirical estimates of the nuclear transparency that were derived in the present study and in [33] comply well and are compatible with the results of the theoretical calculations in Fig. 8*a*.

The empirical data in Fig. 8*a* are also of interest in connection with the possibility of qualitatively estimating of the influence of surface effects on the transparency of nuclei. The ratio of the surface- to the volume-effect contribution varies in proportion to R^{-1}. Since the width of the surface layer of nuclei is approximately constant, effects such as reflection accompanying a transition through the interface between two media in the optical model or the removal of the excitation-quantum cloud from a quasiparticle going over from a medium to a vacuum in field theory [44] may be significant in light nuclei. In view of this, our extrapolation of the data estimated for light nuclei to the region of heavy nuclei may lead to underestimating the transparency of nuclei like ^{181}Ta. Therefore, the fact that the results obtained in the present study agree well with the experimental data reported in [33] for the ^{181}Ta nucleus is indicative of the insignificance of the surface effect in the proton-energy range under investigation, this being consistent with estimates that follow from the theory of finite Fermi systems [44].

The transparency of nuclei to negatively charged pions of kinetic energy about 400 MeV as a function of A is shown in Fig. 8*b* according to the calculations performed on the basis of (22) with the aid of the $\bar{\lambda}$ values from (21). Along with the data of the present study and the estimate of the transparency of carbon nuclei from [42], this figure also displays the results of the experiment that was reported in [45] and which furnished information about the transparency of the Cu and Pb nuclei to negatively charged pions produced in $A(\gamma, \pi^-)$ reactions.

Just like the empirical data, the calculated transparencies in Fig. 8*b* show significant distinctions.

First of all, the distinctions between the values of the rate at which the transparency changes in response to the growth of the mass number A of the nucleus catch the eye. In this respect, the data of the present study and those from [35] are similar, while the A dependence of the transparency in [36] is weaker. The possible explanation for this is that, here and in [35], the dependence of λ on the density of individual nuclei was taken into account, while, in [36], the calculation was performed for nuclei of density corresponding to the radial-parameter value of $r_0 = 1.3$ fm, this density being close to that of the carbon nucleus. At the same time, it follows from the data on the root-mean-square charge radii in (4) that, for nuclei in the $^{12}C-^{207}Pb$ range, the density changes by a factor of about 1.5, so that the disregard of this circumstance may increase the calculated transparency of heavy nuclei and decrease it for nuclei like ^7Li.

The distinction between the empirical estimates of the transparency of Cu and Pb nuclei to negatively charged pions in [45], on one hand, and the data of the present study, on the other hand, is likely to be due to different sensitivities of semi-inclusive cross sections for (γ, π^-) reactions and semiexclusive cross sections for $(\gamma, \pi^- p)$ reactions to inelastic-rescattering effects. The data on the relevant $(\gamma, \pi^- p)$ reactions were obtained by means of an experimental facility that records two particles within narrow solid angles. Therefore, pion rescattering on intranuclear nucleons drives events off the spectrometer acceptance with a higher probability. Such an effect is much weaker in the case of (γ, π^-) reactions. Moreover, the inaccuracy in measuring the photon energy was ± 25 MeV in [45]. Under such conditions, part of the inelastically rescattered pions may remain within the acceptance of the facility used even for considerable variations in energy. According to the result of the analysis performed in [42], the fraction of such events in the reaction $^{12}C(\gamma, \pi^-)$ amounts to about 10% under the kinematical conditions being considered. It is natural to expect that, with increasing mass number of the target nucleus, the contribution of rescattered pions increases, which leads to an increase in the values that are determined for the transparency of heavy and medium-mass nuclei from data on (γ, π^-) reactions.

On the other hand, the disagreement between the data of the present study and the experimental data from [45] for medium-mass and heavy nuclei may partly be due to an overestimated extrapolation of the contribution from surface effects (in just the same way as in the case of protons, which was considered above). For the pion–nucleus interaction, the most significant surface effects are usually attributed to the p-wave gradient term in a pion–nucleus optical potential of the Kisslinger type [46], this term being absent in the Frank–Gammel–Watson model [12]. The

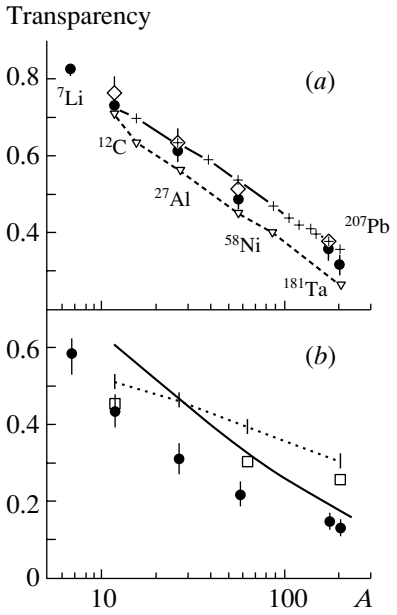

Fig. 8. A dependence of the nuclear transparency to (a) protons and (b) negatively charged pions. The displayed empirical data are given according to (closed circles) the present study, (open diamonds) [33] for $(e, e'p)$ reactions, and (open boxes) [42, 45]. The crosses represent the results of the theoretical calculation based on the Glauber model [22]. The rest of the notation is identical to that in Fig. 6.

measurements of the present study were performed for light nuclei, where there is virtually no constant-density region—the whole nucleus is a diffuse boundary, so that the contribution of the gradient term of the optical potential is present throughout the nucleus. In heavy nuclei, the contribution of this optical-potential component is operative only in a relatively narrow surface layer; therefore, an extrapolation of data obtained in experiments with light nuclei to the region of heavy nuclei on the basis of the model proposed in [12] may lead to somewhat underestimated results for transparencies and mean free paths both in nuclei and in nuclear matter. However, the fact that the estimates obtained in the present study for the neutral-pion mean free path in nuclear matter are in good agreement with those extracted from the experimental data reported in [26], which include data from measurements for medium-mass and heavy nuclei, indicates that, within the model used, the degree of the aforementioned underestimation of the transparency and the pion mean free path in heavy nuclei and in nuclear matter is insignificant.

7. CONCLUSION

In the second resonance region of photon energies, the differential production yields of $\pi^0 p$- and $\pi^- p$

pairs on Li, C, and Al nuclei have been measured versus the proton energy and the azimuthal angle of pion emission.

The resulting experimental data have been analyzed in the distorted-wave impulse approximation on the basis of a model that includes both single and double pion production. The mean free paths of 150- to 270-MeV protons and 50- to 500-MeV neutral and charged pions have been estimated by fitting the calculated reaction yields to their experimental counterparts.

The resulting estimate of the proton mean free path complies with the prediction of the Walecka model [21] and is compatible with the results presented in [19], where the mean free path was estimated on the basis of the proton–nucleus optical potential whose parameters were obtained from a fit to cross sections for elastic proton–nucleus scattering.

At common energy values, the neutral-pion mean free path is in good agreement with the results from [26], which were based on data from the measurement of the semi-inclusive yield of neutral pions from photon interactions with nuclei, and more than two times shorter than the absorption length obtained in [27] on the basis of cross sections for neutral-pion production in collisions of ^{36}Ar nuclei with ^{197}Au nuclei, this being at odds with theoretical estimates of the distinction between these quantities at modest pion energies [32]..

The transparency of nuclei to protons and pions produced in photon interactions with nuclei has been calculated on the basis of empirical data on mean free paths in nuclear matter. For protons of energy 180 MeV, the dependence of the nuclear transparency on the mass number A of the target nucleus is in good agreement with experimental data on $(e, e'p)$ reactions and with the theoretical estimates of the nuclear transparency that are based on the empirical-effective-interaction model [37] and the Glauber model [22]. The resulting transparency of nuclei to charged pions agrees with data on quasifree pion photoproduction in the (γ, π^-) reaction on a carbon nucleus [42] and contradicts the results of a similar experiment with copper and lead nuclei [45]. The transparencies of carbon and aluminum nuclei are satisfactorily described at low pion energies by the theoretical models proposed in [35, 36], but they are systematically below the existing theoretical estimates in the high-energy part of the pion-energy range investigated here.

ACKNOWLEDGMENTS

I am grateful to P.S. Anan'in and N.P. Fedorov for assistance in the measurements, Yu.F. Krechetov and O.K. Saigushkin for stimulating discussions on the problems considered in this article, and the personnel of the Tomsk synchrotron for ensuring the required regime of accelerator operation.

This work was supported in part by the Russian Foundation for Basic Research (project no. 97-02-17765).

REFERENCES

1. S. J. Brodsky, in *Proceedings of the 13th International Symposium on Multiparticle Dynamics* (World Sci., Singapore, 1982), p. 963.
2. A. H. Mueller, in *Proceedings of the XVII Recontre de Moriond* (Editions Frontieres, Gif-sur-Yvette, 1982), p. 13.
3. J. Stachel *et al.*, Phys. Rev. C **33**, 1420 (1986).
4. D. N. Voskresenskiĭ and A. V. Senatorov, Yad. Fiz. **53**, 1521 (1991) [Sov. J. Nucl. Phys. **53**, 935 (1991)].
5. N. C. R. Makins, R. Ent, M. S. Chapman, *et al.*, Phys. Rev. Lett. **72**, 1986 (1994).
6. I. V. Glavanakov, Yad. Fiz. **66**, 819 (2003) [Phys. At. Nucl. **66**, 787 (2003)].
7. I. V. Glavanakov, Yad. Fiz. **49**, 91 (1989) [Sov. J. Nucl. Phys. **49**, 58 (1989)].
8. I. V. Glavanakov, Yad. Fiz. **63**, 2187 (2000) [Phys. At. Nucl. **63**, 2091 (2000)].
9. L. Elton, *Nuclear Sizes* (Oxford, 1961; Inostr. Lit., Moscow, 1962).
10. R. C. Barrett and D. F. Jackson, *Nuclear Sizes and Structure* (Clarendon, Oxford, 1977; Naukova Dumka, Kiev, 1981).
11. H. Genzel, P. Joos, and W. Pfail, *Photoproduction of Elementary Particles* (Springer-Verlag, Berlin, 1973).
12. R. M. Frank, J. L. Gammel, and K. M. Watson, Phys. Rev. **101**, 891 (1956).
13. H. A. Bethe, Ann. Rev. Nucl. Sci. **21**, 93 (1971).
14. I. V. Glavanakov, Yad. Fiz. **55**, 2701 (1992) [Sov. J. Nucl. Phys. **55**, 1508 (1992)].
15. W. T. Eadie *et al., Statistical Methods and Experimental Physics* (North-Holland, Amsterdam, 1971; Atomizdat, Moscow, 1976).
16. I. V. Glavanakov and Y. F. Krechetov, in *Proceedings of the 9th Seminar of Electromagnetic Interaction of Nuclei at Low and Medium Energies* (INR, Moscow, 2001), p. 151.
17. P. U. Renberg *et al.*, Nucl. Phys. A **183**, 81 (1972).
18. A. Nadasen *et al.*, Phys. Rev. C **23**, 1023 (1981).
19. E. D. Cooper, S. Hama, B. C. Clark, and R. L. Mercer, Phys. Rev. C **47**, 297 (1993).
20. G. Li, R. Machleidt, and Y. Zhuo, Phys. Rev. C **48**, 1062 (1993).
21. B. Serot and J. Walecka, Adv. Nucl. Phys. **16**, 1 (1986).
22. V. R. Pandharipande and S. C. Pieper, Phys. Rev. C **45**, 791 (1992).
23. J. W. Negele and K. Yazaki, Phys. Rev. Lett. **47**, 71 (1981).

24. S. Fantoni, B. L. Friman, and V. R. Pandharipande, Phys. Lett. B **104B**, 89 (1981).
25. L. W. Chen, F. S. Zhang, Z. H. Lu, and H. R. Ma, Phys. Rev. C **64**, 064315 (2001).
26. G. N. Dudkin, V. N. Eponeshnikov, Yu. F. Krechetov, and V. A. Trasuchev, Yad. Fiz. **19**, 311 (1974) [Sov. J. Nucl. Phys. **19**, 153 (1974)].
27. R. Holzmann, A. Schubert, S. Hlaváč, *et al.*, Phys. Lett. B **336**, 63 (1996).
28. R. Mehrem, H. Radi, and J. Rasmussen, Phys. Rev. C **30**, 301 (1984).
29. G. N. Dudkin, Candidate's Dissertation in Mathematical Physics (Tomsk, 1978).
30. W. Gassing, V. Metag, U. Mosel, and K. Niita, Phys. Rep. **188**, 365 (1990).
31. J. Carr, H. McManus, and K. Stricker, Phys. Rev. C **25**, 952 (1982).
32. P. Hecking, Phys. Lett. B **103B**, 401 (1981).
33. G. Garino, M. Saber, R. E. Segel, *et al.*, Phys. Rev. C **45**, 780 (1992).
34. I. V. Glavanakov, Yad. Fiz. **31**, 342 (1980) [Sov. J. Nucl. Phys. **31**, 181 (1980)].
35. H. G. de Carvalho, J. B. Martins, O. A. P. Tavares, *et al.*, Lett. Nuovo Cimento **2**, 1139 (1971).
36. N. L. Emets, V. I. Noga, G. D. Pugachev, and Yu. N. Ranyuk, Vopr. At. Nauki Tekh., Ser. Fiz. Vysokikh Énerg. At. Yadra **6** (8), 78 (1973).
37. J. J. Kelly, Phys. Rev. C **54**, 2547 (1996).
38. D. F. Geesaman, R. Gilman, M. C. Green, *et al.*, Phys. Rev. Lett. **63**, 734 (1989).
39. I. V. Glavanakov and V. N. Stibunov, Yad. Fiz. **30**, 897 (1979) [Sov. J. Nucl. Phys. **30**, 465 (1979)].
40. J. Eyink, Interner Bericht Bonn Univ., Bonn-Ir-78-4 (Bonn, 1978).
41. J. A. MacKenzie, D. Branford, J. Ahrens, *et al.*, Phys. Rev. C **54**, R6 (1996).
42. K. Baba, I. Endo, M. Fujisaki, *et al.*, Nucl. Phys. A **306**, 292 (1978).
43. H. J. Yuan, H. L. Lin, G. Fai, and S. A. Moszkowski, Phys. Rev. C **40**, 1448 (1989).
44. D. N. Voskresenskiĭ and O. V. Oreshkov, Yad. Fiz. **50**, 1317 (1989) [Sov. J. Nucl. Phys. **50**, 820 (1989)].
45. K. Baba, I. Endo, M. Fujisaki, *et al.*, Nucl. Phys. A **322**, 349 (1979).
46. L. S. Kisslinger, Phys. Rev. **98**, 761 (1955).

Translated by A. Isaakyan

Physics of Atomic Nuclei, Vol. 67, No. 8, 2004, pp. 1596–1604. Translated from Yadernaya Fizika, Vol. 67, No. 8, 2004, pp. 1618–1626.

ELEMENTARY PARTICLES AND FIELDS
Theory

Graviton Mass, Quintessence, and Oscillatory Character of Universe Evolution

S. S. Gershtein*, A. A. Logunov, M. A. Mestvirishvili, and N. P. Tkachenko*****

Institute for High Energy Physics, Protvino, Moscow oblast, 142284 Russia

Received May 6, 2003

Abstract—On the basis of the field relativistic theory of gravity, an upper limit on the graviton mass, $m_g \leq 1.6 \times 10^{-66}$ g, is obtained at a 95% C.L. by using data on the density parameter $\Omega_{\rm tot}$. Within one standard deviation, the probable value of the graviton mass is $m_g = 1.3 \times 10^{-66}$ g. It is indicated that, according to the relativistic theory of gravity, the existence of quintessence is needed for explaining the accelerated expansion of the Universe. Experimental data on the age of the Universe and on the density of cold matter make it possible to determine the allowed interval of the parameter ν that enters into the equation of state for the quintessence and to indicate the instants of time that correspond to the beginning and cessation of the era of accelerated expansion, as well as the maximum-expansion time, which corresponds to the half-period of the oscillatory evolution of the Universe. © *2004 MAIK "Nauka/Interperiodica".*

1. INTRODUCTION

The discovery of the accelerated expansion of the Universe [1–3] made us revise many well-established ideas of its content and the character of its evolution. One of the popular explanations of accelerated expansion is based on the assumption that the cosmological constant Λ does not vanish, which is equivalent to the existence of a nonzero vacuum energy $\varepsilon_{\rm vac}$ and of the respective negative pressure $P_{\rm vac} = -\varepsilon_{\rm vac}$ [4–8]. This assumption implies an indefinite inflationary expansion of the Universe, the rate of such an expansion being at least 60 orders of magnitude less than the rate of primary inflationary expansion from the Planck scale (the latter is introduced to solve the horizon problem and to explain why the three-dimensional space is flat). However, the observed accelerated expansion of the Universe can also be explained by introducing the concept of quintessence [9–11], which is defined as a special substance in the Universe, its equation of state being

$$P_q = -(1-\nu)\varepsilon_q \quad \left(0 < \nu < \frac{2}{3}\right), \qquad (1)$$

where ε_q is the quintessence energy density and P_q is the quintessence pressure.

In the field relativistic theory of gravity (RTG) [12, 13], the gravitational field is considered as a physical field in Minkowski space; therefore, an indefinite expansion of the Universe is inconsistent with this theory. It was shown in [14] that the concept of quintessence (1) must be introduced in order to explain the observed accelerated expansion of the Universe within RTG. In accordance with RTG, the Universe must undergo a cyclic evolution. The present study was motivated by the appearance of new experimental data and by the importance of the problem.

We will show that, according to RTG, where there is no cosmological singularity and where our three-dimensional space is flat, the existence of a graviton mass with $\nu > 0$ results in that the currently observed accelerated expansion of the Universe will give way to a decelerated expansion, which will then terminate, whereupon the compression of the Universe will begin and continue until the scale factor falls to some minimum value; after that, a new era of expansion will begin.

The ensuing exposition is organized as follows. The fundamentals of RTG are outlined in Section 2. The predictions of RTG for the evolution of the homogeneous and isotropic Universe are presented in Section 3. An upper limit on the graviton mass at a 95% C.L. is obtained in Section 4 from the results of recent measurements of the cosmological parameter $\Omega_{\rm tot}$. A possible value of the graviton mass is estimated within one standard deviation. For the parameter ν, the allowed range of values that is consistent with current data on the age of the Universe and with other measured cosmological parameters is obtained in Section 5. The instant of the beginning and the instant of cessation of the currently observed accelerated expansion of the Universe are estimated

*e-mail: gershtein@mx.ihep.su
**e-mail: logunov@mx.ihep.su
***e-mail: tkachenkon@mx.ihep.su

in Section 6, along with the period of the oscillations of the Universe.

2. FUNDAMENTALS OF RTG

The underlying assumption of RTG is that, just as other fields, the gravitational field is a field in Minkowski space, its source being the energy–momentum tensor generated by all matter fields, including the gravitational field, and conserved in Minkowski space. This approach is in line with that which is adopted in the modern gauge theories of electroweak interactions and in QCD, where conserved charges and the respective currents provide a source of vector fields. Since a source of the gravitational field is provided by the energy–momentum tensor, the gravitational field is described by the rank-2 tensor $\varphi^{\mu\nu}$, and it is owing to this property that the "geometrization" of the theory becomes possible in its subsequent development. The basic set of RTG equations has the form [12, 13] ($\hbar = c = 1$)

$$(\gamma^{\alpha\beta}D_\alpha D_\beta + m_g^2)\tilde{\varphi}^{\mu\nu} = 16\pi G t^{\mu\nu}, \qquad (2)$$

$$D_\nu \tilde{\varphi}^{\mu\nu} = 0, \qquad (3)$$

where D_α is a covariant derivative in Minkowski space specified by the metric tensor $\gamma_{\alpha\beta}$, $\tilde{\varphi}^{\mu\nu}$ is the gravitational-field density, and $t^{\mu\nu}$ is the density of the energy–momentum tensor. Specifically, we have

$$\tilde{\varphi}^{\mu\nu} = \sqrt{-\gamma}\cdot\varphi^{\mu\nu}, \quad \gamma = \det(\gamma_{\mu\nu}) = \det(\tilde{\gamma}^{\mu\nu}),$$
$$t^{\mu\nu} = -2\frac{\delta L}{\delta \gamma_{\mu\nu}},$$

where L is the Lagrangian density for matter and the gravitational field. Equation (3) ensures the conservation of the total energy–momentum tensor and isolates polarization states corresponding to spin-2 and spin-0 gravitons, excluding spin-1 and spin-0′ states (in just the same way as the Lorentz condition in electrodynamics excludes the spin-0 photon). For the set of Eqs. (2) and (3) to be a consequence of the minimum-action principle, that is, of the Euler equations[1)]

$$\frac{\delta L}{\delta \tilde{\varphi}^{\mu\nu}} = 0, \qquad \frac{\delta L_M}{\delta \tilde{\varphi}_k} = 0, \qquad (4)$$

it is necessary and sufficient that the densities of the tensor $\tilde{\varphi}^{\mu\nu}$ and the metric tensor $\tilde{\gamma}^{\mu\nu}$ in Minkowski space enter into the Lagrangian for matter only in the combination [12, 13]

$$\tilde{\varphi}^{\mu\nu} + \tilde{\gamma}^{\mu\nu} = \tilde{g}^{\mu\nu}; \quad \tilde{g}^{\mu\nu} = \sqrt{-g}\cdot g^{\mu\nu};$$
$$g = \det(\tilde{g}^{\mu\nu}) = \det g_{\mu\nu}.$$

Thus, we obtain

$$L = L_g + L_M(\tilde{g}^{\mu\nu}, \tilde{\varphi}_k)$$

and the motion of matter in a gravitational field occurs as if it took place in an effective Riemann space characterized by the metric tensor $g_{\mu\nu}$. All crucial distinctions between the Einstein general theory of relativity and RTG stem from the fact that, within RTG, the gravitational field is considered as a physical field in Minkowski space. It is precisely this approach that inevitably leads to a graviton mass. The equations of gravity that involve a nonzero graviton mass have long since been known (see, for example, [15]). However, they were written only in inertial reference frames because the special theory of relativity was considered to be valid only for such frames. For this reason, these equations were not generally covariant and, in view of this, have not yet received proper attention. In RTG, it is considered that, in Minkowski space, one can use arbitrary reference frames (including accelerated ones) such that the metric coefficients $\gamma_{\mu\nu}$ form a tensor with respect to arbitrary coordinate transformations. This is precisely the reason why Eqs. (2) and (3) are generally covariant.

In RTG, a nonzero value of the graviton mass is required because, otherwise, the gravitational field $\varphi^{\mu\nu}$, generated by the total energy–momentum tensor satisfying the conservation law, possesses a group of gauge transformations [12, 13] (see also [16]). As a result, some observable quantities, including the metric tensor of the effective Riemann space and its curvature, prove to be gauge-dependent. The graviton mass breaks gauge symmetry, thereby making observable quantities independent of arbitrariness, without violating the general covariance of the equations of the gravitational field. In the Lagrangian for the gravitational field, the mechanism of gauge-symmetry breaking via the introduction of a nonzero graviton mass is represented by a term whose structure was unambiguously fixed in [12, 13]. As a result, the equations of motion of the gravitational field and matter take the form

$$R^{\mu\nu} - \frac{1}{2}g^{\mu\nu}R + \frac{1}{2}\left(\frac{m_g c}{\hbar}\right)^2 \qquad (5)$$
$$\times\left[g^{\mu\nu} + \left(g^{\mu\alpha}g^{\nu\beta} - \frac{1}{2}g^{\mu\nu}g^{\alpha\beta}\right)\gamma_{\alpha\beta}\right] = 8\pi G T^{\mu\nu},$$

$$D_\mu \tilde{g}^{\mu\nu} = 0, \qquad (6)$$

[1)] Here, $L_M(\tilde{\gamma}^{\mu\nu}, \tilde{\varphi}^{\mu\nu}, \tilde{\varphi}_k)$ is the Lagrangian density that describes matter and which is associated with the motion of matter fields φ_k in a gravitational field and L is the density of the total Lagrangian, which includes the gravitational-field Lagrangian L_g.

where $R^{\mu\nu}$ and R are the respective curvatures in the effective Riemann space and $T^{\mu\nu}$ is the energy–momentum tensor of matter there,

$$\sqrt{-g}\cdot T^{\mu\nu} = -2\frac{\delta L_M}{\delta g_{\mu\nu}}.$$

Equations (5) and (6) transform covariantly under general coordinate transformations, their form being invariant under Lorentz transformations. Since $m_g \neq 0$, the connection between the effective Riemann space and the metric tensor $\gamma_{\alpha\beta}$ of the underlying Minkowski space is retained in Eq. (5).

Equations (5) and (6) form a complete set of equations. It should be emphasized that relation (6) is precisely an equation that follows from the conservation of the total energy–momentum tensor [or, equivalently, from Eq. (4) for matter fields] rather than an auxiliary condition. With allowance for all of the existing estimates of the graviton mass (see Section 4), Eqs. (5) and (6) comply well with all relativistic gravitational effects observed in the solar system.

3. EVOLUTION OF THE HOMOGENEOUS AND ISOTROPIC UNIVERSE IN RTG

In the case of a homogeneous and isotropic universe, the expression for an interval between events in the effective Riemann space can be expressed in terms of the Friedmann–Robertson–Walker metric as

$$ds^2 = U(t)(dx^0)^2 - V(t) \times \left[\frac{dr^2}{1-kr^2} + r^2(d\Theta^2 + \sin^2\Theta d\varphi^2)\right], \quad (7)$$

where $k = 1$, -1, and 0 correspond to a closed (elliptic), an open (hyperbolic), and a flat (parabolic) universe, respectively.

For the metric in (7), Eqs. (6) take the form

$$\frac{\partial}{\partial t}\left(\frac{V^3}{U}\right) = 0, \quad (8)$$

$$\frac{\partial}{\partial r}\left(r^2\sqrt{1-kr^2}\right) - 2r\left(1-kr^2\right)^{-1/2} = 0. \quad (9)$$

From Eq. (8), it follows that $V^3/U = \text{const}$ or

$$V = \beta U^{1/3}; \qquad \beta = \text{const}. \quad (10)$$

Equation (9) can hold only at $k = 0$.

Thus, it immediately follows from Eq. (6) that the Universe is flat in spatial directions even if there was no primary inflationary expansion. This result was first obtained in [17]. That, in RTG, only one (flat) solution ($k = 0$) is obtained for a homogeneous and isotropic universe, instead of the three Friedmann solutions, is quite natural since Eqs. (5) and (6), together with the equation of state for $T^{\mu\nu}$, form a complete set of equations that has only one solution.

Introducing the proper time

$$d\tau = U^{1/2}dt$$

and the notation

$$a^2(\tau) = U^{1/3},$$

we can recast expression (7) for the interval into the form

$$ds^2 = c^2d\tau^2 - \beta a^2(\tau)[dr^2 + r^2(d\Theta^2 + \sin^2\Theta d\Phi^2)]. \quad (11)$$

With allowance for expression (11), Eq. (5) for a homogeneous and isotropic universe takes the form [12, 13]

$$\left(\frac{1}{a}\frac{da}{d\tau}\right)^2 = \frac{8\pi G}{3}\rho - \frac{1}{6}\left(\frac{m_g c^2}{\hbar}\right)^2 \times \left(1 - \frac{3}{2\beta a^2} + \frac{1}{2a^6}\right), \quad (12)$$

$$\frac{1}{a}\frac{d^2a}{d\tau^2} = -\frac{4\pi G}{3}\left(\rho + \frac{3P}{c^2}\right) - \frac{1}{6}\left(\frac{m_g c^2}{\hbar}\right)^2 \times \left(1 - \frac{1}{a^6}\right), \quad (13)$$

where ρ is the total density of matter and P is the respective pressure.

The constant β that was defined in (10) and which appears in Eq. (12) has a simple physical meaning. If the gravitational field $\varphi^{\mu\nu}$ is a physical field in Minkowski space, the causality principle must hold, which implies that the trajectory of a particle moving in a gravitational field must lie within the light cone in Minkowski space. Given expression (11) for the interval, this leads to the inequality

$$a^2(\tau)\left[a^4(\tau) - \beta\right] \leq 0.$$

Thus, the constant β determines the maximum value of the scale factor [12, 13],

$$a^4_{\max} = \beta.$$

Therefore, an indefinite increase in the scale factor $a(\tau)$—that is, an unbounded expansion of the Universe—is impossible in RTG.[2)]

[2)] Here, we adhere to the conventional term the "expansion" of the Universe, although the Universe is in fact infinite: the coordinate r that appears in expression (11) for the interval varies over the range $0 < r < \infty$. An increase in the distances between galaxies, which is determined from the redshift and which is interpreted in terms of the Doppler effect, is associated with the fact that light from far galaxies is emitted in a gravitational field stronger than the field at the instant of the detection of the light signal by an observer.

In view of Eq. (12), this requirement is satisfied owing to a nonvanishing graviton mass, provided that the matter density ρ is a decreasing function of the scale factor a. According to (12), the minimum value of ρ corresponding to the cessation of expansion ($da/d\tau = 0, a \gg 1$) is

$$\rho_{\min} = \frac{1}{16\pi G}\left(\frac{m_g c^2}{\hbar}\right)^2. \qquad (14)$$

If the equation of state for matter is represented in the form (1), it is well known from the first law of thermodynamics that the dependence of ρ on the scale factor a is given by

$$\rho = \frac{\text{const}}{a^{3\nu}}, \qquad (15)$$

where $\nu = 4/3$ for relativistic matter (radiation and "light" neutrinos) and $\nu = 1$ for baryon matter and cold dark mass. According to (13), cold matter and radiation must lead to the deceleration of expansion. In order to explain the accelerated expansion of the Universe, one has to assume that, in the Universe, there is a "dark" energy $\mathcal{E}_x$ satisfying the condition

$$\left(\rho_x + \frac{3P_x}{c^2}\right) < 0.$$

In this case, it follows from the equation of state (1) that

$$\rho_x + \frac{3P_x}{c^2} = -2\rho_x\left(1 - \frac{3}{2}\nu\right).$$

For the expansion of the Universe to be accelerated, it is therefore necessary that

$$0 \le \nu < \frac{2}{3}.$$

The value of $\nu = 0$ corresponds to the presence of the vacuum-energy density $\varepsilon_{\text{vac}} = \rho_{\text{vac}}c^2$ and the pressure $P_{\text{vac}} = -\varepsilon_{\text{vac}}$. In this case, ρ_{vac} is independent of the scale factor and, over the range $\rho_{\text{vac}} > \rho_{\min}$ [$\rho_{\min}$ is given by (14)], the expansion of the Universe is unbounded according to (12) and (13). For this reason, a nonvanishing value of the vacuum energy density, $\varepsilon_{\text{vac}} \neq 0$, is inconsistent with RTG in Minkowski space. This is quite natural since the vacuum-energy density in a flat space cannot be different from zero. Within RTG, the accelerated expansion of the Universe can be explained only by the presence of quintessence (1) with $\nu > 0$ (strict inequality). In this case, the dark-energy density must decrease with increasing scale factor according to (15). At sufficiently large values of the scale factor, it follows from (12) and (13) that, at a nonzero graviton mass, the expansion of the Universe will turn stop, whereupon the compression of the Universe will begin. This compression will in turn stop at some minimum value of the scale factor, $a_{\min} \neq 0$. To demonstrate this, we note that the negative term on the right-hand side of Eq. (12) increases in proportion to $m_g^2 a^{-6}$ for $a \to 0$. Since the left-hand side of this equation is positive definite, this growth must be compensated for by an increase in the density ρ (at the radiation-dominated stage, the density grows according to the $\rho \sim 1/a^4$ law), but this is possible only if $a_{\min} \neq 0$. As soon as the point $a = a_{\min}$ is reached, a new era of the expansion of the Universe begins. Thus, the term proportional to m_g^2 in Eqs. (12) and (13) removes both a cosmological singularity and the possibility of an indefinite expansion of the Universe. To put it differently, the evolution of the Universe in RTG must be oscillatory owing to a nonzero graviton mass. Current experimental data allow us to set limits on the graviton mass and, on this basis, to estimate the period of the oscillations.

Table 1 (borrowed from [26])

	Ω_{tot}^0
B98 + DMR	$1.15^{+0.10}_{-0.09}$
MAXIMA-1 + DMR	$1.01^{+0.09}_{-0.09}$
B98 + MAXIMA1 + DMR	$1.11^{+0.07}_{-0.07}$
CMB + LSS	$1.11^{+0.05}_{-0.05}$
CMB + SN1a	$1.09^{+0.06}_{-0.05}$
CMB + SN1a+LSS	$1.06^{+0.04}_{-0.04}$

4. Ω_{tot} AND ESTIMATION OF THE POSSIBLE GRAVITON MASS

Soon after the discovery of cosmic microwave background radiation, Sunyaev and Zeldovich [18] performed a detailed quantitative analysis of processes that occurred in the era of hydrogen recombination and photon decoupling from matter. Among other things, they showed that, in the hydrogen-recombination era, adiabatic perturbations (sound waves) in a plasma must have given rise to the angular anisotropy of the observed cosmic microwave background radiation. By studying this anisotropy, one can determine some important cosmological parameters (see also earlier studies of Silk [19] and a

subsequent consideration in [20–22]).[3] The required precision in measuring angular correlations in the spectrum of cosmic microwave background radiation was discussed in detail in [23, 24]. Measurement of angular distributions of cosmic microwave background radiation makes it possible to determine a number of cosmological parameters, including $\Omega^0_{\rm tot}$, which is defined as the ratio of the total matter density ρ to the present-day value of the critical density ρ^0_c,

$$\Omega^0_{\rm tot} = \rho/\rho^0_c (\rho^0_c = 3H^2_0/(8\pi G)),$$

where H_0 is the present-day value of the Hubble constant [25]:

$$H_0 = h(9.77813 \times 10^9 \text{ yr})^{-1}, \quad h = 0.71 \pm 0.07.$$

Jaffe *et al.* [26] performed a global analysis of the BOOMERANG-98 [27] and Maxima-1 [28] experiments, invoking data from the earlier experiment COBE DMR [29], as well as data obtained from the observation of the supernova SN1*a* [1, 2] and large-scale structures in the Universe [30, 31]. The results of this global analysis indicate [26] that the average values of $\Omega_{\rm tot}$ derived from various combinations of experiments exceed unity (see Table 1 taken from [26]).

At a 68% C.L., $\Omega_{\rm tot}$ is [26]

$$\Omega^0_{\rm tot} = 1.11 \pm 0.07, \tag{16}$$

whereas $\Omega^0_{\rm tot}$ in the inflation theory of the early Universe [4–8] is unity to a high degree of precision. For this reason, the fact that the values of $\Omega^0_{\rm tot}$ that were obtained in various experiments systematically exceed unity is of particular interest, even though the results of the analysis in [26] are consistent with the value of $\Omega^0_{\rm tot} = 1$ at a 95% C.L.:

$$\Omega_{\rm tot} = 1.11^{+0.13}_{-0.12}. \tag{17}$$

Assuming that $a \gg 1$ and dividing both sides of Eq. (12) (written for the present-day values) by the square of the Hubble constant, H^2_0, we do indeed arrive at

$$\Omega^0_{\rm tot} = 1 + f^2/6, \tag{18}$$

where $f = m_g c^2/(\hbar H_0)$. It is convenient to represent f as the ratio of the graviton mass to the quantity $m^0_{\rm H}$, which could be called a "Hubble mass":

$$m^0_{\rm H} = \frac{\hbar H_0}{c^2} = 3.8 \times 10^{-66} h\,[\text{g}],$$

$$f = m_g/m^0_{\rm H}. \tag{19}$$

Relations (18) and (19) make it possible to estimate the graviton mass straightforwardly. From formulas (17) and (18), we derive an upper limit on the graviton mass,

$$m_g \le 1.2 m^0_{\rm H} \quad (95\%\ \text{C.L.}).$$

At the same time, this does not rule out the possibility, at a 68% C.L., that, according to (16)–(18), the graviton mass is

$$m_g = (0.8^{+0.2}_{-0.3}) m^0_{\rm H}.$$

Preliminary data from the WMAP experiment [31], which were published quite recently, permit refining the above estimates of the graviton mass. These data yield

$$\Omega^0_{\rm tot} = 1.02 \pm 0.02. \tag{20}$$

At a level of two standard deviations, it then follows that $f^2/6 < 0.06$ with an accuracy of 2σ; that is,

$$m_g \le 0.6 m^0_{\rm H} = 1.6 \times 10^{-66}\ \text{g} \quad (\text{for } h = 0.71).$$

At the same time, the upper limit $\Omega^0_{\rm tot} = 1.04$ in (20) agrees with the lower value in (16) within one standard deviation. This cannot rule out the possibility that

$$\frac{f^2}{6} = 0.04 \text{ and } m_g \approx 0.5 m^0_{\rm H} = 1.3 \times 10^{-66}\ \text{g}. \tag{21}$$

In what follows, this value of the graviton mass is used for further estimates.[4]

5. AGE OF THE UNIVERSE AND LIMITS ON THE QUINTESSENCE PARAMETER ν

Since the time it takes for the scale factor a to increase from its minimum value $a_{\rm min}$ to a value typical of the Friedmann evolution regime is negligible and since the duration of the radiation-dominated stage of expansion is at least four orders of magnitude less than the age of the Universe, we can reckon the age

[3] Sakharov [Zh. Eksp. Teor. Fiz. **49**, 345 (1965)] considered primary quantum fluctuations in the early (cold) Universe. His conclusion was as follows: provided that pressure can be neglected, the amplitudes of adiabatic perturbations in matter have a periodic dependence on the wavelength. Sunyaev and Zeldovich [18] indicated that this circumstance affects the anisotropy of cosmic microwave background radiation that emerges at the end of the hydrogen-recombination era.

[4] It was indicated [25] that all estimates of the graviton mass are based on the assumption that, for $m_g \neq 0$, the potential of a weak gravitational field is of the Yukawa type. This is so in RTG as well [see Eq. (2)]. The best earlier estimate $m_g < 5 \times 10^{-62}$ g was obtained from the gravitational interactions between galaxies in a cluster of size 500 kpc. The above limits rely on observations at distances of about c/H_0 and are therefore four orders of magnitude more stringent.

of the Universe from the beginning of the matter-dominated stage, assuming that the density of cold matter (including baryons) is $\rho_m = \rho_m^0/x^3$, where ρ_m^0 is the present-day density and x is the ratio of the scale factor $a(\tau)$ to its present-day value a_0,

$$x = a(\tau)/a_0.$$

Similarly, the quintessence density can be represented in the form

$$\rho_q = \frac{\rho_q^0}{x^{3\nu}},$$

where ρ_q^0 is its present-day value. Equation (12) then takes the form

$$\left(\frac{1}{x}\frac{dx}{d\tau}\right)^2 = H_0^2\left(\frac{\Omega_m^0}{x^3} + \frac{\Omega_q^0}{x^{3\nu}} - \frac{f^2}{6}\right), \qquad (22)$$

where

$$\Omega_m^0 = \frac{\rho_m^0}{\rho_c^0} \text{ and } \Omega_q^0 = \frac{\rho_q^0}{\rho_c^0}.$$

From Eq. (22), it follows that

$$d\tau = \frac{1}{H_0}\frac{x^{1/2}dx}{\sqrt{F(x)}},$$

where

$$F(x) = \Omega_m^0 + \Omega_q^0 x^{3(1-\nu)} - \frac{f^2}{6}x^3. \qquad (23)$$

Thus, the age of the Universe today t_0 is given by

$$t_0 = \frac{1}{H_0}\int_0^1 \frac{x^{1/2}dx}{\sqrt{F(x)}}. \qquad (24)$$

The time of the beginning (t_1) and the cessation (t_2) of the observed accelerated expansion are

$$t_{1(2)} = \frac{1}{H_0}\int_0^{x_1(x_2)} \frac{x^{1/2}dx}{\sqrt{F(x)}},$$

where x_1 and x_2 are roots of the equation

$$\Omega_m^0 - 2\Omega_q^0\left(1 - \frac{3}{2}\nu\right)x^{3(1-\nu)} + \frac{f^2}{3}x^3 = 0,$$

which is merely the condition that the acceleration in (13) is equal to zero. The maximum time of expansion (that is, the oscillation half-period $T_0/2$) is determined by an integral similar to that in (24); that is,

$$\frac{T_0}{2} = \frac{1}{H_0}\int_0^{x_{\max}} \frac{x^{1/2}dx}{\sqrt{F(x)}},$$

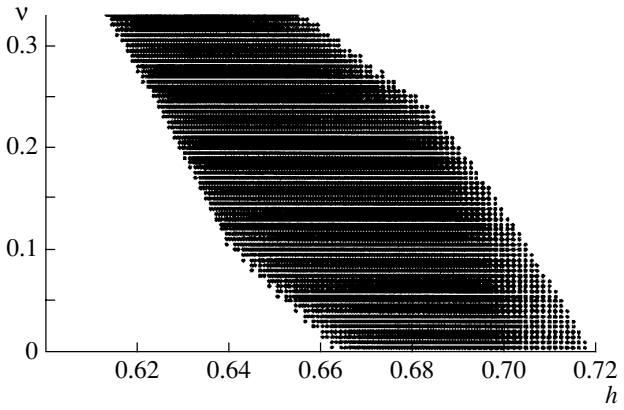

Fig. 1. Region of allowed values of the parameter ν for $\Omega_{\text{tot}} = 1.04$, $0.126 \le \omega_m \le 0.143$, and $13.5 \times 10^9 < t_0 < 13.9 \times 10^9$ years.

where $x_{\max}$ is a root of the equation

$$F(x_{\max}) = 0. \qquad (25)$$

The result obtained in [31] for the age of the Universe today, $t_0 = (13.7 \pm 0.2) \times 10^9$ yr, makes it possible to set limits on the range of the quintessence parameter ν at a nonzero graviton mass. Since the WMAP experiment [31] yielded the value of $\omega_m = \Omega_m^0 h^2 = 0.135^{+0.008}_{-0.009}$ and since $\Omega_q^0 = \Omega_\Lambda^0 = \Omega_{\text{tot}} - \Omega_m^0$ [where, for the graviton mass set to the value in (21), $\Omega_{\text{tot}} = 1.04$], it follows from (23) and (24) that, over the range $\bar{\omega}_m - \Delta\omega_m < \omega_m < \bar{\omega}_m + \Delta\omega_m$, the age of the Universe today acquires an additional dependence on h and ν. Owing to this, one can find the region of allowed values of ν, which prove to be consistent with the interval determined in [31] for the age of the Universe.[5)] The resulting allowed region[6)] is shown in Fig. 1.

It is interesting to note that, for $0.64 < h < 0.67$, the interval adopted here for the age of the Universe today requires the existence of quintessence with $\nu_{\min} > 0$. The value of ν can in principle be determined upon refining data on Ω_m^0 and Ω_Λ^0 (we assume that $\Omega_\Lambda^0 = \Omega_q^0$) and the acceleration q_0. According to (13), we have

$$q_0 = \frac{\ddot{a}_0}{a_0 H_0^2} = \left(1 - \frac{3}{2}\nu\right)\Omega_q^0 - \frac{\Omega_m^0}{2} - \frac{f^2}{6}. \qquad (26)$$

[5)] This interval for the age of the Universe, $13.5 \times 10^9 \le t_0 \le 13.9 \times 10^9$ yr, is chosen here despite the fact that its determination is model-dependent to some extent [see N.P. Tkachenko, IHEP preprint (2003)].

[6)] According to Particle Data Group [25], the allowed interval for h is $0.64 \le h \le 0.78$.

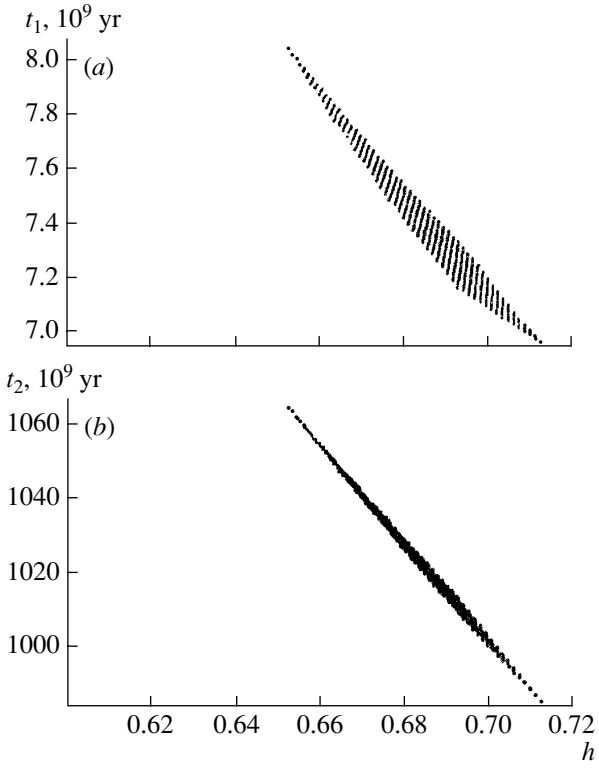

Fig. 2. Time of the (a) beginning (t_1) and (b) cessation (t_2) of the accelerated expansion of the Universe versus h at $\nu = 0.05$ for $\Omega_{\text{tot}} = 1.04$ and $13.5 \times 10^9 < t_0 < 13.9 \times 10^9$ yr and at $\nu = 0.05$ for $0.126 < \omega_m < 0.143$.

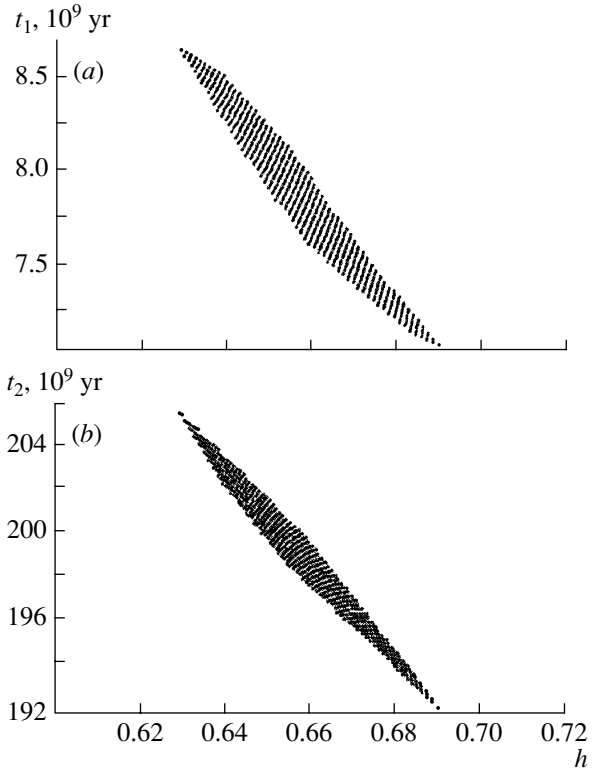

Fig. 3. As in Fig. 2 but for $\nu = 0.20$.

Eliminating the quantity $f^2/6$ from this relation and making use of (18), we arrive at

$$\frac{3}{2}\nu\Omega_q^0 = 1 - q_0 - \frac{3}{2}\Omega_m^0. \qquad (27)$$

The condition

$$q_0 < 1 - \frac{3}{2}\Omega_m^0,$$

which is necessary for the inequality $\nu > 0$ in formula (27) to be valid, is consistent with currently available data. Using Eq. (27), taking the value of $q_0 = 0.32 \pm 0.16$ for the acceleration, and setting $\Omega_m^0 = 0.27$ and $\Omega_q^0 = \Omega_\Lambda^0 = 0.73$ [31], we obtain $\bar{\nu} = 0.25$; within one standard deviation, we have $0.05 < \nu < 0.43$.

6. INSTANTS OF THE BEGINNING AND CESSATION OF THE ACCELERATED EXPANSION AND PERIOD OF OSCILLATIONS

Using the estimate in (21) for the graviton mass and the measured values of $\omega_m = \Omega_m^0 h^2 = 0.135^{+0.08}_{-0.09}$ [31], we can plot the present-day age of the Universe, as well as the instants of the beginning (t_1) and cessation (t_2) of the accelerated expansion, versus h for various possible values of ν (see Figs. 2, 3).

These plots demonstrate that the instant t_1 at which the accelerated expansion begins is not sensitive to variations in the graviton mass and to variations in the parameter ν over the range $(7-8) \times 10^9$ yr, the minimum value of $t_1 \approx 7 \times 10^9$ yr being associated with the maximum h value consistent with the interval chosen for the age of the Universe. The beginning of the acceleration of the expansion of the Universe at $t_1 \approx 7 \times 10^9$ yr explains the observational paradox that the Hubble expansion law is valid even for relatively small distances of about a few tens of Mpc (see, for example, [32]). With increasing ν, the range of h values corresponding to the interval adopted for the age of the Universe is shifted toward lower values of h. For example, we have $0.65 \le h \le 0.71$ at $\nu = 0.05$ and $0.64 \le h \le 0.69$ at $\nu = 0.20$. The instant corresponding to the cessation of the accelerated expansion and, hence, to the beginning of the deceleration, which leads to the termination of the expansion, depends greatly on the parameter ν (see Table 2).

As was indicated above, an indefinite expansion of the Universe is inconsistent with RTG in Minkowski space. For this reason, the only way to explain the observed accelerated expansion of the Universe within RTG is to assume the existence of quintessence or

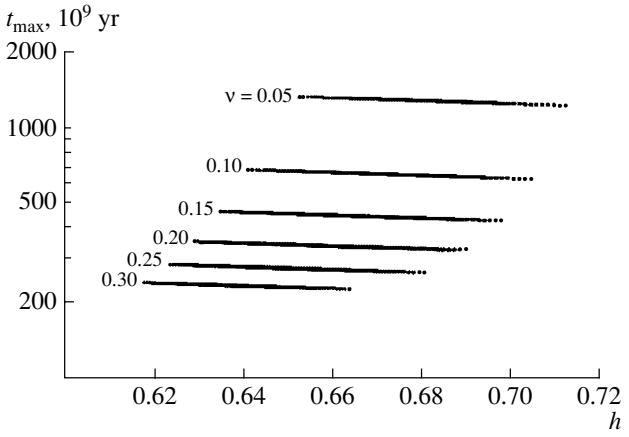

Fig. 4. Time of the maximum expansion of the Universe as a function of h at various values of ν for $\Omega_{tot} = 1.04$, $13.5 \times 10^9 < t_0 < 13.9 \times 10^9$ yr, and $0.126 < \omega_m < 0.143$.

some analogous substance whose density decreases with increasing scale factor, but not faster than in proportion to const/a^2. The termination of the expansion of the Universe follows from the finiteness of the graviton mass in RTG. At this instant, the matter density attains the minimum value in (14).

The scale factor corresponding to the termination of the expansion, x_{max}, is determined by a root of Eq. (25). At small values of ν, it is given by

$$x_{max} \simeq \left(\frac{\Omega_q^0}{f^2/6}\right)^{1/3\nu}$$

to a high degree of precision. In the approximation used here, the relation between the scale factor x_{max} and the scale factor x_2 corresponding to the cessation of the accelerated expansion has the form

$$x_2 = \left(1 - \frac{3}{2}\nu\right)^{1/3\nu} x_{max} \approx \frac{x_{max}}{\sqrt{e}}.$$

Table 2. Instants of beginning (t_1) and cessation (t_2) of the accelerated expansion of the Universe and instant t_{max} of the maximum expansion corresponding to the half-period of oscillations (in billions of years)

ν	t_1	t_2	t_{max}
0.05	7.0–8.2	980–1080	1220–1360
0.10	7.0–8.2	440–485	620–685
0.15	7.1–8.3	275–295	430–460
0.20	7.1–8.3	190–205	325–347
0.25	7.2–8.5	142–149	263–280
0.30	7.5–8.7	109–113	227–235

At the graviton mass set to the value in (21), the time of the maximum expansion (it corresponds to the half-period of oscillations) of the Universe is about 1300×10^9 yr at $\nu = 0.05$, about 650×10^9 yr at $\nu = 0.10$, and 270×10^9 yr at $\nu = 0.25$ (see Fig. 4 and Table 2).

It is of interest that the minimum density value ρ_{min} attained at the instant under consideration is independent of the maximum-expansion time t_{max} and proves to be not overly small. From (14), (18), and (19), we do indeed obtain

$$\frac{\rho_{min}}{\rho_c^0} \approx \frac{f^2}{6} = \Omega_{tot}^0 - 1.$$

At the chosen value in (21), we arrive at $\rho_{min} \simeq 0.04\rho_c^0$.

The idea of an oscillating universe was repeatedly proposed earlier, mainly on the basis of philosophical considerations (see, for example, [33, 34]). This could in principle be expected in the closed Friedmann model for $\Omega_{tot} > 1$. However, the existence of a cosmological singularity and an increase in the entropy from one cycle to another [35] are factors that prevent the realization of the oscillatory regime of evolution in the Friedmann model. These difficulties are removed in RTG for an infinite universe. Moreover, the homogeneity currently observed in the Universe at large scales can be explained by the oscillating character of evolution featuring an infinite number of preceding cycles.

Appealing features of a theory where the evolution of the Universe has an oscillatory character were highlighted by Steinhardt and Turok [36]. In their study, the oscillations of the Universe are due to the introduction of a scalar field φ interacting with matter and to extra dimensions. Those authors argued that the era of accelerated expansion plays a crucial role for entropy conservation throughout each cycle of the evolution. Within RTG, the oscillations of the Universe are governed exclusively by the gravitational field treated as a physical field in Minkowski space and generated by the total energy–momentum tensor of matter [see Eqs. (5) and (6)].

ACKNOWLEDGMENTS

We are grateful to V.V. Ezhela, V.V. Kiselev, V.A. Petrov, P.K. Silaev, N.E. Tyurin, and Yu.V. Chugreev for stimulating discussions.

REFERENCES

1. A. G. Riess *et al.*, Astron. J. **116**, 1009 (1998).
2. S. Perlmutter *et al.*, Astrophys. J. **517**, 565 (1999).
3. P. M. Garnvich *et al.*, Astrophys. J. **509**, 74 (1998).
4. A. H. Guth, Phys. Rev. D **23**, 347 (1981).

5. S. Kato, Mon. Not. R. Astron. Soc. **195**, 467 (1981).
6. A. D. Linde, Phys. Lett. B **108B**, 389 (1982).
7. A. Albrecht and P. J. Steinhardt, Phys. Rev. Lett. **48**, 1220 (1982).
8. A. A. Starobinskii, Phys. Lett. B **117B**, 175 (1982).
9. R. R. Caldwell, R. Dave, and P. J. Steinhardt, Phys. Rev. Lett. **80**, 1582 (1998).
10. R. R. Caldwell and P. J. Steinhardt, Phys. Rev. D **57**, 6057 (1998).
11. J. P. Ostriker and P. J. Steinhardt, Sci. Am. **284**, 46 (2001).
12. A. A. Logunov and M. A. Mestvirishvili, *Relativistic Theory of Gravitation* (Nauka, Moscow, 1989) [in Russian].
13. A. A. Logunov, *Theory of Gravitation* (Nauka, Moscow, 2001) [in Russian].
14. V. L. Kalashnikov, gr-qc/0109060; gr-qc/0202084.
15. V. I. Ogievetsky and I. V. Polubarinov, Ann. Phys. (N.Y.) **35**, 167 (1965), and references therein.
16. R. P. Feynman *et al.*, *Feynman Lectures on Gravitation* (Addison-Wesley, Reading, 1995).
17. A. A. Logunov and M. A. Mestvirishvili, Teor. Mat. Fiz. **61**, 327 (1984).
18. R. A. Sunyaev and Ya. B. Zeldovitch, Astrophys. Space Sci. **7**, 1 (1970).
19. J. Silk, Nature **215**, 1155 (1967); **218**, 453 (1968); Astrophys. J. **151**, 459 (1968).
20. P. J. Peebls and J. T. Yu, Astrophys. J. **162**, 815 (1970).
21. M. L. Wilson and J. Silk, Astrophys. J. **243**, 14 (1981).
22. J. R. Bond and G. Efstathiou, Astrophys. J. **285**, 45 (1984); Mon. Not. R. Astron. Soc. **226**, L655 (1987).
23. G. Jungman *et al.*, Phys. Rev. Lett. **76**, 1007 (1996); Phys. Rev. D **54**, 1332 (1996).
24. J. R. Bond, G. E. Efstathiou, and M. Tegmark, Mon. Not. R. Astron. Soc. **291**, L33 (1997).
25. Particle Data Group, Phys. Rev. D **66**, 1 (2002).
26. A. H. Jaffe, P. A. R. Ade, A. Babbi, *et al.*, Phys. Rev. Lett. **86**, 3475 (2001).
27. P. de Bernardis *et al.*, Nature (London) **404**, 995 (2002).
28. S. Hanany, P. Ade, A. Babbi, *et al.*, Astrophys. J. **545**, L5 (2000).
29. C. Bennett, A. Banday, K. M. Gorski, *et al.*, Astrophys. J. **464**, L1 (1996).
30. A. E. Lange *et al.*, Phys. Rev. D **63**, 042001 (2001); J. R. Bond and A. H. Jaffe, Philos. Trans. R. Soc. London, Ser. A **357**, 57 (1999).
31. C. Bennet *et al.*, astro-ph/0302207 v.2.
32. A. D. Chernin, Usp. Fiz. Nauk **171**, 1153 (2001).
33. A. D. Sakharov, *Scientific Papers* (Tsentrkom., Moscow, 1985), p. 269; Zh. Éksp. Teor. Fiz. **83**, 1233 (1982) [Sov. Phys. JETP **56**, 705 (1982)].
34. É. G. Aman and M. A. Markov, Teor. Mat. Fiz. **58**, 163 (1984); M. A. Markov, Ann. Phys. (N.Y.) **155**, 333 (1984).
35. R. C. Tolman, *Relativity, Thermodynamics, and Cosmology* (Clarendon, Oxford, 1934).
36. P. J. Steinhardt and N. Turok, hep-th/0111030, Vol. 2.

Translated by R. Rogalyov

Physics of Atomic Nuclei, Vol. 67, No. 8, 2004, pp. 1605–1609. Translated from Yadernaya Fizika, Vol. 67, No. 8, 2004, pp. 1627–1631.

FUTURE PUBLICATIONS

Collinearity in the Channels Leading to the Production of Three and Four α Particles in ^{16}Op Collisions at 3.25 GeV/c per Nucleon

E. Kh. Bazarov, V. V. Glagolev, K. G. Gulamov, V. V. Lugovoi, S. L. Lutpullaev, K. Olimov, A. A. Yuldashev, B. S. Yuldashev, and Kh. Sh. Khamidov

Within the phenomenological model of an isotropic phase space, it is shown that an experimentally observed collinearity in the channels involving the production of three and four alpha particles in ^{16}Op collisions is associated with the production of unstable ^{8}Be and ^{9}B nuclei.

Elastic and Inelastic Scattering of 800-MeV Protons on ^{16}O and ^{20}Ne Nuclei

Yu. A. Berezhnoy, V. P. Mikhailyuk, and V. V. Pilipenko

Within the theory of multiple diffractive scattering and the dispersive alpha-cluster model, differential cross sections and polarization observables are calculated for the elastic and inelastic scattering of 800-MeV protons on ^{16}O and ^{20}Ne nuclei. The single-particle nucleon-density distributions obtained within the dispersive alpha-cluster model are used in the calculations. The differential cross sections and polarizations calculated for elastic and inelastic p^{16}O and p^{20}Ne scattering are consistent with available experimental data. The spin-rotation functions calculated for elastic p^{16}O and p^{20}Ne scattering within the model of independent nucleons differ quantitatively from those calculated within the dispersive alpha-cluster model.

Investigation of the Neutron Shell Structure of Even–Even $^{40-56}$Ca Isotopes within the Dispersive Optical Model

O. V. Bespalova, I. N. Boboshin, V. V. Varlamov, T. A. Ermakova, B. S. Ishkhanov, E. A. Romanovsky, T. I. Spasskaya, and T. P. Timokhina

Within the method of matching the experimental data obtained in the neutron-stripping and neutron-pickup reactions on ^{40,42,44,46,48}Ca isotopes, the single-particle energies and probabilities that neutron states are filled are obtained for even–even calcium isotopes. These data are analyzed within the dispersive optical model, and good agreement between the calculated and experimental values of the energies of states is obtained. The dispersive optical potential is extrapolated to the region of unstable ^{50,52,54,56}Ca nuclei. The calculated single-particle energies of bound states in these isotopes are compared with the results of the calculations within the multiparticle shell model, which predicts a new magic number of $N = 34$ for $Z = 20$ nuclei.

Modification of the Jet-Fragmentation Function in Ultrarelativistic Collisions of Nuclei and Its Determination in the Channel Involving the Production of a Leading π^0 Meson

I. N. Vardanyan, I. P. Lokhtin, L. I. Sarycheva, A. M. Snigirev, and K. Yu. Teplov

A modification of the jet-fragmentation function determined by parton-energy losses in dense quark–gluon matter is investigated in channels involving leading-particle production. It is shown that the effect of the softening of the jet-fragmentation function is determined by the angular distribution of gluons emitted in a medium and that it anticorrelates with the effect of the suppression of the total number of jets due to the energy losses of jet partons off the jet cone. The possibility of measuring the jet-fragmentation function with the aid of leading electromagnetic clusters in heavy-ion collisions at LHC energies is analyzed.

1063-7788/04/6708-1605$26.00

General Features of the Single-Spin Asymmetry of Inclusive π-Meson Production in Experiments with a Fixed Target

A. N. Vasiliev and V. V. Mochalov

The results of various experiments that measured the single-spin asymmetry in the inclusive production of π mesons are analyzed in the energy interval from 13 to 200 GeV. The experimental fact that the single-spin symmetry begins increasing at one universal value of the π-meson energy in the c.m. frame is established.

Investigation of the Structure of the Muon Disk at $E_0 \geq 5 \times 10^{16}$ eV According to Data from the Yakutsk Array for Recording Extensive Air Showers

A. V. Glushkov, L. G. Dedenko, and I. E. Sleptsov

The results are presented that were obtained at the Yakutsk array by investigating the time structure of the muon disk in extensive air showers of primary energy in the range $E_0 \geq 5 \times 10^{16}$ eV at distances of 250 to 1500 m from the axis. The measurements were performed with a large muon detector that has an area of 184 m^2 and a detection threshold of $E_\mu \approx 0.5 \sec\theta$ GeV and which began operating in November 1995. Two components having different muon-disk thicknesses were discovered, and this requires strong modifications in the concept of the development of extensive air showers. The problem of the existence of $E_0 \geq 10^{20}$ eV events is considered.

Quasars as a Source of Ultrahigh-Energy Cosmic Rays

A. V. Glushkov

The results are presented that were obtained by analyzing arrival directions for cosmic rays that the Yakutsk array for studying extensive air showers recorded between 1974 and 2002 in the energy range $E_0 \geq 5 \times 10^{17}$ eV for zenith angles in the region $\theta \leq 60°$. It is shown that quasars for which the redshift lies in the region $z \leq 2.5$ can be sources of these rays. Ordered structures are observed in the disposition of quasars and in the cosmic-ray arrival directions. These structures can be associated in one way or another with the large-scale structure of the Universe.

Determination of the Glueball Mass with Allowance for a Relativistic Character of Interaction

M. Dineikhan, S. A. Zhaugasheva, and T. A. Kozhamkulov

Nonperturbative additions to an interaction Hamiltonian that are associated with relativistic motion and a large coupling constant are determined on the basis of an investigation of the asymptotic behavior of the polarization loop for charged scalar particles in an external gauge field. The mass spectrum of a bound state is determined analytically. The mechanism of the emergence of the constituent mass of particles that form the bound state is explained. It is shown that the vector potential and the potential associated with a nonperturbative character of the interaction cancel each other and that the slope of the Regge trajectory is determined in terms of the string-tension tensor.

Upper Limit on the Experimental Estimate of the Diffractive-Dissociation Phenomenon in the Interaction of a Muon Neutrino with Photoemulsion Nuclei According to Data of the E-128 Experiment (Protvino)

O. K. Egorov and V. A. Ryabov

An experimental estimate of the diffractive-dissociation phenomenon in neutrino interaction with photoemulsion nuclei is given. The results were obtained on the basis of data from the SKIF experiment, which was performed in a neutrino beam from the U-70 accelerator (Protvino). The data sample subjected to this analysis included 670 charged-current events of neutrino interactions in the vertex detector used in that experiment. Events in which the Bjorken variable took values in the range $x = 0-0.1$ were selected from this data sample. Upon going over to the variable x', which takes into account the nucleon mass, an upper limit of 0.53 ± 0.07 was set on the contribution of diffractive-dissociation processes to the total charged-current cross section.

Description of Two-Proton Radioactivity on the Basis of Methods of the Quantum Theory of Ternary Nuclear Fission

S. G. Kadmensky

The two-proton decay of spherical nuclei is investigated on the basis of the formalism developed in constructing the quantum-mechanical theory of ternary fission. The proposed method for calculating the amplitudes of partial widths with respect to two-proton decay and the asymptotic behavior of the wave function for a decaying nucleus makes it possible to solve the problem of describing two-proton radioactivity without recourse to the traditionally used (in R-matrix approaches) cumbersome procedure of matching the internal and the external wave function for the decaying nucleus within the three-body formulation. In the diagonal approximation and on the basis of the properties of the potential describing the interaction of the products of two-proton decay, the structure of the wave function for the Cooper pair of two protons bound in the parent nucleus is analyzed, along with the behavior of the wave function describing the potential scattering of the products of binary decay, this being done with allowance for the coupling of decay channels.

Widths and Wave Functions of Decay Nuclear States with Allowance for Channel Coupling

S. G. Kadmensky

The formalism of the quantum theory of fission is used to take into account the coupling of open decay channels in constructing the amplitudes of partial-decay widths and the asymptotic behavior of the wave function for the decaying nucleus not only for fission but also for protonic, alpha, cluster, and other forms of binary decays of nuclei.

Nucleon–Nucleus Optical Potential at Finite Temperatures within a Semimicroscopic Approach Involving Skyrme Forces

V. I. Kuprikov, V. V. Pilipenko, and A. P. Soznik

Within the nuclear-matter approximation, the local-density approximation, and perturbation theory, the approach to constructing a microscopic optical nucleon–nucleus potential at finite nuclear temperatures is developed on the basis of effective density-dependent nucleon–nucleon forces. The real and the imaginary part of the neutron–nucleus optical potential and the mean free paths of neutrons in nuclear matter are calculated at various neutron energies and various nuclear temperatures. The effect of the inclusion of the rearrangement potential on the quantities under consideration is studied, and its importance is demonstrated.

General Formulas for Invariant Functions Describing the Generalized Reaction $\gamma N \to \gamma N$ within the Effective-Lagrangian Method

A. Yu. Loginov and V. N. Stibunov

The crossed channels of the generalized reaction $\gamma N \to \gamma N$ are considered. The coefficients in the transformation from independent helicity amplitudes to invariant functions are calculated. The explicit expressions for the invariant functions are derived with allowance for the contribution from the Born diagrams in the s, u, and t channels and the diagrams for six resonances in the s and u channels. It is shown that the calculated invariant functions satisfy the crossing-symmetry requirements.

Investigation Cosmic Rays at the International Space Station with the Aid of the AMS Detector

V. V. Plyaskin

A brief account of the program of physics investigations that is being implemented by a large international collaboration at the international space station with the aid of the Alpha Magnetic Spectrometer (AMS) is given. The features of the facility under construction are presented, along with some results obtained in a test flight of the spectrometer prototype on board a space shuttle.

Application of Multidimentional Statistical Methods to the Interpretation of Data Measured with the Aid of Multichannel Equipment: KLEM Spectrometer

D. M. Podorozhnyi, E. B. Postnikov, L. G. Sveshnikova, and A. N. Turundaevsky

The study is devoted to a multidimensional statistical procedure for solving problems of reconstructing physical parameters on the basis of data from measurements with multichannel equipment. Within a multidimensional procedure, an algorithm is constructed for estimating the primary energy and the exponent of the power-law spectrum of primary cosmic rays. They are investigated by using the KLEM spectrometer (NUCLEON project) as a specific example of measuring equipment. The results of computer experiments simulating the operation of the multidimensional procedure for this equipment, where the proposed approach is compared with the one-parameter approach presently used in data processing, are given.

Hadronic Production of Prompt J/ψ and ψ' Mesons in the Gluon and c-Quark Fragmentation at High Energies

V. A. Saleev and D. V. Vasin

The transverse-momentum spectra of prompt J/ψ and ψ' mesons from proton–proton interactions are calculated at the Tevatron energy of $\sqrt{s} = 1.8$ TeV. The calculations are based on nonrelativistic QCD, the fragmentation model, the k_T-factorization approach, and the standard parton model. It is shown that, both in the parton model and in the k_T-factorization approach, the contribution from gluon fragmentation exceeds the contribution from c-quark fragmentation. The experimental data of the CDF Collaboration are in accord with the assumption that gluon fragmentation into the octet state $Q\bar{Q}[^3S_1, 8]$ plays a dominant role, the value of the nonperturbative matrix element being the same in the parton model and in the k_T-factorization approach.

Energy Dependence of the Total Cross Section for the Interaction of ^{4}He Ions with Silicon

V. Yu. Ugryumov, I. V. Kuznetsov, E. Byalkovskii, A. Kugler, K. A. Kuterbekov, I. N. Kukhtina, V. F. Kushniruk, V. G. Lyapin, V. A. Maslov, Yu. E. Penionzhkevich, Yu. G. Sobolev, V. Trzaska, G. P. Tyurin, S. V. Khlebnikov, and S. Yamaletdinov

Data from direct measurements of the total cross section for the interaction of ^{4}He ions with silicon nuclei at energies of E < 25 MeV per nucleon are presented. The energy dependence of the parameters of the semimicroscopic potential is determined on the basis of the measured values of the total reaction cross section. This work was performed at the Flerov Laboratory of Nuclear Reactions (Joint Institute for Nuclear Research, Dubna) and the Department of Physics at the University of Jyväskylä (Finland).

Relativistic Inverse Problem for a Superposition of Nonlocal Separable and Local Quasipotentials

Yu. D. Chernichenko

The relativistic inverse problem is solved for the case where the total quasipotential describing the interaction of two relativistic spinless particles of unequal masses is a superposition of a nonlocal separable and a local quasipotential. This consideration is performed within the relativistic quasipotential approach to quantum-field theory. It is assumed that the local component of the total interaction is known and that it admits the existence of bound states. It is shown that the nonlocal separable component of the total interaction can be reconstructed if its local component, the phase-shift increment, and the energies of bound states are known.

Neutrino Geophysics at Baksan I: Possible Detection of Georeactor Antineutrinos

G. Domogatski, V. Kopeikin, L. Mikaelyan, and V. Sinev

In the 1990s, J.M. Herndon proposed a natural nuclear fission georeactor at the center of the Earth with a power output of 3 to 10 TW as an energy source to sustain the Earth's magnetic field. In 2002, R.S. Raghavan indicated that, under certain conditions, antineutrinos generated in the georeactor can be detected by using massive scintillation detectors. We consider the underground Baksan Neutrino Observatory (4800 mwe) as a possible site for developments in geoneutrino physics. There, the intrinsic background level of less than

one event/year in a liquid scintillation ~1000-target-ton detector can be achieved, and the main source of the background is the antineutrino flux from power reactors. We find that this flux is about 10 times lower than at the KamLAND detector site and two times lower than at the Gran Sasso laboratory; therefore, the georeactor hypothesis can be conclusively tested at Baksan. We also discuss possible searches for the composition of the georeactor burning nuclear fuel by analyzing the antineutrino energy spectrum.

QCD and Hybrid NBD on Oscillating Moments of Multiplicity Distributions in Lepton- and Hadron-Initiated Reactions

I. M. Dremin

QCD predictions for moments of multiplicity distributions are compared with experimental data on e^+e^- collisions and their two-NBD fits. Moments of the multiplicity distribution in a two-NBD model for 1.8-TeV pp collisions are considered. Three-NBD model predictions and fits for pp at LHC energies are also discussed. Analytic expressions for moments of hybrid NBD are derived and used to get insight into jet parameters and the multicomponent structure of the processes. An interpretation of observed correlations is proposed.

Study of the ^{4}He + ^{209}Bi Fusion Reaction

A. Hassan, S. M. Lukyanov, Yu. E. Penionzhkevich, L. R. Gasques, L. C. Shamon, and A. Szanto de Toledo

The (^{4}He+^{209}Bi) fusion reaction was investigated at energies near and below the Coulomb barrier. The ^{4}He beam used was produced by the U200M accelerator at FLNR, JINR. The excitation functions for the $2n$, $3n$, and $4n$ evaporation channels from the ^{213}At compound nucleus were measured. To identify the $2n$ and $3n$ evaporation channels, the α-particle energies were measured for ^{211}At and ^{210}At, as well as the half-lives of 7.34 ± 0.04 h and 8.44 ± 0.079 h, respectively. The results are compared with theoretical fusion models and with existing data for the ^{6}He + ^{209}Bi fusion reaction.

On CP-Odd Effects in $K_L \to 2\pi$ and $K^\pm \to \pi^\pm\pi^\pm\pi^\mp$ Decays Generated by Direct CP Violation

E. P. Shabalin

The amplitudes of the decays $K^\pm \to 3\pi$ and $K \to 2\pi$ are expressed in terms of various combinations of the same set of CP-conserving and CP-odd parameters. Extracting the magnitudes of these parameters from the data on the decays $K \to 2\pi$, we estimate the expected CP-odd difference between the values of the slope parameters g^+ and g^- of the energy distributions of "odd" pions in the decays $K^+ \to \pi^+\pi^+\pi^-$ and $K^- \to \pi^-\pi^-\pi^+$.

Physics of Atomic Nuclei, Vol. 67, No. 8, 2004, p. 1610. Translated from Yadernaya Fizika, Vol. 67, No. 8, 2004, p. 1632.

ERRATA

Erratum: "Green's Function Method in the Problem of Complex Configurations in Fermi Systems with Pairing"

[*Physics of Atomic Nuclei* 67, 183–194 (2004)]

S. P. Kamerdzhiev and E. V. Litvinova

In our calculations, numerical errors were made, which led to overestimating some matrix elements of quasiparticle–phonon interaction in the proton subsystem (within the approximations used). Here, we present, in a tabular form, the integrated features of the $E1$ resonance that were rescaled to Sn isotopes by using the parameter value of $f_{ex} = -1.4$, which was taken from the calculations for ^{40}Ca, ^{48}Ca, and ^{56}Ni [1]. As might have been expected, there are sizable distinctions (not greater than 50%, as a rule) only for a pygmy dipole resonance. As to Figs. 1–3, the behavior of the curves there did not undergo any significant changes, with the exception of what is concerned with a sharp peak at $E \simeq 19$ MeV in the region of ^{104}Sn [in a full calculation, the height of this peak decreased to $\sigma(E = 19\ \text{MeV}) = 120$ mb].

Integrated features of the isovector $E1$ resonance in Sn isotopes

Isotope	^{104}Sn		^{120}Sn		^{132}Sn	
Method	1	2	1	2	1	2
EWSR [%]	108.4	108.3	103.6	103.3	96.1	95.8
$\bar{E}$ [MeV]	15.0	15.2	14.4	14.6	13.2	13.4
Γ [MeV]	4.4	1.6	5.0	2.2	4.0	2.0
σ_{int} (0–12 MeV) [%]	20	7	17	11	24	15
σ_{int} (0–$\bar{E}$/2) [%]	1.3	0.17	4.0	0.37	1.4	0.24

The corrected results introduce virtually no changes in the conclusions drawn from our study. In particular, the most interesting conclusion that the inclusion of complex configurations is necessary for describing a pygmy resonance remains in force.

In expression (33), the function $G_1^+(\epsilon)$ was erroneously omitted in the integrand, so that the correct integral must have the form

$$\int \frac{d\epsilon}{2\pi i} G_1^+(\epsilon) M_1^+(\epsilon) G_1^+(\epsilon) M_1^+(\epsilon) G_1^+(\epsilon) G_2^-(\epsilon - \omega),$$

where $G_1^+(\epsilon)$ and $M_1^+(\epsilon)$ are the pole parts of the relevant Green's function and mass operator, respectively.

REFERENCES

1. S. Kamerdzhiev, J. Speth, and G. Tertychny, Nucl. Phys. A **624**, 328 (1997).

Translated by A. Isaakyan

1063-7788/04/6708-1610$26.00